A multiscale modeling framework for the transient analysis of PEM Fuel Cells - From the fundamentals to the engineering practice

Alejandro A. Franco

This document must be cited in the following way:

“ Alejandro A. Franco,

A multiscale modeling framework for the transient analysis of PEM Fuel Cells – From the fundamentals to the engineering practice.

Mémoire d’HDR / HDR Manuscript
Université Claude Bernard Lyon 1, 23rd September 2010 ”

Comitee members:

Philippe Sautet (Professeur, Ecole Normale Supérieure, Lyon, rapporteur),
Bernhard Maschke (Prof. des Universités à l'UCB Lyon 1, rapporteur),
Michael Eikerling (Professeur, Simon Fraser University, Vancouver, Canada, rapporteur)
Patrick Gelin (Directeur de Recherche, IRCELYON, Lyon, examinateur)
Atsushi Ohma (Dr., Nissan Motor Co., Yokohama, Japon, examinateur)
Christian Jallut (Prof. des Universités à l’UCB Lyon 1, président du jury)
Jean Bletry (Prof. des Universités à l’UJF et chercheur senior au CEA, Grenoble, invité)

The professional web page of Alejandro A. Franco is:

http://www.a-franco.fr

Contact e-mail: **alesitofranco@yahoo.fr**

UNIVERSITE CLAUDE BERNARD LYON 1

Numéro d'ordre HDR : 31- 2010

Mémoire
d'Habilitation à Diriger des Recherches (HDR)

Spécialité : Chimie, Procédés, Environment

A multiscale modeling framework for the transient analysis of PEM Fuel Cells
From the fundamentals to the engineering practice

par

Alejandro A. Franco

(PhD., scientist at CEA-LITEN, Grenoble, France)

Soutenue publiquement le 23 Septembre 2010 devant le Jury composé de :

Mr. Philippe Sautet : Professeur, Ecole Normale Supérieure, Lyon……. rapporteur
Mr. Bernhard Maschke : Profeseur des Universités à l'UCB Lyon 1…….rapporteur
Mr. Michael Eikerling : Professeur, Simon Fraser University, Vancouver…… rapporteur
Mr. Patrick Gelin : Directeur de Recherche, IRCELYON, Lyon……. examinateur
Mr. Atsushi Ohma: Dr., Nissan Motor Co., Yokohama…….. examinateur
Mr. Christian Jallut : Prof. des Universités à l'UCB Lyon 1…….président du jury
Mr. Jean Bletry : chercheur senior au CEA Grenoble……..invité

2010

A multi-scale modeling framework for the transient analysis of PEM Fuel Cells

From the fundamentals to the engineering practice

Habilitation pour Diriger des Recherches Manuscript

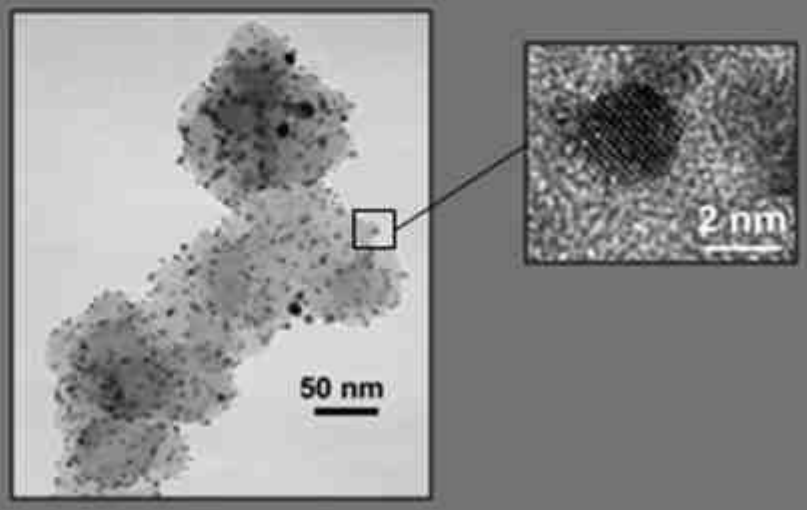

Dr. Alejandro A. Franco

Atomic and Alternative Energies Commission of France (CEA)/
LITEN/DEHT/Laboratory of Components for Fuel Cells and
Electrolysers, and of Modeling (LCPEM)

To my princess in France, to my parents and my family in Argentina…

and to my friends worldwide.

“Lo importante es ser uno mismo”

Mafalda (Quino, argentinean cartoonist, 1932-…).

ACKNOWLEDGEMENTS

It seems that when I was 5 years old I said for the first time to my parents that I wanted to become a "phyisicist" to understand "why and how the World works"... Doing research was a dream for me, and the dream became a reality after many years of effort and dedication...But since I was a child, I also developed a strong interest on a particular field: the electrochemistry. Maybe because electrochemistry is behind the "operation principles" of a large diversity of phenomena in the World...let's think for example on the possible mechanisms behind the appearance of Life in the Earth, the mechanisms making the humain brain working, the power generators one imagine for the future human generations...

Nowadays, it is well accepted that electrochemical devices for energy conversion and storage, such as fuel cells and batteries have a high potentiality to become key technologies for a large diversity of portable, automotive and stationary applications within a future sustainable and ecological energetic network. However, development of durable and inexpensive materials and components is the most important technological challenge that nowadays fuel cell and battery developers are facing. Deep insight based on physical modeling of the materials behavior and aging will advise us how these components with optimal specifications could be made and how they can be integrated into operating devices. I realized that the use of my dreamed "physics" and the associated development of "physical" multiscale models can offer powerful capabilities to simulate the competitions and synergies between mechanisms at multiple spatiotemporal scales (from the atomistic to the cell level). Such a "virtual device" concept can considerably help in proposing innovative procedures (operation strategies and electrodes formulation) to enhance the devices performance and durability. This motivated myself to invent in 2002 a multiscale modeling software for the simulation of electrochemical power generators: the MEMEPhys code, perhaps one of the first codes of this type reported in litterature. Since then, I was literally "absorbed" by the beauty of the field of physical modeling.

After 9 years of developing MEMEPhys learned me that multiscale modeling of electrochemistry is a quite rare discipline with numerous scientific and technical challenges to be still overcome. These challenges can be only tackled on the basis of multidisciplinary, federative and close team work with rigourosity and ethics. Thus, technical success is connected with developing human relationship and scientific collaboration. This is why I want to acknowledge all the people who contributed to my achievement as a scientist.

First of all, I would like to express my sincere gratitude to all the members of the jury for evaluating my H.D.R.: Dr. Atsushi Ohma (Nissan Motor Co., Japan), Prof. Philippe Sautet (Ecole Normale Supérieure de Lyon, France), Prof. Michael Eikerling (Simon Fraser University, Canada), Prof. Bernhard Maschke (Université Claude Bernard Lyon 1, France), Prof. Christian Jallut (Université Claude Bernard Lyon 1, France), Dr. Patrick Gelin (IRCELYON, France), Prof. Jean Bletry (CEA Grenoble, France) *(gracias Jean por esta aventura)*. It was for me a real honour having the appreciation and discussions with all these excellent scientists and great persons.

I would like to sincerely acknowledge the big devotion of all the students and postdocs I advised: Moussa Tembely, Mathias Gerard, Laurent Brochard, Magalie Guinard, Julien Letemplier, Randa Bouchmila, Sylvain Passot, Rodrigo Ferreira de Morais, Daiane Damasceno Borges, Luiz Fernando Lopes Oliveira, Romain Coulon, Hanen Amel, Ali Kachmar, Margaret Gabriel...My deepest gratitude goes to all of them for their excellent job, dedication and perseverance in this exciting field: it was a real pleasure working with all of you. Also, many thanks go to the "new arrivals", Benjamin Deguilhem and Slimane Laref, for having accepted joining my group for postdoctoral positions. Furthermore, many thanks are going to other students I could interact during these years: Mohamed El Hannach, Samir Rachidi, Jenny Jonquille, Guillaume Krosnicki, Galdric Sibiude, Sreejith Pulloor, Anne Gaelle Mercier, Aurore Florent... All these young guys maked alive "MEMELand" through animated scientific discussions but also through highly appreciated contributions including the maintenance of the memorable "MEMELand Tower" built with soda cans ☺...

Science also gave me the possibility to make many collaborators and friends worldwide, including the members of the jury mentioned above. All my gratitude goes to Prof. Alfredo Juan (Universidad Nacional del Sur, Bahia Blanca, Argentina), Dr. David Loffreda (ENS de Lyon, France), Dr. Wolfgang Bessler and Prof. Andreas Friedrich (DLR, Stuttgart, Germany), Dr. Kourosh Malek, Dr. Zheng Shi, Dr. Khalid Fatih and Dr. Xie Zhong (National Research Council of Canada), Tetsuya Mashio (Nissan Motor Co., Japan), Dr. Pascale Pham (CEA LETI, Grenoble, France), Dr. Marie Liesse Doublet (ICG, Montpellier), Dr. Henri Perez (CEA DSM, Saclay, France), Dr. Nicolas Fouquet (PSA, France), Dr. Horacio Corti (CNEA, Argentina), Dr. Thierry Deustch, Dr. Pascale Maldivi, Dr. Serge Gambarelli, Dr. Robert Morel, Dr. Ariel Bregnac, Dr. Yves Samson (CEA INAC, Grenoble, France), Dr. Pascal Fugier (CEA LITEN, Grenoble, France), Dr. André Rakko (Helion Fuel Cells), Prof. Heinz Pitsch (Stanford University, Palo Alto, USA), Prof. Jordi Riera, Dr. Maria Serra and Attila Husar (UPC, Barcelona, Spain), Valéry Parry (SIMAP, Grenoble, France). Thanks a lot to all of you for your friendship. Many thanks also to Prof. Peter Breedveld (Twente University, The Netherlands) for his interest on my work, Dr. Maarten Biesheuvel (Wetsus, The Netherlands) and Prof. Martin Bazant (MIT, USA) for our joint paper on diffuse layers, Dr. Debbie Myers (ANL, USA), Prof. Ernesto Gonzalez (IQSC, Brazil) and Dr. Dane Morgan (Wisconsin Univerisity, USA) for some punctual interactions and useful discussions. Many thanks also to all the people I had the opportunity to meet in the conferences and meetings I participated: scientific discussions with all of them stimulated me a lot.

I address all my deepest gratitude to the Haut Commissaire à l'Energie Atomique, Bernard Bigot, for receiving me in July 2008 for technical discussions. This was a real honour for me. My gratitude is extended to Dr. Paul Lucchesse, Dr. Gerard Gerard Sanchez and Dr. Jean Luc Leray who were present that unforgettable day. I would like to sincerely thank my hosting laboratory and all the colleagues at CEA Grenoble who supported directly or indirectly my research activities. Special thanks go to Nicolas Guillet, Christine Nayoze, Remi Vincent, Eric Mayousse and Sylvie Escribano for stimulating discussions. My gratitude goes also to Didier Marsacq for welcoming me at CEA in 2002 and for giving me the opportunity to experimentally test several "transversal" ideas, like the one "mixing" electromagnetics and electrochemistry. Many thanks also to Pierre Baurens and Pascal Schott for their support and for providing me the intellectual freedom to carry out my PhD thesis between 2003 and 2005, and to Florence Lefevre Joud for recruiting me at CEA in 2005. Special thanks go to Nicolas Bardi for all his support on developing my group when he was heading my lab and for exciting discussions. And all my gratitude goes also to my funders, including CEA internal programs, ANR and EU, as well as the bilateral collaborations with industry as the one I had the honour to establish with Nissan.

My warm acknowledgemnts go to all the professors I had all along my studies in Argentina as they surely contributed on my dedication for science. And my heatiest thanks goes to my princess Maud (te quiero !) and all her family, my parents and all my friends supporting me: Fede Nores Pondal (que grande sos !), Beto et Laura Ramborger (gracias chicos por todo el aguante cada vez que nos vemos), Diego Palacios (aguante la astrofisica !), Judith and Tanuj (merci pour tout !), Tatiana (gracias por todo el apoyo de siempre, ciudadana del miundo !), Andrés, Delphine y los chicos (aguante Belgrano loco !), Carlos Jaime (azucar !), Horacio Emilio Perez Sanchez (ya vamos a ir a Murcia !), Franck, Jung y todos, todos... Para toda mi familia, Mama Beatriz (sos una grande !), Papa Antonio (que grande che haciendo las 300 empanadas en Francia...), Tia Chichi (te quedastes con las ganas de conocer la Torre Eiffel, pero aguante el Gondolieri !), Abu Azu (que vaya marchando el tiramisu y el té para dentro de poquito nomas !), Tio Ruben (sos un campeon de la vida !), primos Silvi, Nati, Rolo, Cristian y tios Perico y Mirtha: gracias a todos por todo el apoyo, el aguante y la buena onda de siempre. Mucha garra !!!

Finally, thanks a lot also to all the people who was present in my defence day: it was a real honour for me.

Now...good reading... !

Alejandro A. Franco

Grenoble, September 23th, 2010

PREFACE

In recent years, Polymer Electrolyte Membrane Fuel Cells (PEMFC) have attracted much attention due to their potential as a clean power source for many applications, including automotive, portable and stationary devices. This resulted in a tremendous technological progress, such as the development of new membranes and electro-catalysts or the improvement of electrode structures. However, in order to compete within the most attractive markets, the PEMFC technologies did not reach all the required characteristics yet, in particular in terms of cost and durability. Because of the strong coupling between different physicochemical phenomena, the interpretation of experimental observations is difficult, and analysis through modeling becomes crucial to elucidate the degradation and failure mechanisms, and to help improving both PEMFC electrochemical performance and durability. The development of a theoretical tool is essential for industrials and the scientific community to evaluate the PEMFC degradation and to predict its performance and durability in function of the materials properties and in a diversity of operating conditions. This manuscript summarizes my scientific research efforts in this exciting topic during the last 9 years in France, including my invention of the MEMEPhys multiscale simulation package, developed on the basis of my childhood passion for the *New Technologies for Energy* in Argentina. My perspectives of adapting this approach to other electrochemical systems such as water electrolyzers and batteries are also discussed.

CONTENTS

ACRONYMS

ADT: Accelerated Degradation Test

AFM: Atomic Force Microscopy

BoL: Beginning of Life

BP: Bipolar Plate

CB: Carbon Black

CCM: Catalyst Coated Membrane

CL: Catalyst Layer

CNT: Carbon Nano-Tubes

COR: Carbon Oxidation Reaction

CV: Cyclic Voltammetry

DFT: Density Functional Theory

DLI-MOCVD: Direct Liquid Injection-Metallo Organic Chemical Vapour Deposition

DRIFT: Diffuse Reflectance Infrared Fourier Transform

ECSA: Electrochemical Surface Area

EDS: Energy Dispersive X-ray Spectroscopy

EIS: Electrochemical Impedance Spectroscopy

EoL: End of Life

EPR: Electron Paramagnetic Resonance

FTIR: Fourier Transformed InfraRed spectroscopy

GDL: Gas Diffusion Layer

HOR: Hydrogen Oxidation Reaction

HPC: High Performance Computing

HR-TEM: High Resolution-Transmission Electron Microscopy

IEC: Ion Exchange Capacity

MC: Monte Carlo

MD: Molecular Dynamics

MEA: Membrane/Electrodes Assembly

MEMEPhys®: *Modele Electrochimique Multiechelle Physique* (Physical Multi-scale Model of Electrochemistry)

MF: Mean Field

ML: Mono-Layer

MPL: Micro-porous layer

NEB: Nudged Elastic Band

NHE: Normal Hydrogen Electrode

NMR: Nuclear Magnetic Resonance

OCC: Open Circuit Conditions

OCV: Open Circuit Voltage

ORR: Oxygen Reduction Reaction

PEMFC: Polymer Electrolyte Membrane Fuel Cell

PEM: Polymer Electrolyte Membrane

PFSA: Perfluoro Sulfonic Acid

PNP: Poisson-Nernst-Planck

PTFE: Poly-Tetra-Fluoro-Ethylene

RDE: Rotating Disk Electrode

RH: Relative Humidity

RRDE: Rotating Ring Disk Electrode

SANS: Small-Angle Neutron Scattering

SAXS: Small-Angle X-ray Scattering

SECM: Scanning Electrochemical Microscopy

SEM: Scanning Electron Microscopy

TEM: Transmission Electron Microscopy

XPS: X-ray Photoelectron Microscopy

XRD: X-Ray Diffraction

SYMBOLS

Latin letters

C_j reactant or ion concentration *(mol.m^{-3})*

$C_{SO_3^-}$ Nafion® sulfonates concentration *(mol.m^{-3})*

d compact layer thickness *(m)*

D_j reactant, water or ion diffusion coefficient *(m^2.s^{-1})*

$D_{i,Kn}$ reactant Knudsen diffusion coefficient *(m^2.s^{-1})*

E_w equivalent weight of the PEM *(kg.mol^{-1})*

$f = F/RT$

F Faraday's constant *(96485 C.mol^{-1})*

$g_{j^{z+}}$ ionic conductivity *(S.m^{-1})*

k_i kinetic reaction parameter *(m.s^{-1})*

L diffuse layer thickness *(m)*

l_{CL} CL thickness *(m)*

l_{GDL} GDL thickness *(m)*

l_{IN} ionomer layer thickness *(m)*

J_i reactant or ion molar flux *(mol.s^{-1}.m^{-2})*

m mass *(kg)*

M molar mass *(kg.mol^{-1})*

$n^{\max}$ maximal number of available adsorption sites per unit of catalyst surface *(m^{-2})*

N_A Avogadro's number *(6.022.10^{23} mol^{-1})*

P gas or liquid water pressure *(Pa)*

r catalyst or pore radius *(m)*

R ideal gas constant *(8.314 $J.K^{-1}.mol^{-1}$)*

S_{MEA} geometrical surface of the Membrane-Electrodes Assembly *(m^2)*

T absolute temperature *(K)*

t_{OT} simulated operation time (*s*)

v_i electrochemical reaction rate *($mol.s^{-1}.m^{-2}$)*

$\overline{V_i}$ molar volume of water and Nafion® *($m^3.mol^{-1}$)*

Greek letters

γ specific surface area *($m^2.m^{-3}$)*

ΔG Gibbs energy for a single (electro-) chemical reaction *($J.mol^{-1}$)*

ε electric permittivity *($C^2.N^{-1}.m^{-2}$)*

θ_s covering fraction of free sites

θ_i covering fraction of the intermediate reaction specie

$\vec{\theta}$ covering fraction of dipoles opposed to the catalyst surface

$\overleftarrow{\theta}$ covering fraction of dipoles oriented towards the catalyst surface

τ tourtousity

$\wp$ porosity

η electrostatic potential difference through the compact layer *(V)*

λ number of water molecules per sulfonate site

μ dipolar moment of a water molecule *(0.617×10^{-29} C.m)*

ρ_i platinum or carbon density *($kg.m^{-3}$)*

σ electronic surface density *($C.m^{-2}$)*

ϕ electrostatic potential in the electrolyte phase *(V)*

ψ electrostatic potential in the electro-active phase (Pt and C) *(V)*

OVERVIEW

In France, the *accreditation to supervise research* (or H.D.R., from the French spelling *Habilitation pour Diriger de Recherches*) is a national diploma of higher education that it is possible to obtain after a PhD. It allows the candidates to access to the body of university professors, to become PhD thesis supervisor or to be elected as *Thesis Rapporteur* by PhD or other H.D.R. applicants. The H.D.R. is based on the evaluation of the scientific results and career of the candidate, the originality of his approach in a field of science and validates its ability to define and succeed in a research program in sciences or technology and its ability to supervise young researchers. My motivation for applying to this diploma stems from a personal lifelong goal to pursue an academic career, in relation with my scientific interests in the field of physical electrochemistry.

As no formal consign or constraint exists, different styles and approaches are possible to write a H.D.R. manuscript: some people choose to describe in a very detail way their scientific life achievements in terms of supervision work or responsibilities, some other people provide an overview of their technical work or provide a “collection package” of their key publications in international journals, and others look for an equilibrated review between technical details and scientist life achievements. The latter is my personal choice for my manuscript here. For this reason, this manuscript is far of providing a detailed technical review of my work: for further information I invite the reader to refer to my journal publications.

The following is the structure I suggest for this manuscript. First of all, Chapter I includes my biography and personal experiences, from my first steps as Physics student in my country, Argentina, until my scientific career development in France.

In Chapter II I report a state-of-the-art on PEMFC research on performance and durability for stationary and automotive applications. The Chapter highlights key on going experimental and modeling efforts to achieve fast wide-spread commercialisation of these technologies. The scientific motivations for the development of my physical multi-scale modeling approach of PEMFC are in particular underlined.

My modeling approach (MEMEPhys mutliscale simulation package) is presented in Chapter III in relation with the PEMFC materials degradation and their durability prediction as a function of the operation conditions, initial material loadings and electrodes micro-structure.

Chapter IV reports a collection of applicative examples of my approach to address the practical problems of catalyst, support and membrane degradation as well as the competition and synergies between degradation processes and external contaminants.

Finally, in Chapter V, I conclude and discuss the short and mid-term perspectives of my research activities.

The end of this manuscript includes several Appendixes reporting my detailed Curriculum Vitae and list of publications, a short discussion on the application of my modeling approach to other electrochemical systems, a short summary of the infinite-dimensional Bond Graph theory underlying the mathematical structure of my multi-scale model, a copy of some of my papers published in international journals, and the bibliography used.

Good reading!

Dr. Alejandro A. Franco

Grenoble, France, July 12th, 2010

CHAPTER I

My scientific career

"Ciencia y humanismo han de ser un abrazo
y no un muro entre razón y sentimiento."

Pablo Serrano, spanish sculptor, 1908-1985.

I.1 – My first "Argentinean steps" as a "New Energies" scientist

I was born in Bahia Blanca city, in the south east of Argentina, in December 10, 1977. It seems that my passion for physical sciences started very early in my life. Even if my parents told me that until I was 4 years old I wanted to become a doctor…but in medicine.

At 5 years old, maybe motivated by my preferred television series "Cosmos: a Personal Voyage" (presented by the American astronomer Carl Sagan) I started to become attracted by Physics and Astrophysics.

Within this context, I used to enjoy my time by designing on the paper several kinds of machines, including a car to go to the moon (that I built in scale 1:4…), machines to eliminate spatial junk, space shuttles and "perpetual" machines (trying to violate the thermodynamics principles…) to produce electricity. My interest on finding new ways of producing energy started probably there. A book entitled "Renewable Energies" which my parents offered me when I was 11 years old definitively marked my life: I filed my first patent at 13 years old (1992) after designing a hydrogen-based machine to produce clean energy with high energy production efficiency (≈60%).

The machine was called "CEAM" (from the Spanish spelling *Central Energetica Alternativa Multiproposito*…I confess I did not know about the existence of "CEA" at that moment of my life!) and it was based on the hydrogen use cycle. It worked through the interplaying between different modules: a small aeolian system was used to generate electricity used in turn in a water electrolyzer to produce hydrogen. The hydrogen was then burned inside a boiler. The combustion product, water vapor, was used to drive a first turbine that, through a bicycle dynamo, allowed lighting a small lamp. The heat produced by the combustion was used to

heat water in a secondary circuit and the vapor produced drived a second turbine allowing lighting a second lamp. The remaining vapor was used to heat a small greenhouse (with a Bonsai living inside…) and then condensed and re-injected into the electrolyzer in a novel way (Figure I.1). I presented this machine in the National Student Science Fairs during the 1992-1996 period, winning several prizes (Figure I.2). I had there the opportunity to discuss with specialists and engineers, which allowed me to improve the machine year afer year. Each time I am coming back to Argentina, it is nice to see again, with some nostalgia, the "CEAM" machine in my grandmother house…still working (!).This was definitively my first experience in the field of the *New Technologies for Energy.* These activities were part of a very active student life where I also participated in several competitions in (rap) music, literature and mathematics (Mathematics Olympiads). I should say that my high school provided me a great adaptability, open minding and numerous values that I bring with me nowadays.

After finishing my high school studies with excellent marks (9.98/10 of global average over 6 years), in March 1997 I started my studies in Theoretical Physics in the *Universidad Nacional del Sur* (U.N.S.) in Bahia Blanca [[1]]. The overall duration of the study is 5 years, thus it is equivalent to the French *Master Research 2* level. This university was founded in 1956, and it is an independent and autonomous institution, one of the most important universities in Argentina. At present, there are 16 Departments and about 2600 faculty members, 50 first degree courses completely free of charge for about 24000 regular students and 51 postgraduate courses for about 1300 students enrolled in specializations, Master and PhD degree programs.

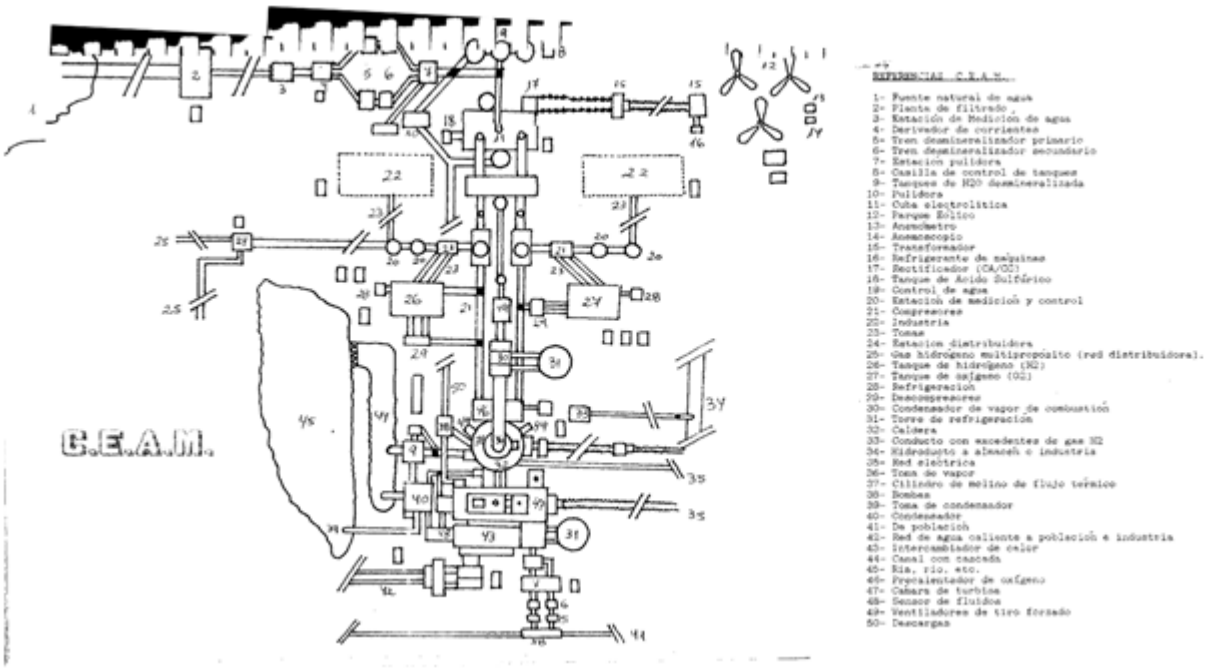

Figure I.1: My first patented hydrogen-based energy machine (see Appendix I).

Figure I.2: Presentation of my "CEAM" machine in some National School Science Fairs in 1992 (left), in 1993 and in 1995 (right).

In the U.N.S. I completed courses in applied Mathematics, and classical and modern Physics. From 1998 I started to work as *"Ayudante de Catedra"* (assistant professor) where I was giving theoretical lectures and supervising exercise sessions with groups of 20-70 students in the field of General Physics, Classical Mechanics, Electromagnetism, Thermodynamics and Quantum Mechanics, for students in Physics, in Electrical Engineering,

in Biology and in Pharmacology. This was a nice experience complementary to my work of tutor of high school students I used to do at home. The following is the list of the courses I gave (the student levels are indicated):

General Physics - Practice (480 h)	1998	1st and 2nd year of University degree	UNS
Classical Mechanics - Practice (240 h)	1999	1st and 2nd year of University degree	UNS
Thermodynamics - Practice (140 h)	2000	1st and 2nd year of University degree	UNS
Electrodynamics - Practice (100 h)	2000	2nd year of University degree	UNS
Quantum Mechanics – Practice (480 h)	2001	3rd year of University degree	UNS

Figure I.3: The U.N.S (left) and a view of Bahia Blanca city (right).

In July 1999 (third year of my Physics studies) I decided to pass the admission exam for the *Insituto Balseiro* (Balseiro Institute) [2]. The *Instituto Balseiro* is an academic institution founded in 1955, chartered by the *Universidad Nacional de Cuyo* and the *Comision Nacional de Energia Atomica* (C.N.E.A.) [3]. The institution is located in Bariloche city, at the foot of the Andes in the midest of the Nahuel Huapi National Park in the Argentinean Patagonia. The *Instituto Balseiro* teaches Physics, Nuclear Engineering and Mechanical Engineering at an undergraduate level, and Physics, Nuclear Engineering and Medical Physics at graduate and post-graduate levels. This institution is one of the most prestigious research centers in Latin America, world-wide recognized: its special characteristics, both, in students' training and research, makes it a unique institution in the region.

The undergraduate students are admitted after a tough examination where 30 are selected out of around 100-150 applicants per year. They are all given a full scholarship which allows them to be devoted full-time to their studies. Nowadays, the *Instituto Balseiro* has around 90 undergraduates, 160 graduate students, and 80 professors. It also offers advanced courses, international workshops, schools, and PhD and Master programs open to all students in Argentina and the rest of Latin America. This has allowed many non-Argentinean students to

come to Bariloche seeking excellence in education and research. The *Centro Atomico Bariloche* is the research institution. Both are intimately linked since students do experiments in the labs of the Center and professors are all active researchers there (a sine-qua-non condition which enhances the teaching quality). The nearly 160 researchers, in all areas including physics and engineering, are mainly employees of the C.N.E.A. and/or of the National Science Research Council (C.O.N.I.C.E.T.). The Institute has produced as a spin off one of the few high-tech companies in Argentina, INVAP, which has built and exported several research nuclear reactors (whose work led to the first research nuclear reactor in Latin America (1957), as well as the region first commercial nuclear reactor, Atucha I, in 1974), radars, satellites and nuclear medical equipment. All these institutions have nucleated the largest density of scientists and engineers of Argentina and most probably in Latin America.

Figure I.4: A view of the Instituto Balseiro (left) and a view from San Carlos de Bariloche city (*Nahuel Huapi* lake) (right).

I succeed the challenging admission exams (50 problems of mathematics and physics to be solved in no more than 5 hours…) to then really enjoy my time in the *Instituto Balseiro*. I remember me reading Physics textbooks under a reputed descendant of Newton's apple tree in front of the library garden. I discovered there the field of the non-equilibrium thermodynamics, non-linear dynamics phenomena, solid-state physics, surface science and…electrochemistry. In 1999, I designed a machine extending the classical Lorenz's chaotic waterwheel [4,5], with the goal of producing electric power from chaotic motion, exploiting irreversible thermodynamics principles. A Lorenzian chaotic waterwheel is just like a normal waterwheel except for the facts that the buckets leak. Water pours into the top bucket at a steady rate and gives to the system energy while water leaks out of each bucket at a steady rate and removes energy from the system. If the parameters of the wheel are set correctly, the wheel will exhibit chaotic motion: rather than spinning in one direction at a constant speed, the wheel will speed up, slow down, stop, change directions, and oscillate

back and forth between combinations of behaviors in an unpredictable manner. I did not file any patent with this machine, but I had a nice mark from my professors ...

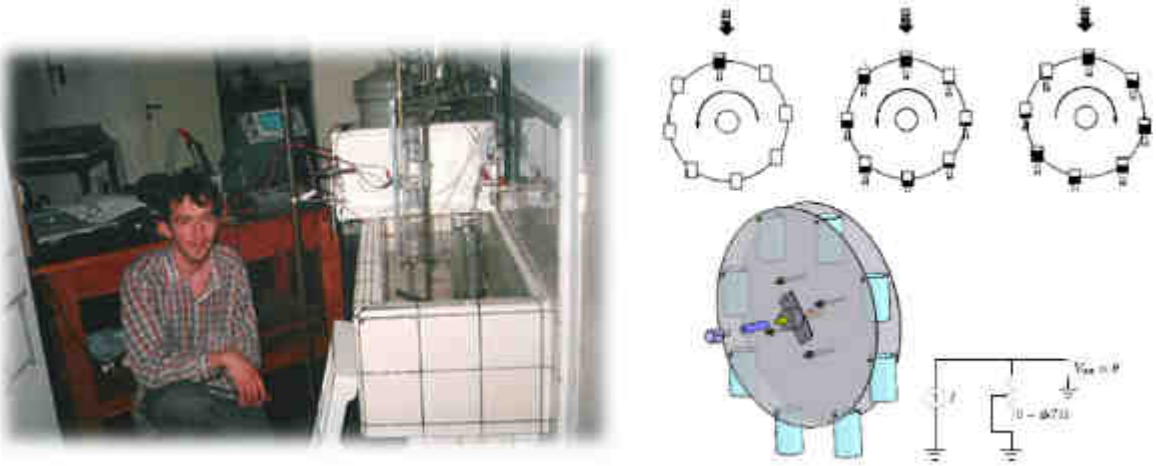

Figure I.5: My version of the Lorentz's chaotic wheel (left) and operation principle (right).

In September 2000 I came back to the U.N.S., finishing my studies in Theoretical Physics in November 2001 and obtaining the highest average of my promotion (9.68/10 of global average over 5 years). By the end of 2000, I heard from the director of the Physics department, Prof. Alfredo Juan, about an internship for a one-year work in the topic of hydrogen (!)-related Technologies (Fuel Cells) being proposed at the *Commisariat à l'Energie Atomique* of France (CEA) [6] in Grenoble, France, by Prof. Jean Bletry (a researcher on Solid State Physics, now retired from CEA) and Dr. Didier Marsacq (nowadays the director of the CEA-LITEN, see below). Naturally, because of the topic, I applied, and after my application was accepted, I left Argentina to France in December 31st 2001.

Then, the French adventure started…and the one-year stay became a "permanent" stay…

I.2 - My arrival to France

I started to work at CEA in January 2, 2002. The CEA, re-called from January 2010 the *Commissariat à l'Energie Atomique et aux Energies Alternatives* (Atomic Energy and Alternative Energies Commission), it is a French national institute established in October 1945 by Charles de Gaulle. A leader in research, development and innovation, the CEA mission statement has two main objectives:

- ✓ to become the leading technological research organization in Europe

- ✓ and to ensure that the nuclear deterrent remains effective in the future.

The CEA is active in three main fields:

- ✓ energy,
- ✓ information and health technologies,
- ✓ and defense and national security.

In each of these fields, the CEA maintains a cross-disciplinary culture of engineers and researchers, building on the synergies between fundamental and technological research. In 2006, the total CEA workforce consisted of 15332 employees (52 % of whom were in management grades). Across the whole of the CEA (including both civilian and military research), there were 1017 PhD students and 278 post-docs. In 2004, the civilian programs of the CEA received 55 % of their funding from the French government, and 35 % from external sources (partner companies and the European Union). The remaining 10 % was provided from a fund dedicated to the decommissioning and clean-up of civilian nuclear plants. The military programs are mainly funded directly by the French Ministry of Defence.

The CEA is based in nine research centers in France, each specializing in specific fields. The laboratories are located in the Paris region, the Rhône-Alpes, the Rhône valley, the Provence-Alpes-Côte d'Azur region, Aquitaine, Central France and Burgundy. The CEA benefits from the strong regional identities of these laboratories and the partnerships forged with other research centers, local authorities and universities.

Figure I.6: CEA research centers (left) and a view of CEA-Grenoble (right).

My 2002 work took place in the division which is nowadays called “LITEN”. LITEN (Laboratory for Innovation in New Energy Technologies and Nanomaterials) is a CEA institute located for the most part in Grenoble and in Chambery (city close to Grenoble, within the National Institute of Solar Energy -INES-). It is one of Europe newest and most important

research centers in the new energy technology field. It works to support the country efforts to diversify its energy mix through more effective use of renewables, in particular to meet energy requirements in transport, housing and mobile electronics. It also seeks to make French businesses more competitive. Involved in 350 research partnership contracts every year, LITEN works hand in hand with French industry. It is one of the CEA laboratories with the most patents (96 new applications filed in 2008 and a portfolio of 324 international patents). LITEN research activities are focused

- ✓ on solar energy,
- ✓ low-energy buildings,
- ✓ future transport applications (hydrogen, fuel cells and batteries),
- ✓ and nanomaterials for energy and methods guaranteeing their safe use.

LITEN is the leading centre for new energy technologies, and in particular fuel cells, in France and it is working on research contracts with regional, national and international industrial partners (e.g. Sofileta, Acxys, Apollon Solar, Photowatt, STMicroelectronics, Mecachrome, EDF, PSA, Jusung...). Its research work covers complete technological processes, from basic components to prototypes integrated into a system for the purposes of demonstration. LITEN has several first-class technological platforms, clean rooms for testing equipment and processes, and heavy equipment for characterization and testing. In addition, LITEN has access to the other CEA Grenoble facilities and sets up joint laboratory facilities with its industrial partners. LITEN is also developing its activity on the international scene with its participation in European projects (35 projects underway for FP6 and 7) and specific efforts in the direction of the Asian market concerning solar energy, hydrogen vector, energy storage, energy microsources, organic energy. Partnerships involving solar energy and hydrogen as a new energy vector are also taking shape in the Middle East.

When I arrived to CEA, because of my background I was expecting to work on Fuel Cells theoretical modeling, instead I was asked to perform experiments. Overcoming my first disappointement, I discovered there the experimentalist viewpoints and approaches, as I prepared myself numerous catalysts and Membrane-Electrodes-Assemblies (MEA) and carried out several electrochemical testing. This experience has been an inflexion point in my professional life which definitively consolidates my PEMFC theoretical and modeling expertise of nowadays.

Until December 2002, my work consisted on the development and the electrochemical characterisation of a new kind of fuel cell with anionic polymeric electrolyte for portable applications. The main challenge was to develop an anionic ink to fabricate the electrodes, as in contrast to standard acidic PEMFC, does not largely exist. Some first tests by using

methanol as the fuel provided encouraging results. Furthermore, I set up measurements techniques to distinguish reversible and irreversible performance degradations. By extending previous published experimental works proving that the presence of a permanent magnetic field inside the electrodes is likely to increase the performances of the PEMFC, I designed, based on mathematical modeling, a new type of cathode including permanent magnetized particles. These permanent magnets support the chemical species transfer in the cathode via the Kelvin magnetic force. This force attracts the oxygen with paramagnetic properties towards the catalytic sites and pushes back the diamagnetic water molecules. From my simulations, I suggested an optimized micro-structural distribution of magnetized particles in the electrode to envisage a significant increase in the electrochemical activity towards the Oxygen Reduction Reaction (ORR). I then did some first experimental testing with encouraging results. I filed a patent with this idea by August 2002, and these activities were pursued by a PhD student I advised in 2008, as described below, and continue until nowadays.

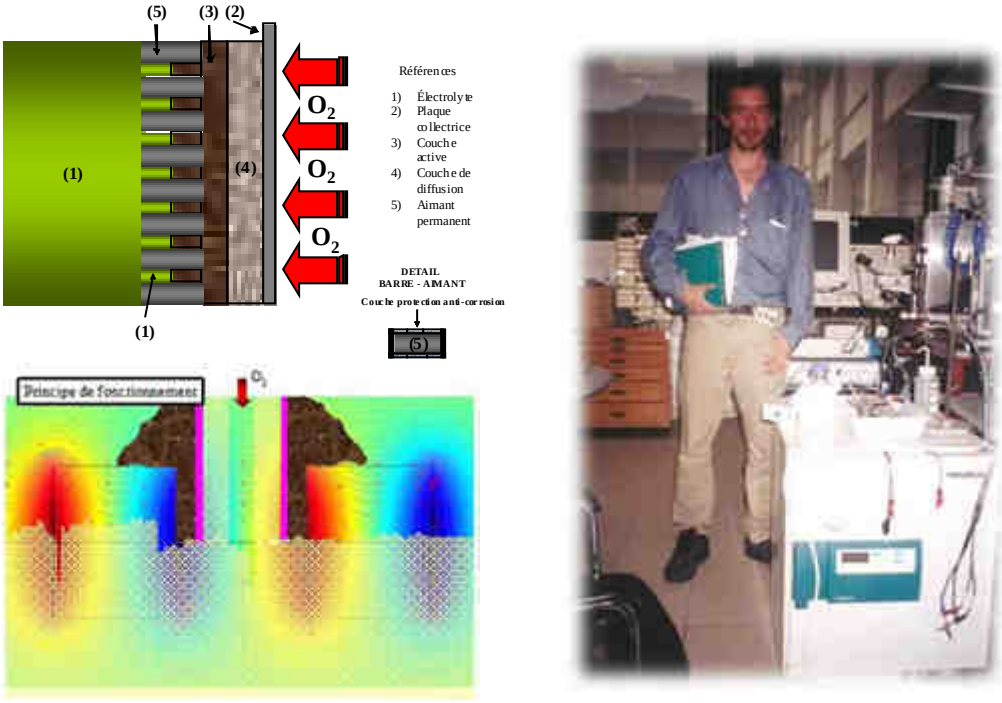

Figure 1.7: My 2002 patent on the use of magnetic micro-particles to enhance the ORR in PEMFC cathodes (left), 3D numerical calculation of resulting O_2 concentration between two permanent magnets (in pink: the catalyst, in light yellow: the electrolyte, in brown: the catalyst-support) (left); and my "magnetic" fuel cell experiment in 2002 (right).

During these exciting research times, the CEA proposed me a PhD position on PEMFC modeling with a lot of theory work in perspective (!). I was delighted to accept.

I.3 - My PhD thesis at CEA-Grenoble: from mathematics to physics

After my application passed the standard examination process by the CEA High Commissioner, I started my PhD thesis in January 2nd 2003, almost one year after my arrival to France. At the university level, I has been supervised by Professor Bernhard Maschke and Professor Christian Jallut, both from the *Laboratoire d'Automatique et de Génie des Procédés* (Laboratory of Automatic Control and Chemical Engineering) in the *Université Claude Bernard Lyon-1*.

When I discussed in my 2002 recruitment interview with my future PhD advisor at CEA, Pascal Schott, the main goals of the PhD project were stated as: the development of a new mathematical framework, based on *infinite-dimensional Bond Graphs* (see Chapter III and Appendix III), to model in a modular/flexible way the different interplaying physicochemical phenomena inside an operating PEMFC. However, two pertinent questions in my PhD kick-off meeting from the responsible of the PEMFC modeling group at that moment, Pierre Baurens, have aroused my curiosity: *"What is the role of the electrochemical double layer in PEMFC operation? How does the double layer looks like in PEMFC environments and how does it impact the transient behavior of the cell?"*. Those simple but deep questions became the main motivation for all my subsequent PhD work, with my Physics background having again a main role.

In order to analyze the experimental results of Electrochemical Impedance Spectroscopy (EIS) on PEMFC electrodes (or Catalyst Layers -CLs-), I developed a new mutli-scale mechanistic model to understand the dynamic behavior of a MEA. This model is new In the sense that it is fully built within an irreversible thermodynamics and electrodynamics framework, and depended on the internal PEMFC physical parameters, such as the effective electrode surface, the electric permittivity of the materials, the reaction kinetics and the diffusion coefficients of the reactive species.

The model resulted from the coupling of a microscopic scale transport phenomena description of charges (electrons and protons) through the electrode and the ionomer electrolyte within, a spatially distributed microscopic model of the reactant diffusion (hydrogen and oxygen) through the ionomer covering the Pt/C particles (agglomerate-like model), and a spatially distributed nanoscopic description of the ionomer-Pt/C interface. This interfacial model was based on an internal description of the electrochemical double layer dynamics, coupling the transport phenomena in the diffuse layer and the electrochemical reactions and water adsorption in the compact layer, without using classical empirical Butler-Volmer models. This multi-scale model introduced many couplings between different physical domains, such as diffusion-migration transport and detailed electrochemistry. I have

formulated this multi-scale model in the formalism of infinite-dimensional Bond Graphs (presented in the Appendix III). In this way a modular structure is given to the system where the couplings between the modules are defined in accordance with the laws of thermodynamics and physics allowing the later inclusion of other physico-chemical phenomena or their re-use in other electrochemical systems. These key properties were used for the further developments of this model that I made after my PhD. Finally the Bond Graph model has been used to calculate the causalities of the different couplings, using the commercial code 20-Sim® [7], and to give the model a computational structure. The numerical resolution has been carried out in Matlab/Simulink® coupled to Comsol Multiphysics® -known as Femlab® in 2005- (finite elements method). The system dynamics, depending on the current, the temperature, the reactant pressures, and the structural composition of the electrodes was simulated. The model allowed evaluating the sensitivity of the EIS to operating conditions and electrodes composition, and it gave access to the contributions of the different phenomena and constitutive layers. An experimental validation of the model was carried out on a specific bench and single cell. The simulations were found to be in good agreement with experimental results.

I did not file any patent from this thesis work, but I participated in 5 international conferences (3 oral presentations) and published 3 papers in peer-reviewed international journals (2 regular and 1 proceedings). In 2005, I was recipient of a finalist prize for the Young Scientific Award of the *International Society for Solid State Ionics* (see Appendix I).

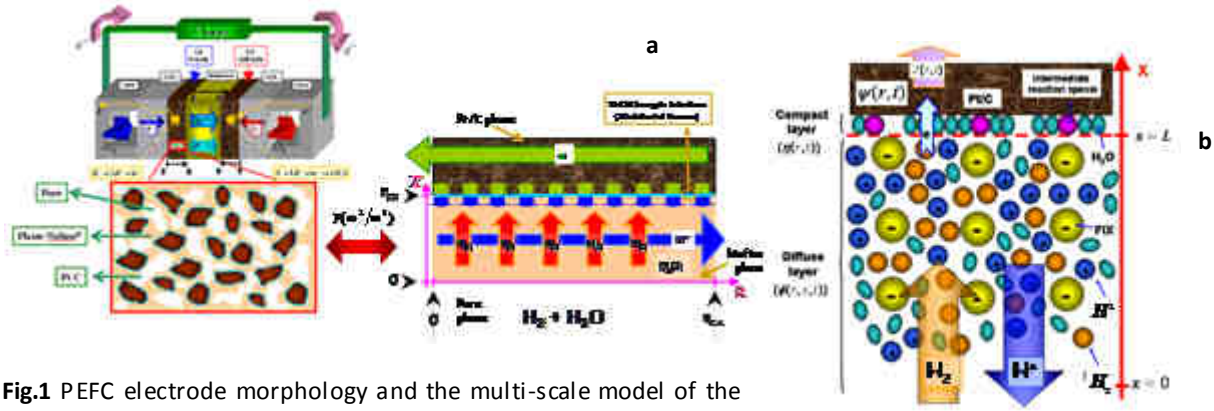

Fig.1 PEFC electrode morphology and the multi-scale model of the volumetric electrode (example of the anode) and localization of the nanoscopic model (a). Detail of the nanoscopic interface model (b).

Figure I.8: My PhD thesis multi-scale model of PEMFC (Source: [8]).

My PhD thesis work served as a strong basis for the development of my model MEMEPhys® (from the French spelling *Modèle Electrochimique Multi-Echelle Physique*) which became a reference for PEMFC modeling at CEA (see Chapter III). As the best of my knowledge, this model introduced for the first time in the published PEMFC modeling litterature, a continuum

nano-scale theory to scale up *ab initio* atomistic data into kinetic models and describing the feedback between the electrochemical double layer structure and the effective nano-catalysts reactivity properties. The non-equilibrium thermodynamics framework and the elementary kinetic approach used within, naturally opened powerful capabilities to address more complex problems such as the MEA materials degradation which I started to look closely by the end of 2005 (see Chapters II and III).

All along my PhD I contributed in the CEA Grenoble communication program "La Recherche fait Ecole", organized by the Division of Scientific Communication, and consisting in researchers presentations in the Grenoble region high schools on topics of actuality (e.g. nanotechnologies, etc). I had in charge the module *"Fuel Cells"* where I was presenting three times per year the CEA research work on fuel cells and hydrogen-related technologies to young high school students. This program is a nice experience for the researcher as the technical language has to be adapted to a young audience without a strong background on physical chemistry. I really enjoyed the spontaneity of the students' questions and interacting with them on their future career plans, as well as telling them how it is the scientist life. This is an activity that I am pursuing nowadays (see below).

After my PhD defence in November 28th, 2005, I was proposed, by Dr. Florence Lefebvre (the head of my lab at that moment) to a permanent research position in the CEA. As simultaneously, I was considering an offer of postdoctoral position by Prof. Heinz Pitsch from Stanford University in USA, it was for me difficult to choose. Finally, I decided to stay in Grenoble and continue my "French adventure"...

I.4 – My career as permanent researcher at CEA-Grenoble

My permanent research position at CEA officially started on December 5th 2005. As a member of the permanent staff I started to work on the extension of my model MEMEPhys® to address the PEMFC materials aging under automotive-like operation conditions. The mechanistic feedback between the instantaneous performance and the intrinsic MEA aging processes, such as Pt catalyst oxidation, dissolution and ripening, or the C support corrosion, has been implemented in my PhD thesis model. This allowed taking into account, at each simulated time step, both the effect of the cell potential decay on the materials aging and the effect of the materials aging on the cell potential decay. This powerful characteristic was a natural consequence of the modular mathematical structure of MEMEPhys®, and thus, it allows the prediction of material properties evolution (e.g. the temporal evolution of the interlinked activity, selectivity and stability properties of the electrocatalyst). The prediction of

the cell potential degradation, such as MEA durability as a function of the cell operating conditions and the initial MEA design parameters, also arises from our model. Furthermore, our model allows providing temporal multi-scale analysis and insights on the competitions between the different degradation mechanisms, crucial pre-requisites in engineering practice (see Chapter III).

2006 was a year where I advised my first Master Research student and where I submitted several project proposals to get funding, as project manager or as modeling working package (WP) responsible in proposals submitted by my colleagues. From the beginning of 2007, my activities started to develop very quickly through different projects funded by the National Research Agency (A.N.R.), as well as students and postdoctoral researchers funded by the CEA and industrial partnerships, as summarized in the following.

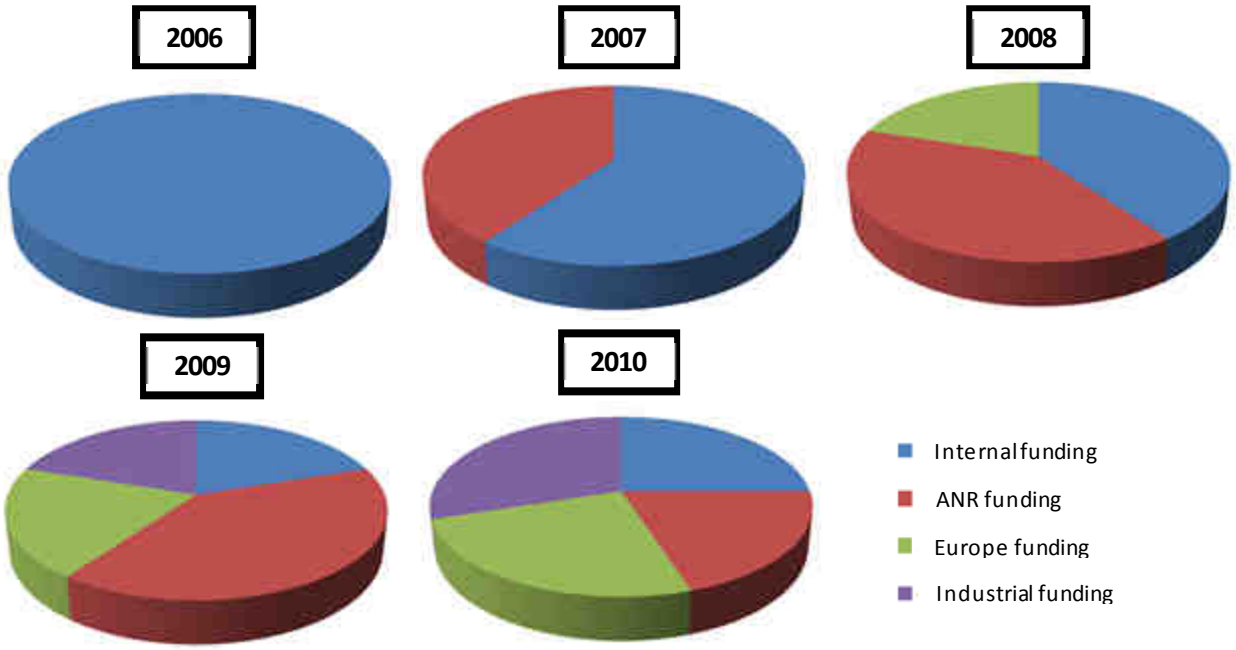

Figure I.9: the funding resources of my modeling activities.

I.4a – Projects

From 2007, I was or I am still Modeling WP leader in different National and International projects, including:

- **DVD-AME: Understanding the impact of transient operation conditions on PEMFC materials degradation** (January 2006 – March 2009)
  - ✓ **Funding:** National Research Agency (A.N.R.)

- ✓ **Partners:** CEA, CNRS/*Laboratoire de Catalyse* (LACCO), CNRS/*Service de Propriétés Moleculaires et Structures* (SPRAM)
- ✓ **Description of my contribution:** This project aimed to analyze the durability and degradation of operating MEA submitted to stressing conditions required by the PEMFC automotive applications. The studies were focused on the state of the art MEA made with PFSA (PerFluoroSulfonatedAcid) polymers, Pt/C as catalyst and carbon fibres based-Gas Diffusion Layers (GDL) containing more or less PTFE. Apart from the materials, the influence of the MEA preparation processes on the performance or on the components degradation has been also considered. The aim of this research work was to enhance our understanding of the operating MEA degradation in order to be able to propose solutions at the component level or concerning the operating modes. The proposed methodology has been to observe the evolution of the MEA performance and properties when submitting the whole MEA or components to *in situ* or *ex situ* aging protocols (half-cells and single cells tests) in order to determine the parameters limiting the durability and the mechanisms involved. The study has been based on physico-chemical analyses performed before and after aging, including electrochemical measurements to determine the interaction between aging and the electrodes properties, mechanical tests and transport properties analyses to determine the Polymer Electrolyte Membrane (PEM) evolution, and micro-structural observations to relate the evolution of performance and properties to materials modifications. This project provided useful experimental data to check the predictions obtained by the simulation package MEMEPhys® and are nowadays integrated within the model. Furthermore, the MEMEPhys® model provided some theoretical support to understand the experimental observations carried out in the project.

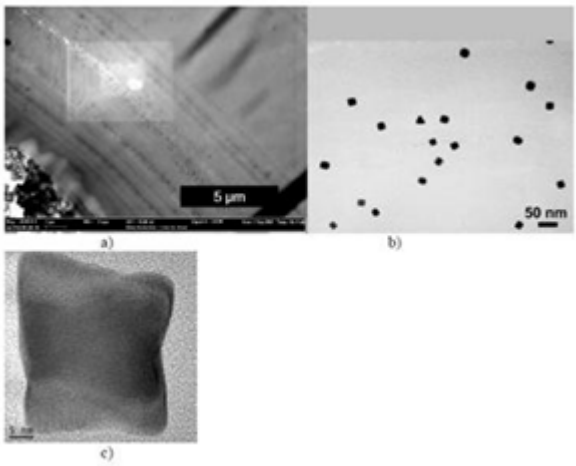

Figure I.10: Example of result within the context of DVD-AME project (observed Pt precipitation in the PEM after MEA on/off operation during 1000 h, and detail of the formed cristallites (c)).

- **POLIMPAC: Analysis of the Impact of Pollutants on PEMFC Performance** (January 2007 – March 2010)
  - ✓ **Funding:** National Research Agency (A.N.R.)
  - ✓ **Partners:** CEA, *Institut de Recherche sur la Catalyse et l'Environnement de Lyon* (IRCELyon), Helion Fuel Cells, *Institut Français du Pétrole* (IFP), CNRS/*Laboratoire de Science et Ingénierie des Matériaux et Procédés* (SIMAP)
  - ✓ **Description of my contribution:** this project focused on identifying and analyzing the impact of external pollutants (from atmospheric air, fuel reforming, distribution network…) on the electrochemical performance of a Pt-based PEMFC. Single cells and stacks were tested and specific studies of the Pt reactivity to the pollutants in real operational conditions were done. Within this project I was leading a whole WP dedicated to the multi-scale modeling of the behavior of the MEA in presence of external pollutants. Among my most relevant results, for the first time in the community, I developed a model describing the degradation of the cathode C corrosion when the anode is being operated with CO-contaminated H_2. The model allowed predicting the fact that under specific automotive operating conditions (current cycles I_{min}-I_{max} with I_{min}>0) the anode contamination with small amounts of CO (2-5 ppm) mitigates the cathode catalyst C support corrosion and improves the long-term MEA durability compared to the case of a MEA operated with pure H_2 (degradation rate 3 times lower). The modeling studies have been also extended to the study of the interplaying between the anode CO contamination and PEM degradation with the same conclusions. These results have been fully validated by experiments carried out at CEA and allowed 4 patents applications. These results can have considerably impact on industry as this could allow the use of a less purified and thus cheaper H_2 feed in the PEMFC (see Chapter IV).

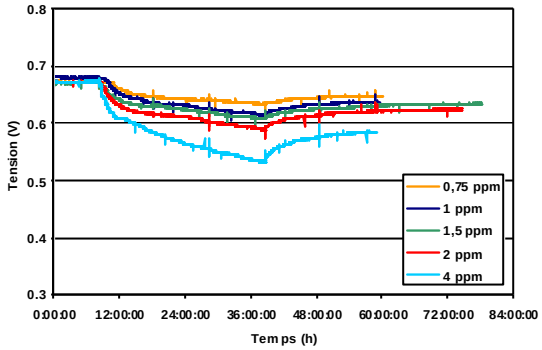

Figure I.11: Example of result within the context of POLIMPAC project (experimental impact of SO_2 concentration in the PEMFC cathode on the global cell performance).

- **OPTICAT: Development of new metallic electro-catalysts for PEMFC cathodes** (January 2007 – March 2010)
  - ✓ **Funding:** National Research Agency (A.N.R.)
  - ✓ **Partners:** CEA, CNRS/*Laboratoire de Catalyse* (LACCO), CNRS/*Service des Propriétés et Structures Moleculaires* (SPRAM), RECUPYL SAS, SOLVIONIC SA.
  - ✓ **Description of my contribution:** this project dealt with the development of new multi-metallic catalysts and CLs formulations in order to reduce Pt loading and improve the PEMFC behavior and lifetime. The CLs studied in this project have been made either with a Pt/C ink deposited on membrane or GDL, or by a direct coating of catalytic nano-particles on a C support constituted by the Micro-Porous Layer (MPL) of a GDL. In this last case, the used coating processes included vacuum technologies (e.g. Direct Liquid Injection-Metallo Organic Chemical Vapour Deposition -DLI-MOCVD-) or electro-deposition. CLs and MEAs have been electrochemically tested and characterized. A reprocessing method of the electrode waste has been furthermore developed, together with a technico-economical study to quantitfy the cost of each process used to prepare the CLs. Jointly with my students, I developed a theoretical approach allowing to predict both performance (electroactivity to the ORR) and degradation of Pt-M (with M being a transition metal) nano-structured catalysts. This new proposed model, (unique in literature), parameterized with *ab initio* data (e.g. obtained from Density Function Theory -DFT- calculations), has been successfully used to understand the nano-structure-activity-stability relationships of Pt_xCo_y nanoparticles and thus in the diagnostics and interpretation of experimental observables (e.g. EIS). This work was clearly the first illustration of the versatility of MEMEPhys® approach to address materials with different chemical composition and nano-structure (see Chapter IV).

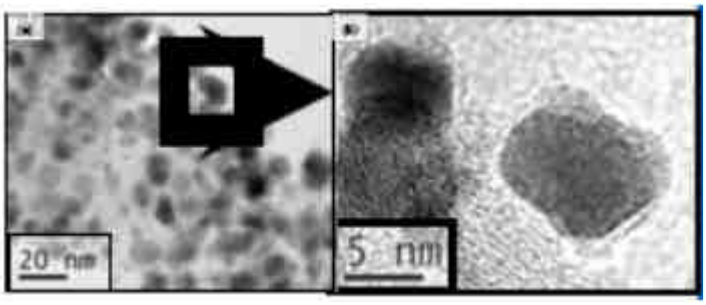

Figure I.12: Example of result within the context of OPTICAT project (HR-TEM images of Pt_3Co nanoparticles prepared by DLI-MOCVD on a GDL support).

- **DECODE: Understanding the impact of water transfer onto PEMFC materials degradation** (January 2008 – December 2011)
  - ✓ **Funding:** European Commission (FP7)
  - ✓ **Partners:** CEA, Solvay Solexis S. p. A. (Italy), Volvo Technology A.B. (Sweden), *Zentrum für Sonnenenergie- und Wasserstoff-Forschung Baden-Württemberg* (ZSW*)* (Germany), SGL Technologies GmbH (Germany), European Commission DG - Joint Research Centre Institute for Energy (JRC-IE) (Belgium), Adam Opel GmbH (Germany), Dana Sealing Products – Victor Reinz GmbH (Germany), *Friedrich-Alexander-Universität Erlangen-Nürnberg* (Germany), Chalmers University of Technology (Sweden), *Deutsches Zentrum für Luft- und Raumfahrt e.V.* (DLR) (Germany).
  - ✓ **Description of my contribution:** The aim of the DECODE project is to elucidate the materials degradation mechanisms in PEMFC with special focus on the influence of liquid water and in a second phase to modify components to achieve a significant improvement of PEMFC durability. The project is structured into several WPs for the investigation of various components of PEMFC. DECODE focuses both on detailed component characterisation and also subsystem (short stack) testing and analysis. Components are tested in long-term operation in short stacks under realistic and technical conditions thereby leading to naturally aged components. The components of PEMFC investigated in the project consist in the CLs, PEM, GDLs, MPLs and bipolar stacks, with both *in situ* and *ex situ* analysis. A special strength of the project is the large modeling activity which is expected to significantly advance knowledge and understanding of the processes leading to degradation and also to deliver the tools to describe aging and performance degradation. Within this project, I was the leader of the WP devoted to the modeling of the MEA degradation. This allowed the implementation of water transport phenomena in MEMEPhys® and exploring its impact on the degradation processes, and how these degradation processes affect in turn the local water transport properties (see Chapter IV).

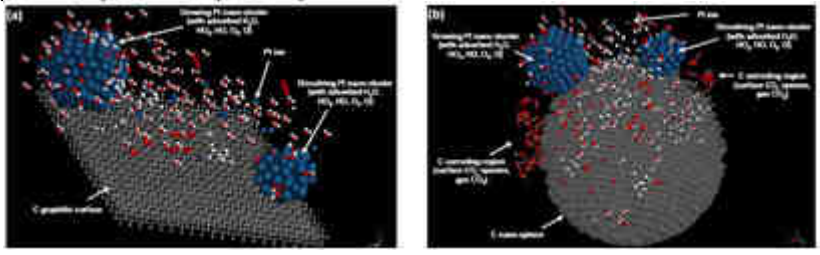

Figure I.13: Example of result within the context of DECODE project (atomistic level models of the electrochemical Ostwald's ripening on C graphite surface and C nanosphere).

- **ARCAPAC: Bottom-up design approach of PEMFC electrodes** (December 2008 – January 2012)
  - ✓ **Funding:** National Environment and Energy Management Agency (A.D.E.M.E.)
  - ✓ **Partners:** CEA, CNRS/*Laboratoire de Catalyse* (LACCO), *Université de Tours*, Helion Fuel Cells.
  - ✓ **Description of my contribution:** this project consists in developing new CL architectures based on "bottom-up" nano-science technologies, which would allow decreasing Pt loadings up to the µg/cm^2 order. MEMEPhys® modeling approach supports these developments by providing interpretation of experimental tests and by proposing guidelines for CL "bottom-up" architecture design with improved performance. In particular, the purpose of this work is to develop a kinetic model describing the Hydrogen Oxidation Reaction (HOR) and ORR on organically-capped Pt nano-particles elaborated by Dr. Henri Perez at CEA-Saclay/DSM. DFT approach is used and theoretical descriptions of the electrochemical double layer surrounding these nano-particles are being developed. The kinetic model will collect some of the elementary events, catalytic or not, the final aim being the comparison of the calculated electrochemical observables with the experimental results.

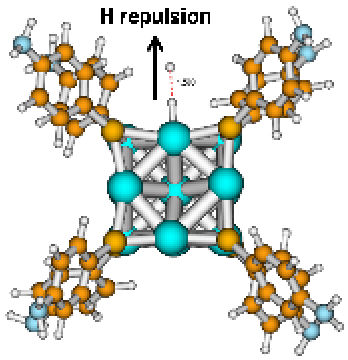

Figure I.14: Example of result within the context of ARCAPAC project (*ab initio* calculation of the repulsion of H from the organically-capped Pt nanoparticle).

- **CATIMINHY: Development of new architectures of PEMFC electrodes** (December 2008 – January 2012)
  - ✓ **Funding:** National Research Agency (A.N.R.)

- ✓ **Partners:** CEA, *Université Joseph Fourier*, National Institute of Technology of Grenoble (INPG), Siliflow S.A.S., Paxitech Fuel Cells, Rhodia,
- ✓ **Description of my contribution:** Innovation in PEMFC components is limited by the preponderant use of a few traditional fabrication technologies. Moreover, a specific aim is to reduce the Pt loading because of its increased cost. This project proposes a technological breakthrough consisting in the preparation of CLs by hybrid printing technologies, where most of the components can be deposited successively, without hot pressing. Thanks to the enhancement of interfaces, the limitation of the contact resistances, the thinning of the various layers, this concept brings gains in performances and an optimization in the Pt loading. These processes, allowing an automated production by batch, are now being applied by the realization of a pilot line for conventional MEA, Catalyst Coated Membrane (CCM) type. Within this project, I am leader of the WP devoted on applying MEMEPhys® to understand the impact of different MEA architectures (e.g. catalyst loading gradients across the CLs thicknesseses) on the PEMFC performance and durability. Until today, the model suggested some "optimal" configurations and electrode structures allowing mitigating the cathode C corrosion and PEM degradation. This has been successfully demonstrated by experiments, and allowed filing 2 patents (see Chapter IV and Appendix I).

- **AIRELLES: Development of MEA for PEM-Water Electrolysers** (January 2009 – December 2011)
  - ✓ **Funding:** National Research Agency (A.N.R.)
  - ✓ **Partners:** CEA, Helion Fuel Cells, CNRS/*Laboratoire de Catalyse* (LACCO), *Institut Laplace*.
  - ✓ **Description of my contribution:** AIRELLES project proposes fundamental and technological research and development actions in the field to MEA for PEM-Water Electrolysers (PEM-WE). This project proposes to develop and manage lifetime tests of innovating catalysts, PEM and MEA following a protocol that fit the use of a PEM-WE coupled to intermittent renewable energies. Within this project, we analyze and try to better understand degradation phenomena of a PEM-WE, a topic not largely adressed in the international scientific community. My group is now adapting MEMEPhys® to describe the relevant physicochemical phenomena in a PEM-WE including detailed description of the elementary kinetic reactions on Ir_xO_y and Ru_xO_y catalysts from *ab initio* DFT data (see Appendix II).

- **ARTEMIS: Start up time reduction and fuel cells system optimization for electric emergency application** (January 2009 – December 2011)
  - ✓ **Funding:** National Research Agency (A.N.R.)
  - ✓ **Partners:** CEA, National Institute of Technology of Grenoble, Polytechnical Institute of Lorraine, Helion Fuel Cells.
  - ✓ **Description of my contribution:** This project addresses the problem of the start-up phase time reduction and sustainability for PEMFC stationary applications, under specific operating conditions. This project aims on defining the optimal strategy for stops and stand-by modes under reactive gases, in order to significantly reduce the start-up time (about thirty seconds today, this start-up time should be closer to the second at least) and the MEA degradation due to the materials aging: this will reduce the quantity of batteries required, having an impact on the structure and the system cost. The second task of the project is to explore the specific operating conditions (rapid power on, low power operation and low temperature startup) to develop solutions preventing rapid degradation of the MEAs. I am providing here theoretical support to get insights about the main degradation mechanisms behind these particular operating conditions, and to suggest via MEMEPhys®, start-up strategies to enhance the MEA durability.

- **KSU-NANO: Development of new C-based nanomaterials for energy applications** (January 2009 – December 2011)
  - ✓ **Funding:** King Saud University (Saudi Arabia)
  - ✓ **Partners:** King Saud University, CEA
  - ✓ **Description of my contribution:** this project focuses on the development of durable electrocatalyst supports for PEMFC. In particular, attention is focused on fullerene-like materials.

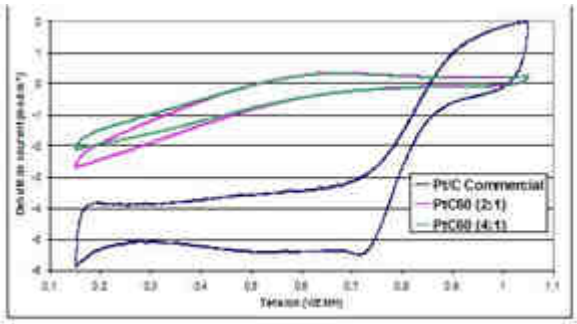

Figure I.15: Example of experimental result within the context of KSU-NANO project (performance of different Pt_nC_{60} electrocatalysts towards the ORR).

- **Modeling the role of Nafion® on PEMFC electrodes performance** (March 2010 – February 2011)
  - ✓ **Funding:** Nissan Motor Co. (Japan) & CEA
  - ✓ **Partners:** Nissan Motor Co. (Japan), CEA, National Research Council of Canada (NRC) – Institute for Fuel Cell Innovation.
  - ✓ **Description of my contribution:** Recent PEMFC CL models account for agglomerate formation and bimodal porous architecture and rationalize Pt effectiveness and water balance. A complete structural picture is, however, still controversial. Major debates include composition and size of Pt/C agglomerates, structure/distribution and function of ionomer; structure and distribution of water, and heterogeneous wetting properties of CL. Insights into these structural details is vital for understanding interfacial properties: nature and abundance of active interfaces and contribution to current generation (Pt|vapour, Pt|ionomer, Pt|water in pores). It is also pivotal to understand mechanism of proton and electron transport. Recent efforts to unravel structure formation in CL involved self-organization, adsorption and physicochemical and transport properties of CL. This project focuses on the description of the CL structure in more details. Moreover, we intend to unravel the effect of ionomer on electrochemical activity of Pt and the global relation between microstructure, ionomer morphology, electrochemical reaction and performance. My contribution within this project is to develop an elementary kinetic model of the ORR on Pt from atomistically-derived parameters, accounting for the impact of the CL ionomer structural properties on the electrochemical reactivity or performance of the PEMFC.

Incoming projects involving my research activities include:

- **PREMIUM ACT: Predictive Modeling for Innovative Unit Management and Accelerated Testing Procedures of PEFC** (starting by the end 2010, duration: 3 years)
  - ✓ **Funding:** European Commission (JTI)
  - ✓ **Partners:** CEA, IRD Fuel Cells A/S (Denmark), *Politecnico di Milano* (Italy), ICI CALDAIE (Italy), Soprano (France), European Commission DG - Joint Research Centre Institute for Energy (JRC-IE), *Deutsches Zentrum für Luft- und Raumfahrt e.V.* (DLR) (Germany).
  - ✓ **Description of my contribution:** PREMIUM ACT is an ambitious project on the durability of PEMFC, targeting one of the main hurdles still to overcome before

successful market development of stationary fuel cell systems. PEMFC systems are now very near, or even already comply with market requirements for cost and performance. But durability targets, up to several tens of thousands of hours, are much more difficult to reach. PREMIUM ACT proposes a very innovative approach, combining original experimental work on PEMFC systems, stacks and MEA, including locally resolved studies of components durability, components characterization and multi-scale modeling. I am the modeling WP responsible in this project where MEMEPhys® will be used to go further in the understanding of the competition between degradation mechanisms and to predict accelerated aging procedures representative of real-life degradation (see my discussions on this problem in Chapter II).

- **MMM@HPC: Development of multi-scale modeling and high performance computing methods for materials** (starting by the end of 2010, duration: 3 years)
  - ✓ **Funding:** European Commission (FP7)
  - ✓ **Partners:** CEA, Karlsruhe Institute of Technology (Germany), CINECA Bologna (Italy), CSC - IT Center for Science (Finland), Korea Institute of Science and Technology (Korea), Nokia Research Center (Finland), Sony (Germany), Science and Technology Facilities Council (UK), University of Mons (Belgium), University of Patras (Greece).
  - ✓ **Description of my contribution:** This project focuses on the application of multi-scale modeling methodologies to improve materials and nanostructured objects. The project combines *ab initio*, Coarse Grained Molecular Dynamics (CGMD) and continuum level modeling efforts and covers different application domains, such as microelectronics devices, bio-sensors and Li-ion batteries. This project will provide to my group a first opportunity to extend our multi-scale modeling approach of the electrochemistry from PEMFC to Li-Ion batteries.

I.4b – Advised students and collaborators

From 2006 until present I got several Master Research and PhD students scholarships (Tables I-1 and I-2) and five scholarships for postdoctoral researchers (Table I-3). Some of them have been obtained from applications to internal CEA call for proposals, other ones from applications to the transversal *CEA Nanosciences program* and other ones from bi-lateral collaborations with research institutes and industrials.

I should say that all these talented students and collaborators worked/are working hard to help my group to develop and develop our modeling approach.

Until today, I advised 8 Master Science students, 7 PhD students (+2 incoming) and 3 postdoctoral researchers (+2 incoming) on different aspects of fuel cells electrocatalysis, nanomaterials degradation phenomena and MEMEPhys® model development. To this list reported here, I should add some interactions with other students being advised by other colleagues at CEA (e.g. PhD thesis of Mathias Gerard, Oct07-Sep10, on the Modeling and experimental study of the PEMFC-system interaction, in relation with the PEMFC materials degradation). I always encouraged my collaborators to file patents and publish their work if the quality is sufficiently good. The consequence of that is that the majority of my students and collaborators have already a paper published, a patent filed or an oral presentation in international conference given.

Advised students	Period	Topic	Level	Publications/ Patents
Hanen Amel (internal CEA funding)	Jun10-Oct10	Microstructural resolved modeling of water transfer in PEMFC CL (Pore Network Approach)	MSc. *(MR2)*	Expected
Julien Letemplier (internal CEA funding)	Jun10-Oct10	Modeling of PEMFC materials aging	MSc. *(MR1)*	Expected
Randa Bouchmila (internal CEA funding)	Jun09-Jui10	Multi-scale modeling of the ORR activity properties and aging phenomena of nano and microstructured electrodes for PEMFC applications.	Chemical Engineering student (3rd year) at CPE Lyon (*année de césure école d'ingénieur*)	✓ 1 presentation in international conferences ✓ 2 patents
Sylvain Passot (internal CEA funding)	Sep07-Aug08	Multi-scale modeling of Pt_xCo_y catalysts aging in PEMFC	Chemical Engineering student (3rd year) at CPE Lyon (*année de césure école d'ingénieur*)	✓ 7 presentations in international conferences ✓ 3 publications in international journals
Magalie Guinard (internal CEA funding)	Mar08-Aug08	Multi-scale modeling of PEMFC anode CO poisoning: impact on performance and durability.	MSc. *(MR2)*	✓ 8 presentations in international conferences ✓ 2 publications in international journals ✓ 1 patent
Mathias Gerard (internal CEA funding)	Mar07-Sep07	Multi-scale modeling of carbon catalyst-support corrosion in PEMFC.	MSc. *(MR2)*	✓ 6 presentations in international conferences ✓ 2 publications in international journals ✓ 1 patent
Laurent Brochard (internal CEA funding)	Apr06-Aug06	Multi-scale Modeling of Transfers in PEMFC.	Student (3rd year) at Ecole Polytechnique (*stage en enterprise)*	---
Moussa Tembely (internal CEA funding)	Mar06-Sep06	Multi-scale Modeling of Pt-Catalyst Degradation in PEMFC Environments.	MSc. *(MR2)*	✓ 4 presentations in international conferences ✓ 2 publications in international journals

Table I-1: Advised engineering and Master Science students.

Advised PhD students	Period	Topic	External collaborations	Publications/ Patents
? (DLR/CEA co-funding)	Sep10-Aug13	Modeling and experimental anaylisis of PEMFC aging	German Aerospace Center (DLR-Stuttgart)	Expected
Ana Balan (internal CEA funding)	Sep10-Aug13	Multi-scale modeling of PEMFC aging	---	Expected
Luiz Fernando Oliveira Lopes (internal CEA funding)	Oct09-Sep12	Multi-scale modeling of physicochemical phenomena in PEM-water electrolysers.	Laboratory of Automatics and Chemical Engineering (LAGEP) (CNRS, University Lyon 1)	✓ 1 publication in international journals (in preparation)
Sylvain Passot (Air Liquide-Axane Fuel Cells/CEA co-funding)	Oct09-Sep12	Impact of pollutants mixtures on the PEMFC performance: experimental and modeling approach	Air Liquide-Axane Fuel Cells	✓ 1 publication in international journals (in preparation)
Daiane Damasceno Borges (internal CEA funding)	Sep09-Aug12	Multi-scale modeling of the role of Nafion® in the charge transport properties of PEMFC electrodes	CEA/INAC (Dr. Gerard Gebel's group)	✓ 1 publication in international journals (in preparation)
Romain Coulon (CEA/DLR co-funding)	Feb09-Jan12	Multi-scale Modeling of the Nafion® Membrane Degradation under PEMFC Automotive Operating Conditions	German Aerospace Center (DLR-Stuttgart)	✓ 4 presentations in international conferences ✓ 3 publications in international journals
Seng-Kian Cheah (Direction of Militar Applications of France)	Nov08-Oct11	Investigation of H_2 pollutants impact on PEMFC nanomaterials performance and degradation	Institute of Catalysis of Lyon (IRCE Lyon, France)	✓ 4 presentations in international conferences ✓ 3 publications in international journals
Rodrigo Ferreira de Morais (internal CEA funding)	Oct08-Sep11	*Ab initio*-based kinetic modeling of the HOR and ORR reactivity properties of Pt and Pt_xNi_y nanoparticules for PEMFC applications	Ecole Normale Superieure de Lyon, Laboratory of Chemistry (ENS, France)	✓ 5 presentations in international conferences ✓ 4 publications in international journals
Guillaume Krosnicki (KSU funding)	Oct08-Sep11	Development and Electrochemical Characterization of Fullerene-based Nanomaterials as Electrocatalysts in PEMFC	University of Strasbourg (LCMOPS, France)	✓ 2 publications in international journals ✓ 3 patents
Federico Nores Pondal (CNEA-CEA funding)	Mar08-Dec08	Preparation and electrochemical testing of magnetized MEA for enhanced ORR.	CNEA, Argentina	✓ 2 patents

Table I-2: Advised PhD students.

Advised postdoctoral researchers	Period	Topic	External collaborations	Publications/ Patents
?	Sep10-Aug11	Multi-scale Modeling of the HER Electrocatalytic Properties of Ni-N-based Bio-inspired Molecules as Cathodic Materials for Photosensitive Electrolyzers.	CEA/INAC and CEA-Life Science Division (DSV)	Expected
Dr. Slimane Laref (CEA Nanosciences Program funding)	Sep10-Aug11	Multi-scale Modeling of Li-Ion Batteries	University of Montpellier (France)	Expected
Dr. Ali Kachmar (Nissan Motor Co. and CEA co-funding)	Mar10-Feb11	Understanding the role of Nafion® on the PEMFC ORR	Nissan Motor Co. and NRC-IFCI (Vancouver, Canada)	Expected
Dr. Ali Kachmar (CEA Nanosciences Program funding)	Jan09-Feb10	Multi-scale Modeling of the HER Electrocatalytic Properties of Ni-N-based Bio-inspired Molecules as Cathodic Materials for Photosensitive Electrolyzers.	CEA/INAC and CEA-Life Science Division (DSV)	✓ 1 presentation in international conferences ✓ 2 publications in international journals ✓ 1 patent
Dr. Margaret A. Gabriel (CEA Nanosciences Program funding)	Oct08-Mar10	Multi-scale Modeling of the ORR Electrocatalytic Properties of Metallofullerenes as Cathodic Materials for PEMFC	CEA/INAC	✓ 2 presentations in international conferences ✓ 3 publications in international journals ✓ 3 patents

Table I-3: Advised postdoctoral researchers.

I.4c – Other scientific collaborations

From my PhD time until nowadays, I developed several scientific collaborations with several high level researchers at the national and international level. Some of them have been originated from projects and some other ones from networking in scientific meetings and conferences. Some of these collaborations induced bilateral project contracts. These collaborations are supported on strong complementarities within the field of PEMFC electrocatalysis and degradation. Within the context of some of them I could realize some scientific stays in worldwide recognized institutes. The list (non-exhaustive) of my ongoing scientific collaborations, outside the projects partners' punctual actions listed in Section I.4a, includes:

- **National Research Council of Canada (NRC) – Institute for Fuel Cell Innovation (IFCI) (Vancouver, Canada)**
  - ✓ **Context:** scientific collaborative research CEA-NRC agreement.
  - ✓ **Details:** a collaborative work is ongoing to develop a modeling approach allowing predicting simultaneously performance degradation and changes in the mesostructure of the MEA (CGMD and multi-scale kinetic simulations). In 2008 I visited the IFCI and gave and invited seminar. For the period June-July 2009 I hosted Dr. Kourosh Malek in my laboratory (summer scientific visiting position), and in last May 2010 I was hosted by Dr. Malek in NRC. Until today, this collaboration produced 2 presentations in international conferences and 1 paper submitted to an international journal (see Appendix I).

- ***Deutsches Zentrum für Luft- und Raumfahrt e.V.*** **(DLR) (Stuttgart, Germany)**
  - ✓ **Context:** joint PhD thesis student Romain Coulon
  - ✓ **Details:** from 2006 I am collaborating with Dr. Wolfgang Bessler on the topic of elementary kinetics modeling. From beginning 2009 we are co-advising a PhD thesis now ongoing at CEA-Grenoble (Romain Coulon) on the subject "Microstructural-resolved modeling of the PEMFC membrane degradation".

- ***Comision Nacional de Energia Atomica*** **(CNEA),** ***Centro Atomico Constituyentes*** **(CAC) (Buenos Aires, Argentina)**
  - ✓ **Context:** - - -
  - ✓ **Details:** I have an ongoing informal collaboration in the topic of electrochemistry and thermodynamic properties of PEMs with Prof. Horacio Corti who is the director of the Chemistry Department of the CNEA/CAC. Prof. Corti invited me to give oral presentations of our approach in two Iberoamerican conferences occurred in Argentina (2006 and 2007, see Appendix I). Federico Nores Pondal, PhD student in the group of Prof. Corti, worked with me in 2008 at the CEA/LCPEM on my magnetic patent for 8 months (cf. Table I.2).

- ***Ecole Normale Supérieure de Lyon*** **(ENS-Lyon) (Lyon, France)**
  - ✓ **Context:** PhD thesis student Rodrigo Ferreira de Morais
  - ✓ **Details:** Prof. Philippe Sautet and Dr. David Loffreda co-advise with me an ongoing PhD thesis at CEA-Grenoble (Rodrigo Ferreira de Morais) on the subject

"Ab initio-based kinetic modeling of the reactivity properties of Pt_xNi_y nanoparticules for PEMFC applications". They provide us a strong advice and help on the DFT technique and catalysis fundamentals.

- ***Institut de Recherche sur la Catalyse et l'Environnement de Lyon*** (**IRCELyon) (Lyon, France)**
  - ✓ **Context:** PhD thesis student Seng-Kian Cheah
  - ✓ **Details:** Together with the head of my laboratory, Dr. Olivier Lemaire, I am co-advising with Prof. Patrick Gélin an ongoing PhD thesis at CEA-Grenoble (Seng-Kian Cheah) on the subject "Investigation of H_2 pollutants impact on PEMFC nanomaterials performance and degradation". I was also working with Prof. Gélin within the context of the POLIMPAC project, who carried out useful Fourier Transformed. InfraRed spectroscopy (FTIR) and Mass Spectrometry analyses of the adsorption properties of different pollutants (e.g. CO) on nano-structured metallic electrocatalysts (e.g. Pt nanoparticles supported on Carbon Black -CB-). These experimental studies allow validating some detailed mechanisms implemented in MEMEPhys®.

- **Air Liquide / Axane Fuel Cells**
  - ✓ **Context:** joint PhD thesis student Sylvain Passot
  - ✓ **Details:** we are collaborating in the topic of PEMFC anode and cathode contamination and co-advising the PhD thesis of Sylvain Passot.

- ***Institut de Physique et de Chimie des Materiaux de Strasbourg*** **(Strasbourg, France)**
  - ✓ **Context:** PhD thesis student Guillaume Krosnicki
  - ✓ **Details:** I am collaborating with Prof. Delphine Felder Flesch within the context of Guillaume Krosnicki's PhD thesis. We work together on the design and preparation (e.g. via chemical synthesis) of C_{60}-based catalysts and catalyst-supports for PEMFC applications.

- ***Université de Montpellier* (Montpellier, France)**
  - ✓ **Context:** postdoctoral researcher Slimane Laref
  - ✓ **Details:** I am now collaborating with Prof. Marie-Liesse Doublet on the topic of multi-scale modeling of Li-ion batteries, from atomistic to the cell level. We are in particular interested on the development of a mechanistic understanding of aging mechanisms and on the adaptation of MEMEPhys® to these systems. I will co-advise the postdoctoral position of Dr. Slimane Laref with her.

- ***Laboratoire d'Automatique et de Génie de Procédés* (LAGEP) (Lyon, France)**
  - ✓ **Context:** PhD thesis student Luiz Fernando Oliveira Lopes
  - ✓ **Details:** this collaboration continues after my PhD thesis at CEA (January 2003 – November 2005) co-supervised by Prof. Christian Jallut and Prof. Bernhard Maschke from the *Laboratoire d'Automatique et de Génie de Procédés* (LAGEP) (UMR 5007). Prof. Jallut is now the PhD advisor of Luiz Fernando in the field of multi-scale modeling of PEM-WE.

- **CEA-Grenoble/INAC (Grenoble, France)**
  - ✓ **Context:** internal collaboration
  - ✓ **Details:** I am collaborating with Dr. Thierry Deutsch in the topic of High Performance Computing (HPC). We were jointly supervising one postdoctoral researcher work at CEA-Grenoble: Dr. Margaret Gabriel on the subject "Multi-scale modeling of electrochemical processes in fullerene-based nanoobjects for PEMFC applications". Together with Dr. Pascale Maldivi and Dr. Valentina Vetere, I have co-supervised Dr. Ali Kachmar, postdoctoral researcher, on the subject "Multi-scale modeling of the reactivity properties of bio-inspired catalysts for PEMFC and PEM-WE applications". Furthermore, I am collaborating with Dr. Gerard Gebel from the CEA/INAC on the topic of Nafion® membranes.

- **CEA-Grenoble/*Direction des Sciences du Vivant* (Grenoble, France)**
  - ✓ **Context:** CEA Nanosciences program
  - ✓ **Details:** I am collaborating with Dr. Vincent Artero on the fundamental understanding of the mechanisms behind bio-inspired-based electrocatalysis for low-temperature H_2 production (hydrogenases). Jointly with CEA/INAC (see

previous item), I was supervising a postdoctoral researcher (Dr. Ali Kachmar) on the subject “DFT-based multi-scale kinetic modeling of the PNP molecules electroactivity towards the HOR and proton reduction for hydrogen production”. A second postdoctoral researcher will continue this work starting in the incoming months.

- **CEA-Grenoble/LETI/*Département microTechnologies pour la Biologie et la Santé* (Grenoble, France)**
  - ✓ **Context:** internal collaboration
  - ✓ **Details:** I am collaborating with Dr. Pascale Pham within the context of a research focused on the modeling of electrochemical processes inside the human brain (CNT-based micro-electrodes for the *in situ* treatment of the Parkinson’s disease). I have been invited to take part of a working group focused on the understanding of the “electrochemical double layer effects in biological systems”. The nano-scale interfacial theory within MEMEPhys® has been remarkably adapted to their case and used to model the temporal behavior of the CNT-based electrodes in relation with experimental EIS interpretation.

Some other past and ongoing interactions include Peugeot-Citroên SA. (PEMFC degradation), Stanford University (multi-scale modeling methods for fuel cells -Prof. Heinz Pitsch’s group, Department of Mechanical Engineering-: in 2007 I did a short visiting position in Prof. Pitsch’s group to work in fuel cells electrocatalysis issues and I gave two invited seminars in Stanford Campus), Massachusetts Institute of Technology (USA) (modeling of electrochemical interfaces -Prof. Martin Bazant, Department of Mathematics-: from this collaboration I published a joint paper with Prof. Bazant and Dr. Maarteen Biesheuvel -Wageningen University, The Netherlands- on the modeling of steric effects in PEMFC diffuse layers).

Furthermore, I have also triggered transversal collaborations between different laboratories in France. One example is the collaboration developed between CEA/INAC and CEA/LITEN on the context of development of nano-structured fuel cell catalysts by using “nano-aggregates sources” (see Chapter III). Another example is a possibly incoming collaboration between the ENS Lyon and the CEA/INAC within the context of HPC for PEMFC electrocatalysis.

I.4d – Scientific responsibilities

At the CEA internal level,

- ✓ from January 2009 I became the responsible of the PEMFC Modeling activities of my laboratory LCPEM. The group is nowadays constituted of 4 permanent researchers-engineers and 15 students and postdoctoral researchers (Figure I.16). The group has a recognized expertise in electrocatalysis, CL, PEM and GDL degradation, water/charge/reactants transport in the CL, PEM and GDL and thermal and mechanical stresses. Several models, from the atomistic to the system level scale, have been developed in the last 15 years to respond the particular and general project needs, on standard PEMFC (degradation, bimetallics, pollutants, water transfer, PEM mechanical stress…), PEM-WE and on exotic cells (bio-inspired catalysts, Si-based fuel cells…). The combination of all these competences in a same modeling group is unique in France. From the second semester 2009 we started to work on the modeling of Li-Ion batteries, activity which will increase the number of our staff members (+ 1 permanent + 2 postdoctoral researchers) from September 2010. In practice I have in charge the management of the scientific computing resources for our laboratory, and the coordination of our modeling activities. Within this context, I am in charge of organizing a scientific prospective of our ongoing actions, to improve our scientific production and reactivity towards the projects and our hierarchy requirements, through regular meetings and seminars where each member present the progress on his work or address general topics in the field of fuel cells modeling. I am also in charge of following that the scientific production is in agreement with the LITEN Quality rules (intellectual property protection of software developed, user/developer manuals of in-house software, copy-protected storage of simulation results…) and of the reporting to the head of my laboratory and to the head of my department.

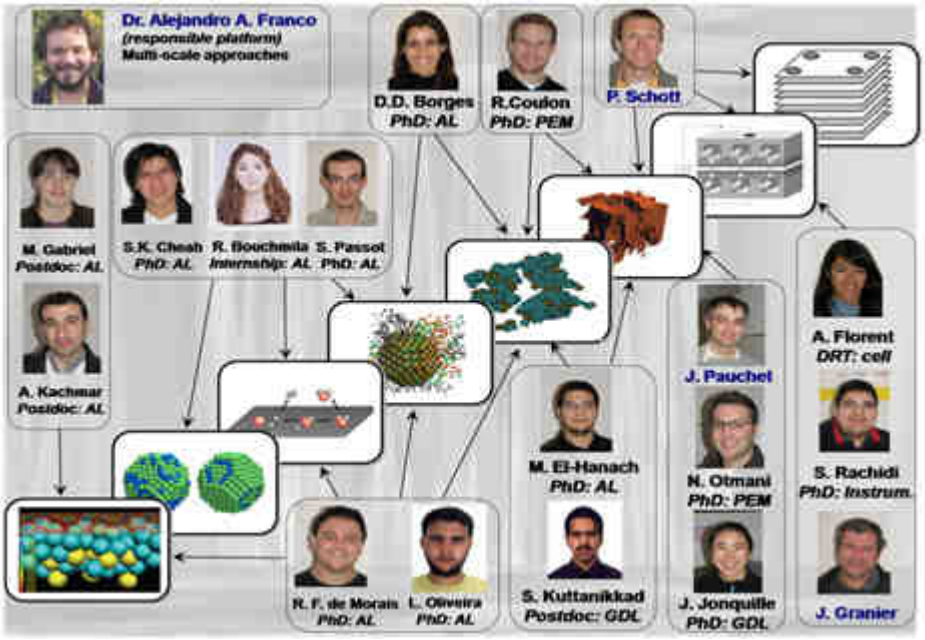

Figure I-16: My LCPEM modeling group as in spring 2010.

- ✓ From 2007, I am part of the CEA "Nanocatalysis working group" dedicated to propose new research topics on the field of physical electrochemistry and develop transversal collaboration between the different CEA laboratories. Within this context, I have written a full report, internally communicated at CEA, reviewing the state-of-the-art of the developments in the field of nanomaterials electrochemical behavior in PEMFC environments, and suggesting novel scientific approaches (combining experiments and multi-scale modeling) to help CEA to be among the international leaders in the subject of fuel cells and electrochemical systems for energy.
- ✓ In 2009, I has been nominated "CEA expert" on the field of physical electrochemistry, nanosciences and PEMFC modeling, a kind of internal recognition for my research achievements.
- ✓ I pursue my contribution to the CEA Grenoble program "La Recherche fait Ecole", always in charge of the presentations on fuel cells and hydrogen-related technologies (Figure II.17).

Figure I-17: My participation in the CEA Grenoble program "La Recherche fait Ecole".

At the national level,

- ✓ I am member of the project reviewer committee of the P-NANO program (topic: nano-sciences) from the National Research Agency. Within this context, I use to evaluate project proposals submitted every year to this program call for proposals.

At the international level, I have nowadays several scientific responsibilities:

- ✓ Firstly, I am member of the reviewer staff in several international journals of electrochemistry. Up to present I reviewed 104 papers submitted for publication in the following journals: "*Solid State Ionics*", "*Fuel Cells: from fundamentals to systems*", "*Electrochimica Acta*", "*Journal of the Electrochemical Society", "Journal of Solid State Electrochemistry", "International Journal of Hydrogen Energy", "Mathematical and Computer Modeling od Dynamical Systems", "Industrial & Engineering Chemistry Research", "Electrochemistry Communications", "Thin Films" and "Journal of Power Sources".*
- ✓ In late 2008 the publisher Pan Stanford [9] invited me to edit a book on the topic of PEMFC degradation R&D. This book is entitled *Polymer Electrolyte Fuel Cells: Science, Applications and Challenges*. This book focuses on the recent research progresses on the fundamentals understanding of the materials degradation phenomena in PEMFC, for automotive applications. The key features of this book are:

- it discusses great potential of fuel cells for automotive applications as well as the technological challenges for their widespread commercialization On a multidisciplinary basis, this book provides a complete and comprehensive critical review on crucial scientific topics related to PEMFC materials degradation, and ensures a strong complementary between experimental and theoretical analysis (experimental accelerated aging methods in *ex situ* and *in situ* conditions, stability properties of nanoparticles, structural and physicochemical characterization methods of degradation, detailed theoretical modeling, elementary mechanisms, nano-electrocatalysts and carbon support behavior under realistic operation conditions...) and preparation techniques (technologies of nano-electro-catalysts, membranes and carbon support elaboration…) with several practical applications for both the research and the industry communities;
- Includes contributions by leading authors in the field written with the student in mind comprising of a good balance of theoretical and experimental chapters. The book includes 15 Chapters prepared by internationally recognized researchers worldwide representing key research institutes, universities and industrials in the field of PEMFC R&D and physical electrochemistry such as Johnson Matthey Technology Centre (UK), National Research Council (Canada), Peugeot Citroen SA (France), Nissan Motor Co. (Japan), Instituto de Quimica de Sao Carlos (Brazil), Argonne National Laboratory (USA), Georgia Technology Institute (USA), Technical University of Gratz (Austria), Queen's University (Canada), Universitat Politecnica de Barcelona (Spain), Universidad de Alicante (Spain) and CEA-Grenoble (France) (see the book plan in Appendix I).
- Includes an extensive bibliography for further reading.

The audience for this book is Engineers, researchers (from both industry and academics) and students on physicochemistry, electrochemistry and material science. The delivery date for the full book is October 31st 2010.

✓ I am Active Member of two international societies of electrochemistry: the American Electrochemical Society (ECS) and the International Society of Electrochemistry (ISE). Within this context I am for example solicited for the organization of the ECS and ISE conferences (see below).

- ✓ Until now, I co-chaired two international conferences on fuel cells nanomaterials (*Nanoenergy Conference* -Paris 2008- and *International Symposium on Physical Modeling and Simulation of Electrochemical Processes in Fuel Cells and Experimental Validation* -Karlsruhe 2009-) and I has been part of the advisory committee (see Appendix I).
- ✓ I am the Corresponding Organizer of the incoming *International Symposium on Physical Modeling of Electrochemical Processes in Fuel Cells and Experimental Validation* which will take place as a part of the *61st Meeting of the International Society of Electrochemistry* (Nice, September 26th-October 1st 2010):
    - this symposium will focus on fundamental understanding of the electrochemical mechanisms and the physical modeling of structure and properties of complex media in fuel cells, including (but not restricted to) Polymer Electrolyte (PEMFC) and Solid Oxide (SOFC) fuel cells. In particular, the symposium emphasizes the relevant physico-chemical and electrochemical processes, as well as non-linear operation of the cell as a whole. This Symposium is extended to PEM-WE modeling. Organized through several sessions, we are soliciting contributions on modeling-based diagnostics, and advanced design of materials and cells that will provide a balanced topical view on recent progress and the pertinent challenges. The outmost premises are that fuel cells could be markedly improved, in spite of proven demonstrations of fuel cell powered vehicles and devices in recent years. Topics will include:
        - o fundamentals of electrocatalytic phenomena in fuel cell environments: elementary pathways, double-layer and solvation effects
        - o nanostructure-activity-stability relationships and influence of the electrocatalyst support and the electrolyte
        - o prediction of experimental observables (e.g. CV, EIS...) from atomic-scale and relevant elementary kinetic modeling
        - o modeling-based prediction of fuel cell components transport properties: water, reactants and charge transfers in electrode, diffusion and electrolyte media
        - o modeling of materials degradation phenomena (e.g. catalyst support corrosion, catalyst oxidation/ripening, membrane degradation...)
        - o modeling of materials thermo-mechanical stresses

- modeling of materials poisoning (e.g. PEMFC catalyst CO poisoning...) and extreme working conditions (e.g. PEMFC cold start...)
- electrode and cell level modeling: transport and transfer phenomena, electrode performance and durability optimization
- stack and system level modeling: mass and heat transfer, design optimization
- system dynamics and control approaches : non-linear behavior of fuel cell potential
- nano-meso scale statistical computational methods of fuel cell materials including DFT, MD, CGMD and meso-dynamics
- mean-field (MF) and Monte-Carlo (MC) methods
- Computational Fluid Dynamics (CFD) methods
- Direct Numerical Simulation (DNS) methods
- multi-scale methods: hybrid Monte-Carlo-CFD, model reduction and upscaling techniques
- contributions on experimental validation techniques: *in situ* chemical, electrical and microstructural characterization, imaging techniques and spectroelectrochemistry, model experiments for determination of model parameters

- The symposium is organized through several plenary lectures (40 minutes) and invited presentations (20 minutes) to be given by internationally recognized researchers; as well as through contributed oral presentations (20 minutes) and poster communications. The program will be published online in the incoming weeks.

✓ I am co-organizer with colleagues from Imperial College of London (UK), University of California Berkeley (USA) and Yamanashi University (Japan) of the incoming *International Symposium on Fuel Cells: materials, properties and mechanisms,* which will take place as a part of the *62nd Meeting of the International Society of Electrochemistry* (Niigata, Japan, September 11th- 16th 2010).

✓ I am contributing in the CEA/LCPEM working group involved in the ISO committee for the definition of the pollutants tolerance norms in PEMFC.

Figure I-18: Nice and Niigata ISE meetings brochures.

I.4e – Scientific production

I participated as a regular and invited speaker (plenary, semi-plenary and key lectures) in numerous international conferences and workshops (*Electrochemical Society Meetings*, *International Society of Electrochemistry Meetings*, *Congresses of the International Society of Theoretical Chemical Physics*, *PEFC Durability and Performance Conferences*, *International Society for Solid State Ionics meetings*, international workshops on PEMFC degradation and modeling…) all around the world (Bertinoro 2003, Spa 2004, Santorini 2004, Lucerne 2005, Baden-Baden 2005, Québec 2005, Barcelona 2006, Vienna 2006 and 2009, Lyon 2006, Buenos Aires 2006, Chicago 2007, Palo Alto 2007, Miami 2007, Zurich 2008, Phoenix 2008, Vancouver 2008 and 2010, Seville 2008, Ulm 2008, Torino 2008, San Francisco 2009, Santa Barbara 2009, New York 2010…). I gave also invited lectures in several national conferences and workshops (organized by the *Société Française de Chimie and the Société Française de Physique*), as the plenary lecture I will give in the incoming *Journées de la Matière Condensée* (Troyes, France, August 2010) on the role of Nanosciences in PEMFC technology development (see Appendix I).

Moreover, I gave invited seminars in some high level institutes in foreign countries, including Heidelberg University (2006), Stanford University (2007 and 2009), National Research Council of Canada (2008 and 2010), University of California Santa Barbara (2009), University of New York (2010) (Figure I.19) (see my detailed CV in Appendix I).

Figure I-19: One of my presentations (NRC-IFCI, Vancouver, Canada, 2010).

Furthermore, I gave an invited 3-hours presentation of my whole work to the High Commissioner of CEA, Prof. Bernard Bigot at CEA-Saclay in July 2008. It was an honour for me to present him my work and I really appreciated his kindness and support to develop my group.

Furthermore, at beginning 2010, I have been invited to write two book chapters:

- a Chapter on the topic "PEMFC degradation modeling and analysis" in the book *Polymer electrolyte membrane and direct methanol fuel cell technology (PEMFCs and DMFCs) - Volume 1: Fundamentals and performance*, edited by Dr Christoph Hartnig (BASF Fuel Cell GmbH) and Dr-Ing. Christina Roth (Technische Universität Darmstad), to be published in Woodhead (Cambridge, UK). This Chapter is being to be delivered in Summer 2010.
- a Chapter on the topic of "Modeling of Direct Alcohol Fuel Cells" in the book *Direct Alcohol Fuel Cells Technologies: research and development*, being edited by Prof. Ernesto Gonzalez (Instituto de Quimica de Sao Carlos, Brazil) and Prof. Horacio Corti (CNEA, Argentina), to be published in Springer. The Chapter will be delivered in spring 2011.

Finally, I am author of several scientific papers in international journals and conference proceedings and of several patents, and my work on degradation modeling is now being internationally recognized through several citations in papers appeared in international journals and proceedings (see my detailed CV in Appendix I).

I.5 – My future plans

My short-term career perspective consists in continue coordinating the LCPEM Modeling activities, offering a scientific framework ensuring a high level scientific production, in the field of modeling, and a high reactivity towards the projects and hierarchy requirements. Within this context, a new permanent researcher has been recruited to reinforce my group from September 2010 and to help me on the adaptation of my model MEMEPhys® for Li-ion batteries. I am expecting a real team work on this.
Furthermore, I would like to continue my scientific collaborations all around the world and developing new ones with both academics and industrials. At mean/long term, I would like to do a 1-year scientific stay in a foreign country, maybe in North America, Canada or USA.

From a technical viewpoint I am planning to continue developing my multi-scale modeling approach in general, through different projects (some of them as main coordinator), collaborations and by advising students. My objective is continuing having high scientific (publications, conferences) and patents productions. Generally speaking, I want to continue being very active into the field of multi-scale modeling of electrochemical systems and nano-sciences, and into international committees of experts (e.g. through the edition of books and reviews, conferences organizations…).
More at long term, based on the scientific excellence, I would like to evolve in my CEA career, and continue contributing into the international recognition of our laboratories.
Personally speaking, I do not exclude the possibility of coming back to Argentina at long-term. My education basis has been constituted by my country and I would reward that in the future.

CHAPTER II

Electrocatalysis and aging phenomena in PEMFC

"Common sense is the collection of prejudices acquired by age eighteen."

Albert Einstein, German born American Physicist, 1879-1955.

II.1 – From the "Gas battery" controversy to the modern PEM Fuel Cells

Despite their modern high-tech aura, fuel cells actually have been known to science for more than 150 years. Though generally considered a curiosity in the 1800s, fuel cells became the subject of intense research and development during the 1900s.

William Grove (1811 -1896), a Welsh judge, inventor and physicist, developed an improved "wet-cell battery" in 1838 [10] which used a platinum electrode immersed in nitric acid and a zinc electrode in zinc sulfate to generate about 12 Amps of current at about 1.8 Volts. Based on this work, Grove discovered that by arranging two platinum electrodes with one end of each immersed in a container of sulfuric acid and the other ends separately sealed in containers of oxygen and hydrogen, a constant current would flow between the electrodes. The sealed containers held water as well as the gases, and he noted that the water level rose in both tubes as the current flowed.

In 1800, British scientists William Nicholson and Anthony Carlisle had described the process of using electricity to decompose water into hydrogen and oxygen (electrolysis). But combining the gases to produce electricity and water was, according to Grove, "a step further that any hitherto recorded." Grove realized that by combining several sets of these electrodes in a series circuit he might "effect the decomposition of water by means of its composition." He soon accomplished this feat with the device he named a "gas battery", the first fuel cell [11].

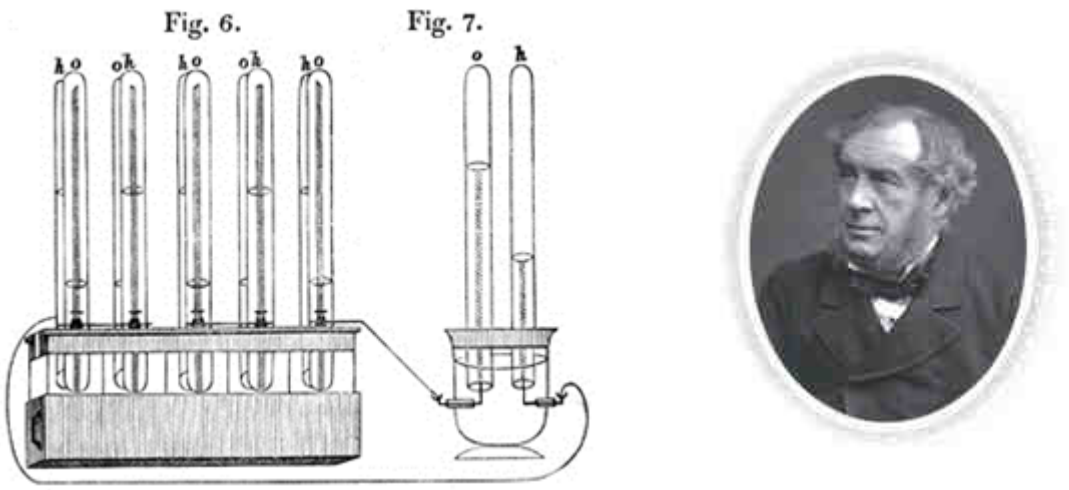

Figure II.1: William Grove's drawing of his "Gas Battery" or first fuel cell in 1843 (Source: [11]).

After some controversy generated by some contemporary researchers (e.g. Christian Schönbein (1799-1868) who believed that the gas battery oxygen did not contribute to the production of current, but that it was produced by the combination of hydrogen with water), Grove provided strong experimental evidence that producing current required both hydrogen and oxygen [11]. However, he also raised questions about the detailed mechanisms behind the production of heat and "novel gaseous and liquid products", questions that he could not answer with the equipment and theory available to him. We should recall that when Grove unveiled his gas battery, the scientific community was still struggling to understand the basic principles of chemistry and electricity, matter and energy. The laws of thermodynamics were still being refined, the electron was yet to be discovered, and theories to explain the nature of matter and energy abounded. In this scientific climate, the gas battery was both an enigma and a source of passionate arguments. For example, among the available theories at that moment, the so-called "contact theory" of Alessandro Volta (1745 - 1827) introduced to refute Galvani's notion of a special electricity intrinsic to animals, supposed that the mere contact between different conductors (especially metals) was able "to set the electric fluid in motion" [12]. A rival "chemical theory" supposed that a chemical reaction generated the electricity [13].

One of the major founders of the modern physical chemistry, Wilhelm Ostwald (1853-1932), described Grove's gas battery as "of no practical importance but quite significant for its theoretical interest" [14]. In his book *Electrochemistry: History and Theory*, published in 1896, Ostwald wrote,

> *"It was a puzzle [...] how gases separated by a thick layer of liquid were able to combine with the help of the catalytic power of platinum [...] The process of representing natural phenomena as mechanical ones had been completely mastered by the science of that time.*

Even today it is generally valid as an undoubted postulate. But we are now finding that one cannot achieve a proper representation of reality in this way. This is a point where science begins to follow another path. This is the formation of appropriate new concepts and the corresponding training in the capacity to conceive a correlation between phenomena that would not have been possible on the mechanical model.... The mechanical view of reality is being replaced in our time by concepts of energy."

At the end of his book, Ostwald solved "the puzzle of Grove's gas battery" and wrote,

"The answer is contained in the fact that oxidizing agents are always substances that form negative ions or make positive ions disappear; the reverse is true of reducing agents.... Oxygen and hydrogen are nothing more than oxidizing and reducing agents."

The gas battery in the 19th century spurred research and the testing of theories. While the understanding of the basic science improved, no practical device emerged despite several attempts. Scientists and engineers soon learned that they would have to overcome many hurdles if this new technology was to be commercialized. By the end of the 19th century, the internal combustion engine was emerging and the widespread exploitation of fossil fuels sent the fuel cells in the way of “scientific curiosity”.

The chemist Ludwig Mond (1839 -1909) spent most of his career developing industrial chemical technology such as soda manufacturing and nickel refining. In 1889, Mond and his assistant Carl Langer described their experiments with a fuel cell using air and industrial coal gas [15]. They attained 0.6 Amps.m^{-2} (vs. surface area of the electrode) at 0.73 Volts. Mond and Langer's cell used electrodes of thin, perforated platinum. They were the first researchers to introduce the term “fuel cell”.

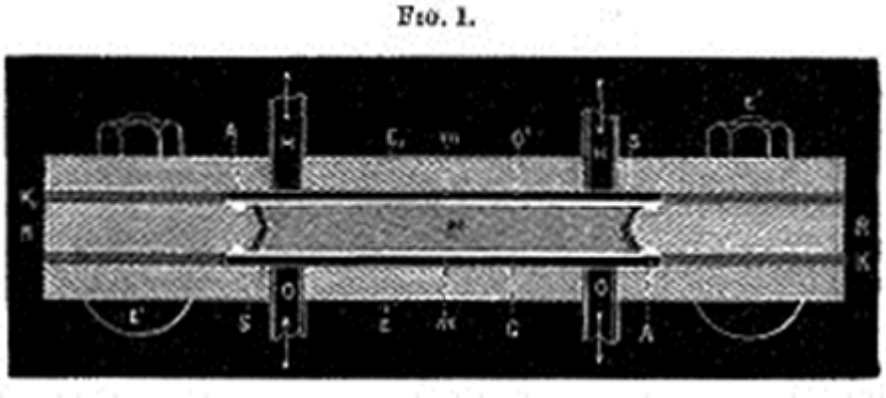

Figure II.2: Fuel Cell design by Ludwig Mond and Carl Langer in 1889 (Source: [15]).

At the same time, Charles Alder Wright (1844–1894) developed a similar fuel cell, and his publication gives an idea of the limitations of those times in terms of the “leakage of gasses

from one chamber to another", and from the "infinitesimal currents generated" [16]; even with considerable amount of platinum, he concluded that it would cost too much to be practical. The French team of Louis Paul Cailleteton (1832-1913) came to the same conclusion in 1894. In describing their improved Grove cell they noted that "only precious metals" would work and so deemed the process impractical [17].

Emil Baur (1873 -1944) of Switzerland conducted wide-ranging research into different types of fuel cells during the first half of the twentieth century. Baur's work included high temperature devices (using molten silver as an electrolyte) and a unit that used a solid electrolyte of clay and metal oxides [18]. In the 1940s, other researchers added monazite sand to a mix of sodium carbonate, tungsten trioxide, and soda glass "in order to increase the conductivity and mechanical strength" of his electrolyte [17]. Many of the designs during this period experienced unwanted chemical reactions, short life ratings, and disappointing power output. However, the work of Baur and others on high-temperature devices paved the way for both the Molten Carbonate Fuel Cells (MCFC) and SOFC devices of today [19,20].

To a certain extent, fuel cells remained a solution in search of a problem. As Europe plunged toward the Second World War, the problem suggested itself to the British Francis Bacon (1904 -1992) who in 1932 began his research into fuel cells. Early cell designers used porous platinum electrodes and sulfuric acid as the electrolyte bath. Using platinum was expensive and using sulfuric acid was corrosive. Bacon improved on the expensive platinum catalysts with a hydrogen and oxygen cell using a less corrosive alkaline electrolyte (potassium hydroxide (KOH)) and inexpensive nickel electrodes. It took Bacon until 1959 to perfect his design, when he demonstrated a fuel cell producing 5 kW of power, enough to power a welding machine or to be integrated into the Royal Navy submarines [21].

In 1955, Willard Grubb, a scientist working at the company *General Electric*, made a major advance in acidic fuel cells using liquid electrolytes: he developed the first proton-conducting polymer electrolyte: a sulphonated polystyrene ion-exchange membrane. In 1958, Leonard Niedrach, another *General Electric* chemist, designed a way of depositing platinum onto this membrane. The improvements made through the combined efforts of Grubb and Niedrach ultimately produced in 1959 the "Grubb-Niedrach cell" or the first "modern" PEMFC [22].The unit was fueled by hydrogen generated by mixing water and lithium hydride. The cell was compact and portable, but its platinum catalysts were expensive. *General Electric* and NASA developed this technology together resulting in its use on the Gemini space project, constituting the first commercial use of a fuel cell. The main objective of this project was to test the operational durability of fuel cell systems with a view to replacing batteries with fuel cells to provide electric power and drinking water to the crew in the spacecrafts.

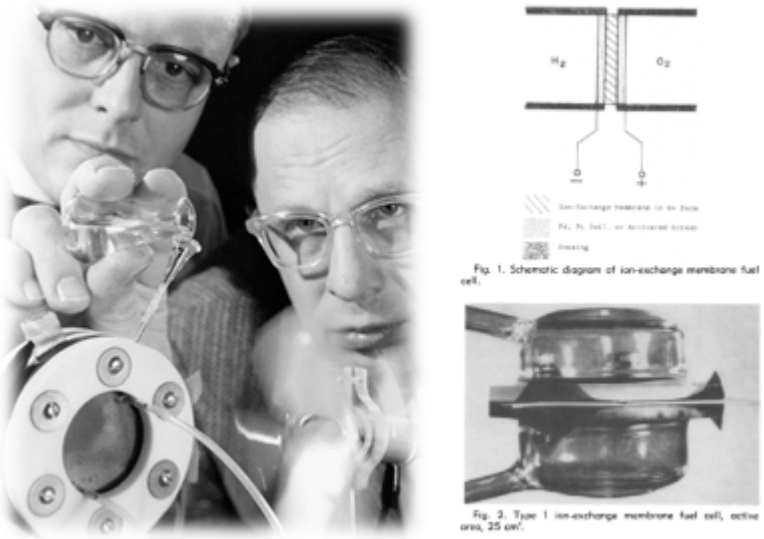

Figure II.3: General Electrics' Thomas Grubb (in the left) and Leonard Niedrach (in the right) run a fan with a diesel powered PEMFC in April 1963; Right: their fuel cell design (Source: [22]).

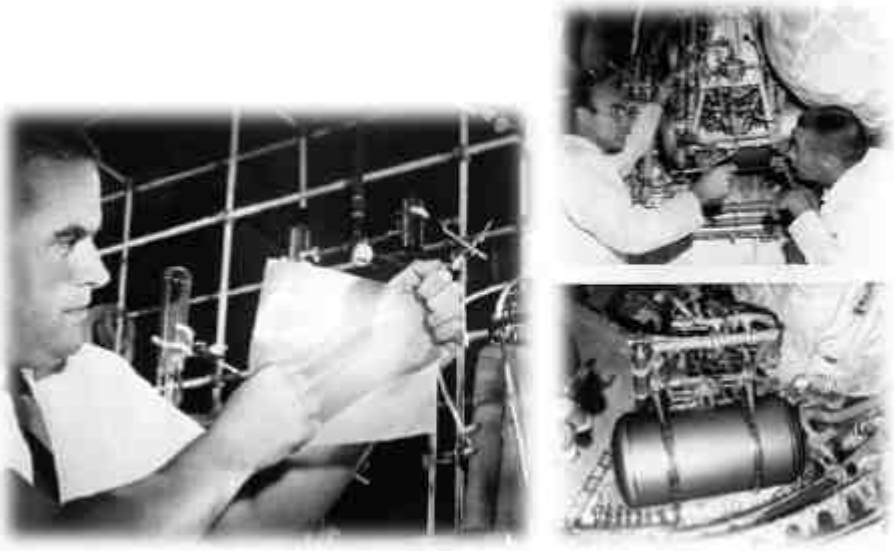

Figure II.4: A General Electric's researcher with a polymer electrolyte in 1965 (left); PEMFC in the Gemini space program (right).

In the same 1959, Harry Ihrig, an engineer for the *Allis Chalmers Manufacturing Company*, demonstrated a 20-horsepower tractor that was the first vehicle ever powered by a fuel cell. The tractor was equipped with 1008 individual Bacon alkaline cells, using propane, generating a total power of 15 kW. Using the same technology, *Allis Chalmers* would go on to create a golf cart, submersible, and fork lift in the early 1960s.

In 1966 *General Motors* demonstrated the first vehicle for urban use powered by a 5 kW Bacon alkaline fuel cell: the GM Electro-Van. The fuel cell was fueled by both super-cooled

liquid hydrogen and liquid oxygen, and had a maximal durability of (only!) 1000 hours. The GM Electro-Van had one large tank for the hydrogen and one for the oxygen and contained 150 metres of piping throughout the rear of the vehicle, turning this 6-seat van into a 2-seater with barely enough room for 2 passengers. The GM Electro-Van top speed was between 100 - 115 $km.h^{-1}$, with autonomy of 200 km. After the GM Electro-Van was built, tested and shown off to journalists in 1966, the project was scrapped largely because of safety reasons (GM experienced an incident with the hydrogen tank which exploded) and because it was cost-prohibitive. According to the journalists at those times, "the platinum used in the fuel cell was enough to buy a whole fleet of vans" and there was absolutely no supporting hydrogen infrastructure in place at that time.

Figure II.5: The first vehicles powered by fuel cells.

In 1965, Walther Grot, a researcher of *Dupont de Nemours* designed a new kind of proton-conducting polymer, which proved to be superior in performance and durability to sulfonated polystyrene of Grubb: the sulfonated tetrafluoroethylene based fluoropolymer-copolymer or Nafion® [23]. Nafion® is a PerFluoroSulfonic Acid (PFSA) and its unique ionic properties are a result of incorporating perfluorovinyl ether groups terminated with sulfonate groups onto a tetrafluoroethylene (Teflon®) backbone. In 1966 this material started to be used in the Gemini space program for a significant number of flights, even if NASA decided to replace the PEMFC by the less expensive Bacon's alkaline fuel cells in the Apollo program and in the space shuttle. Anyway, Nafion® discovery constituted a breakthrough and rapidly became the reference electrolyte material for PEMFCs.

Figure II.6: Walther Grot, the discoverer of Nafion® at Dupont in the 1960s (Source: [23]).

Since the mid-1980s, PEMFC development has included stationary power applications.

The Canadian firm *Ballard Power Systems* launched full-scale PEMFC development in 1983 and in 1987 demonstrated the potential for high power density by incorporating Nafion® membranes in their fuel cells. In 1989, *Ballard Systems* introduced a 5 kW hydrogen and air PEMFC stack, and in 1991 they began operating a 250 kW plant in a military airport in Indiana, USA.

In the late 1980s and early 1990s, some research institutes in USA, such as Los Alamos National Lab and Texas A&M University experimented with ways to reduce the amount of platinum required for PEMFC. Thin-film electrode technology was pioneered initially at Los Alamos National Laboratory to design the first modern PEMFC electrocatalyst layers, composite structures consisting of proton-conducting ionomer material and noble-metal (platinum) catalyst supported on carbon [24, 25, 26]. It was maybe at this point that the global race by the private sector to develop PEMFCs started. The relatively low operating temperatures and short start-up and transient-response times made it possible to achieve compact, high density designs, and it became “economically feasible” to commercialize the cells. Because of these advances, PEMFC developers started eyeing markets that could not be served by other kinds of fuel cells (like Phosphoric Acid Fuel Cells -PAFC-), i.e. automobile, residential, and compact commercial applications.

The Japanese government initiated in 1993 a program for research and development on PEMFCs for use in transportation and commercial applications. The toughening of environmental regulations in North America pressed automobile manufacturers operating in that market to establish long-term environmental strategies, and thus they set about developing fuel-cell vehicles. Notably, the Japanese automobile industry began such development in 1992, and built the first test vehicles in the middle of the 1990s.

In 1994, *Daimler Benz* demonstrated its first NECAR I (New Electric CAR) fuel cell vehicle at a press conference in Ulm, Germany. In 1995, *Ballard Systems* tested PEMFC in buses in Vancouver (Canada) and Chicago (USA) and later in experimental vehicles made by *Daimler Chrysler*. PEMFC have also supplied power to unmanned blimps and to nautical buoys.

The product was developed further by *Ballard Systems* and *Daimler Chrysler* in the late 1990s and the companies achieved a total power output of 75 kW with their *Mark 900 unit*. This signaled that the stack was finally able to meet the performance targets for transportation applications and to nowadays PEMFC technology remains the choice of the automotive industry.

The Japanese firm *Tokyo Gas* started the development of PEMFC systems for residential uses in 1998. Early in 2000, the company *AeroVironment* selected PEMFC technology to provide nighttime power for its solar-powered Helios long-duration aircraft. The goal was to make an unpiloted aircraft that could fly continuously for up to six months by using photovoltaic panels during the day to run electric motors and electrolyze water. At night, the PEMFC was to run the motors by converting the hydrogen and oxygen back into water. Several test flights were made from 2001 to 2003. Iceland opened the first commercial hydrogen station in 2003 as a part of the country initiative to implement a hydrogen economy.

The creation of the Fuel Cells Network (Reseau PACo) by the Ministry for Research in 1999 has furthered the rise of strong partnerships between public and private sector research institutes and fostered the setting up of dedicated PEMFC companies such as Axane (Air Liquide) or Helion Fuel Cells (Areva). In my country, Argentina, H_2 is now being used to produce residential electricity or to directly use mixed with Compressed Natural Gas in demonstration combustion cars. [27].

The last years have seen some major developments in terms of PEMFC technology and the transportation industry (Figure II.7, e.g. of the French firm *Peugeot Citroën*). Several companies have made very public commitments to the development of PEMFC vehicles and most have cars operating on the roads in demonstration programs, and the government of numerous countries worldwide promoted the current “explosion” in hydrogen fuel cell development. The high level of activity in this sector has given a natural boost to PEMFC research and development. In addition, the use of PEMFC units for portable and small stationary applications has rapidly increased over the last few years as these sectors have begun to expand and enjoy a strong period of growth.

Finally, from the early 2000s climate change debates, PEMFC attracted additional interest to improve the environment concerning atmospheric and noise pollution. Indeed, feed with pure

hydrogen, generating units and other similar applications will compete with, then replace diesel engines which emit particles, NO_x, and are particularly noisy. A real advantage will be obtained by the fact that hydrogen, even if produced by natural gas reforming with CO_2 emission, is used by a higher efficiency system. Moreover, in the middle-long term, the technological deployment of fuel cells will allow the setting-up of a real hydrogen economy which will have a major impact on reduction of greenhouse gases emissions if hydrogen is produced by CO_2-neutral processes (reforming with sequestration or production by renewable energy).

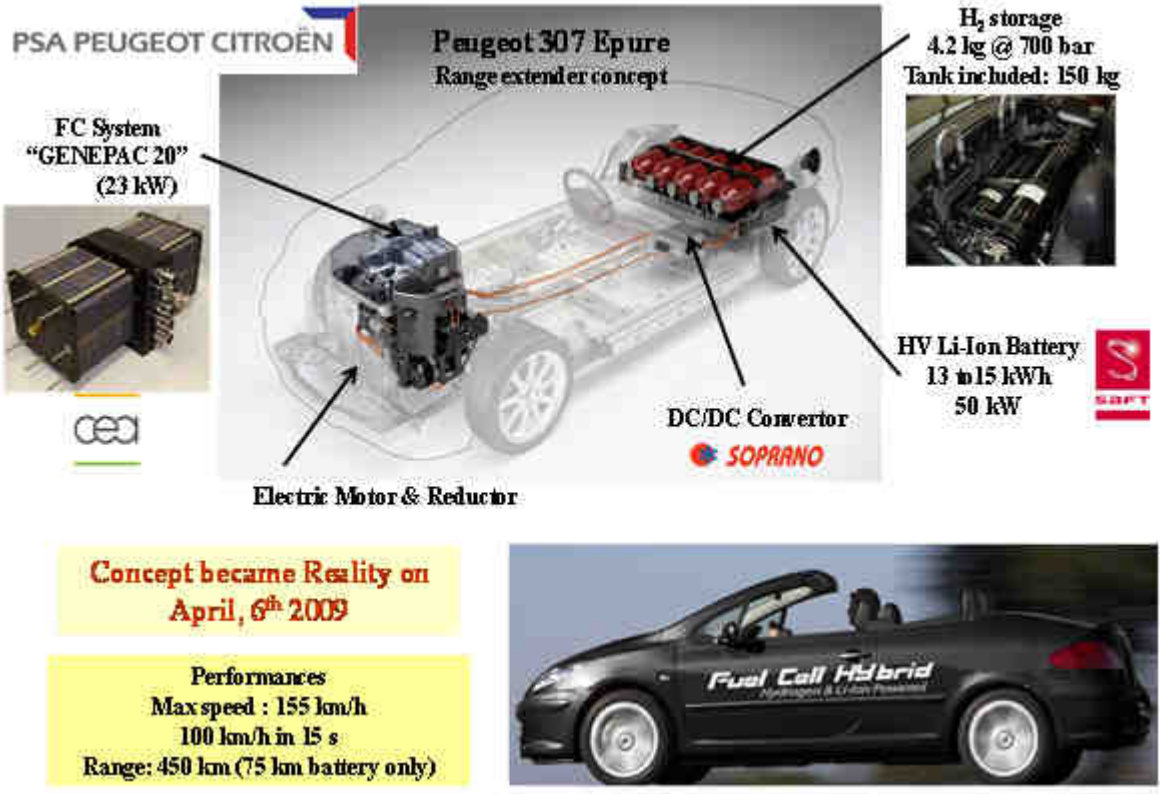

Figure II.7: PSA Peugeot-Citroën fuel-cell powered car (Source: [28]).

II.2 – Modern PEMFCs and the role of physical modeling

Despite the tremendous technological progress achieved in PEMFCs during the last 50 years from the first Grubb-Niedrach cell, PEMFCs are still not largely commercialized. In order to compete within the most attractive markets, the PEMFC technologies did not reach all the required technical characteristics yet, in particular in terms of cost and durability [29,30].

To better explain the fundamental underlying reasons of that, let first summarize how a modern PEMFC is made. A view of a single cell showing individual components is shown in Figure II.8. An individual cell consists of a cathode, an anode, and a separating PEM (usually, Nafion®). Each electrode has an electrocatalyst layer (the CL), and a gas diffusion layer (GDL). The CLs can be attached to either the membrane (i.e. to form a MEA) or at times to the GDL material. Each individual cell produces a voltage of about 0.6-0.7 V; to produce a suitable voltage, individual cells are "stacked" to form a fuel cell stack. The individual cells are electrically connected in series by bipolar plates (BP), and special end plates terminate the stacks to provide the compressive forces needed for stack structural integrity. The BP provide conducting paths for electrons between cells, distribute the reactant gases across the entire active MEA surface area (through flow channels integrated into the plates), remove waste heat (through cooling channels), and provide stack structural integrity as well as barriers to anode and cathode gases. Directly adjacent to the BP are the GDLs, which typically consist of two layers as macroporous substrate layer and a MPL. The GDLs are gas permeable and help distribute gases to the CLs, conduct electrical current, and also provide a network of paths for liquid water to move from the MEA to the flow channel. The macroporous substrate layer consists of a carbon fiber matrix with a large void volume, typically 75-85%, and a primarily hydrophobic MPL consisting of CB mixed with fluoropolymer. The cathode GDL normally has an attached MPL; the anode GDL may or may not have a MPL. In modern MEAs, the electrocatalysts are nano-particles of Pt or Pt alloys deposited on high-surface area C supports. The nano-particles increase the active catalytic surface area per unit mass of the Pt pr Pt alloys. Ionomer is also included in the CL for proton transport, with Nafion® still being the standard material.

The overall operating principle of a PEMFC is relatively simple. Hydrogen is fed to the cell and oxidized at the anode (HOR), while oxygen, usually carried in an air feed stream, is reduced at the cathode (ORR). The protons produced at the anode are conducted through the PEM to the cathode. Since the PEM is not electronically conductive, the electrons released at the anode have to flow along an external circuit, thereby generating useful electric power, and eventually recombine with the protons on the cathode side to produce water. CLs are maybe the most complex components in a PEMFC as they have to manage simultaneously processes occurring at different spatio-temporal scales, as the electrochemical reactions and the ionic, reactants and (liquid and vapor) water transport phenomena.

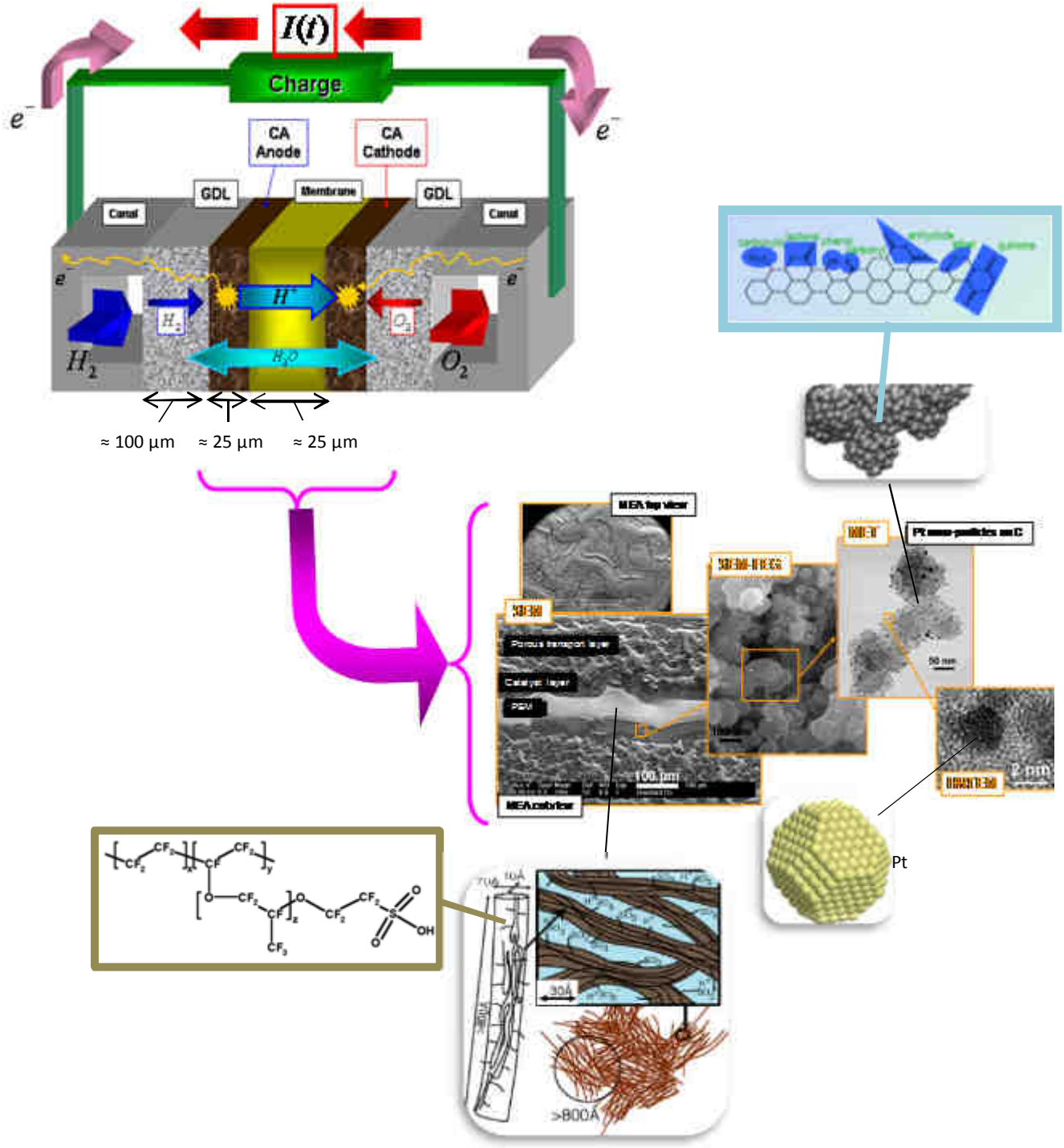

Figure II.8: A modern PEMFC and some models of the materials chemistry.

Today, the most widely deployed PEMFCs cost about 275 US$/kW for transportation and 4500 US$/kW for stationary applications (by contrast, a diesel generator costs 800 to 1500 US$/kW, and a natural gas turbine can be 400 US$/kW or even less) [31]. According to the USA Department of Energy (DOE), the cost targets for successfully competition of PEMFC

with alternative technologies are significantly lower: 30-50 US$/kW for transportation and 750 US$/kW for stationary applications. Current automotive prototypes use over 2 g Pt/kW of electricity: the DOE goal is to develop PEMFC needing only 0.2 g Pt/kW by 2015.

One of the reasons of this high cost is still that the most preferred catalyst in PEMFCs is Pt, whose resources are both limited and costly (Figure II.9): it corresponds to about 40% of the MEA cost as the standard global Pt loading used to be about 0.5 mg/cm^2. Nafion® ionomer is also expensive with a cost of around 700 US$/m^2.

Furthermore, the commercialization of PEMFC systems will result in an increasing demand of precious metals (e.g. Pt, Ru, Pd, Au…). Without their recycling after PEMFC lifetime, the long-term availability in nature of these metals could become a serious limitation. Hence, precious metal recycling is also critical to the long-term economic sustainability of PEMFC [32].

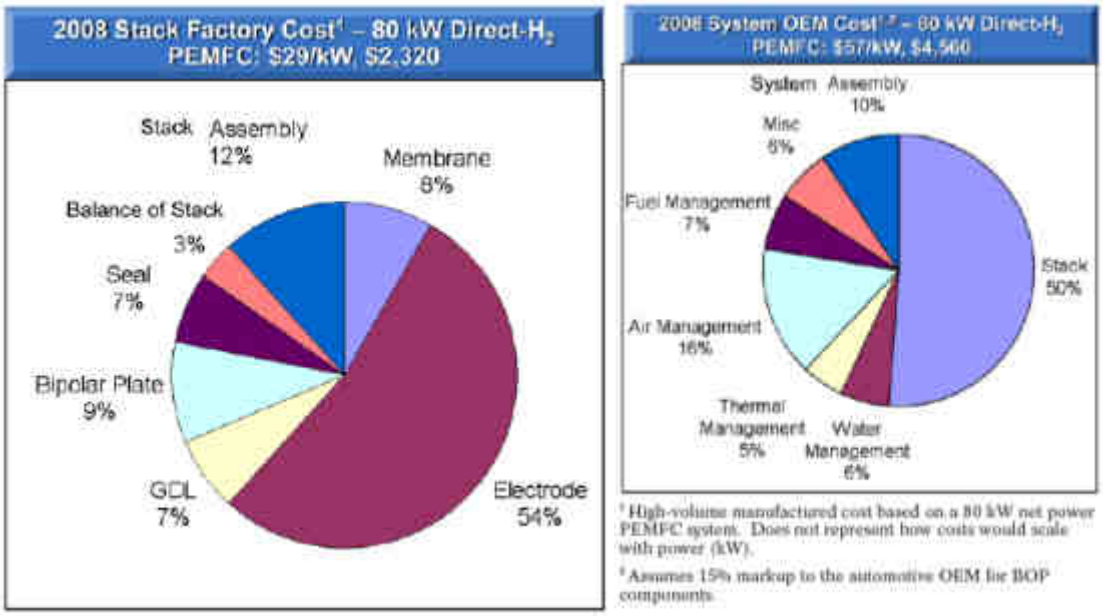

Figure II.9: Typical cost of the PEMFC components in 2008 (Source:[33]).

Broadly speaking, improved performance in PEMFC and reduced Pt loading can be achieved by enhancing the rates of transport and/or electrochemical reaction, and by increasing the surface/volume ratio of interfacial areas where reactions/transport take place. This can be achieved by, e.g.,

- engineering the transport properties or processes in specific areas optimizing the components structural properties (e.g. CLs) by keeping Pt, CB and Nafion® materials
- optimizing (i.e. changing) the chemistry of these materials (e.g. by replacing Pt catalyst by multi-metallics, etc.).

In any case, it is first necessary to identify the prevailing limitations and their location, and to understand their origin. *In situ* measurements to obtain the relevant information are difficult due to the confined and electrochemically active environment of PEMFC, the complexity of the couplings, and the often transient nature of the processes. Rational models based on the fundamental physico-chemical processes together with experimental observation are thus a powerful tool to gain a more complete understanding of the operation of the PEMFCs at the different relevant scales, from the atomistic (e.g. electrocatalysis) up to the cell level (e.g. water management). Excellent review papers discussing the benefits of using theory to improve for fuel cells have been already published [34,35].

Different simulation approaches of the PEMFC performance have been developed during the last 20 years [36,37]. These models quite well describe water management and thermal phenomena occurring in PEMFC for different operating conditions. Even if electrochemical reactions are assumed to occur through simple "global steps", with kinetic rates described through empirical *Butler-Volmer equations* neglecting the nano-scale electrochemical double layer structure impact on the effective electro-catalytic properties (e.g. [38], and see my discussions in [8]).

In a pionnering paper, Springer *et al.* [39] reported an isothermal, one-dimensional, steady-state model of a complete PEMFC. In particular, the model predicted an increase in PEM resistance with increased current density and demonstrated the great advantage of a thinner PEM in alleviating the resistance problem. Bernardi and Verbrugge [40,41] proposed a one-dimensional mathematical model of the PEMFC for liquid water transport in porous electrodes assuming a constant liquid water volume fraction and no interactions between liquid and gas flows. A numbers of CL models had been then developed, including the interface models [39,40,41], the thin film models [42], the agglomerate models [43,44,45,46,47,48,49,50,51,52,53], and the thin film agglomerate models [50,51,52]. Using the agglomerate model, the researchers at NRC of Canada studied the optimum performance of PEMFC for a number of optimization parameters: type of agglomerate, CL thickness, CL porosity, distribution of Nafion® content, Pt loading, etc. [53,54,55,56,57,58,59]. Besides these models, the works of Wang and Wang [60,61] treated the CL as an individual zone with various conservation equations employed in the modeling of transient study and various time constants for the transient transport phenomena were proposed.

As for the investigation of two-phase flow, Wang *et al.* [62] pioneered the research on this issue through analytical and numerical methods. A thereshold current density was proposed to distinguish the scenarios between single- and two-phase regimes of water distribution and transport. In the subsequent works of their group, sophisticated models [63,64,65,66] were

developed to simulate the flooding and liquid water distribution in PEMFCs. The so-called *mature multiphase mixture formulation* with single set of conservation equations was employed to mimic the two-phase transport process. Another analytical model performed by Pasaogullari *et al.* [67], focusing on the liquid water transport in hydrophobic electrode, indicated that capillary transport dominates the water remove from flooded GDLs. The model of Natarajan and Van Nguyen [68,69], which considered the evaporation or condensation of liquid water, also demonstrated the importance of its transport on cell performance.

The growing use of nano-sciences (with the development of atomistic modeling approaches, such as DFT or Molecular Dynamics -MD- [70]) and nano-techonologies (with the development of modern techniques of materials structural and chemical characterization at the nano-scale [71]) are encouraging to understand and thus to control the fundamental structure and behavior of the PEMFC materials at the atomic and molecular level. This includes the determination of the controlling elementary reaction pathways and intrinsic kinetics involved in the ORR over Pt and Pt based alloys and their potential dependent behavior and the understanding of the influence of the extrinsic reaction environment including the surface coverage, alloy composition, solution phase and electrochemical potential. New functionalities or lower Pt loadings (e.g. via the development of multi-metallic catalysts with lower Pt loading, e.g. [72]) are made available by manipulation of matter at this scale or through specificities of the nano-dimensions, where the physical and chemical properties of materials differ from those of the bulk matter. DFT has been largely used to explore different PEMFC reactions in absence of interfacial electric field (e.g. ORR steps in [73,74,75,76,77,78,79,80,81,82]). *Ab initio* or the first principles molecular dynamics (AIMD) method, based on Carr and Parrinello's approach [83], has been applied in the study of electrochemistry [84]. *Reactive Force Field* approaches are now being used to study the ionomer/water/catalyst interfaces during an electrochemical reaction [85]. Neurock *et al.* developed a detailed first principle approach that employs a *double-reference method* to simulate the influence the electrochemical potential on the chemistry at the metal/solution interface [86]. In this method the aqueous solution metal interface and the interfacial potential drop are explicitly treated. However the choose of an appropriate water surface structure is critical in establishing the appropriate electrochemical and electrocatalytic behavior. This method has been applied to study some electrochemical steps involved in the ORR, methanol oxidation and CO poisoning reactions on Pt (e.g. [87,88]). Novel CGMD models have been also developed to predict the micro-structural self-organization of the CLs and to understand its impact on the effective transport and electrochemical properties [89].

Unfourtunately, high electrochemical activity and/or reduced Pt loading does not necessary implies enhanced durability. Because other concerns were more pressing at the time, only a few PEMFC researchers studied lifetime issues before the early 2000s. Now, however, the

emphasis has shifted from designing PEMFC systems and improving their short term performance to improving fuel cell reliability and lifetime and thus making PEMFC definitively cost competitive. At least 3000 to 5000 operational hours are required for automotive applications [31], up to 20000 hours for transportation and up to 40000 hours for stationary applications [31]: as a comparison, present life time of PEMFC under automotive solicitations rarely exceeds 1000 hours. A maximum rate of degradation from 2 to 10 µV/hour (-40°C to + 40°C) is wished for the majority of the applications (less than 10% power degradation is needed). As a result, the number of published studies of fuel cell reliability, lifetime, and cost has increased dramatically in the last 10 years. Several of these studies revealed severe degradation of PEMFC materials as the individual components are exposed to an aggressive combination of strong oxidizing conditions, liquid water, strongly acidic conditions, high temperature, high electrochemical potentials, reactive intermediate reaction products, a chemically reducing atmosphere at the anode, high electric current, and large potential gradients.

The large-scale development and commercialization of PEMFC energy passes now necessarily by elucidating MEA aging mechanisms in order to help improving both PEMFC electrochemical performance and durability…

II.3 – PEMFC materials aging mechanisms and performance loss

It is largely observed that the nano/microstructural properties of the Pt or Pt-alloy-based CL and the PEM evolve during PEMFC operation, even at normal (i.e. not under zero) operating temperatures. These spatiotemporal nano/microstructural changes translate into irreversible long-term cell potential degradation (Figure II.10).

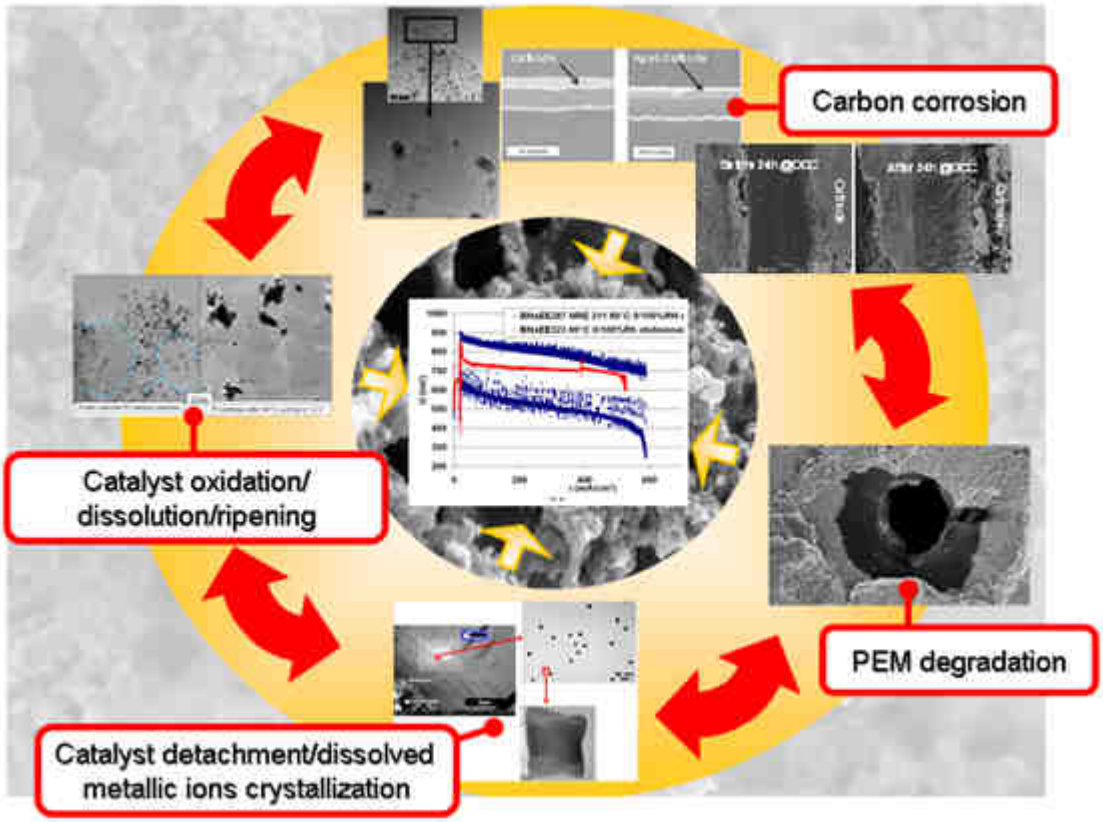

Figure II.10: Some interplay between (electro-) chemical aging phenomena inducing the PEMFC performance degradation.

Different methods are typically used for the investigation of degradation processes and mechanisms in PEMFCs. The main topic is the loss of electrochemical performance, which is mainly analyzed by i-V characteristics. Additional information is derived from EIS investigations that allow deconvoluting the effect of some degradation processes (e.g. the PEM aging manifested as proton resistance increase over time [90]). The cyclic voltammetry (CV) [91] allows determining a change of the active catalyst surface area (or electrochemical surface area -ECSA-). Furthermore, current density mappings and neutron scattering and imaging measurements are frequently performed to obtain local information about the operating conditions. *In situ* characterization generally provides information about performance degradation through changes in electrical properties but rarely provides direct information on the degradation mechanisms, nor on the degradation processes themselves [92]. For this purpose *ex situ* structural characterizations are necessary to complement the electrochemical characterizations in single-cells. Typical analytical methods for *ex situ* characterization are X-ray Photoelectron Spectroscopy (XPS) [93], Scanning Electron Microscopy (SEM), Transmission Electron Microscopy (TEM), Scanning Tunneling Microscopy (STM) [94], Atomic Force Microscopy (AFM) [95], X-Ray Diffraction (XRD) [96],

Infrared Spectroscopy (IR), and porosimetry. Structural analyses are performed by SEM, TEM, STM, and AFM; additionally XRD is used for the investigation of particle distributions of the catalysts and their changes. The investigation of surface composition of the components like CL, GDL, and BP is performed by XPS. XRD and TEM analysis are the two main techniques to study the catalyst size and distribution changes. The advantage of the XRD is that it provides a good statistical overview of the catalysts size distribution in the CLs [97]. On the other hand, TEM images give the direct information of the location of particle growth in the CL that can be useful to analyze the mechanisms [98,99].

Unfourtunately, the limitation of these *ex situ* characterization techniques is that they do not provide direct *in operando* information on how the different mechanisms are interplaying in the PEMFC, and thus we should be very careful with the conclusions that one can made from *post mortem* observations. Moreover, the ways of how degradation mechanisms occur are expected to be strongly sensitive to the PEMFC operation modes. This fact is illustrated in Figure II.11 which shows the experimentally measured impact of three PEMFC operation modes (open circuit conditions with circulating H_2 and O_2 -OCC-, galvanostatic conditions and current-cycled conditions) on the cell potential evolution, at two different temperatures. At 60°C, the galvanostatic operation mode is revealed to be more severe for the MEA, and at 80°C, the worst performance corresponds to the MEA operated with a current-cycled mode.

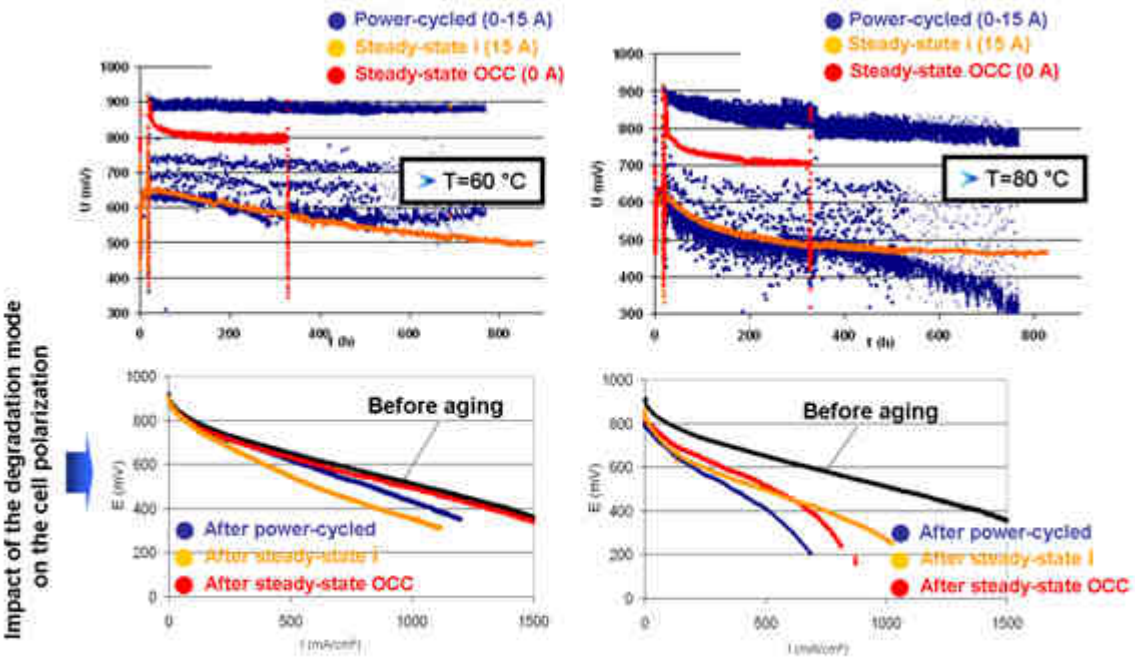

Figure II.11: Impact of the operation mode of a MEA on its associated performance degradation at 60°C and 80°C. Standard CEA/LCPEM Pt-MEA (one MEA per experiment), single cell, H_2/air, P_A=P_C=1.5 bar, RH_A=0%, RH_C=100% (for the OCC experiment, the rapid potential evolution at 320 h correspond to the measurement of a polarization curve) (Source: [100]).

Even if some understanding can arise from the combination of electrochemical and structural characterizations, these trends are too complex to be interpreted only on the basis of experimental data: the development of a theoretical understanding or modeling of the underlying mechanisms reveals again as a powerful complementary tool, not only to provide experimental interpretation, but also to suggest operation modes that mitigate MEA degradation (predictive capabilities).

Furthermore, it should be underlined that durability studies in the PEMFC research community are now more automotive application-oriented meaning hard conditions to be applied like dynamic loading, start/stop tests, etc. but with a lifetime objective of 3000-5000 hours (cf. Section II.2) allowing real or almost real case experiments. Stationary applications present different specifications and thus different operating strategies are needed to manage start-up, shutdown, as well as the nominal operation, with required lifetime of 40000 hours which does not allow the "real case" methodology but clearly calls for an accelerated aging methodology (or accelerated durability testing -ADT-). The use of physical modeling to get insights on the possible competitions and synergies between aging mechanisms can be relevant to design short term (and thus, cheaper) experimental testing representative of long-term operation.

The large amount of research work that is being done worldwide clearly highlights the complexity and the remaining experimental and theoretical challenges to fully understand PEMFC materials aging mechanisms under realistic operating conditions. As described in the following, different "frameworks" or approaches are conducted to tackle this problem (to limit this manuscript scope, I exclude from my discussion the aging of BP/flow fields, gaskets, stacks and other system components -moreover, details about these components are often proprietary-).

- ✓ ***Framework of analysis #1: "separation" between the individual materials aging***

The possible competition and interactions between the PEMFC materials aging mechanisms remain unclear, and very few studies have been reported regarding this in literature (e.g. our work in [101] -Figure II.12-): for simplicity reasons, each individual material is usually the focus of separate aging studies, as reviewed in the following.

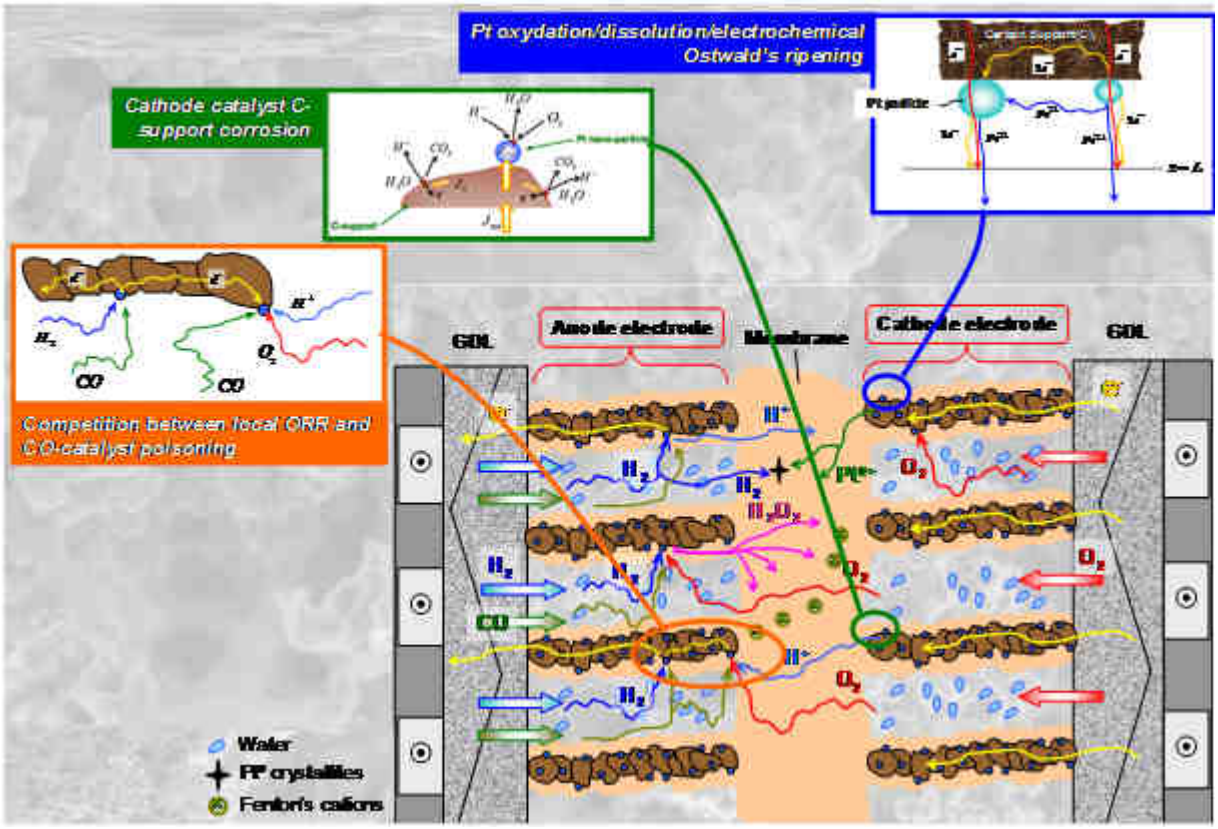

Figure II.12: Some electrochemical aging mechanisms inducing the irreversible PEMFC performance loss (in orange: ionomer, brown: C, blue: Pt) (Source: [101]).

a) Catalyst degradation. Although Pt nano-particles are very stable in acidic electrolytes at low electrode potentials, considerable dissolution of cathodic Pt takes place at high potentials representative of typical PEMFC cathode operating conditions (potential between 0.7 and 1.1 V vs. NHE) [102]. Both steady-state and drive-cycle conditions produce extensive catalytic oxidation, dissolution and redistribution of the Pt atoms [103, 104]. Extensive nano-particle coarsening and redistribution is also observed, leading to the reduction of the ECSA and to the loss of the electrochemical activity [105]. Furthermore, TEM observations performed after PEMFC operation show the formation of Pt single nano-crystals within the PEM [106]: the location of the precipitated Pt (in the anode, in the cathode or in the PEM) is believed to be primarily controlled by the availability of hydrogen which permeates from the anode to the cathode and of oxygen which permeates from the cathode to the anode. In fact, Pt that has migrated from the cathode to the PEM could undergo repeated oxidation by crossover oxygen and reduction by crossover hydrogen [107]. Therefore, distribution patterns and the particle size of migrated Pt are strongly dependent upon the relative concentrations of the crossover oxygen and hydrogen from the two electrode sides.

Higher concentrations of crossover hydrogen and oxygen yield sharper and narrower Pt bands with larger Pt aggregates, while lower concentrations yield wider distributions with smaller Pt crystals.
Furthermore, it has been speculated that hydrogen shortage at the Pt surface results in electrochemical decomposition of water to produce an additional current, as well as protons and oxygen [107]. It has been suggested that the oxygen produced causes oxidation of Pt to PtO, which undergoes anodic Pt dissolution and eventual migration to the PEM as well.

Some researchers have claimed that oxygen starvation within the cathode (related for example to mal-disttribution or interruption of air supply) could also enhance degradation of Pt-C materials [108]. These authors have suggested that oxygen-starved conditions within the cathode can "drive" the reduction of protons into hydrogen, and a subsequent heterogeneous chemical reaction between hydrogen and the remaining oxygen produces H_2O. The authors have suggested that this reaction could generate heat and hot spots in the MEA which will enhance the Pt particle coarsening. However only short-term experiments (<10 hours) have been reported and mechanistic interpretations of the causes remain unclear.

Alternatively, it has been shown that the specific activity and stability of PEMFC electrodes can be improved by alloying Pt with some transition metals (e.g. Co, Ni, V…): these electrodes also achieve lower global Pt loadings compared to pure Pt-based electrodes. Among these Pt-alloys, Pt-Co nano-materials have been widely studied as promising alternative catalysts for PEMFC applications, showing enhanced ORR activity and better stability than pure Pt materials [109, 110, 111]. Because composition combinatorial methods for improving Pt_xCo_y activity and stability have had limited success, several studies have been dedicated to the understanding of the Pt-Co nanostructure impact on its activity and stability properties [112,113]. The CL elaboration method and coordination of Co with Pt atoms could also affect the performance and durability [114]. However detailed Pt_xCo_y degradation mechanisms are still very poorly understood. Only few papers are devoted to the experimental study of the long term (> 300 h) durability of these materials [110,111,115].

b) Catalyst C support degradation. CB catalyst-support is thermodynamically unstable at typical cathode operating conditions (potential > 0.2 V vs. NHE at 25°C) [116]. Despite that C corrosion reaction reveals to be quite slow at common PEMFC operating temperatures (< 120°C) with a steady non-zero current demand, severe CB

structure damage has been observed after PEMFC power-cycled and start up/shut down operation representative of automotive applications [117,118,119,120]. In-line direct gas mass spectroscopy analysis has successfully detected intermittent peaks of CO_2 emission in exhausted gas from the cathode, indicating that C corrosion occurs during the load cycle in the PEMFC [121, 122]. Several experimental studies let believe that this degradation is due to the presence of oxygen in the anode [123]: the presence of the oxygen in the anode induces a reverse proton current between the electrodes increasing the cathode C oxidation, which can manifest as dramatic structural changes in the cathode (e.g. porosity increase, electrode thickness decrease) (cf. Figure II.12). In contrast, the anode thickness appeared to be no changed. According to Tang *et al.* [118], after a shut down operation, if the anode exhaust port is not closed, air can gradually diffuse into the anode side, creating an oxygen/hydrogen boundary. Furthermore, it is believed that mal-distribution or anode local interruptions of hydrogen supply (the so-called *fuel starvation* phenomenon) enhances oxygen permeation from the cathode into the anode [123]. According to Fuller and Gray [124] as well as Darling and Jayne [125] formation of liquid water drops in the anodic channel could also locally block the hydrogen access to the CL. The starved region can also develop from poor anode flow dynamics that can lead to development of a nitrogen filled region in the channels. When C corrosion occurs, the C support in the cathode CL is reduced in volume and connectivity, which causes also Pt particles to become isolated or less effective to ORR (C corrosion-driven Pt coarsening [126]). The CL then suffers from reduction of ECSA, which leads to irreversible performance degradation. Furthermore, Pt is believed to bond with the C support through the interaction between Pt and π electrons of the graphene sheets in the C support: the weaker the π bond (sp2-hybridized C), the weaker the interaction, thus C corrosion can also induce Pt particle detachment, but this depends clearly on the chemistry of the C and of the Pt-C bond [127,128].
Moreover, CB corrosion can also contribute onto the delamination between the CL and the PEM, and/or between the CL and the GDL.

c) PEM degradation. The PFSA PEM aging is a very complex issue as it can derive from combined effects between electrochemical, physicochemical and mechanical mechanisms. Regarding the chemical and electrochemical degradation, hydrogen peroxide (H_2O_2) can be formed at the surface of the Pt particles, if H_2 and O_2 coexist (from crossover) in the CLs. Being the H_2O_2 a highly oxidative reagent with a high reduction potential (1.77 V vs RHE) it may deteriorate the ionomer in the PEM (maybe

even inside the CLs), through the formation of radical species, such as OH° and OOH°, according to a mechanism not yet fully understood [129]. The decomposition of H_2O_2 to give the peroxide radical species is definitely increased by the presence of traces of metal ions (Fenton's cations) such as iron [130,131], copper [132] or titanium [133], but the degradation of the PFSA PEM is described even in the absence of these pollutants [134].

Formation of H_2O_2 has been detected in an operating PEMFC [135]. However, some researchers suggest the direct formation of radicals on Pt catalyst, from the molecular H_2 and O_2 reaction on the surface, may be the main cause of degradation, although H_2O_2 can also be formed during the cathodic ORR, in particular if Pt-M catalysts (with M being a transition metal element) are used [136,137]. However, the study of these mechanisms is very difficult because H_2O_2 decomposition rate is extremely high on Pt and Pt-M catalysts [138].

Chemical decomposition of the ionomer produces fluoride ions (measured in PEMFC effluent water), probably in the form of HF, which in turn may deteriorate other materials used in MEA and cell stacks. Furthermore, PEM degradation facilitates reactants cross-over between the electrodes, and hence the performance drop ("mixed-potential phenomenon"). By using XPS methods in multi-layered MEA, Chen and Fuller demonstrated that H_2O_2 emission rates are strongly dependent on the PEM relative humidity, oxygen partial pressure and PEM thickness [139]. Shim *et al.* recently reported accelerated experiments showing that the anode side of the PEM was more deteriorated under H_2-O_2 supply conditions, and that the cathode side of the PEM was more deteriorated under H_2-air supply conditions [140]. In other paper, Hatanaka *et al.* carried out an open-circuit durability test with a fluoride emission rate (FER) measurement for intentionally Pt-precipitated PEM with and without CLs [141]. The FER of the PEM with Pt-band was clearly higher than that of the PEM without Pt band. The results showed that precipitated Pt surely contributes to the PEM degradation. On the other hand, the PEM with both Pt-band and CLs showed much higher FER, clearly showing that the Pt-band might not be the main cause of PEM degradation. Furthermore, it has also been also claimed that crossover oxygen promotes the degradation of the PFSA PEM in the presence of Pt [107].

The F-NMR, IR or Raman spectroscopy can also allow determining the chemical structure and composition of the polymers and their functional groups, and thus to elucidate if some chains scissions or bonds modifications have occurred [145]. Studies of the PEM degradation also include analyses of their functional properties (proton conductivity, water sorption, gas transport, mechanical strength) strongly related to their structure. Water sorption, conductivity and permeability can be measured to

evaluate the transport properties modifications after degradation [142, 143, 144, 145]. Mechanical diagnostics are also used to evaluate the mechanical strength modifications that can be caused by weakening, thinning, pinholes, cracks, for example after local dryings, or by chains physical reorganisations like chains entanglement loss. Other techniques like Small Angle Neutron and X-ray Scattering (SANS and SAXS), already used to determine the physical structure of the polymer membranes [146,147], could also help to evidence their physical degradation caused by chains reorganization.

Finally, although the recast ionomer in the CLs is susceptible to undergo the same degradation mechanisms as the PEM, few studies have been carried out on this subject.

d) GDL/MPL degradation. Many PEMFC researchers have noted that the way the GDL interacts with water evolves during lifetime tests. The evolution seems to occur at the microstructural level (micrometer to submicrometer) but can be seen macroscopically. Water sprayed on the surface of a fresh GDL bounces off as spherical beads, but water sprayed on the surface of a lifetime-tested GDL adheres to the surface. Evidently, the PEMFC operating environment gradually changes the GDL from hydrophobic to hydrophilic, which can irreversibly degrade PEMFC operation as the water-content levels and transport properties of those media change. For example, gas convection and diffusion are hindered through a GDL after lifetime testing [148,149,150,151,152,153]. After prolonged exposure to the strong oxidative conditions at the cathode of an operating PEMFC, C atoms on the GDL surfaces can oxidize to form carboxyl groups or phenols, which are hydrophilic. As a result, the GDL C surface becomes more hydrophilic, causing a gradual increase in cathode water uptake during lifetime tests. To study the loss of hydrophobicity of the GDL or the MPL, Wood *et al*. have performed ADT of GDL materials [154].These tests aged GDL materials in liquid water, and varied oxygen concentrations and temperature during the aging process. The researchers showed that hydrophobicity decreases with time and increases with temperature and that adding O_2 molecules to the aging process reduced the hydrophobicity more than did elevated temperature alone.

The C powder in the MPL can also be corroded in the environment of an operating fuel cell. Porosimetry measurements can indicate that carbon is lost from the MPL during fuel cell operation [154]. The mercury and water porosimetry measurements have shown that the GDL pore structure changes during lifetime tests. Largepore (30-60 µm diameter) volume has decreased, while small-pore volume increases. The loss

in large-pore volume is likely due to irreversible compression due to the fuel cell compression. However, there are only a few literature papers which examine mechanical degradation and review the effect of compression of GDL on the performance of PEMFC [155,156].

Ex situ ADT methods, for example by using half-cells or Rotating Disk Electrodes (RDE), have been also developed to study materials aging mechanisms [157,158,159,160]. A typical example of an ADT, is fixing the electrode potential at high values (e.g. 1.4 V) in order to study C degradation. Based on the experimental data obtained under these conditions, it is currently concluded that state-of-the-art Pt, C and PEM materials will never reach durability requirements and that alternative materials are necessary for future CL materials [165,161,162,163,164]. In our opinion, these conclusions merit to be reconsidered, as potentials higher than 1.2 V (the zero-current cathode potential) are probably unrealistic under normal PEMFC operating conditions, where, furthermore, we expect a strong interaction of the aging mechanism under study with reactants, charge and water transfers, HOR and ORR and other materials degradation mechanisms. The analysis approaches of the experimental data aiming to "separate" aging phenomena in PEMFCs, may lead to contradictory interpretations. For example, Schulze *et al.* claimed that (classical) global (two-electrodes) EIS can be used as a method to characterize the losses of the electrochemical performance and to distinguish between the degradation processes in the anode and in the cathode [165], in contradiction to the three-electrode EIS experimental work reported by Kuhn *et al.* [166] showing that anode and cathode contributions to PEMFC performance cannot be separated by using classical EIS. Other authors recently claimed that the contribution of each single aging phenomenon can be "separated" from experiments by using mathematical control analysis [167]: from the analysis above, in our opinion this is seems difficult to do in general operation conditions, as the interplaying between aging mechanisms remains still unclear. We have demonstrated in some of our group publications that different degradation mechanisms combined can improve the MEA durability -e.g. [168]-, compared to the case where only a single degradation process occurs (see further examples within this sense in Chapter IV) (Figure II.13). In other words, because of the strong non-linear phenomena taking place in the PEMFC, super-position principle does not apply to degradation phenomena, and thus the impact of a set of interplaying individual materials aging mechanisms on the global cell potential, could be not higher, even lower, that the impact of one or few of these mechanisms considered separately. Thus, within a PEMFC control perspective (extremely important issue for the cell operation into an end-user device) it will be necessary to develop reduced mathematical models derived from more complete physical models accounting for the interplaying between aging

mechanisms. Similar discussions can be made regarding other empirical approaches such as in [169].

- ✓ ***Framework of analysis #2: "damaging" impact of external contaminants on the materials***

The intrinsic materials aging mechanisms can generate products which contaminate the catalyst or PEM [170]. However, the problem of the understanding of the materials aging phenomena becomes more complex if we consider that a realistic PEMFC would also operate with H_2 and O_2 contaminated with external impurities (Table II.1).

Contaminant	Result	Characteristics
Anode CO contamination	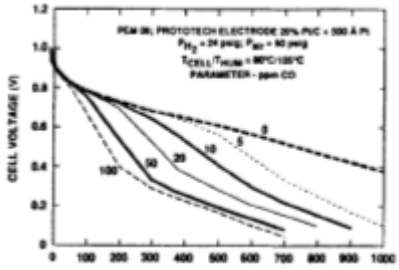 Polarization curves for a PEM fuel cell at 80°C in the presence of low CO levels in the H_2 anode feed stream. The CO levels in ppm are specific next to each curve. Other experimental conditions are specified in the figure [171].	Reversible effect
Cathode SO_2 contamination	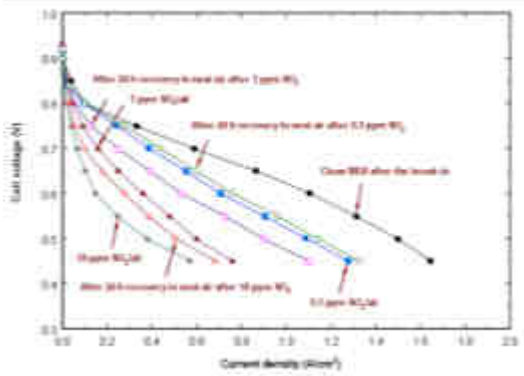 Effect of SO_2 concentration in air on cell performance at 118.5 µmoles of dosage T_{cell}=70°C, TD(A/C)=80/70°C, P(A/C)=101/101 kPa, Stoic.(A/C)=1.2/2.0, RH_{inlet}=100% [172].	Irreversible effect

Table II.1: Some examples of impact of external pollutants on PEMFC performance degradation.

Industrially, hydrogen is mainly produced by high temperature reforming processes using methane or coal which incorporates high level of impurities, such as carbon monoxide (CO), hydrogen sulfide (H_2S), ammonia (NH_3), organic sulfur-carbon, and carbon-hydrogen compounds [173]. The main part of those pollutants is then removed by using pressure swing adsorption units. However, this purification process becomes more complicated and thus more expensive if we wish to reach ultra-low concentrations of contaminants in hydrogen. In

order to avoid an impact of hydrogen cost on the PEMFC development, specifications for the produced hydrogen must be oriented to the most critical impurities for the cell. As a consequence, the quality of the hydrogen produced must be in line with the end-use application. A balance between cell performance/durability, and hydrogen production cost needs to be found [174, 175]. In this industrial framework, international cooperation is in progress on the ISO standardization of hydrogen fuel specification for road vehicles and stationary applications of PEMFC.

The impact of CO on the PEMFC anode performance has been widely studied experimentally and by modeling, and many mitigation methods have been proposed. In the more recent years, the impacts of H_2S and NH_3 have become an important subject of work. It is well accepted that the major impact of CO and H_2S contaminants on PEMFC anode is a kinetic effect due to poisoning of the electro-catalyst, while NH_3 mainly affects the ionomeric membrane by reducing the ionomer conductivity [176]. In both cases, significant performance degradation can be induced. In order to enhance the CO tolerance, bimetallic catalysts such as Pt-Ru, Pt-Mo and Pt-Sn have been proposed [177, 178]: however, the mechanisms underlying these tolerance improvements and the possible impact of the external contaminant on the intrinsic stability properties of the nano-particles still remain unclear.

In the other side, even if the PEMFC is operating with pure hydrogen (instead of reformate gas), the expected working conditions are still different from those met in prototypes for demonstration programs. This comes from the fact that PEMFC cathode air breathing from polluted atmospheres may diminish the cell performance: in most cities one can find several pollutants (CO, NO_x, SO_x, NaCl, O_3, etc.), which will poison the cathode catalysts and even the anode catalysts if some air permeation occurs through the PEM [179].

There is some experimental evidence to think that some of these external anode and cathode contaminants can enhance the damage of the PEMFC MEA materials [180]. However, possible mitigation effects of intrinsic materials aging mechanisms by the injection of these contaminants have not been considered in the literature before our group work published in 2008 and 2009 (see Chapter IV) [168, 181]. Most of the contamination experiments reported in literature are done under stationary power (galvanostatic) conditions (i.e. not totally automotive representative) and very few works reported long-term studies on the associated impact on the performance [182]. As the best of our knowledge, our publications [168, 183] are the first ones addressing the long-term impact of contaminants under current cycled conditions representative of automotive applications. This kind of dynamical operation can in fact favour the contaminated-induced mitigation of intrinsic materials aging evoked before, in contrast to galvanostatic operation (see Chapter IV).

Finally, even if some work has been carried out to understand the impact of some pollutants mixtures on the PEMFC individual CLs behavior, the global PEMFC dynamical behavior in presence of both anode and cathode contaminants appears to be unexplored in literature [184]. Again, there is no reason to disconsider possible synergetic effects between individual contaminants impacts.

✓ ***Framework of analysis #3: Butler-Volmer-modeled PEMFC aging mechanisms***

Despite numerous reviews reported on the experimental degradation research [185,186], very few reviews have been published on the topic of modeling of aging phenomena (e.g. [187]). The reason is maybe that most of these models have been only very recently developed. I discuss now some of the key ingredients behind these models and the underlying challenges (Table II.2) [188]. I focus here this discussion only on MEA materials degradation.

Mechanism	Example
Pt/C-ionomer interface delamination	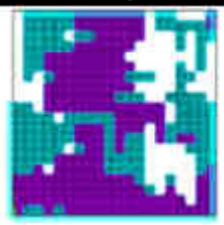 Rong *et al.*: Model region for the contact between ionomer and catalyst powder; purple domain represents the C/Pt agglomerate and the cyan domain represents ionomer [217].
C corrosion	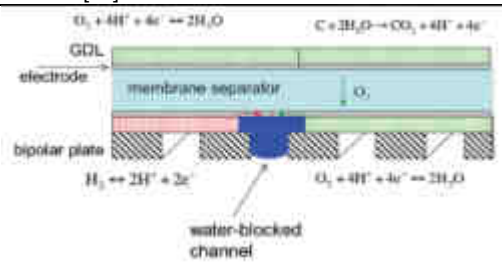 Fuller *et al.*: Impact of hydrogen concentration heterogeneities on cathode C corrosion [189].
PEM degradation	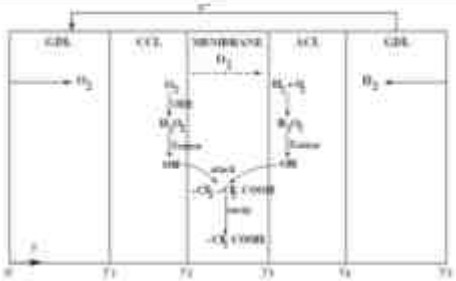 Shah *et al.*: A schematic of the MEA and definitions of the positions along the thickness coordinate *y*. A schematic of the peroxide/radical formation, backbone unzipping, and side-chain cleavage is also shown [213].

Table II.2: Examples of published models at the continuum level describing PEMFC materials aging.

Regarding catalyst aging, Darling and Meyers have proposed a mechanistic model, based on empirical parameters, of the Pt oxidation/dissolution in a PEMFC, largely cited by experimentalists in subsequent papers [190]. By using empirical Butler-Volmer equations written in terms of the CL potential, the authors calculate the Pt surface coverage by oxides and the rate of Pt dissolution into the ionomer, assuming that the ORR rate is not affected by Pt oxidation (ORR is modeled as a global $4e^-$ reaction). The rate of electrochemical Pt dissolution was described as a function dependent on the coverage of Pt oxide and the Pt particle size. The same authors then extended this model including Pt diffusion in the PEM and in the anode ionomer assuming bimodal particle-size distribution [191]. The results successfully predicted that ECSA loss is much quicker during potential cycling than potential holdings at any potential. Bi and Fuller [192] added the phenomenon of Pt-band formation as a result of the chemical reduction of diffused Pt ion by crossover hydrogen at a specific plane in the PEM. Holby *et al.* [193,194,195], used a similar model and simulated ECSA loss assuming various initial nano-particle size distributions: he concluded that the initial nano-particle size distribution significantly affects the long-term ECSA loss and that hydrogen crossover accelerates the loss. Takeshita *et al.* proposed a simple 1D model to describe the Pt particle size evolution in various positions of a cathode CL [196]. More recently, further physical models of Pt ripening have been developed predicting the evolution of catalyst size distributions in good agreement with experimental data [197,198]. The evolution of the catalyst-size distribution in these models is described based on the Ostwald ripening mechanism where the smaller particles dissolve and the monomer thereby released is consumed by the large ones [199]. Lifshitz and Slyozov [200] and Wagner [201] have developed an elegant asymptotic solution for the evolution of an ensemble of particles during Ostwald ripening (known nowadays as the *LSW theory*). All these Pt ripening models disconsider realistic limitations for electrons and Pt^{z+} transport between the nano-particles (e.g. the catalyst support and the surrounding electrolyte are assumed to be perfect charge conductors) but this could be not sufficient enough to study Pt ripening on corroding CB or how Pt ripening is impacted by water content inhomogeneities within the CL (see Chapter III).

Bi *et al.* developed a simple model to describe the Pt band position [202]. This model is based on steady state Fickean diffusion equations in terms of the rates of hydrogen and oxygen crossover in the PEM separator. The results have been successfully compared with H_2/air potential cycling experiments. Pt metal was not observed between the Pt band and the cathode in either Bi *et al.* study or in Ohma *et al.* work [203]. One possibility is that the Pt atomic concentrations were too low to be detected in SEM and TEM images. But Ohma explained that any deposited Pt atoms can redissolve at high mixed potential location and the Pt ions move further towards the anode. The Pt band formation in the PEM is believed to occur because of the suppressed hydrogen crossover by H_2/O_2 catalytic combustion reaction

on Pt that was deposited in the PEM. Within this context, Atrazhev *et al.* introduced a model to calculate the Butler-Volmer potential of a catalytic particle immersed inside a PEM (mimicking Pt precipitated after dissolution from the cathode) [204].This potential is assumed to result from a "mixed potential" of ORR and HOR as the PEM is permeable to both O_2 and H_2. The model demonstrates that the particle potential is dependent on the particle location, as ORR and HOR are driven by the diffusion of crossover gases through the PEM and the local proton transport, in agreement with some experimental data [205].

Regarding C corrosion, Reiser *et al.* have proposed a one dimensional static model devoted to the calculation of the PEMFC electrode/electrolyte electro-potential profiles when the anode is partially exposed to air, in order to define the conditions that could be favorable for the cathode Carbon Oxidation Reaction (COR) [123]. By using a numerical finite element method, the authors solve a Poisson equation coupled with a conservation equation of the electric charges and an empirical Bulter-Volmer description of the global HOR and ORR. A similar model has been more recently proposed by Meyers and Darling [206]. The model describes how a mal-distribution of hydrogen across the fuel electrode can induce both oxygen permeation from the cathode to the anode, and cathode C corrosion in the fuel starved region. Implications of this reverse current mechanism are explored by simulating a cell with a non-uniform distribution of hydrogen along the fuel channel in both steady state and transient operation. The mathematical model is a one dimensional representation taking into account the reactants transport in the channels and the Bulter-Volmer equations. Fuller and Gray [124] proposed a two dimensional extension of these models, to calculate the electric-potential profile under conditions of partial hydrogen coverage in the anode (other variations are also available: e.g. [207]). CFD model versions describing the PEMFC operating conditions which enhance C corrosion have been also developed [208,209,210].

C loss during a PEMFC operation is investigated with a physical model by Takeuchi and Fuller [211], including reactants permeation through the PEM, and global reaction kinetics for the HOR, ORR, and the COR. C loss phenomena under ordinary fuel cell operation conditions are identified in this work. The effects of these are less severe than start-up and H_2 partial starvation, but they are large enough to affect the cell performance after a long-time operation. The model quantifies the effects that cell voltages, activity for oxygen reduction, humidity, and temperature have on the rate of C loss. The authors found that a more rapid kinetics for ORR promotes C loss by lowering the electrolyte potential at the PEMFC cathode.

In spite of the low level of the understanding on the PEM degradation mechanisms, there have been some models published for the case of their chemical degradation. Kundu *et al.* developed a semi-empirical model assuming hydrogen crossover from the anode to cathode,

peroxide radical formation on the cathode/membrane interface, PEM degradation caused by the radical attack, fluoride formation and transportation, membrane thinning, and OCV change by hydrogen crossover increase [212]. While there showed a good agreement in fluoride emission, the model seems to need various refinements with further advancement of the understanding on the mechanism.

Shah *et al.* recently published a complete single-cell model that incorporates chemical degradation of the PFSA PEM [213]. The model is based on conservation principles and includes a detailed description of the transport phenomena. A degradation submodel describes the formation of hydrogen peroxide via distinct mechanisms in the cathode and anode, together with the subsequent formation of radicals via Fenton reactions involving metal-ion impurities. The radicals participate in the decomposition of reactive end groups to form carboxylic acid, hydrogen fluoride, and CO_2. Degradation is assumed to proceed through unzipping of the polymer backbone and cleavage of the side chains. Known trends with respect to operating conditions are qualitatively captured.

Further models have been reported implementing elementary kinetic approaches based on the empirical Butler-Volmer theory to analyse the products of PFSA PEM degradation [214].

Kima *et al.* recently proposed a model allowing the calculation of the steady-state cell potential loss as function of an interfacial delamination between the CL and the GDL, but without link with materials degradation phenomena [215]. Rong *et al.* [216,217], presented an FEM model to describe debonding and delamination between ionomer and C/Pt agglomerate during humidity and temperature cycles. They estimated the strain in the ionomer phase caused by humidity cycles and predicted initiation time of delamination between the inomer and C and showed that those mechanical changes can happen and can affect the PEMFC performance. Delamination can be also an issue when water in the CL freezes. Mench *et al.* [218,219,220] presented a 1D transient model for this phenomenon. They showed that ice lens formation between the CL and the PEM or the diffusion medium and the catalyst can cause an unrecoverable damage.

Regarding atomistic modeling (Table II.3), on the basis of a DFT approach, Jacob studied oxides structure and the composition of bulk Pt-electrodes in electrochemical environments at elevated Butler-Volmer electrode potentials [221].

Atrazhev *et al.* [222] proposed that the peroxide radical can be formed directly on Pt surface, instead of through hydrogen peroxide, using DFT calculations. This mechanism allows peroxide radicals to be formed on the cathode whose potential is too high to form hydrogen peroxide by two electron reduction of oxygen and therefore can elucidate some experimental results suggesting radical formation on the cathode [223, 224,225]. The chemical degradation mechanisms of the PEM were studied quantum-chemically for hydrocarbon [226] and for PFSA PEMs [227]. The latter showed the possibilities of a new decomposition mechanism of

peroxide radicals attack to undissociated SO_3H side chain terminals and of the attack by hydrogen radicals, which can be formed by the reaction between a hydrogen molecule and a peroxide radical, to any position of the polymer, in addition to the previously proposed mechanism [228] of peroxide radicals attack to remaining non-fluorinated main chain terminals and following unzipping reactions.

Tian and Anderson [229] showed by DFT calculations that Co is oxidized before Pt on PtCo alloy and that Pt as edge sites is easier to be oxidized than Pt on the terrace. adsorptions of OH and H_2O on different surface models including Pt(111), $Pt_{15}Co(111)$, and $Pt_3Co(111)$ at 0.25 ML coverage were systematically investigated and reversible potentials for a series of reactions occurring in the initial stage of electrode dissolutions were obtained The latter result suggests that Pt dissolution is initiated at the edge site.

Some other techniques can be used in order to study the stability properties of the nanomaterials at the atomistic level. Monte Carlo (MC) models have been developed to describe nano-particles ripening, but not still for Pt [230]. By using MD simulations, Chen and Chan studied the mobility of Pt clusters up to 200 atoms on HOPG [231]. They predicted a generally high mobility of these clusters on the HOPG surface. A connected two-particle aggregate with a neck was observed over a period of a few ns, suggesting the possible stability of a networked structure which was also observed in experiments for larger particles. Zhou [232] carried out a MD simulation for charged Pt surface in contact with Nafion® containing water. The simulation suggested Pt disintegration caused by the interaction between Pt and the sulfonic acid terminal of Nafion® and instantaneous temperature rise at the interface up to 2000 K. This temperature rise, however, seems too high to be realistic.

Surprisingly, no atomistic-level modeling has been published on the topic of C corrosion. A paper on this last topic is now being submitted resulting from a collaborative work between NRC in Canada and my group [233] (see Chapter III and IV).

Mechanism	Example
Pt oxidation	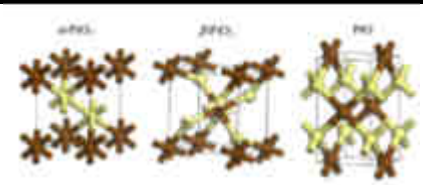 Jacob: Bulk-unitcells of the three most stable Pt-oxides: α-PtO_2, β-PtO_2, PtO. Dark spheres indicate Pt atoms, while bright ones are oxygens [221].
Pt coarsening	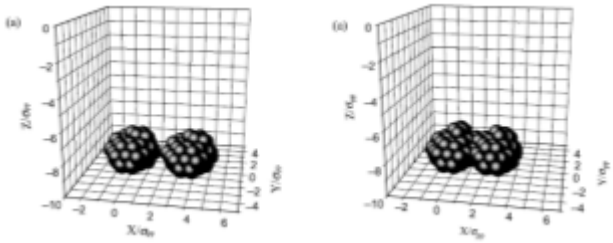 Chen *et al.*: Two clusters with 50 Pt atoms during aggregation (left: before, right: after 2 ns) [231].
Bimetallic nanoparticles reconstruction	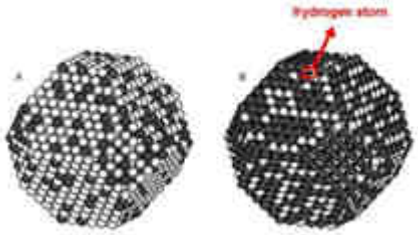 Zhu *et al.*: Impact of the environment on the nanoparticle reconstruction Structures of $Rh_{0.5}Pt_{0.5}$ clusters at 304 K predicted by MD simulations (a) in the absence of hydrogen and (b) in the presence of hydrogen. Pt atoms are white, Rh atoms are grey, and H atoms are black [234].
Bimetallic nanoparticles electrochemical dissolution	 Greeley and Norskov: impact of bimetallic catalysts composition on their stability (dissolution potential) [239].

Table II.3: Examples of published atomistic models addressing the PEMFC materials stability and aging.

Despite that these kinetic and atomistic models provide very useful information, they present several drawbacks that make them not appropriate enough to predict MEA durability under automotive operation conditions:

- *No prediction of cell potential evolution and MEA durability.* These kinetic models use to represent steady-state regimes with time-independent local operating conditions (e.g. local water content within the CL) and they show for instance poor predictive capability. One reason is that many of these models are parametrized by using *ex situ* experiments which are not representative enough of real operating conditions (e.g. potential between 1.2 and 1.6 Volts in [207]). Another reason is that they do not take into account the impact of the modeled aging phenomena on the structural and physicochemical properties of the MEA materials (e.g. variation of conductivity, variation of porosity, variation of contact resistances…). In other words, the instantaneous feedback between performance and aging, occurring in real PEMFC operation, is not taken into account: they describe which operating conditions affect a given degradation process (e.g. C corrosion) but do not describe the impact of this degradation process on the instantaneous performance (any prediction of the transient behavior of the PEMFC MEA electrochemical observables, such as the cell potential degradation, is provided).
- *Aging mechanisms addressed in a separated (uncoupled) way.* Most of the available kinetic models focus on Pt-based MEA, where Pt and C materials are treated as a single phase (no distinction between Pt and C phases). As in the *ex situ* experimental approaches, each material aging phenomenon has been the subject of individual modeling studies. However, in realistic PEMFC environments, aging mechanisms of the different individual materials are expected to compete or interact (cf. our previous discussions).
- *Potentiostatic-potentiodynamic simulations.* In most of the available kinetic degradation models, the Butler-Volmer electrode potential is the input variable, the output being a material corrosion rate and the cell current. Implicitly, it is assumed that the potential of the nano-materials is equal to the external/macroscopic applied potential. Again, the cell potential evolution and the associated MEA durability cannot be predicted in this way. The majority of the single-cell tests available in the literature are made with the current being the input variable.
- *Use of the classical Butler-Volmer theory.* This empirical theory, largely used in the PEMFC modeling community [235], describes electrochemical (electron-transfer) reactions on ideal planar electrodes. By using empirical Butler-Volmer equations written in terms of the electrode potential (as done e.g. in [190,191,206]) (Figure II.13), oxide formation and corrosion reactions (on Pt and C) are implicitly supposed to take place in the bulk, just outside the catalyst/Nafion® interfacial electrochemical double layer. Thus the possible inter-relation with ORR intermediate reaction species and the parasite water adsorption on the catalyst or C surface, expected in realistic PEMFC

environments [236], is not taken into account. In fact, the electrochemical double layer capacity is usually assumed to be constant (i.e. the electrochemical double layer structure is assumed to be uncoupled from the elementary reactions). In our opinion this could be an important assumption as the electrochemical interface is expected to evolve under transient conditions (such as in the case of aging nano-particles), and the structure of the electrochemical double layer influences in turn the electron transfer rate and thus the effective electro-activity properties of the catalyst surface. Disconsidering these issues can lead to contradictory interpretations (e.g. in [207] it is predicted that the increase of the ORR rate enhances C corrosion, but in [209] the opposite is also predicted). More generally, experimental evidence has been reported by Adzic *et al.* that Butler-Volmer equations are inappropriate for describing HOR and ORR reactions on Pt surfaces [237]. There is also some experimental evidence for nano-sized electrodes, where pronounced nano-scale non-linear effects of charge transfer in the surrounding electrolytic environment are important and cannot be explained using conventional theories [238]. Furthermore, the use of such a macroscopic Butler-Volmer theory cannot be really justified for describing electron transfer reactions on nano-materials with an evolving structure (in fact, standard transition-state theory assumes that the "catalyst" properties, by definition of "catalyst", are time-invariant or recovering its morphology after reaction). For example, water splitting and hydroxyl adsorption are speculated to modify the surface Pt-alloys dissolution thermodynamics [239]: thus, the stability properties of nano-structured catalysts (e.g. facility to oxidize) can be strongly affected by the electrochemical reactions of interest in PEMFC environments, such as the HOR or the ORR. Structure and interatomic distance can also change during reactant (H_2 or $O_{2)}$ exposure [240] or liquid adsorption. For example, surface segregation of Pt-Rh nanoclusters is dramatically altered by hydrogen chemisorption: in the absence of hydrogen, the cluster surfaces are Pt-rich, but in the presence of hydrogen, the cluster surfaces can be Rh-rich ("reversing segregation" or "reconstruction" phenomena) [241].

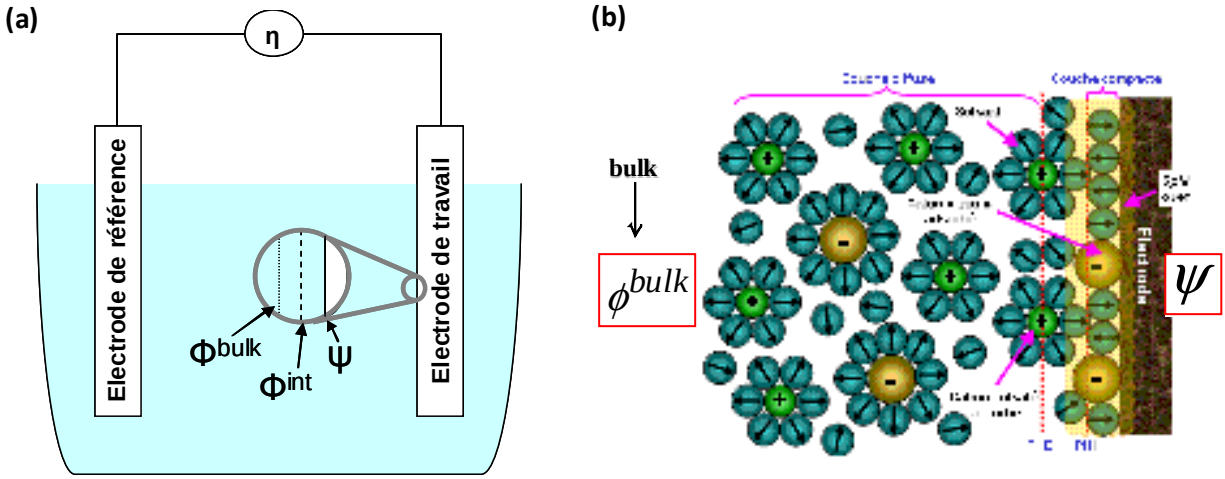

Figure II.13: (a) Typical electrochemical cell and definitions of potentials; (b) classical detailed representation of the electrochemical double layer. Butler-Volmer approach: double layer structure neglected, current function of the overpotential $i = f(\eta)$; transition-state theory: double layer structure neglected, kinetics written as functions of the electrode potential $v_i = f(E) = f\left(\psi - \phi^{bulk}\right)$; our approach: double layer structure accounted explicitily, kinetics written as functions of the surface potential $v_i = f\left(\eta^F\right) = f\left(\psi - \phi^{int}\right)$; Source: [8]).

- <u>*No* connection *between kinetic and ab initio models.*</u> In general, most of the available degradation kinetic models do not provide a connection with first-principles and surface science data at the atomistic scale. Most of the degradation mechanisms described in literature (e.g. for Pt oxidation/ dissolution in [190]) come from experimental fitting, without checking the thermodynamic consistency of the proposed pathways at the atomistic level. Very few efforts have been reported on the use of *ab initio* data to build degradation (kinetic) models (e.g. our work in [242,243], see Chapter III). First-principles or *ab initio* calculations (such as DFT method) can be used to predict important quantities such as adsorbate atomic structures and bonding energies, and provide key information on the reaction mechanisms and pathways. However, most of the *ab initio* studies available in literature focus on the calculation of the stability properties of the catalyst materials [244,245]. Greeley and Norskov have recently proposed a procedure to estimate trends in the thermodynamics of binary surface alloy dissolution in acidic media from DFT calculations [239]. This procedure is used to analyze the dissolution of solute metal atoms from various surface alloys, both with and without water splitting and hydroxyl adsorption, and dissolution of the so-called "skin" structures from bulk binary alloys. Despite these promising theoretical features, application of atomistically-resolved methods for modeling the electrochemical processes in a PEMFC-like environment remains a major challenge:

description of the coupling between chemistry and the electric field at the atomic scale is not an easy task. Some tentative steps in this direction have been already reported, but under non-realistic (zero absolute temperature) or very restricted (low Butler-Volmer overpotential, or system close to equilibrium) PEMFC operating conditions [246]. In general, no realistic descriptions of the interface are provided: e.g. Nafion® and catalyst-support electronic structure probably have an impact on the specific electro-catalytic properties.

Furthermore, because of its macroscopic character, the Butler-Volmer theory is not appropriate enough (as it is too macroscopic to capture key phenomena at the nano-scale) for matching atomistic physics with experimental observables. Perhaps too little effort has been expended in linking kinetic modeling with *ab initio* approaches in a way to preserve the underlying physics at the nano-scale. Moreover, because of the short time scales as well as the quasi-equilibrium conditions, real-time computation that couple these atomistic models with continuous descriptions of transport phenomena in a fuel cell still remain out of reach. In our opinion, there is great value in exploring and creating theoretical tools to enable quantitative interpretation and prediction of fundamental chemistry and electrochemistry into PEMFC engineering practice. This requires modeling at appropriate length/time scales and creating bridges between such scales, as well as better communication between theory and experiments. The exciting challenge is now to develop models accounting for degradation in order to match more realistic (closest to final application) PEMFC operating conditions, and to predict MEA durability (i.e. cell potential evolution).

II.4 – Conclusions

In recent years, PEMFCs have attracted much attention due to their potential as a clean power source for many applications: traction of vehicles by the replacement of the thermal generators, portable applications (cellular phones, laptop computers…) and the production of stationary electricity.

For example, stationary systems providers have now demonstrated, all over the world, the ability of low temperature PEMFCs to answer their customers' needs as far as performance, efficiency, environmental goals are concerned. Cost and durability are now the main hurdles in the path of the commercial success of these systems. Demonstrating a durability of several thousands of hours, up to 40000 hours for some applications, is thus now the prime requirement. The longer the durability, the higher the price customers will be ready to pay for their investment. Demonstrating such a long life-time in real operating conditions within an autonomous system is a real challenge. System failures often impair satisfactory

demonstrations of the stack reliability. Statistical proof of a repeated success in achieving a long life time asks for a large number of units operating at customers facilities, which is very costly. Before launching such large scale demonstrations, necessary when approaching market maturity, fuel cell system providers need a reliable prediction of their product's lifetime.

The main bottleneck now, if one wants to shorten the "time to market" for new PEMFCs, is that one needs an efficient method to take into account durability targets in all R&D actions on components and unit operating management strategies. A simple "try and error" method is manageable to get system durability from a few hundreds to a few thousands of hours. It is practically impossible when one wants to get from a few thousands of hours up to several tens of thousands of hours.

So called ADT protocols are easy to establish. One can indeed easily reach very short lifetimes with PEMFCs! But what is needed, are representative accelerated testing procedures. As an example, the selection of MEA for durability relies on accelerated tests. When testing MEA A, B and C with these procedures, if MEA B shows better durability, it is important that in the system MEA B will indeed provide the longer lifetime.

In my group, we aim to demonstrate that a reliable method, based on combined experimental and modeling approach, can be established to predict system lifetime, to propose validated representative ADT, and to benchmark components and improve operating strategies with respect to a durability target.

Predictive modeling is a requisite to establish this methodology for PEMFC. Durability of a PEMFC is the result of a very complex set of interrelated events, with competitive effects but also synergies between degradation processes. By accelerating one phenomenon, one usually creates conditions that are no more representative of the subtle balance between reactions in the real operating conditions. One can thus either overestimate degradation rates (leading to developing very highly resistant membranes, support carbons or catalysts for conditions never encountered in a real system), or underestimate degradation because some negative feedback loops are not taken into account. Only a physically based, multi-scale and multi-temporal model can provide the tool to combine all possible degradation phenomena and analyse their global impact on durability in a given set of operating conditions.

As an input for this model, one has to understand the fundamentals of degradation. Specific experimental data is needed, to correlate degradation and deterioration phenomena to operating conditions for stationary applications, and identify the paths leading to failure

phenomena. This experimental part is an effort to obtain data on degradation quantitatively and reproducibly, since the understanding of kinetics of various degradation processes are the key of final lifetime prediction.

We are convinced that this goal of establishing the proof of concept for lifetime prediction methodology, will, in the meantime, provide valuable data on degradation mechanisms for use in other research projects, either for other applications, or for material, components and system research and development.

CHAPTER III

Our modeling approach

"The task of Physics is not to find out how Nature is. Physics concerns what we can say about Nature."

Niels Bohr, Danish Physicist, 1885-1962.

III.1 – The key role of multi-scale modeling in industry

Computational modeling plays nowadays an extremely important role in several disciplines and research fields, such as in nuclear research, geology, meteorology and oceanography. But a concurrent increase of computational resources and efficient marketing techniques has revolutionized prototype development and optimization also in many key worldwide industries. In automotive and aerospace R&D for example, both cornerstone industries of the worldwide economy, prototype development has been almost completely moved from the workbench to the virtual drawing board, a plan which helped both industries to maintain their competitiveness in the global market.

With the accelerating trend towards development of PEMFC components based on micro- and nano-structured materials, the development of simulation approaches for simultaneous *in silico* prediction, characterization and optimization of these materials and components properties emerges as a new grand challenge in engineering and computational sciences. An unified multi-disciplinary approach towards the deployment of models, tools, algorithms and simulation and visualisation techniques is required to transform isolated solutions for specific problems into comprehensive, industry-ready platforms which are capable of predicting the properties of complex PEMFCs on the basis of their constitutive elements. While many techniques exist to address the specific questions and processes in the PEMFC, a lack of integration of the existing methods in readily available multi-scale modeling platforms has to date limited a large impact of PEMFC materials-modeling techniques in the industries.

The emergence of a wide array of novel catalysts, supports and membranes based on materials structured at the nano-scale, opens exciting opportunities to accelerate the

materials-research development by *in silico* experiments. Many of these materials can nowadays be characterized with *ab initio* quantum mechanics methods which open the door to first-principles description and optimization of materials properties in a bottom-up approach. In order to fulfill this promise, these data must be transferred in a series of hierarchical simulations to much larger length- and time-scales than can be addressed with *ab initio* modeling alone.

In fact, in order to contribute to real-world applications and to translate basic understanding into marketable products, PEMFC behaviour must be understood in the context of complex interplaying assemblies and materials. Based on this idea, it is necessary to develop a comprehensive strategy to replace some traditional experimentation, which is often costly (e.g. the long-term cell degradation tests) if not impossible (e.g. *in operando* visualization of the electrochemical double layer structure), by *in silico* experimentation for the PEMFC materials sciences.

Simulation strategies for nano- and micro-scale based PEMFC materials behavior in realistic operation modes (including degradation), must in fact span a large time and length-scale comprising many orders of magnitude. Given the complexities of multi-scale calculations, modeling the cell performance at a larger scale will not be possible by simply extending nano-scale simulation methods to increasingly larger systems. Instead, multi-scale simulation methods, which integrate information from high-accuracy calculations at small length and time scales into large-scale models, represent a promising approach to achieve quantitative materials modeling. Despite much research in this direction in other research fields, there are few demonstrated examples to date which address present day PEMFC R&D requirements of the world-wide industry and research communities.

There is a decades worth of experience in the development and application of individual software packages to address the specific problems in materials-science modeling in European research laboratories. This has resulted in a multitude of software programs, many of which can exploit HPC architectures, well suited for performing particular challenging tasks. In contrast to biosciences where most molecular simulations focus on proteins and/or DNA, there is little standardization in materials-science modeling, because of the vast internal complexity of the materials being developed.

In contrast to modeling in the automotive and aerospace industries, simulations in the materials sciences are presently far from being "whole device" simulators, where an entire unit is described at the functional level (usually macroscopic, i.e., long time-scales) on the basis of its components at the microscopic level (nanometer length scales, picosecond time-

scales). Such "whole device" simulators must therefore encompass components addressing the behavior of the material at a variety of length and time scales.

While there exists a number of standalone algorithms for integrating "adjacent" time and length scales into specific software packages (see, e.g., the QM/MM methodology), at present, there is no unified methodology to meet the challenges in multi-scale materials science simulation.

The global research strategy of my group at CEA is to establish a novel methodology which aims to provide an open, extensible, and maintainable infrastructure as a framework for performing PEMFC materials simulations at disparate scales. In particular, we aim to develop a model at the cell level (MEMEPhys®) allowing to capture nano- and micro-scale processes fingerprints onto the macroscopic electrochemical observables revelant for engineering practice, and from thus, to predict nano- and micro-structured materials activity, tolerance to contaminants and durability in conditions as close as possible to the realistic PEMFC environments (Figure III.1).

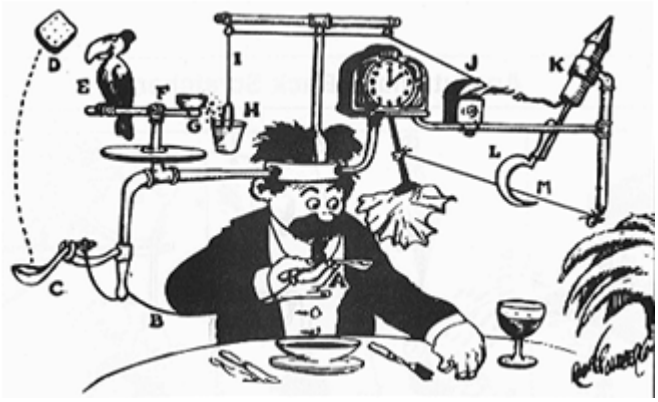

Figure III.1: Obviously, multi-scale modeling does not consist on developing a complex model just to reproduce the same results that it can be already obtained from simpler macroscopic models (Source: [247]).

III.2 – Our research approach of PEMFC materials aging

In the last 9 years I have developed with my group a research approach aiming firstly, on a deeper understanding of the fundamental electrochemistry and coupling of the physico-chemical phenomena responsible of the PEMFC MEA aging under steady-state and transient operating conditions; and secondly, on providing a predictive physical-based methodology of both PEMFC performance and durability. This approach strongly combines

experimental and theoretical efforts at different materials and components scales and are done inside my laboratory but also in collaboration with other teams within CEA and worldwide (cf. Chapter I). These efforts provide

- an homogeneous description of the degradation investigations which allows comparable evaluation of the experiments performed in different laboratories,
- the suggestion of guidelines to reduce the amount of Pt iand to mprove the design of the PEMFCs for enhanced performance and durability
- the recommendation of PEMFC dynamical operating strategies for mitigating MEA degradation
- the suggestion of experimental methods for accelerated and non-accelerated aging and off-line testing.

Figure III.2 illustrates my research approach structure. The “global mechanistic model” in Figure III-2, refers to my MEMEPhys® model, described below, and supported by the parallel development of models addressing some specific physicochemical mechanisms and generating parametrical inputs for the global model (e.g. *ab initio* calculations of elementary electrochemical kinetic barriers) (see following Sections). Other complementary work includes *ex situ* electrochemical characterization of the MEAs, CLs and the PEM with model materials (preparation approaches include DLI-MOCVD, electrodeposition and nanoaggregates sources, see Table III.1). These characterizations allow some uncoupling of the physico-chemical phenomena and are adjusted to the specific demands of the modeling. The techniques are described in Table III.3. All these experimental studies include potentiostatic, cyclic voltammetry and EIS analyses.

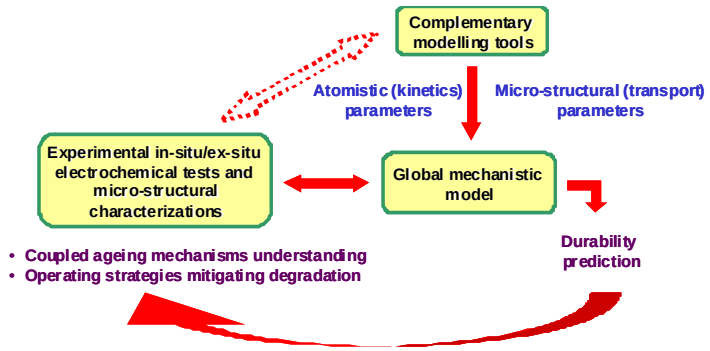

Figure III.2: Global organization of our research approach.

Technique	Specifications
Chemical synthesis (@CEA-LITEN/LCPEM)	✓ Low temperature method. ✓ Low cost method: simple set up and good scability. ✓ Formation of nanoparticles (alloys) on CB, C fibers or CNT. 
Electrodeposition (@CEA-LITEN/LCPEM)	✓ Low temperature method. ✓ High Pt utilization. ✓ Formation of nanoparticles (alloys) on GDL or CNT. 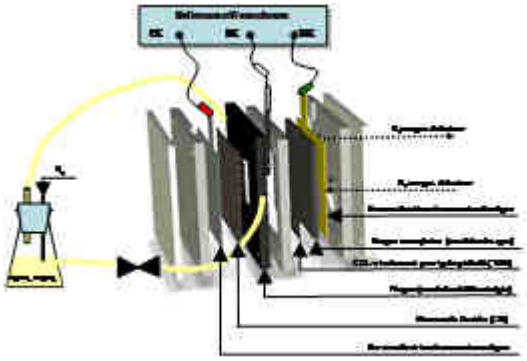

Table III.1: Used preparation approaches of model CLs and MEAs.

Technique	Specifications
Nanoaggregates-source (@CEA-INAC)	✓ Intermediate temperature method ✓ Formation of nanoparticles (alloys and Pt-skin) on GDL 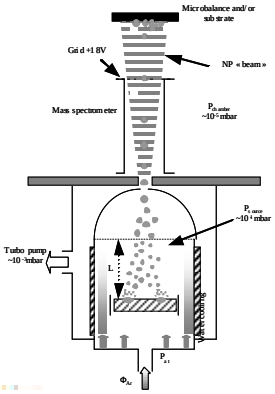
DLI-MOCVD (@CEA-LITEN/ Laboratory of Surface Technologies)	✓ Intermediate temperature method ✓ Use of metallic chemical precursors ✓ Formation of nanoparticles (bulk-truncated) on GDL 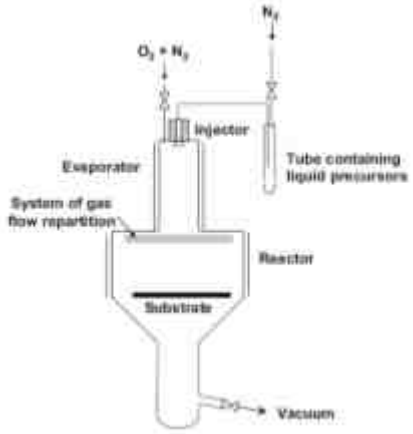

Table III.1 (continued): Used preparation approaches of model CLs and MEAs.

Technique	Measurements
RDE, RRDE (@CEA-LITEN/LCPEM)	✓ Study of catalyst activity, selectivity and stability through a constant reactant supply. ✓ Study of reaction mechanisms. 
Half-cell (@CEA-LITEN/LCPEM)	✓ Understanding of the mechanisms in conditions close to the fuel cell environment. 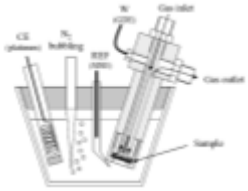
Single cell (@CEA-LITEN/LCPEM)	✓ Static and dynamic operating conditions. ✓ Performance and durability studies in real conditions. ✓ Water at the outlet are analyzed to identify potential degradation products. 
SEM, TEM, HR-TEM, XRD, EDS, XPS (@CEA-LITEN/LCPEM and SIMAP)	✓ Micro-structural characterizations of the home-made MEA before and after aging tests: impact of aging on structural changes (e.g. Pt migration, catalyst evolution, C-support degradation). ✓ Catalyst size and distribution. ✓ Catalyst lattice parameter (alloys). ✓ Catalyst composition. ✓ 3D tomography 

Table III.2: Experimental tools used to validate MEMEPhys®.

Technique	Measurement
DRIFT spectroscopy (@IRCELyon)	✓ Detailed information on the adsorption properties of contaminants on the catalyst surface and on the chemical nature of the reaction products. 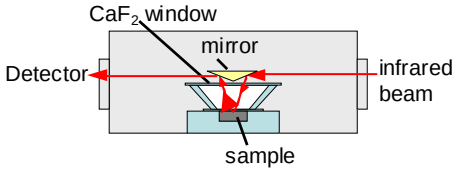
SECM (@CEA-INAC/SPRAM)	✓ Local induction of accelerated electrochemical aging on electrodes through chemically active species generation within the confined space between the micro-electrode and the studied material. ✓ Possibility to perform an easy parametric study on catalyst synthesis by means of an array of small synthesis batches with slightly varying conditions between each other. ✓ Electrochemical data (e.g. activity, catalyst and C-support conductivities…) during accelerated material aging. 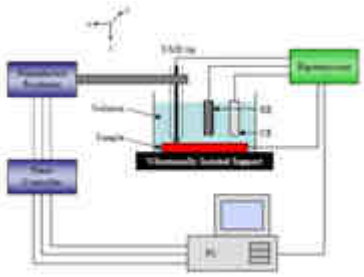
Mass spectrometry (@IRCELyon and CEA-LITEN/LCPEM)	✓ Detection of the species released by the PEMFC operation (e.g. CO_2 product from cathode C corrosion) 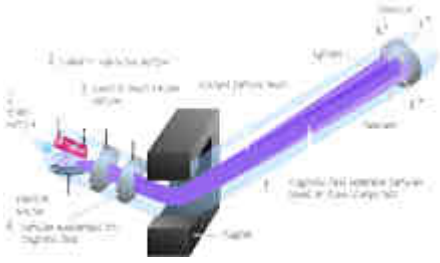

Table III.2 (continued): Experimental tools used to validate MEMEPhys®.

Technique	Measurement
EPR (@CEA-INAC)	✓ Detection of radical formation (OH°, OOH°…) in aged MEA and in an operating PEMFC MEA (*in situ*). 
NMR (@CEA-INAC)	✓ Structural analyses with solid-state NMR on aged PEM samples. ✓ Information on the chemical structures as well as data on the crystalline, amorphous or semi-crystalline state of materials. 

Table III.2 (continued): Experimental tools used to validate MEMEPhys®.

III.3 – MEMEPhys®: our multi-scale model for PEMFC transient analysis

MEMEPhys® is a transient, multi-scale and multi-physics single cell model accounting for the coupling between self-consistent physical-based mechanistic descriptions of the PEM and the CL phenomena (e.g. reactants, water and charge transport and detailed electrochemistry) and different materials aging mechanisms. [8,248,249,250]. The model was designed to connect atomistic phenomena (elementary kinetic processes) with macroscopic electrochemical observables (e.g. polarization curves - i-V characteristics -, EIS…) with reasonable computational efforts by using *ab initio* and surface science databases [8,126,168,242,243, 248, 249, 250, 251,252,253,254,255,256,267]. Such a model is a multi-scale one in the sense

that it is made of a set of interconnected sub-models describing the phenomena occurring at different scales in the PEMFC. However, this description remains macroscopic in the sense that it is based on irreversible thermodynamics concepts particularly adapted for the description of non-equilibrium physicochemical systems, as they are extensively used in chemical engineering: use of conservation laws coupled to closure equations (e.g. flux expressions, chemical rate models, thermodynamic models…). A good way to derive such a model is to use the Bond Graph approach [257,258,259,260]: this approach allows building the model as a modular collection of reusable sub-models through the concept of port power-conjugate variables, in particular for distributed-parameter systems [261]. Such an approach allows to easily modify the sub-models and to test new assumptions as it is computationally causal-independent (see Appendix III). The advantages of the Bond Graph approach utilization in chemical engineering and fuel cells modelling have been already demonstrated [8,,262,263].

The parameterization of MEMEPhys® is carried out on the basis of home-made and commercial MEAs characteristics, single-cell tests and specific *ex situ* experiments, and specific atomistic models developed (see below). For some sub-parts of the model, an estimation strategy from experimental results is applied and the parameters time evolution is analysed. According to the complex nature of such a model and prior to any estimation procedure, a structural identifiability analysis of some sub-parts has been made, following an already developed mathematical procedure I have developed, in order to check the theoretical feasibility of the estimation.

In contrast to the standard Butler-Volmer-based PEMFC models, our approach describes (mechanistically) the feedback between the instantaneous performance and the intrinsic MEA aging processes: that means that the model takes into account, at each simulated time step, both the effect of performance on aging and the effect of aging on performance. This powerful characteristic arises naturally from the coupled structure of our model, and thus, it allows the prediction of material properties evolution (e.g. the temporal evolution of the interlinked activity, selectivity and stability properties of the electrocatalyst). The prediction of the cell potential degradation, such as MEA durability as a function of the cell operating conditions and the initial MEA design parameters, also arises from our model. Furthermore, our model allows carry out temporal multi-scale analysis (e.g. simulation of the EIS shape evolution during the MEA degradation, cf. [126, 249]) and provides insights on the competitions and synergies between the different degradation mechanisms.

More generally, in contrast to the classical theories used to describe the PEMFC electrochemical behavior, in our approach the PEMFC environment is seen as a fully non-equilibrium physicochemical system. The nano/micro-structural properties of the PEMFC

electrodes (e.g. catalyst active surface area, cathode thickness…) are not time-invariant: they are defined as instantaneous state-variables.

I emphasize that the characteristics of my modeling approach represent important prerequisites for engineering practice to understand the synergies and interactions between the aging phenomena, to interpret PEMFC behavior under realistic operating conditions, to predict the MEA degradation and durability as a function of its initial nanomaterials composition and nano/microstructure, and to find new operation strategies to mitigate the degradation.

In the following I discuss in a general way the key concepts supporting our multi-scale model. For full mathematical details, we invite the readers to refer to our publications.

III.3a – General assumptions

The main assumptions for the model used to get the simulations results reported in Chapter IV, are described in the following:

- ✓ 1D+1D+1D model. It resolves transport phenomena along the channels and across the GDL, and transport phenomena and detailed electrochemistry across the MEA and the ionomer film + electrochemical interface at the micro-nano-scales inside the CLs (see the following Sections). Mechanical and gravitational aspects are not described;
- ✓ isothermal conditions are assumed (however, the temperature is explicitly accounted in the different transport and electrochemical parameters). The model is not valid for temperatures below than 4°C. Ice formation is not taken into account. Other specific models describing the electrochemistry under 0°C have been developed in my group in the past, and the connection with MEMEPhys® will be subject of interest within the incoming months;
- ✓ at the initial *in silico* PEMFC state (t_{OT} = 0 s), the physicochemical properties of the CLs and the PEM are assumed to be isotropic and homogeneous throughout their entire volume (e.g. catalyst, ionomer and C are supposed to be homogeneously distributed within the CL volume; contact angle, porosity, ionic conductivity, electrical conductivity in the C phase, electric pemittivities, etc. are assumed to be space-independent). These assumptions can be easily changed within the model (e.g. to simulate the PEMFC behavior with initial Pt gradients across the CL thickness or on its surface) as explained in Chapter V;
- ✓ no distinction is done between the electrostatic potential in the catalyst and the electrostatic potential in the C support;

- ✓ the diffusion layers are often composed of either a single GDL or a composite structure of a GDL and a MPL. In our model we only describe the GDL;
- ✓ as a first approximation, the model excludes the degradation of the anode, GDL and the corrosion of the channels as well as the mechanical degradation of the layers.
- ✓ at the present status, the model does not describe ionomer degradation within the CLs.

To mimic the actual morphology of the CLs, a spherical thin film-agglomerate approach along with a one-dimensional two-phase model is developed to investigate the transient evolutions of various model properties as well as performance and durability.

In the particular case of an isothermal PEMFC fed with pure oxygen and hydrogen fully saturated with water vapor we assume that the PEM and electrodes are already fully humidified at t_{OT} = 0 s (PEMFC starting operation time). In these conditions, it is not necessary to take into account the transient pore phase flooding by liquid water in the electrode. The additional water production in the cathode is assumed to be evacuated through the liquid phase with zero thermodynamic resistance (no chemical potential gradient). These comments are extensive to water description in the GDL. Pressure drop is supposed to be negligible in the GDL and pore phase. Furthermore, in this case hydrogen and oxygen pressures drops across the CL can be neglected [250].

III.3b - Global algorithm

From an algorithmic point of view, the multi-scale kinetic model MEMEPhys® is supported on two interacting "cores" [101,126] (Figure III.3):

(i) the first one describes the interactions between the different non-aging phenomena (e.g. HOR and H_2 transport in the anode, ORR and O_2 transport in the cathode, H_2O transport within all the MEA) [248]

(ii) the second one describes the degradation processes such as catalyst oxidation, dissolution and ripening in the cathode, catalyst poisoning in the anode and/or cathode, C corrosion in the cathode and PEM degradation [126].

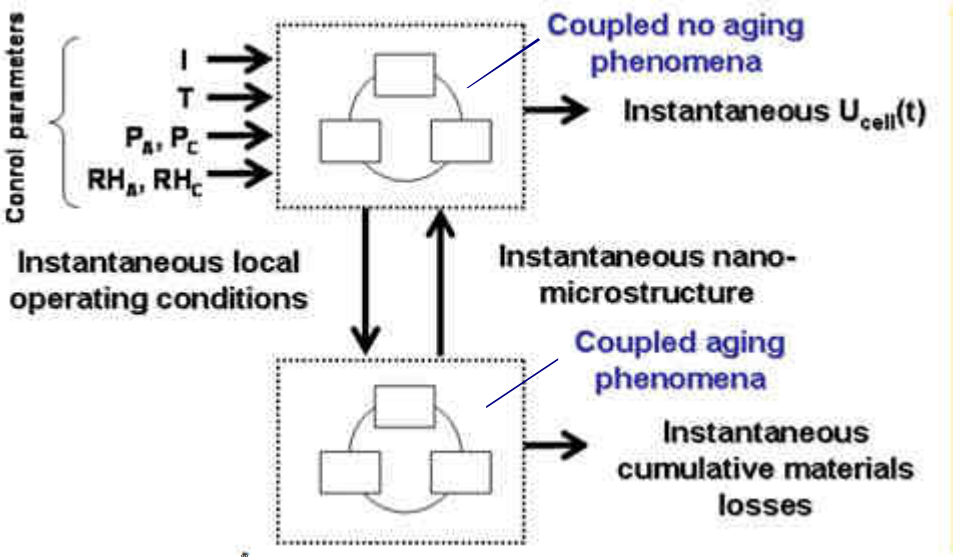

Figure III.3: MEMEPhys® model algorithmic structure (description of the feedback between instantaneous performance and aging: prediction of durability).

The first core provides to the second one a multi-dimensional vector containing local operating conditions (e.g. local liquid water content across the CL thickness) at the simulated time "t" (instantaneous state variables). The second core returns to the first one a multi-dimensional vector containing information about the new electrocatalytic and transport properties induced by the local CL or PEM structure degradation. This feedback allows calculating cell potential decay. The relationships between the structural changes and the electrocatalytic and transport properties changes (e.g. between C mass loss by corrosion and effective electronic conductivity of the CL) are provided by continuum mathematical functions (e.g. *continuity equations* relating catalyst nano-particles dissolution kinetics with their surface area evolution or equations relating the C corrosion kinetics with the C surface area evolution, built on the basis of fractal C structures -see below-) or by databases (or "libraries") previously generated by using atomistic-level structural resolved models such as DFT, MC or CGMD (Figure III.4) (see below).

The model combines "on the-fly" numerical simulation at four scales (Figure III.5):

(i) one at the nano-scale describing the structural changes of the electrochemical double layer surrounding the catalyst and C nano-particles during the degradation process. These nano-scale models consist of a non-equilibrium compact layer sub-model describing the competitive adsorption of the intermediate reaction species, of the parasite water molecules and oxide formation on both catalyst and C, and of a non-equilibrium diffuse layer sub-model in the electrolyte, describing

the transport (electro-migration and diffusion) of protons and metallic ions (produced by the catalyst dissolution) close to the nano-particules.

(ii) one at the micro-scale describing the reactants transport phenomena (diffusion) at the catalyst/C agglomerates level

(iii) one at the meso-scale describing the transport phenomena of reactants (diffusion), charges (electro-migration) and water (diffusion and electro-osmosis) through the MEA thickness (including hydrogen, oxygen and nitrogen crossover through the membrane). Inside the CLs, a description of the water condensation phenomena is included.

(iv) one at the macro-scale describing multi-species transport and water condensation phenomena within the GDL.

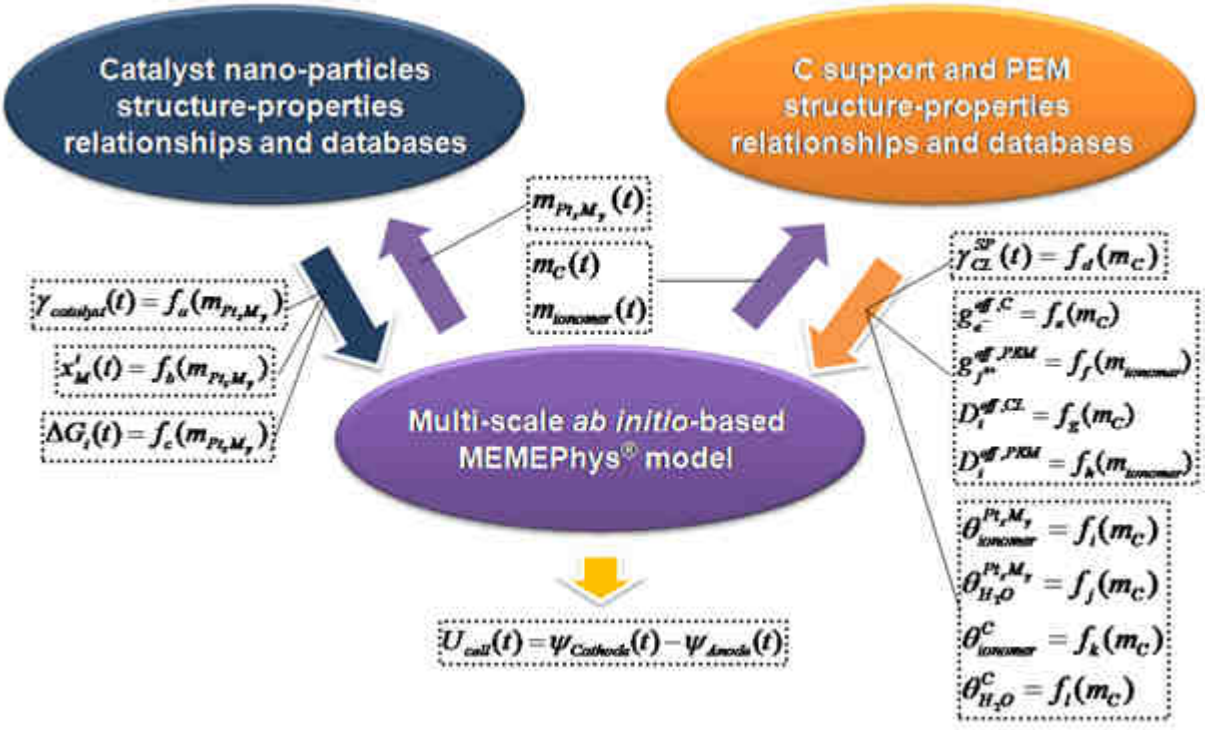

Figure III.4: MEMEPhys® structure-properties relationships to simulate catalyst nano-particles, C support and PEM degradation.

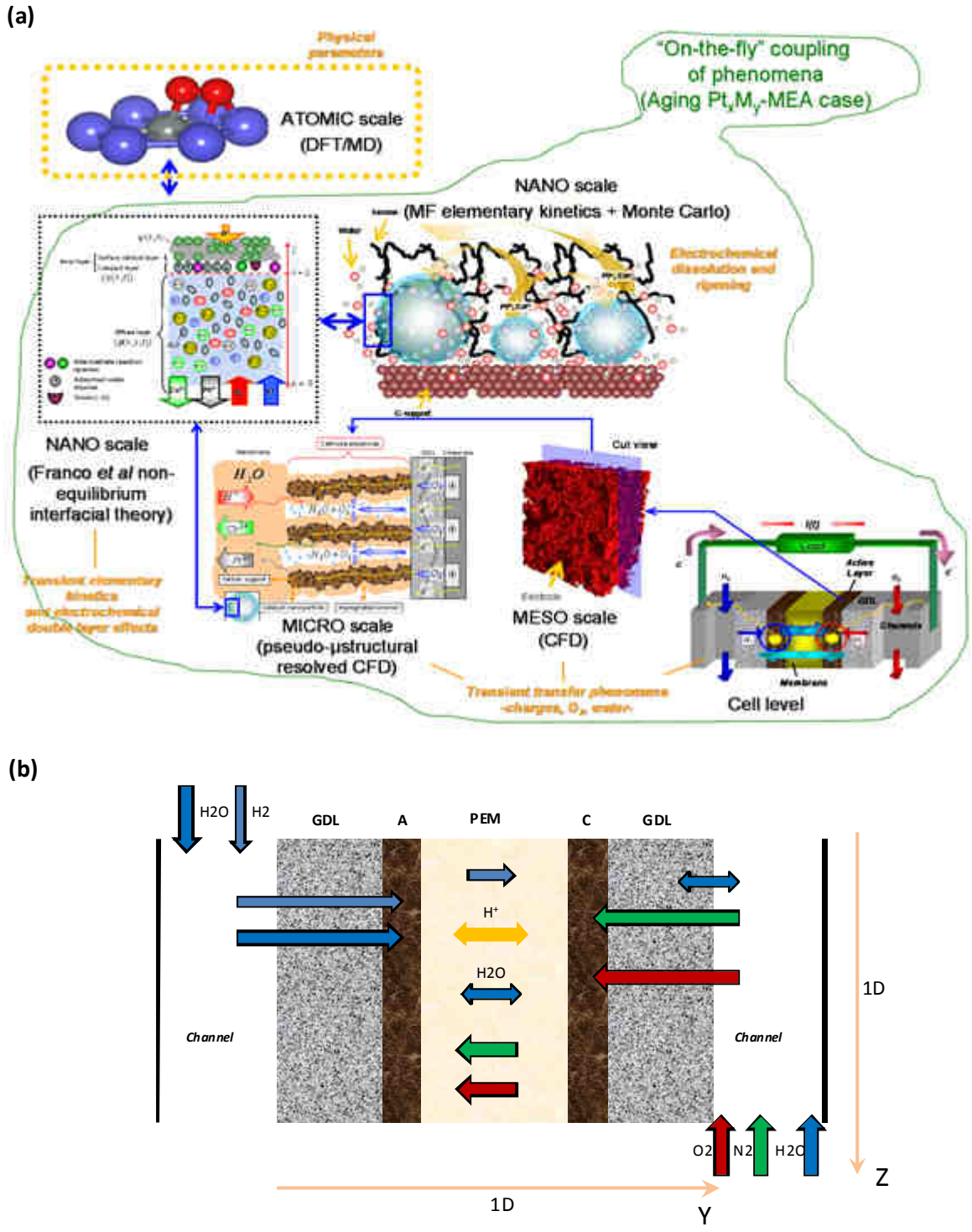

Figure III.5: (a) accounted scales within MEMEPhys®, (b) modeled components (Source: [101]).

III.3c – Electrochemical databases

In our approach, all the materials are treated as separated (but interconnected) phases (e.g. Pt electrochemistry and C corrosion in [126, 168, 255]). All the chemical and electrochemical processes are modeled as series-parallel elementary kinetic steps.

For the electrochemical sub-models, the nano-particles are mapped onto surfaces (Pt(111) and C sheet). Thus our electrochemical models neglect side effects (i.e. edge or corner sites on a nano-particle), but this is still sufficient for predicting relevant CL potential evolution trends. Full elementary kinetic modeling of reactions on 3D nano-particles still remains a challenge for theory [264,265].

We are using both our own DFT calculations and literature DFT data to determine the thermodynamically favourable elementary reactions and reaction pathways occurring at the atomistic scale on the electrocatalyst surface (e.g. ORR involving O_2 dissociation and H_2O formation on Pt(111) or $Pt_3Ni(111)$, see Figure III.6 for the pathways possibilities, before DFT discrimination). We use energy barriers (transition states) estimated/calculated either by previously published DFT works or by our DFT models in periodic conditions in order to calculate the kinetic rate constants for each single reaction step involved in the HOR, ORR and poisoning reactions [266,267,268]. To calculate the thermodynamics of the materials dissolution and corrosion (e.g. Co dissolution) from DFT data, we are using an extension of the approach proposed in [239] the methodological details being given elsewhere [242,243,256].

The corresponding atomistic kinetics is then implemented into the non-equilibrium nano-scale models of MEMEPhys® collecting all the elementary events, catalytic or not, to simulate the electrochemical observables. The nano-scale models introduce the electric field effect correction without empirical parameters and open interesting perspectives to scale up atomistic data into macroscopic models in a robust way (see below). The impact of the catalyst chemistry and nano-structure on the electrodes and cell potentials can be then captured.

Some examples of elementary reactions studied and used within MEMEPhys® are reported in Table III.3 and Figure III.7.

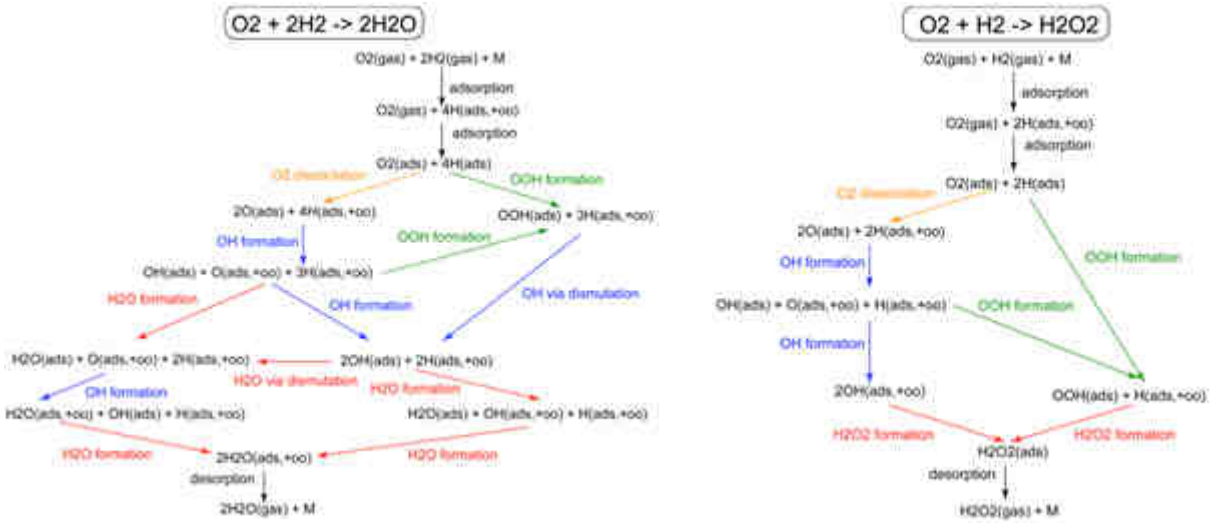

Figure III.6: Possible formation routes of H_2O and H_2O_2 on Pt and Pt-based catalysts explored using DFT calculations.

HOR/ORR/H2O2	Contamination reactions	Degradation reactions
$H_{2(gas)} + 2s \Leftrightarrow 2H_{(ads)}$ $H_{2(gas)} + s \Leftrightarrow H_{(ads)} + H^+ + e^-$ $H_{(ads)} \Leftrightarrow s + H^+ + e^-$	<u>CO poisoning</u> $CO_{(gas)} + s \Leftrightarrow CO_{(ads)}$ $CO_{(ads)} + H_2O \Leftrightarrow CO_2 + 2H^+ + 2e^-$ $(Pt-O) + (Pt-CO) \Leftrightarrow 2Pt + CO_2$ $(Pt-OH) + (Pt-CO) \Leftrightarrow 2Pt + CO_2 + H^+ + e^-$ $Os + COs \Rightarrow CO_2 + 2s$	Pt oxidation/dissolution $Pt \Leftrightarrow Pt^{2+} + 2e^-$ $Pt + H_2O \Rightarrow Pt(OH)_{(ads)} + H^+ + e^-$ $Pt(OH)_{(ads)} \Leftrightarrow Pt(O)_{(ads)} + H^+ + e^-$ $Pt(O)_{(ads)} + 2H^+ \Leftrightarrow Pt^{2+} + H_2O$
$O_{2(gas)} + 2s \Rightarrow O_{2(ads)}$ $O_{2(ads)} \Leftrightarrow 2O_{(ads)}$ $O_{(ads)} + H^+ + e^- \Leftrightarrow OH_{(ads)}$ $OH_{(ads)} + H^+ + e^- \Leftrightarrow H_2O_{(ads)}$ $2OH_{(ads)} \Leftrightarrow H_2O_{(ads)} + O_{(ads)}$ $2OH_{(ads)} \Leftrightarrow H_2O_{2(ads)} + s$ $O_{(ads)} + OH_{(ads)} \Leftrightarrow OOH_{(ads)} + s$ $O_{2(ads)} + H^+ + e^- \Leftrightarrow OOH_{(ads)}$ $OOH_{(ads)} \Leftrightarrow O_{(ads)} + OH_{(ads)}$ $OOH_{(ads)} + H^+ + e^- \Leftrightarrow H_2O_{2(ads)}$ $H_2O_{(ads)} \Leftrightarrow H_2O_{(gas)} + s$ $H_2O_{2(ads)} \Leftrightarrow H_2O_{2(gas)} + s$	<u>NO_2 poisoning</u> $NO_{2(gas)} + s \Leftrightarrow NO_{2(ads)}$ $NO_{2(ads)} \Leftrightarrow NO_{(ads)} + O_{(ads)}$ $NO_{(ads)} + O_2H_{(ads)} \Rightarrow HNO_3 + 2s$	C corrosion $C + H_2O \Rightarrow C(H_2O)_{(ads)}$ $C + H_2O \Rightarrow C(OH)_{(ads)} + H^+ + e^-$ $C(H_2O)_{(ads)} + C(OH)_{(ads)} \Rightarrow C(OOH)_{(ads)} + 2H^+ + 2e^-$ $C(OOH)_{(ads)} \Rightarrow CO_2 + H^+ + e^-$
	<u>SO_2 poisoning</u> $SO_{2(gas)} + s \Leftrightarrow SO_{2(ads)}$ $SO_{2(ads)} \Leftrightarrow SO_{(ads)} + O_{(ads)}$ $SO_{(ads)} + OH_{(ads)} + O_2H_{(ads)} \Rightarrow H_2SO_4 + 3s$	PFSA-side chain degradation $\sim CF_2COOH + HO^\bullet \Rightarrow \sim CF_2COO^\bullet + H_2O$ $\sim CF_2COO^\bullet \Rightarrow \sim CF_2^\bullet + CO_2$ $\sim CF_2^\bullet + HO^\bullet \Rightarrow \sim CF_2OH$ $\sim CF_2OH \Rightarrow \sim C(O)F + HF$ $\sim C(O)F + H_2O \Rightarrow \sim COOH + HF$ $\sim CF_2COOH + 2HO^\bullet \Rightarrow \sim COOH + 2HF + CO_2$
		<u>Fenton's reactions</u> $H_2O_2 + Fe^{2+} \Leftrightarrow Fe^{3+} + HO^\circ + HO^-$ $H_2O_2 + Fe^{3+} \Leftrightarrow Fe^{2+} + HOO^\circ + H^+$ $HOO^\circ + Fe^{3+} \Leftrightarrow Fe^{2+} + O_2 + H^+$ $H_2O_2 + HO^\circ \Leftrightarrow H_2O + HOO^\circ$ $HO^\circ + Fe^{2+} \Leftrightarrow Fe^{3+} + HO^-$

Table III.3: Some typically accounted elementary reactions within MEMEPhys®.

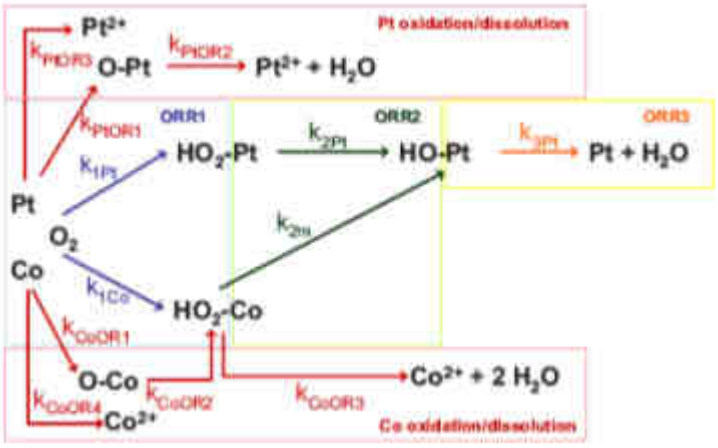

Figure III.7: Example of our *ab initio* determined ORR steps coupled with Pt and Co oxidation/dissolution reactions to simulate the ORR activity evolution during Pt_xCo_y aging (Source: [242,243]).

In my group, the DFT calculations are nowadays being performed with the Vienna *Ab initio* Simulation Package (VASP) [269,270] for periodic systems (e.g. the ORR and HOR on metallic surfaces, in collaboration with ENS from Lyon), with the ADF (Amsterdam Density Functional) Package [271] for non-periodic systems (e.g. bio-inspired molecules) and BigDFT (CEA *ab initio* code, being developed by the CEA/INAC) [272] for some particular systems (e.g. metallofullerenes). As example, methodological details about our VASP calculations on Pt(111) are provided in Appendix IV [266]: for the determination of the transition states, the Nudged Elastic Band (NEB) method is used [273].

Here we present an example of one of our ongoing calculations. First of all the $Pt_3Ni(111)$ surface have been modeled using three different terminations: 1) one called *bulk-truncated,* a surface termination that preserve the bulk stoichiometry for all the layers, 2) one called *skeleton*, a surface termination built to represent the chemical leaching of Ni atoms of the first layer (bulk truncated termination exposed to the electrochemical environment), and 3) one called *skin*, a surface that has only Pt atoms in the first layer and a PtNi stoichiometry varying from the second to the third atomic layer. It is important to point out that these three different $Pt_3Ni(111)$ materials present different catalytic properties and we are interested to understand the higher activity (up to X 90) that they present compared to Pt/C catalysts [112]. From our *ab initio* comparisons of $Pt_3Ni(111)$ surface terminations against Pt(111), the following trends can be underlined:

- ✓ atomic hydrogen on $Pt_3Ni(111)$ has the same stability (adsorption energy) than on Pt(111). The preferential site change from top and hollow on bulk-truncated to a bridge site on skeleton;

- ✓ atomic oxygen is 0.3 eV more stable on $Pt_3Ni(111)$ than on Pt(111). We can observe even change on stability of 70 meV from bulk-truncated to skeleton. There is not change on the preferential site from Pt(111) to $Pt_3Ni(111)$;
- ✓ molecular oxygen has a small difference (0.16 eV) in stability from Pt(111) to $Pt_3Ni(111)$ bulk truncated and a much higher difference (0.51 eV) from Pt(111) to $Pt_3Ni(111)$ skeleton. This change in stability is followed by a change on the preferential site, from a Top_Bridge (TB) in bulk truncated to a Top_Top (TT) on skeleton;
- ✓ the hydroxide OH species has the same behavior than molecular oxygen, with a gain of 0.51 eV in stability between Pt(111) to $Pt_3Ni(111)$.

From a reactivity point of view in Pt(111):

- ✓ the barrier of O_2 dissociation is 0.08 eV smaller than the barrier for formation of hydroperoxyl (OOH) at low coverage suggesting that the two most evocated routes for water formation (O_2 dissociation and OOH formation) are thermodynamic possible;
- ✓ the barrier of O_2 dissociation in low coverage (0.35 eV) is half compared with higher coverage (0.75) calculated by Mavrikakis [274];
- ✓ cluster calculations overestimate the barriers for O_2 dissociation and OH formations.

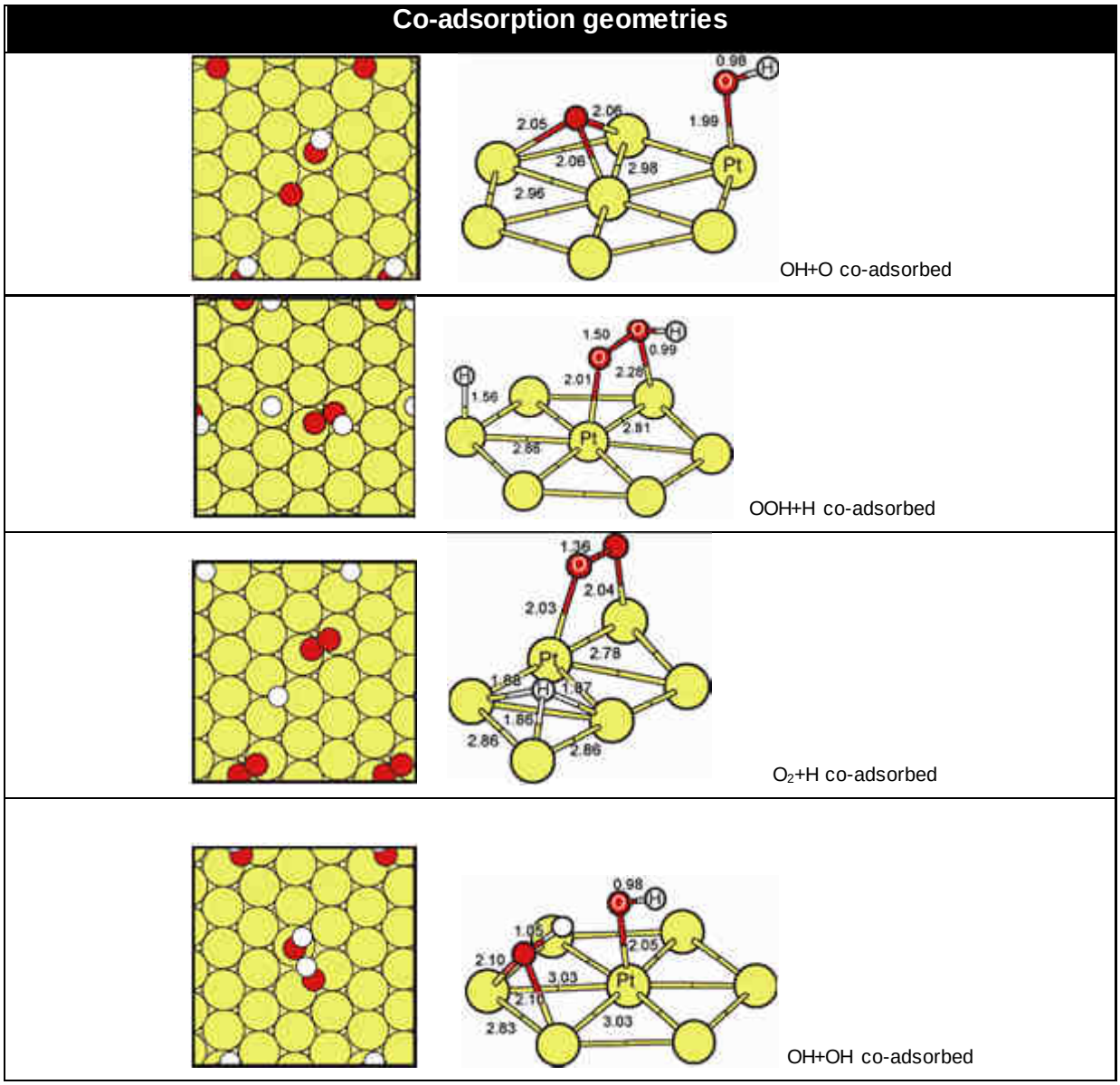

Figure III.8: Examples of calculated co-adsorption geometries for the elementary steps of the ORR on Pt(111).

Name of the adsorbed	Range in eV	The most stable site:
Atomic Hydrogen (H)	(-0.46 < -0.51)	*Top* and *hollow fcc* are competitive
Atomic Oxygen (O)	(-0.84 < -1.22)	*Hollow fcc*
Molecular Oxygen (O_2)	(-0.63 < -0.80)	*fTT* (mix of two *top* sites)
Hydroxide (OH)	(-1.73 < -1.78)	*bOHbri_Hhcp* (mix of *bridge* and *hollow hcp* sites)
Molecular water (H_2O)	(-0.29)	*H_2Otop_2Hbri* (mix of top and bridge sites)
Hydroperoxyl (OOH)	(-1.06 < -1.27)	*O_2 bri_Hbri* (mix of *bridge* sites)
Hydrogen peroxide (H_2O_2)	(-0.32 < -0.33)	*bT_fcc_OHtop* (mix of *hollow fcc* and *top* sites)
(O + O)	(-1.55 < -2.22)	*Ofcc_Ofcc*
(O + H)	(-1.57 < -1.64)	*Ofcc_Hfcc*
(H_2O + O)	(-1.19 < -1.57)	
(O_2 + H)	(-1.10 < -1.23)	*fTT_Hfcc*
(OH + H)	(-1.16 < -1.25)	*OHbri_Hhcp*
(OH + OH)	(-3.32 < -3.92)	*bOHtop_Hbri_bOHbri_Hfcc*
(H + OOH)	(-1.48 < -1.77)	*Htop_fTTOOH_Hbri*
(O + OH)	(-2.57 < -2.92)	*Ofcc_OHtop_Hhcp*

O_2	-0,49
O	-3,37
H	-2,73
H_2O	-0,6
OH	-2,06
O_2H	-1,04

Table III.4: Example of calculated co-adsorption energies (left) and values reported in published literature [275] (right).

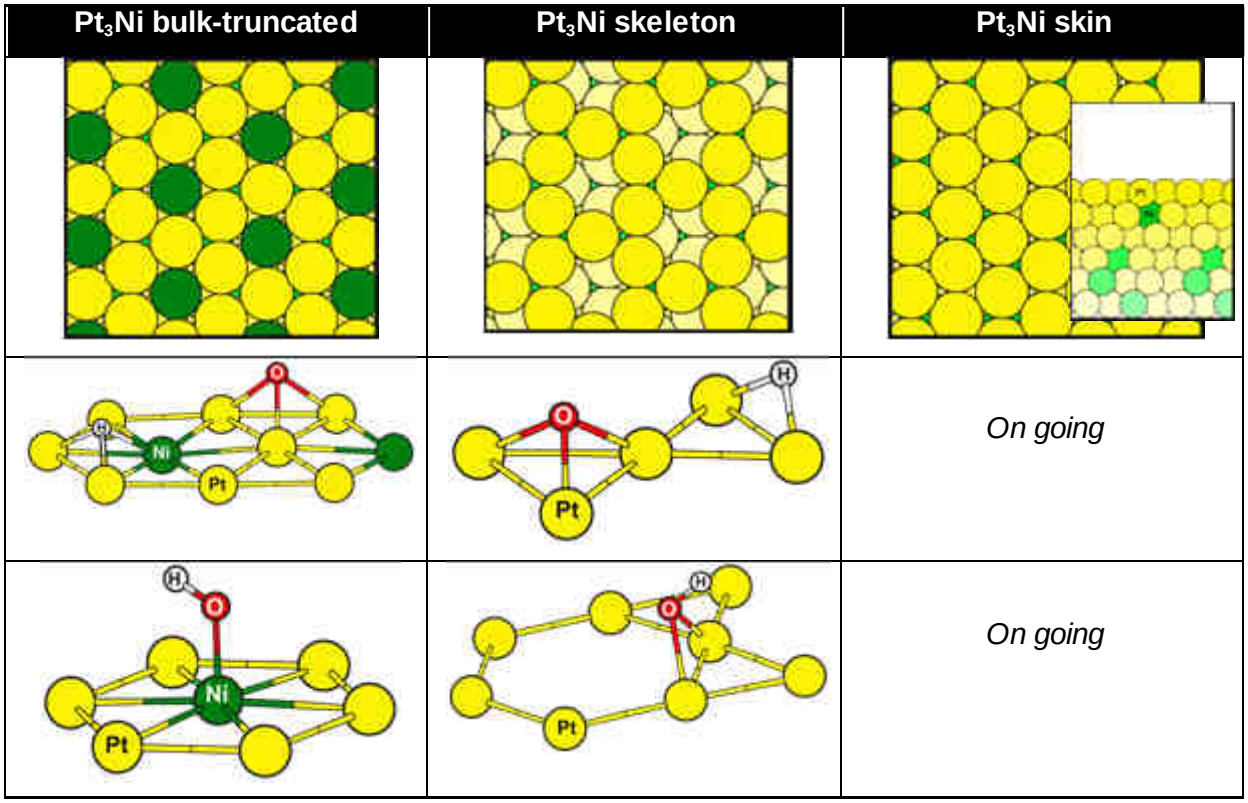

Figure III.9: Examples of optimized co-adsorption geometries for the ORR on $Pt_3Ni(111)$.

Name of the adsorbed	Range in eV	The most stable site:
Atomic Hydrogen (H)	(-0.42 < -0.48)	*holPt$_2$Ni_Ptfcc*
Atomic Oxygen (O)	(-0.94 < -1.50)	*OholPt$_2$Ni_Ptfcc*
Molecular Oxygen (O$_2$)	(-0.71 < -0.96)	*fTB_TNiBPt$_2$_Ptfcc*
Hydroxide (OH)	(-1.65 < -1.99)	*bBOHPtNi_OholPt$_2$Ni_Pthcp*
(O + H)	(-1.44 < -1.90)	*OholPt$_2$Ni_Ptfcc_HtopPt*

Name of the adsorbed	Range in eV	The most stable site:
Atomic Hydrogen (H)	(-0.42 < -0.56)	*bri_short_bent*
Atomic Oxygen (O)	(-1.30 < -1.57)	*3hol_1lay_Nifcc*
Molecular Oxygen (O$_2$)	(-0.93 < -1.41)	*TT_short*
Hydroxide (OH)	(-1.98 < -2.38)	*bBOH_short_HholNihcp*
(O + H)	(-1.62 < -2.09)	*O_3hol1layNifcc_H_3hol1layNihcp*

Table III.5: Example of calculated co-adsorption energies for $Pt_3Ni(111)$ bulk truncated (up) and $Pt_3Ni(111)$ skeleton (bottom).

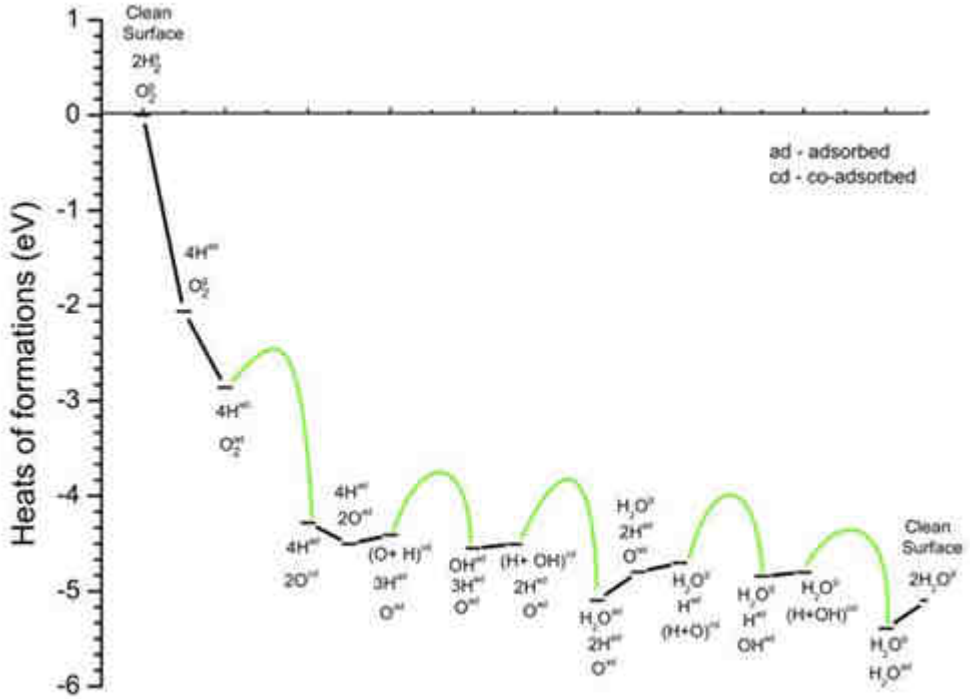

Figure III.10: Calculated H_2O formation energy profile.

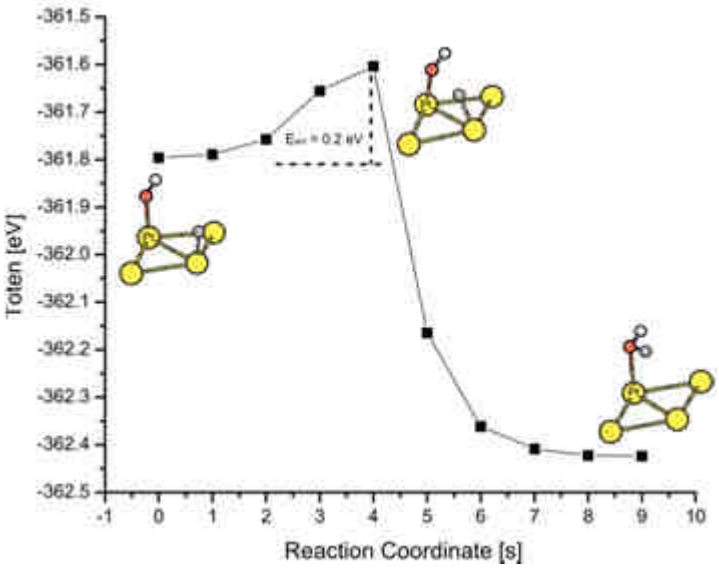

Figure III.11: Example of NEB calculation for the water formation on Pt(111).

Calculated Transition-States for the elementary steps of the ORR on Pt(111)

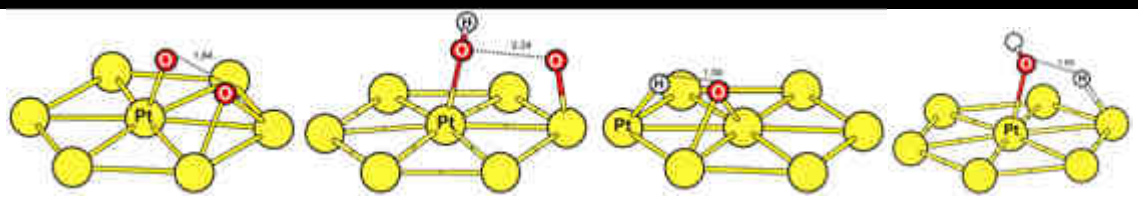

Step	Barrier in eV
O_2 dissociation	0.31
OH formation	0.90
H_2O formation	0.20
OOH formation	0.39

Step	Barrier in eV
O_2 dissociation	**0,65**
OH formation	**1,37**
H_2O formation	**0,24**
OOH formation	**0,05**

Figure III.12: Examples of our calculated possible transition-states for the ORR on Pt(111), associated barriers (below at the left) and comparison with results obtained from Pt_{59} clusters by Jacob *et al.* (below, at the right).

Another example is our DFT studies on the proton reduction mechanism catalyzed by the complexes $[Ni(P_2^HN_2^H)_2]^{2+}$, bio-inspired from the hydrogenases [276]. A detailed analysis of the reactive isomers has been carried out together with the localizations of the Transition States and energy minima. We observed that the reactive catalytic specie is a biprotonated Ni(0) complex, that can show different conformations and that can be protonated on different sites. The energies of the different conformations and bi-protonated species have been calculated and discussed by us in [276]. Energy barriers for two different reaction mechanisms have been identified in solvent and in gas phase. Frequencies calculations have been performed

to check the nature of the energy minima and for the calculations of entropic energetic terms and Zero Point Energies. We show that only one conformation is mostly reactive. All the other conformations are non-reactive in their original form and they have to pass through conformational barriers in order to become reactive.

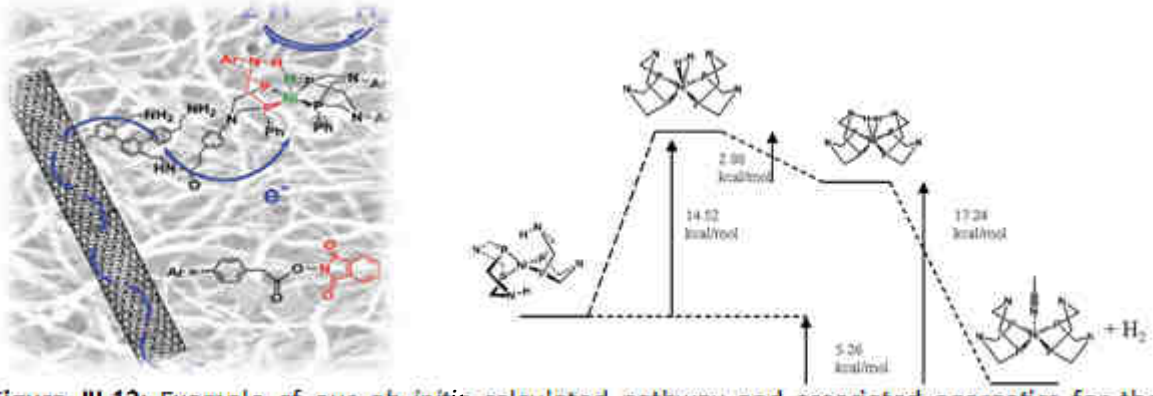

Figure III.13: Example of our *ab initio* calculated pathway and associated energetics for the H_2 production on $[Ni(P_2{}^{H}N_2{}^{H})_2]^{2+}$ supported on CNT (Source: [276]).

The interest of using metallofullerenes as PEMFC catalysts has been also evaluated by us using DFT [268]. Because of the stability of C_{60}, these materials have interesting properties to reduce C corrosion or Pt degradation in standard CLs. The enthalpies for the multi-step ORR adsorbates on $C_{59}Pt$ and $C_{60}Pt_n$ were determined and the structures generally resemble that predicted for adsorbates on a Pt surface. The hydrogen atom was more strongly bound on a C atom near the Pt than on the Pt atom itself. Water was bound to the Pt atom with a binding energy of 0.56 eV, but had negative binding energies on the C_{60}-like backside of this metallofullerene, which is consistent with the insolubility of C_{60} in water. Enthalpies for some possible ORR reactions were determined. As in Pt surfaces, it looks like the OH will poison the electrocatalytic sites. In addition, because of the strong adsorption of the hydrogen to all parts of the fullerene, it seems that hydrogen may poison the electrocatalytic sites also. This will slow down the production of water on the PEMFC cathode.

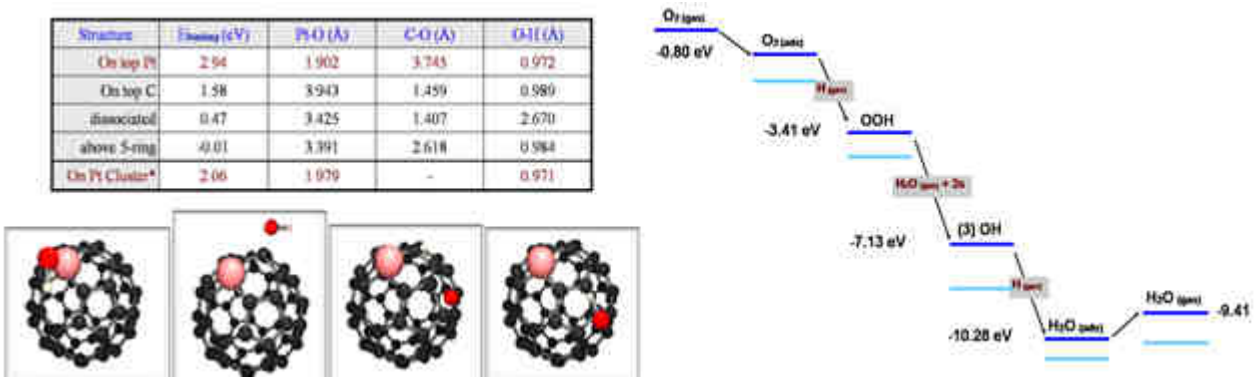

Figure III.14: Example of our *ab initio* calculated pathway and associated energetics for the ORR on $C_{60}Pt$.

III.3d – Structure-properties relationships and databases

The instantaneous MEA materials structural evolutions (e.g. ECSA, C surface area, PEM porosity) in the simulated PEMFC operation, induced by the catalyst dissolution and ripening, C corrosion and PEM chemical degradation, are determined at each simulation time-step as functions of the elementary degradation chemistry kinetic equations described in our previous papers [126,168,242,243] and recalled later in this Chapter.

For example, in order to relate the specific Pt surface area $\gamma_{catalyst}$ ($m^2.m^{-3}$) with the Pt degradation kinetics induced by both electrochemical Ostwald ripening and dissolution into the surrounding electrolyte (water+ionomer) (Figure III.15), we adopt the continuity equation [277]

$$\frac{\partial \Phi}{\partial t} + \frac{\partial}{\partial r}\left(\frac{\partial r}{\partial t}\Phi\right) = \Gamma(y,z,t) \tag{1}$$

where $\Phi(r,y,z,t)$ is the distribution function given by

$$\Phi(r,y,z,t) = \lim_{\Delta r \to 0} \frac{N(r, r+\Delta r, y, z, t)}{\Delta r} \tag{2}$$

where $N(r, r+\Delta r, y, z, t)$ is the number of catalyst nano-particles per unit of CL volume with size (radius) comprised between r and $r+\Delta r$. In equation (1) $\Gamma(y,z,t)$ is a source/sink term which allows accounting for the Pt dissolution and diffusion towards the PEM (i.e. it is function of the total Pt mass supported on C, $m_{catalyst}(y,z,t)$, calculated from an elementary kinetics approach, cf. our papers [249,253]), for the Pt nano-particles coarsening induced by C corrosion (cf. our papers [126,168]) and for the finite Pt^{z+} lateral inter-particles conductivity (related to the local water content in the vicinity of the nano-particles) and the finite lateral inter-particles electronic conductivity of the CB (eventually decreasing as a consequence of C corrosion) (the last three aspects being the subject of a publication by us [278] and will not be detailed here). The radius evolution is obtained from the equation

$$\frac{1}{\nu_m}\frac{\partial r}{\partial t} = j_i - j_k \tag{3}$$

where the kinetic rates j are function of the nano-particles radius (surface energy effect), the Pt^{2+} concentration and the electrostatic potential jump through the compact layer developing

on the nano-particles surface (see below the interfacial nano-scale submodel), as in our papers [243,249].

The specific catalyst surface area $\gamma_{catalyst}$ at the coordinates (y,z) in the macro-scale (cf. Figures III.5 and III.24) is obtained from

$$\gamma_{catalyst}(y,z,t) = 4\pi \int_0^{\infty} \Phi(r,y,z,t) r^2 dr \tag{4}$$

within the assumption of spherical nano-particles. This surface evolution affects in turn the electrostatic potential in the CL (see below).

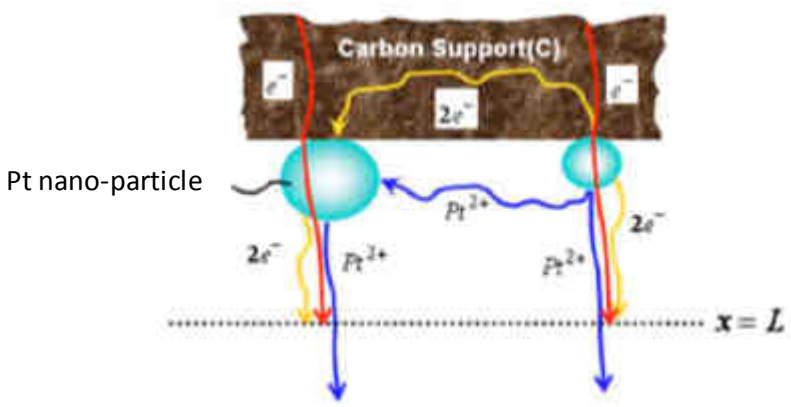

Figure III.15: Model of Pt electrochemical Oswald ripening within MEMEPhys® (Source: [249,253]).

For accounting for the electrocatalytic properties changes during bimetallic catalyst nano-particles degradation (e.g. Pt_xCo_y), we perform a series of MC simulations for different nano-particles sizes (different number of atoms) and different compositions (stoichiometries) to build a database providing the catalyst specific surface area $\gamma_{catalyst}$ and *i-layer* composition x_M^i of the nano-particles as function of their mass [242,243]

$$\gamma_{catalyst} = f_a(m_{Pt_xM_y}) \tag{5}$$

$$x_M^i = f_b(m_{Pt_xM_y}) \tag{6}$$

The energy barriers of the single electrochemical steps under consideration (e.g. ORR) are given by

$$\Delta G_i = f\left(\left\{x_M^i\right\}\right) = f_c\left(m_{Pt_xM_y}\right) \quad (7)$$

obtained by interpolation of thermodynamic data and/or DFT calculations carried out for different catalyst stoichiometries and structures. The three functions (5-7) impact in turn the calculated CL potential (cf. Figure III.4).

For the MC calculations, Sutton-Chen multi-atomic potential is applied with an annealing method to simulate the pseudo-equilibrium atomic repartition of each structure [279]. This potential provides the total nanoparticle energy *U* as the addition of terms that describes the two-body repulsive interaction between the atoms *i* and *j* separated by a distance r_{ij}, and of many-body cohesion terms associated with atom *i:*

$$U = \sum_i^{N_{atoms}} \left[\frac{1}{2} \varepsilon^{AB} \sum_{j \neq i}^{N_{atoms}} \left(\frac{\sigma^{AB}}{r_{ij}} \right)^{n^{AB}} - c^A \varepsilon^A \sqrt{\sum_{j \neq i}^{N_{atoms}} \left(\frac{\sigma^{AB}}{r_{ij}} \right)^{m^{AB}}} \right] + xE_{ads}^{Pt} + yE_{ads}^{M} \quad (8)$$

In Eq. (8), ε^{AB} is the so-called energy parameter, σ^{AB} is the lattice constant, c is a dimensionless parameter, and n and m are positive integers with $n > m$. The last two terms account for possible adsorbed-induced reconstruction effects on bi-metallic nano-particles [256]. One example of MC calculated Pt_xCo_y nanoparticle structure is presented in Figure III.15. According to Ma *et al.* [280], atomic surface segregation is primarily determined by the surface energy and the atomic size. This is the physical explanation. However, surface segregation could also be understood by statistical concepts. Indeed, our MC simulations (Figure III.16a) show that surface composition is strongly dependent on global volume composition. That is to say that for compositions far from 50/50, the surface is mainly composed of atoms which are in the majority. Thus, for $Pt_{75}Co_{25}$, it is Pt which preferentially segregates to the surface but for $Pt_{25}Co_{75}$, it is cobalt which preferentially segregates to the surface (more electrochemically unstable configuration). When the surface top-layer is enriched in one element, the second layer is enriched in the other element. The simulations also suggest the formation of percolated Pt-rich and Pt-rich regions, which agrees with some analysis recently published based on HR-TEM characterizations [281].

It is also possible to couple “on-the-fly” MC calculation of the structures evolution on time with the degradation kinetics within MEMEPhys® and this is presented elsewhere [188,282] (Figure III.16b).

(a)

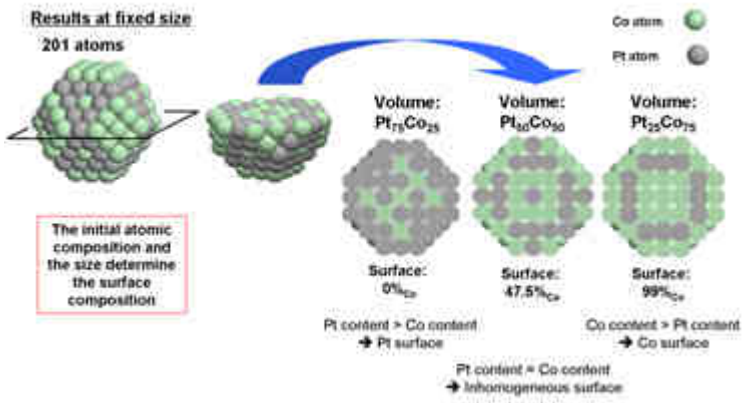

(b)

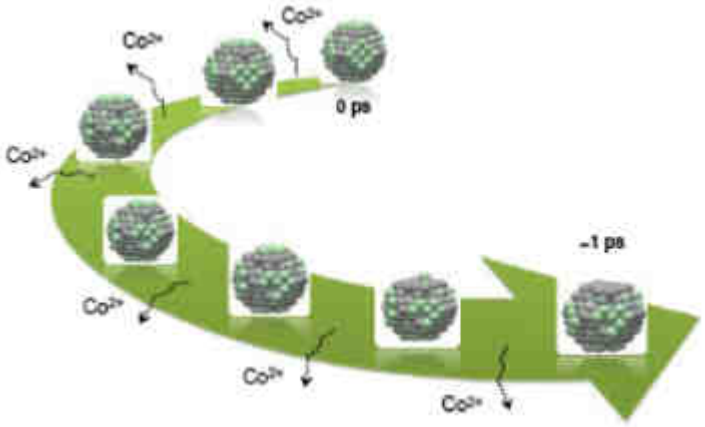

Figure III.16: (a) Cut views of nanoparticles of 201 atoms (1.6 nm) after MC simulations for three different atomic compositions ($PtCo_3$ is expected to be more unstable because it has more *Co* atoms at the surface); (b) "on-the-fly" Kinetic MC simulation of a PtCo nano-particle dissolution [242, 243].

For accounting the cathode CL (PEM) transport properties changes induced by C corrosion (ionomer degradation) we can use for example spatially averaged fractal representations of the CLs to describe the impact of C (ionomer) mass loss on the micro-structural properties changes, such as the evolution of the C instantaneous surface area or effective diffusion coefficients in the CL. We have used this approach for example in [126,168,181] to relate the temporal evolution of the cathode thickness and C surface area with the C corrosion kinetics, by representing the carbon phase as a two-dimensional Sierpinski carpet projected in the cathode thickness direction (Figure III.17). Another example of application of this kind of fractal approach, on PEM degradation, is provided in Figure III.18.

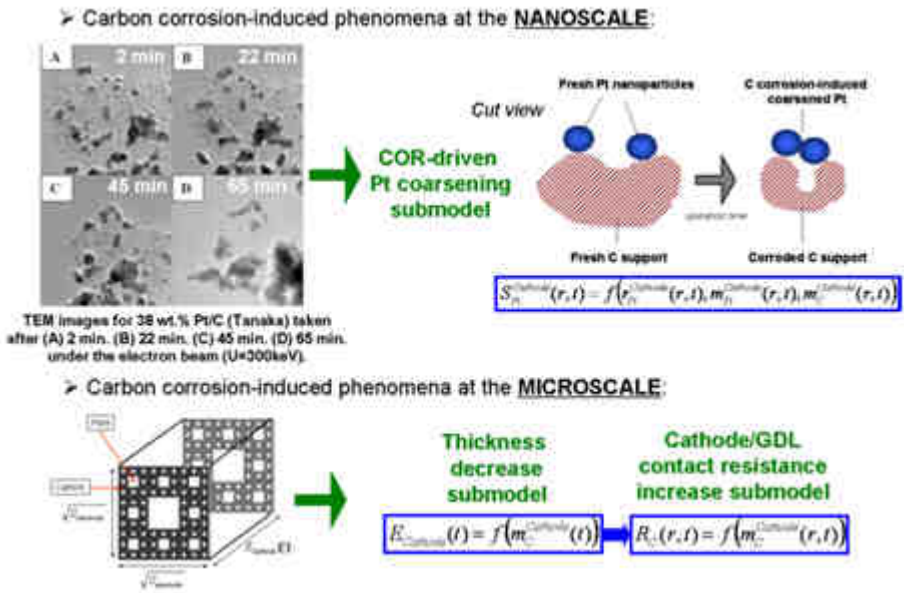

Figure III.17: C corrosion-induced phenomena accounted within MEMEPhys® (at the nano-scale: support corrosion-driven catalyst coarsening; at the micro-scale: cathode thickness decrease and cathode/GDL contact resistance decrease) (Source: [126, 168]).

Other simpler approaches can be used. Again, for the case of PEM degradation, in order to take into account the degradation-induced structural evolution impact on the proton conductivity g_{H^+}, based on the approach proposed by Choi *et al.* [283] we write

$$g_{H^+} = \frac{\wp_{PEM}}{\tau_{PEM}} \left[\frac{F^2}{RT} \left(D^{\Sigma}_{H^+} \cdot C^{\Sigma}_{H^+} + D^{G}_{H^+} \cdot C_{H^+} + D^{E}_{H^+} \cdot C_{H^+} \right) \right] \tag{9}$$

where the conductivity is expressed as the sum of three contributions (Figure III.19): the bulk diffusion of protons, the diffusion via a proton hoping mechanism (Grotthus mechanism) and the surface diffusion in a hydration shell in the vicinity of the sulfonated groups. In equation (9) $D^{i}_{H^+}$ are the diffusion coefficients and $C^{i}_{H^+}$ are the concentration of protons, either in the "bulk" (middle of the pore) or at the surface of a pore. The expression $\wp_{PEM} / \tau_{PEM}$ is the ratio between the PEM porosity and tortuosity, where [284]

$$\frac{\wp_{PEM}}{\tau_{PEM}} = \frac{1}{\tau_{PEM}} \frac{\lambda}{\lambda + \frac{m^{dry}_{Nafion}}{\rho_{Nafion} V_{H_2O}} \frac{1}{n_{SO_3^-}}} \tag{10}$$

Where λ is the number of water molecules per sulfonate group and $n_{SO_3^-}(y,z,t)$ is the remaining number of moles of sulfonate groups in the PEM calculated from the kinetic equations describing the side-chain degradation (see below and Appendix IV, cf. Table III.3).

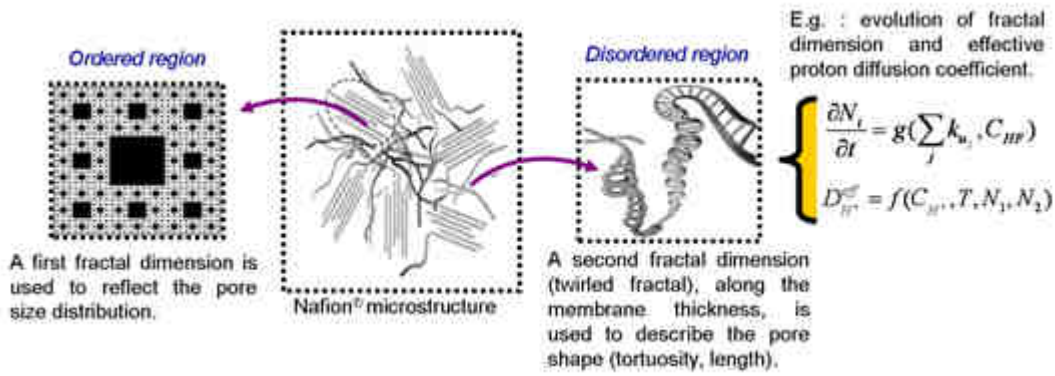

Figure III.18: PEM microstructural model used within MEMEPhys® (the degradation chemistry allows the prediction of the effective transport parameters evolution) (Source: [101]).

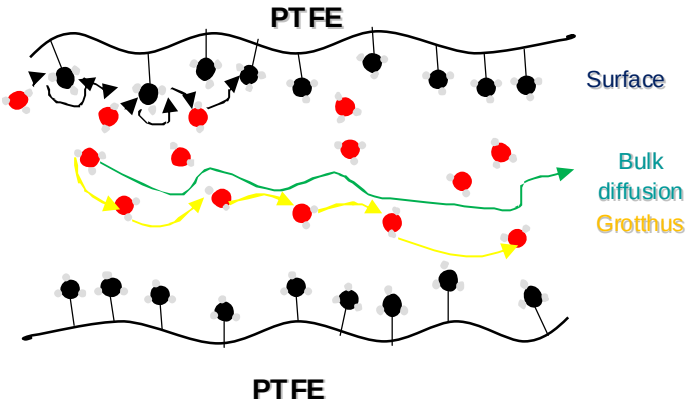

Figure III.19: Schematic representation of a Nafion® pore with proton transport.

To improve these "geometrical" representations of the CL and PEM micro-structure, averaged parameters can be alternatively determined by micro-scale resolved models that are directly describing the morphological structure and aging-induced temporal topological changes. Within this case, micro-structures can be generated *in silico* by stochastic methods (e.g., MC description of the carbon agglomerates distribution in the CL, or simpler stochastic CL reconstruction [285]), atomistic methods (e.g. CGMD [286]) or by using experimentally determined structures (e.g. TEM 3D-tomography [287]). On the basis of these structural predictions, the transport properties of chemical species (e.g. H_2, H_2O, O_2, N_2) and of charge (effective conductivities for protons and electrons) can be derived. This allows the assessment of parameters such as the overall electrical conductivity, and the surface area of mutual contact of catalyst and electrolyte particles arranged in different interpenetrated

percolating networks. The dependence of these parameters on volume fractions, layer thickness, and size of electrolyte and catalyst particles can be studied.

For example, within this context, thanks to a fruitful ongoing collaboration with NRC-IFCI from Vancouver (cf. Chapter I), CGMD simulations of a CL has been used to build a structural database for CLs with different C contents in terms of interpolated mathematical functions describing the impact of the C mass loss (induced by corrosion) on the evolution of the ionomer coverage on Pt and C, the electronic conductivity of the CB, the C surface area and the Pt surface area (which re-organizes during the C corrosion process) (cf. Figure III.4). These functions are then integrated into the kinetic model of MEMEPhys® to simulate the impact of C corrosion on the MEA performance decay (Figure III.20 and see Chapter IV) [233]. CGMD methods, which are actively researched in a large number of application areas, combine units of the material into larger fragments (called "beads"), which can be modeled efficiently using law-timescale methods, such as Brownian dynamics. Parametrization of the interactions of these units requires feedback from atomistic simulations. The details on this methodology for performing studies of self-organization in PEMFC CLs mixtures have been described by my Canadian colleagues Malek *et al.* in [286, 288], where they represent all atomistic and molecular species, i.e., Nafion® ionomer chains, solvent molecules, water, hydronium ions, carbon and Pt particles, by spherical metallic, polar, nonpolar, and charged beads with pre-defined sub-nanoscopic length scale.

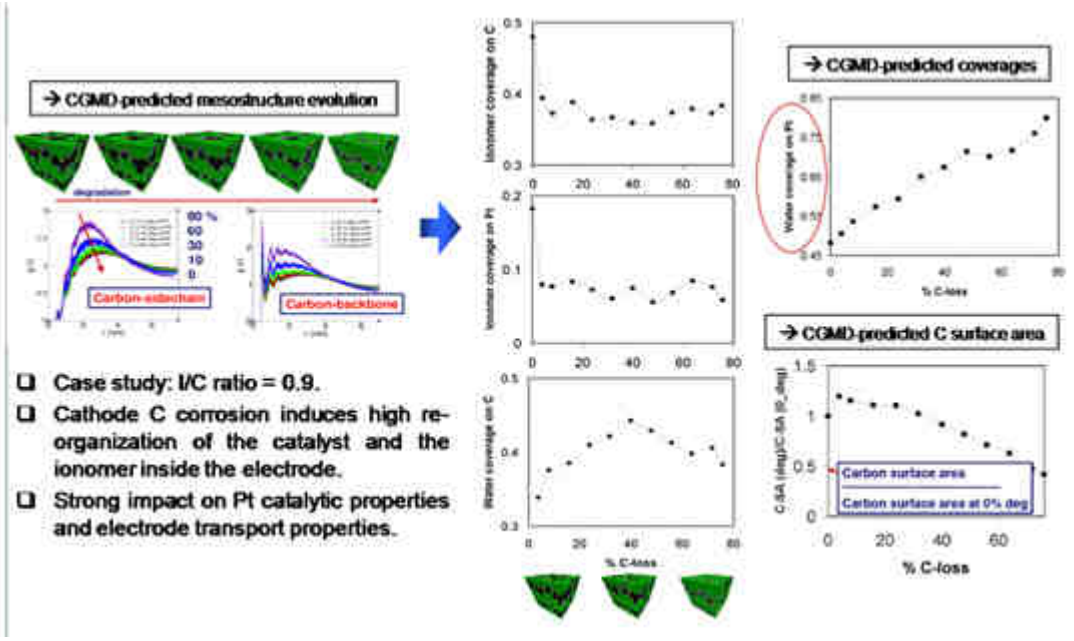

Figure III.20: CGMD calculation of the cathode CL re-organization during the C corrosion (Source: [233]).

Pore network modeling (PNM) can be used to estimate relationships between H_2 and O_2 transport properties and the liquid water saturations in the CLs with a given pore-size distribution estimated by experiments, MC or CGMD. PNM is an efficient method to investigate multiphase transport in porous media. It was used in petroleum field during decades and was recently applied to water management inside the GDL of the PEMFC [289,290]. In my group, 2D and 3D structural models are developed to study the effects of the pore size distribution, wetting properties and the electrochemical activity on the liquid water transport and then on the global performance of the CLs. A pore network is built to represent the porous structure of the CL, and a transient simulation is carried out to simulate water production and water transport inside this network. In this model

- ✓ the water transport in the CL is driven by the capillary pressure;
- ✓ the invasion algorithm consist on calculating the path of liquid water produced in active agglomerates until it reached a breakthrough point in the CL/GDL interface;
- ✓ a statistical study is used to calculate an average breakthrough number while the active agglomerates are chosen randomly.

Partial liquid saturation in the pores is computed for investigating the link between the local wetting properties and the gas access to the active zones where the ORR happens.

The results show that liquid water distribution inside the cathode strongly depends on the hydrophilicity of the pores. This distribution has a direct influence on the gas diffusion (Figure III.21 and III.22).

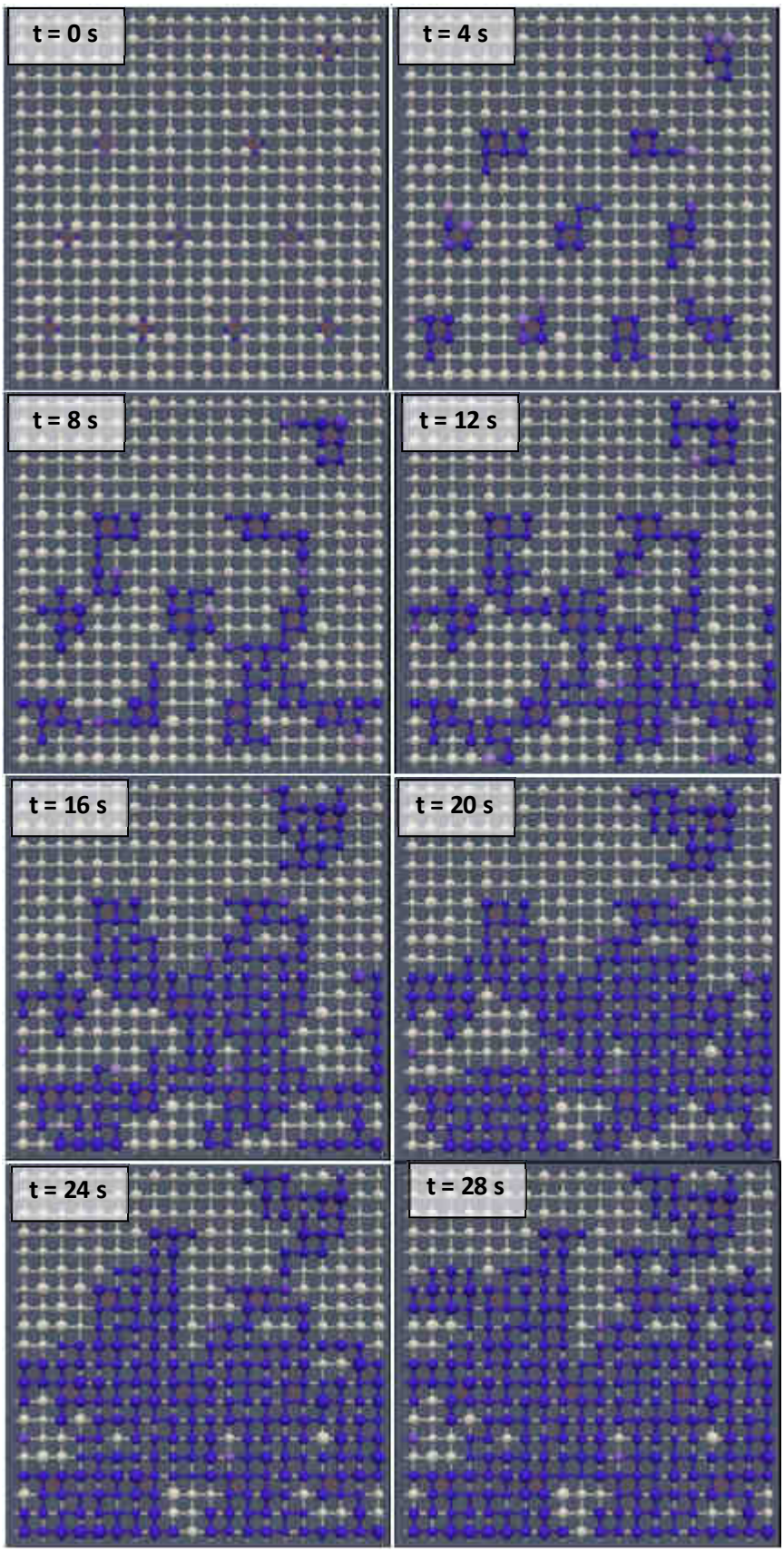

Figure III.21: Example of PNM simulation of water transfer through the secondary pores of a cathode (the red circles represent the active agglomerates, PEM in the back, GDL in the top) (Source: [291]).

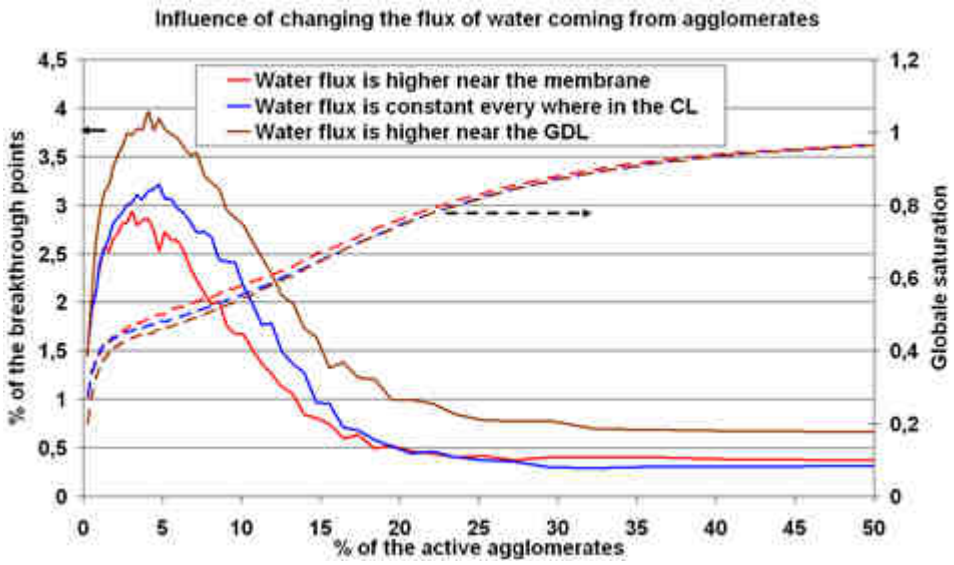

Figure III.22: Example of global saturation calculated by a PNM simulation of water transfer through the secondary pores of a cathode (Source: [291]).

III.3e – Model modules

In this section we provide an overview of the key components behind MEMEPhys®. For more details see Appendix IV and the incoming review in [188].

The channels modules. These modules consist on simple models resolving the convection transport phenomena of H_2, vapor H_2O and gas contaminants (e.g. CO or H_2S) along the anode channel, and of O_2, N_2, vapor H_2O and gas contaminants (e.g. NO_2 or SO_2) along the cathode channel (cf. Figure III.5). Liquid water transport is neglected inside the channels. Both co-flow (H_2 inlet in front of Air inlet) and counter-flow (H_2 inlet in front of the Air outlet) operation modes can be adopted.

The corresponding conservation equations are written in the form

$$\frac{\partial C_i}{\partial t} = -\nabla_z . J_i + S(z,t) = -\nabla_z . \left(C_i v_g\right) + \frac{J_i\left(y = l_{GDL}, z, t\right)}{l_{channel}} = -\nabla_z . \left(C_i \left(-K_P \nabla P_g^T\right)\right) + \frac{J_i\left(y = l_{GDL}, z, t\right)}{l_{channel}} \qquad (11)$$

where K_P is a constant factor and where the total gas pressure P_g^T is given by (assuming ideal gas behavior)

$$P_g^T = \sum_i C_i RT \qquad (12)$$

The source term in Equation (11) is proportional to $J_i(y = l_{GDL}, z, t)$ which is the molar flux at the boundary GDL/channel calculated by the GDL model (see below).

The GDL modules. There have been many approaches in the literature proposed to model the GDL [292, 293, 294]. The approach taken depends upon how the rest of the PEMFC is modeled. There are several types of flow models for porous media, such as Fick diffusion, the Stefan-Maxwell equations, as well as numerous other derivations based upon these equations.

We adopt here the classical Stefan-Maxwell-Knudsen diffusion equations combined with the Darcy convection equation to resolve the transport phenomena of H_2, biphasic H_2O (liquid and vapor) and gas contaminants through the anode GDL thickness, and of O_2, N_2, biphasic H_2O and gas contaminants through the cathode GDL thickness (Figure III.23).

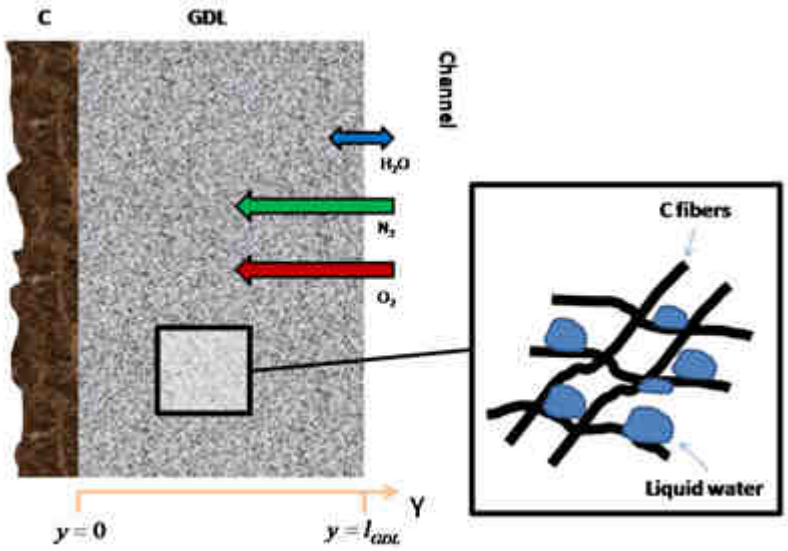

Figure III.23: Cathode GDL model (case of operation without gas contaminants).

The conservation equations for the individual gas species are written

$$\frac{\partial}{\partial t}\left((1-s)\wp_{GDL}C_i\right)+\nabla_y.\left(C_i v_g + j_i^d\right)=S(y,z,t) \qquad (13)$$

where $\wp_{GDL}$ is the GDL porosity and s is the liquid water saturation (fraction of pore volume occupied by liquid water) defined as function of the liquid water concentration $C_{H_2O,l}$ as in [295].

In equation (13) j_i^d is the species diffusion flux and the source term S only is non zero for H_2O as it describes the rate of water evaporation-condensation following [296]

$$S = \begin{cases} H_0^+(1-s)\left(C_{H_2O} - C_{H_2O}^{sat}(T)\right) & \text{if } C_{H_2O} \geq C_{H_2O}^{sat}(T) \\ H_0^- s\left(C_{H_2O} - C_{H_2O}^{sat}(T)\right) & \text{if } C_{H_2O} < C_{H_2O}^{sat}(T) \end{cases} \quad (14)$$

where H_0 are the Heaviside functions and $C_{H_2O}^{sat}(T)$ refers to the saturation concentration.

The gas velocity v_g in equation (13) is assumed to obey the Darcy law for flow in porous media

$$v_g = -\frac{\kappa_{rg}(s)K}{\mu_g}\nabla P_g^T = -\frac{(1-s)^3 K}{\mu_g}\nabla P_g^T \quad (15)$$

where P_g^T follows equation (12). K is the absolute permeability of the GDL (function of $\wp_{GDL}$ and the GDL pore mean radius, for example through the Kozeny-Carman relationship [297]) and μ is the dynamic viscosity of the gas. $\kappa_{rg}(s)$ is a term added into Darcy law to represent the relative permeability of the porous GDL to the gas phase, given by an empirical fit.

The diffusion flux j_i^d in equation (13) comes from the solution of the Stefan-Maxwell-Knudsen equations

$$-\frac{P}{RT}\nabla_y x_i - \frac{x_i}{RT}\nabla_y P_g^T = \frac{\vec{j}_i^{\,d}}{D_{i,Kn}} + \sum_{j=1}^{n}\frac{x_j \vec{j}_i^{\,d} - x_i \vec{j}_i^{\,d}}{D_{ij}^{eff}} \quad (16)$$

where x_i represents the molar fraction of species *i*. The effective binary diffusion coefficients D_{ij}^{eff} are defined by scaling the standard binary diffusion coefficient using the porosity and a Bruggeman's correction coefficient [298,295]

$$D_{ij}^{eff} = \left((1-s)\wp_{GDL}\right)^{\frac{\log_{10}(\wp_{GDL}/\tau_{GDL})}{\log_{10}(\wp_{GDL})}} D_{ij} \quad (17)$$

The Knudsen diffusion coefficient $D_{i,Kn}$ is function of the GDL pore radius r_{pore}^{GDL} as determined from the kinetic theory of gases and as usually considered in PEMFC modeling [299]

$$D_{i,Kn} = \frac{2}{3} r_{pore}^{GDL} \sqrt{\frac{8RT}{\pi M_i}} \tag{18}$$

For the liquid water, the conservation equation is written

$$\frac{\partial}{\partial t}\left(sC_{H_2O,l}\right) + \nabla_y.\left(sC_{H_2O,l} v_l\right) = -S(y,z,t) \tag{19}$$

with the source term representing the water production by condensation (cf. equation (14)), and the liquid water velocity is assumed to obey Darcy law

$$v_l = -\frac{\kappa_{rl}(s)K}{\mu_l}\nabla P_l = -\frac{s^3 K}{\mu_l}\nabla P_l \tag{20}$$

μ_l is the liquid viscosity, $\kappa_{rl}(s)$ is the relative liquid permeability of the GDL given by an empirical fit. The liquid pressure P_l is due to both to the capillary pressure (P_c) and the gas pressure (P_g) according to [300]

$$P_l = P_g + P_c = P_g + \gamma_s \cos(\vartheta)\left(\frac{\wp_{GDL}}{K}\right)^{1/2} \Im(s) \tag{21}$$

where γ_s is the liquid surface tension constant, ϑ is the contact angle between the liquid and solid phases and $\Im(s)$ is the capillary function that relates the water volume fraction to the capillary pressure (here the well known *Udell function* is used [301]).

For the electron transport along the GDL C fibers, the conservation equation is written as

$$0 = \nabla_y.\left(-g_{e^-}^{GDL,eff}\nabla_y\psi\right) = \nabla_y.\left(-\left(1-\wp_{GDL}\right)^{\frac{\log_{10}((1-\wp_{GDL})/\tau_{GDL})}{\log_{10}(1-\wp_{GDL})}} g_{e^-}^{GDL}\nabla_y\psi\right) \tag{22}$$

where $g_{e^-}^{GDL}$ is the intrinsic GDL electronic conductivity.

All these equations are solved with appropriate boundary conditions connected to the channel and CL models, and are not detailed here.

The CL modules. The CL constitute the most novel modules within MEMEPhys® as they include

- ✓ a meso-scale description of the reactant species (H_2, O_2, gas contaminants), charges (including dissolved metallic ions) and liquid water transport through the secondary pores along the CL thickness, and charges and water transport within the ionomer phase along the CL thickness
- ✓ a micro-scale description of the reactants and contaminants transport across the ionomer film covering the C agglomerates (and eventually across the C agglomerates volume, see below),
- ✓ a nano-scale description of the electrochemical interface phenomena on both catalyst and C surfaces, modeling the diffuse layer structure under non-equilibrium conditions and the detailed elementary reaction kinetics (e.g. ORR, contamination reaction, catalyst dissolution…) taking place within the compact layer (cf. Figure III.5 and see below).

Figure III.24 shows the CL model and the detail of the meso-scale. Figure III.25 presents two kinds of micro-scale agglomerate models that can be implemented within MEMEPhys®: one being representative of C support without primary pores, and the second one with primary pores the choice depending on the electrode design specifications.

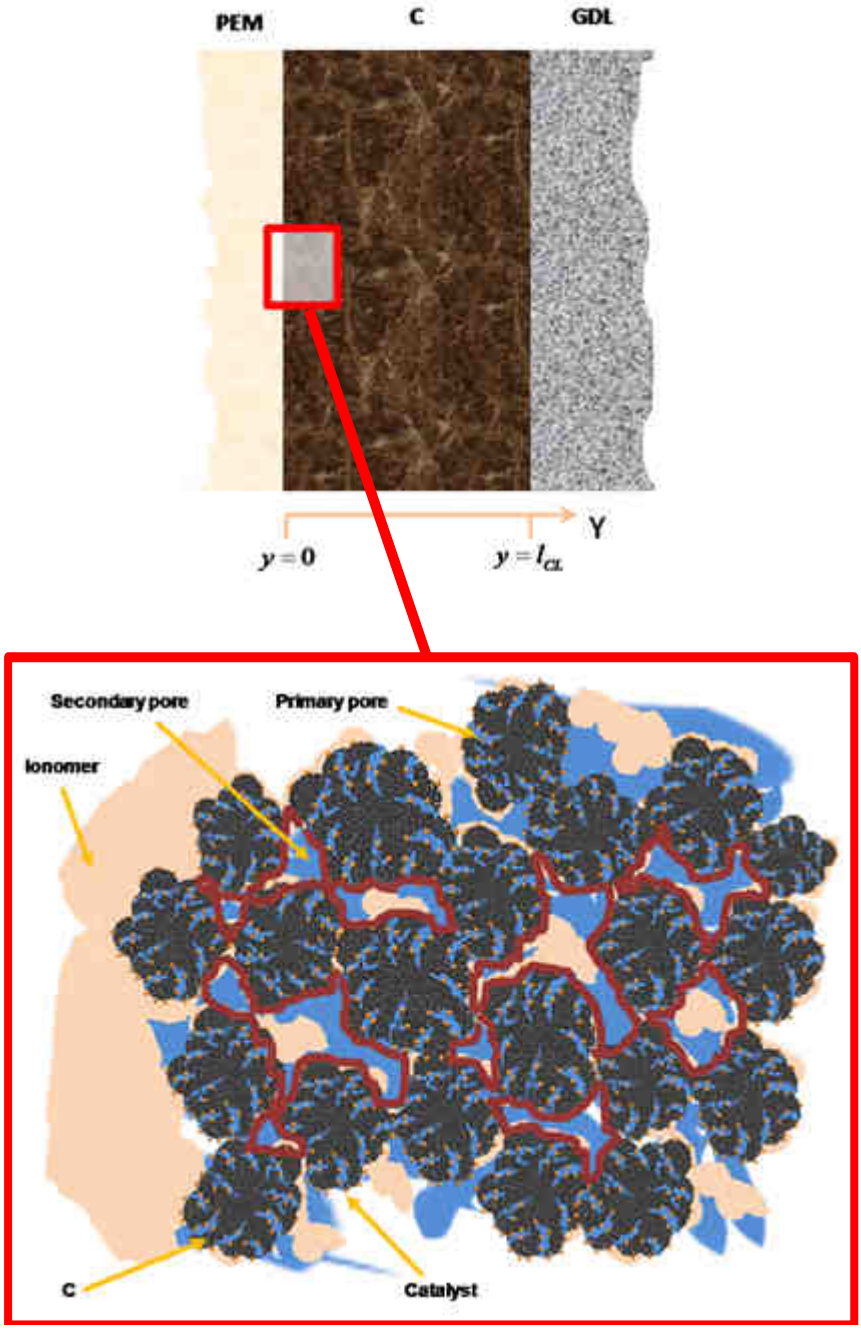

Figure III.24: CL model at the macro and meso-scale where the boundaries defining the specific surface area of secondary pores γ^{SP} are indicated (in the figure, case of C support with primary pores).

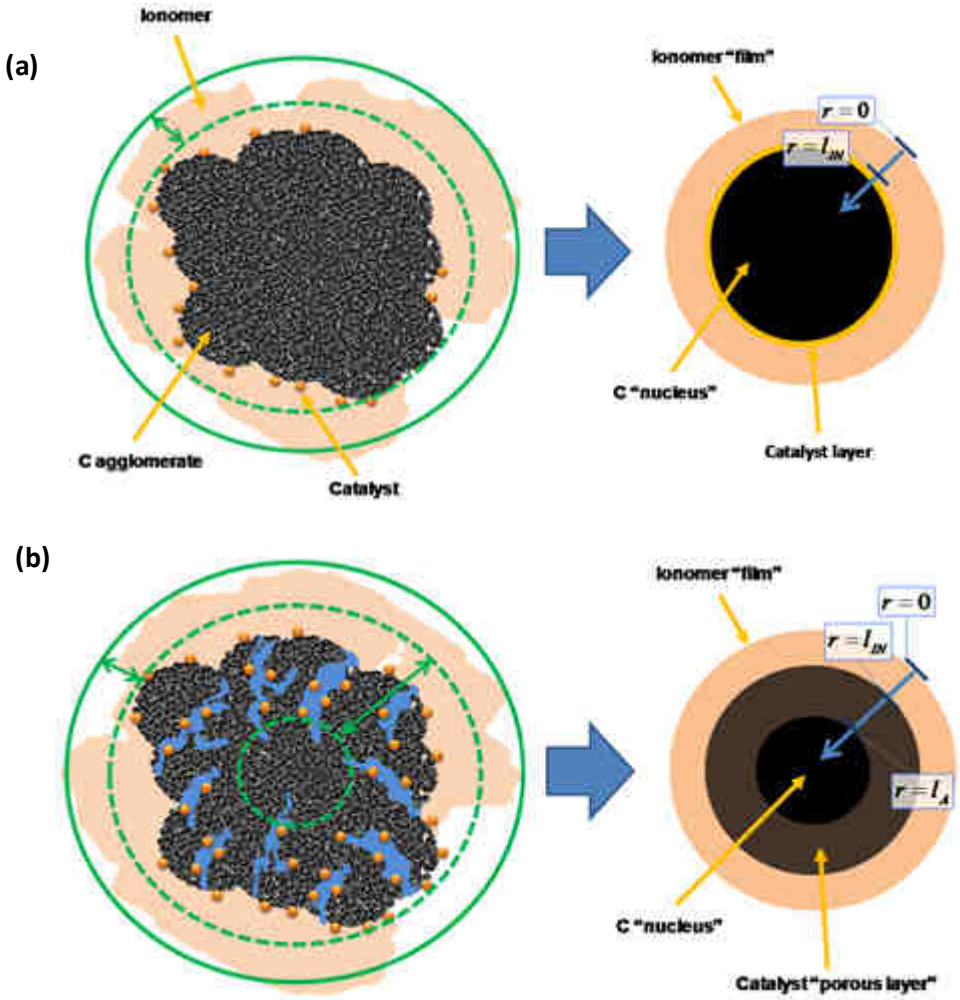

Figure III.25: Modelled C agglomerates, under the spherical hypothesis, without (a) and with (b) primary pores. In particular, the ionomer phase is indicated.

Meso-scale: at the meso-scale level (transport through the CL secondary pores), the conservation equations for the individual gas species are written

$$\frac{\partial}{\partial t}\left((1-s)\wp_{CL}^{SP}C_i\right)+\nabla_y.\left(C_i v_g + j_i^d\right)=S(y,z,t)+R(y,z,t)=S(y,z,t)+\gamma^{SP}J_i(r=0,y,z,t) \qquad (23)$$

where S is as in (13), R describes the rate of mass transfer between the ionomer film coating around the agglomerates and the secondary pores (this is similar to our previously published model in [8,248]) and the other terms are defined as in (13).

γ^{SP} ($m^2.m^{-3}$) refers to the specific surface area of C secondary pores ("contact surface area" between the ionomer and the secondary pores per unit of CL volume). Because of the chemical-governed self-organization of the materials within the CL [286], $\wp_{CL}^{SP}$, τ_{CL}^{SP} and γ^{SP} are functions of the catalyst, ionomer and C mass contents, and their values can be estimated

either from experimental data, geometrical considerations or atomistic simulations [302]. When aging of one or several of these materials occurs, the CL structure is expected to evolve. As a first approximation, we assume here that $\wp_{CL}^{SP}$, τ_{CL}^{SP} and γ^{SP} only evolve with C corrosion -C mass loss- (ionomer degradation in the CL is not described yet within the model) following the geometrical or atomistic based databases already discussed in Section III.3d. As C corrosion can be inhomogeneous within the CL (e.g. PEM side vs. GDL side differences or air inlet vs. air outlet differences induced by different local water contents, see below the description of the corrosion kinetics), $\wp_{CL}^{SP}$, τ_{CL}^{SP} and γ^{SP} are in fact functions of Y and Z coordinates. Catalyst degradation, inducing changes on its morphology, size and dispersion on the C support probably contributes on the CL meso-structure evolution [303]: this is something that we would like to explore in the future, in particular, in collaboration with the colleagues from NRC in Vancouver.

The gas velocity and the species diffusion fluxes in equation (23) are written in a similar way to equations (15) and (16), with the Knudsen coefficients $D_{i,Kn}$ and the absolute permeability K being also functions of the C mass (through the secondary pores mean radius), thus of time if the C degradation is included in the simulation [181].

For the liquid water in the secondary pores $C_{H_2O,l}$, the conservation equation is analogous to equation (19)

$$\frac{\partial}{\partial t}\left(sC_{H_2O,l}\right)+\nabla_y.\left(sC_{H_2O,l}v_l\right)=-S(y,z,t)+W(y,z,t)=-S(y,z,t)+ \\ +\gamma^{SP}k\left(C_{H_2O,Ionomer}(y,z,t)-C_{H_2O,l}(y,z,t)\right) \tag{24}$$

where $W(y,z,t)$ is the rate of water transfer (desorption/absorption) from the ionomer film to the secondary pores (a linear kinetics is assumed). The liquid water velocity is calculated in a similar way to the GDL (cf. equation (20)).

For the electron transport across the C in the CL, we have

$$\nabla_y.\left(-g_{e^-}^{CL,eff}\nabla_y\psi\right)=\nabla_y.\left(-\left(\wp_{CL}^{C}\right)^{\frac{\log_{10}\left(\wp_{CL}^{C}/\tau_{CL}^{C}\right)}{\log_{10}\left(\wp_{CL}^{C}\right)}}g_{e^-}^{CL}\nabla_y\psi\right)=S_{e^-}(y,z,t)=\pm\gamma_{catalyst}J(y,z,t)+ \\ +\gamma^{SP}J_{COR}(y,z,t) \tag{25}$$

where $\wp_{CL}^{C}$ is the C support volume fraction (function of time if C corrosion is included in the model), $\gamma_{catalyst}$ depends on time if the catalyst dissolution and ripening and/or the C corrosion-driven catalyst coarsening (cf. equation 4) are included in the simulation. Again,

$\gamma_{catalyst}$ can also depend on space because of the degradation inhomogeneities induced, for example, by the local water content within the CL (cf. equation 4). $J_{COR}(y,z,t)$ is the local current density related to the C corrosion kinetics (Figure III.26, cf. [126])

$$J_{COR}(y,z,t) = \sum_i \nu_i^{COR} \tag{26}$$

where ν_i^{COR} are the elementary reactions depending on the local water content in the ionomer phase $C_{H_2O,ionomer}$ [126].

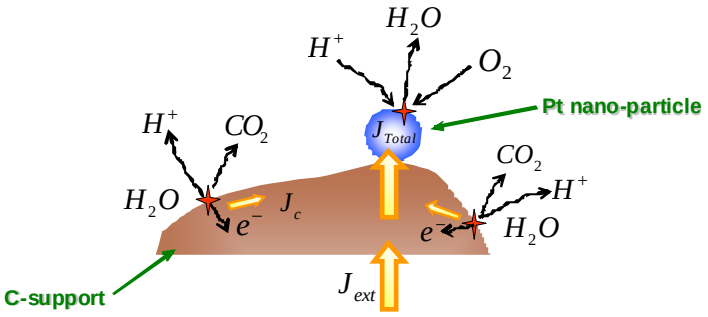

Figure III.26: Nano-scale parasitic current related to C corrosion (Source: [126]).

Equation (25) allows calculating $J(y,z,t)$ which is the nano-scale current density produced (anode)/consumed (cathode) by the catalyst nano-particles (see below).

Inside the CLs, protons and parasitic ions (coming from catalyst dissolution) are assumed only to move within the hydrated ionomer phase, and not through the liquid water in the secondary pores. There is still large debate regarding the mechanisms of ions and water transport within thin ionomer films [304].

For the case of C agglomerates without primary pores (cf. Figure III.25), the conservation equations for the ions (protons and dissolved metal) transport through the ionomer phase, outside the nano-scale diffuse layer (cf. Figure III.5, [248]) are written as

$$\nabla_y.\left(J_{k^{z+}}\right) = \nabla_y.\left(-\left(\varepsilon_{CL}^{ionomer}\right)^{\frac{\log_{10}\left(\varepsilon_{CL}^{ionomer}/\tau_{CL}^{ionomer}\right)}{\varepsilon_{CL}^{ionomer}}} D_{k^{z+}}(\lambda)\left(fzC_{k^{z+}}\nabla_y\phi + \nabla_y C_{k^{z+}}\right) + x_{k^{z+}}J_{H_2O}\right) = S_{k^{z+}}(y,z,t) =$$
$$= \pm\gamma_{catalyst}J_{k^{z+}}(x=0,y,z,t)$$

(27)

$$\nabla_y.\left(-\nabla_y\phi\right)=\frac{F}{\varepsilon_{ionomer}}(C_{H^+}(y,z,t)+zC_{M^{z+}}(y,z,t)-C_{SO_{3^-}}) \tag{28}$$

where the source terms are functions of the nano-scopic ionic fluxes at x = 0 (i.e. at the boundary between the nano-scale diffuse layer and the meso-scale ionomer phase -see below-) and where $C_{SO_{3^-}}$ is the ionomer sulfonate groups concentration, assumed to be constant even if its value can change with local hydratation for example. In equations (27) the ions diffusion coefficients are functions of the local water content λ (number of water molecules per sulfonate group) and $x_{k^{z+}}$ is a molar fraction. The ionomer volume fraction $\wp_{CL}^{ionomer}$ in the CL without primary pores, is given by

$$\wp_{CL}^{ionomer}=1-\wp_{CL}^{C}-\wp_{CL}^{SP} \tag{29}$$

In our model, water transport in the ionomer phase is described through two “classical” competing phenomena: water electro-osmosis and water diffusion, i.e.

$$\frac{\partial\left(\wp_{CL}^{ionomer}C_{H_2O,ionomer}\right)}{\partial t}+\nabla_y.\left(-\wp_{CL}^{ionomer}{}^{\frac{\log_{10}\left(\wp_{CL}^{ionomer}/\tau_{CL}^{ionomer}\right)}{\log_{10}\left(\wp_{CL}^{ionomer}\right)}}\left(D_{H_2O,ionomer}(\lambda)\nabla_y C_{H_2O,ionomer}+\alpha_{EO}(\lambda)J_{H^+}\right)\right)= \tag{30}$$

$$=\Omega(y,z,t)-W(y,z,t)=\gamma_{catalyst}J_{H_2O}(x=L,y,z,t)-W(y,z,t)$$

where $J_{H_2O}(x=L,y,z,t)$ is the flux of produced water at the catalyst surface (related to the electrochemical reactions kinetic rates, see below). In equation (30) only the protons are assumed to contribute to the electro-osmotic drag (in principle the metal ions could also contribute). The electro-osmotic parameter $\alpha_{\mathrm{EO}}(\lambda)$ is given by the empirical relationship in [305].The water diffusion coefficient and $\lambda=f(C_{H_2O,ionomer})$ is given as in [8].

Micro-scale: regarding now the micro-scale models for the agglomerates (cf. Figure III.25), a diffusion equation for the reactants (hydrogen, oxygen and contaminants) is solved in spherical coordinates through the ionomer film surrounding the C agglomerate. For the case without primary pores

$$\frac{\partial C_{i,ionomer}}{\partial t} = -\frac{1}{r^2}\frac{\partial}{\partial r}\left(r^2 D_i \frac{\partial C_{i,ionomer}}{\partial r}\right) \quad (31)$$

with boundary conditions at r = 0 given by the Henry laws

$$C_i(r=0,t) = \frac{p_i}{H_i} \quad (32)$$

where H_i is the Henry coefficients (as a first approximation, the reactants are assumed to absorb in the hydrated ionomer from the liquid water-free secondary pore phase -not from liquid water-). The boundary condition at $r = l_{IN}$ is given by

$$J_i(r = l_{IN} \approx x = L,t) = -\sum_i \nu_i \quad (33)$$

where ν_i are the electrochemical kinetic rate associated to the *i* consumption on the catalyst surface. The case of the C agglomerates with primary pores is described elsewhere [188].

Nano-scale: the processes occurring at the interface between the catalyst and electrolyte are manifold and strongly influenced by the surrounding environment and the external parameters (temperature, pressure, and electrode potential). In addition, these external parameters can affect the morphology and composition of the CL, especially in case where nano-particles are used as catalyst material. A consistent theoretical description of such complex catalytic systems is a real challenge. During my PhD thesis, I proposed a novel model within a continuum framework to describe in a detailed way the electrochemical interface in the vicinity of the catalyst under non-equilibrium conditions [8,250]. This nano-scale model, which is a key part of MEMEPhys®, is constituted of a 1D-diffuse layer sub-model and a 1D-compact layer submodel, as represented in Figure III.27 for the case of bimetallic catalysts.

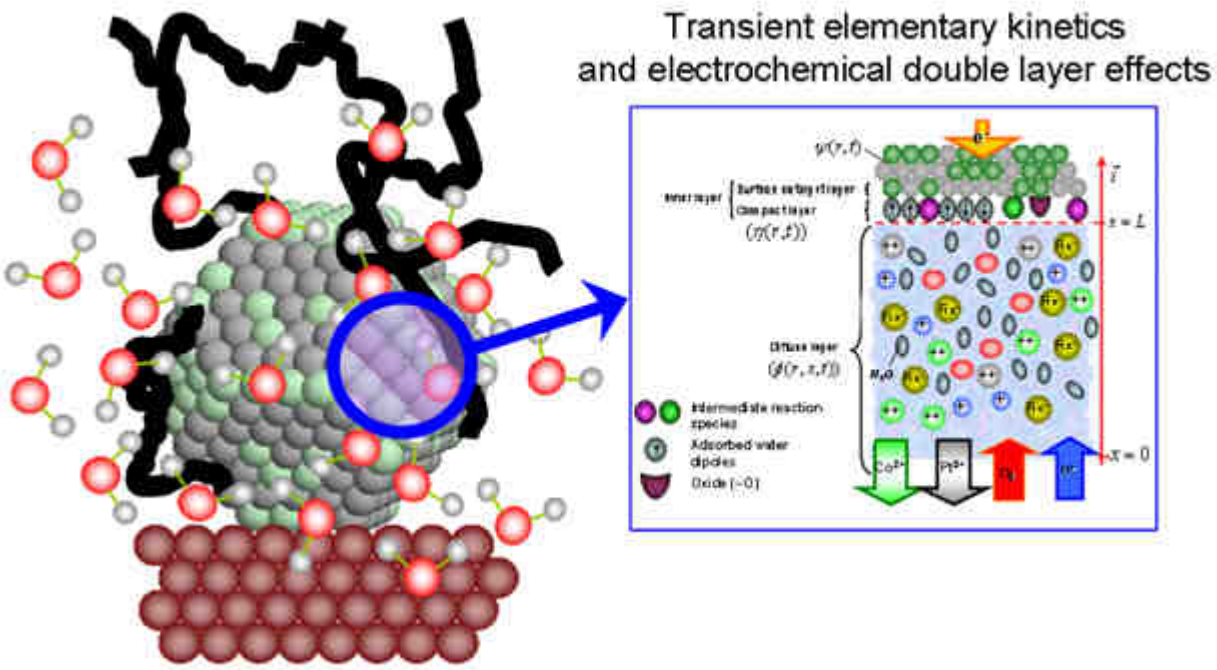

Figure III.27: Nano-scale interfacial model (case of Pt_xCo_y catalyst degradation) (at the left, the "black lines" represent the ionomer) (Source: [242,243]).

The 1D-diffuse layer sub-model describes the transport by diffusion and electromigration of H^+ and M^{z+} close to the catalyst surface and coupled with the electric field generated by the resulting net charge distribution. All species are considered as punctual (diluted solution theory), so the inter-particle electrical interaction is neglected. The solvation effects and convection by water are not considered. The catalyst nano-particles are assumed to be sufficiently separated to avoid diffuse layer overlapping effects.

Combining the flux related to the Fick diffusion force and to the electrical force, with the mass balance, we obtain the equations representing the ions concentration (Nernst-Planck equations):

$$\frac{\partial C_{H^+}}{\partial t} = -\nabla_x . \vec{J}_{H^+} = -\nabla_x . (-D_{H^+} \nabla_x C_{H^+} - fD_{H^+} C_{H^+} \nabla_x \phi) \tag{34}$$

$$\frac{\partial C_{M^{z+}}}{\partial t} = -\nabla_x . \vec{J}_{M^{z+}} = -\nabla_x . \left(- D_{M^{z+}} \nabla_x C_{M^{z+}} - zfD_{M^{z+}} C_{M^{z+}} \nabla_x \phi\right) \tag{35}$$

where $\phi(x, y, z, t)$ is the electrical potential in the electrolyte diffuse layer, which is calculated from the Poisson equation

$$\frac{\rho}{\varepsilon_{DL}} = \frac{F}{\varepsilon_{DL}}(C_{H^+} + zC_{M^{z+}} - C_{SO_3^-}) = -\nabla_x{}^2\phi \tag{36}$$

The extension of the PNP equations for the case of more than one parasitic ion M^{z+} naturally arises and it is not detailed here.

It is important to note that equations (34-36) are introduced because at the nano-scale level (near to the electrified surface where the electron transfer takes place) the electroneutrality cannot be assumed, and because there is not any supporting electrolyte (the conductivity of the ions in this diffuse layer medium is not infinite).

The boundary conditions at $x=0$ ("bulk" concentrations and electrostatic potential ϕ, cf. Figure III.27) for equations (34-36) are calculated by the ion transport models through the ionomer phase at the meso-scale (cf. equations (27-28)). The boundary conditions at $x=L$ are given by

$$J_{H^+}(x=L,y,z,t) = \pm\sum_i \hat{v}_i \tag{37}$$

$$J_{M^{z+}}(x=L,y,z,t) = \sum_j \hat{v}_j^{diss} \tag{38}$$

where $\hat{v}_i$ are the electrochemical kinetic rates involving protons and $\hat{v}_j^{diss}$ the electrochemical kinetic rates associated to the metallic dissolution from the catalyst (only valid in the cathode CL).

We deduce the boundary condition of equation (36) at $x=L$ from the Gauss theorem applied around the compact layer [248,250]

$$\frac{\partial\phi}{\partial x}(x=L,y,z,t) = -\frac{\sigma(y,z,t)}{\varepsilon_{CL}} \tag{39}$$

where the catalyst electronic charge density $\sigma(y,z,t)$ is calculated from the balance equation at each time-step of the kinetic simulation [248]

$$J(y,z,t) = \pm F\sum_i \hat{v}_i \mp \sum_j \hat{v}_j^{diss} \pm \frac{\partial\sigma}{\partial t} \tag{40}$$

For the C/electrolyte interface, a similar approach can be employed as described in [126].

Note: The net charge ρ in equation (36) can change with the local hydratation $C_{H_2O,ionomer}$ at the meso-scale (equation (30)) or with the chemistry of the ionomer. However, this is difficult to capture based only on the PNP approach. In order to evaluate these possible effects, within a collaborative work with the experimental group of Dr. Gerard Gebel at CEA/INAC, we have implemented a MC model to calculate the diffuse layer structure formed in the charged surface/electrolyte interface, for different volume water fractions. The model extends the approach previously developed by Kasemo *et al.* [306 307] which consists to distribute the ionomer and water into a 3D lattice and then perform the interaction between them. The length of the lattice uses to be around 50-100 nm to simulate the ionomer close the catalyst surface. The behavior of the system is first considered be governed only by hydrophobic and hydrophilic interactions. The total energy is minimized by using the Metropolis algorithm and the equilibrated structure is obtained. An interesting feature observed is the phase separation of the hydrophobic polymer chain and water: the structure obtained depends on the water content (Figure III.28). Once these calculations are finished, we introduce a random net charge distribution ρ on the ionomer beads in contact with water, and we optimize the electrostatic energy accounting for the interactions between the net charged beads, the interaction with the images and with the charged plane with surface charge densities σ taken from MEMEPhys® calculations. We get then the equilibrated net charge distribution $\rho_{\min}$ and associated electrostatic potential ($\rho_{\min}$ corresponds to the charge distribution with minimal energy (Figure III.28)). By taking the average of the electrostatic potential at each bead layer (Figure III.29), a database is constructed providing the continuum interpolated functions

$$\begin{cases} \rho_{\min}(x=L) = f(\text{water fraction}, \sigma) \\ \phi(x=L) = f(\rho_{\min}) \\ \mathrm{C}_{\mathrm{H}^+}(x=L) = \dfrac{\rho_{\min}(x=L)}{F} + C_{SO_3^-} \end{cases} \quad (41)$$

that can be used in MEMEPhys® instead of the PNP equations.

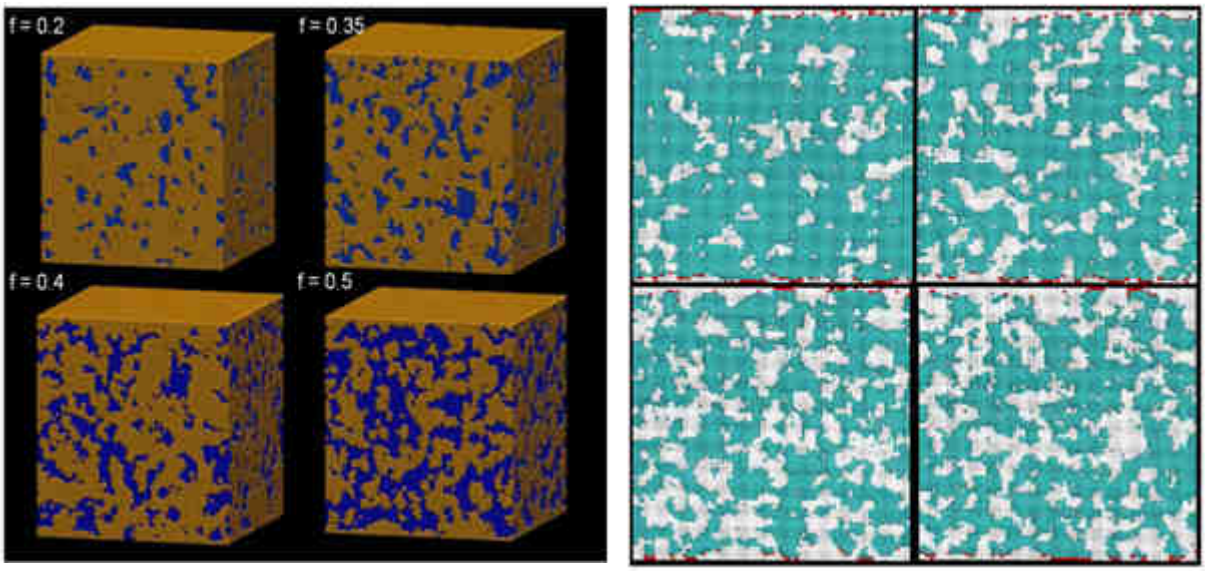

Figure III.28: Calculated impact of water fraction on the interfacial ionomer-water structure (left); calculated net charge distribution (red points) (right). The metal walls are on top and in the bottom of the box (periodic boundary conditions are used) (Source: [308]).

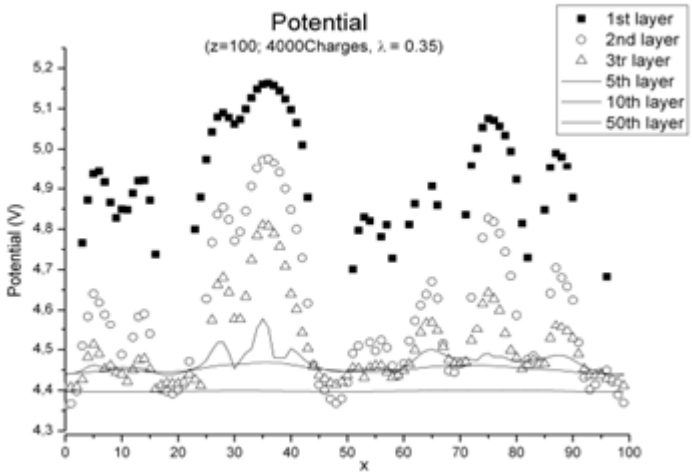

Figure III.29: Example of calculated electrostatic potential along the metal surface (left) (Source: [308]).

Regarding now the chemical and electrochemical processes taking place in the compact layer, they are modeled as series-parallel elementary kinetic steps (see for example our paper [243] and Appendix IV). In our approach, for a given metallic element *M* (Pt or a transition metal, in the case of a bimetallic) at the catalyst level, we have

$$\theta^M + \theta_O^M + \theta_i^M + \vec{\theta^M} + \overleftarrow{\theta^M} + \theta_{ionomer}^M + \theta_{j^+}^M = 1 \qquad (42)$$

where θ^M is the surface coverage by free sites on M surface atoms, θ_O^M is the M-surface coverage by oxides, θ_i^M is the M-surface coverage by the adsorbed reaction intermediates (e.g. OH, OOH for an ORR), and $\vec{\theta^M}$ (respectively $\overleftarrow{\theta^M}$) are the water covering fractions with effective dipoles oriented towards (respectively opposed) the M-surface. $\theta_{ionomer}^M$ is the poisoning ionomer coverage on the catalyst (recently implemented within the context of C corrosion, see Chapter IV) and $\theta_{j^+}^M$ is the coverage by specifically adsorbed ions (relevant for liquid electrolytes). A similar approach is used for describing C corrosion [126, 255].

In order to take into account the effect of catalyst degradation (structure evolution) on the activity and stability properties, we extend classical elementary kinetic modeling by implementing time-dependent kinetic parameters (associated with each step) given by [243]

$$k_i \propto \frac{k_B T}{h} \exp\left(-\frac{1}{RT} \left[\Delta G_i(t) + f_1(\eta_F(t)) + f_2(\theta_i(t)) \right] \right) \tag{43}$$

where the energy barrier $\Delta G_i(t)$ is given by equation (7). The second term in the second exponential argument is a function (dependent on the metal work function and Fermi energy, and independent of Butler-Volmer-like symmetry factors "α", see my previous work, Appendix III in [8]) of the electrostatic potential jump $\eta_F(t)$ between the catalyst surface and the electrolyte (zero for no electron transfer steps), through the compact layer (cf. Figure III.27), and accounts for the effect of the interfacial electric field on the electrochemical reactions [8].

For the general case of a bimetallic Pt_xM_y surface, $\eta_F(t)$ is given by [243,250]

$$\eta_F(t) = -\frac{\sigma.d}{\varepsilon_{CL}} - \frac{\left(x_M^S(t).a_M.\theta^M + \left(1 - x_M^S(t)\right).a_{Pt}.\theta^{Pt}\right).n^{\max}.\Theta_{H_2O}.\mu.\sinh[\ X(\sigma,\theta_i)]}{\varepsilon_{DL}} + \vartheta\left(\sigma, C_{j^+}(x=L)\right) \tag{44}$$

In equation (44), the first term accounts for the compact layer thickness contribution to the potential jump, the second one for the effective dipolar layer contribution, and the third one for solvation and ions specific adsorption effects (not detailed here) (the other parameters

are defined in [243]). X is an intermediate variable function of σ and θ_i, and is the solution of the transcendental equation

$$\frac{\sinh[X]}{\frac{1}{\Theta_{H_2O}}\frac{x_M(t).\left(\theta^M+\theta_i^M\right)+\left(1-x_M(t)\right).\left(\theta^{Pt}+\theta_i^{Pt}\right)}{x_M(t).\theta^M.a_M+\left(1-x_M(t)\right).\theta^{Pt}.a_{Pt}}+\cosh[X]}=\frac{d^3}{A\mu\varepsilon_{CL}}\sigma-\frac{k_BTd^3}{A\mu^2}X \qquad (45)$$

solved at each time step of the kinetic simulation [243].

The third term in the second exponential argument in (43) represents a function of the instantaneous coverage by the different adsorbate intermediates (excluding water). This term allows correcting the activation barriers by the repulsion-attraction energy between the adsorbates (this is analogous to a Temkin's isotherm term). It can be estimated empirically (usually assumed to be linear with the coverage) or from DFT data.

The instantaneous coverage of the reaction intermediates are calculated from balance equations written in terms of the elementary kinetic rates of adsorption/desorption processes,

$$\frac{n^{\max}}{N_A}\frac{d\theta_i}{dt}=\sum_j v_j\pm\sum_k \hat{v}_k \qquad (46)$$

where v_j is the kinetic rate associated to an electron-less elementary step and $\hat{v}_k$ the kinetic rate associated to an electrochemical elementary step, being written in a general way

$$\hat{v}_k=k_{f,m}\prod_{j\in R_{f,m}}c_j^{\nu'_j}-k_{r,m}\prod_{j\in R_{r,m}}c_j^{\nu''_j} \qquad (47)$$

where c refers either to a surface coverage or a volume concentration (see some examples in our papers in Appendix IV).

The coverage of free sites is given by

$$\theta_s=\frac{1-\sum_i\theta_i-\theta_{ionomer}}{1+\Theta_{H_2O}a\cosh[X]} \qquad (48)$$

as already detailed in [126]. The poisoning by water molecules is calculated following the approach we introduced in [250]. The ionomer coverage on the catalyst can be assumed to be

negligible, with constant values, or derived from CGMD simulations for example (e.g. on C corrosion in [233], see Chapter IV).

The output of the nano-scale model is the local electrostatic potential at the catalyst level according to

$$\psi(y,z,t) = \eta_F(y,z,t) + \phi^{\text{int}}(y,z,t) \tag{49}$$

where ϕ^{int} is the electrostatic potential at the boundary between the compact and diffuse layers, calculated from the PNP equations. This is again in contrast with some classical Butler-Volmer models where the (electrode) potential value is used to be "imposed" or "controlled", instead of the current.

Regarding the catalyst degradation, for example, the following balance equation allows calculating the instantaneous Pt catalyst mass content at the CL level based on the elementary catalyst degradation kinetics in Table III.3

$$m_{Pt}(y,z,t) = m_{Pt}(y,z,t=0) - \int_0^t \left(\sum_j v_j^{diss} \right) M_{Pt} \gamma_{catalyst}(y,z,t) V_{CL@(y,z)} dt \tag{50}$$

where M_{Pt} is the Pt molar mass. The procedure is analogous for bimetallics (see Appendix IV). For the C/electrolyte interface, a similar elementary kinetic approach is employed as described in [126]. The following balance equation allows calculating the instantaneous C mass content in he CL level based on the elementary C corrosion kinetics in Table III.3

$$m_C(y,z,t) = m_C(y,z,t=0) - \int_0^t \left(\sum_j v_j^{COR} \right) M_C \gamma^{SP}(y,z,t) V_{CL@(y,z)} dt \tag{51}$$

The PEM module. This module, developed within the context of a collaboration with DLR institute from Stuttgart, resolves the water, proton and crossover species transport phenomena across the PEM thickness. In particular, the module includes a description of the

movement of parasitic metallic ions (e.g. Pt^{2+}, Co^{2+}), Pt^{2+} re-crystallization, H_2O_2 diffusion and chemical attack of the Nafion® ionomer side chains via Fenton's cations (with assumed concentration as a first approximation), cf. Table III.3. The PEM is assumed not electron conductive. Again, the feedback between the evolution of the structure of Nafion® and its transport properties (proton conductivity and water diffusion coefficient) is accounted explicitly (e.g. cf. equation (10)).

In the PEM oxygen, hydrogen and hydrogen peroxide transports are assumed to be governed by the independent Fickian diffusion equations solving the local concentrations C_j

$$\frac{\partial C_{O_2}}{\partial t} = -\nabla_y.(J_{O_2}) = -\nabla_y.(-\frac{\wp_{PEM}}{\tau_{PEM}} D_{O_2} \nabla C_{O_2}) \quad (52)$$

$$\frac{\partial C_{H_2}}{\partial t} = -\nabla_y.(J_{H_2}) + S(y,t) = -\nabla_y \cdot (-\frac{\wp_{PEM}}{\tau_{PEM}} D_{H_2} \nabla_y C_{H_2}) - kC_{Pt^{2+}}(y,t) C_{H_2}(y,t) \quad (53)$$

$$\frac{\partial C_{H_2O_2}}{\partial t} = -\nabla_y.(J_{H_2O_2}) + S_{H_2O_2}(y,t) = -\nabla_y \cdot (-\frac{\wp_{PEM}}{\tau_{PEM}} D_{H_2O_2}(\lambda) \nabla_y C_{H_2O_2}) + S_{H_2O_2}(y,t) \quad (54)$$

where the sink term in equation (53) allows accounting for the Pt ions reduction by H_2 crossover, and the one in equation (54) is related to the Fenton's reactions decomposing H_2O_2. N_2 and contaminants crossover through the PEM are neglected. For the proton, parasitic ions and water transport, the equations are analogous to the ones in the CL ionomer medium.

Degradation can be accounted for here via equation (10). For example, if we consider as a first approximation that the chemical degradation occurring in the PEM is only due to the radical-induced cutting of side chains, we have

$$\text{HOOC - R (-S)} + \text{HO}\cdot \Leftrightarrow \text{HOOC - R} + \text{A (DEG)} \quad (55)$$

where *R* represents a back bone chain, *S* a side chain and *A* the molecule which results from cutting the side chain. The evolution of the concentration of sulfonated groups will depend on

the concentration of hydroxide radicals, the former concentration of side chains and the degradation constant k_{DEG} following [284]

$$\frac{dC_{SO_3}}{dt} = -k_{DEG} \cdot C_{SO_3} \cdot C_{HO^{\cdot}} = -v_{DEG} \tag{56}$$

Hydroxyl radicals are formed via the decomposition of hydrogen peroxide through the so-called Fenton's reactions detailed in Table III.3. The time-dependent concentrations of the different intermediates and reaction products are given by the following system of differential equations,

$$\frac{dC_i}{dt} = \sum_i v_i - \sum_j v_j \tag{57}$$

These expressions allow the calculation of the side chain concentration over time and thus, the evolution of the PEM ionic conductivity.

III.4 – Numerical algorithm

MEMEPhys® numerical algorithm is developed by combining a C language code with Matlab-Simulink and Comsol Multiphysics commercial software. This algorithm contains a CEA in-house developed temporal multi-scale solver (variable time step), which allows managing simultaneously simulated processes occurring at different time scales (e.g. nanoscale on-catalyst adsorption mechanisms with typical time scales of ≈ 10^{-6} s, and reactants transport phenomena with typical time scales of ≈ 10^{-1} s). Spatial discretization (e.g. through the CL thickness) can be done through fix or adaptative meshing depending on the case under study. The commercialization possibilities of this algorithm are nowadays under consideration by CEA.

The inputs of the model are the current, temperature, anode and cathode outlet pressures, anode and cathode stoecheometries, anode and cathode relative humidities. With the exeption of the temperature, all these inputs can be time-dependent (e.g. time-dependent current for EIS simulations). The main output of the model is obviously the cell potential and the anode and cathode potentials (at the channel level),

$$U_{cell}(t) = \psi_{Cathode}(t) - \psi_{Anode}(t) \quad (58)$$

a magnitude strongly dependent on operating conditions and initial MEA compositions (e.g. initial catalyst and ionomer loadings). We emphasize that because of the material degradation, the electrode potentials $\psi_{Cathode}(t)$ and $\psi_{Anode}(t)$ (and thus $U_{cell}(t)$) can evolve with time even at fixed current, temperature, reactant pressures and relative humidity.
Other outputs of the model are the materials properties state, the amount of degradation products released and any state-variable in the model (e.g. proton concentration at the compact layer level, or electronic charge density at the nanoscale).

III.5 – Conclusions

We realize that there is a multitude of challenges and solutions in multi-scale simulation, which are unlikely and only inefficiently met by the development of large monolithic computer codes, which may at best address a small fraction of the possible questions. Instead multi-scale simulation methods, which integrate information from high-accuracy calculations at small length and time scales into large-scale models represent a promising approach to achieve quantitative PEMFC materials modeling on the basis of detailed descriptions of the nano-scale building blocks.

In this Chapter I reported some of my research efforts going in this sense, in particular through the design of the MEMEPhys® model. MEMEPhys® is a bottom-up approach providing the link between atomistic dominated mechanisms and macroscopic electrochemical observables. In our opinion, this physical model is providing promising perspectives in engineering practice as it is dependent on the MEA design parameters at different scales (from nano to macro) and sensitive to the transient operating conditions. The model manages simultaneously performance and durability of the MEA, an interesting feature to design ADT or to provide modeling-based recommandations for end-users. The powerful capabilities of this model are illustrated in the next Chapter through several application examples.

CHAPTER IV

Application examples

"Essentially, all models are wrong, but some are useful."

George Box, British Statistician, 1919-…

IV.1 – Performance

One of the applications that MEMEPhys® is to understand the influence of the different PEMFC components, MEA designs and structural parameters (e.g. at the CL level) on the global PEMFC performance, and thus suggesting technical improvements.

Figure IV.1a shows polarization curves (i-V characteristics) calculated without degradation mechanisms for two kind of cathode GDLs under operation with O_2 and Air. Figures IV.1b and IV.1c show the methodology employed for calculating this kind of polarization curves: the calculated transient evolution of the cell potential is shown, including the simulated pre-conditioning phase and the plotted polarization curves generated by current steps (alternatively, i-V characteristics can be obtained by simulating current ramps -like in CV experiments-, not shown here). Thus, the model can emulate "real" experimental methodologies as it is fully transient.

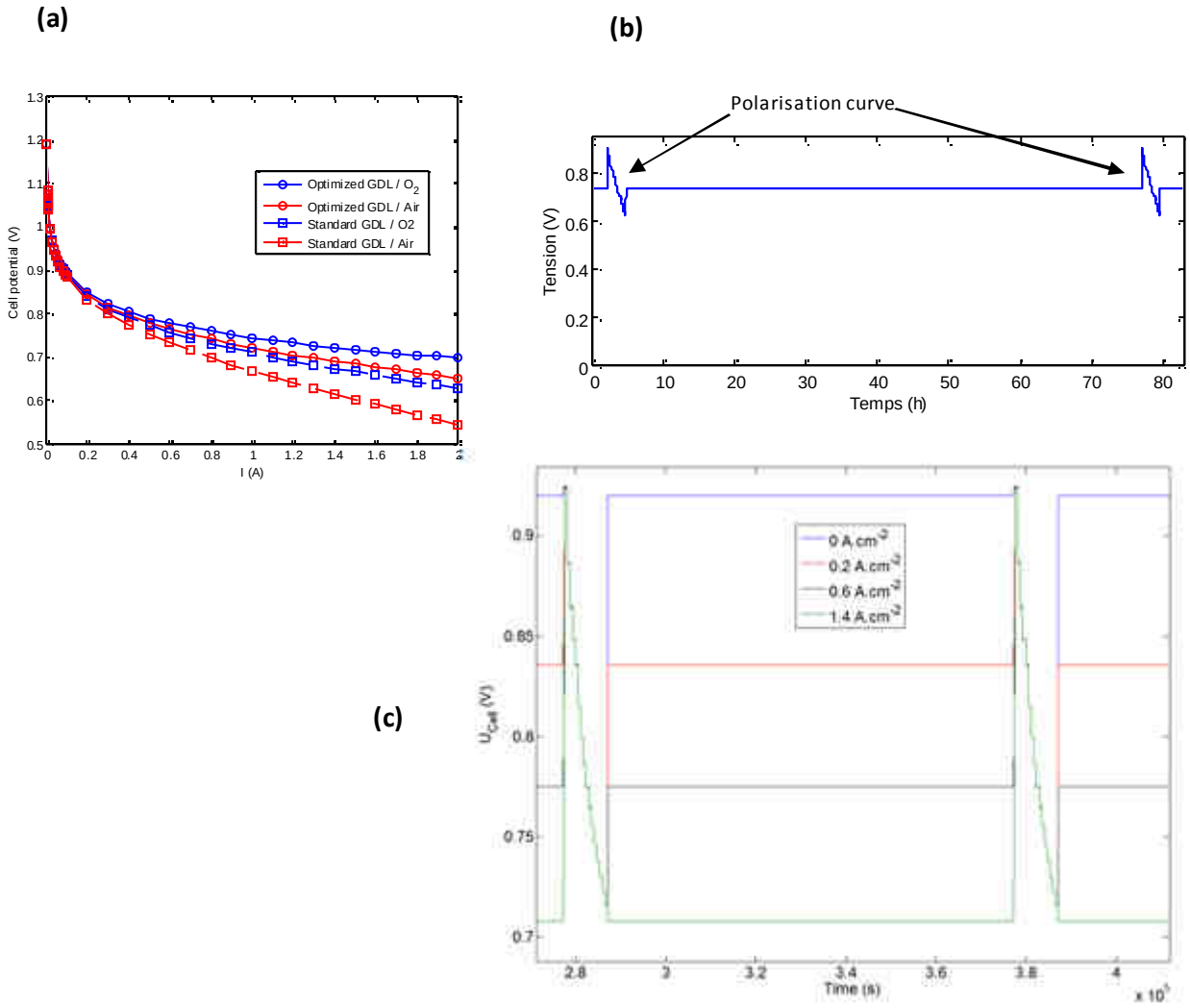

Figure IV.1: (a) Calculated i-V characteristics for two kinds of cathode GDLs operating with pure O_2 and Air; (b) simulation approach employed to calculate the polarization curve (and eventually, its evolution on time); (c) detail of the procedure per "current steps" -shown for 4 pre-conditioning currents- (P_A=P_C=1.5 bar, pure H_2, pure O_2, T = 80°C, S_{MEA} = 2 cm^2, WPt_A =0.1 $mg_{Pt}.cm^{-2}$, WPt_C = 0.3 $mg_{Pt}.cm^{-2}$; structural parameters propertary CEA).

The EIS technique forms a good diagnostic tool for evaluating performance owing to its ability to "separate" the impedance responses of the various transport processes occurring simultaneously in PEMFCs [309]. Generally, the high-frequency region (>100 Hz, in general) of an impedance spectrum reflects the charge transport in the CL, whereas the low-frequency region (< 10^{-2} Hz, in general) represent mass transport in the GDL, the CL and the PEM. The relative importance of the transport processes depend on the steady-state value of the current at which the EIS experiment is conducted. At low overpotentials when the mass transport resistance is not significant, the main contributor to the impedance can be the charge transport in the CL. At moderate overpotentials proton, gas, and water transport

begin to contribute to the total impedance of the cell. At high overpotentials gas diffusion in the GDL and the catalyst layer become dominant, especially when air is used as the oxidant. Figure IV.2 shows impedance spectra calculated in the frequency range of 1 MHz to 10^{-2} Hz at given stationary currents illustrating again the transient characteristics of MEMEPhys®. The behavior observed in this example agrees with typical experimental results [8,310,311].

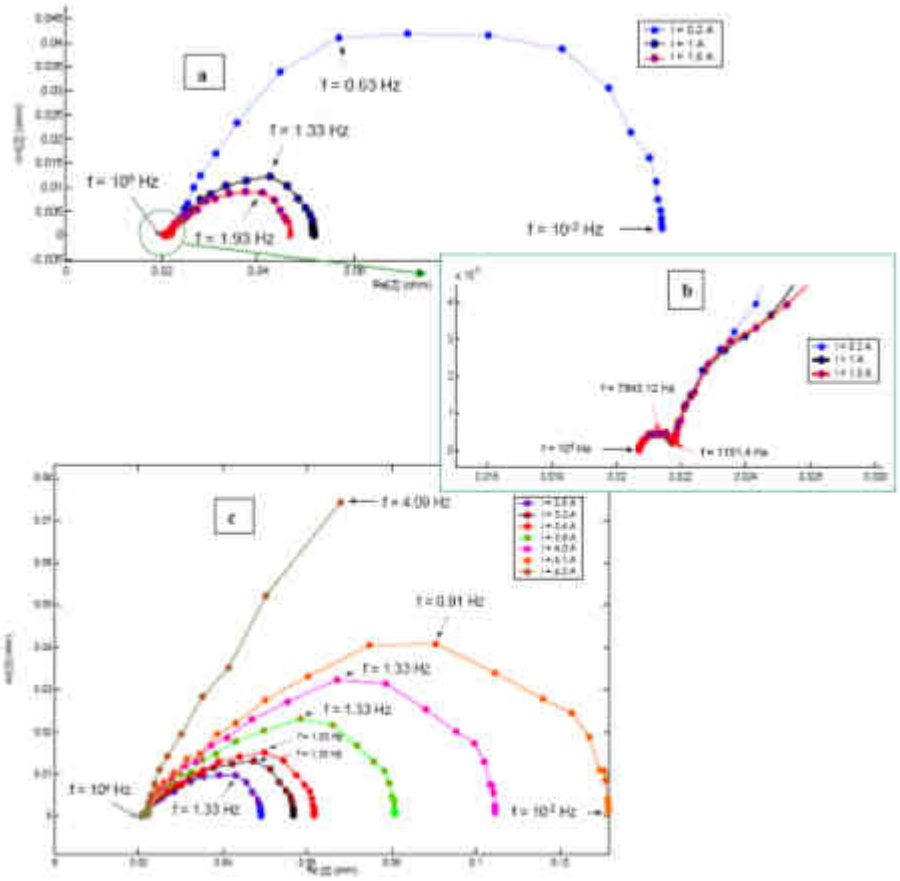

Figure IV.2: Example of calculated EIS sensitivity to the nominal current (Source: [8]).

A summary of the behavior of different nanoscale state-variables along a polarization curve is shown in Figure IV.3, for two different ORR pathways. In particular, the model captures the impact of the type of pathway on the surface charge density, surface potential and reaction intermediates coverage vs. current.

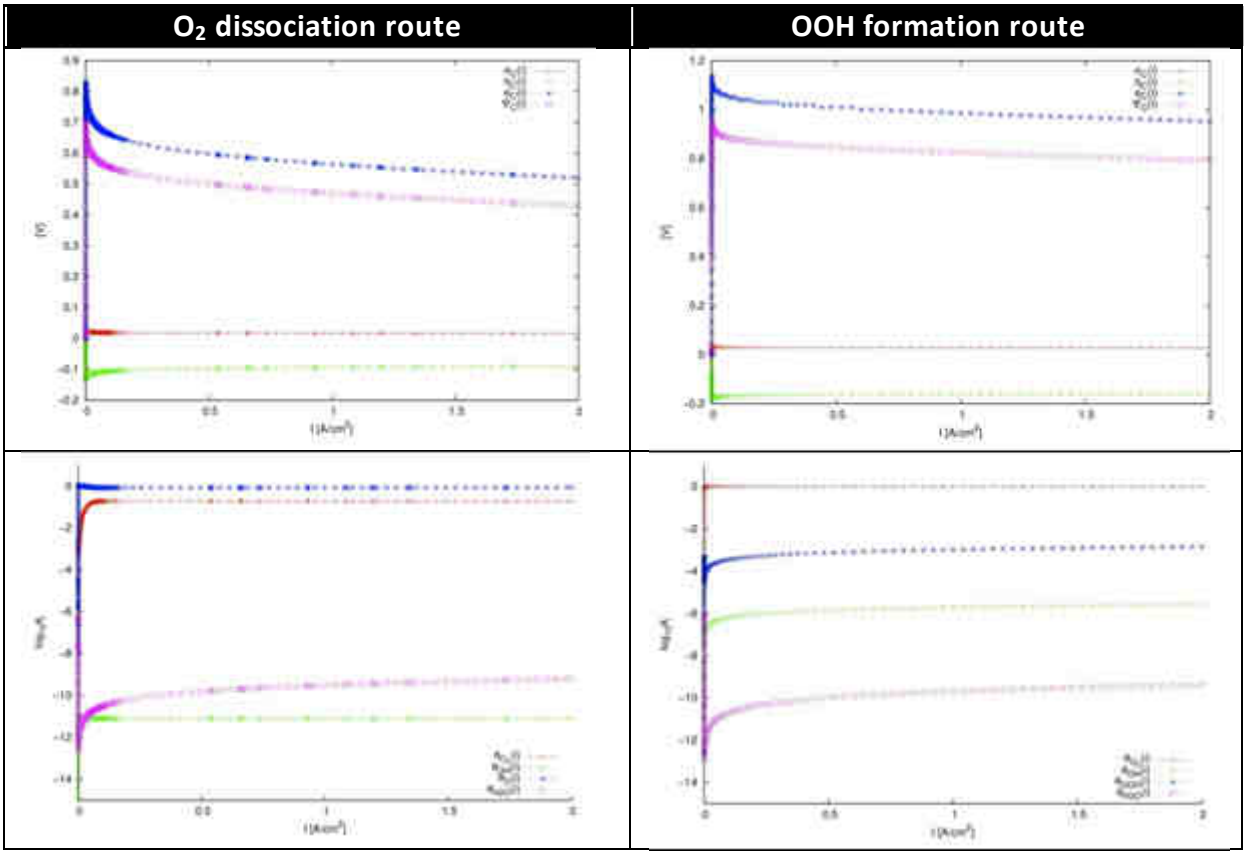

Figure IV.3: Example of calculated cathode nanoscale state-variables along a polarization curve corresponding to a PEM+cathode model (comparison between two different ORR pathways).

The content of Nafion® ionomer in the CL affects simultaneously the gas permeability, the catalytic activity and the ionic resistance. Hence, an optimum Nafion® content in the CL is necessary for good performance, something already studied for many groups worldwide (e.g. [312]). Figure IV.4a shows, in an illustrative way, the calculated impact of the cathode ionomer loading (%wt) on the i-V characteristics. For the operation and structural parameters of that case, the CL performance strongly decreases if it has "too much" ionomer content. This latter behavior may be due to blocking of the catalyst sites, reduced gas permeability, and increased mass transport polarization. The transport limitation results from an increase in the distance through which the reactants has to permeate and diffuse. These results helped on the optimization of the CEA cathode CLs, through examples not shown here, allowing filing 2 patents (Figure IV.4b).

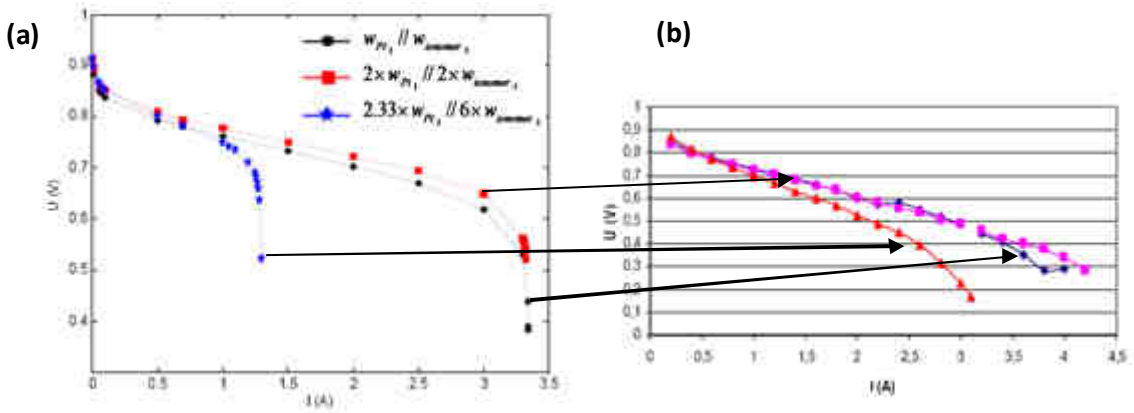

Figure IV.4: (a) Calculated impact of the cathode ionomer loading on the PEMFC polarization curve; (b) experimental validation (P_A=P_C=1.5 bar, T = 80°C, S_{MEA} = 2 cm^2).

The impact of the chemistry and nano-structural properties of the catalysts on the PEMFC performance can be easily captured by using MEMEPhys®, if the appropriate thermodynamic and/or *ab initio* DFT data are available. Figure IV.5 shows the modeling calculation results of the ORR activity of pure Pt compared to different homogeneous (bulk-truncated alloys) Pt_xCo_y catalysts [242, 243]. Activity of the different systems can be ranked as PtCo>Pt_3Co>Pt>$PtCo_3$, in excellent qualitative agreement with in-house experiments carried out in a half cell with catalysts Pt by DLI-MOCVD process (details of elaboration and half-cell test are provided in our team paper [313]).

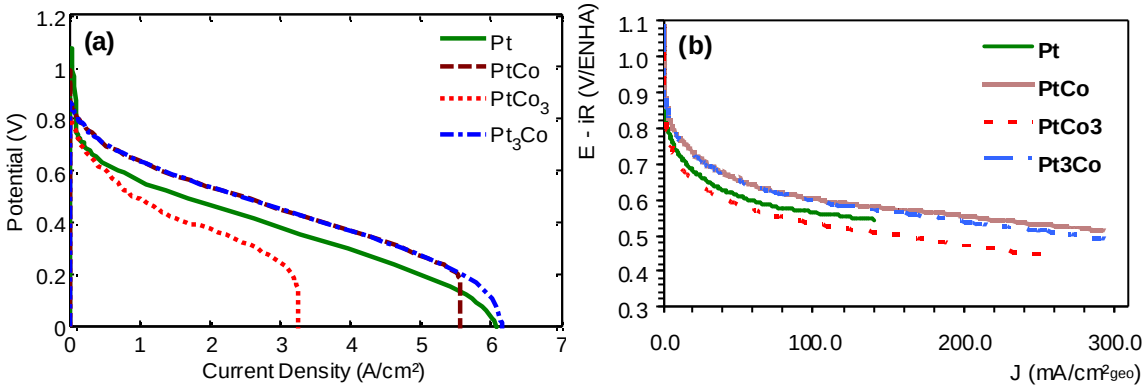

Figure IV.5: (a) Instantaneous polarization curves obtained from multi-scale model simulations for Pt_xCo_y. Morphological assumptions: initial particle size: 2 nm; initial catalyst surface area: 0.01m²; homogeneous profile. (b) Experimental activity results for Pt_xCo_y and Pt elaborated by DLI-MOCVD and tested in a half cell (Source: [242, 243]).

The interest as PEMFC catalysts of more exotic materials can be also evaluated using MEMEPhys®.

Based on DFT calculations we carried out on the proton reduction mechanism catalyzed by the complexes $[Ni(P_2^HN_2^H)_2]^{2+}$ (cf. Chapter III), a kinetic model has been developed and integrated into the MEMEPhys® nano-scale module to calculate the electrochemical observables. Figure IV.6 shows the predicted impact of counter-ion concentration on the V-i characteristics in good comparison with dedicated experiments carried out in a half-cell. This model has been recently extended to describe the competition of the HOR with CO adsorption and electro-oxidation, founding that this Pt-free material offers a better tolerance to CO than the pure Pt [276]. This modeling work allowed 1 patent application at beginning of 2010.

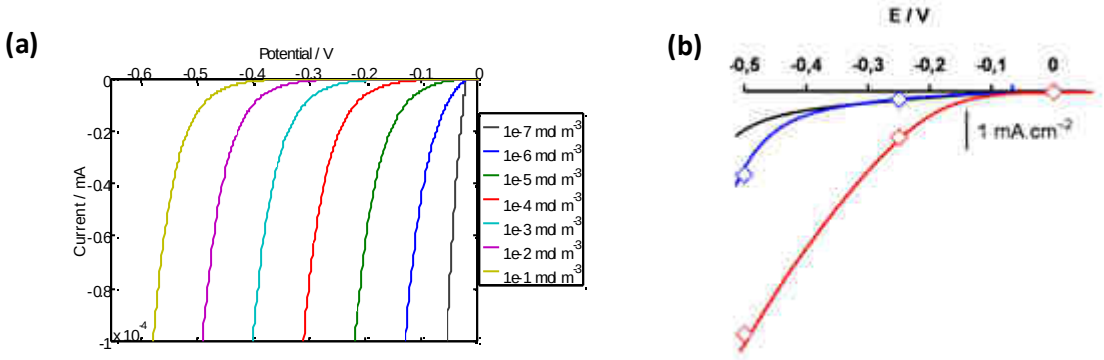

Figure IV.6: (a) calculated V-i characteristics of the $[Ni(P_2^HN_2^H)_2]^{2+}$ catalyst as function of the counter-ion concentration in the electrolyte (CH_3CN^{2-}); (b) experimental V-I characteristics -red curve- (Source: [276,314]).

Another example of the flexibility of MEMEPhys® to analyze materials is shown in Figure IV.7 on the calculated electrochemical response of a membrane-Pt-C_{60} cathode (cf. Chapter III). We report here the calculated i-V characteristics of this material, with an elementary kinetic model developed on the basis of *ab initio* calculations (cf. Chapter III), by comparing the case without and with mixture with CB: because of the semi-conductor properties of these materials, CB clearly increases the global cathode performance. This modeling work triggered 3 patent applications in 2009, and some of these metallofullerenes have been synthesized in our laboratory by chemical addition of Pt or Pd [315,316] with different controlled stoichiometries (Pt_nC_{60} with n = 1, 2 or 4 and Pd_mC_{60} with m = 1, 2, 4 or 10) (Figure IV.8). The electrocatalytic activity of these materials has been tested in RRDE, half-cell and fuel cell. MEAs have been realized by classical method. In RRDE tests, metallofullerenes show a good electrocatalytic activity to the oxygen reduction reaction, similar to commercial Pt/C 20 wt% (Johnson Matthey®). ORR on both Pt_4C_{60} and $Pd_{10}C_{60}$ follows "a four-electron path" leading water. In PEMFC, metallofullerene-CLs, e.g. Pt_4C_{60} and $Pd_{10}C_{60}$, show interesting performance (P = 530 mW.cm^{-2} and 375 mW.cm^{-2} at 1 A.cm^{-2}) but still need to be optimized (Figure IV.9). The materials offers relative stability properties (500 h of durability test @ 0.1

A.cm^{-2}) as the hydrophobic properties of the C_{60} "protect" the CB from water and thus from corrosion (cf. Figure IV.7).

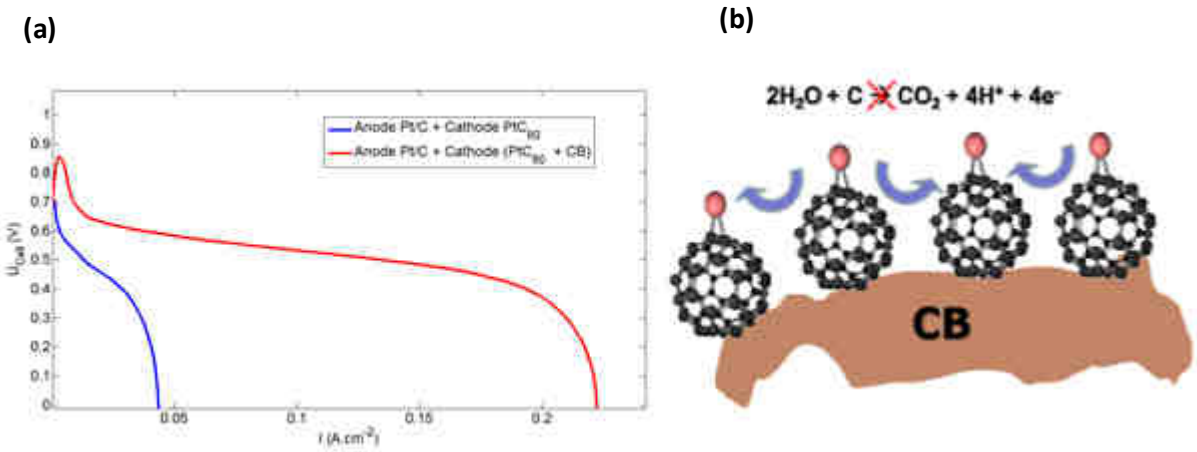

Figure IV.7: (a) calculated polarization curves of a PtC_{60}-based PEMFC cathode without and with CB; (b) possible microstructure of the CL with CB.

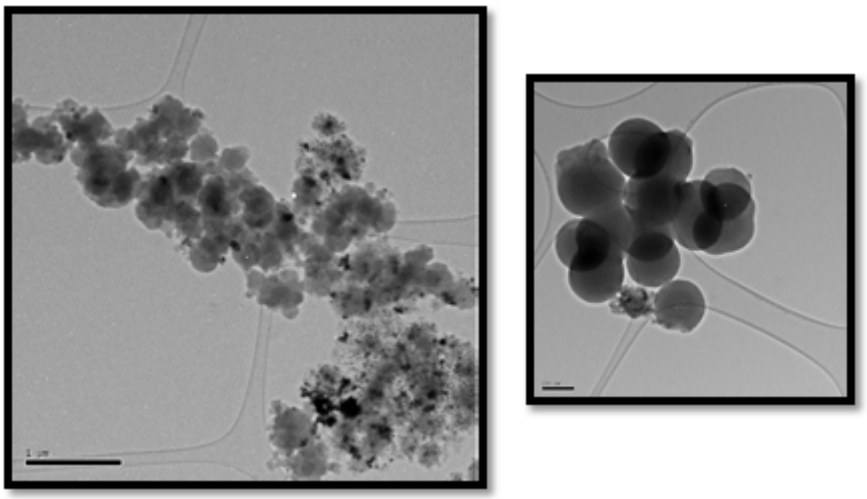

Figure IV.8: TEM images of the prepared PtC_{60}-based electrocatalyst.

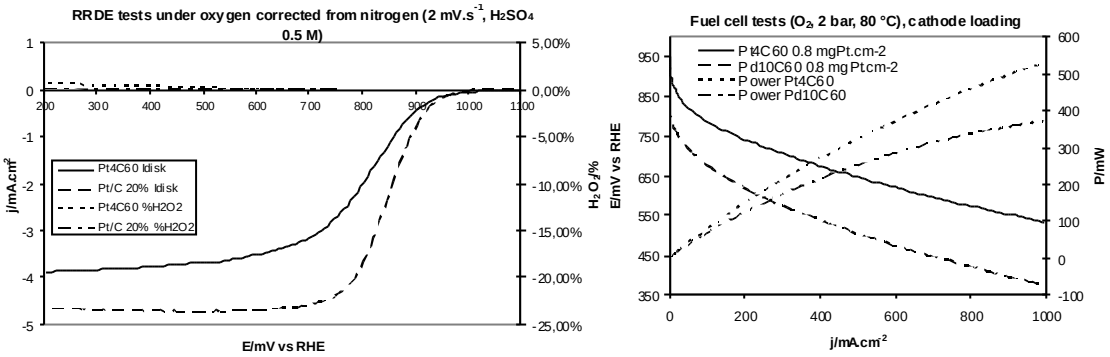

Figure IV.9: experimental polarization curves of Pt_nC_{60} and Pd_nC_{60}-based PEMFC cathode with CB.

An *in silico* MEMEPhys®-based electrocatalyst "benchmarking" is reported in Figure IV.10, showing the sensitivity of the model to the type of reaction kinetics and thus, again, to the catalyst chemistry and nano-structure. For further examples of application of MEMEPhys® to materials, I invite the reader to refer to my publications listed in Appendix I, some of them included in Appendix IV.

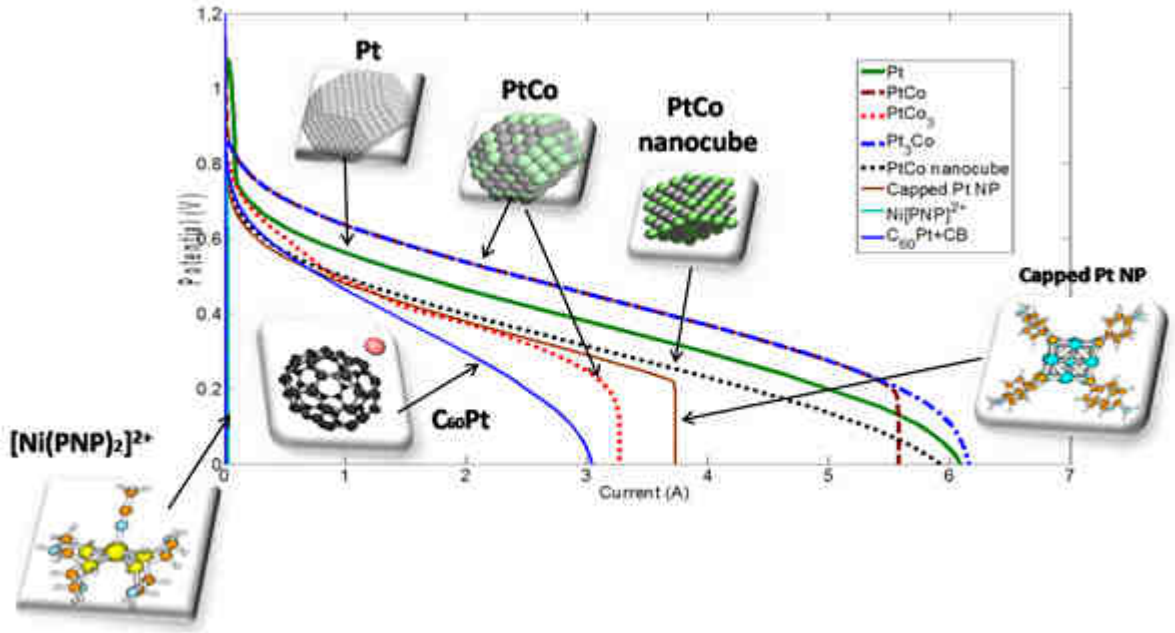

Figure IV.10: *in silico* MEMEPhys®-based electrocatalyst "benchmarking" (all the calculations have been made with P_A=P_C=1.5 bar, RH_A=RH_C=100 %, T = 25°C, S_{MEA} = 5 cm^2).

IV.2 – Performance degradation

The aging-related micro-structural changes are strongly dependent on the operating conditions (stressors) like temperature, relative humidity, potential, load cycles, mechanical stress, contaminants, fuel starvation…It is very difficult to predict at long-term the cell potential without knowing the cell current state, and it is very difficult to know the cell state without looking at the "history" of the input stressors. This means that it is necessary to know the path that the input stressor followed before it reached its current value: the MEA nanomaterials degradation mechanisms are strongly history-dependent or hysteric phenomena.

As MEMEPhys® is a transient model, it can emulate experimental degradation conditions close to the "real" ones. Figure IV.11 shows the impact of the pre-conditioning cathode relative humidity, at OCV conditions, on the transient evolution of the cell potential and i-V

characteristics by accounting for the cathode Pt degradation (oxidation, dissolution and electrochemical ripening) and C corrosion (cf. Chapter III). OCV conditions and high relative humidities enhance these degradation mechanisms. The model clearly highlights the importance of choosing an appropriate pre-conditioning phase to get a long-term durability. The impact of the pre-conditioning phase on the intrinsic materials degradation is a topic, surprisingly, not still largely addressed in literature.

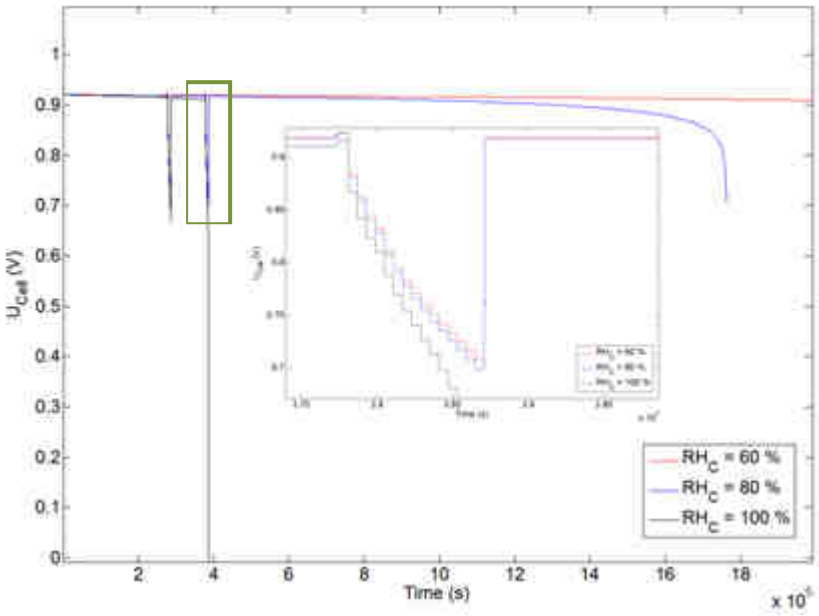

Figure IV.11: Calculated impact of the pre-conditioning cathode relative humidity on the i-V characteristics and durability (I = 0 A, P_A=P_C=1.5 bar, T = 80°C, S_{MEA} = 25 cm^2).

The model has been successfully used to enhance the cathode CL structure to mitigate the reversible and irreversible performance degradations (Figure IV.12). The impact of water flooding on the MEA performance decay was well reproduced by the model: the increase of Pt loading per unit of CL pore volume enhances potential decay as the local water production and thus flooding is enhanced, which can in turn enhance Pt dissolution and C corrosion (both, water content-dependent mechanisms). These modeling studies concerned 1 patent application and allowed to my laboratory the optimization of CL regarding the performance stability.

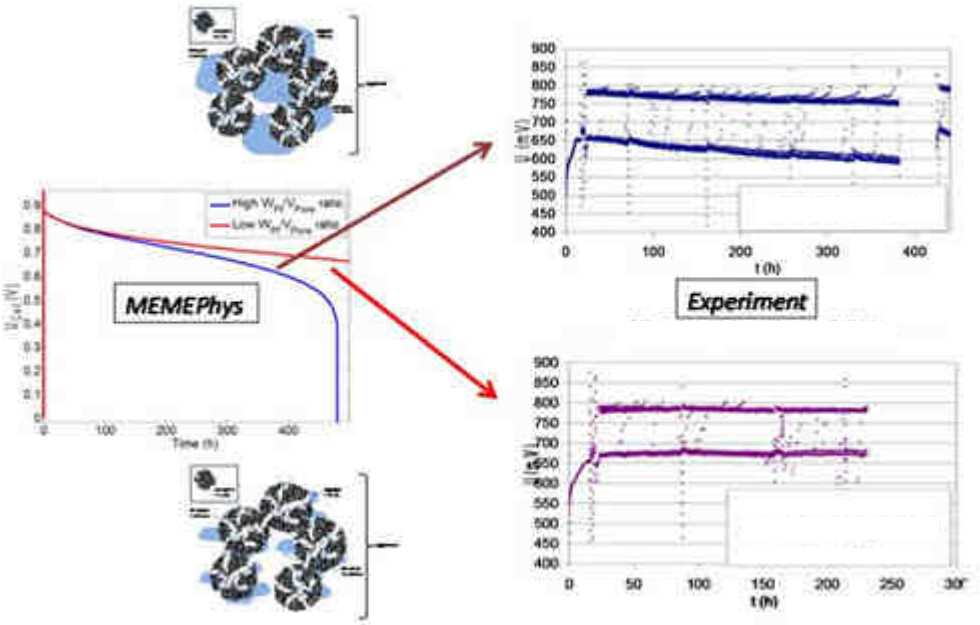

Figure IV.12: Calculated impact of the Pt loading per unit of CL secondary pores volume on the performance decay, and comparison with experiments (Source: [317]).

IV.3 – Catalyst aging

The specificity of the aging of the catalyst itself can be studied with some detail using MEMEPhys®. Figure IV.13a displays some examples of the calculated evolution of the Pt catalyst-size distribution during the Pt oxidation, dissolution and electrochemical ripening mechanisms described in Chapter III and Appendix IV, in a simulated PEMFC cathode. This figure clearly highlights the model sensitivity to the initial CL nano-structure -catalyst size distribution (normal and lognormal are compared)-. The sensitivity of the lognormal model to the cathode RH is illustrated in Figure IV.13b (mean radius illustrated): Pt^{2+} diffusion between the nano-particles (ripening) is enhanced as the local water content increases. The associated impact of this on the cathode potential is shown in Figure IV.13c, which underlines the importance of water management on performance degradation.

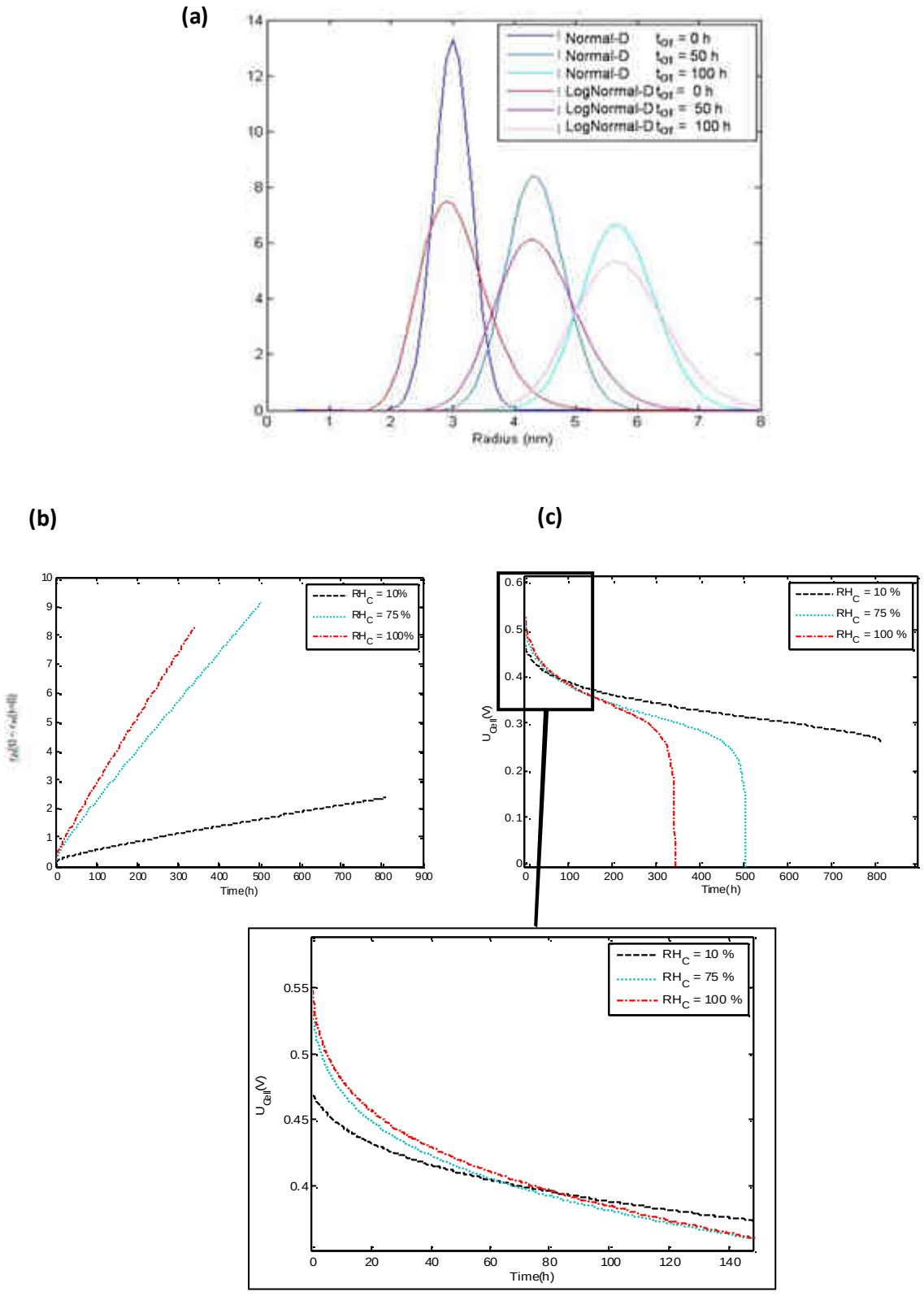

Figure IV.13: (a) Calculated evolution of the Pt size distribution (D) for two initial configurations (RH_C= 80%); (b) calculated impact of the cathode RH on the mean Pt radius increase (case of a normal distribution); (c) associated impact on the cathode performance decay (P_C=1.5 bar, T = 80°C, I = 0.75 A.cm^{-2}).

In Figure IV.14 we show an example of calculated time evolution of the specific Pt surface area $\gamma_{catalyst}$, during oxidation, dissolution and ripening: the area decay rate increases with the electrode potential (which decreases with current) in qualitative agreement with experimental data that used to be obtained by CV.

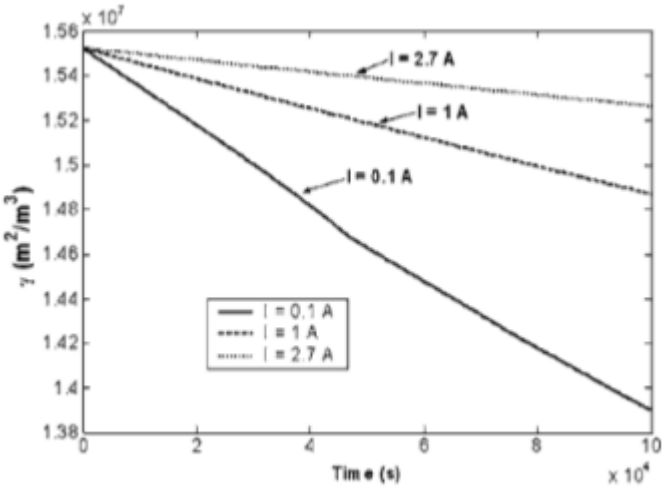

Figure IV.14: Calculated impact of the nominal current on the specific surface area decay (Source: [249,253]).

Figure IV.15 shows the simulated EIS temperature sensitivity, for different nominal currents, after t_{OT} simulated operation. In all the cases, because the hydrated Nafion® phase proton conductivity increases with temperature, the high-frequency intersection point with the real axe shifts toward the Nyquist plan origin. At I = 0.5 A we note that the low-frequency inductive arc diameter is smaller at the highest temperature. Otherwise, at I = 1 A the inductive loop is not greater at 353 K, and a low-frequency capacitive arc appears. Also, it can be observed that for all current levels the size of the high-frequency capacitive arc is smaller at the highest temperature. This is explained by the enhancement of the ORR with temperature. However, low-frequency capacitive arcs are bigger at the highest temperature. Temperature favors both Pt oxidation/dissolution and ripening, which leads to decreasing faster the specific catalytic area and to increase faster the local nano-scale current density J. Then, the increase of J leads to an earlier oxygen transport limitation at the catalyst level and a bigger low frequency arc magnitude at the highest temperature. Even though simulated time is the same for both 313 and 353 K EIS, the EIS at 353 K provides the signature of a "more aged" cathode.

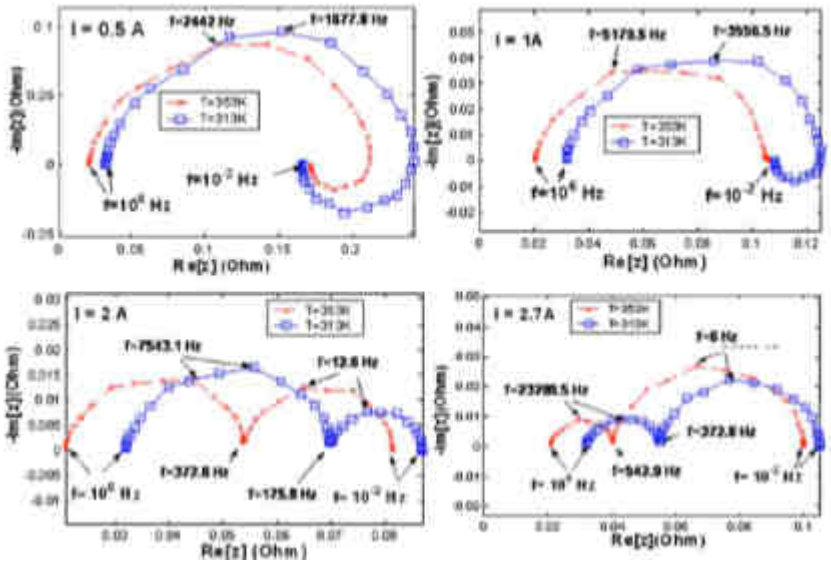

Figure IV.15: Impact of the Pt degradation on the EIS evolution (Source: [249,253]).

The calculated time evolutions of the EIS pattern for three nominal currents are shown in Figure IV.16, emphasizing the temporal multi-scale character of the model. In the three cases it is noted that a long simulated operating time strongly affects the EIS shape.

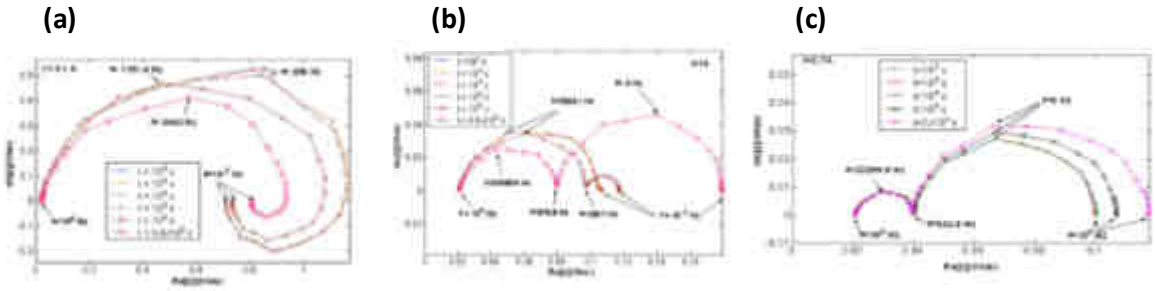

Figure IV.16: Calculated impact of the operation time on the EIS for (a) I = 0.1 A; (b) 1 A; (c) I = 2.7 A (Source: [249,253]).

On the basis of our model, we have studied the degradation and the degradation-induced ORR evolution on Pt_xCo_y electro-catalytic nanoparticles in a PEMFC cathode. Within this context, an *ab initio*-based kinetics description of Pt and Co oxidation/dissolution and the ORR has been coupled to a description of the atomic nano-particle re-organization (segregation, surface energy minimization) as a function of the cumulative Pt and Co mass losses: the time-evolution of the Pt-Co surface and volume ratios at the nano-particle level is simulated according to bulk-truncated and to annealed structural models (cf. Chapter III).

Figure IV.17 shows modeling results for bulk-truncated Pt_xCo_y aging versus Pt aging for two constant demanded current densities. For low currents (0.1 A/cm², Figure IV.17a) our model

predicts a potential "collapse" after 4.9x10^{7}s for PtCo and after 5.9x10^{7}s for Pt_3Co, thus PtCo degradation is faster than Pt_3Co. The observed potential "collapse" occurs when the cathode catalyst surface area (driven by the temporal evolution of the catalyst dissolution) becomes too small to ensure the demanded current. Low current durability simulations can be summarized by Pt_3Co>PtCo>$PtCo_3$. For intermediate currents (0.5 A/cm², Figure IV.17b) our model predicts a potential collapse after 4.10^{7}s for PtCo and after 6.10^{7}s for Pt_3Co ($PtCo_3$ is not represented in this graph because of its predicted very fast degradation), thus we have the same trend. The Co dissolution rate is higher than Pt dissolution rate, and the Co dissolution rate is higher for higher Co volume contents (cf. [243]): this explains why in the two durability rankings (for low and intermediate current) the durability decreases as the Co volume content increases. Regarding Pt nano-particles (in these simulations with a mass higher than the Pt contents in the Pt_xCo_y case), durability increases as the nominal current increases, as previously reported by us in [253] and in agreement with experimental knowledge.

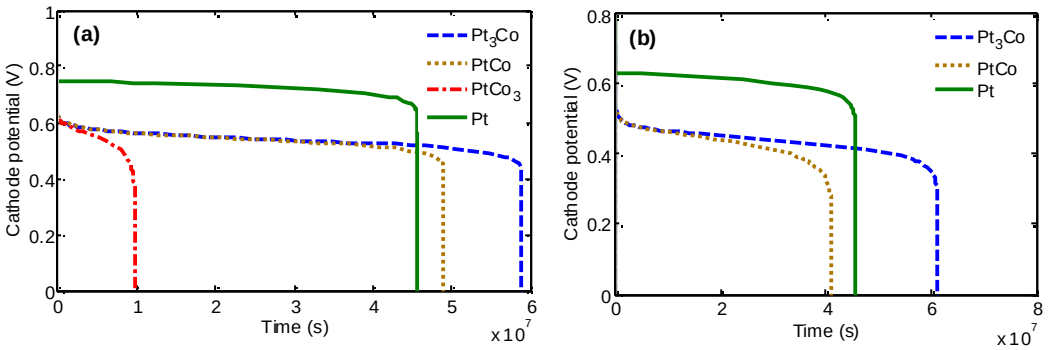

Figure IV.17: Model durability simulation results for Pt_xCo_y at a constant demanded current density. Morphological assumptions: initial particle size: 2 nm; initial catalyst surface area: 0.01 m²; homogeneous profile. (a) 0.1 A.cm^{-2} (b) 0.5 A.cm^{-2} (Source: [242, 243]).

Co dissolution is strongly related to the demanded current density (or applied potential). This fact is illustrated by the Figure IV.18a simulation results on bulk-truncated Pt_3Co: dissolved amount of Co increases as the current decreases. Calculated Pt dissolution rate (not shown here) is considerably lower than the Co dissolution rate (the Pt dissolution rate increases as the Co content in the nano-particle decreases) and the homogeneous nano-particles become more and more like a skeleton-structured nano-particle (the transition element dissolves leaving "holes" in a Pt matrix, like a "French emmental cheese"), exactly as determined by some experiments such as in Stamenkovic *et al.* paper [112]. As we detail in [313] in-house FEG-TEM, TEM and XPS analysis on aged electrodes showed unambiguously that the Co disappears from the nanoparticle composition after RDE aging experiments, regardless of their initial composition (Figures IV18.b and IV.18c).

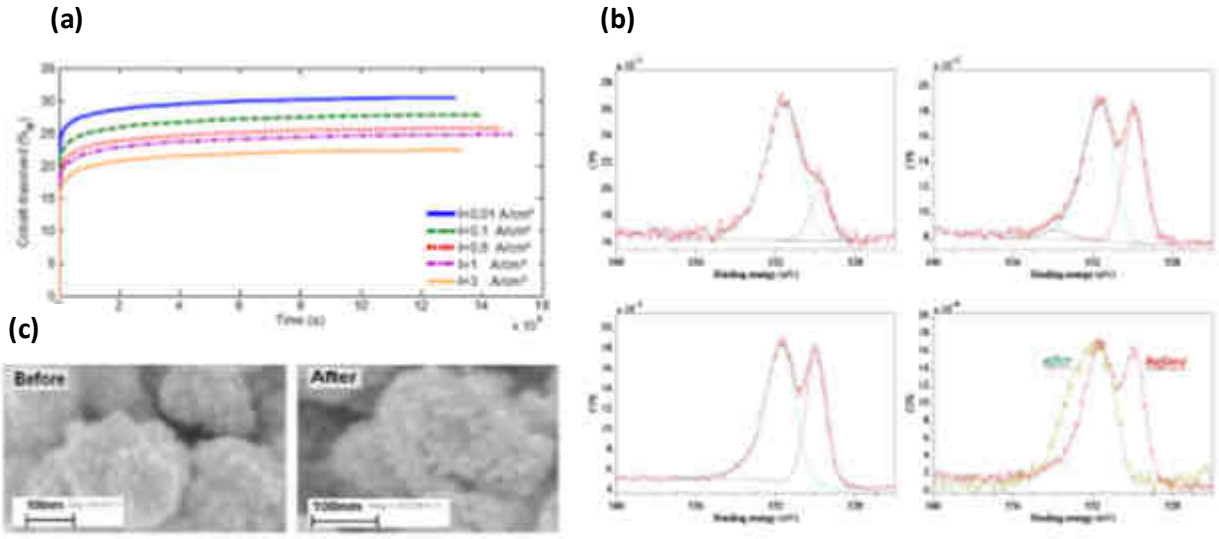

Figure IV.18: (a) Calculated evolution of the amount of dissolved Co^{2+} (Pt_3Co, homogeneous); (b) FEG-SEM images of Pt_3Co material before and after aging ; (c) XPS oxygen *1s* spectra for the fresh Pt_3Co (up corner left), PtCo (up corner right), $PtCo_3$ (down corner left) and superposed spectra of the PtCo material before and after electrochemical aging (Source: [243,313]).

IV.4 – Catalyst support degradation

We studied the cumulative effect of an anodic ORR (induced by O_2 crossover from the cathode to the anode) on cathode carbon catalyst-support loss (C corrosion) under fuel starved and ordinary (e.g. constant current) PEMFC operation conditions in [126] and in [255]. The effects of C corrosion at constant current are less severe than start-up and full H_2 partial starvation, but they are large enough to affect the cell performance after a long-time operation.The design factors of the MEA and operational factors such as humidity and temperature also affect carbon loss. The influence of these parameters is not always simple, and the coupling of these several factors was addressed with MEMEPhys® to elucidate the rate of carbon loss under normal PEMFC operation.

Figure IV.19 shows the simulated long-term behavior of the anode, cathode and cell potentials, for two static nominal currents. Firstly, we can note that cathode and cell potential decrease with time because of the COR-driven degradation mechanisms. When the cathode carbon phase is degraded, the cathode thickness and the Pt active area decrease with time, the latter following the C corrosion-driven platinum coarsening mechanism described in [126]. In analogous way to the modeling of catalyst degradation, for both nominal currents at a given t_{OT} (longer than 1000 hours), the simulated cathodic potential decreases dramatically. This potential failure occurs when the cathode Pt active area (driven by the temporal

evolution of the cathode thickness in our fractal model of that paper) becomes too small to ensure the demanded current I_{ext}.

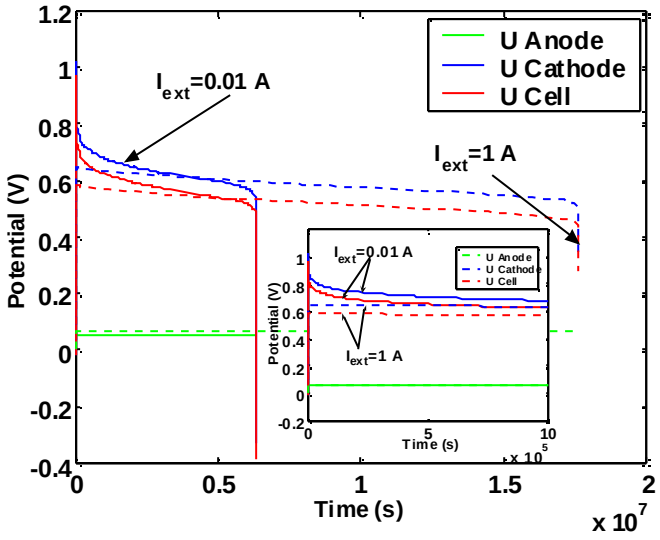

Figure IV.19: calculated impact of the cathode C corrosion on the temporal evolution of the electrodes and cell potentials (Source: [126]).

Figure IV.20a shows the impact of the external current on the cumulative C mass loss, for two simulated operation times. It can be observed that when the current increases, the cathodic potential decreases, and then the COR becomes slower: lost C mass is higher at lower currents, in agreement with *ex situ* experimental behaviors. This suggests that, in order to mitigate cathode C oxidation during start up/shut down H_2 flow experiments, it seems better operate the MEA at intermediate/high current values. Figure IV.20b shows the impact of the anode O_2 concentration in the H_2 flow on the cumulative C mass loss: the calculated trend clearly highlights that O_2 bleeding techniques, used to enhance the anode tolerance to external pollutants such as CO, can dramatically damage the cathode C catalyst support.

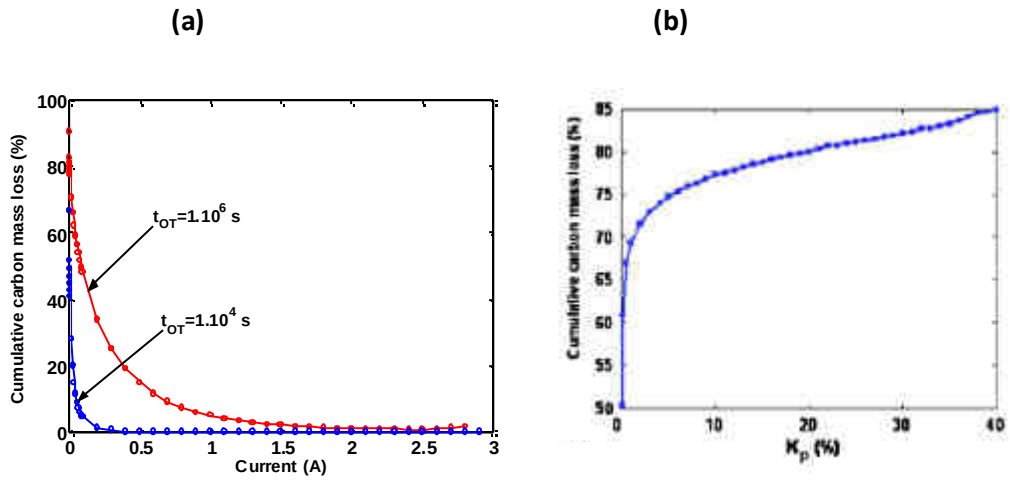

Figure IV.20: (a) impact of the nominal external current on the on the cumulative carbon mass loss for two simulated operation times; (b) impact of the O_2 concentration in the anode on the cumulative C mass loss (Source: [126]).

As shown in Figure IV.21a, the model captures the impact of the initial cathodic Pt loading on the cumulated C mass loss. Increasing the Pt mass in the cathode increases considerably the C support damage, trend in agreement with some experimental results [318]. Hence, it is clear that the cathodic ORR plays a major role on the COR (cf. equation (25) and Figure III.26), by directly consuming the electrons produced by the corrosion reaction (the cathode Pt "catalyses" the C corrosion). The slopes of these curves decrease as the Pt loading increases: this is due to the fact that the Pt active area decreases during the simulated PEMFC operation (COR-driven coarsening mechanism), and then, COR is slowed down. Figure IV.21b illustrates the calculated impact of the initial Pt nano-particle mean size on the cumulative C mass loss for two simulated operation times. An interesting feature captured by the model is that increasing the initial Pt size reduces the cumulative C mass loss, as the catalyst (of C corrosion) specific surface area $\gamma_{catalyst}$ decreases. This theoretical behavior is in agreement with the experimental trends provided by Stevens *et al.* [319] and by Adjemian [320]. The above analysis also means that a mechanism such as the electrochemical Ostwald ripening (contributing to $\gamma_{catalyst}$ decrease with time) can contribute to slowing down the COR process (see below).

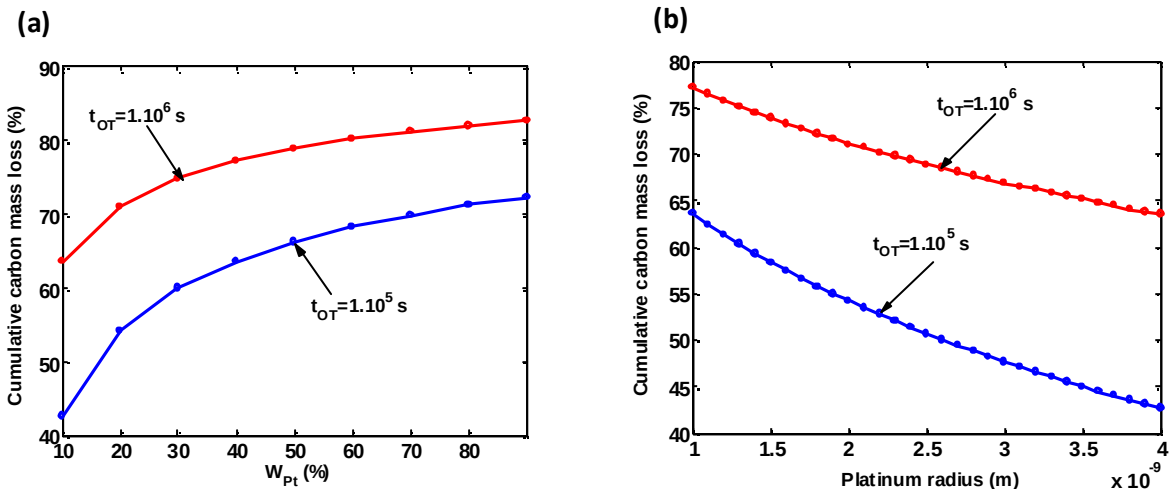

Figure IV.21: (a) calculated impact of the cathode Pt mass ratio on the cumulative carbon mass loss for two simulated operation times; (b) calculated impact of the Pt nano-particles mean radius on the cumulative carbon mass loss for two operation times (Source: [126]).

More recently, in collaboration with NRC-IFCI from Vancouver, we have improved the structural description of this model by using CGMD data (see Appendix I). By employing extensive CGMD simulations, we analyzed micro-structure of CL as a function of C loss and in view of ionomer and water morphology, water and ionomer coverage, and overall changes in C surface. These ingredients are integrated into MEMEPhys® to capture the impact of the structural changes on the PEMFC performance decay. In principle, such multi-scale simulation studies allow relating the aging of CL to the selection of C particles (sizes and wettability), catalyst loading and the level of ionomer structural changes during the CL degradation process.

When the cathode C is degraded the Pt active surface area decreases with time (Figures IV.22a and IV.22b), the latter due to the catalyst nano-particules re-organization with the C support corrosion. An interesting feature can also be pointed out from Figure IV.22c: at short-term operation, the catalyst surface area increases with time instead of decreasing. This is a fingerprint of the fact that at the beginning of the C corrosion process, catalyst in smaller pores becomes exposed to water and ionomer.

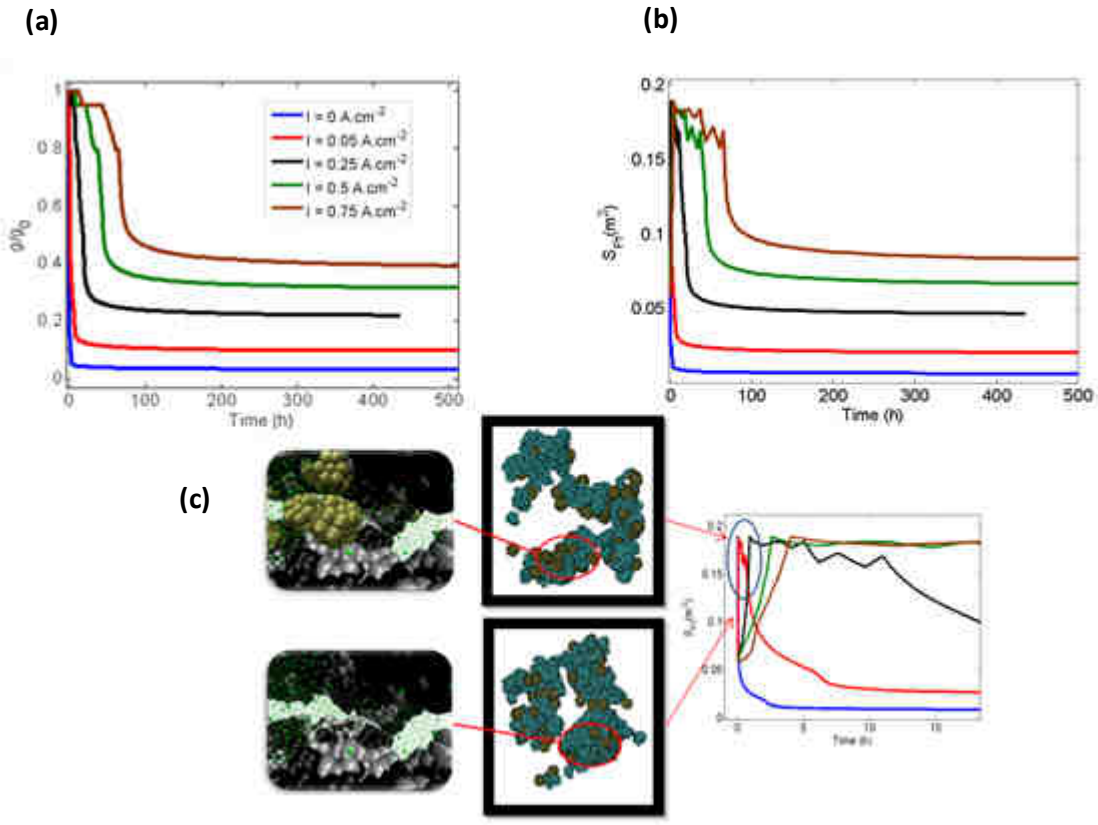

Figure IV.22: (a) calculated CB conductivity evolution using the CGMD database within MEMEPhys for different fixed currents; (b) associated Pt surface area evolution; (c) detailed view of the Pt surface area evolution (Source: [233]).

Figure IV.23 shows the associated Pt ad-species (OH, OOH, H_2O) and adsorbed ionomer coverage evolution during the C corrosion for two current densities, 0 (OCV condition) and 0.75 A.cm^{-2}. This coverage evolution is a consequence of the C corrosion-induced Pt re-organization. The main features are that the OH coverage increases with time i.e. the catalyst activity decreases. The ionomer coverage is higher at the higher current which agrees with the experimental data reported by Markovic *et al*. [321]. Figure IV.24 shows the corresponding C corrosion ad-species (OH, OOH) and ionomer coverage evolution. At long-term operation, the ionomer coverage becomes higher than the water coverage, and the difference in those coverage decreases as the current increases (as the degradation rate, and thus the electrode re-organization, decreases). Furthermore, the C oxide ad-layer increases as the current increases, implicating an increased stability of the C at high currents ("passivation" effect).

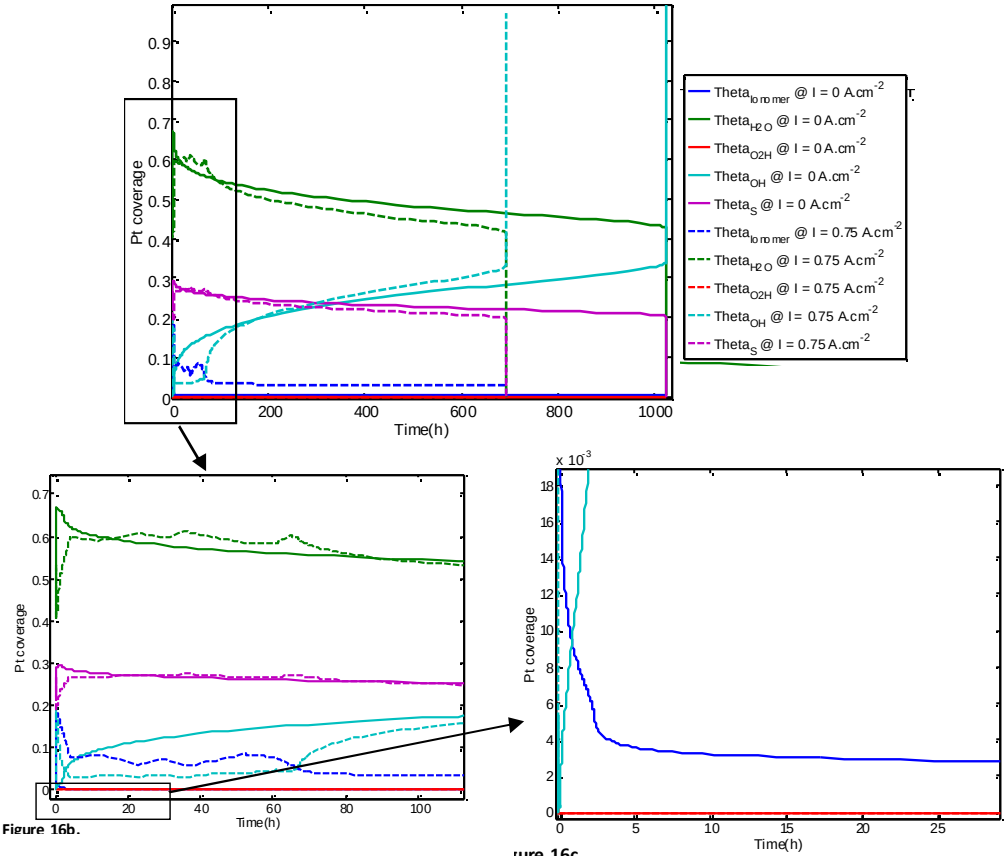

Figure IV.23: calculated evolution of the Pt-ad-species coverage during the C catalyst support corrosion (Source: [[233]]).

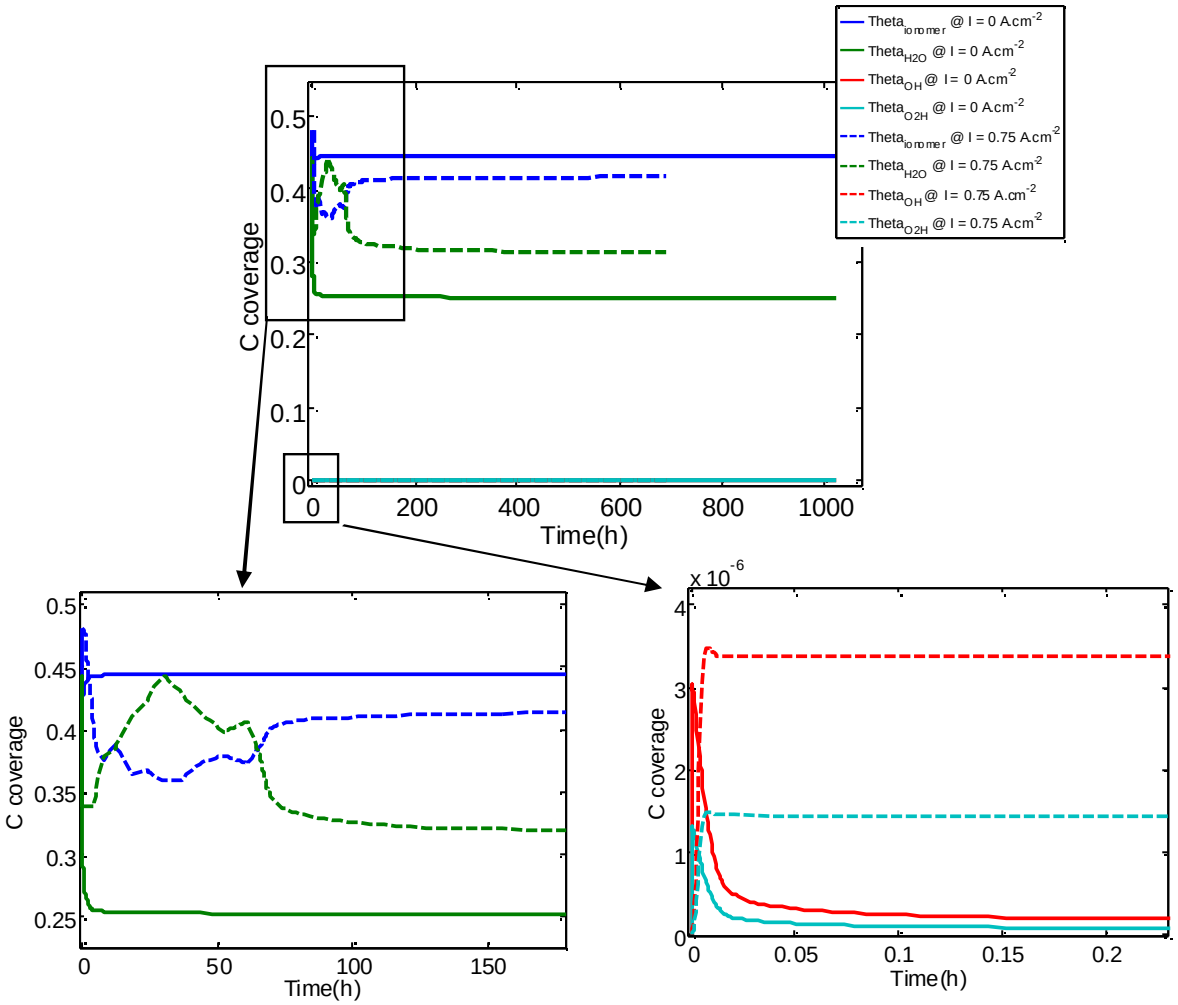

Figure IV.24: calculated evolution of the C-ad-species coverage during the C catalyst support corrosion (Source: [233]).

In Figure IV.25 we report the calculated MEA "durability" as function of the nominal current density, for the full model and for a model where $\theta^{Pt}_{ionomer} = 0$ and $\theta^{C}_{ionomer} = 0$. The durability is calculated here as the simulated time when the potential "collapse" occurs. We underline that the ionomer adsorption on both Pt and C clearly increases the MEA durability for any current density. This can be understood from the associated cumulative C mass loss and Pt active surface area loss at 0.5 A.cm^{-2} provided in the same figure: the ionomer adsorbed on C "protects" it from water and thus mitigates the C corrosion reaction and the associated catalytic activity loss. This mitigation effect, captured here for Nafion®, should be lower or higher depending on the chemical nature of the ionomer.

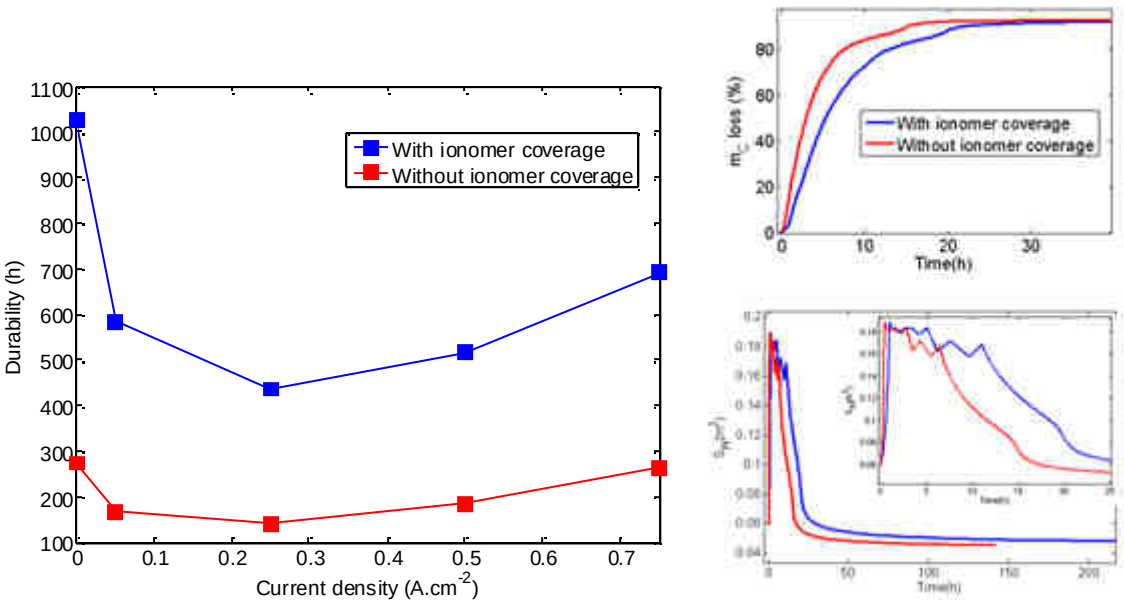

Figure IV.25: calculated durability for the model without including the ionomer coverage and with including the ionomer coverage, and the associated cumulative C mass loss and Pt surface area evolution at I = 0.5 A.cm^{-2} (Source: [233]).

IV.5 – Ionomer degradation

In Figure IV.26, we compare the calculated i-V characteristics for a fully hydrated PEMFC accounting for the PEM side-chain degradation (induced by H_2O_2 formed in the anode, cf. Table III.3, and diffusion into the PEM), under the conditions defined in [284]. We can observe that the influence of the PEM degradation on the cell potential decay is negligible until t_{OT} = 1000 h. For longer operation times, the impact of PEM degradation on the performance becomes pronounced. The same Figure shows the temporal evolution of the cell potential at several given currents. We observe a strong influence on the cell potential for currents above 0.5 A. This shows how operating conditions influence degradation behavior.

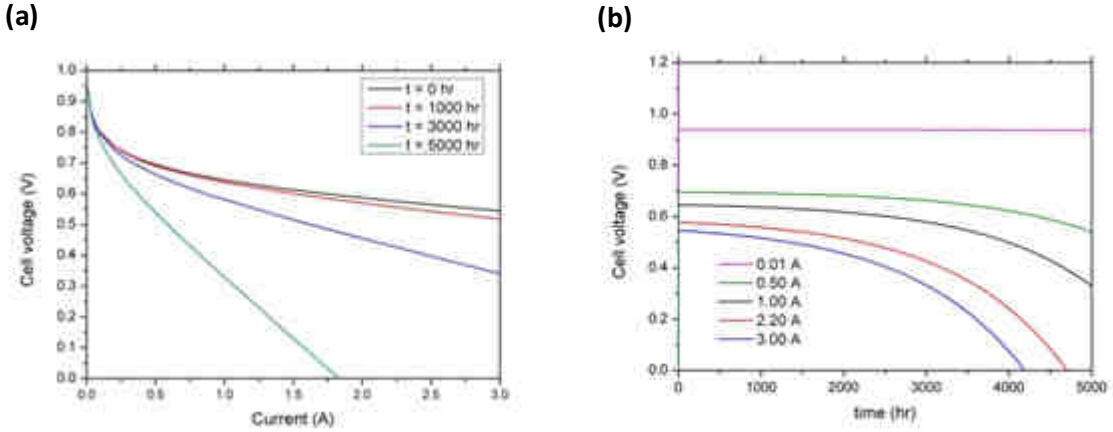

Figure IV.26: (a) calculated polarization curves for different t_{OT}; (b) calculated temporal evolution of the cell potential for different currents (Source: [284]).

The associated evolution of the PEM conductivity versus time is shown in Figure IV.27 for different currents. The PEM conductivity is continuously decreasing over time. The slope of the curve is decreasing as well, suggesting that the conductivity would reach a constant value at the end of the life of the cell. Figure IV.27 also shows the same data plotted as PEM conductivity versus current. Both plots show that the increase of PEM resistance with time is only little dependent on current.

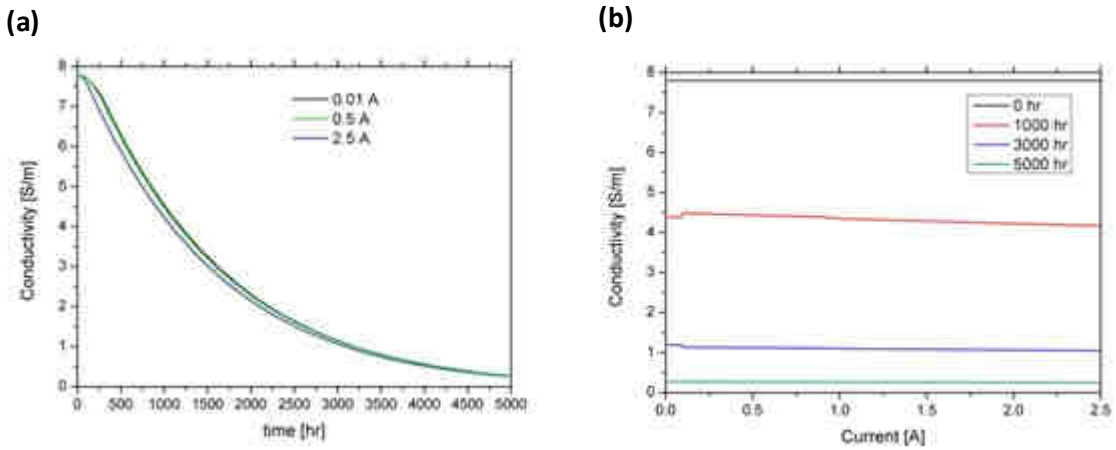

Figure IV.27: (a) evolution of the PEM conductivity over time for different nominal currents; (b) impact of the nominal current on the PEM conductivity at different t_{OT} (Source: [284]).

Figure IV.28 shows the PEM conductivity plotted versus time for different PEM thicknesses of 25, 50 and 100 µm. We observe an only little impact of the thickness on the conductivity evolution. Therefore, material properties stay largely unchanged from a thin PEM to a thick PEM. The same Figure shows an enlargement of the last 1000 h. We observe here that the conductivity of the thicker PEM remains higher than that one of the other PEMs. We show also the concentration of sulfonic acid groups in the PEM over time. Here we observe that for the 100 µm case, the concentration is higher, which means the degradation is smaller. These findings lead to the conclusion that even if a thin PEM has a smaller resistance due to its little thickness, it is slightly more sensible to degradation.

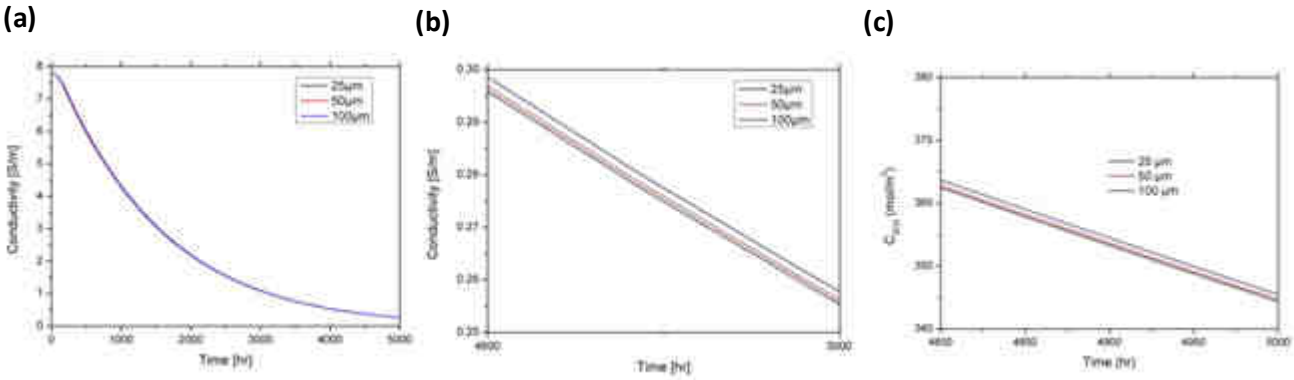

Figure IV.28: (a) PEM conductivity evolution for several thicknesses; (b) enlargement of the last 1000 h; (c) SO_3^- concentration for the last 200 h of the simulations (Source: [284]).

IV.6 – Competition between materials aging mechanisms

In order to illustrate the capabilities of our model to study competitions between different degradation mechanisms, we focus here on some few examples. For further studies, I invite the reader to consult my group publications (see Appendix I).

- ✓ ***Competition between cathode C corrosion and PEM degradation.***

In Figure IV.29 we report the calculated cell potential evolution for a model only accounting for cathode C degradation (a), and the calculated potential evolution for a model accounting for both PEM + C degradation (b), at different fixed nominal currents.

For the first case we observe a dramatic potential collapse, a clear signature of the electro-active area loss (driven by the C support corrosion). We can observe also an optimal current with maximal durability (0.5 A), as already shown by us in [126]. For the second case, the current offering the maximal durability corresponds to the OCV, and we observe a "bell-shaped" potential collapse which provides a signature of the effect of the PEM degradation. In our opinion this feature is interesting for experimental interpretation of cell potential evolutions, to identify the aging process dominating the performance loss.

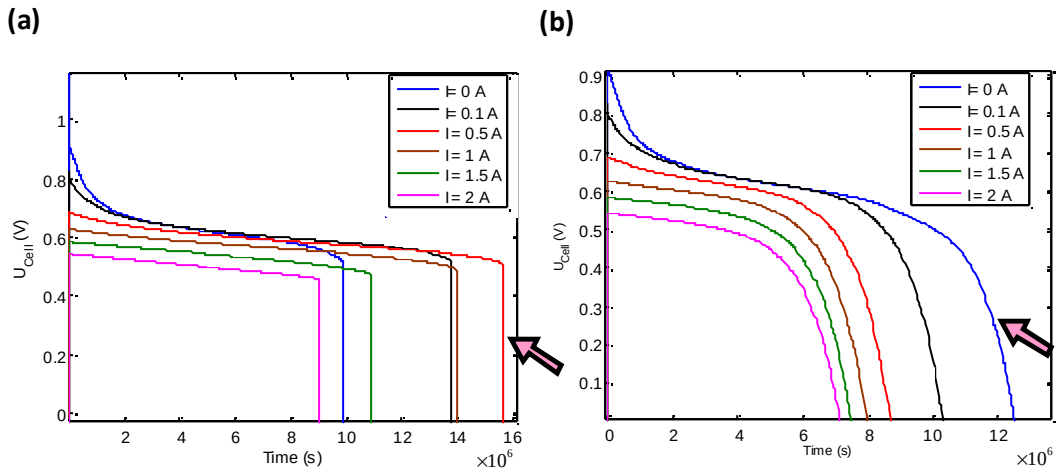

Figure IV.29: (a) calculated cell potential evolution with the model accounting for C corrosion (and induced Pt coarsening) for different nominal currents; calculated cell potential evolution with the model accounting for both PEM + C degradation for different nominal currents (Source: [101]).

Figure IV.30 displays the calculated cell potential evolution at fixed current, for a model only accounting for the cathode C corrosion (and induced Pt coarsening) and for a model accounting for both PEM side-chain degradation + C corrosion, for two PEM thicknesses (25 µm and 50 µm). The potential behavior overlaps for the two models applied to the PEM with initial thickness of 50 µm, which indicates that the C corrosion is the dominating aging mechanism. In contrast to this, for the 25 µm PEM case, the coupled model provides a lower durability compared to the model only accounting for the C corrosion.

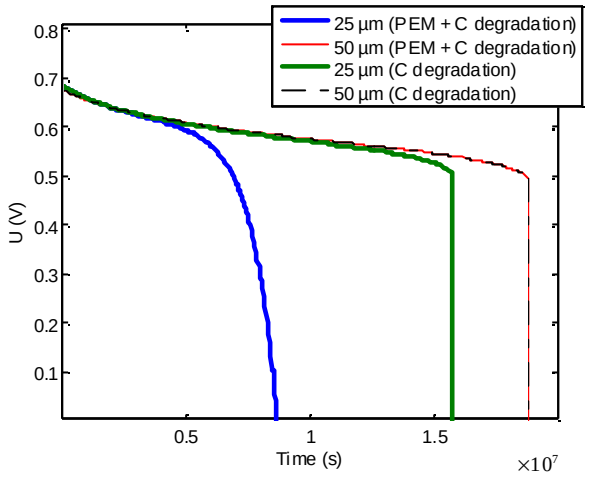

Figure IV.30: Calculated cell potential evolution with a model accounting for PEM + C corrosion vs. a model only accounting for C corrosion (and induced Pt coarsening), for two different PEM thicknesses (Source: [101]).

If we look at the associated calculated cumulative C mass losses (Figure IV.31a) and calculated C corrosion-driven Pt surface area decrease (Figure IV.31b) for the 25 µm case, it

can be concluded that the PEM side-chain degradation mitigates the cathode C corrosion! This is because of the calculated decrease of the PEM proton conductivity (from the PEM degradation model) which contributes to decreasing the proton reverse current (from the cathode to the anode) and thus mitigates the C corrosion in the cathode. These results provide some explanation of some experimental data showing that cathode C support corrodes less with PEMs which have some facility to degradate their conductivity [100].

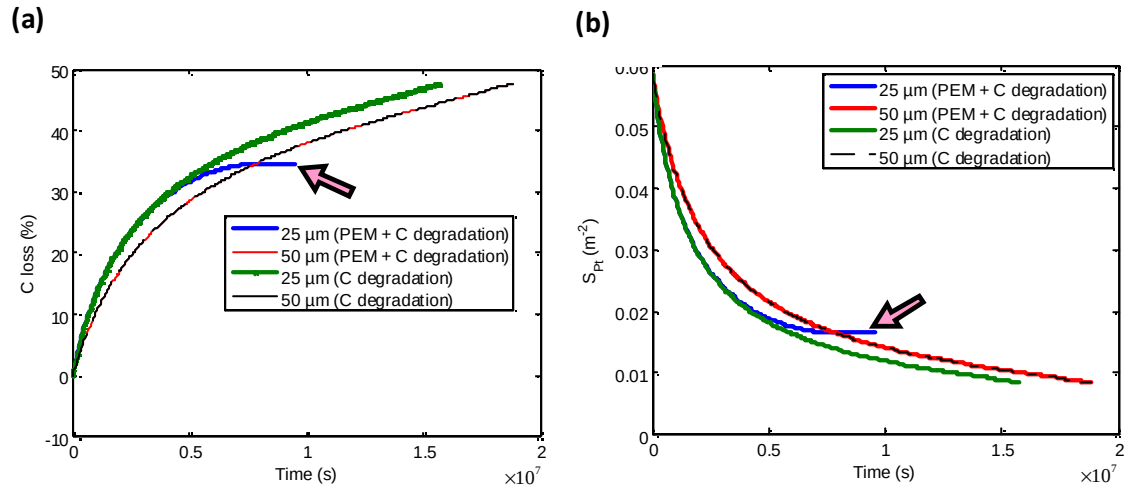

Figure IV.31: Model accounting for PEM + C degradation vs. model accounting for only C degradation; a) calculated cumulative C mass loss, b) calculated C corrosion-driven Pt surface area decrease, for two different initial PEM thicknesses (Source: [101]).

✓ ***Competition between cathode C corrosion and Pt degradation.***

In Figure IV.32 we show simulation results corresponding to a model coupling cathode Pt oxidation/dissolution and ripening with cathode C corrosion. Figure IV.32a shows the simulated impact of the catalyst loading (assuming no catalyst electrochemical degradation) on the cumulative C mass loss, and Figure IV.32b shows the simulated impact of the initial catalyst loading (assuming simultaneous catalyst dissolution/ripening and C corrosion) on the cumulative C mass loss, for three nominal currents. For both cases, at each nominal current, the C mass loss increases as the Pt loading increases (Pt catalyzes C corrosion, as described in the previous Section, i.e. the ORR on Pt affects the C corrosion rate). Furthermore, at each initial Pt loading, the C mass loss increases as the nominal current decreases. An interesting feature, arising from the comparison of the two simulated cases, is that when Pt electrochemical ripening is considered (dissolution and re-deposition) the C corrosion process appears to be mitigated (lower C mass loss for each initial Pt loading and at each nominal current). This is because ripening induces the increase of the Pt nano-particles mean radius and thus the decrease of the catalyst specific surface area $\gamma_{catalyst}$, and

thus C corrosion appears to be less and less “catalyzed”, in agreement with experimental data [319]. These simulations assume that the C electronic conductivity between the Pt nano-particles does not change with the C corrosion process: the C electronic conductivity decrease can in turn slow down the Pt ripening process (cf. Chapter III).

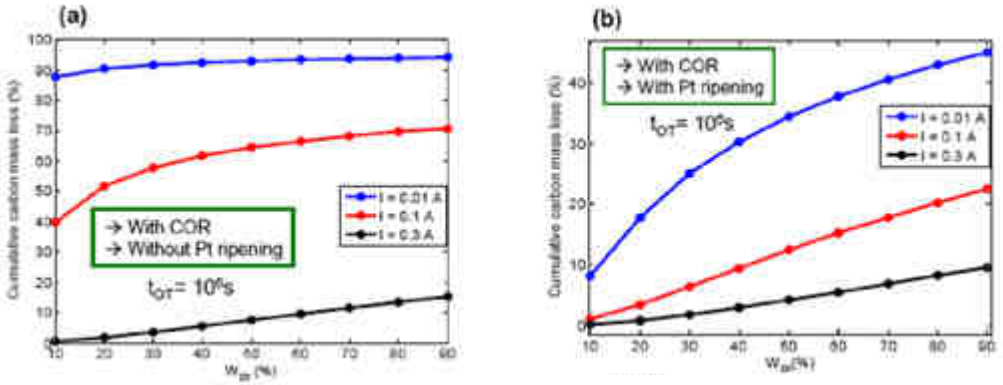

Figure IV.32: (a) calculated impact of the catalyst loading (assuming no catalyst dissolution/ripening) on the cumulative C mass loss; (b) simulated impact of the initial catalyst loading (assuming coupling with catalyst dissolution/ripening) on the cumulative carbon mass loss.

✓ ***Competition between PEM, C and Pt degradation.***

The model can address simultaneously the competition between PEM, C and Pt degradation, resolving the possible heterogeneities along the cathode channel. Figure IV.33 shows one calculation example for a PEMFC operated in counter-flow mode. The calculated impact of a square cycle operation on the global performance decay is shown in Figure IV.33b with the corresponding deconvolution of the contribution of the different aging mechanisms (for the seak of simplicity, only the potentials at I_{max} are shown). Differences between the cumulative materials mass losses in the air inlet and in the air outlet are observed because of the water content inhomogeneities (Figure IV.33c): in particular, Pt and C degradation are higher in the air inlet as the calculated liquid water content is higher than in the outlet. Liquid water favors both corrosion reactions. These trends have been validated experimentally in our group (Figure IV.33d). Different degradation behaviors at co-flow are obtained (not shown here).

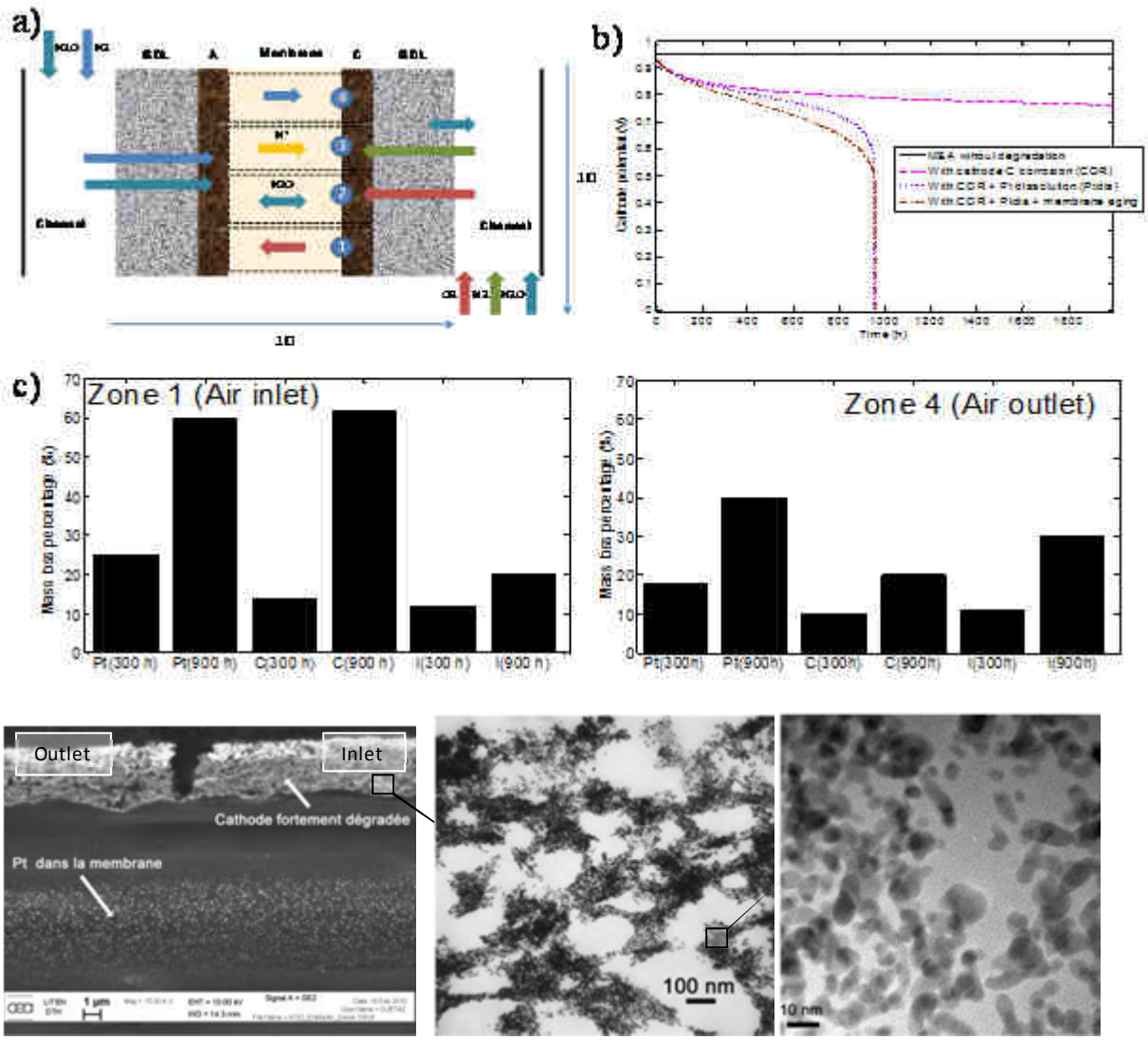

Figure IV.33: (a) simulation of a PEMFC operated in counter-flow mode; (b) calculated impact of a square cycle operation (0.1-0.5 A.cm^{-2}, period=30 min) on the performance decay and deconvolution of the contribution of the different aging mechanisms; (c) calculated cumulative materials mass losses in the air inlet side and in the air outlet side of the cathode and PEM; (d) some TEM images (T = 27 °C, P_A=P_C=1.5 bar, RH_A= RH_C=100%, $S_{electrode}$= 25 cm^2, WPt_A= 0.1 mg.cm^{-2}, WP_C= 0.25 mg.cm^{-2}) (Source: [322]).

IV.7 – Impact of external contaminants on performance

Two examples are provided here on the use of MEMEPhys® to address the external contaminants impact on the performance: an anodic one (CO) and a cathodic one (NO_2). Other situations, such as cathodic SO_2 contamination and mixtures of contaminants are under study and will be presented the H.D.R defence day.

✓ ***Anode CO contamination: impact on the PEMFC performance***

Figure IV.34 shows the calculated impact of the CO concentration in H_2 on the anode i-V characteristics (overpotential here) of an *in silico* half cell with pure Pt. It is clear that the pure Pt catalysts are seriously poisoned by CO: the overpotential increases at any current with the CO concentration. These results are well consistent with the well known experimental poisoning effect of CO on pure Pt catalyst [171,256].

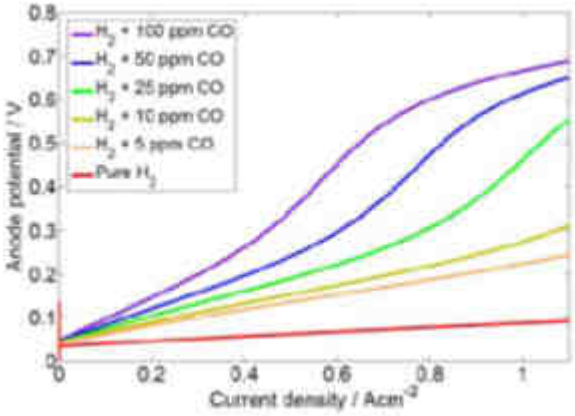

Figure IV.34: calculated anode i-V characteristics of an *in silico* Pt-based half cell for different CO concentrations in H_2 (T= 25°C) (Source: [256]).

Figure IV.35a displays the calculated impact of the anode CO concentration on the cell performance decay at a given current (CO introduced at t = 4 h and removed at t = 52 h): the impact of the CO on the performance decay is slower for lower CO concentrations (Figure IV.35c), in agreement with experiments (see Figure IV.36b). The anode Pt ad-species coverage evolutions corresponding to the 10 ppm case are reported in Figure IV.35b. The calculated impact of the anode CO concentration on the whole cell i-V characteristics is reported in Figure IV.36a, also in good agreement with experimental knowledge [171].

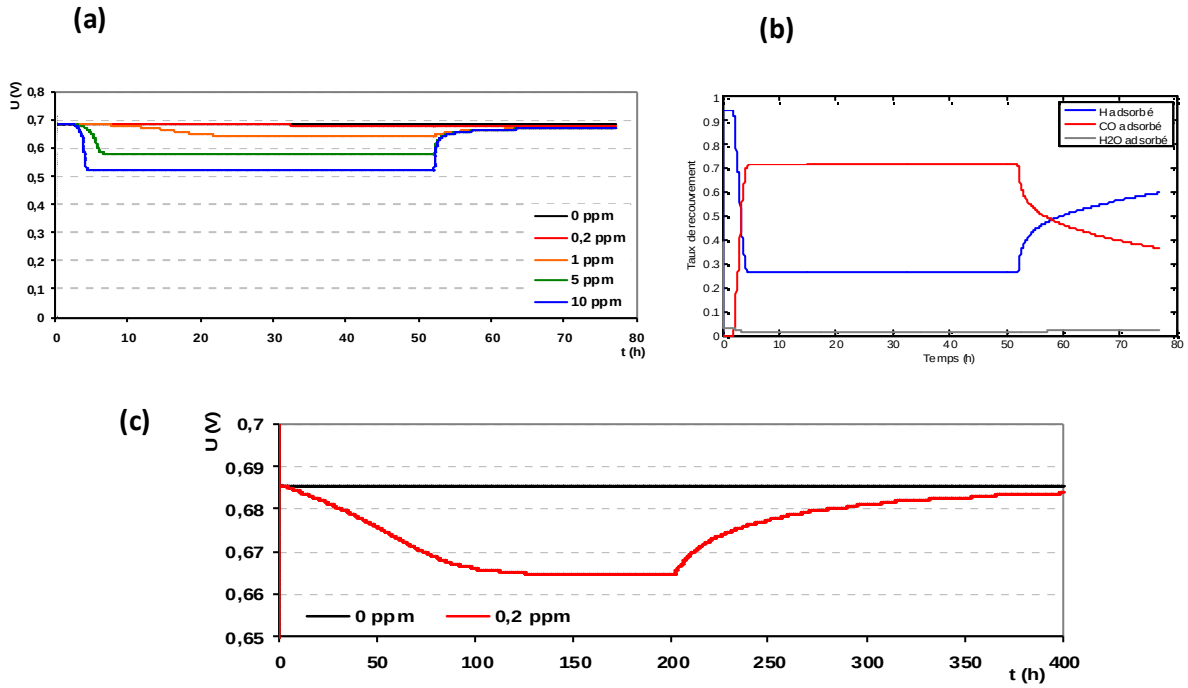

Figure IV.35: (a) calculated impact of the anode CO concentration on the cell performance decay (CO introduced at t = 4 h and removed at t = 52 h); (b) anode Pt ad-species coverge evolution corresponding to the 10 ppm case; (c) calculated performance evolution for the 0.2 ppm case (CO introduced at t = 0 h and removed at t =200 h) (I=0.6 A.cm^{-2}, T=70°C; P_{anode}=$P_{cathode}$=1.5 bar, RH_{anode}=$RH_{cathode}$ = 60%).

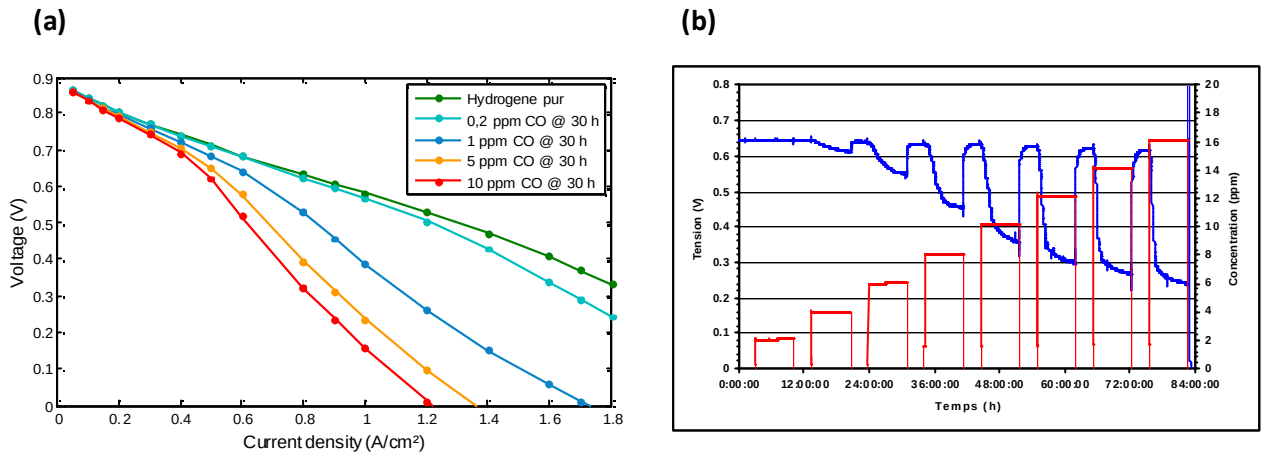

Figure IV.36: (a) calculated impact of the anode CO concentration on the i-V characteristics; (b) in-house experimental data (T=70°C, P_{anode}=$P_{cathode}$=1.5 bar, RH_{anode}=$RH_{cathode}$ = 60%; for (b) I=0.6 A.cm^{-2}).

.

The early work of Prigogine [323] on non-equilibrium thermodynamics initiated numerous studies on self-oscillating reaction systems far from equilibrium. According to this theory, in heterogeneously catalyzed surface reactions, far from thermodynamic equilibrium, new phenomena may develop, such as instabilities, oscillations, chemical waves or chaotic behavior. From the highly non-linear couplings in PEMFC electrochemistry, these self-oscillating phenomena can be expected, in particular under operation in presence of external impurities [324]. Oscillatory phenomena are not uncommon in electrochemical systems [325], and are fully compatible with irreversible thermodynamics principles. For example, metal dissolution and deposition is reported to give potential oscillations in alkaline solutions [326]. It is also found that galvanostatic potential oscillations appear when some small organic molecules such as formic acid and formaldehyde are electro-oxidized at the anode [327]. Potential oscillations are also found with the anodic oxidation of H_2 on Pt electrodes when metal cations such as Cd^{2+}, Cu^{2+}, Sn^{2+}, Bi^{3+}, and Ag^{+} are present in the electrolyte solution [328,329]. These oscillations are believed to be due to the coupling of hydrogen oxidation and the electro-sorption and/or electro-deposition and dissolution of the metal ions.

For some galvanostatic conditions, the pure Pt anode a self-oscillatory behavior of the anode potential was observed using MEMEPhys®. As shown in Figure IV.37 the anode potential oscillates in the range of 0.18 V – 0.7 V under a constant current of 20 mA (10 mA.cm-²) when H_2 contains from 30 to 100 ppm of CO. Rather constant amplitude was observed after the onset of oscillations, which was earlier for higher CO concentration. In the case of 16 ppm of CO, the anode potential increases but the poisoning effect is not strong enough to reach oscillation. Without CO in H_2, oscillation was not observed. Figure IV.37b is a detailed view of the results with 30 ppm CO. It shows that the potential increases gradually from 0.18 V up to 0.7 V, and then drops abruptly down to 0.18 V in a periodical way.

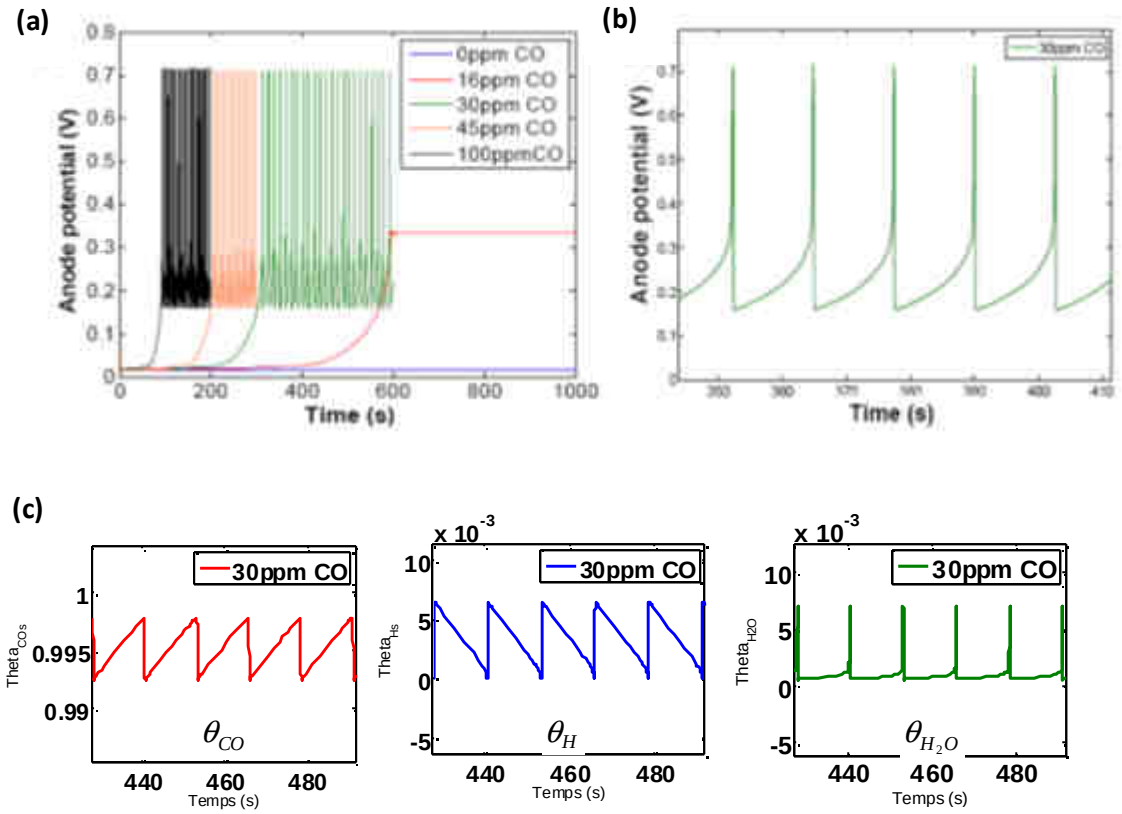

Figure IV.37: (a) calculated evolution of the anodic potential with Pt-based half-cell under constant current of 20 mA (40 mA.cm^{-2}) for different CO concentrations; (b) detailed view of (a) for 30 ppm of CO in H_2; (c) coverage evolutions corresponding to (b) (Source: [256]).

Experiments on half cells under similar conditions were carried out in order to confirm the simulation results. The experiment results are shown in Figure IV.38. Qualitatively, they are in good agreement with our simulation results. As seen in Figure IV.38a, like in simulation results (Fig. 37 (a)) the potential self-oscillations start earlier for higher CO concentration (30). The detailed behavior of self-oscillations is observed in Figure IV.38b, where periodic gradual potential increase was followed by abrupt potential drop. The potential self-oscillatory behavior under the poisoning effect of CO has only been reported elsewhere for bimetallic catalysts [330,331,332]. Although Zhang *et al.* mentioned the possibility of total recovery of Pt catalyst performance after CO poisoning, this was done by stopping the supply of CO to the catalyst [333]. This potential self-oscillatory behavior is thus reported here for the first time.

The phenomenon of potential self-oscillations can be explained by considering the reactions of CO adsorption and CO electro-oxidation by water (cf. Table III.3). The increase of anode potential is due to the gradual poisoning of CO on the Pt catalysts. As a consequence, the availability of free sites for H_2 oxidation to sustain the same electrical current is consistently decreased. Therefore, the anode overpotential increases continuously to enhance the HOR rate to compensate the loss of reaction sites. The adsorption rate of CO is proportional to its

concentration. So that, a higher CO concentration then means a higher poisoning rate. Thus, the onset of oscillation is the earliest for the highest CO concentration. The abrupt potential drop is due to the fast kinetics of CO electro-oxidation from water**.** A fast electrooxidation of adsorbed CO resumes the free sites for HOR which decreases again the anode overpotential abruptly down to initial potential (Figure 37c).

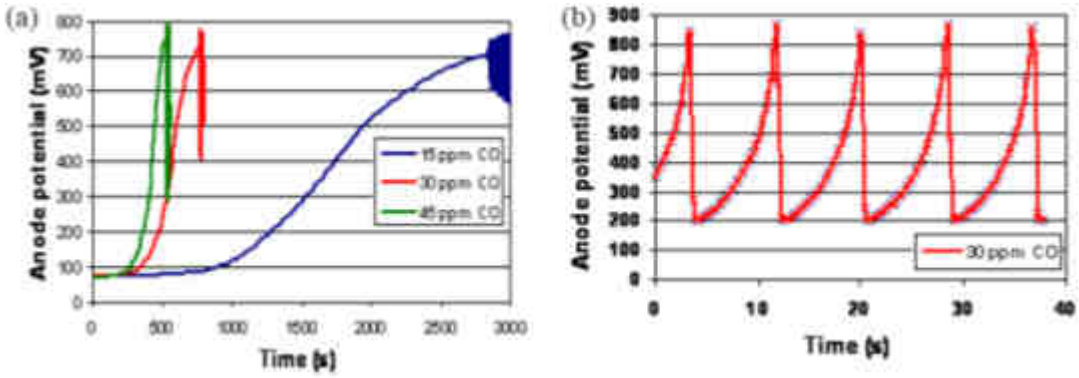

Figure IV.38: (a) experimental measurements of the anodic potential of a pure Pt-based half-cell with different CO concentrations in H_2 under constant current of 40 $mA.cm^{-2}$; (b) detailed view of (a) for 30 ppm of CO in H_2 (Source: [256]).

The great interest in self-oscillatory phenomena in catalytic reactions on metal surfaces is, for a large part, caused by the possibility to perform the catalytic processes more efficiently using unsteady-state operation. The oscillation cycles of the different products may have different forms and surface phases with respect to each other; this can produce valuable information on the mechanism of such reactions. This study is another proof of the bivalent character of MEMEPhys® to address both engineering and fundamental issues. A CO detector in H_2 has been designed based on this modeling work and 1 patent was filed.

- ✓ ***Cahode NO_2 contamination: impact on the PEMFC performance.***

The impact of NO_2 was investigated through a parametrical study which consisted in evaluating the effect of NO_2 concentration, fuel cell temperature and current density on the cell potential evolution. Using MEMEPhys®, it was then possible to understand these results and to identify the main mechanistic pathways.

As shown in Figure IV.39, the impact of NO_2 is characterized by a clear drop of the performance followed by a stabilization of the voltage. In our operating conditions, an untypical phenomenon of “voltage wave” (transient increase of the potential followed by its

decrease) was observed. The recovery phase shows that the impact of NO_2 is reversible. It seems that the return under pure air is done in two steps: a fast increase of performance followed by a slower rate.

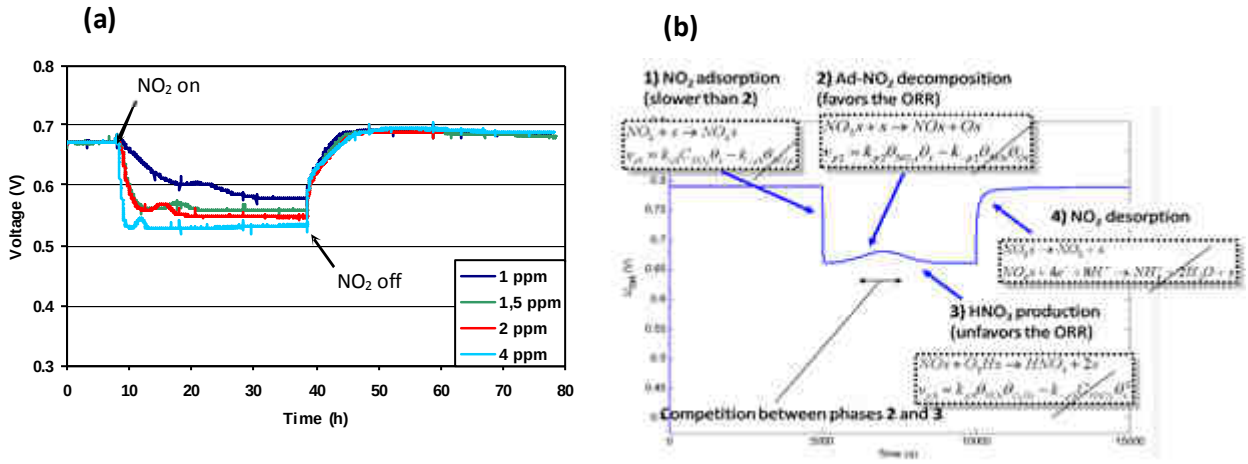

Figure IV.39: (a) evolution of experimental single cell performance for different concentrations of NO_2 in air, followed by pure air (T_{cell} = 70 °C, $P_{anode} = P_{cathode}$ = 1.5x10^5 Pa, $RH_{anode} = RH_{cathode}$ = 60 %); (b) calculated results (same conditions with $RH_{anode} = RH_{cathode}$ = 100 %).

Our proposed elementary kinetic mechanism in Table III.3 allows explaining the impact of NO_2 on PEMFC performance: when NO_2 is introduced in the air feed stream, it first adsorbs on the catalyst, which causes the initial performance drop and the following stabilization by covering part of the active sites. Then adsorbed O (dissociation) is produced contributing to increase the ORR rate (where O is an intermediate) and thus, during a certain time, inducing a performance increase. Adsorbed NO is finally released as HNO_3–like species by reacting with ORR O_2H intermediates decreasing the ORR rate, and causing performance to drop again (cf. Figure IV.39b). These competitive reactions explain the observed “voltage wave”. After that, reactions equilibrate and performance becomes stable.

Experimental EIS were recorded every ten hours, but for better clarity only three of them are shown in Figure IV.40: after 8 hours under pure air, at the end of the pollution phase and after 20 hours recovery. The impact of NO_2 pollution is associated to an increase of the resistance attributed to the charge transfer (first half-arc). Mass transport resistance (second half-arc) is not affected. This is consistent with NO_2 adsorption on the catalyst and partial occupation of the reaction sites. The EIS after recovery confirm the reversibility of the NO_2 impact. It is also observed that performance decrease level and rate are more important when NO_2 concentration increases (Figure IV.41). The “potential wave” arrives earlier and lasts shorter when NO_2 concentration increases: the competitive reactions of O production and HNO_3 release are favored. Finally the reversibility of the NO_2 impact was observed until

at least 4 ppm, which is much higher than the NO_2 concentration that can be encountered in real PEMFC operation.

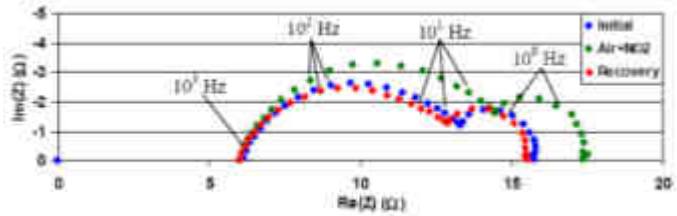

Figure IV.40: Evolution of EIS under pure air, air+NO_2 2 ppm and after 20 hours recovery. T_{cell} = 70°C, i = 0.6 A/cm², P_{anode} = $P_{cathode}$ = 1.5x10^5 Pa, RH_{anode} =$RH_{cathode}$ = 60 %, st_{H2} = 1,2, stAir = 2.

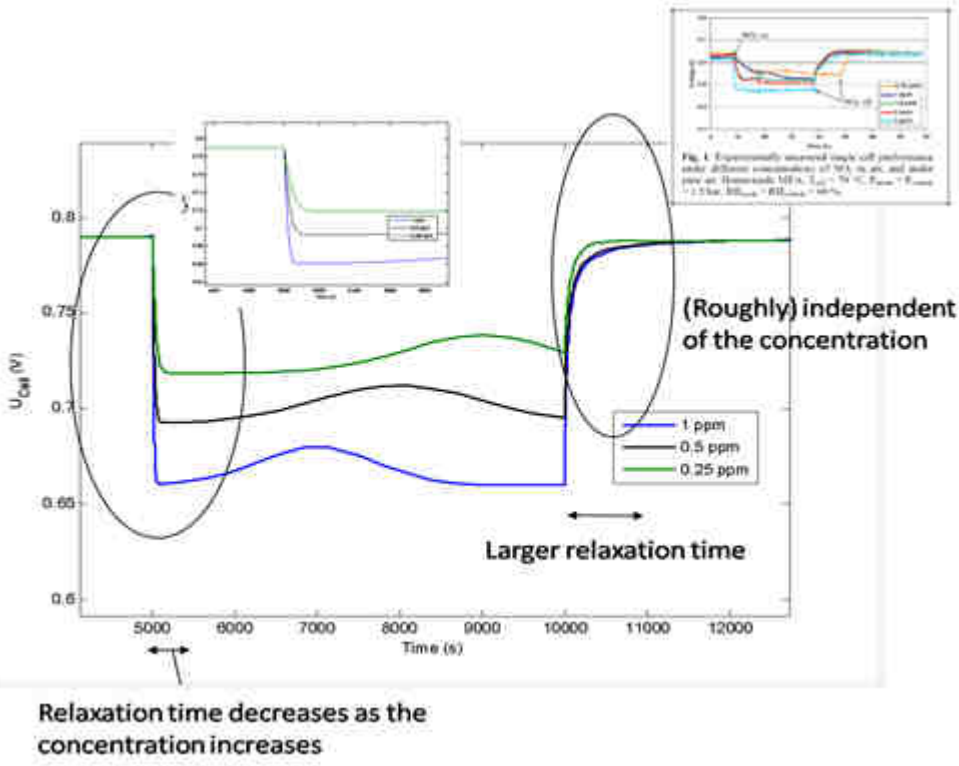

Figure IV.41: Impact of NO_2 concentration on the PEMFC potential dynamics (modeling in the left, experimental in the right).

The voltage wave is also shorter and appears earlier when current density increases (Figure IV.42). This is coherent with the increase of adsorbed O_2H coverage with current, and thus the enhancement of the NO_2 desorption reaction. This causes the quantity of adsorbed NO to decrease, enhancing in turn the reaction producing HNO_3. Concerning the recovery phase, the come back to initial performance under pure air is faster. The two different slopes are more clearly visible for intermediate current density. Other parameters have been studied, as discussed in [334].

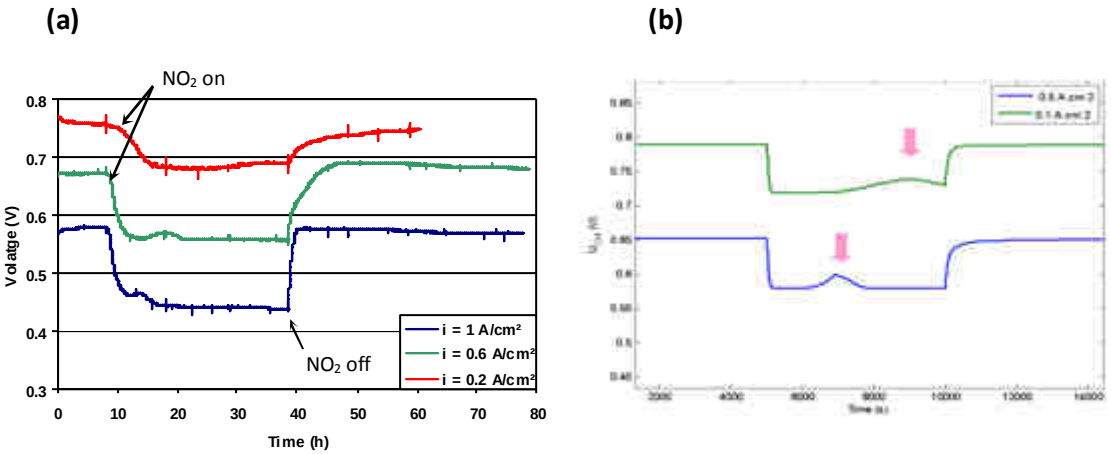

Figure IV.42: (a) Evolution of experimental single cell performance for different current densities under NO_2 in air, followed by pure air (C_{NO2} = 1.5 ppm, T = 70 °C, $P_{anode} = P_{cathode}$ = 1.5x10^5 Pa, $RH_{anode} = RH_{cathode}$ = 60 %); (b) calculated results (same conditions with $RH_{anode} = RH_{cathode}$ = 100 %).

IV.8 – Synergies between pollutants and materials aging mechanisms

✓ *Synergies between cathode C corrosion and anode CO poisoning.*

On the basis of our approach, we have investigated the impact of the injection of CO in the anode feed stream of a PEMFC on the long-term (at least 600 h) MEA performance degradation, under current-cycled operation representative of transport application conditions. First of all, we proposed an elementary kinetic mechanism within MEMEPhys® describing the transient behavior of a PEMFC MEA in the presence of CO at the anode, and accounting at the same time for the C catalyst-support corrosion phenomena in the cathode. In the anode side, competitive CO/H_2 adsorptions and electro-oxidations on Pt are accounted for, as well as the local anodic ORR and the detailed descriptions of the cathodic ORR and the cathodic C corrosion [168, 255].

Numerical simulations suggest that under specific operating conditions, CO injection in the anode feed stream could be used to mitigate C catalyst support corrosion of the cathode electrode under current-cycled operating conditions (Figure IV.43). This interesting feature is here explained by the anodic reactivity between the CO and the membrane crossover O_2, the last one being the "driving force" of the cathode→anode proton pumping effect believed to be the mechanism responsible for the cathode C catalyst-support corrosion. CO reacts with O_2 on the surface of Pt, allowing the decrease of the anodic ORR rate and thus the reverse proton current and the cathode C corrosion. Experiments have been carried out showing

results in qualitative agreement with theoretical behaviors, and demonstrating that the CO effect on the cell potential degradation is strongly dependent on the current-cycle mode. In particular, we studied the impact of two endurance tests on the PEMFC performance degradation, under both pure H_2 (and air in the cathode side) and H_2+5 ppm CO (and air in the cathode side):

- ✓ 30 minute phase with the current density set to 0 $mA.cm^{-2}$, followed by a 30 minute phase with the current density set to 0.54 $mA.cm^{-2}$ (protocol $0/I_{max}$).
- ✓ 30 minute phase with the current density set to 0.108 $mA.cm^{-2}$, followed by a 30 minute phase with the current density set to 0.54 $mA.cm^{-2}$ (protocol I_{min}/I_{max}).

The short and long-term degradation of the PEMFC performance under the $0/I_{max}$ protocol is stronger under H_2+CO than under pure H_2 operation. In these conditions, the anode Pt-catalyst CO contamination is the main mechanism contributing to the performance degradation. In contrast, the long-term degradation of the PEMFC performance under the I_{min}/I_{max} protocol is lower under H_2+CO compared to pure H_2 operation: I_{min}/I_{max} protocols are expected to induce more fuel starvation than $0/I_{max}$ protocols and thus a more significant cumulative anodic O_2 concentration which can react with CO. This synergy between O_2 and CO reduces both the CO poisoning on the anode side and the O_2-driven proton pumping effect responsible for the cathodic C catalyst-support corrosion: we have filed 2 patents on this C corrosion mitigation method which constitutes in our opinion an interesting example on the use of our model as a predictive tool for proposing innovations in the PEMFC operation modes [335]. Furthermore, it can be noted that the anodic CO injection can also reduce PEM chemical attack induced by the OOH° and OH° radicals formed by coexistence of H_2 and O_2 on some anodic Pt sites. Microstructural analyses (SEM, HR-TEM) and chemical (XPS) characterizations on fresh and aged MEA (with and without CO) confirms the mechanisms [336] (see Appendix I).

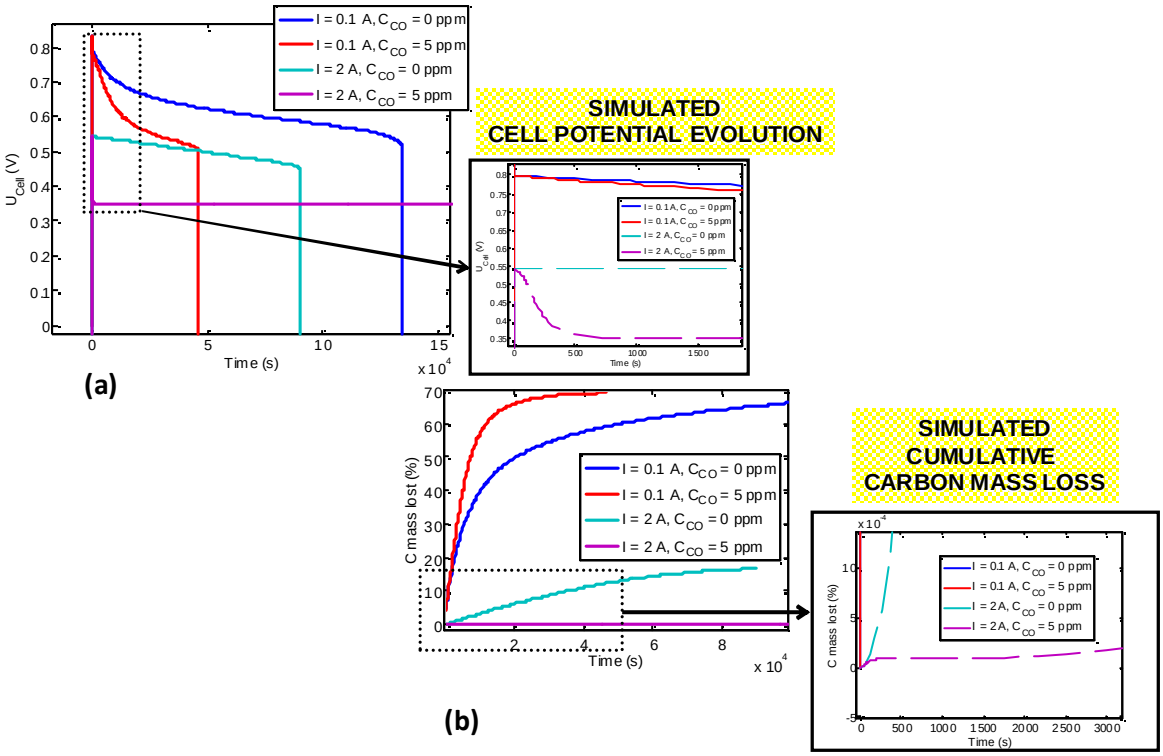

Figure IV.43: (a) calculated temporal evolution of the cell potential at two different currents and two different anodic CO concentrations; (b) associated cumulative C mass loss (Source: [168]).

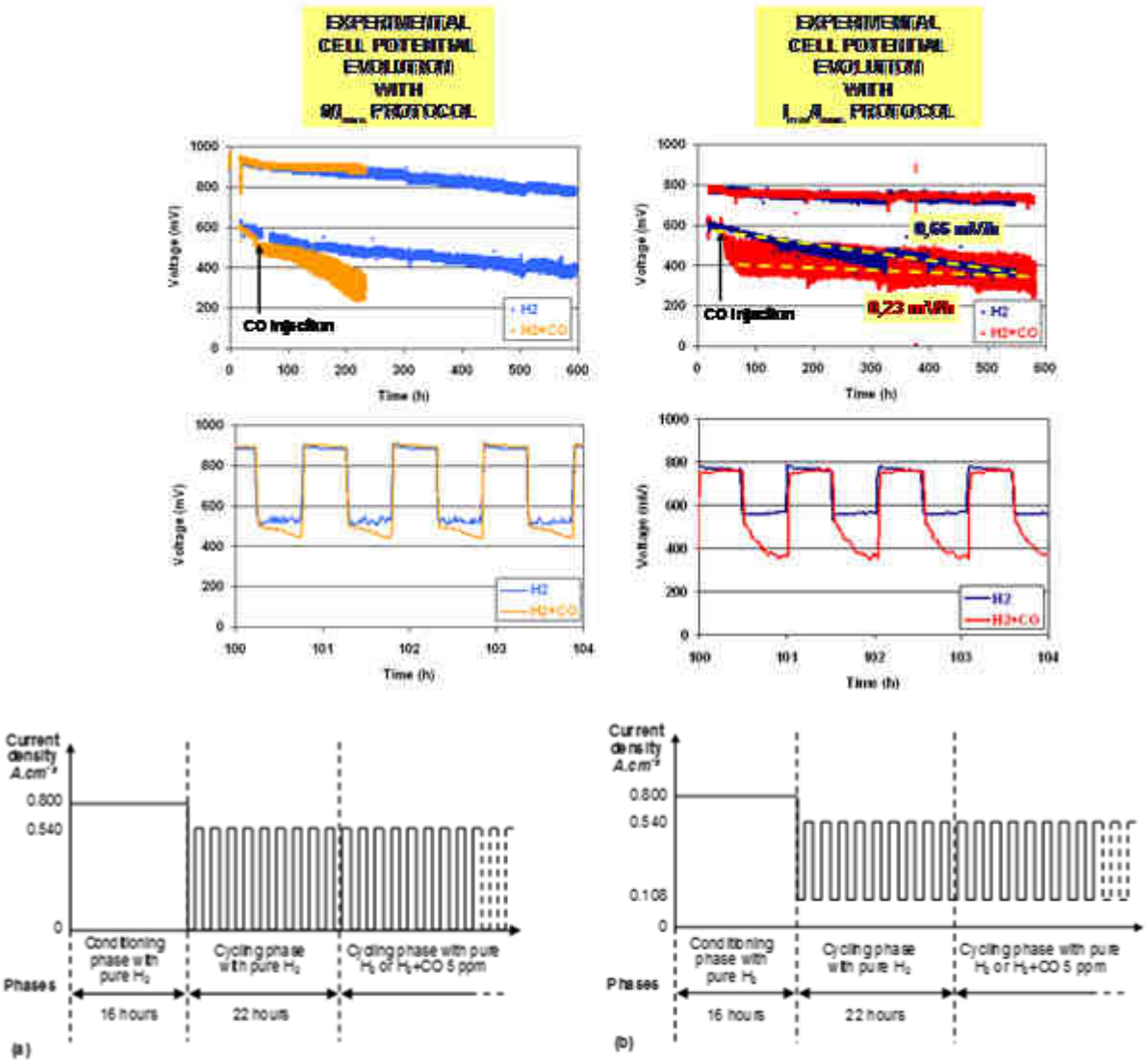

Figure IV.44: Experimental performance degradation for $0/I_{max}$ current cycle protocol under pure hydrogen and H_2+CO 5 ppm (a), experimental performance degradation for I_{min}/I_{max} current cycle protocol under pure hydrogen and H_2+CO (b) (Source: [168]).

Furthermore, in collaboration with IRCELyon (cf. Chapter I), experiments were carried out with Pt/C using DRIFT spectroscopy and mass spectrometry, to analyse the detailed interaction between the CO and the catalyst, and to analyse the gas composition in the reaction chamber, respectively.

The Pt/C catalyst was reacted with gases in the sequence of $H_2 \rightarrow CO \rightarrow O_2 \rightarrow CO \rightarrow O_2 \rightarrow CO \rightarrow O_2 \rightarrow CO \rightarrow O_2$. The IR spectra show IR bands characteristic of a-top adsorbed CO on Pt surface atoms. Pre-adsorbed species on Pt/C catalyst prior to CO adsorption were observed to be affecting the resulting CO coverage on Pt surface. The CO

coverage was higher if H_2 was pre-adsorbed than if O_2 was pre-adsorbed. The oxidation of the CO adsorbed on Pt (CO_{ad}) by O_2 was not complete, as evidenced by the existence of a weak IR band corresponding to residual CO linearly adsorbed on Pt.

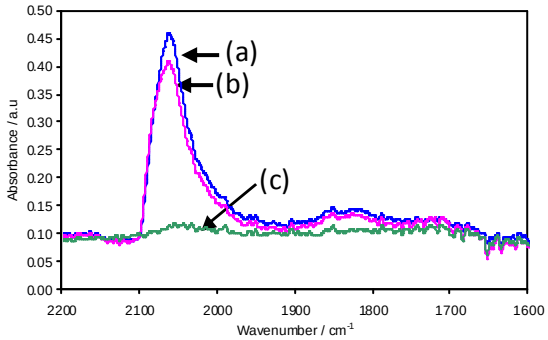

Figure IV.45: DRIFT spectra recorded after reaction of (a) CO with H_2 pre-adsorbed Pt/C catalyst, (b) CO with O_2 pre-adsorbed Pt/C catalyst, and (c) O_2 with CO pre-adsorbed Pt/C catalyst. The 2060 cm^{-1} band intensity at is proportional to the amount of a-top adsorbed CO on Pt surface (Source: [337]).

From mass spectrometry measurements, it was observed that the kinetics of CO_{ad} oxidation by O_2 gas was slow, being even significantly slower than when Pt/C was contacted with O_2 prior to CO adsorption (Figure IV.46(b)). Thus, our suggested mechanism to remove O_2 from the Pt by CO (and thus to mitigate the reverse proton pumping effect) is a performant reaction, and air bleeding, classically proposed to mitigate the CO Pt poisoning, can strongly contribute onto the cathode C corrosion as O_2 could prefer reacts through an anodic ORR (enhancing the reverse proton pumping effect), confirming our calculation results (cf. Figure IV.20b).

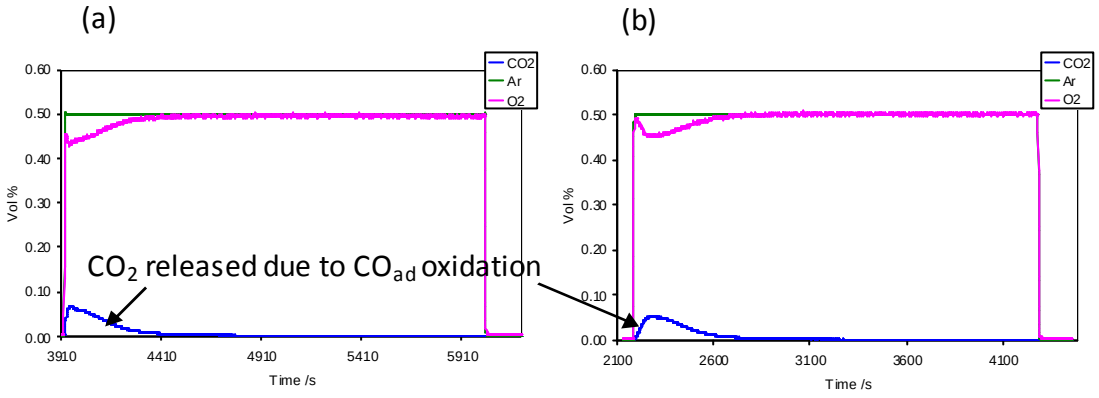

Figure IV.46: Variation of O_2 and CO_2 concentrations vs time upon reaction of adsorbed CO on Pt/C with O_2 gas; Prior to reaction with O_2 gas, Pt/C was contacted successively with (a) H_2 and CO, (b) O_2 and CO (Source: [337]).

The particle size distribution of the Pt/C catalyst was measured from TEM micrographs (Figure IV.47). The mean particle diameter was shown to slightly increase after Pt/C was reacted with the sequence of gases (H_2→ CO→ O_2→ CO→ O_2→ CO→ O_2→ CO→ O_2). This interesting result points out the necessity of use modeling to provide understanding of this phenomenon.

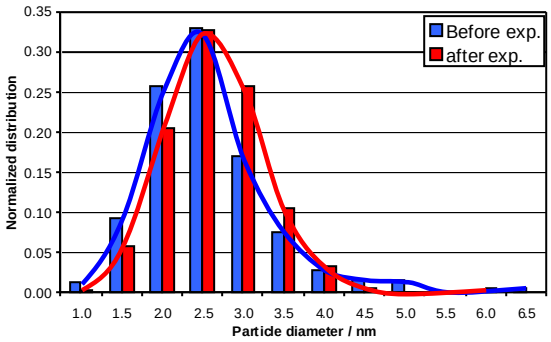

Figure IV.47: Pt/C catalyst particle size distribution before and after reaction with the sequence of gases (H_2→ CO→ O_2→ CO→ O_2→ CO→ O_2→ CO→ O_2) (Source: [337]).

From a technological perspective, in conclusion, in order to minimize the impact of the presence of CO in H_2 on PEMFC performance under I_{min}/I_{max} cycle operation, the use of CO-tolerant catalysts (e.g. Pt-Ru, Pt-Sn…) on the anode side could be envisaged. On the basis of these interesting results, this work has been extended to more complex current cycles, representative of different PEMFC applications (not discussed here). In particular, we have shown that, even if in the short-term CO strongly impacts the performance, it can improve the long-term durability of the PEMFC. This could allow the use of a less purified and thus cheaper H_2 feed in the PEMFC.

- ✓ ***Impact of CO poisoning on anode Pt_xCo_y degradation.***

Pt_xCo_y bimetallic catalyst particles have been simulated by using the annealing MC method (cf. Chapter III). It was considered that the catalyst was under CO rich environment, and under full coverage of CO. Basically it was found that the adsorption of CO does not induce any surface reconstruction phenomena as observed for the case of other bimetallic catalysts, such as PtRu.

An *ab initio*-based kinetic model that is able to describe the performance of a PEMFC anode under the influence of CO+H_2 was developed within MEMEPhys®. The results have shown that the Pt_3Co catalyst has a higher CO tolerance than the pure Pt.

The polarization curves are shown in Figure IV.48**.** Compared to pure Pt catalyst, the anode overpotential of Pt_3Co does not exhibit big increment under H_2 + CO. According to our model,

the presence of Co reduces the adsorption energy of CO on Pt sites thus the coverage of CO is also reduced. Therefore, the decrease in free sites that bring to increase of overpotential due to CO adsorption does not occur on Pt_3Co catalyst as for the case of pure Pt.

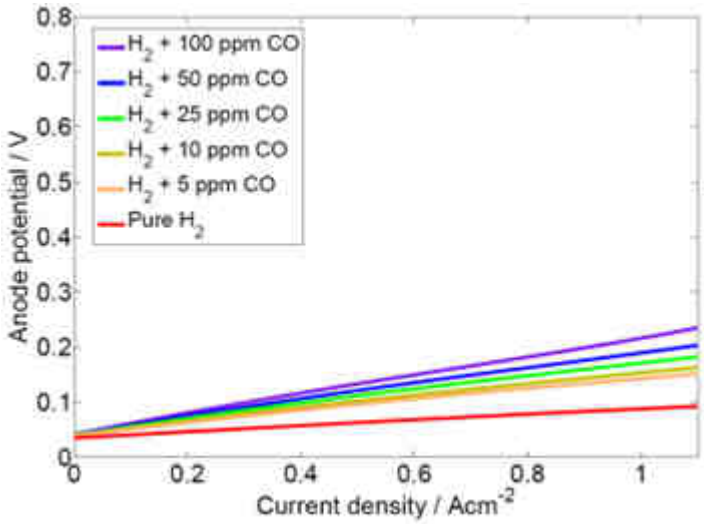

Figure IV.48: Anodic polarization curve of a half-cell loaded with pure Pt_3Co catalysts with radius of 2 nm under the influence of different CO concentrations (Source: [256]).

Performances with PtCo and Pt_3Co catalysts and H2 + 10 ppm CO under galvanostatic conditions were compared. The results in Figure IV.49 show that the anode potential for Pt_3Co is constant whereas a gradual anode potential increase is observed for the PtCo catalyst. These observations are attributed to the difference of stability between Pt_3Co and PtCo catalysts. For Pt_3Co, MC simulation shows that the particle has a Pt skin structure. Therefore, Co atoms are "protected" from dissolution into the electrolyte as a result of oxidation. In contrast to this, PtCo catalyst has surface Co atoms which can be oxidized easily. Thus, the performance of PtCo is degrading and the anode overpotential is increasing with time due to the loss of Co atoms. Although the performance of Pt_3Co is stable (Co dissolution is negligible) with particle size of 2 nm, Co dissolution could be observed when the Pt_xCo_y particle size is less than 1.5 nm (not shown here).

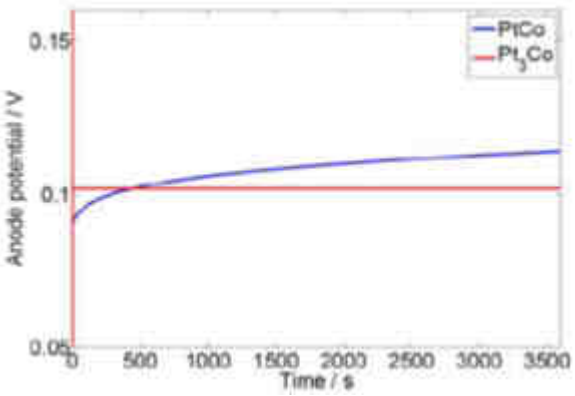

Figure IV.49: Simulated anode potential for PtCo and Pt_3Co catalysts for H_2 + 10 ppm CO under 0.5 $A.cm^{-2}$ constant current (Source: [256]).

PtCo catalysts were further investigated to understand the influence of CO concentration in H_2 on the Co dissolution. As explained before, the Co dissolution is a crucial phenomenon that increases the anode overpotential thus degrading the performance. Therefore, Co dissolution needs to be limited. As seen in Figure IV.50a, Co dissolution is lower for higher CO concentration in the short term. Nonetheless, an opposite behavior was observed for a longer duration. The amount of Co dissolved from the PtCo catalyst increases with the CO concentration as shown in Figure IV.50b. These opposite behaviors can be explained by considering the CO coverage and overpotential increase due to CO coverage. At the beginning, CO is adsorbed on the catalyst and slows down the Co dissolution. This effect is more pronounced for higher CO concentration, as the CO coverage on the catalyst is higher. Thus, Co dissolution is lower for higher CO concentration. However, the anode overpotential increases at the same time due to the higher CO coverage (as explained before in the case of pure Pt). The high anode overpotential will promote Co dissolution and this effect will become stronger than that of CO coverage after a certain time. This means that high CO concentration could promote Co dissolution in long term. Experimental tests are ongoing in my group to check this result.

To the best of our knowledge, the study of CO impact on Co dissolution kinetics has never been reported in the literature before.

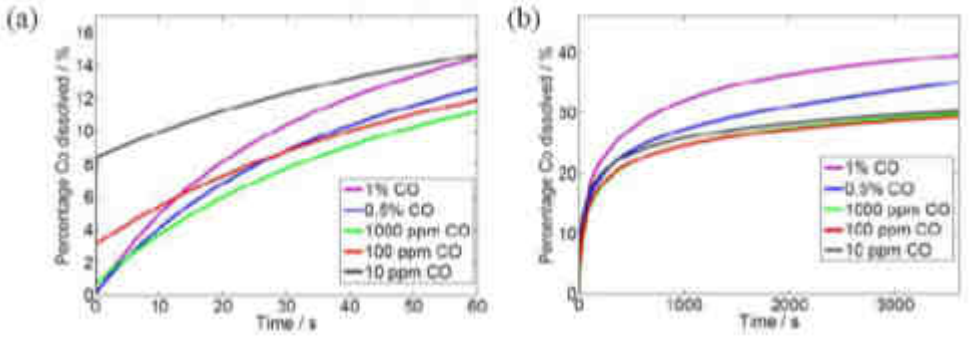

Figure IV.50: Percentage of Co dissolved from PtCo catalyst versus operation time with H_2 + CO mixtures, under 0.5 A.cm^{-2} constant current. (a) Calculation results for the first 60 s; (b) calculation results for the long run (Source: [256]).

IV.9 – Conclusions

Because of the high complexity of the PEMFC MEA in terms of structural properties and of the strong coupling between different physicochemical phenomena, interpretation of experimental observations is difficult, and analysis through mathematical modeling becomes crucial in order to establish nano/microstructure-performance relationships, to elucidate MEA degradation and failure mechanisms, and to help improve both PEMFC electrochemical performance and durability.

For industry application of such a modeling, the approach should be flexible and easily adaptable: a single modeling tool to address a diversity of problems is strongly necessary to get fast results instead of redeveloping one code for each particular problem.

In this Chapter I have illustrated through some application examples my research team efforts to develop MEMEPhys®. The main goals are to study electrochemical, hysteresis and aging phenomena in PEMFC MEA and to predict MEA nanomaterials durability as a function of several operation conditions.

Among the examples I presented in this Chapter, we can underline: 1) the study of the ORR evolution and CO-contaminated HOR on Pt_xCo_y aging nanoparticles (prediction of durability as function of the composition) and other exotic materials (metallofullerenes, Pt-free catalysts), 2) the identification of synergies between the PEM, cathode C and Pt degradation, 3) the analysis of the contribution of each degradation mechanism on the global cell performance reversible and irreversible decay, 4) the impact of contaminants on the transient response of the cell potential, 5) the use of anodic CO contamination as a mitigation method of cathode C degradation and PEM aging (a modeling prediction experimentally validated, and triggering several patents applications).

CHAPTER V

Conclusions and perspectives

"Programs must be written for people to read, and only incidentally for machines to execute"

Abelson & Sussman, Structure and Interpretation of Computer Programs

PEMFCs have attracted much attention due to their potential as a clean power source for many applications: traction of vehicles by the replacement of the thermal generators, portable applications (cellular phones, laptop computers…) and the production of stationary electricity. This resulted on a tremendous technological progress, such as the development of new membranes and electro-catalysts or the improvement of electrode structures. However, in order to compete within the most attractive markets, the PEMFC technologies did not reach all the required characteristics yet, in particular cost and durability.

My research efforts aim to contribute in developing deep insights on PEMFC physical electrochemistry and aging phenomena thanks to a strong combination of targeted experiments with multi-scale theoretical modeling.

On the basis of a diversity of collaborations with teams within CEA, France, Europe, NorthAmerica, SouthAmerica and Asia, the main objective of our research work is to develop a modeling approach addressing MEA electrocatalysis and degradation providing

- ✓ understanding of different electrochemical and aging mechanisms and their interplaying at the material, component, MEAs and cell levels
- ✓ a physical-based interpretation tool of experimental observables (i-V characteristics, EIS…)
- ✓ a physical-based tool useful for PEMFCs design through the determination of nanostructure-activity-durability relationships for the MEA materials
- ✓ a physical-based tool predictive of MEAs durability under realistic automotive operating conditions
- ✓ recommendation of operating protocols mitigating degradation of MEA for automotive applications
- ✓ recommendation of ADT representative of long-term PEMFC operation

Within this sense, I developed with my team a new transient multi-scale mechanistic model of the detail PEMFC MEA electro-catalysis, based on a non-equilibrium thermodynamics approach (MEMEPhys® model). The approach couples meso/micro-scale transport descriptions of reactants, charges and water within the cell with a spatially distributed model of the nano-scale electrochemical catalyst/electrolyte interface in presence of non-equilibrium electro-catalytic processes. These processes are described on the basis of an elementary kinetic approach built on atomistic and surface science data, without using empirical Butler-Volmer equations. Furthermore, on a physical basis, the model describes the feedback between the instantaneous performance and the intrinsic material aging processes. It provides new insights on the interplaying between the different aging phenomena (catalyst oxidation/dissolution/electrochemical ripening, dissolved catalyst movement within the MEA, PEM degradation, C-support corrosion, catalyst poisoning by external pollutants…) and analyses the MEA response sensitivity to operating conditions, initial catalyst/C/ionomer loadings and temporal evolution of the electro-catalytic activity. The MEA durability can be thus predicted in *in situ* PEMFC conditions.

MEMEPhys® is nowadays a reference PEMFC model at CEA as it has been successfully applied to address the impact of materials degradation processes on performance decay and to conclude that the coupling between several degradation and/or contamination mechanisms does not necessarily has a more negative impact that each degradation or contamination mechanism impact taken individually. This is explained because of the development of positive synergies. In this manuscript I illustrated that through several examples, one of them that could have important implications for the hydrogen production industry, such as the use of an anodic CO contamination to mitigate cathode C corrosion and PEM degradation.

Furthermore, understanding the morphology and properties of the PEMFC and its components on the atomic scale is indispensable in order to gain insights into the macroscopic behavior, such as its performance and durability. While pure *ab initio* calculations are usually restricted to quite idealized model systems, with the proposed work we gain significant new insights in the structure and properties of the electrode/electrolyte-interface, one of the linkages in a PEMFC, where our present knowledge is still rudimentary. Thus, the impact of the materials structural properties on the electrochemistry is revealed, through for example our studies on the impact of Nafion® re-organization on the C corrosion kinetics or the Pt_xCo_y nano-particles degradation.

With my group, we are now planning to continue exploring possible synergies between degradation mechanisms (Figure V.1) and developing MEMEPhys® by improving the description of the structural representation of the CLs, PEM and GDLs. The powerful multi-scale capabilities of the numerical solver open exciting perspectives to integrate detailed kinetics and further structural-resolved data. Moreover, we are now working in the "on-the-fly" coupling between PNM and MEMEPhys® to simulate water transport, detailed electrochemistry and degradation phenomena in realistic 3D CL structures. Further experimental validation of some points (e.g. CO induced Pt_xCo_y dissolution) is ongoing and other ones (e.g. detailed *ex situ* catalysis study of NO_2/Pt interaction reactions) are planned.

Further development of the model is still necessary to include descriptions of other realistic phenomena such as mechanical stresses and non isothermal operating conditions. Moreover, analytical approximations are certainly of interest within the perspective of implementing this kind of models in PEMFC stacks and systems, and this is also something that we are starting to look closer (see my first collaborative work in this sense in [338] and in Appendix IV).

I am also planning to extend MEMEPhys® to Li-Ion batteries and other electrochemical systems (see Appendix II). All this work will be done through different projects (some of them as main coordinator), collaborations and by advising students.
Generally speaking, my short-term career perspective consists now in continue coordinating the LCPEM Modeling activities, contributing to develop a scientific framework ensuring a high quality scientific production, rigor and a high reactivity towards the projects and hierarchy requirements. Furthermore, I would like to continue my scientific collaborations all around the world (including Argentina, my country) and developing new ones with both academics and industrials. I want to continue being very active into the field of multi-scale modeling of electrochemical systems and nano-sciences (publications, patents), and into international committees of expertise (journals review and books edition conferences organizations…). I will continue trying to contribute into the international recognition of our laboratories in the field of PEMFC electro-catalysis and degradation.

I have been enjoying a marvelous experience in our efforts to understand more deeply the workings of the electrochemistry. I hope to continue the learning, for that will automatically continue the enjoyment…

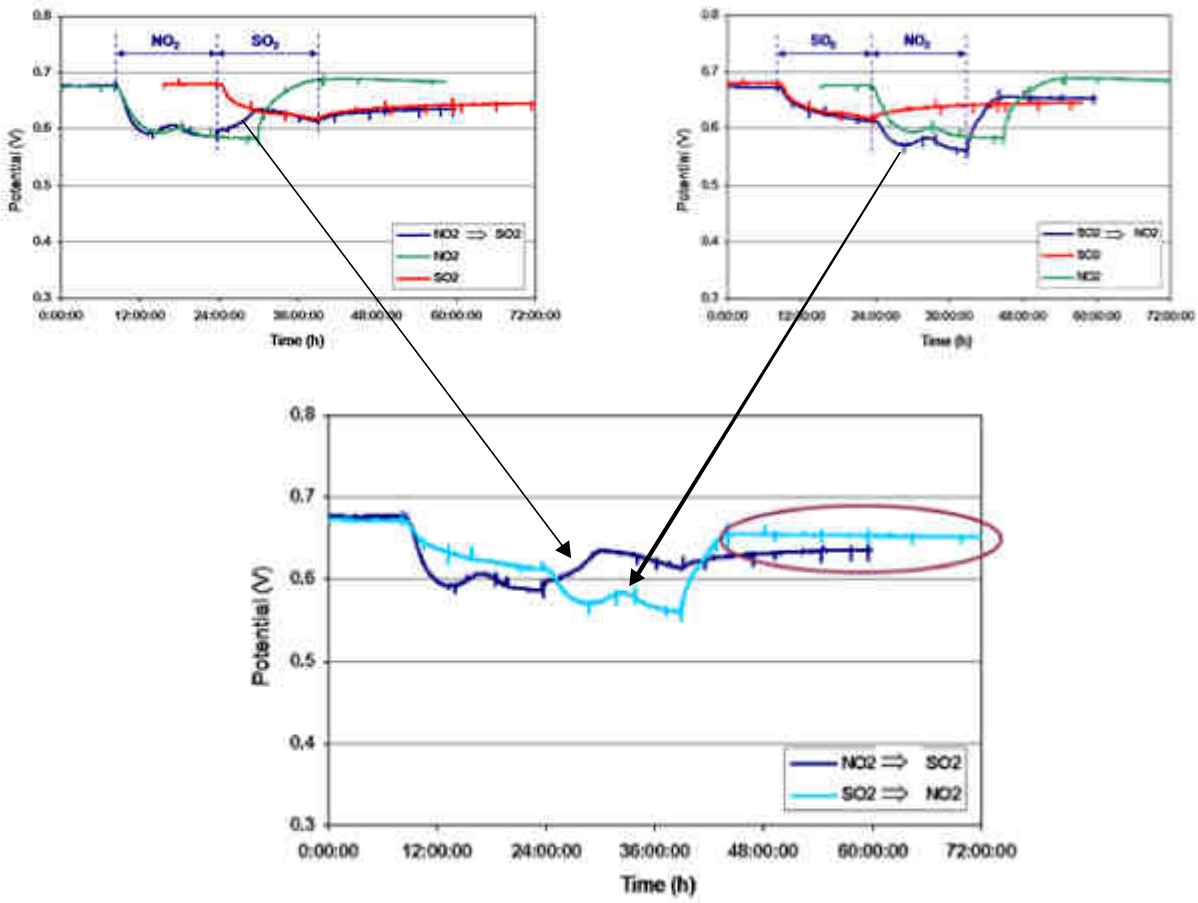

Figure V.1: An *"Avant Première"* of the incoming intriguing issues within my research…(e.g. impact of the NO_2/SO_2 injection sequence on the cathode potential evolution (Source: [339]).

Appendix I

My detailed Curriculum Vitae

CURRICULUM VITAE

(as in July 2010)

Dr. Alejandro A. Franco

"Theoretical physics from fuel cells

to other electrochemical devices"

Personal information

Date of birth: December 10, 1977

Place of birth: Bahia Blanca, Argentina

Marital status: Single

Citizenship: Argentinean-Italian

EDUCATION

2009-2010 - HDR diploma in preparation (authorization for HDR registration obtained in July 2009 after examination of the Scientific Committee of the Université Claude Bernard Lyon-1, Ecole Doctorale de Chimie, Procédés et Environment).

2003-2005 - PhD in Automatics (*Physical Chemistry*), Université Claude Bernard Lyon-1.

- Qualification: *excellent with congratulations of the jury*.
- Place of work: CEA-Grenoble/LITEN

- Advisors: Prof. Bernhard Maschke, Prof. Christian Jallut (CNRS/LAGEP UMR 5007)
- Theme of the thesis: Development of a novel theoretical framework for the multi-scale modeling of electrochemical processes in Polymer Electrolyte Membrane Fuel Cells (PEMFC).

1997-2001 - M.Sc. in Theoretical Physics (*Licenciatura en Fisica*, *equivalent to "BAC+5" in France*), Department of Physics, *Universidad Nacional del Sur* (Bahia Blanca, Argentina) and *Instituto Balseiro, Comision Nacional de Energia Atomica* (Bariloche, Argentina)

- Graduated with honour diploma, over-all grade average: **9.68/10** (award to the best average in Physics career)
- Specialities: non-equilibrium thermodynamics, electrodynamics, solid-state physics and quantum mechanics.

1991-1996 - High School studies in the *Escuela de Ciclo Basico* and *Escuela Normal Superior* (E.N.S.) (Bahia Blanca, Argentina)

- Graduated with honour diploma, over-all grade average: **9.98/10** (diploma equivalent to the *"BAC-S"* in France).

SCIENTIFIC EMPLOYMENT

2005-present - Member of the permanent research staff of the CEA/LCPEM.

- *Research interests:* electro-catalysis, physical electrochemistry, irreversible thermodynamics, non-linear dynamics phenomena, quantum mechanics, solid-state physics, nano-materials, multi-scale modeling and theory of modern fuel cells.

- From May 2009, *responsible of the Electrochem. Systems Modeling Group* at the CEA/LITEN/DEHT/LCPEM, by decision of the head of my laboratory. I have in charge the management of the scientific computing resources for our laboratory, and the coordination of all our modeling activities, being carried out by 4 permanents and 15 non permanents (11 PhD students, 3 postdocs and 1 Msc. Student). Within this context, I am in charge of organizing a scientific prospective of our ongoing actions, to improve our scientific production and reactivity towards the projects requirements, through mensual meetings and seminars where each member present the progress on his work or address general topics in the field of fuel cells modeling. I am also in charge of following that the scientific production is in agreement with the LITEN Quality rules (intellectual property protection of software developed, user/developer manuals of in-house software, copy-protected storage of simulation results…).

- *Working-Package Leader in several on-going French and European projects including:*

  - CATHYMINHY (ANR "PAN-H", 2008-2012) (where I am modeling Working Package -WP- leader): development of new MEA elaboration processes for PEMFC.
  - POLIMPAC (ANR "PAN-H", 2007-2010) (modeling WP leader): identification and analysis of the impact of external pollutants (from atmospheric air, fuel reforming, distribution network…) on the electrochemical performance of a Pt-based PEMFC.
  - OPTICAT (ANR "PAN-H", 2007-2010) (modeling WP leader): development of novel multi-metallic catalysts in order to reduce catalyst layer Pt loading.
  - DVD-AME (ANR "PAN-H", 2006-2008) (contributor): characterization of the state-of-art MEA aging, through studies performed with PEFC operating under power-cycled conditions representative of automotive applications.
  - DECODE (EU PCRD 7, 2008-2011) (modeling WP leader): study of the impact of the water management on PEMFC aging.
  - ARCAPAC (ADEME, 2008-2012) (modeling WP leader): bottom-up design of PEFC electrodes with improved performance and durability (capped Pt nano-particles systems).
  - AL NANO (King Saud University-CEA, 2009-2011) (modeling WP leader): nanostructured materials for PEMFC.
  - PREMIUM ACT (EU PCRD 7, starting by the end 2010, duration: 3 years) (modeling WP leader): modeling-based predictive methodology of PEMFC and DMFC durability.
  - MMM@HPC (EU PCRD 7, starting by the end 2010, duration: 3 years) (modeling WP leader): multi-scale modeling of Li-Ion batteries.

- *Several on-going scientific collaborations including:*

  - Nissan Motor Co.: modeling the impact of ionomer structural properties on the ORR reactivity in PEMFC electrodes (Mr. Tetsuya Mashio, Dr. Atsushi Ohma)
  - National Research Council of Canada-Institute for Fuel Cell Innovation: micro-structural resolved modeling of PEMFC MEA (Dr. Koroush Malek)
  - Stanford University: multi-scale modeling methods for fuel cells (Prof. Heinz Pitsch's group, Department of Mechanical Engineering)
  - Massachusetts Institute of Technology (MIT): steric ionic effects in electrochemical interfaces (Prof. Martin Bazant, Department of Mathematics)
  - DLR-Stuttgart: modeling of detailed electrochemistry (Dr. Wolfgang Bessler)
  - ENS Lyon: *ab initio* modeling of electrocatalytic phenomena (Prof. Philippe Sautet, Dr. David Loffreda)
  - IRCE-Lyon: catalysis, surface science experiments (Prof. Patrick Gelin)
  - CNRS/LAGEP: non equilibrium thermodynamics, chemical engineering, infinite dimensional Bond Graphs applied to PEMFC and PEM-WE modeling (Prof. Christian Jallut, Prof. Bernhard Maschke)
  - Université de Montpellier: modeling of Li-ion batteries (Prof. Marie Liesse Doublet)
  - CEA-Grenoble/INAC: quantum chemistry, HPC (Dr. Thierry Deutsch, Dr. Pascale Maldivi, Dr. Valentina Vetere)

- CEA-Grenoble/LETI/Département microTechnologies pour la Biologie et la Santé : modeling of electrochemical processes inside the humain brain (Parkinson's disease) (Dr. Pascale Pham)
- CEA-Grenoble/DSV: understanding the electrochemical behavior of Pt-free bio-inspired materials for H_2 production (Dr. Vincent Artero).

➢ Member of the CEA "Nano-catalysis" working group

➢ Advisor of several PhD, MSc. students and post-doctoral researchers (see list of collaborators, Chapter I)

➢ Regular participant as speaker in the CEA-Grenoble scholar scientific programs « La Recherche fait école » and « Fête de la Science ».

2003-2005 – PhD thesis in Theoretical Physical Chemistry at CEA-Grenoble/LITEN.

2002- One-year-period visiting scientist at the CEA-Grenoble/LITEN

➢ Research on micro-anionic-polymer electrolyte fuel cells for portable applications:
- Development and characterisation of novel **anionic** polymeric electrolytes and fabrication of electrodes; electrochemical characterization.
- Conceptual modeling of transport and electrochemical phenomena in the core of the anionic micro-fuel cell.
- Conception and development of a magnetized electrode for the paramagnetic pumping of oxygen in a micro-fuel cell cathode (patent filled in December 4th 2002, number FR 2848341 A1 20040611 (French) WO 200454018 A1 20040624 (French)).

1998-2001 - Assistant teacher at the Department of Physics, Universidad Nacional del Sur (Bahia Blanca Argentina)

➢ Animation of theoretical lectures and supervision of exercise sessions with groups of 20-70 students in the field of General Physics, Classical Mechanics, Electromagnetism, Thermodynamics and Quantum Mechanics, for students in Physics, in Electrical Engineering, in Biology and in Pharmacology.

1997-2001 – Several research activities during the MSc. preparation within the field of non linear dynamics (classical mechanics), electrodynamics and superconductivity (with 2 internal publications within the *Comision Nacional de Energia Atomica*, Bariloche, Argentina).

SOME ADVISED STUDENTS AND POST-DOCs AT CEA

(See complete list in Chapter I)

- Postdoctoral researchers

  - **(Oct 08-Mar10)** Dr. Margaret A. Gabriel. Subject: Multi-scale Modeling of the ORR Electrocatalytic Properties of Metallofullerenes as Cathodic Materials for PEMFC and PEM-WE. Our research in this topic generated 3 patents, 2 presentations in international conferences (MODVAL and ECS Meeting) and 3 publications in first class international journals (*PCCP*, *ECS Trans.*).
  - **(Jan 09-Feb10)** Dr. Ali Kachmar. Subject: Multi-scale Modeling of the HER Electrocatalytic Properties of Ni-N-based Bio-inspired Molecules as Cathodic Materials for Photosensitive Electrolyzers. Our research in this topic generated 1 patent, 2 presentations in international conferences (ECS Meeting) and 3 publications in first class international journals (*J.Phys.Chem.C, J.Electrochem. Soc., ECS Trans.*).

- PhD students

  - **(Oct 09-Sep12)** Luiz Fernando Oliveira Lopes. Subject: Multi-scale Modeling of Physicochemical Phenomena in PEM-WE.
  - **(Oct 09-Sep12)** Sylvain Passot. Subject: Understanding the Impact of Pollutants Mixtures on the Electrochemical Performance and Durability of PEMFC: a Experimental and Modeling Approach.
  - **(Sep 09-Aug12)** Daiane Damasceno Borges. Subject: Multi-scale Modeling of the Ionic Transport Properties of Nafion® in the PEMFC Electrodes.
  - **(Feb09-Jan12)** Romain Coulon. Subject: Multi-scale Modeling of the Nafion® Membrane Degradation under PEMFC Automotive Operating Conditions. Up to now our reseach in this PhD thesis generated 4 presentations in international conferences (MODVAL and ECS Meetings) and 3 publications in first class international journals (*J. Electrochem. Soc.*, *ECS Trans.*).
  - **(Nov08-Oct11)** Seng-Kian Cheah. Subject: Investigation of H_2 pollutants impact on PEFC nanomaterials performance and degradation. Up to now our research in this PhD thesis generated 4 presentations in international conferences (ECS Meetings) and 3 publications in first class international journals (*J. Electrochem. Soc.*, *ECS Trans.*).
  - **(Oct08-Sep11)** Rodrigo Ferreira de Morais. Subject: *Ab initio*-based kinetic modeling of the HOR and ORR reactivity properties of Pt_xNi_y nanoparticules for PEMFC applications. Up to now our research in this PhD thesis generated 5 presentations in international conferences (ECS Meetings) and 4 publications in first class international journals (*J. Electrochem. Soc.*, *ECS Trans.*).
  - **(Oct08-Sep11)** Guillaume Krosnicki (co-supervised with Dr. O. Lemaire, CEA/LITEN/LCPEM). Subject: Development and Electrochemical Characterization of Fullerene-based Nanomaterials as Electrocatalysts in PEMFC and PEM Electrolyzers. Up to now our research in this PhD thesis

generated 3 patents and 2 publications in first class international journals (*J. Phys. Chem.*).

- **(Oct07-Sep10)** Mathias Gerard (advice for his modeling work). Subject: PEMFC Degradation under Oxygen Starvated Conditions: Interaction with the Management System.
- **(Apr08-Dec08)** Federico Nores Pondal -CNEA Centro Atomico Constituyentes, Argentina-. Subject: Development, Electrochemical Characterization and Modeling of Magnetic Cathodes for the Enhancement of the ORR Activity in PEFC.

➢ Stages

- **(Jun09-Jun10)** Randa Bouchmila, Chemical Engineering student (3rd year) at CPE Lyon: *année de césure école d'ingénieur* at CEA/LCPEM. Subject: Multi-scale Modeling of the ORR activity properties and Degradation Phenomena of Nanosctructured MultiMetallic Nanoparticles for PEMFC applications. Up to now our research in this *stage* generated 2 patents and 1 presentation in international conferences (ECS Meeting).
- **(Sep07-Aug08)** Sylvain Passot, Chemical Engineering student (3rd year) at CPE Lyon: *année de césure école d'ingénieur* at CEA/LCPEM. Subject: Multi-scale Modeling of Pt_xCo_y Electrocatalysts Degradation in Transient PEMFC Operating Conditions. Our research in this *stage* generated 7 presentations in international conferences (MODVAL, International Society of Electrochemistry Meetings, International Society of Theoretical Chemical Physics, ECS Meetings) and 3 publications in first class international journals (*J. Electrochem. Soc.*, *ECS Trans.*)
- **(Mar08-Aug08)** Magalie Guinard, MSc. (MR2). Subject: Multi-scale Modeling of PEFC Anode CO Poisoning: Impact on Electrochemical Performance and Durability. Our research in this *stage* generated 1 patent, 8 presentations in international conferences (MODVAL, International Society of Electrochemistry Meetings, International Society of Theoretical Chemical Physics, ECS Meetings) and 2 publications in first class international journals (*Electrochim. Acta*, *ECS Trans.*)
- **(Mar07-Sep07)** Mathias Gerard, MSc. (MR2). Subject: Multi-scale Modeling of Carbon Catalyst-Support Corrosion in PEFC Environments. Our research in this *stage* generated 1 patent, 6 presentations in international conferences (MODVAL, International Society of Electrochemistry Meetings, International Society of Theoretical Chemical Physics, ECS Meetings) and 2 publications in first class international journals (*J. Electrochem. Soc.*, *ECS Trans.*)
- **(Apr06-Aug06)** Laurent Brochard, student at Ecole Polytechnique (3rd year): *stage en entreprise* at CEA/LCPEM. Subject: Multi-scale Modeling of Transfers in PEFC.
- **(Mar06-Sep06)** Moussa Tembely, MSc. (MR2). Subject: Multi-scale Modeling of Pt-Catalyst Degradation in PEFC Environments. Our research in this *stage* generated 4 presentations in international conferences (MODVAL, International Society of Electrochemistry Meetings, International Society of Theoretical Chemical Physics, ECS Meetings) and 2 publications in first class international journals (*J. Electrochem. Soc.*, *ECS Trans.*).

AWARDS

2005 – **Awarded by the International Society for Solid State Ionics** (ISSI): finalist for the ISSI Young Scientist Award

2002 – **Gold medal** from the Bahia Blanca (Buenos Aires province) government (**best higher education award of 1997-2001 period** - University over-all grade average: **9.68/10**)

1995 – **Award** from the "International Rotary Club" (best "Young Scientist 1995", Bahia Blanca, Argentina).

1991-1996 – **Several Argentinean awards** in the "Olympiads of Mathematics and Sciences" (secondary school).

INTERNATIONAL CONFERENCES AND MEETINGS ORGANIZED

- Organizer of the incoming International Symposium on Fuel Cell Modeling and Experimental Validation in the 62st Annual Meeting of the International Society of Electrochemistry (Niigata, September 11 – 16, 2011).
- Corresponding (Main) Organizer of the incoming International Symposium on Fuel Cell Modeling and Experimental Validation in the 61st Annual Meeting of the International Society of Electrochemistry (Nice, September 26 – October 1, 2010).
- I co-chaired the International Symposium on Fuel Cell Modeling and Experimental Validation –Karlsruhe, Germany, 2009-.
- I have been part of the Scientific Advisory Committee and co-chaired the international conference on energy nanomaterials Nanoenergy 2008 -Paris, France, 2008-.
- Co-chairperson of the International Workshop on "High Temperature Fuel Cells and Degradation Mechanisms", CARISMA European Network, Grenoble, July 5-6, 2007.

.

MEMBERSHIPS

- American Electrochemical Society (ECS) Active Member
- International Society of Electrochemistry (ISE) Active Member
- Member of the *Société Française de Physique*

OTHER EXPERT ACTIVITIES

- Member of the project evaluation committee of the ANR P-NANO program.
- Member of the reviewers staff in several international journals of electrochemistry. Up to present I reviewed 104 papers submitted for publication in the following journals: "*Solid State Ionics*", "*Fuel Cells: from fundamentals to systems*", "*Electrochimica Acta*", "*Journal of the Electrochemical Society", "Journal of Solid State Electrochemistry", "International Journal of Hydrogen Energy", "Mathematical and Computer Modeling od Dynamical Systems", "Industrial & Engineering Chemistry Research", "Journal of the American Chemical Society (JACS)" and "Journal of Power Sources".*

INVITED SCIENTIST RESEARCH VISITS

Invited visiting scientist at

- National Research Council, Institute for Fuel Cell Innovation (Vancouver, Canada), May 1st-31, 2010.
- Stanford University, Department of Mechanical Engineering (California, US), Prof. Heinz Pitsch's group, November 8-13, 2007. Stanford University - Palo Alto USA.
- Heidelberg University (Interdisciplinary Center for Scientific Computing), Heidelberg, November 6-12, 2006.
- Universidad Politecnica de Catalunya (UPC), Barcelona (Spain), January 3-12, 2006.

PhD THESIS

[1] A.A. Franco, " A physical multi-scale model of the electrochemical dynamics in a polymer electrolyte fuel cell – An infinite dimensional Bond Graph approach"; PhD Thesis Université Claude Bernard Lyon-1 (France) no. 2005LYO10239 (2005) http://tel.archives-ouvertes.fr/tel-00110968/en/.

BOOKS AND BOOK CHAPTERS

[1] A.A. Franco, **invited editor**, book title: *Polymer Electrolyte Fuel Cells: Science, Applications and Challenges* (publisher: Pan Stanford-Imperial College, London), to appear

in October 2010. Field: PEFC nanomaterials and degradation with confirmed contributions of several internationally recognized researchers (e.g. Sarah Ball -Johnson Matthey Co., UK-, Debbie Myers -Argonne National Lab, USA-, Tetsuya Mashio -Nissan Co., Japan-, Kourosh Malek –National Research Council, Canada-, Victor Hacker -Gratz University, Austria-, Nicolas Fouquet -PCA Peugeot Citroên, France-…).

Outline of the book:

INTRODUCTION/PROLOGUE – PEMFC generalities, operation principles, application domains, presentation of the book outline.

CHAPTER I: PEMFC technologies for automotive applications – Dr. Nicolas Fouquet (Peugeot Citroën SA, France). History of PEMFC application in cars, how a PEMFC works into a real automotive system, hybridation with batteries, requirements in terms of cost-performance-durability, challenges…from an automotive industrial point of view.

CHAPTER II: "Control strategies at the system level to mitigate performance degradation of PEMFC – Prof. Jordi Riera, Dr. Maria Serra and Dr. Attila Husar (Universitat de Barcelona, Spain). System-level control strategies to enhance PEMFC performance and durability.

CHAPTER III: "PEMFC MEA elaboration methods" – Pascal Fugier, Dr. Etienne Quesnel and Dr. Sebastien Donet (CEA-LITEN, France) Review on MEA elaboration methods with standard materials.

CHAPTER IV: "Ex situ electrochemical characterization methods of PEMFC nanomaterials degradation"- Dr. Deborah Myers and Dr. Xiaoping Wang (Argonne National Laboratory, USA). Review on available ex-situ electrochemical tools –e.g. RRDE, half-cells, electrochemical FTIR, electrochemical AFM…- useful for analysis of nanomaterials degradation.

CHAPTER V: "Microstructural characterization approaches of PEMFC nanomaterials" - Dr. Zhong Xie (NRC-IFCI, Canada). Review on HR-TEM, XPS, 3D-imagenery of nanoparticles…useful for psotmortem analysis.

CHAPTER VI: "Instability of nanocatalysts in PEMFC environments: a state of the art" - Dr. Sarah Ball (Johnson Matthey, UK). Review on experimental knowledge on catalysts degradation mechanisms.

CHAPTER VII: "Catalysts supports for PEMFC applications: performance and stability issues" - Prof. Ernesto R. Gonzalez (Instituto de Quimica de Sao Carlos, Brazil). Critical review on catalysts supports: CB, CNT, TiO2…, impact on catalyst electronic structure, support stability and degradation mechanisms.

CHAPTER VIII: "Membrane degradation mechanisms in PEMFC" - Prof. Tom Fuller and Dr. Panos Trogadas (Georgia Institute of Technology, USA). Review on knowledge on membrane degradation mechanisms, experimental approaches.

CHAPTER IX: "Gas Diffusion Layers in Polymer Electrolyte Fuel Cells: structural, transport and stability properties" – Prof. Jon Pharoah (Queen's-RMC Fuel Cell Research Centre, Canada). Review on GDL, transport and stability properties.

CHAPTER X: "Effects of Fuel and Air Impurities on PEMFC electrodes performance" - Dr. Zheng Shi (NRC-IFCI, Canada). PEMFC anode and cathode contaminants. Impact of performance and durability, ex-situ and single cell tests, electrochemical characterization, challenges.

CHAPTER XI: "In-situ characterization methods of PEMFC materials degradation, synergies between degradation mechanisms" – Viktor Hacker (University of Gratz, Austria). State of the art of experimental studies of the materials degradation in in-situ conditions, synergies between degradation mechanisms, synergies between materials degradation and reactants contamination.

CHAPTER XII: PEMFC modeling 1: from the atomistic to the structural-resolved approches. Dr. Tetsuya Mashio (Nissan Motor Co., Japan) and Dr. Kourosh Malek (NRC-IFCI, Canada). Atomistic modeling tools to assess degradation phenomena, prediction of activity/selectivity/stability properties of nanocatalysts and supports, prediction of electrodes and membranes microstructures and transport properties.

CHAPTER XIII: PEMFC modeling 2: from the structure-resolved to the multi-scale kinetic approches – Dr. Alejandro A. Franco (CEA-LITEN, France). Continuum modeling tools to assess degradation phenomena, prediction of observables from elementary kinetic approaches, modeling at the cell and system level, multi-scale techniques, prediction of performance and durability.

CHAPTER XIV: Design of shape and nanostructure-controlled catalyst nanoparticles for PEMFC applications - Prof. Jose Solla-Gullon, Dr. F. J. Vidal-Iglesias, Dr. E. Herrero, Prof. J. M. Feliu and Prof. A. Aldaz (University of Alicante, Spain). Synthesis methods of shape and nanostructure-controlled catalysts with improved activity and stability, structural and electrochemical characterizations, single-cell tests.

CONCLUSIONS – Conclusions and further work, open questions, challenges.

[2] A.A. Franco, **book chapter** on multi-scale modeling of PEMFC materials degradation, Book title: *Polymer Electrolyte Fuel Cells: Science, Applications and Challenges* (publisher: Pan Stanford-Imperial College, London, UK), to appear in October 2010.

[3] A.A. Franco, **book chapter** PEMFC degradation modeling and analysis, Book title: Polymer electrolyte membrane and direct methanol fuel cell technology (PEMFCs and DMFCs) - Volume 1: Fundamentals and performance, edited by Dr Christoph Hartnig and Dr-Ing. Christina Roth (publisher: Woodhead, Cambridge, UK). This Chapter will be delivered in summer 2010.

[4] A.A. Franco, **book chapter** Modeling of Direct Alcohol Fuel Cells, Book title: *Direct Alcohol Fuel Cells Technologies: research and development*, being edited by Prof. Ernesto Gonzalez (Instituto de Quimica de Sao Carlos, Brazil) and Prof. Horacio Corti (CNEA, Argentina), to be published in Springer. The Chapter will be delivered in spring 2011.

PATENTS

[1] 9 other patents being filled in 2010 (5 as first author)

[2] V. Vetere, **A.A. Franco (co-author)**, A. Kachmar, P. Maldivi, « Méthode pour augmenter l'activité catalytique des molécules bio-inspirées à base de phosphore et d'azote pour application électrolyte de l'eau et pile à combustible », FR patent (2010).

[3] R. Vincent, S. Escribano, **A.A. Franco (co-author)**, « Méthode pour diminuer les dégradations réversibles et irréversibles des cathodes dans les assemblages membrane-électrodes des piles à combustible à membrane échangeuse de protons », FR patent (2010).

[4] A.A. Franco (first author), O. Lemaire G. Krosnicki, « Méthode pour augmenter la durabilité des supports catalytiques carbonés dans les assemblages membrane-électrodes des piles à combustible à membrane échangeuse de protons », FR patent (2009).

[5] A.A. Franco (first author), O. Lemaire G. Krosnicki, « Méthode pour augmenter la performance électrochimique des assemblages membrane-électrodes des piles à combustible à membrane échangeuse de protons à base de metallofullenes », FR patent (2009).

[6] O. Lemaire, **A.A. Franco (co-author)**, B. Barthe, N. Bardi, « Stratégie de fonctionnement pour limiter l'impact du SO_2 sur la performance électrochimique de la cathode d'une pile à combustible à membrane échangeuse de protons », FR patent (2009).

[7] A.A. Franco (first author), O. Lemaire, « Méthode en fonctionnement reversible pour limiter le vieillisement des assemblages membrane-électrodes des piles à combustible à membrane échangeuse de protons », FR patent (2009).

[8] O. Lemaire, **A.A. Franco (co-author)**, N. Guillet, « Capteur de CO par auto-oscillations de potentiel dans une électrode anodique », FR patent (2008).

[9] A.A. Franco (first author), O. Lemaire, S. Escribano, « Méthode pour limiter le vieillissement par corrosion du support catalytique carbone à la cathode des piles à combustible à membrane échangeuse de protons », FR patent (2008).

[10] A.A. Franco (first author), C. Nayoze, C. Roux, D. Marsacq; « Pile à Combustible comportant une Cathode Magnétique à Pompage Statique », FR patent (2002).

[11] A.A. Franco (first author), "Small-scale electric power generator with looped hydrogen electrochemistry", AR patent (1992).

INVITED SEMINARS IN FOREIGN UNIVERSITIES AND INSTITUTES

[1] A.A. Franco, *"Elementary kinetics concepts in PEMFCs: multi-scale-multi-physics for the MEA activity, selectivity and durability enhancement"*, **invited seminar** given at the NRC-IFCI, Vancouver (BC, Canada), May 17, 2010.

[2] A.A. Franco, *"Multi-scale degradation processes in PEM Fuel Cells: towards a mechanistic predictive tool of the MEA durability"*, **invited seminar** given at the University of Santa Barbara California (CA, USA), July 16, 2009

[3] A.A. Franco, *"Dissolution of multimetallic nanoparticles: which mechanism for which impact on PEM Fuel Cells performance degradation?"*, **invited seminar** given at the Stanford University (Department of Mechanical Engineering) (CA, USA), May 28, 2009.

[4] A. A. Franco, *"Multi-scale modeling of degradation mechanisms in PEFC"*, **invited seminar** given at the NRC-IFCI, Vancouver (BC, Canada), July 25, 2008

[5] A.A. Franco, *"Transient Multi-scale Modeling of Coupled Ageing Mechanisms in PEFC"*; **invited lecture** given at the Stanford University, Department of Mechanical Engineering (CA, USA), November 12, 2007.

[6] A.A. Franco, *"A multi-scale non-equilibrium theory of interfacial electrochemical processes"*, **invited lecture** given at the Heidelberg University (Interdisciplinary Center for Scientific Computing), Heidelberg (Germany), December 6, 2006.

[7] A.A. Franco, *"Modelo dinámico mecanístico multi-escala para el análisis de transientes de PEMFC"*, **invited seminar** given at the Universidad de Buenos Aires (Chemistry Department), Buenos Aires (Argentina), August 22, 2006.

[8] A.A. Franco, *"Physical Electrochemistry for Fuel Cells Innovation"*, **invited lecture** given at the Universidad Politecnica de Catalunya (UPC), Barcelona (Spain), January 5, 2006.

INVITED ORAL PRESENTATIONS IN INTERNATIONAL CONFERENCES

[1] A.A. Franco, *"The role of condensed matter physics in Fuel Cells technology"*, **invited plenary lecture** at the 12th Journées de la Matière Condensée, Société Française de Physique (Troyes, France), August 23-25, 2010.

[2] A.A. Franco, *"Multi-scale modeling of nano-materials aging mechanisms in PEMFCs"*, **invited lecture** at the 10th International Conference of Electrified Interfaces (ICEI), (Geneva, New York, USA), June 20-25, 2010.

[3] A.A. Franco, *"A Multi-scale modeling methodology for the description of electrochemical processes in Fuel Cells: from theory to the engineering practice"*, **invited plenary lecture** at the French and American Young Engineering Scientists Symposium (YESS NANO 09), Soleil Synchroton (L'Orme des Merisiers, France), November 15-18, 2009.

[4] A.A. Franco**,** *"Multi-scale modeling-based prediction of PEM Fuel Cells MEA durability under automotive operating conditions"*, **invited oral presentation** at the 216th Meeting of the American Electrochemical Society (ECS), Vienna (Austria), October 4-9, 2009.

[5] A.A. Franco, *"Multi-scale degradation processes in PEM Fuel Cells: towards a mechanistic predictive tool of the MEA durability"*, **invited plenary lecture** at the *International Workshop of Modeling of Electrocalysis in Fuel Cells*, University of Santa Barbara California (Santa Barbara, USA), July 12-16, 2009.

[6] A.A. Franco, *"Multi-scale modeling of coupled nanomaterials degradation mechanisms in PEM Fuel Cells"*, **invited oral presentation** at the 215th Meeting of the American Electrochemical Society (ECS), San Francisco (CA, USA), May 24-29, 2009.

[7] A.A. Franco, *"Physical-based modeling of PEM fuel cells degradation – Part I: Physicochemical concepts for the durability prediction of Pt_xM_y nanostructured catalysts"*, **invited oral presentation** at the 6th Symposium on Fuel Cell Modeling and Experimental Validation (MODVAL 6), Karlsruhe (Germany), March 25-26, 2009.

[8] A.A. Franco, O. Lemaire, *"Physical-based modeling of PEM Fuel Cells Degradation – Part II: Using anode CO contamination as a mitigation method of cathode carbon corrosion and PEM aging"*, **invited oral presentation** at the 6th Symposium on Fuel Cell Modeling and Experimental Validation (MODVAL 6), Karlsruhe (Germany), March 25-26, 2009.

[9] A.A. Franco, *"On the instability of nanostructured catalysts in PEFC environments: new mechanistic insights"*, **invited plenary lecture** at the International Conference "Nano-Energy 2008", Paris (France), October 21-23, 2008.

[10] A.A. Franco, *"Materials degradation mechanisms in PEFC"*, **invited lecture** at the International Workshop on Accelerated Testing in Fuel Cells, Ulm (Germany), October 6-7, 2008.

[11] A. A. Franco, *"Degradation issues in PEFC: new insights from a multi-scale mechanistic viewpoint"*, **invited oral presentation** at the 59th Annual Meeting of the International Society of Electrochemistry (ISE), Seville (Spain), September 7-12, 2008.

[12] A.A. Franco, *"Multi-scale modeling of coupled degradation mechanisms in PEFC environments: theoretical insights and experimental validation"*, **invited oral presentation** at the Conference of the International Society for Theoretical Chemical Physics, Vancouver (Canada), July 19-24, 2008.

[13] A. A. Franco, *"A non-equilibrium thermodynamics viewpoint of degradation phenomena in fuel cells"*, **invited oral presentation** at the 5th Symposium on Fuel Cell Modeling and Experimental Validation (MODVAL 5), Winterthur (Switzerland), March 11-12, 2008. (organized by the Institute of Computational Physics -ICP-, Winterthur).

[14] A.A. Franco; *"Transient Multi-scale Modeling of Coupled Aging Mechanisms in PEFC - A theoretical tool for experimental interpretation and advanced MEA design"*, **invited lecture** at the 3rd Annual conference "Performance and Durability 2007", American Knowledge Foundation & Department of Energy (DOE), Miami (Florida, USA), November 15-16, 2007.

[15] A.A. Franco, *"Aging mechanisms in Polymer Electrolyte Fuel Cells: when electrode design meets theory: the CEA-Grenoble approach"*, **invited plenary lecture** at the HYFUSEN 2007 Conference (Iberoamerican Conference on Hydrogen and Fuel Cells Technologies), organized by the CNEA (Argentinean Nuclear Commission), Posadas (Argentina), June 12-15, 2007.

[16] A. A. Franco, *"Transient multi-scale modeling of aging mechanisms in a Polymer Electrolyte Fuel Cell: an irreversible thermodynamics approach"*, **invited oral presentation** at the 216th Meeting of the American Electrochemical Society (ECS), Chicago (IL, USA), May 6-11, 2007.

[17] A.A. Franco, *"Modelo dinámico mecanístico multi-escala para el análisis de transientes de PEMFC"*, **invited lecture** at the II JIPCH Conference (Iberoamerican Conference on Hydrogen and Fuel Cells Technologies), organized by the Iberoamerican network of Hydrogen Technologies and the CNEA (Argentinean Nuclear Commission), Buenos Aires (Argentina), July 24-26, 2006.

[18] A.A. Franco, "*A multi-scale physical model of Polymer Electrolyte Fuel Cells: an infinite-dimensional Bond Graph approach"*, **invited oral presentation (Young Scientist Award Final Ceremony)** at the Solid State Ionics Conference, Baden-Baden (Germany), July 17-22, 2005.

OTHER PRESENTATIONS IN INTERNATIONAL CONFERENCES

[1] A.A. Franco, S. Escribano, R. Vincent, L. Guetaz, *"Resolving the role of water transport on the competitive degradation mechanisms in a PEMFC MEA: a modeling approach"*, **oral presentation** at the 61st Annual Meeting of the International Society of Electrochemistry (ISE), Nice, September 26-October 1st, 2010.

[2] A.A. Franco, K. Malek, *"Degradation mechanisms in PEMFC: new insights from a mesostructural resolved kinetic modeling approach"*, **oral presentation** at the 217th Meeting of the American Electrochemical Society (ECS), Vancouver, April 25-30, 2010.

[3] A.A. Franco, S.-K. Cheah, O. Lemaire, *"Hysteresis phenomena in PEM Fuel Cells materials degradation: a multi-scale modelling viewpoint"*, **oral presentation** at the 217th Meeting of the American Electrochemical Society (ECS), Vancouver, April 25-30, 2010.

[4] A.A. Franco, O. Lemaire, *"Competitions and synergies between electrochemical aging mechanisms in PEM Fuel Cells"*, **oral presentation** at the 217th Meeting of the American Electrochemical Society (ECS), Vancouver, April 25-30, 2010.

[5] A.A. Franco, *"Nanostructured electrocatalysts degradation in PEM Fuel Cells: key role of the electrochemical interface in engineering practice"*, **oral presentation** at the 216th Meeting of the American Electrochemical Society (ECS), Vienna, October 4-9, 2009.

[6] A.A. Franco, B. Barthe, O. Lemaire, *"Mechanistic Investigations of NO_2 Impact on ORR in PEM Fuel Cells: A Coupled Experimental and Multi-scale Modeling Approach"*, **oral presentation** at the 216th Meeting of the American Electrochemical Society (ECS), Vienna, October 4-9, 2009.

[7] R. Coulon, W. Bessler, A.A. Franco, *"Modeling chemical degradation of a polymer electrolyte membrane and its impact on fuel cell performance"*, **oral presentation** at the 216th Meeting of the American Electrochemical Society (ECS), Vienna, October 4-9, 2009.

[8] M.A. Gabriel, T. Deutsch, A.A. Franco, *"Fullerene-Based Materials as Catalysts for Fuel Cells"*, **oral presentation** at the 216th Meeting of the American Electrochemical Society (ECS), Vienna, October 4-9, 2009.

[9] A. Kachmar, V. Vetere, P. Maldivi, V. Artero, A.A. Franco, *"Bio-Inspired Materials for H2 Production and Oxidation: Multi-scale Mechanistic Modeling of the Electrocatalytic Processes on $[Ni(PNP)_2]^{2+}$ Complexes"*, **oral presentation** at the 216th Meeting of the American Electrochemical Society (ECS), Vienna, October 4-9, 2009.

[10] A.A. Franco, B. Barthe, O. Lemaire, *"Using anode CO contamination as a mitigation method of cathode carbon corrosion in PEMFC"*, **oral presentation** at the 215th Meeting of the American Electrochemical Society (ECS), San Francisco, May 24-29, 2009.

[11] A.A. Franco, S. Escribano, O. Lemaire, *"Polymer electrolyte membrane degradation in fuel cells environments : interplaying with Pt and C nanomaterials aging mechanisms – A mutliscale modeling viewpoint"*, **oral presentation** at the 215th Meeting of the American Electrochemical Society (ECS), San Francisco, May 24-29, 2009.

[12] A.A. Franco, S.K. Cheah, R. Ferreira de Morais, *"Non-equilibrium Interfacial Electrochemical Phenomena in Aging PEM Fuel Cells: A New Theory for Multi-scale Simulation of Nano-structured Catalysts Degradation and Durability Prediction"*, **oral presentation** at the 215th Meeting of the American Electrochemical Society (ECS), San Francisco, May 24-29, 2009.

[13] M.A. Gabriel, T. Deutsch, A.A. Franco, *"Modeling of electro-catalytic phenomena in fullerene-based nano-objects for PEFC applications"*, **oral presentation** at the 6th Symposium on Fuel Cell Modeling and Experimental Validation (MODVAL 6), Karlsruhe, March 25-26, 2009.

[14] P. Fugier, A. A. Franco, S. Passot, E. Billy, S. Mailley, L. Guetaz, N. Guillet, *"Pt_xCo_y catalysts for PEFC applications: new understanding on the impact of particles nano-structure on performance degradation"*, **oral presentation** at the Fundamentals and Developments of Fuel Cells Conference, Nancy (France), December 10-12, 2008.

[15] A. A. Franco, S. Passot, N. Guillet, L. Guetaz, B. Barthe, M. Guinard, M. Gerard, O. Lemaire, *"Synergies between ageing mechanisms in PEFC environments: new insights from a multi-scale/multi-physics modeling investigation and experimental validation"*, **oral presentation** at the Fundamentals and Developments of Fuel Cells Conference, Nancy (France), December 10-12, 2008.

[16] A.A. Franco, *"Synergies Between Ageing Mechanisms in PEFC Environments: New Insights from a Multi-Scale/Multi-Physics Modeling Viewpoint"*, **oral presentation** at the 2nd EuChems Chemistry Congress, Torino (Italy), September 16-20, 2008.

[17] A. A. Franco, S. Passot, E. Billy, S. Mailley, L. Guetaz, N. Guillet, P. Fugier, *"Degradation of nano-structured Pt_xCo_y catalysts in PEFC: new insights from a multi-scale modeling approach"*, **oral presentation** at the 59th Annual Meeting of the International Society of Electrochemistry (ISE), Seville (Spain), September 7-12, 2008.

[18] A. A. Franco, S. Passot, M. Guinard, M. Gerard, *"Coupling of ageing mechanisms in PEFC environments: new insights from a multi-scale modeling investigation"*, **oral presentation** at the 59th Annual Meeting of the International Society of Electrochemistry (ISE), Seville (Spain), September 7-12, 2008.

[19] O. Lemaire, A. A. Franco, M. Guinard, B. Barthe, N. Guillet, *"PEFC anode long-term CO contamination impact on intrinsic catalyst and C-support ageing mechanisms: new advances on durability understanding"*, **oral presentation** at the 59th Annual Meeting of the International Society of Electrochemistry (ISE), Seville (Spain), September 7-12, 2008.

[20] A.A. Franco, *"Solid state physics in Fuel Cells Electrochemistry: theory and experiments"*, **oral presentation** at the V France-Spain Conference on Solid State Physicochemistry, Clermont-Ferrand (France), April 2-4, 2008.

[21] A. A. Franco, S. Passot, P. Fugier, *"Transient multi-scale modeling of Pt_xCo_y catalysts degradation in PEFC environments"*, **oral presentation** at the 213th Electrochemical Society Meeting, Phoenix (AZ, USA), May 18-23, 2008.

[22] A. A. Franco, M. Gerard, *"Transient model of carbon catalyst-support corrosion in a PEFC: multi-scale coupling with Pt electro-catalysis and impact on performance*

degradation", **oral presentation** at the 213th Electrochemical Society Meeting, Phoenix (AZ, USA), May 18-23, 2008.

[23] A.A. Franco, *"Coupled aging mechanisms in PEFC: a theoretical multi-scale viewpoint"*, **oral presentation** at the CARISMA European Network Workshop: High Temperature Fuel Cells, and ageing mechanisms, Grenoble July 5-6, 2007.

[24] A.A. Franco, "*Modeling the behavior of nano-structured electro-catalysis in PEFC environments: looking for activity/stability relationships"*, **oral presentation** at the CARISMA European Network Workshop: "Catalysts for PEFC applications", oral comm., Paris, May 16 2007.

[25] A.A. Franco, C. Jallut, B.M. Maschke, *"A multi-scale Bond graph model of the electrochemical dynamics in a Polymer Electrolyte Fuel Cell"*, **oral presentation** at the 17th International Symposium on Mathematical Theory of Networks and Systems (MTNS), Kyoto (Japan), July 24-28, 2006.

[26] A. A. Franco, M. Tembely, P. Schott, Christian Jallut, Bernhard Maschke*, "A Multi-Scale Dynamic Mechanistic Model for Transient Analysis of PEFCs"*, **oral presentation** in the World Hydrogen Energy Conference 16, Lyon (France), June 13-16, 2006.

[27] A. A. Franco, P. Schott, C. Jallut, and B. Maschke, *"A multi-scale Bond Graph model of physico-chemical phenomena in a fuel cell"*; **oral presentation** at the *5th MATHMOD Conference*, Vienna (Austria), February 7-10, 2006.

[28] A.A. Franco, P.Schott, C. Jallut, B. Maschke; "*A Multi-scale Dynamic Mechanistic Model for Transient Analysis of Volumetric Electrodes*", **poster presentation** at the Solid State Ionics Conference, Baden-Baden (Germany), July 17-22, 2005.

[29] A.A. Franco, P. Schott, C. Jallut, B. M. Maschke, *"A multi-scale dynamic mechanistic model for transient analysis of PEFC"*; **oral presentation** at the *3rd European Fuel Cells Forum*, Luzern (Switzerland), July 4–8, 2005.

[30] A.A. Franco, P. Schott, C. Jallut, B.M. Maschke, *"A multi-scale dynamic mechanistic model for transient analysis of electrochemical cells"*; **oral presentation** at the 207th Meeting of the Electrochemical Society, Québec (Canada), May 15-20, 2005.

[31] A. A. Franco, P. Schott, C. Jallut, B. Maschke; "*A multi-scale dynamical model of a PEFC electrode"*; **oral presentation** at the *JDMACS Conference*, Lyon (France), September 5-9, 2005.

[32] A.A. Franco, P. Schott, C. Jallut et B. Maschke; "*Modeling an Electrochemical Interface Dynamics using the Displacement Current and a Dynamic Dipolar Layer"*, **poster presentation**, Computational Electrochemistry Workshop, Santorini (Greece), September 26-29, 2004.

[33] A.A. Franco, P. Schott, C. Jallut, B. Maschke; "*Modeling an Electrochemical Interface Dynamics using the Displacement Current and a Time Varying Dipolar Density"*, **poster presentation**, 10th International Conference on Electrified Interfaces, Spa (Belgium), July 11-16, 2004.

→ Several other presentations and seminars in France (CEA, CNRS, GDR meetings, *Société Française de Chimie*…) (2003-2009).

PUBLICATIONS IN INTERNATIONAL JOURNALS

(in italic, the name of my supervised students and postdoctoral researchers).

[1] Alejandro A. Franco, *Sylvain Passot*, *Seng Kian Cheah*, Olivier Lemaire, Christel Faure, *Chem. Rev.*, *"PEM Fuel Cells contamination: mechanisms and challenges from experiments and physical modeling"*, submitted (2010).

[2] Max P. Eschenbach, *Romain Coulon*, **Alejandro A. Franco**, Joseph Kallo and Wolfgang G. Bessler, *"Multi-scale simulation of fuel cells: from the cell to the system"*, *Solid State Ion.* (2010), doi:10.1016/j.ssi.2010.06.041

[3] *Margaret A. Gabriel*, Thierry Deustch, Luigi Genovese, *Guillaume Krosnicki*, Olivier Lemaire and **Alejandro A. Franco**, *"Metallofullerenes as fuel cell electrocatalysts: a theoretical investigation of adsorbates on $C_{59}Pt$"*, *Phys. Chem. Chem. Phys.* (2010), doi: 10.1039/b927111b

[4] *Margaret A. Gabriel*, Thierry Deustch and **Alejandro A. Franco**, *"Fullerene-based Materials as Catalysts for Fuel Cells"*, *ECS Trans.*, **25** (22) (2010) 1.

[5] *Ali Kachmar*, Valentina Vetere, Pascale Maldivi and **Alejandro A. Franco**, *"Bio-inspired materials for H_2 production: multi-scale mechanistic modeling of the underlying electrocatalytic processes"*, *J. Phys. Chem. C*, submitted (2010).

[6] Valérie Parry, Jean-Charles Joud, Olivier Lemaire and **Alejandro A. Franco**, *"XPS investigation of the PEMFC active layers aging: characterization of the mitigating role of an anodic CO contamination on cathode degradation"*, *J. Power Sources*, submitted (2010).

[7] Kourosh Malek and **Alejandro A. Franco**, *"Microstructral-based Modeling of Aging Mechanisms in Catalyst Layers of Polymer Electrolyte Fuel Cells"*, *J. Phys. Chem. C*, in preparation (2010).

[8] Alejandro A. Franco and Wolfgang Bessler, *"Are fuel cells deterministic?"*, *Fuel Cells*, submitted (2010).

[9] *Romain Coulon*, Wolfgang Bessler and **Alejandro A. Franco**, *"Modeling chemical degradation of a Polymer Electrolyte Membrane and its impact on Fuel Cell performance"*, *ECS Trans.*, **25** (35) (2010) 259.

[10] *Seng-Kian Cheah*, Olivier Lemaire, Patrich Gélin and **Alejandro A. Franco**, *"CO Induced Reconstruction of Pt_xCo_y Electrocatalytic Nanoparticles in a PEM Fuel Cell Anode under transportation Operating Conditions"*, *ECS Trans.*, **25** (35) (2010) 275.

[11] *Rodrigo Ferreira de Morais*, David Loffreda, Philippe Sautet and **Alejandro A. Franco**, *"Towards a Multi-scale Modeling Methodology for the Prediction of the Electro-activity of PEM Fuel Cell Catalysts"*, *ECS Trans.*, **25** (24) (2010) 167.

[12] **Alejandro A. Franco**, *Sylvain Passot*, Pascal Fugier, *Emmanuel Billy*, Nicolas Guillet, Laure Guetaz, Eric De Vito and Sophie Mailley, *"Pt_xCo_y catalysts degradation in PEFC environments: Mechanistic insights – Part II: MOCVD elaboration and electrochemical characterization"*, *J. Electrochem. Soc.,* **157** (6) (2010) B943.

[13] **Alejandro A. Franco**, *Sylvain Passot*, Pascal Fugier, *Emmanuel Billy*, Nicolas Guillet, Laure Guetaz, Eric De Vito and Sophie Mailley, *"Pt_xCo_y catalysts degradation in PEFC environments: Mechanistic insights – Part I: Multi-scale modeling"*, *J. Electrochem. Soc.,* **156** (2009) B410.

[14] **Alejandro A. Franco**, *Romain Coulon*, *Rodrigo Ferreira de Morais*, *Seng Kian Cheah*, *Ali Kachmar* and *Margaret A. Gabriel*, *"Multi-scale modeling-based prediction of PEM Fuel Cells MEA durability under automotive operating conditions"*, *ECS Trans.*, **25** (1) (2009) 65.

[15] **Alejandro A. Franco**, Benoît Barthe, Ludovic Rouillon and Olivier Lemaire, *"Mechanistic investigations of NO_2 impact on ORR in PEM Fuel Cells: a coupled experimental and multi-scale modeling approach"*, *ECS Trans.*, **25** (1) (2009) 1595.

[16] **Alejandro A. Franco**, *Romain Coulon*, Sylvie Escribano and Olivier Lemaire, *"Polymer Electrolyte Membrane degradation in Fuel Cells environments: interplaying with Pt and C nanomaterials aging mechanisms - A multi-scale modeling viewpoint"*, *ECS Trans.*, accepted (2009).

[17] **Alejandro A. Franco**, *Seng Kian Cheah* and *Rodrigo Ferreira de Morais*, *"Non-equilibrium interfacial electrochemical phenomena in aging PEM Fuel Cells: a new theory for multi-scale simulation of nano-structured catalysts degradation and durability prediction"*, *ECS Trans.*, accepted (2009).

[18] **Alejandro A. Franco**, *Magalie Guinard*, Benoît Barthe, Olivier Lemaire, *"Impact of carbon monoxide on PEFC catalyst carbon support degradation under current-cycled operating conditions"*, *Electrochim. Acta*, **54** (22) (2009) 5267.

[19] P. Maarten Biesheuvel, **Alejandro A. Franco** and Martin Z. Bazant, *"Diffuse charge effects in Fuel Cell membranes"*, *J. Electrochem. Soc.,* **156** (2) (2009) B225.

[20] **Alejandro A. Franco**, *Sylvain Passot*, Pascal Fugier, *Emmanuel Billy*, Nicolas Guillet, Laure Guetaz, Eric De Vito and Sophie Mailley, *"Transient multi-scale modeling of Pt_xCo_y catalysts degradation in PEFC environments"*, *ECS Trans.*, **13** (17) (2008) 29.

[21] **Alejandro A. Franco**, Benoît Barthe, *Mathias Gerard*, *Magalie Guinard* and Olivier Lemaire, *"Carbon catalyst-support corrosion in Polymer Electrolyte Fuel Cells: mechanistic insights"*, *ECS Trans.*, **13** (15) (2008) 35.

[22] Alejandro A. Franco and *Mathias Gerard*, *"Transient model of carbon catalyst-support corrosion in a PEFC: multi-scale coupling with electro-catalysis and impact on performance degradation"*, *J. Electrochem. Soc.*, **155** (4) (2008) B367.

[23] Alejandro A. Franco, *"Transient multi-scale modeling of aging mechanisms in a Polymer Electrolyte Fuel Cell: an irreversible thermodynamics approach"*, *ECS Trans.*, **6** (10) (2007) 1.

[24] Alejandro A. Franco and *Moussa Tembely*, *"Transient multi-scale model of aging mechanisms in a PEFC cathode"*, *J. Electrochem. Soc.*, **154** (7) (2007) B712.

[25] Alejandro A. Franco and *Mathias Gerard*, *"Transient Multi-scale Modeling of coupled aging mechanisms in PEFC – A theoretical tool for experimental interpretation and advanced MEA design"*, In *Proc. 3rd Fuel Cells Durability and Performance Conference*, Miami, USA (2007).

[26] Alejandro A. Franco, *Moussa Tembely* and *Mathias Gerard*, *"Aging mechanisms in Polymer Electrolyte Fuel Cells: when electrode design meets theory"*, in *Proc. HYFUSEN Conference*, organized by CNEA and the *Iberoamerican Society of Hydrogen and Fuel Cells*, Posadas, Argentina (2007) 10.

[27] Alejandro A. Franco, Pascal Schott, Christian Jallut and Bernhard Maschke, *"A multi-scale dynamic mechanistic model for transient analysis of PEFC"*, *Fuel Cells*, **7** (2007) 99.

[28] Alejandro A. Franco, Christian Jallut and Bernhard Maschke, *"A multi-scale Bond Graph model of the PEFC physicochemistry"*, *MCDMS*, accepted (2007).

[29] Alejandro A. Franco, Christian Jallut and Bernhard Maschke, *"Multi-scale Bond Graph Model of the Electrochemical Dynamics in a Fuel Cell"*, in *Proc. 5th MATHMOD Conference*, (Eds. I Troch and F. Breitenecker), Vienna, Austria (2006) P103.

[30] Alejandro A. Franco and *Moussa Tembely*, *"Modelo mecanistico multi-escala para el analisis de transientes de PEMFC"*, in *Proc. of the 2nd Iberoamerican Conference on Hydrogen and Fuel Cells*, Buenos Aires, Argentina (2006) 1.

[31] Alejandro A. Franco, *Moussa Tembely*, Christian Jallut and Bernhard Maschke, *"A Multi-scale Dynamic Mechanistic Model for Transient Analysis of PEFCs"*, in *Proc. World Hydrogen Conference* (WHEC) 16, Lyon, France (2006) 572.

[32] Alejandro A. Franco, Pascal Schott, C. Jallut, B. Maschke, *"A dynamic mechanistic model of an electrochemical interface"*, *J. Electrochem. Soc.*, **153** (6) (2006) A1053.

[33] Alejandro A. Franco, Pascal Schott, C. Jallut, B. Maschke, *"Un modèle multiéchelle dynamique d'une électrode volumique de PEFC"*, *revue e-STA* **2** (3) (2005), http://www.see.asso.fr/esta/index-suite.php.

[34] Alejandro A. Franco, Pascal Schott, C. Jallut and B. Maschke, *"A Multi-scale Dynamic Mechanistic Model for Transient Analysis of PEFCs"*, in *Proc. 3rd European PEFC Forum*, (Ed. C. Hebling) Lucerne, Switzerland (2005) B063.

[35] Alejandro A. Franco, *"Using chaotic Lorenz' waterwheels as electricity generators", Coleccion de articulos de los estudiantes del Instituto Balseiro,* CNEA, San Carlos de Bariloche, Argentina (1999).

[36] Alejandro A. Franco, *"Inversed mechanical pendulum: new relationships between chaotic regimes and periodic frictions", Coleccion de articulos de los estudiantes del Instituto Balseiro ,* CNEA, San Carlos de Bariloche, Argentina (1999).

LANGUAGES AND INFORMATICS SKILLS

- Languages:

- Spanish: mother tongue.
- French: fluent (I live in France since January 2002).
- English: fluent (read, written and spoken).
- Italian: scholar
- Portuguish: scholar

- Informatics: Windows and Linux ; experimental electrochemistry acquisition software (Coreware®, ZPlot®, VoltaMaster® …); software of command/control RSView32® ; software of scientific computing COMSOL Multiphysics®, FLUENT®, Matlab-Simulink®, 20-Sim®, Mathematica®, VASP, ADF, GROMACS, generic Monte Carlo and Kinetic Monte Carlo software, Hyperchem®, Materials Studio®, C, C++, Fortran.

MISCELLANEOUS

- Sports: Football, tennis, trekking.

- Leisure: Piano, chess game, reading (particularly about astrophysics and cosmology).

References available upon request

Appendix II

Application to other electrochemical systems

The multi-scale modeling approach behind MEMEPhys®, combining *ab initio*-based elementary kinetics with transport phenomena at different scales and materials degradation, can be easily adapted to other electrochemical systems such as Direct Methanol Fuel Cells (DMFC), SOFC, PEM-WE, Li-ion batteries, electrodeposition experiments and biological systems. In the following some examples of ongoing actions in my group within this context are discussed.

- ✓ ***PEM-WE***

A highly promising method of hydrogen production is the PEM-based electrolysis of water which offers a number of advantages for the electrolytic production of hydrogen and oxygen in comparison with conventional wateralkali electrolysers. PEM-WEs enjoy ecological cleanness, much smaller mass and overall dimensions, high degree of gas purity (more than 99.99% for hydrogen), the possibility of producing compressed gases (up to 200 bars and more) for direct pressurized storage without additional power inputs and at higher safety levels.

However, this technology is in the early stages of research on materials development. There are substantial technical challenges related to efficiency, cost (IrO_2, RuO_2 and Pt-based catalysts are currently used to split water into H_2 and O_2) and lifetime. The last point is one of the main shortcomings towards the large-scale development and commercialization of this technology. Like in PEMFCs, the microstructural properties of the electrodes evolve during the electrolysis processes limiting the PEM-WE lifetime. Another problem is the stability of the currently used membrane materials towards high pressure operation.

Again, analysis through physical modeling becomes crucial to elucidate the underlying physicochemical mechanisms. However, as the best of our knowledge, any physicochemical

model allowing predicting the PEM-WE performance and durability as function of its operation conditions and MEA composition/structure (catalyst loading, micro-porosities…) has been reported in the scientific literature.

As PEM-WEs are, structurally and phenomenologically speaking, similar to PEMFCs, the objective of my ongoing work is to adapt our transient multi-scale mechanistic model MEMEPhys®, to describe in a detailed way the physicochemical phenomena occurring in the CLs and PEM of the PEM-WE. This approach, developed within a storng interaction with the CEA/LCPEM experimental team, will provide deeper insights on the competitions and synergies between electrochemical processes that are crucial to optimize the MEA properties as well as to suggest operating conditions to enhance their performance and durability:

This new model, called SyhPEMEM® by us, is still supported on a multi-scale framework describing the link between atomistic-dominated (surface nanoelectrochemistry) and micro-scale-dominated (produced H_2, O_2 transfers) processes. The approach includes first principles-based descriptions of the elementary H_2O splitting reaction steps (Hydrogen Evolution Reaction -HER- and Oxygen Evolution Reaction -OER-) on the catalysts (e.g. IrO_2, RuO_2 for the anode, and Pt for the cathode), and catalyst oxidation/dissolution, cathode carbon corrosion and membrane degradation will be implemented soon. One of the theoretical challenges within this work is to describe the electrochemical double layer effects under biphasic regimes (at high currents, H_2 and O_2 bubbles can form) which can require implementing modeling methods such as Kinetic MC.

The model already allows predicting, in good agreement with experimental results, the PEM-WE behavior as function of the operation mode (power-cycled, stationary operations) and the CL structural (e.g. porosity) and compositional (catalyst/ionomer loadings) parameters.

A paper with a first version of this PEM-WE model is in preparation [340].

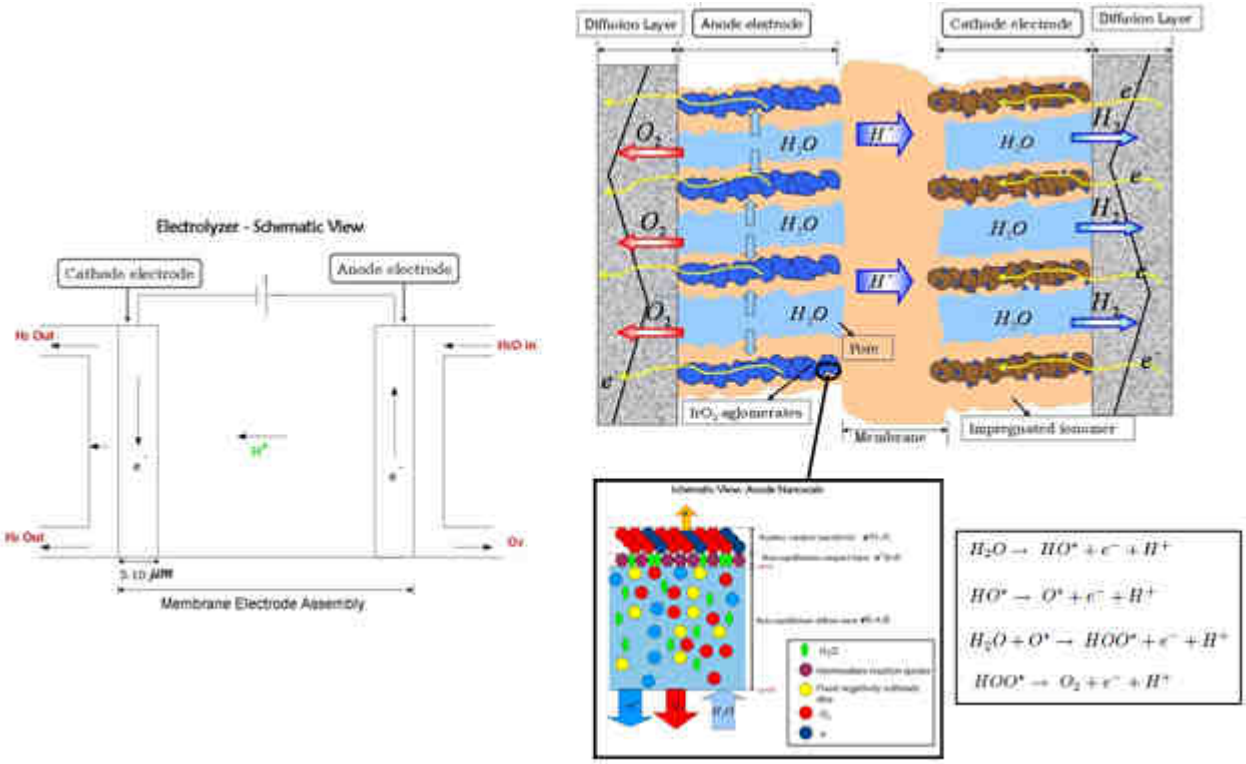

Figure A-II.1: SyhPEMEM® model (Source: [340]).

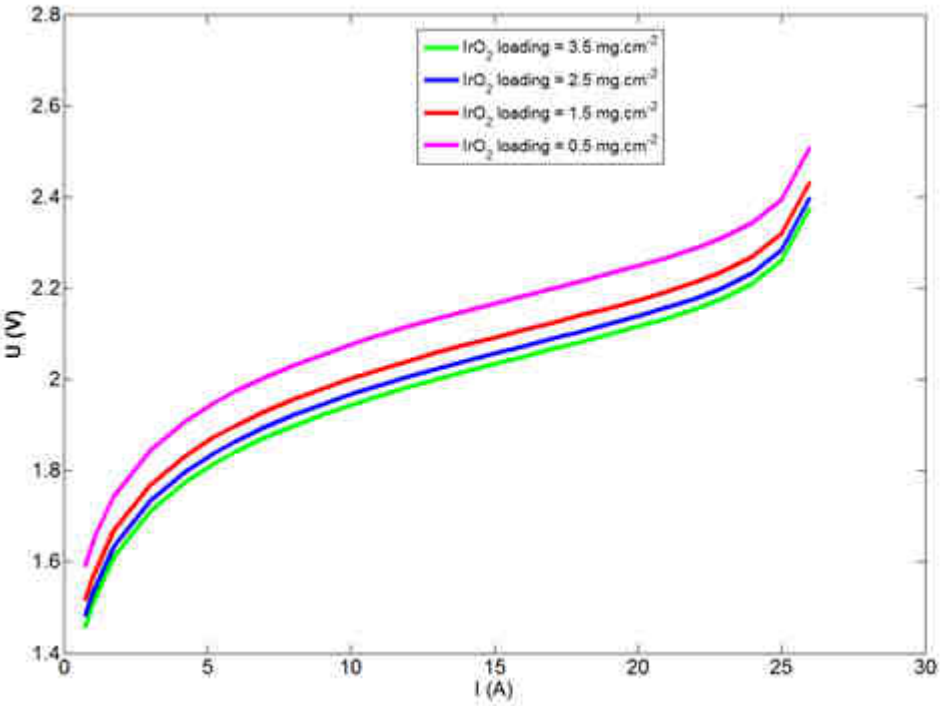

Figure A-II.2: Example of calculation with SyhPEMEM® model (impact of anode IrO_2 loading on the i-V characteristics) (Source: [340]).

✓ ***Lithium-ion batteries***

Lithium-ion batteries are a type of rechargeable battery, current in portable electronics, automotive and aerospace applications because of their high energy-to-weight ratios and slow self-discharge when not in use. In a Lithium-Ion battery, lithium ions move from the anode electrode to the cathode electrode through a polymer electrolyte during discharge, and from the cathode to the anode during charge. The anode materials are usually metal oxides or graphite. The cathode is generally made of oxides (e.g. lithium cobalt oxides, lithium manganese oxides) or polyanions (e.g. lithium iron phosphates). It is experimentally known that depending on the materials choice for the anode, cathode, and electrolyte, the performance (voltage, charge capacity), durability (materials degradation rate), and safety of a Lithium-ion battery can change dramatically. However, until now, in comparison with PEMFCs, only few works have been reported on the detailed understanding of the underlying electrochemical processes beside the Lithium-Ion battery operation. More precisely, a theoretical work remains to be done to understand the mechanisms related to the insertion of Lithium ions in the covalent matrices used as an electrode, in order to improve the performance and durability of the batteries. A major reason for this shortcoming lies in the difficulty of the theoretical treatment of the chemistry in systems under electrostatic polarization in which complex atomic bonds of very different nature coexist, such as covalent bonds and ionic bonds.

Another objective of the oingoing work of my group is to adapt MEMEPhys® for the description of the electrochemical processes inside the Li-Ion batteries, including degradation phenomena. This occurs now through three steps:

- use of DFT for the calculation of the thermodynamic properties of the electrolyte and electrodes materials (e.g. towards the Li ion insertion process).
- use of Non Equilibrium Thermodynamics Theory to describe the electrochemical interfaces far from the equilibrium conditions (simulating interfacial electrolyte properties such as free energy for interfacial ion transfer, and structural and transport properties of solid electrolyte interphase, as well as the solid electrolyte formation in the anode).
- use of Hybrid MC-MF approach to describe the transport processes of Li ions as well as the kinetics of the insertion processes into the electrodes. This will allow simulating the experimental observables (e.g. charge as function of time).

A comparison with experimental data will allow the validation and the understanding of the behavior of these batteries, and opening doors for the improvement of the present technologies.

Appendix III

Infinite-dimensional Bond Graphs

An originality of our multi-scale irreversible thermodynamics approach is that it constitutes a modular model. That means that the model represents explicitly the different physical phenomena as nonlinear sub-models in interaction.

Such developed model is a multi-level one in the sense that it is made of a set of interconnected sub-models describing the phenomena occurring at different level in the PEMFC. However, this description remains macroscopic (suitable for engineering applications) in the sense that it is based on irreversible thermodynamic concepts as they are extensively used in chemical engineering: use of conservation laws coupled to closure equations (flux expressions, chemical rate models, thermodynamic models). By using the infinite-dimensional Bond Graph theory, the model is built as a collection of interconnected and reusable sub-models through the concept of port power-conjugate variables. Such an approach allows to easily modify the sub-models and to test new assumptions keeping the mathematical structure of the model and the couplings. As an example, the following paper, published by us in 2006, in collaboration with the LAGEP, shows the infinite-dimensional Bond Graph representation of the coupling between the physicochemical phenomena (disconsidering degradation in this example) within MEMEPhys®.

Proceedings: 5th MATHMOD Vienna, February 2006 (I.Troch, F.Breitenecker, eds.)

MULTI-SCALE BOND GRAPH MODEL OF THE ELECTROCHEMICAL DYNAMICS IN A FUEL CELL

A.A. Franco[a], P. Schott[a], C. Jallut[b] and B.M. Maschke[b]

[a] CEA-Grenoble/ Laboratoire de Pile à Combustible, France
[b] LAGEP, UMR 5007 CNRS/ Université Claude Bernard, France

Corresponding Author: A.A. Franco,
Commissariat à l'Energie Atomique (CEA) /DRT/DSEN/SGPAC/ Laboratoire de Pile à Combustible
17 rue des Martyrs, 38000 Grenoble, France
Phone: +33 4 38 78 63 75, Fax: +33 4 38 78 25 56
E-mails: alejandro.franco@cea.fr ; alesitofranco@yahoo.fr

Abstract. Electrochemical impedance spectroscopy is a widely used experimental technique for the transient analysis of Polymer Electrolyte Fuel Cells. Experimental results are usually analyzed using equivalent circuit models which have to be fitted to each operation point and do not offer a direct access to internal physical parameters of the electrodes. The goal of this paper is to present a novel multi-scale mechanistic Membrane-Electrode Assembly model based on the distributed-parameter Bond Graph language (irreversible thermodynamics and electrodynamics) and depending on the internal physical parameters. It is constituted of a transport phenomena description through the thickness of the electrodes and membrane and a physical description of the electrochemical interface between the Carbon (C)/Platinum (Pt) and Nafion® phases at a nanoscopic scale. We show how the Bond Graph language, extended to spatial multi-scale modelling, allows to structure this model in a modular way and to relate the multiple phenomena involved in fuel cell electrodes operation. Our model is mainly dedicated to the diagnostic of the dynamic fuel cell operation, and to define electrodes properties. Our approach allows to predict the influence of working conditions and operating point on the characteristics of the impedance spectra. The sensitivity of the simulations results to inputs like nominal current, temperature, reactant pressure and Nafion® and platinum loadings in the electrodes are in good agreement with experimental results.

1. Introduction

Electrochemical impedance spectroscopy (EIS) is a widely used experimental technique for the transient analysis of *Polymer Electrolyte Fuel Cells* (PEFC) [3]. Experimental results are usually analyzed using equivalent circuit models which have to be fitted to each operation point and do not offer a direct access to internal physical parameters of the electrodes [1]. In these models, charge transfer is typically represented by ideal resistors and mass transport by complex impedances. The interfacial accumulation of intermediate reaction species and the electrochemical double layer at the metal/electrolyte interface are represented by capacitive elements. One drawback of this approach is that these models are not predictive and their parameters values have to be fitted at each fuel cell working point (given by the nominal current, the temperature and the reactant species concentration). Also, due to the fact that the AC circuit components are a global linear representation of the nanoscopic physical mechanisms involved, an analogical circuit involving three or more circuit elements can often be arranged in various ways and still produce similar impedance responses. Other authors [10] derive analytical expressions of the impedance dependence with nominal current, supposing simple electrochemical mechanisms in the electrodes: the analytical expressions obtained are not reusable (they have to be recalculated if one changes a mechanism or couple it with other physicochemical phenomena); furthermore, analytical computations of complex impedances become impossible for more complicated mechanisms.
In this paper we propose a novel multi-scale mechanistic *Membrane-Electrodes Assembly (MEA)* dynamic model [4] [5] [6] [11] [12] [13] based on the *distributed-parameter Bond Graph language* [8] [9] (irreversible thermodynamics and electrodynamics) and depending on the internal physical parameters.
Our model is composed of an *anodic* and *cathodic electrodes* and an *membrane electrolyte* mechanistic sub-models (the electrodes of some micrometers thickness are separated by a 20 to 100 micrometer thick membrane). The electrodes are constituted of catalyst/electronic conductor particles (*Pt/C phase*) (of 100 nanometers size, and supposed to be uniformly distributed in the electrode volume) immersed in a protonic conductor medium (*Nafion® phase*) (of maximum 10^{-5} m thickness) and a void fraction (*pore phase*) (Fig.1). An *electrochemical double layer* is formed at the nanometric vicinity of the Pt/C phase (Fig. 2). The multiscale model results of the coupling of a microscale proton and electron transport description through the electrode thickness, a spatially distributed microscale model of the reactant (H_2 in the anode, O_2 in the cathode) diffusion through the Nafion® layer, and a spatially distributed nanoscopic model of the Pt/C-Nafion® interface. The last one is constituted of a *diffuse layer* and a *compact layer*. The diffuse layer is composed of spatially moving proton ions, of counter-ions representing the negatively charged and spatially fixed sulfonate groups of the Nafion® phase, and of water

molecules. The compact layer is formed by adsorbed water molecules at the surface of the Pt/C phase, and intermediate reaction species of the electrochemical reactions (converting H_2 into protons and electrons in the anode, and O_2, protons and electrons into water in the cathode). In a first step, we consider here the case of isothermal fuel cells fed with pure hydrogen and oxygen fully saturated with water vapour. Additional water production is evacuated through the liquid phase. In these conditions it appears not necessary to take into account the *gas diffusion layers* of a typical fuel cell [3]. The model computes dynamically the potential difference between the two electrodes in response to a time dependent current demand $I(t)$ (and depending on P_a, P_c -total anodic and cathodic pressures in the pore phase- and T -PEFC temperature-).

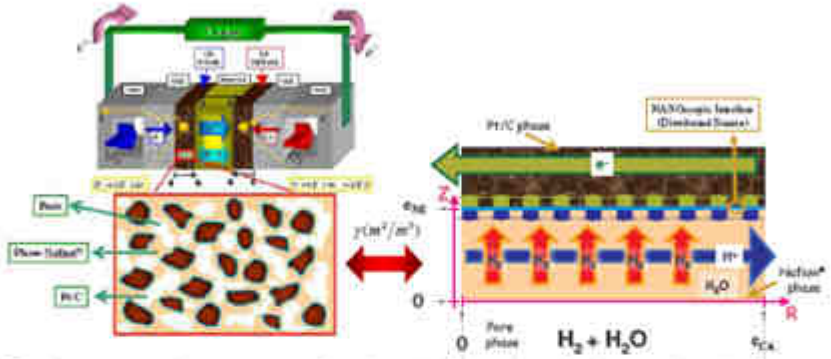

Fig. 1: The electrode morphology and the multi-scale model of the volumetric electrode (example of the anode) and localization of the nanoscopic interface model. The reactant specie (hydrogen) diffuses through the impregnated Nafion® layer, protons and electrons are produced at the nanoscopic interface, and evacuated through the electrode thickness.

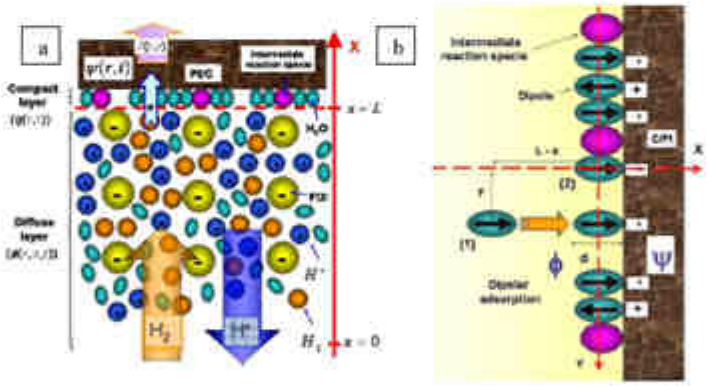

Fig. 2: a) A schematic representation of the nanoscopic interface model (anodic case): the reactant specie (hydrogen) arrives to the compact layer where the electron transfer reaction takes place. Protons are produced at $x = L$ and evacuated through $x = 0$. b) Intermediate reaction species and dipolar water adsorption on the Pt surface (cf. Section 3).

2. The microscale sub-models

The reactant (noted by i) transport through the impregnated Nafion® layer thickness is given by:

$$\vec{J}_i = -(C_i D_i / RT)\vec{\nabla}_{r,z}\mu_i \quad \text{and} \quad \partial C_i / \partial t = -\nabla_{r,z}.\vec{J}_i \tag{1}$$

where $\mu_i(r,z,t)$ is the chemical potential of the i specie, $C_i(r,z,t)$ is the molar concentration (mol.m^{-3}), $J_i(r,z,t)$ the molar flux (mol.m^{-2}.s^{-1}), D_i the diffusion coefficient in the Nafion® phase, T the temperature (K) and R the ideal gas constant. The corresponding Bond Graph representation is shown in Fig.3 as the interconnection of five multiport elements (C, 0, R, 1 and DTF) linked by bonds which are associated to a pair of conjugated variables (thermodynamic flux and effort) and a product with power unity (we show also the

causality chosen for our simulations). The element **C** has as pair of conjugated port (external) variables, the variation of the concentration and the chemical potential of the reactant specie ($\partial C_i/\partial t, \mu_i$) (it represents the matter accumulation with internal energy associated U). The element **0** represents the balance equation in (1) as well as the assumption of local equilibrium of the irreversible thermodynamics [6]. The element **R** represents the diffusion process of the reactant specie, defined by the energy dissipative relation in (1) relating the two conjugated variables ($J_i, \nabla\mu_i$) (the module chosen here for this element is DC_i/RT). The element denoted by **1**, the dual of the **0** junction, ensures the respect of sign convention (we define the flux as the opposite of the generating force). The central element denoted by **DTF** represents the interconnection between the storage (element **C**) and the dissipative (element **R**) parts of the model. It combines two adjoint differential relations: the definition of the generating force as the gradient of the chemical potential $\nabla_x\mu_i$ and of the conservation law by the divergence of the flux $\nabla_x J_i$. Furthermore, the **DTF** element (which is the dissipative counterpart of the models given in [7]) defines the two boundary variables obtained by the Stokes' theorem [2] applied to the volume of the modelled system: at $z = 0$ (Nafion®/pore boundary), the reactant chemical potential $\mu_i(z=0,t)$ is imposed by the element Se (thermodynamic effort source) (corresponding to the Henry's relations in Section 4); at $z = \epsilon_M$ (reactant transport microscale/nanoscale boundary), the reactant molar flux is imposed (through a port) by the transport model at the nanoscale (continuity of fluxes at the interface between the two scales $J_i(r, z=\epsilon_M, t) = J_i(r, x=0, t)$).

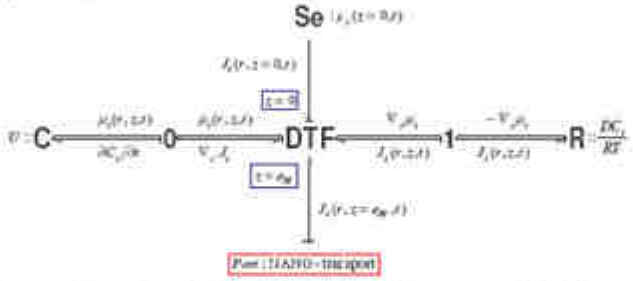

Fig. 3: Infinite-dimensional Bond Graph of the hydrogen (anode) or oxygen (cathode) transport through the thickness of the Nafion® layer covering the Pt/C phase.

The local electronic current $i_{e^-}(r,t)$ in the Pt/C phase at the microscale is given by:

$$i_{e^-}(r,t) = -S_{MEA}\, g_{e^-} \nabla\psi(r,t) \text{ and } \nabla\left[i_{e^-}(r,t)/S_{MEA}\right] = S_{e^-}(r,t) \qquad (2)$$

where $\psi(r,t)$ is the local electronic electrical potential, computed by the nanoscopic sub-models, g_{e^-} is the electronic conductivity and S_{MEA} is the MEA surface according the direction R. The local production or consummation is given by $J(r,t)\gamma = S_{e^-}(r,t)$. $J(r,t)$ is the current density (A/m²) boundary condition at the nanoscale where γ is the *specific active area* (in m².m⁻³) (cf. Fig.1).

The Bond Graph of Fig.4a represents this model as the interconnection of four multi-port elements (because here we have neglected the electronic accumulation in (2), we have not energy accumulation through a **C** element). The element **0** represents the balance equation in (2) and relates the element **DTF** to an element **coupling** (cf. Section 3) relating $S_{e^-}(r,t)$ with the current density $J(r,t)$, boundary condition at the nanoscale (cf. Section 3).

The element denoted by **R** represents the electronic transport through the electrode thickness and it is defined by the dissipative relation in (2) relating the two conjugated variables ($i, \nabla_x\psi$) (the module associated is here g_{e^-}).

The element **DTF** represents the interconnection between the part connected to the nanoscale model and the energy dissipative part of the model (element **R**). It combines the definition of the generating force as the gradient of the electronic potential $\nabla_x\psi$ and the conservation law by the divergence of the current density $\nabla_x[i/S_{MEA}]$. This **DTF** defines also the two boundary variables: at $r = 0$ (electrode/gas diffusion layer boundary), the electronic current $i(r=0,t)$ is imposed by a first element **Sf** (thermodynamic flow source) ($i_{e^-}(r=0,t) = I(t)$ - global current delivered, input of the model); at $r = \epsilon_{CL}$ (electrode/membrane boundary), the electronic current is imposed by a second element **Sf** ($i_{e^-}(r=\epsilon_{CL},t) = 0$).

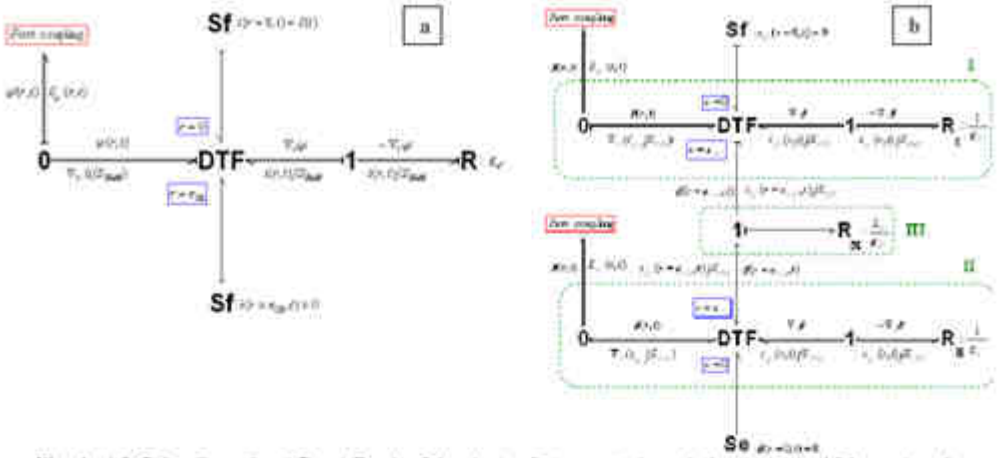

Fig. 4: a) Infinite-dimensional Bond Graph of the electronic transport through the electrode thickness (anode or cathode) with the causality chosen for our simulations. b) Infinite-dimensional Bond Graph of the protonic transport through the AME thickness. The resistances can be modulated by water transport [6].

At the microscopic scale the electroneutrality for protons in the Nafion® phase can be assumed because we are far of the electrified surface (Pt/C-Nafion® nanoscopic interface) [5] [6], so the protonic current is given by:

$$i_{H^+}(r,t) = -S_{MEA}\,g_{H^+}\,\nabla_r\phi(r,t) \quad \text{and} \quad \nabla_r\left(i_{H^+}(r,t)/S_{MEA}\right) = S_{H^+}(r,t) \tag{3}$$

where $\phi(r,t)$ the local protonic electrical potential in the Nafion® phase and g_{H^+} the protonic conductivity. The proton production (anode) and consummation (cathode) are given by the distributed source $S_{H^+}(r,t) = J(r,t)/r$, where $J(r,t)$ is calculated by the microscopic electron transport model.

The Bond Graph representation of the proton transport through the electrodes thickness is analogous to the electronic one (parts (I) -cathode- and (II) -anode- in Fig.4b) (because of the electroneutrality, we have not element C). The elements DTF define the two boundary variables: in (II), at $r = 0$, the ionic potential is imposed by an element Se ($\phi(r=0,t) = 0$ as *reference potential*). In (I), at $r = 0$, the ionic current is imposed by an element Sf ($i_{H^+}(r=0,t) = 0$); at $r = e_{CL}$ (electrode/membrane boundary), the protonic current $i_{H^+}(r = e_{CL},t)$ is imposed by the membrane sub-model (III) on (II), and the potential $\phi(r = e_{CL},t)$ is imposed on (I). The element R_M in (III) represents the protonic transport through the membrane. It combines also the definition of the gradient of the ionic potential $\nabla_r\phi$ and the divergence of the protonic current density $\nabla_r\left(i_{H^+}/S_{MEA}\right)$. As an example in Fig.4b, this sub-model is discretized in one mesh (its module is so equal to L_M/g_{H^+}). The element denoted by 1 represents $i_{H^+}(r = e_{CL},t)/S_{MEA} = i_{H^+}(r = e_{CL},t)/S_{MEA}$ (continuity of current).

3. The nanoscale sub-models

The diffuse layer part of the nanoscale sub-model (cf.Fig.2a) takes into account the transport by diffusion and electrical migration of reactants, depending on the electric field generated by the resulting charge distribution. All the species (H^+, H_2, O_2, FIX^- and water) are supposed to be punctual (interparticle interaction neglected). Solvatation by water and convection are not considered here. The reactant transport is treated as in the microscopic model (cf. equation (1)). The H^+ transport close to the interface Pt/C-Nafion® is governed by (electroneutrality cannot be assumed [4] [5] [6]):

$$-\left[D_{H^+}C_{H^+}/RT\right]\nabla_r\tilde{\mu}_{H^+} = J_{H^+} \quad \text{and} \quad \partial C_{H^+}/\partial t = -\nabla_r J_{H^+} \tag{4}$$

$$(F/\varepsilon_{CD})(C_{H^+} - C_{FIX}) = -\nabla_r^2\phi + \varepsilon_{CD}\nu_{CD}\,\partial^2\phi/\partial r^2 \tag{5}$$

where $\tilde{\mu}_{H^+} = \mu_{H^+} + F\phi$ (electrochemical potential), $\phi(r,x,t)$ is the electrical potential in the electrolyte (neglecting the magnetic effects [6] [14] [15]) and C_{FIX} the sulfonate concentration in the Nafion® electrolyte.

At $x = L$, the Frumkin's overpotential [4] [5] [6] [11] [12] allows the development of the electrochemical reaction on the Pt surface. This potential discontinuity (cf. Fig.2a) is given by:

$$\eta(r,t) = \psi(r,t) - \phi(r, x = L, t) \tag{6}$$

According to the superposition principle [4] [5] [6] [14] [15], $\eta(r,t)$ is also given by:

$$\psi(r,t) - \phi(r, x = L, t) = \eta(r,t) = -(\sigma/\varepsilon_{CC})d + \Gamma(\sigma)/\varepsilon_{CD} \tag{7}$$

where the first term is linked to the thickness of the compact layer d, and the second one to its dipolar nature. In (7), σ is the electronic surface density on Pt, ε_{CC} is the electric permittivity of the compact layer, ε_{CD} the electric permittivity of the diffuse layer (supposed independent of temperature) and Γ is the surface dipolar density (in debye/m^2) given by $\Gamma = \mu(\vec{n} - \overleftarrow{n})$ where μ is the dipolar moment of a water molecule, $\vec{n}$ (respectively $\overleftarrow{n}$) the number of dipoles per surface unit towards (respectively opposed) to the metal (cf. Fig.2b).

The oriented adsorption of molecules is described here by the two equilibrium reactions $H_2O + s \leftrightarrow \overleftarrow{H_2O} - s$, where s is a free site of adsorption on the metal surface. The application of the mass action law gives:

$$\vec{n}\Big/\left(n_s\Theta_{H_2O}\right) = \vec{K} = \exp\left[-\Delta\vec{G}^*/RT\right] = \exp\left[-\left(-\Delta G_c^0 \mp \frac{\mu\sigma}{\varepsilon_{CC}} \mp \frac{A\mu^2}{d^3}\left(\frac{\vec{n} - \overleftarrow{n}}{n^* + \vec{n} + \overleftarrow{n}}\right)\right)\Big/RT\right] \tag{8}$$

where n_s is the number of free sites per surface unit, Θ_{H_2O} the activity of the surface free water (supposed to be constant), and $\Delta\vec{G}^*$ is the sum of the Gibb's free energies associated to the adsorptions: the first term represents the chemical energy of adsorption (supposed to be independent of the dipolar orientation), the second one the electrostatic energy corresponding to the necessary work to bring a dipole from infinity to the surface, and the third one the interdipolar interaction energy. n^* denotes the sum of free sites and occupied sites by intermediates per surface unit. We can demonstrate [5] that from (8) we can write $\Gamma = -an_s\Theta_{H_2O}\mu Sinh[X]$, with $X = (\mu/(kT\varepsilon_{CC}))\sigma + (A\mu^2)/(kTd^3)\left(\vec{n} - \overleftarrow{n}\Big/n^* + \vec{n} + \overleftarrow{n}\right)$ and $a = 2\exp(-\Delta G_c^0/RT)$ ($A = \zeta[3]/2\pi\varepsilon_{CD}$, ζ being the Riemann's function). $X(\sigma)$ is calculated from:

$$aSinh[X]\Big/\left(\frac{n^*}{n_s\Theta_{H_2O}} + aCosh[X]\right) = \sigma\left(d^3/\varepsilon_{CC}A\mu\right) - X\left(kTd^3/A\mu^2\right) \tag{9}$$

Finally, we obtain for the Frumkin's overpotential:

$$\boxed{\eta(r,t) = \frac{\sigma}{\varepsilon_{CC}}d - \frac{an_s\Theta_{H_2O}\mu Sinh[X(\sigma)]}{\varepsilon_{CD}}} \tag{10}$$

A Tafel-Heyrovsky-Volmer reaction mechanism [4] [5] [6] [11] [12] [13] for the anodic hydrogen oxidation is used to calculate the temporal evolution of n^* (and so of n_s) in (9) and (10):

$$\left.\begin{array}{ll} H_2 + 2s \leftrightarrow 2Hs & \text{(Tafel)} \\ s + H_2 \leftrightarrow Hs + H^+ + e^- & \text{(Heyrovsky)} \\ Hs \leftrightarrow s + H^+ + e^- & \text{(Volmer)} \end{array}\right\} \quad \left.\begin{array}{l} v_{TAF} = k_{TAF}\theta_r^2 C_{H_2}(r,L,t) - k_{-TAF}\theta_H^2 \\ v_{HEY} = k_{HEY}\theta_r C_{H_2}(r,L,t)e^{(1-\alpha_{HEY})f\eta} - k_{-HEY}\theta_H C_{H^+}(r,L,t)e^{-\alpha_{HEY}f\eta} \\ v_{VOL} = k_{VOL}\theta_H e^{(1-\alpha_{VOL})f\eta} - k_{-VOL}\theta_r C_{H^+}(r,L,t)e^{-\alpha_{VOL}f\eta} \end{array}\right\} \tag{11}$$

where v_{TAF}-v_{HEY} and v_{VOL} are the associated reaction step rates written as functions of $\eta(r,t)$. In these expressions θ_r the surface coverage by free sites, θ_H, the surface coverage by the monoatomic hydrogen adsorbed, k_i and k_{-i} are the standard kinetics constants, α_i the symmetry factors, $f = F/RT$ (F the Faraday's constant). In the cathode, a Damjanovic reaction mechanism [4] [5] [6] [11] [12] [13] for the cathodic oxygen reduction is used:

$$\left.\begin{array}{ll} O_2 + H^+ + e^- + s \leftrightarrow O_2Hs \ \text{(Dmj 1)} & v_1 = k_1\theta_s C_{H^+}(r,L_c,t)C_{O_2}(r,L_c,t)e^{-\alpha_1\beta(V-U)} - k_{-1}\theta_{O_2Hs}e^{(1-\alpha_1)\beta(V-U)} \\ O_2Hs + H_2O + 2s \leftrightarrow 3OHs \ \text{(Dmj 2)} & v_2 = k_2\theta_{O_2Hs}\Theta_{H_2O}\theta_s^2 - k_{-2}\theta_{OHs}^3 \\ OHs + H^+ + e^- \leftrightarrow H_2O + s \ \text{(Dmj 3)} & v_3 = k_3\theta_{OHs}C_{H^+}(r,L_c,t)e^{-\alpha_3\beta(V-U)} - k_{-3}\theta_s\Theta_{H_2O}e^{(1-\alpha_3)\beta(V-U)} \end{array}\right\} \quad (12)$$

The surface coverages θ_{Hs}, θ_{O_2Hs} and θ_{OHs} are given by the balance equations:

$$\left.\begin{array}{l} (n^{max}/N_A)(d\theta_{Hs}/dt) = -v_{VOL} + v_{HER} + 2v_{OER} \\ (n^{max}/N_A)(d\theta_{O_2Hs}/dt) = v_1 - v_2 \\ (n^{max}/N_A)(d\theta_{OHs}/dt) = 3v_2 - v_3 \end{array}\right\} \quad (13)$$

where N_A is the Avogadro's number. For the surface dipolar coverage oriented towards (opposed) the metal, we have:

$$\vec{\theta} = \frac{a}{2}e^{\pm\alpha} \Big/ \left(\frac{1}{\Theta_{H_2O}} + \frac{\theta_{Hs}}{\theta_s}\frac{1}{\Theta_{H_2O}} + aCosh[X]\right) \quad \text{(anode)}, \qquad \vec{\theta} = \frac{a}{2}e^{\pm\alpha} \Big/ \left(\frac{1}{\Theta_{H_2O}} + \frac{\theta_{O_2Hs}+\theta_{OHs}}{\theta_s}\frac{1}{\Theta_{H_2O}} + aCosh[X]\right) \quad \text{(cathode)} \quad (14)$$

and using (13) with $\theta_s + \theta_{Hs} + \vec{\theta} + \overleftarrow{\theta} = 1$ (respectively $\theta_s + \theta_{O_2Hs} + \theta_{OHs} + \vec{\theta} + \overleftarrow{\theta} = 1$), we compute θ_s and $\pi_c\sigma$ is calculated through the charge conservation law in the metal/electrolyte interface [4] [5] [6] (Fig.2a) which is,

$$J(r,t) - J_{Far}(r,t) = J(r,t) - F(v_{HER} - v_{VOL}) = -\partial\sigma/\partial t \quad \text{(anode)} \quad (15)$$

$$J(r,t) - J_{Far}(r,t) = J(r,t) - F(v_1 + v_3) = \partial\sigma/\partial t \quad \text{(cathode)} \quad (16)$$

where J_{Far} is the faradaic current density.

The Bond Graph in Fig.5, represents, in the anode (the discussion for the cathode is analogous and is not presented here), the coupling between the diffuse layer, compact layer and electrochemical reactions models, where we show the causality chosen for our simulations. This Bond Graph is constituted by the diffuse layer sub-Bond Graphs, an element **MC**, two elements **0**, one element **1** and one sub-Bond Graph (denoted **Reaction**) associated to the electrochemical reactions (11).

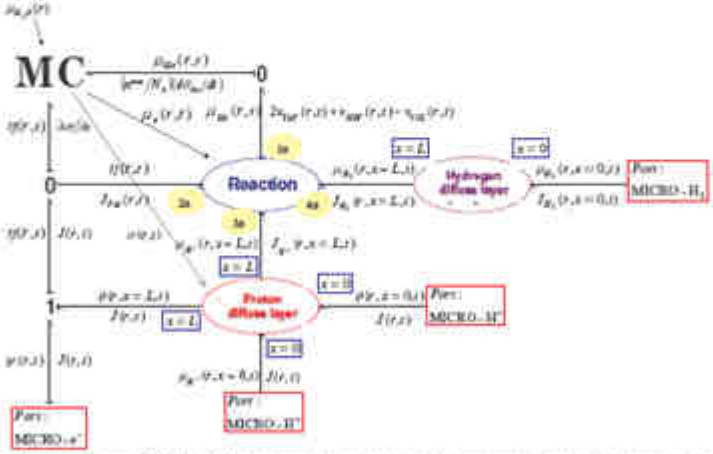

Fig. 5: The distributed-parameter Bond Graph representation of the anodic nanoscopic model where we show the causality chosen for our simulations.

At $x = 0$ the Bond Graph associated to the hydrogen and proton diffuse layer models have its ports connected to the hydrogen and proton microscale models through the power-conserving 2-ports elements **coupling** (cf. Fig.7b) fundamental to the multiscale coupling in heterogeneous media [2]. We identify a fourth port (denoted **MICRO-e⁻**) which is connected to the microscale electronic transport model also through an element **coupling** representing: the equality of the electronic potentials at the boundary of the two scales $\varphi(r,t)^{MICRO} = \varphi(r,t)^{NANO}$ and the continuity of the current between the two scales $J(r,t)\gamma = S_\gamma(r,t)$ (as we

discuss in [6]). The current density $j(r,t)$ is imposed by the electronic microscale model; the nanoscale model returns to the last one the electronic potential $\varphi(r,t)$.

The element **MC** represents a modulated variable capacitance with σ and with the number of free sites n_s (using the definition of *differential capacity* $C_{dl}(\sigma) = d\eta/d\sigma$ [5] [6]). It has two ports in the anodic case: a first one as pair of conjugated variables, the variation of the surface coverage and the chemical potential of the intermediate reaction specie Hx $\left(\left[n^{tot}/N_A\right]d\theta_{H_x}/dt \;,\mu_{H_x}(r,t)\right)$, and a second one as pair of variables the variation of the electronic charge density and the Frumkin's overpotential$(\partial\sigma/\partial t,\eta(r,t))$. This element represents the accumulation (adsorption) of the water molecules on the catalytic surface and it has three signals (denoted by the arrows): 1) an input signal which indicates that this element can be modulated by the chemical potential of water μ_{H_2O} in the diffuse layer (this would allow to couple the model with a model describing water transport, through Θ_{H_2O} in (10)); 2) an output signal towards the element **Reaction**, which gives the chemical potential of the free sites $\mu_s(r,t)$ covering the catalytic surface; 3) an output signal towards the element **proton diffuse layer**, which gives the electronic charge density $\sigma(r,t)$. The element **1** represents the potential balance (from (6)) $\varphi(r,t) = \eta(r,t) + \phi(r,x=L,t)$, and the element **0** with three ports, represents the current density balance (15) for H_2 oxidation. The element **0** with two ports, expresses the intermediate specie balance (13) (H_2 oxidation).

The element **Reaction**, has four ports: the port denoted by **4a**, connected to the element **hydrogen diffuse layer**, which imposes the chemical potential of the hydrogen at $x=L$ $\mu_{H_2}(r,x=L,t)$; the port denoted by **3a**, linked to the protonic transport model in the diffuse layer, which imposes the chemical potential of the protons at $x=L$ $\mu_{H^+}(r,x=L,t)$; the port denoted by **2a**, which has as conjugated variables the faradaic current $J_{Far}(r,t)$ and the Frumkin's overpotential $\eta(r,t)$; and the port denoted by **1a**, which has as conjugated variables the rate balance (from (13)) $-v_{VOL}+v_{HEY}+2v_{TAF}$, and the chemical potential of the intermediate specie μ_{H_x}.The element **reaction** has associated the Bond Graph shown in Fig.6a. It is constituted by: an element TF (II) of modulus F coupling the efforts ($\eta(r,t)$ and $F\eta(r,t)$) between them in a ratio F and the fluxes ($J_{Far}(r,t)$ and $J_{Far}(r,t)/F$) between them in the inverse ratio; one part composed by three elements **MR**, energy-dissipative, representing the reaction kinetics (11) modulated by the chemical potential $\mu_s(r,t)$ (the constitutive relations associated to these elements are non linear, defined in function of the *electrochemical affinities* $\tilde{A}_k$ [6]); and one part (I) which represents a junction structure relating the port-variables to the elements **MR**.

The element **hydrogen diffuse layer** has the associated infinite-dimensional Bond Graph shown in Fig.6b. We find here the same structure as that of the microscale model of reactant transport through the impregnated Nafion®. The **DTF** here defines also the boundary variables: at $x=0$, the reactant chemical potential $\mu_i(r,x=0,t)$ is imposed by the microscale model of reactant transport through the impregnated Nafion®; at $x=L$ (diffuse layer/compact layer boundary), the reactant molar flux $J_i(r,x=L,t)$ is imposed by the reaction model at the compact layer ($J_{H_2} = -(v_{TAF}+v_{HEY})$, $J_{O_2}(r,x=L,t) = -v_1$); $C_{H_2}(r,L,t)$ and $C_{H^+}(r,L,t)$ (in (11)) are obtained from the diffuse layer model.

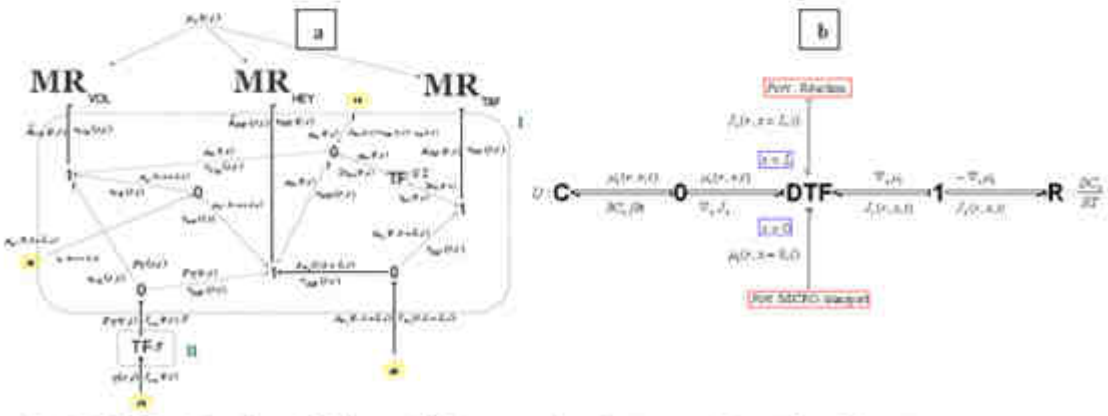

Fig. 6: a) The Bond Graph of the Tafel-Heyrovsky-Volmer mechanism of hydrogen oxidation. b) The distributed parameter Bond Graph representation of the dynamic model of reactant transport (hydrogen) through the (anodic) diffuse layer.

Finally, the element proton diffuse layer in Fig.5, has the associated infinite-dimensional Bond Graph shown in Fig.7. It is composed by the connection of two sub-parts: a first one describing the protonic transport (I) and a second one describing the potential φ dynamics and its coupling with the proton accumulation (III). These sub-parts are linked through a power-conserving element TF (II) associated to a energy transfer coupling the efforts ($E(r,x,t)=-\nabla_x\varphi$ and $FE(r,x,t)$) between them. The sub-part (I) is constituted by the interconnection of four multi-port elements: **0**, **R**, **1**, **0** et **DTF**. The element **0** represents the balance equation in (4) and the assumption of local equilibrium of the irreversible thermodynamics. The element **C** representing the accumulation of protons, is included in the element **CI**, described later. The element **R** represents the protonic transport in the diffuse layer, defined by the energy dissipative relation in (4) relating the two conjugated variables ($J_{H^+},\nabla_x\tilde{\mu}_{H^+}$) (the module associated to this element is here RT/DC_{H^+}). The junction **1**, ensures the respect of the sign convention (flux opposed to the thermodynamic effort) and the effort balance (from the expression of the electrochemical potential): $-\nabla_x\tilde{\mu}_{H^+}=-\nabla_x\mu_{H^+}-FV_x\varphi=-\nabla_x\mu_{H^+}+FE$. Always in the sub-part (I), the element **DTF** represents the interconnection between the energy accumulative (element **CI** in the sub-part (III)) and the dissipative (element **R**) parts. It combines the two adjoint differential relations: the thermodynamic force expressed as the gradient of the protonic electrochemical potential $\nabla_x\tilde{\mu}_{H^+}$ and the conservation law through the divergence of the flux $\nabla_x J_{H^+}$. At the boundaries of this **DTF** we have: at $x=L$ (diffuse layer/compact layer boundary), the protonic molar flux $J_{H^+}(t,x=L,t)$ is imposed by the reaction model at the level of the compact layer ($J_{H^+}(t,x=L,t)=(v_{MV}+v_{VOL})$ in the anode, $J_{H^+}(t,x=L,t)=(v_1+v_3)$ in the cathode); at $x=0$ (port noted :1), the coupling between the nano and microscales takes place through two relations: firstly, according to the electroneutrality assumption at the microscale we have $\mu_{H^+}(t,x=0,t)^{NANO}=\mu_{H^+}(t,t)^{MICRO}=\mu_0+RT\ln C_{HC}$ which represents the equality of the chemical potentials at the boundary between the two scales. Secondly, the continuity of the molar fluxes at the boundary between the two scales $S_{H^+}(t,t)=J(t,t)\gamma$ ($J_{H^+}(t,x=0,t)=J(t,t)$), as a consequence of the global current conservation [6]). These two relations define a power-conserving connection element between the scales, noted by **coupling** in Fig.7b [2].
In the sub-part (III) the element denoted by **0** represents the current balance $J(t,t)=F\tilde{J}_{H^+}(t,x,t)+\partial\tilde{D}(t,x,t)/\partial t$ which can be deduced by taking the divergence of the Ampere's law [6] according to the coordinate x.
The element denoted by **1** which relates the **0** to the **DTF** (*), ensures the sign convention $E(t,x,t)=-\nabla_x\varphi$. The **DTF** (*) combines the two adjoint differential relations: the opposite of the electric field expressed as the gradient of the ionic potential $\nabla_x\varphi$ and the conservation law of the total current density expressed by the divergence of the flux $\nabla_x J$. The source of flux Sf impose a divergence of the total current density $\nabla_x J$ null (so this density is independent of the coordinate x). At the boundaries of this **DTF** we have: at $x=L$ (diffuse layer/compact layer boundary), the current density $J(t,t)$ imposed by the microscale electronic model (cf. Fig.4a). The diffuse layer model computes the ionic potential $\varphi(t,x=L,t)$; through the port at $x=0$, the potential $\varphi(t,x=0,t)$ is imposed by the microscale protonic model, and the diffuse layer model computes $S_{H^+}(t,t)=J(t,t)\gamma$.
In an analogous way, the elements **coupling** can be associated to these connections between scales, but we will not detail this here. The **DTF** (**) combines the electric field $E(t,x,t)$ with $-\varepsilon_{CD}\partial\varphi/\partial t$. At the boundary $x=L$ of this element, an element **MSe** (modulated effort source) imposes the electric field $E(t,x=L,t)$, computed from the modulation signal σ (through the Gauss'theorem applied at the compact layer [4] [5] [6] ($\partial\varphi/\partial x(L,t)=-\sigma/\varepsilon_{CC}$)) coming from the sub-model describing the water adsorption in the compact layer (element **MC** in Fig.5). At $x=0$ the source of flux Sf impose $-\varepsilon_{CD}\partial\varphi/\partial t=0$, because our microscale model doesn't describe the intrinsic dynamics of the ionic potential (we have not a D'Alembert equation at this scale). The power exchanged through this port is then zero. Finally, the element denoted in Fig.7a by **CI**, has three ports: a first one with conjugated variables ($\partial\mu_{H^+}(t,x,t),\partial C_{H^+}/\partial t$) connected to the transport sub-part (I), a second one with the variables ($\varphi(t,x,t),\nabla_x J$) connected to the **DTF** (*), and a third one with the conjugated variables ($\nabla_x E,-\varepsilon_{CD}\partial\varphi/\partial t$) connected to the **DTF** (**). This element represents the coupling between the matter accumulation $\partial C_{H^+}/\partial t$ (capacitive behaviour), and the D'Alembert equation (5) (behaving like an inertia [6]).

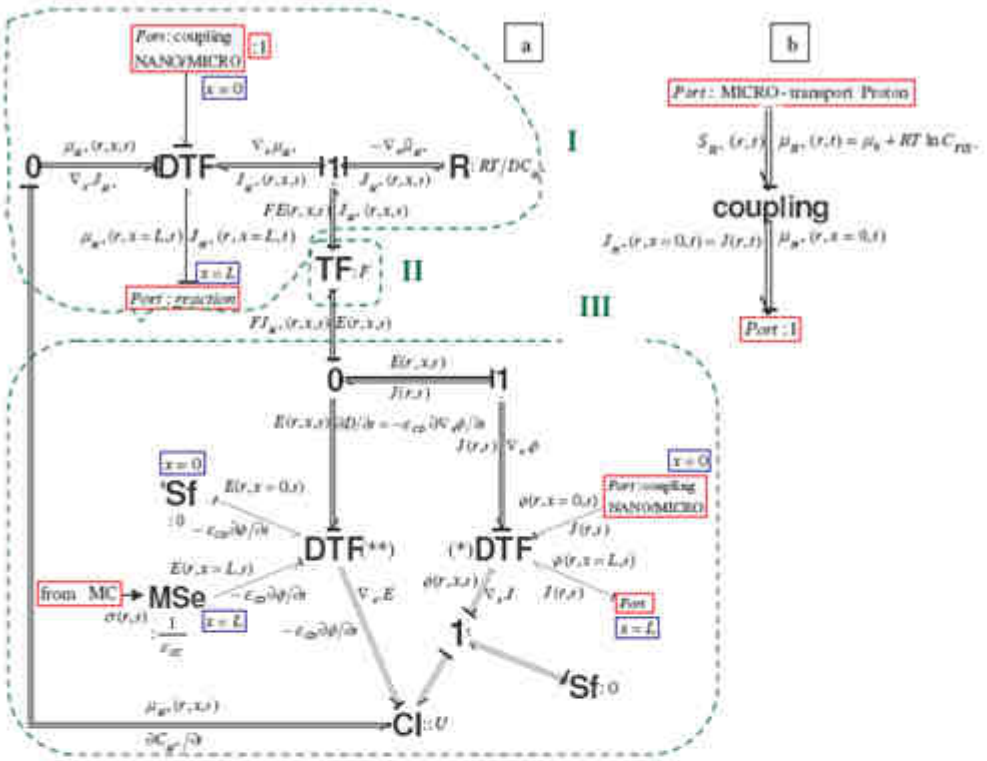

Fig. 7: a) The distributed parameter Bond Graph representation of the proton transport dynamic model in the diffuse layer (nanoscale). b) Element coupling between the protonic micro and nanoscales sub-models.

4. Some simulations results

The model was implemented under Fenlab®/Simulink®/Matlab® and the simulations have been performed on an Intel® Pentium® 4 processor 2 GHZ, 1 Go of RAM. The used physicochemical parameters for the simulations shown here are [6]: $\gamma = 5.59\times10^{7}$ (m²/m³); $\varepsilon_M = 50\times10^{-4}$, $\varepsilon_{H} = 10^{-7}$, $\varepsilon_{Cb} = 15\times10^{-4}$ (m); $S_{MR} = 2.1\times10^{-4}$ (m²); $L = 10^{-9}$ (m); $C_{FR} = 1200$ (mol/m³); $\alpha_{REF} = \alpha_{VOL} = 0.5$, $\alpha_1 = 0.8$, $\alpha_2 = 0.99$; $\Delta G_c^0 = 1$ (kJ/mol); $k_{TAF} = 10^{-1}$ $k_{MET} = 10^{-8}$ $k_{-RH} = 10^{-6}$ $k_{-VOL} = 10^{-5}$ $k_3 = 10^{8}$ (m/sec); $k_{-TAF} = 10^{-1}$ $k_{VOL} = 10^{-2}$ $k_{-1} = 10^{-5}$ $k_2 = 10^{8}$ $k_{-2} = 10^{-2}$ $k_{-3} = 1$ (mol/(m².sec)); $k_1 = 10^{4}$ (m⁴/(mol.sec)); $\varepsilon_{CCA} = 6\times\varepsilon_0$, $\varepsilon_{CCC} = 4\times\varepsilon_0$, $\varepsilon_{CDA} = \varepsilon_{CDC} = 20\times\varepsilon_0$ (C/(Volt.m)); $\lambda = 14$. The empirical relations used here [6]:

- $C_{R_1}(z=0,t) = \dfrac{P_A - P_{sat}}{1.09\times10^{6}\times\exp(77/T)}$, $C_{R_2}(z=0,t) = \dfrac{P_C - P_{sat}}{5.08\times10^{7}\times\exp(-498/T)}$ (Henry's laws) with $P_{sat} = 10^{-5}\times\exp\left(23.1961 - \dfrac{3816.44}{T - 46.13}\right)$ (bars)
- $\Theta_{H_2O} = 1.435 + 0.0022\lambda - \dfrac{2.75}{\lambda} - 0.13\ln\lambda$;
- $D_{R_1} = 2.97\times10^{-14}\times T\times10^{\frac{\left[1.35\times(298-T)+0.01\times(298-T)^2\right]}{T\times\lambda}} = g_{R_1}/fC_{FR}$ (m²/sec)
- $D_{R_2} = 3.92\times10^{-14}\times\exp(0.025\times T)$ (m²/sec)
- $\mu_i(p,T) = \mu_{i0}(T) + RT\ln a_i$ (thermodynamic property) where a_i is the activity (for ideal solutions –our assumption–: $a_i = C_i\lambda$

The dynamic PEFC potential $U_{cell}(t)$, as response to a current perturbation $I(t)$, is calculated through:

$$U_{cell}(t) = \psi_C(r=0,t) - \psi_A(r=0,t) \tag{17}$$

Based on time simulations, the frequency response and the impedance spectrum of the system can be derived (Fast Fourier Transform on the input and output -signals). A small sinusoidal signal (e.g. 15 mA) has been superimposed on the fixed (DC) current level $\bar{I}$ for frequencies ranging from 0.01 Hz to 10^5 Hz. In Fig.8a and 8b we show the sensitivity of the simulated MEA polarisation curve and EIS to the Nafion® and platinum loadings. Our model allows to compute optimal loadings values in good agreement with experimental results as we show elsewhere [6]. The Fig. 8c shows the influence of the nominal current $\bar{I}$ on the EIS. The increase of the demanded current leads to the diminution of the amplitude of the half-circles: the capacitive effect diminishes, in accordance with well know experimental results [6] [10]. Similar studies can be performed for temperature and pressures sensitivity, and other dynamical PEFC behaviours (current steps, cyclic voltammetry…) can be simulated [6].

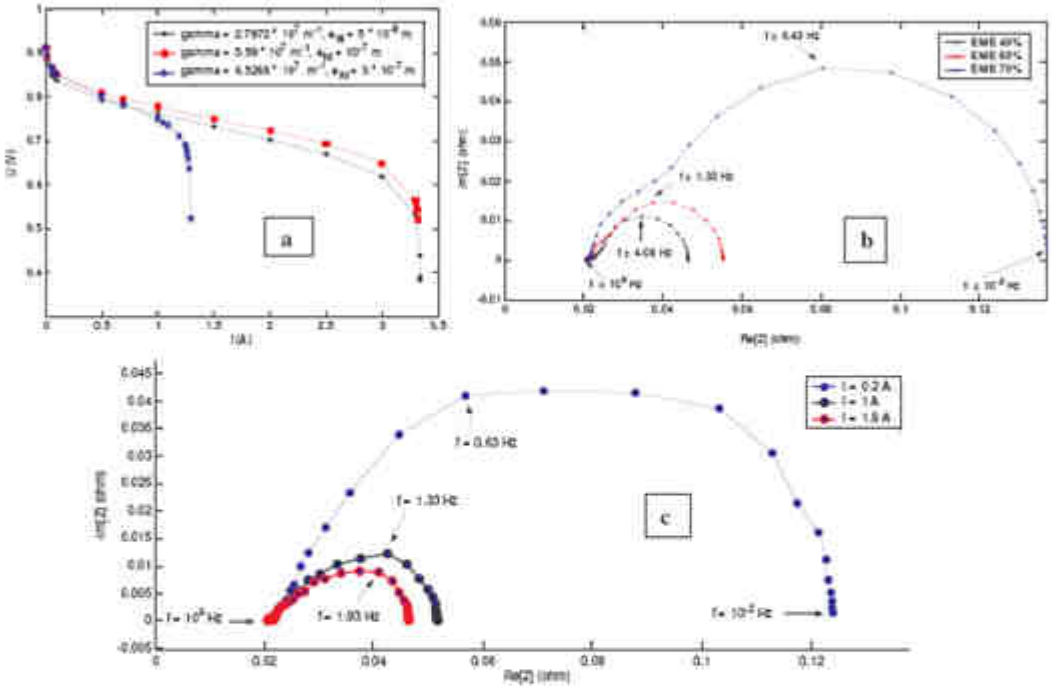

Fig. 8: Some simulation results - a) Sensitivity of the polarisation curve to the electrodes Nafion® and platinum loading ($T = 353$ K, $P_A = P_C = 1.5$ bar) b) EIS spectra sensitivity to the electrodes Nafion® and platinum loadings ($T = 353$ K, $P_A = P_C = 1.5$ bar, $\bar{I} = 1$ A) c) EIS spectra sensitivity to the nominal current $\bar{I}$ ($T = 353$ K, $P_A = P_C = 1.5$ bar).

5. Concluding Remarks

We propose a new mechanistic model for the dynamic simulation of a polymer electrolyte fuel cell Membrane-Electrodes Assembly. Our model results of the coupling of a microscale transport phenomena description through the electrodes and the electrolyte thickness, a spatially distributed microscale model of the reactant diffusion through the Nafion® layer covering the Pt/C particles, and a spatially distributed nanoscopic description of the Nafion®-Pt/C interface. This interfacial model is based on an internal description of the *double layer* dynamics, coupling the transport phenomena in the *diffuse layer* and the electrochemical reactions in the *compact layer*.

The model is based on a distributed-parameter Bond Graph description of the coupling between irreversible thermodynamics and electrodynamics. The use of the Bond Graph language has allowed to hierarchize this multiscale model and to formulate it in modular way, so that it is reusable and could be adapted to other electrochemical systems (solid oxide fuel cells, Lithium-ion batteries) or coupled to another physico-chemical phenomena (catalytic aging mechanisms, water transport...[4] [6]).

Our model is mainly dedicated to the diagnostic of the dynamic fuel cell operation, but it can help also to define electrodes properties (optimisation of platinum/Nafion® loadings) [6]. Furthermore, the model can evaluate the contribution of different physicochemical phenomena into the PEFC performance. Unlike classical analogical models based on equivalent circuits, our approach allows to predict the influence of working conditions and operating point on the characteristics of the impedance spectra. The sensitivity of the simulations results to inputs like nominal current, temperature, reactant pressure and electrodes Nafion® and platinum loadings are in good agreement with experimental results [6]. We have now started a parametric identification study of our model [6].

6. References

[1] Berthier F., J.-P. Diard et R. Michel, *Distinguishability of equivalent circuits containing CPEs. Part I. Theoretical part*; Journal of Electroanalytical Chemistry 510 (2001) 1–11.

[2] Eberard D., Lefevre L. and Maschke B.M., *Multiscale coupling in heterogeneous diffusion processes: a port-based approach*, Proc. International Conference PhysCon 2005, August 24-26, 2005, Saint Petersburg, Russia.

[3] Eikerling M., Kornyshev A.A. and Kulikovsky A., *Can theory help to improve fuel cells?*; The Fuel Cell Review (December 2004-January 2005).

[4] Franco A.A., Schott P., Jallut C. and Maschke B.M., *A Multiscale Dynamic Mechanistic Model for Transient Analysis of Electrochemical Cells*. Orally presented in Symposium "T1: Modeling of Electrochemical Systems" 207th Meeting of the Electrochemical Society (Québec, May 15-20), abstract #1296.

[5] Franco A.A., Schott P., Jallut C. and Maschke B.M.; *A Multiscale Dynamic Mechanistic Model for Transient Analysis of PEFCs*. In: Proc. 3rd European PEFC Forum, Luzern, 2005, paper #B063.

[6] Franco A.A., A Physical Multiscale Model of the Electrochemical Dynamics in a Polymer Electrolyte Fuel Cell (Original title: Un modèle physique multiéchelle de la dynamique électrochimique dans une pile à combustible à électrolyte polymère), PhD Thesis Université Claude Bernard Lyon-1 (France), in press.

[7] Maschke B.M. and Van der Schaft A.J., *Canonical interdomain coupling in distributed parameter systems: an extension of the symplectic gyrator*; In: Proc. of the ASME IMECE New York (2001).

[8] Van der Shaft A.J. and Maschke B.M., *Hamiltonian formulation of distributed-parameter systems with the boundary energy flow*, Journal of Geometry and Physics, 42 (2002), 166-194.

[9] Van der Schaft A.J. and Maschke B.M., *Compositional modelling of distributed-parameter systems; In: Advanced topics in control systems theory*, Chapter 4, pp.115-154, Springer (2004).

[10] Walkiewicz S., Bautista M., Bultel Y., Diard J.P. Electrochemical Impedance Spectroscopy study of the PEMFC behaviour (original title: *Etude par spectroscopie d'impédance électrochimique du comportement en fonctionnement d'une PEMFC*); 14ème Forum sur les Impédances Electrochimiques (Paris, January 14, 2002), 221-230 .

[11] Franco A.A., P.Schott, C. Jallut et B. Maschke; *A Multiscale Dynamic Mechanistic Model for Transient Analysis of Volumetric Elecrodes*. Presented in the Solid State Ionics Conference (SSI-15, Baden-Baden, July 17-22, 2005).

[12] Franco A.A.; *A physical multiscale model for transient analysis of electrochemical cells: an infinite-dimensional Bond Graph approach*. Finalist for the "Young Scientist Award 2005" of the Solid State Ionics Conference (SSI-15, Baden-Baden, July 17-22, 2005), and orally presented.

[13] Franco A.A., P. Schott, C. Jallut et B. Maschke; *Un Modèle Multiéchelle Dynamique d'une Electrode de PEFC*. Proceedings and orally presented in the JDMACS 2005 (Lyon, September 5-9, 2005).

[14] Franco A.A., P. Schott, C. Jallut et B. Maschke; *Modelling an Electrochemical Interface Dynamics using the Displacement Current and a Time Varying Dipolar Density*. Presented in the 10th International Conference on Electrified Interfaces (Spa, July 11-16, 2004).

[15] Franco A.A., P. Schott, C. Jallut et B. Maschke; *Modelling an Electrochemical Interface Dynamics using the Displacement Current and a Dynamic Dipolar Layer*. Presented in the Computational Electrochemistry Workshop (Santorini, September 26-29, 2004).

Appendix IV

My papers selection

In this Appendix, I present a selection of my papers published in peer-reviewed international journals. But the reader is very welcome to consult my published papers not included here.

Metallofullerenes as fuel cell electrocatalysts: A theoretical investigation of adsorbates on $C_{59}Pt$

Margaret A. Gabriel,[ab] Luigi Genovese,[c] Guillaume Krosnicki,[b] Olivier Lemaire,[b] Thierry Deutsch[a] and Alejandro A. Franco*[b]

Received 22nd December 2009, Accepted 17th May 2010
First published as an Advance Article on the web
DOI: 10.1039/b927111b

Nano-structured catalyst degradation in state-of-the-art polymer electrolyte membrane fuel cells (PEMFCs) is one of the main shortcomings that limit the large-scale development and commercialization of this technology. During normal operating conditions of the fuel cell, the PEMFC lifetime tends to be limited by coarsening of the cathode's Pt-based catalyst and by corrosion of the cathode's carbon black support. Because of their chemical properties, metallofullerenes such as $C_{59}Pt$ may be more electrochemically stable than the Pt/C mixture. In this paper we investigate, by theoretical methods, the stability of oxygen reduction reaction (ORR) adsorbates on the metallofullerene $C_{59}Pt$ and evaluate its potential as a PEMFC fuel cell catalyst.

1. Introduction

Although platinum is an effective catalyst for the 'hydrogen oxidation reaction' (HOR) and the 'oxygen reduction reaction' (ORR) in Polymer Electrolyte Membrane Fuel Cells (PEMFCs), it is also an expensive one. Besides the cost, traditional electrodes also have stability problems associated with Pt 'dissolution', Pt 'ripening',[1,2] and erosion of the carbon black support[3] during fuel cell operation. The ORR, on the commonly used Pt/carbon black catalyst, is slow compared to the Hydrogen Oxidation Reaction.[4] Thus, it is an ongoing interest of the fuel cell community to reduce or even replace the platinum used in fuel cell electrodes.

Alloying Pt with some transition metals has been shown to improve the specific activity and stability of PEMFC electrodes, with the advantage of lower global Pt loadings. In particular, Pt-Co nanomaterials have been widely studied and show enhanced ORR activity and better stability than pure Pt materials.[5–7]

Metallofullerenes have also been suggested as alternative catalysts with ultralow Pt loading.[8] Since a fullerene is quite stable, a metallofullerene might be stable enough to reduce the carbon corrosion, while still allowing catalytic activity on the metal atom(s). Metallofullerenes consist of endofullerenes, heterofullerenes, and exofullerenes. Platinum metallofullerenes exist as heterofullerenes and exofullerenes. $C_{59}Pt$, a heterofullerene which can be manufactured by laser ablation,[9,10] is essentially a C_{60} molecule that has had one of its carbon atoms replaced by a platinum atom.

The HOR mechanism is well understood on PEMFC platinum-bulk or platinum nanoparticle catalysts, but the ORR is still poorly understood. Several mechanisms for the ORR have been proposed, including the 'Damjanovic mechanism'[11–13] as well as a mechanism that has H_2O_2 as an intermediate.[14,15] H_2O_2 is an undesirable intermediate, however, as it chemically attacks the ionomer and membrane in the PEMFC.[15]

Previous work by Jacob *et al.*,[16–19] Balbuena *et al.*,[20,21] and by Michealides and Hu[22,23] has investigated ORR adsorbates and the formation of water on platinum clusters. In this paper, we adopt a similar methodology to investigate the ORR mechanism on $C_{59}Pt$ to help evaluate its feasibility as a PEMFC catalyst. Under the assumption that the ORR occurs through intermediate species adsorbing onto the $C_{59}Pt$ molecular surface, stable structures for these intermediates are found through density functional theory (DFT) calculations. Interpretation of the results and their consequences on the expected $C_{59}Pt$ activity towards the ORR is discussed.

2. Methodology

A single metallofullerene was used in these calculations. Every adsorbate was placed on the molecular surface at several different places and the structure was minimized with DFT. The lowest energy adsorbate–metallofullerene structure is what is reported here. Spin states were checked.

The DFT calculations were done in BigDFT,[24,25] which is based on Daubechies wavelet functions.[26] The basis set is systematic and is controlled by one parameter, the grid size. Based on the scaling property of wavelets, two levels of resolutions (a fine and a coarse grid) are used to adapt the mesh of the basis set in order to describe the wavefunctions. Two parameters (fine and coarse radius multipliers) control the adaptivity of the mesh around each atom. The extension of the fine (coarse) mesh around each atom is calculated by multiplying the fine (coarse) radius multiplier by a value that depends on the energy of the highest occupied state for each

[a] *INAC/SP2M/L_Sim, Commissariat à l'Energie Atomique et aux Energies Alternatives (CEA)-Université Joseph Fourier, 17 rue des Martyrs, 38054 Grenoble cedex 9, France*
[b] *DRT/LITEN/DEHT/LCPEM, Commissariat à l'Energie Atomique et aux Energies Alternatives (CEA), 17 rue des Martyrs, 38054 Grenoble cedex 9, France*
[c] *European Synchrotron Radiation Facility, 6 rue Horowitz, BP 220, 38043 Grenoble, France*

isolated atom. The BigDFT results of model systems, like methane and cyclobutane, have been favorably compared to plane wave results.[29]

Hamann–Goedecker–Hutter GGA norm-conserving pseudopotentials,[27] optimized for use with the exchange-correlation functional of Perdew, Burke, and Ernzerhof,[28] were used in these calculations. The platinum atom was described by a semicore ($5g^{-}$ + 18) pseudopotential, which has 8 electrons more than the non-semicore pseudopotential, but can be adequately described with a reasonable grid size since the mesh is adaptive. A grid size of 0.40 bohr was used, while the fine radius multiplier for the atoms was 9 and the coarse radius multiplier was 5. Additionally, the formation energy for $C_{60}Pt$ has been compared for three different functionals within BigDFT. The formation energy for PW91[28] was within 0.13 eV of the results presented in Section 3.1.1 and the results for PBE0,[30] a hybrid functional, were about 0.79 eV more endothermic. Since the PBE0 calculations are not necessarily more accurate for the systems studied here, and they are considerably slower, PBE96 has been used.

A manual search, in conjunction with minima hopping,[31–33] allowed the best sites for ORR adsorbates such as OH, water, and OOH to be found. Minima hopping uses short molecular dynamics runs to try to find new lower potential minima, which may not be minima that would be found by a manual search of possible adsorbate sites.

Electric field and solvation effects, which would be present in a fuel cell, are not discussed in this article, as the DFT calculations are intended to be used as input into a statistical mechanics based model of the electrochemical interface in a fuel cell,[34] which is itself used in a full multiscale model of a fuel cell.[35]

3. Results

3.1 The stability of $C_{60}Pt$

All of the carbon atoms are equivalent in C_{60} and, as Fig. 1b shows, are involved in two [6:5] bonds and one [6:6] bond. A [6:5] bond divides a 6-membered ring from a 5-membered ring and, likewise, a [6:6] bond divides two 6-membered rings. There is only one possible way to replace a carbon atom with a platinum atom to form $C_{60}Pt$.

After this substitution was done, this $C_{60}Pt$ molecule was

(a) (b)

Fig. 1 C_{60}, where (a) is a three-dimensional view and (b) is a projection of several rings in the structure. The central carbon shown is at the center of two 5-membered rings and one 5-membered ring.

allowed to relax. The area around the Pt atom was puckered outwards (Fig. 2a), as demonstrated by the slight 'cage radius'[1] increase from 3.55 Å in C_{60} to 3.58 Å in $C_{60}Pt$.† The puckering is also shown by the lengthening of bonds. The [6:5] bond length between the Pt and C is 1.97 Å and the [6:6] bond lengths between the Pt and C are shorter, 1.93 Å. In C_{60}, typical [6:5] C–C bond lengths are 1.45 Å and typical [6:6] C–C bond lengths are 1.40 Å. Only two other bonds noticeably lengthened and they were part of the 6-membered rings of which the platinum was a part. Otherwise, the fullerene bonds are essentially unchanged.

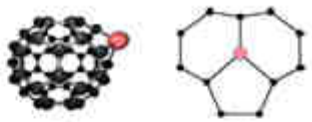

(a) (b)

Fig. 2 $C_{60}Pt$, where (a) is a side view of the Pt which shows how the metallofullerene is 'puckered', and (b) is a projection of the front view and only includes the structure immediately around the gray platinum atom. The platinum is at the center of two 6-membered rings and one 5-membered ring.

This structure compares well to previous theory papers.[9,10,15,36] Chiangpeng *et al.*[36] studied several metallofullerenes, not including platinum, by using the local spin density approximation and found structures similar to what other studies, including this one, find for a platinum heterofullerene. Poblet *et al.*,[10] Hayashi *et al.*,[9] and Campanera *et al.*[37] used DFT within various versions of the program ADF.[27,38]

3.1.1 The formation of $C_{60}Pt$.

The formation energy, E_f, of $C_{60}Pt$ is obtained using the reaction below

$$C_{60} + Pt_{triplet} \rightarrow C_{60}Pt + C_{triplet} \quad (1)$$

in order to yield the equation

$$E_f = E_{C_{60}Pt} + E_C - E_{C_{60}} - E_{Pt} \quad (2)$$

for E_f, which was found to be 5.76 eV. $E_{C_{60}Pt}$ and $E_{C_{60}}$ are the total energies for those molecules in the singlet state and E_C and E_{Pt} are the energies for a single atom in the triplet state. The value of 5.76 eV compares well to the formation energy of 5.24 eV found by Hayashi *et al.*,[9] but both values indicate a highly endothermic formation reaction and thus it is energetically preferable for the species to exist as C_{60} and Pt. This explains why high energy densities (like laser ablation) are required to produce this kind of material.

However, a large energy barrier is likely present that prevents the $C_{60}Pt$ from breaking its Pt–C bonds. The energy to break a Pt–C bond should be over 2 eV,[40,41] so $C_{60}Pt$ would not be expected to attain enough energy in the normal operation of the fuel cell (around 350 K in a low temperature PEMFC) to break these bonds. This is supported by the DFT calculations in which there was no sign of the platinum atom breaking its bonds, even when minima hopping was done. The apparent high barrier for the dissolution of this

† 'Cage radius' is defined as the average distance of every atom in the cage from the cage center.

metallofullerene suggests that it could remain stable in a low-temperature PEMFC.

3.2 Adsorption intermediates

The stability of each ORR intermediate was investigated on a single $C_{59}Pt$ molecule and the enthalpies found for the most stable structures are tabulated in Table 1. Both manual searches, where the adsorbate was placed at various sites on the molecular surface, and minima hopping were done. The adsorbates investigated were the H atom and the OH, OOH, O_2, and H_2O molecules.

3.2.1 Hydrogen atom. The sites investigated for the hydrogen atom included sites on the side of the molecular surface opposite of the Pt, sites around the Pt, and sites on the Pt. After relaxation, even if the hydrogen atom was started in the middle of a bond or ring, the hydrogen was on top of a carbon atom or near the platinum, with one high energy exception. This is consistant with calculations done for graphite and graphene.[42] Like in graphene, the carbon atom nearest the hydrogen adsorbate is puckered above the molecular surface, but, since the surface is hard to define in a fullerene, this is shown by the lengthening of 0.08 to 0.1 Å for the bonds of this carbon atom.

When the hydrogen was on top of a carbon that was on the reverse side of the fullerene or was on top of a carbon atom that was a next-nearest neighbor to the platinum, the binding energy ranged from 1.94–2.18 eV (Fig. 4c and 4d). When the hydrogen was on top of the carbon of the Pt-C [6:5] bond, the binding energy ranged from 2.32–2.42 eV (Fig. 4b). If the hydrogen was partially on top of the platinum, its binding energy ranged from 2.49–2.68 eV (Fig. 4a). However, the most stable binding site (Fig. 3) found for hydrogen was on top of the carbon involved in the Pt-C [6:6] bond, at a C–H distance of 1.11 Å, and this energy was 2.95 eV. The enthalpies and some distances for all of the structures attempted can be seen in Fig. 3. The most stable structure found by Jacob[18] on pure Pt clusters was an on-top site with an energy of 2.73 eV and a Pt-H distance of 1.54 Å.

The strong hydrogen adsorption, even on the reverse side of the metallofullerene, has implications for the PEMFC HOR and hydrogen storage,[43] especially for 'hydrogen spillover'.[44] Any hydrogen atoms, produced by a dissociative adsorption of molecular hydrogen on the $C_{59}Pt$ molecular surface, will not be easily released from the metallofullerene molecular surface. The hydrogen atoms (adsorbed protons) will likely have difficulty participating in the ORR reactions or being actually utilized as a fuel.

Table 1 Reaction enthalpies for possible ORR reactions. The binding energy is the negative of the adsorption energy. OH and H, in particular, have such strong binding tendencies, that they may poison the catalytic sites

System	Enthalpy (eV)
$OH_{(gas)} + s \rightarrow OH_{s(ads)}$	−3.43
$H_2O_{(ads)} + s \rightarrow H_2O_{s(ads)}$	−0.56
$OOH_{(gas)} + s \rightarrow OOH_{s(ads)}$	−1.98
$O_{2(gas)} + s \rightarrow O_{2s(ads)}$	−1.71
$H_{(gas)} + s \rightarrow H_{s(ads)}$	−2.95

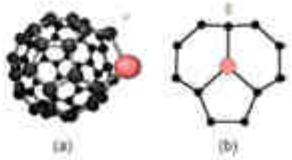

Fig. 3 Two most stable H adsorption sites on $C_{59}Pt$, where (a) shows a three-dimensional side view of the most stable adsorption site and (b) shows a projection of the area around the Pt atom (dark grey). The two H sites (light grey) are above the C involved in the Pt-C [6:6] bond. The carbon atoms are in black and the projection is made onto the plane formed by the three carbon atoms neighboring the platinum, in the more stable structure. The two structures differ in energy by only 0.03 eV.

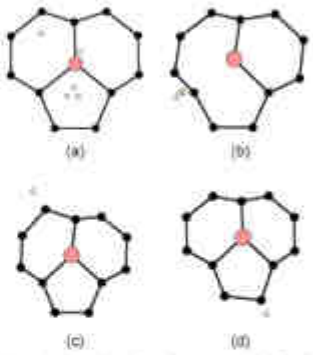

Fig. 4 Projections for other sites that were tried for the hydrogen atom. Every set of hydrogen atoms is projected onto the metallofullerene structure for the most stable adsorbate in the set. The binding energy ranges are: (a), 2.49 to 2.68 eV; (b), 2.32 to 2.42 eV; (c), 2.18 eV; and (d), 1.94 eV. The adsorbate sites found on the reverse side of the metallofullerene are not shown here. The less stable sites also have caused the most structural distortion around the platinum atom.

3.2.2 OH. The hydroxyl group was also tested on several sites, both near the platinum atom and on the reverse side of the metallofullerene. The most stable site (Fig. 5) found had the oxygen on top of the platinum, with the hydrogen atom pointed towards the 5-membered ring. The OH bond length was 0.97 Å and the oxygen was 1.96 Å above the platinum. Another structure, with the hydrogen pointing slightly upwards, was only 0.13 eV less stable. The optimal structure is actually quite similar to that found for OH on a Pt cluster[16] and OH on C_{60}.[45] In the Fidati *et al.* article, the OH is also on top of an atom (carbon, in this case) and also points slightly up and towards a 5-membered ring.

In the article by Jacob on Pt clusters, the OH is on top of a Pt atom and the hydrogen is pointing towards an fcc triangle. He finds an OH distance of 0.97 Å and an Pt-O distance of 1.98 Å, both of which are close to the values for $C_{59}Pt$ found in our calculations. His value of 105.4° for the Pt-O-H angle is close to the angle of 109.9° found for $C_{59}Pt$. However, the adsorption energy for the most stable site in $C_{59}Pt$ is 3.37 eV,

Fig. 5 OH on $C_{59}Pt$. The OH is effectively on top of the Pt atom and will tend to block other adsorbates from binding near the Pt, especially since the OH has such a strong binding energy. The colors and projection method are the same as in Fig. 3. Oxygen is shown in medium gray.

considerably larger than Jacob's value of 2.04 eV. Both of these energies are so much larger than kT at the normal low temperature PEMFC operating temperatures (T = 313–353 K), that OH would not be expected to easily desorb from the molecular surface.

3.2.3 Water. The most stable water adsorption site found (Fig. 6) has the oxygen above the platinum, but not quite on top. The hydrogen atoms point away from the platinum and between some of the 6-membered carbons. The H–O–H angle is 102.1° and the OH distances are 1.00 and 0.97 Å. The Pt–O distance is 2.30 Å and the Pt–O–H angles are 95°. For a Pt cluster, Jacob finds a Pt–O distance of 2.39 Å, an H–O–H angle of 105.1°, and OH distances of 0.97 Å. The Pt–O–H angles are 94 and 98° on the Pt cluster. The adsorption energy for Jacob's on-top site is 0.60 eV while Michaelides and Hu[42] find that at low water coverage on a Pt cluster, the water also prefers to have the oxygen on an on-top site with an adsorption energy of 0.34 eV. The adsorption energy for water on $C_{59}Pt$ was 0.56 eV and this is consistent with the numbers found by these other researchers.

C_{60} is almost completely insoluble in polar or hydrogen bonding solvents,[46] including water.[47] Consistent with this, the binding energies for water on the reverse side of $C_{60}Pt$ were repulsive.

3.2.4 OOH. The hydroxyl adsorbate sites were primarily obtained by minima hopping. The most stable structure (Fig. 7) had an adsorption energy of 1.98 eV. One of its oxygens is on top of the Pt, the second oxygen is over the 5-membered ring, and the hydrogen atom points towards the fullerene. The O–O–H angle is 101.9° and the Pt–O–O angle is 125.2°. The O–O distance is 1.47 Å and the O–H distance is 0.98 Å. The distance between the platinum and the on-top oxygen is 1.96 Å.

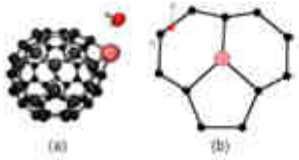

Fig. 6 Water on $C_{59}Pt$. The colors and projection method are the same as in in Fig. 3. Oxygen is shown in medium gray.

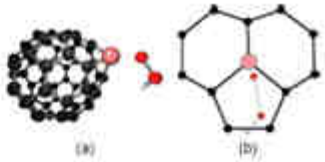

Fig. 7 OOH on $C_{59}Pt$. This molecule is on top of the Pt and will tend to block catalytic activity. It is also a rather bulky molecule and blocks the 5-membered ring. The colors and projection method are the same as in Fig. 3. Oxygen is shown in medium gray.

Jacob finds similar numbers for OOH on a Pt cluster, as do Ma and Balboena.[28] However, unlike OOH on $C_{59}Pt$, OOH in these Pt cluster calculations is almost planar to the surface. The adsorption energy found by Jacob is 1.03 eV.

An OOH on $C_{60}Pt$ structure was found that was only 0.09 eV less stable and it is quite similar in its distances and angles to the most stable structure discussed above, except for the Pt–O distances. It has the O–O bond perpendicular to the Pt–C [6:6]-bond. So, the Pt is almost equidistant to both oxygen atoms, with distances of 2.06 and 2.36 Å. A third structure, an additional 0.05 eV less stable, is very similar to the most stable one and is in almost the same position above the fullerene.

3.2.5 Molecular oxygen. The most stable O_2 adsorbate site (Fig. 8) found had one of its oxygen atoms on the [6:6]-carbon and the other pointing towards the platinum atom. However, the O_2 was not aligned with the Pt–C [6:6] bond, but at an angle to this bond. This structure had an adsorption energy of 1.71 eV. The C–O distance was 1.41 Å and the O–O distance was 1.53 Å while the distance between the platinum atom and the nearest oxygen was 2.06 Å. The Pt–O–O angle was 83.0° while the C–O–O angle was 96.3°.

The most stable molecular oxygen structure Jacob found had the oxygen molecule along the bond between two platinum atoms with an adsorption energy of 0.49 eV.

4. Discussion: reactivity in a fuel cell

The calculations of adsorbate structures and enthalpies can be used to help understand what might happen during fuel cell operation. The enthalpies of the reactions discussed in this section can be found in Table 2.

Fig. 8 O_2 on $C_{59}Pt$. The O_2 is not in an ideal position to react with gaseous hydrogen to form OOH. The colors and projection method are the same as in Fig. 3. Oxygen is shown in medium gray.

Table 2 Reaction enthalpies for possible ORR reactions. The only reactions shown that are endothermic involved adsorbed H, which may be able to poison the catalytic surface

System	Enthalpy (eV)
$O_{2(ads)} + H_{(gas)} \rightarrow OOH_{(ads)}$	−2.51
$OOH_{(ads)} + H_2O_{(gas)} + 2s \rightarrow 3\ OH_{(ads)}$	−4.38
$H_{(ads)} + OOH_{(ads)} \rightarrow 2\ OH_{(ads)}$	−3.23
$OH_{(ads)} + H_{(gas)} \rightarrow H_2O_{(ads)}$	−2.36
$O_{2(ads)} + H_{(ads)} \rightarrow OOH_{(ads)} + s$	0.45
$O_{2(ads)} + H_{(gas)} \rightarrow OOH_{(ads)}$	−2.51
$O_{2(gas)} + H_{(ads)} \rightarrow OOH_{(ads)}$	−1.26
$OH_{(ads)} + H_{(ads)} \rightarrow H_2O_{(ads)} + s$	0.60
$OH_{(ads)} + H_{(gas)} \rightarrow H_2O_{(ads)}$	−2.36

Q3 Table 3 The energies and structural parameters for all H on $C_{59}Pt$ calculations are described in this table. Every calculation refers to the projection describing the position of the hydrogen atom, with the exception of the calculations on the reverse side of the metallofullerene, for which a projection was not done. Two of the values for the metallofullerene reverse side were on top of a carbon atom. The third value for the metallofullerene reverse side was above a 6-membered ring

Q4 Hydrogen run	$E_{binding}$ (eV)	Pt–H (Å)	C–H (Å)
Not shown	−0.14	8.93	2.43
4d	1.94	3.35	1.11
Not shown	2.12	8.63	1.11
Not shown	2.14	8.03	1.11
4c	2.18	3.47	1.11
4b	2.32	2.34	1.12
4b	2.38	2.32	1.13
4b	2.39	2.36	1.12
4b	2.40	2.47	1.11
4b	2.40	2.35	1.12
4b	2.42	2.52	1.11
4a	2.49	1.70	3.14
4a	2.51	1.66	2.33
4a	2.59	1.64	2.46
4a	2.65	1.67	2.80
4a	2.68	1.65	2.57
3b	2.92	2.45	1.12
3b	2.95	2.60	1.11

4.1 Adsorbates and reactions

Every adsorbate studied had a strongly exothermic adsorption energy. Since all but the H atom preferred sites on or near the Pt atom, this indicates that these substances could poison the catalyst. The large binding energies also strongly suggest that the most likely way to remove the adsorbates from the fullerene is to have them react to form water. In fact, water has the weakest binding energy of all of the adsorbates studied.

H and OH seem like the most likely poisoners of the fullerene catalytic surface, as they have highly exothermic adsorption energies on the Pt atom and, for the H, on the carbon atoms. The ability of H to poison the metallofullerene depends on the concentration of H available in the physicochemical environment and this may not be high enough to completely occupy the molecular surface, especially given the fullerene–water repulsion, as discussed below. Since there may not be enough H to occupy the molecular surface sites, it is possible there may be other adsorbates with which the hydrogen can react. Unfortunately, probable ORR reactions involving adsorbed hydrogen to form OOH or H_2O are endothermic (0.45 and 0.60 eV, respectively). Similar reactions involving gaseous hydrogen are exothermic (−2.51 and −2.36 eV, respectively), though slightly less exothermic than the adsorption of hydrogen. These reactions with gaseous H may allow the ORR to proceed, however. A reaction involving gaseous oxygen and adsorbed hydrogen to form adsorbed OOH is exothermic by −1.26 eV, and this may also allow the ORR to proceed. However, there will probably be significant reorganization of the metallofullerene molecular surface in order to allow this reaction to occur, which implies a potential energy barrier. Adsorbed hydrogen can also be involved in a reaction with adsorbed OOH to form OH, which is a highly exothermic reaction (−3.23 eV), but this is probably not fast enough to get rid of the adsorbed hydrogen and the ORR will be slowed down. Additionally, adsorbed OOH must already exist for this reaction to happen.

OH has the strongest binding energy of the adsorbates studied. It is still less likely than hydrogen to poison the catalytic surface since there are less sites for it, and, to produce OH, there must be several precursor reaction steps. The most likely method of getting rid of the OH on the molecular surface is by a reaction with gaseous hydrogen, but as mentioned previously, hydrogen adsorption has a more favorable enthalpy.

In Fig. 9, one example of a potential reaction path is shown. This is a mechanism commonly used to describe the ORR on a platinum-based catalyst and is presented here in order to analyze the pathway on this metallofullerene. Every reaction step, except for the desorption of water from the catalyst, is highly exothermic. However, barriers are expected in between every one of these reaction steps. There are not enough catalytic sites in this metallofullerene to allow for an efficient series of reactions, and the available sites are expected to be far apart. Also, the adsorbates would need to move about the molecular surface in order for the reactions to proceed.

Water has a slight preference to be adsorbed rather than gaseous which may slow down the overall ORR reaction, as it occupies reaction sites. However, in the 'Damjanovic mechanism', water is one of the reactants, so the adsorbed water can be used up that way. The reaction of water vapor with OOH to form three adsorbed OH groups is highly exothermic (−4.38 eV), but the reaction with adsorbed water is still very exothermic (−3.83 eV) and is also energetically favorable. This

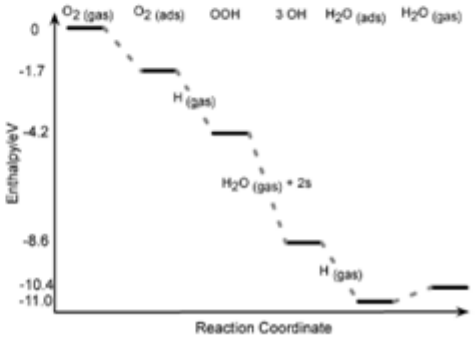

Fig. 9 One possible reaction pathway for the ORR.

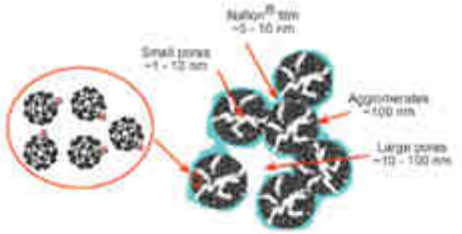

Fig. 10 Possible mesostructural view of a metallofullerene based PEMFC electrode where the inset is an artistic visualization of the active layer. The scale of the electrode is about 400 nm and the scale of the metallofullerene active layer visualization is about 20 Å.

reaction uses up to three sites, however, and is not likely to occur at a fast rate due to this. If the microstructure of a fuel cell metallofullerene-based electrode is similar to that of a platinum nanocluster-based electrode,[33] there will be pores in the material (Fig. 10). Liquid water allows protons to access these pores and a repulsive water–fullerene interaction may inhibit the access of these protons to the catalyst. This would negatively affect all fuel cell reactions.

5. Conclusions and further directions

The enthalpies for the multi-step ORR adsorbates on $C_{60}Pt$ were determined and the structures generally resemble that predicted for adsorbates on a platinum surface. The hydrogen atom was more strongly bound on a carbon atom near the platinum than on the platinum atom itself. Water was bound to the platinum atom with a binding energy of 0.56 eV, but had negative binding energies on the C_{60}-like reverse side of this metallofullerene, which is consistent with the insolubility of C_{60} in water.

Enthalpies for some possible ORR reactions were determined. As in platinum, it looks like the electrocatalytic sites will be poisoned by some of the adsorbates. In addition, because of the strong adsorption of the hydrogen to all parts of the fullerene, it seems that hydrogen may poison the electrocatalytic sites also. This will slow down the production of water on the PEMFC cathode.

These enthalpies, along with reaction barriers, estimates of vibrational entropies, and an estimate of catalytic surface area, can also be used as input into the multiscale kinetic model of Franco *et al.*[11] This can then be used to predict current–voltage curves that can be compared to experiments.[46]

Acknowledgements

This work was performed using HPC resources from GENCI-CINES (Grant 2009-x2009082232) and CEA-CCRT. M.A.G. acknowledges the CEA Nanoscience Program and French Project LN3M Project No. ANR-05-CIGC-003 for funding.

References

1 A. V. Virkar and Y. Zhou, *J. Electrochem. Soc.*, 2007, **154**, B540–B547.
2 A. A. Franco and M. Tembely, *J. Electrochem. Soc.*, 2007, **154**, B712–B723.
3 A. A. Franco and M. Gerard, *J. Electrochem. Soc.*, 2008, **155**, B367–B384.
4 S. Thomas and M. Zalbowitz, *Fuel Cells-Green Power*, Los Alamos National Laboratory, Los Alamos, New Mexico, USA, 1999.
5 A. Franco, S. Pasoot, P. Fugier, C. Arglade, E. Billy, L. Guetaz, N. Guillet, E. De Vito and S. Mailley, *J. Electrochem. Soc.*, 2009, **156**, B410.
6 S. Ball, S. Hudson, B. Theobald and D. Thompsett, *Electrochem. Soc. Trans.*, 2007, **11**, 1267.
7 S. Ball, S. Hudson, J. Hui Leung, A. Russell, D. Thompsett and B. Theobald, *Electrochem. Soc. Trans.*, 2007, **11**, 1247.
8 S. Silva, J. Perez, R. Torresi, C. Luengo and E. Ticianelli, *Electrochim. Acta*, 1999, **44**, 3565–3574.
9 A. Hayashi, Y. Xie, J. M. Poblet, J. M. Campanera, C. B. Lebrilla and A. L. Balch, *J. Phys. Chem. A*, 2004, **108**, 2192–2198.
10 J. M. Poblet, J. Munoz, K. Winkler, M. Cancilla, A. Hayashi, C. B. Lebrilla and A. L. Balch, *Chem. Commun.*, 1999, 493–494.
11 A. Damjanovic and V. Brusic, *Electrochim. Acta*, 1967, **12**, 615–628.
12 O. Antoine, Y. Bultel and R. Durand, *J. Electroanal. Chem.*, 2001, **499**, 85–94.
13 A. Franco, P. Schott, C. Jallut and B. Maschke, *Fuel Cells*, 2007, **07**, 99–117.
14 M. Tarasevich, A. Sadkowski and E. Yeager, *Comprehensive Treatise of Electrochemistry*, Plenum Press, 1983.
15 R. Borup, J. Meyers, B. Pivovar, Y. S. Kim, R. Mukundan, N. Garland, D. Myers, M. Wilson, F. Garzon, D. Wood, P. Zelenay, K. More, K. Stroh, T. Zawodzinski, J. Boncella, J. E. McGrath, M. Inaba, K. Miyatake, M. Hori, K. Ota, Z. Ogumi, S. Miyata, A. Nishikata, Z. Siroma, Y. Uchimoto, K. Yasuda, K.-i. Kimijima and N. Iwashita, *Chem. Rev.*, 2007, **107**, 3904–3951.
16 T. Jacob, *Fuel Cells*, 2006, **06**, 159–181.
17 T. Jacob and W. A. Goddard III, *J. Phys. Chem. B*, 2005, **109**, 297–311.
18 T. Jacob, B. V. Merinov and W. A. Goddard III, *Chem. Phys. Lett.*, 2004, **385**, 374–377.
19 T. Jacob, R. P. Muller and W. A. Goddard III, *J. Phys. Chem. B*, 2003, **107**, 9465–9476.
20 Y. Ma and P. B. Balbuena, *Chem. Phys. Lett.*, 2007, **447**, 289–294.
21 Y. Wang and P. B. Balbuena, *J. Chem. Theory Comput.*, 2005, **1**, 935–943.
22 A. Michaelides and P. Hu, *J. Am. Chem. Soc.*, 2001, **123**, 4235–4242.
23 A. Michaelides and P. Hu, *J. Chem. Phys.*, 2001, **114**, 513.
24 L. Genovese, A. Neelov, S. Goedecker, T. Deutsch, S. A. Ghasemi, A. Willand, D. Caliste, O. Zilberberg, M. Rayson, A. Bergman and R. Schneider, *J. Chem. Phys.*, 2008, **129**, 014109.
25 *BigDFT*, http://inac.cea.fr/L_Sim/BigDFT.
26 I. Daubechies, *Ten Lectures on Wavelets*, SIAM, Philadelphia, 1992.
27 C. Hartwigsen, S. Goedecker and J. Hutter, *Phys. Rev. B: Condens. Matter Mater. Phys.*, 1998, **58**, 3641–3662.
28 J. P. Perdew, K. Burke and M. Ernzerhof, *Phys. Rev. Lett.*, 1996, **77**, 3865–3868.
29 J. Perdew, in *Electronic Structure of Solids*, 1991.
30 J. P. Perdew, M. Ernzerhof and K. Burke, *J. Chem. Phys.*, 1996, **105**, 9982–9985.
31 S. Goedecker, *J. Chem. Phys.*, 2004, **120**, 9911.
32 S. Roy, S. Goedecker and V. Hellmann, *Phys. Rev. E: Stat., Nonlinear, Soft Matter Phys.*, 2008, **77**, 056707.
33 S. E. Schönborn, S. Goedecker, S. Roy and A. R. Oganov, *J. Chem. Phys.*, 2009, **130**, 144108–9.
34 A. A. Franco, P. Schott, C. Jallut and B. Maschke, *J. Electrochem. Soc.*, 2006, **153**, A1053–A1061.
35 J. M. Campanera, C. Ik, A. L. Balch, I. Perez and J. M. Poblet, *Chem.–Eur. J.*, 2005, **11**, 2730–2742.
36 D. Changgong, Y. Jinlong, C. Xiangyuan and C. Chan, *J. Chem. Phys.*, 1998, **111**, 8481–8485.

37 *ADF*, http://www.scm.com, SCM, Theoretical Chemistry, Vrije Universiteit, Amsterdam, The Netherlands.
38 G. te Velde, F. Bickelhaupt, S. van Gisbergen, C. Fonseca Guerra, E. Baerends, J. Snijders and T. Ziegler, *J. Comput. Chem.*, 2001, **22**, 931.
39 C. Fonseca Guerra, J. Snijders, G. te Velde and E. Baerends, *Theor. Chem. Acc.*, 1998, **99**, 391.
40 R. Kapadia, J. B. Pedley and G. B. Young, *Inorg. Chim. Acta*, 1997, **265**, 235–239.
41 H. Gross, C. T. Campbell and D. A. King, *Surf. Sci.*, 2004, **572**, 179–190.
42 Y. Ferro, F. Marinelli and A. Allouche, *J. Chem. Phys.*, 2002, **116**, 8124–8131.
43 K. Meletov, I. Tsilika, S. Assimopoulos, G. Kourouklis, S. Ves, I. Bashkin, V. Kulakov and S. Khasanov, *Phys. Status Solidi B*, 2001, **223**, 459.
44 P. C. Mitchell, A. J. Ramírez-Cuesta, S. F. Parker, J. Tomkinson and D. Thompsett, *J. Phys. Chem. B*, 2003, **107**, 6838–6845.
45 E. Fileti, R. Rivelino, F. de Brito Mota and T. Malaspina, *Nanotechnology*, 2008, **19**, 365703.
46 R. Ruoff, D. S. Tse, R. Malhotra and D. C. Lorents, *J. Phys. Chem.*, 1993, **97**, 3379–3383.
47 Y. Marcus, A. L. Smith, M. Korobov, A. Mirakyan, N. Avramenko and E. Stukalin, *J. Phys. Chem. B*, 2001, **105**, 2499–2506.
48 M. A. Gabriel, T. Deutsch, G. Krosnicki, O. Lemaire and A. A. Franco, in preparation.

ECS Transactions, 25 (24) 167-173 (2010)
10.1149/1.3316123 ©The Electrochemical Society

Towards a Multiscale Modeling Methodology for the Prediction of the Electro-activity of PEM Fuel Cell Catalysts

Rodrigo Ferreira de Morais[a,b], David Loffreda[b], Philippe Sautet[b] and Alejandro A. Franco[a]

[a] Commissariat à l'Énergie Atomique/DRT/LITEN/DTH/Laboratory of Components for Fuel Cells and Electrolyzers, and of Modeling (LCPEM), 17 rue des Martyrs, F-38054 Grenoble, cedex 9 (France) - E-mail corresponding author: rodrigo.ferreira-de-morais@cea.fr
[b] Université de Lyon, Institut de Chimie de Lyon, Laboratoire de Chimie, Ecole Normale Supérieure de Lyon and CNRS, 46 Allée d'Italie, F-69364 Lyon, France
E-mail corresponding author: ferreira.de.morais@ens-lyon.fr

In this study, density functional theory (DFT) calculations are presented for molecular and atomic oxygen adsorption on the Pt(111) surface at low coverage. The final goal is the atomistic description of oxygen dissociation kinetics in order to feed a multiscale kinetic model which simulates the Polymer Electrolyte Membrane Fuel Cell (PEMFC) electrochemical behavior. For molecular oxygen, the most favorable adsorption structure is top-top and shows an adsorption energy of -0.80 eV in agreement with previous studies. For atomic adsorption, only the threefold fcc and hcp hollow sites are stable at this coverage (-1.22 eV and -0.85 eV, respectively), in contrast with previous results.

1. Introduction

The current limitations of the present PEMFC technologies which restrict their economical viability are essentially the cost of the catalyst and its stability. The reference pure metal catalyst for PEMFC cathodes is Pt since it exhibits the highest electrocatalytic activity for the oxygen reduction reaction (ORR) [1]. Despite the progresses on reducing the amount of Pt, the typical loading still remains high and costly for widespread electrodes marketing. For this reason, Pt-M alloy nanoparticles (with M being a transition metal element) have been proposed as an alternative material to solve this question. Some bimetallic (PtCo, PtNi) systems exhibit an enhanced activity for ORR and a better stability compared to pure Pt [2, 3]. Up to now the fundamental reasons of such an improvement have not been elucidated from a kinetic point of view and only a few theoretical investigations have tackled the question of the ORR kinetics on pure Pt [4-9] and Pt alloys [4, 10, 11] at the atomistic level. The main theoretical efforts (reaction pathways and activation barriers) have been oriented towards the study of the oxygen dissociation on pure Pt catalyst modeled either by Pt cluster models or by periodic surfaces. However, a complete description of ORR kinetics for pure Pt and PtNi surfaces is still missing and the influence of the morphology of the nanoparticles onto kinetics is not solved yet.

The purpose of this work is the elaboration of a multiscale methodology to address the key questions of PEMFC for various pure Pt and PtNi catalysts. In a first step, density functional theory (DFT) is used to describe the ORR at the atomistic scale. Then, the objective is the implementation of the corresponding atomistic kinetics into a microscale model that can collect all the elementary events, catalytic or not. The final aim is the comparison with the experimental results.

In the following, initial DFT results related to the oxygen dissociation on Pt(111) will be presented and discussed through the stability of the initial (molecular oxygen) and final

(atomic oxygen) adsorption states. The same approach is currently considered on the different alloy terminations of the $Pt_3Ni(111)$ surface, however the corresponding results will be published in a forthcoming full-length article.

2. Methodology

Our methodology to simulate the multiphysics and multiscale phenomena inside the PEMFC consists of two specific parts. The first one is the development of a complete data base of the rate constants for the elementary chemical and electrochemical reactions occurring on the fuel cell catalyst. This task is carried out with *ab initio* quantum calculations (using DFT method). The second one is the application of this data base into a multiphysics/multiscale kinetic model. This model, called MEMEPHYS, it has been developed during the last 8 years at CEA by Franco *et al.* [12]. The model is built in a multidisciplinary framework, using concepts of nonequilibrium thermodynamics and electrodynamics in order to scale up atomistic data into numerically coupled elementary kinetic models which allow simulating experimental observables (e.g. polarization curves, electrochemical impedance spectroscopy or cyclic voltammetry) [13-14]. MEMEPHYS model includes a detailed description of the nanoscale electrochemical interface between the catalyst and the electrolyte, accounting for the impact of the electrochemical reactions on its structure. To do so, two specific regions are simulated. The first one is called inner layer with the descriptions of the metal surface, where the adsorption of the intermediate reactions species of ORR or HOR, the water and the pollutants occurs. The second one, called diffuse layer, describes the diffusion of the ions and counter ions. From the descriptions of these two regions, embedded into a micro and mesoscale description of transport phenomena in the PEMFC Membrane-Electrodes Assembly, the model calculates the nanoscale surface potential (through the inner layer) and the electrodes potentials as function of the cell operating conditions (nominal current, temperature, relative humidity, reactant pressures).

The figure-1 shows the different scales inside the MEMEPHYS approach. This model can be used to simulate observable, and compare DFT calculations with experimental results. [4-6]

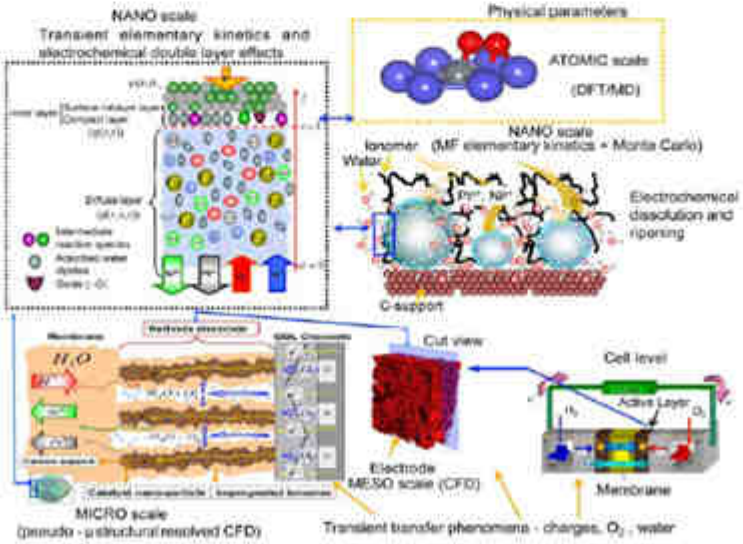

Figure 1: PEMFC multiscale model discussed in [12].

The DFT calculations are performed with the Vienna *Ab initio* Simulation Package (VASP) [15, 16]. The generalized gradient approximation (GGA) is used with the Perdew-Burke-Ernzerhof exchange-correlation functional [17] and the projector augmented-wave method (PAW) [18]. The plane-wave basis set expansion is limited at a cut-off of 400 eV. The coverage chosen here on the Pt (111) surface (1/12 ML) is associated with a $(2\sqrt{3}\times2\sqrt{3})$ supercell throughout the study. The numerical integration in the Brillouin zone is performed on a (3×3×1) Monkhorst-Pack k-point mesh [19]. The Pt surface is modeled by a periodic slab composed of five metal layers and a vacuum of 14 Å (Figure-2). Adsorption is considered only on one side of the slab. During all the geometry optimizations, the degrees of freedom of the adsorbate and the three uppermost metal layers are relaxed while the two lowest platinum planes are frozen in a bulk-like optimal geometry (Pt-Pt distance of 2.81 Å). Spin polarization is included in order to account for the open shell nature of the O_2 molecule.

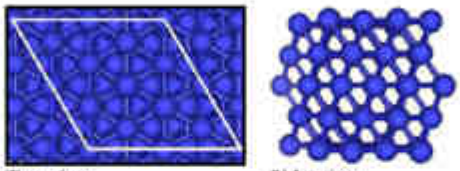

Top view Side view

Figure 2: Surface model and supercell to describe the Pt (111) surface, with 12 Pt atoms per layer.

3. Results and Discussion

Adsorption of atomic oxygen on Pt (111) – There are four possible high symmetry adsorption sites: one-fold top (T), two-fold bridge (B), three-fold fcc (F) and hcp (H) hollow sites. At coverage 1/12 ML the T and B sites are not stable, in contrast with previous articles [12]. From these sites, the oxygen atom diffuses to the hollow sites. Figure 3 shows the two possible stable sites at this coverage. These results are in qualitative agreement with previous publications [7, 20] using periodic boundary conditions (PBC) at a higher coverage ½ ML.

As usual, the adsorption energy of oxygen is obtained as follows:

(1) $$E_{ads} = E\,(N\times O/Pt) - N/2\;E(O_2\ gas) - E\,(clean\ Pt)$$

The fcc site is more stable than the hcp position with a stability gain of 0.37 eV (E_{ads}= -1.22 eV for fcc according to Table-1). This result agrees with P. Légaré's DACAPO value (-1.03 eV) [20] and with previous calculations at higher ¼ ML coverage (-1.08 eV) [21]. Other authors define the binding energy with a reference to a gas phase oxygen atom= -4.59 eV in Ref. [22] (1/9 ML), -3.88 eV in Ref. [11] (1/4 ML) and -3.73 eV in Ref. [9] (1/4 ML). In our case, we find -4.55 eV for 1/12 ML. For cluster models, the binding energy appears to be largely sensitive to the considered size (from -2.08 eV for $Pt_{6,3}$ to -4.20 eV for $Pt_{8,10,9}$ [23] and -3.37 eV for Pt_{35} [5]). If one excludes the weakening of the adsorption energy at high coverage [20, 22], the observed discrepancies between PBC and cluster models can be inferred to the systematic error (for PBC, the thickness of the slab, the choice of the GGA functional and for clusters, the spurious edge effects).

Table 1: Adsorption energy (eV), magnetic moment for O_2 (μB), O-O and Pt-O distances (Å) for O_2 and O adsorption and for coadsorption of 2O atoms on Pt (111). The coverage is 1/12 ML (or 1/6 ML for the coadsorption).

Molecular adsorption	E_{ads} (eV)	d(O-O) (Å)	d(Pt-O) (Å)	m_{O2} (μB)
TT	-0,80	1,36	(2,03; 2,03)	-0,93
TB fcc hollow site	-0,77	1,40	(2,18; 2,17; 2,02)	0,04
TB hcp hollow site	-0,63	1,39	(2,23; 2,22; 2,03)	0,01
Isolated atomic adsorption				
Fcc hollow site	-1,22	-	(2,05; 2,06; 2,06)	-
Hcp hollow site	-0,85	-	(2,06; 2,06; 2,06)	-
Atomic coadsorption				
F+F (TT dissociation)	-2,00	-	(2,07; 2,05; 2,05) (2,04; 2,07; 2,08)	-
F+F (TB fcc dissociation)	-2,22	-	(2,04; 2,08; 2,04) (2,08, 2,04, 2,04)	-
H+H	-1,56	-	(2,03; 2,08; 2,05) (2,08, 2,03, 2,05)	-

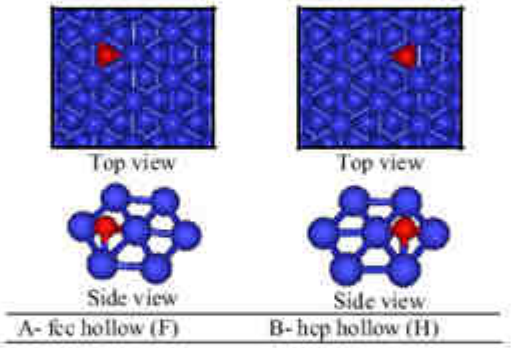

Figure 3: Atomic oxygen adsorption on a Pt (111) surface.

Adsorption of O_2 on Pt (111) – Different initial adsorption structures have been tested but among them only 3 are found stable (cf. Figure-4). The most stable adsorption structure TT (-0.80 eV), corresponds to a flat configuration of the oxygen molecule on the Pt surface where the two oxygen atoms are located close to two adjacent top sites. The two other forms TB(Pt_{fcc}) and TB(Pt_{hcp}) are metastable (-0.77 eV and -0.63 eV, respectively) and they are associated with a position in which one oxygen atom is located above a top site and the second one above a bridge position. These results are in quantitative agreement with Eichler *et al.* (-0.72 eV for TT, -0.68 eV for TB(Pt_{fcc}) and -0.58 eV for TB(Pt_{hcp}), at a coverage of ¼ ML with a ($\sqrt{3}\times2$) supercell) [12], in fair agreement with Xu *et al.* (-0.62 eV for TT, -0.61 eV for TB(Pt_{fcc}) and -0.45 eV for TB(Pt_{hcp}), at a coverage of ¼ ML with a (2×2) supercell) [11]. Low temperature scanning tunneling microscopy shows two types of species for O_2 adsorbed on Pt(111) [24], and from simulations of the STM images by M.-L. Bocquet *et al.* [21], these species have been assigned to the TT and the TB(Pt_{fcc}) structures in agreement with our present results.

Spin unrestricted calculations has been performed since O_2 in gas phase is paramagnetic. Between the three stable adsorption structures only TT presents a significant

magnetic moment (-0.93 μB). This result is twice what has been found by Eichler *et al* (0.4 μB for TT), but agrees with Bocquet *et al.* (0.89 μB). The other two stable sites have a magnetic moment close to zero.

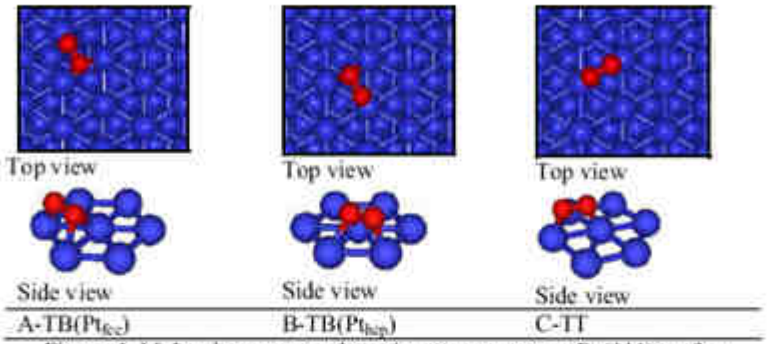

Figure-4: Molecular oxygen adsorption structures on a Pt (111) surface.

Coadsorption of two oxygen atoms on Pt (111) – In order to prepare the study of the dissociation of molecular oxygen, the possible coadsorption structures of two adjacent oxygen atoms have been examined. As it is shown on a Figure-5 three different configurations are possible by combining the stable and competitive adsorption sites F and H.

Starting from the TT structure for the molecular adsorption state, the dissociation might occur following a homolytic cleavage of the O-O bond on Pt and the pathway would end on a coadsorption state composed of two oxygen atoms sitting in fcc hollow sites (F+F from TT in Table-1). This process is exothermic (-1.20 eV). If now the TB(Pt$_{fcc}$) structure was considered for the initial geometry, the final dissociated state would be a coadsorption structure with adjacent oxygen atoms positioned in hcp hollow sites (H+H). The exothermicity is then smaller. In contrast, for a dissociation pathway starting from the second TB(Pt$_{hcp}$) structure, the final dissociated state would then correspond to a coadsorption of two fcc hollow sites (F+F from TB) with a larger exothermicity.

The coadsorption effect can be estimated by comparing the adsorption energy of the two adjacent oxygen atoms with the sum of the adsorption energy of the corresponding isolated adsorption sites. For F+F coadsorptions (from TT or TB), this difference is positive (0.11-0.22 eV/O atom), so it means that the coadsorption phenomenon is destabilizing in this case (repulsion through the Pt surface, since the two O atoms share a common Pt atom). For H+H, the situation is reverse. The difference becomes negative (-0.07 eV/O atom) meaning that the coadsorption is stabilizing in this case. Notice that here no Pt atom is shared between the two Pt$_3$ hollow sites.

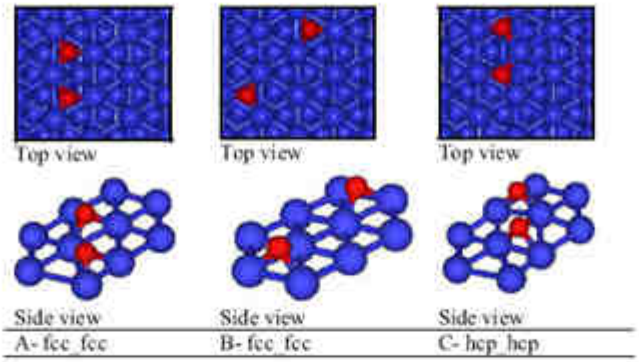

Figure-5: Coadsorption of 2 adjacent atomic oxygen atoms on Pt (111).

4. Conclusions

In this study, the molecular and atomic oxygen adsorption structures have been investigated on the Pt (111) surface at a low coverage on the basis of DFT calculations.

For the adsorption of atomic oxygen only, the threefold fcc and hcp hollow sites have been found stable at coverage 1/12 ML (top and bridge sites diffuse to hollow sites). In the case of molecular oxygen adsorption three competitive structures have been obtained in agreement with previous theoretical studies (TB(Pt_{fcc}), TB(Pt_{hcp}), TT). The investigation of the coadsorption states coming from oxygen dissociation shows a large variation for the thermicity of this reaction. According to Hammond principle, this means that the activation energy barrier must change significantly as a function of the coverage for the chosen pathway.

The next step of this study is the determination of the dissociation transition states in order to evaluate the kinetic rate constants at this atomistic scale.

Acknowledgments

This work is funded by the French National Research Agency (ANR) through the program "PAN-H", within the context of the project "MAFALDA" (ANR-08-PANH-014-02 contract). The authors thank IDRIS at Orsay, CINES at Montpellier and PSMN at Lyon, for CPU time and assistance (project 609).

References

1. J. K. Nørskov, J. Rossmeisl, A. Logadottir, L. Lindqvist, J. R. Kitchin, T. Bligaard and H. Jónsson, J. Phys. Chem. B, **108**, 17886 (2004).
2. Vojislav R. Stamenkovic, Ben Fowler, Bongjin Simon Mun, Guofeng Wang, Philip N. Ross, Christopher A. Lucas, Nenad M. Marković, Science **315**, 493 (2007).
3. Vojislav R. Stamenkovic, Bongjin Simon Mun, Karl J. J. Mayrhofer, Philip N. Ross, and Nenad M. Marković, J. Am. Chem. Soc., **128**, 8813 (2006).
4. Timo Jacob and William A. Goddard, Chem. Phys. Chem., 7, 992 (2006).

5. Timo Jacob, Fuel Cells, **6,** 159 (2006).
6. Timo Jacob and William A. Goddard III, J. Am. Chem. Soc., **126,** 9360 (2004).
7. A. Eichler, F. Mittendorfer, and J. Hafner, Phys. Rev. B, **62**(7), 4744 (2000).
8. Eichler, A.; Hafner, J. Phys. Rev. Lett., **79**, 4481 (1997).
9. Kandoi, S.; Gokhale, A. A.; Grabow, L. C.; Dumesic, J. A.; Mavrikakis, M. Catal. Lett., **93**, 93 (2004).
10. Timo Jacob and William A. Goddard, III, J. Phys. Chem. B, **108,** 8311 (2004).
11. Xu, Y.; Ruban, A. V.; Mavrikakis, M. J. Am. Chem. Soc., **126**, 4717 (2004).
12. A. A. Franco, R. Coulon, R. F. de Morais, S.-K. Cheah, A. Kachmar, M. A. Gabriel, J. Electrochem. Soc., **25** (1), 65-79 (2009).
13. Alejandro A. Franco, Pascal Schott, Christian Jallut, and Bernhard Maschke, J. Electrochem. Soc., **153,** A1053 (2006).
14. A. A. Franco, P. Schott, C. Jallut, and B. Maschke, Fuel Cells, **7,** 99 (2007).
15. G. Kresse and J. Hafner, Phys. Rev. B, **47**, RC558 (1993).
16. G. Kresse and J. Furthmüller, Phys. Rev. B, **54**, 11169 (1996).
17. J. P. Perdew, K. Burke, and M. Ernzerhof, Phys. Rev. Lett., **77,** 3865 (1996).
18. G. Kresse, D. Joubert, Phys. Rev. B, **59,** 1758(1999).
19. H. J. Monkhorst and J. D. Pack, Phys. Rev. B, **13,** 5188 (1976).
20. P. Légaré, Surface Science, **137**, 580 (2005).
21. M.-L. Bocquet, J. Cerdà, and P. Sautet, Phys. Rev. B, **59,** 15437 (1999).
22. Zhihui Gu and Perla B. Balbuena, J. Phys. Chem. C, **111,** 9877 (2007).
23. Timo Jacob, Richard P. Muller, and William A. Goddard, III, *J. Phys. Chem.*, **107**, 9465 (2003).
24. B. C. Stipe, M. A. Rezaei, W. Ho, S. Gao, and M. Persson, and B. I. Lundqvist, Phys. Rev. Lett. **78**, 4410 (1997).

ARTICLE IN PRESS

SOSI-11946; No. of Pages 4

Solid State Ionics xxx (2010) xxx–xxx

Contents lists available at ScienceDirect

Solid State Ionics

journal homepage: www.elsevier.com/locate/ssi

Multi-scale simulation of fuel cells: From the cell to the system

Max P. Eschenbach [a], Romain Coulon [a,b], Alejandro A. Franco [b], Josef Kallo [a], Wolfgang G. Bessler [a,c,*]

[a] German Aerospace Center (DLR), Institute of Technical Thermodynamics, Pfaffenwaldring 38-40, 70569 Stuttgart, Germany
[b] Commissariat à l'Energie Atomique (CEA), DRT/LITEN/DTH/LCPEM, 38000 Grenoble, France
[c] Universität Stuttgart, Institute of Thermodynamics and Thermal Engineering (ITW), Pfaffenwaldring 6, 70550 Stuttgart, Germany

ARTICLE INFO

Article history:
Received 31 August 2009
Received in revised form 15 June 2010
Accepted 17 June 2010
Available online xxxx

Keywords:
Multi-scale
Modeling
Simulation
Software
Fuel cell

ABSTRACT

In the current fuel cell modeling literature there is a gap between "physics-oriented" cell-level models and "application-oriented" system-level models. This paper presents a computational approach to close this gap by directly coupling cell-level and system-level simulation software. It allows to integrate a detailed description of electrochemistry and 2D transport into a system model within SIMULINK, allowing a direct feedback between system requirements and cell processes. By decoupling time scales between cell and system, the computational speed can be significantly enhanced. The method is applicable to both, polymer electrolyte fuel cells (PEFC) and solid oxide fuel cells (SOFC). Here, we show application in the context of PEFCs. Local membrane water management and electrochemical performance is made accessible on the system-level, where it can be used for visualization and control purposes.

1. Introduction

Modeling and simulation techniques are becoming increasingly important for both, understanding fundamental processes in fuel cells, and supporting design and optimization of fuel cell systems. Yet, there is a considerable gap in scales (both temporal/spatial scale and complexity scale) between fundamental models on one side and component models on the other side. Lower-scale models are usually "physics-oriented" and include detailed descriptions of electrochemical kinetics [1–3], transport processes (both gas-phase and liquid) [4,5] and structure [6]. Higher-scale models are "application-oriented" and use simplified (semi-)empirical descriptions for fuel cell and balance-of-plant components (e.g., blowers, heat exchangers, and humidifiers). System examples include fuel cell cars [7,8], hybrid power plants [9,10], and portable power systems [11]. In the fuel cell literature, there is so far only limited coupling between lower-scale and higher-scale models.

This paper describes and demonstrates a computational approach for a direct dynamical coupling of cell and system-level. It is based on a detailed description of electrochemistry and 2D transport using the in-house software DENS [12], component and system description using the commercial software SIMULINK, and a software interface that allows to couple the two codes. The approach accounts for the direct feedback between system requirements (e.g., load changes) and electrode processes. The method is applicable to both, polymer electrolyte fuel cells (PEFC) and solid oxide fuel cells (SOFC). Here we show application in the context of PEFCs.

2. Cell-level model

The two-dimensional model of the PEFC is shown schematically in Fig. 1. It represents transport along a single channel and through the thickness of the membrane-electrode assembly (MEA). The governing equations are given in Table 1. Gas-phase transport in anode and cathode channels is described by 1D Navier-Stokes equations. Membrane water management includes diffusion and electro-osmotic drag as formulated by Weber and Newman for a vapor-equilibrated membrane [4]. The dependence of transport coefficients on membrane humidity is calculated according to Weber and Newman (diffusion coefficient) [4] as well as Meier and Eigenberger (drag coefficient and proton conductivity) [13]. The partial differential equations are discretized via finite-volume techniques; the number of grid points used for the present study is 10×5 (along channel and through MEA).

The model is based on a number of simplifying assumptions (single-phase water transport, i.e., no occurrence liquid water; isothermal conditions; no transport losses in gas diffusion layers; and Butler-Volmer kinetics with constant exchange current density). These assumptions will be relaxed in future studies, although the model is already able to represent experimentally observed behavior (see below). It should be emphasized that, from a system-level view, the model is considerably more complex than what has been used in previous studies [14].

A comparison of cell-level model predictions with experimental single-cell measurements is shown in Fig. 2. The experiments were

* Corresponding author. German Aerospace Center (DLR), Institute of Technical Thermodynamics, Pfaffenwaldring 38-40, 70569 Stuttgart, Germany. Tel.: +49 711 6862 603.
E-mail address: wolfgang.bessler@dlr.de (W.G. Bessler).

0167-2738/$ – see front matter © 2010 Published by Elsevier B.V.
doi:10.1016/j.ssi.2010.06.041

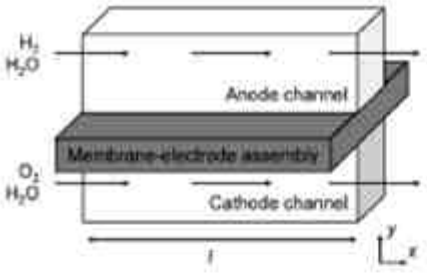

Fig. 1. Schematic representation of the two-dimensional PEFC cell-level model.

carried out on a 50 cm² single-cell with a multi-channel meander flow field at a pressure of 2 bar. A Nafion 112 membrane with in-house electrodes (platinum loading 0.8 g/cm²) was used. Exchange current densities of the Butler–Volmer equations used in the model were obtained via fit to experimental electrochemical impedance data (Zahner Electrochemical Workstation IM6; impedance data analyzed with an R(RC)(RC) equivalent circuit representing the two electrodes and the membrane resistance). The resulting agreement between simulated and experimental polarization behavior (Fig. 2) is good. The model-based analysis of polarization losses shows that the dominant losses originate from the cathode electrochemistry, which is in agreement with previous observation [15].

3. System-level model

In order to demonstrate the feasibility of the multi-scale coupling approach, a simple system-level model is used representing the single-cell test bench. The system-level model is shown in Fig. 3. Dynamic simulations were performed using galvanostatic loads, and a generic load profile was employed for test purposes. Since the cell-level model uses voltage as input, the galvanostatic load profile is transformed into a voltage signal via a proportional-integral (PI) controller. The current signal also enters the gas supply modules for lambda control of the fuel and air streams. Humidification is realized by temperature-dependent fourth-order saturation pressure correlations.

4. Multi-scale simulation

The cell-level model equations shown in Table 1 are implemented as C code in the in-house software DENIS [12]. For stationary (steady-state) simulations, all time derivatives are set to zero and the resulting equation system is solved with a Newton algorithm. For dynamical simulations, the equation system is time-integrated with adaptive time stepping using the implicit stiff solver LIMEX [16]. The system-level model is implemented in SIMULINK. Transient numerical solution of the model uses the explicit Bogacki–Shampine method as implemented in SIMULINK ("ode3"). A fixed time step of 0.5 s is used as a compromise between real-time capability and the steady-state assumption at each time step described below.

The coupling between cell and system levels is established via a SIMULINK system function ("S-function"). This software interface makes the full DENIS functionality available in SIMULINK block. Inputs to the block are gas inflow composition and rate at anode and cathode, temperature, pressure, cell voltage, and system time. The block returns gas outflow composition and rate, cell current and power, as well as spatially resolved cell properties such as local humidity.

It is important to note that the numerical solver on the cell-level runs independently of the system-level solver. This opens a computationally elegant way of decoupling time scales: While the system-level model is always solved dynamically, the cell-level model can be solved either dynamically or in steady-state mode. In the latter case, for each time step of the system-level model, the cell-level model provides a stationary solution for the respective input conditions. This allows a significant increase in computational speed. The requirement for using time-scale decoupling is that processes on the cell-level (electrochemical reactions, cell-scale transport) are fast compared to processes on the system-level (feedback of control loops, inertia of balance-of-plant components) and can be assumed in continuous equilibrium. For many system applications, this assumption holds true.

As a result of coupling two different solvers, processor multi-core usage is achieved. While standalone DENIS or SIMULINK applications are only able to run on a single core, coupling of the codes results in a increase in CPU usage without parallel implementation. Moreover, multiple DENIS blocks can be used within a single SIMULINK model, for example, representing multiple representative single-cells in a fuel cell stack.

Table 1
Summary of the governing equations of the cell-level model. See [12] for details and definition of symbols.

Gas-phase transport in supply channels (x dimension, anode and cathode)	
Continuity	$\frac{\partial \rho}{\partial t} = -\frac{\partial \rho v_x}{\partial x} + \frac{2h_{ch}}{A_{ch}} \sum_i \dot{r}_{\Gamma,i}$
Momentum conservation	$\frac{\partial \rho v_x}{\partial t} = -\frac{\partial \rho v_x^2}{\partial x} - \frac{\partial p}{\partial x} - \frac{2h_{ch}}{A_{ch}} \tau_w$
Species conservation	$\frac{\partial \rho Y_i}{\partial t} = -\frac{\partial \rho v_x Y_i}{\partial x} - \frac{\partial j_i^{diff}}{\partial x} + \frac{2h_{ch}}{A_{ch}} \dot{r}_{\Gamma,i} M_i$
Ideal gas law	$p = \rho R T \sum_i Y_i / M_i$
Electrode kinetics at the electrodes (anode and cathode)	
Butler–Volmer equation	$i = i^0 \left[\exp\left(\frac{0.5 z F \eta_{act}}{RT}\right) - \exp\left(-\frac{0.5 z F \eta_{act}}{RT}\right) \right]$
Activation overpotential	$\eta_{act} = \Delta\phi - \Delta\phi_{eq,ref}(T_{gas})$
Water management of polymer membrane (y dimension)	
Continuity	$\frac{\partial \lambda}{\partial t} = -\frac{(1+n_d)\, i}{z F \rho_{dry}} \frac{\partial \lambda_{y,0}}{\partial y}$
Drag and diffusion flux	$\lambda_{y,0} = \lambda_0 - \lambda_{d,0} + \left(-\frac{n_d \lambda_{y,0}}{\rho_{dry}} + \frac{\lambda_{y,0} \lambda_{d,0}}{\rho_{dry}} \frac{\rho_{dry}}{\rho_{d,0}} \right) \frac{n_d i}{z F D_\lambda \rho_{dry}}$
Potential distribution (y dimension)	
Cell voltage	$E = \phi_{mem,ca} - \phi_{mem,an}$
Potential step (anode and cathode)	$\Delta\phi = \phi_{mem} - \phi_{sol}$
Ionic charge transport (solid electrolyte)	$\frac{\partial}{\partial y}\left(\sigma_{sol} \frac{\partial \phi_{sol}}{\partial y}\right) = 0$

Please cite this article as: M.P. Eichenbach, et al., Multi-scale simulation of fuel cells: From the cell to the system, Solid State Ion. (2010), doi:10.1016/j.ssi.2010.06.041

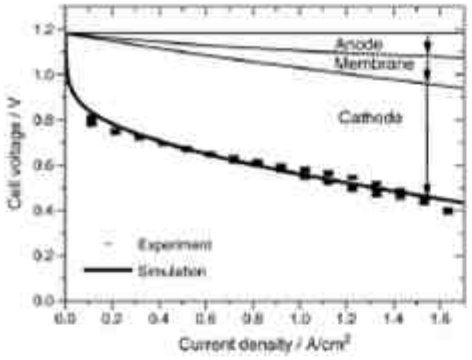

Fig. 2. Comparison of cell-level model predictions (including distribution of polarization losses) with experimental current–voltage characteristics of a single cell operated at 80 °C and 2 bar on fully humidified air and fully humidified H_2.

5. Results and discussion

Fig. 4 shows an exemplary load profile imposed by the system-level model, as well as the resulting voltage response and average membrane lambda value given by the cell-level model. The simulations shown here were performed for a pressure of 3 bar in order to reflect conditions of improved water management for elevated stack operating temperatures. The solid lines show the results for decoupled cell and system time scales (dynamic system-level solution, steady-state cell-level solution at each system-level time step). The dashed lines show the results for full dynamic coupling. On the scale of Fig. 4, the difference is not resolved for current and voltage profiles. Yet, there is a notable difference in membrane lambda at low load, showing the slow response of membrane water transport on load changes. Regarding simulation time there is a considerable difference between the two simulation modes. When decoupling time scales, the computational time is 11 min on a dual-core 2.66 GHz processor desktop computer for the 17 min physical time simulation

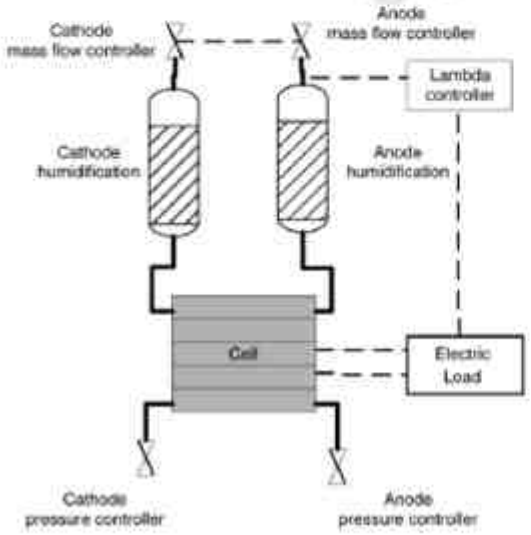

Fig. 3. Schematic representation of the fuel cell system-level model.

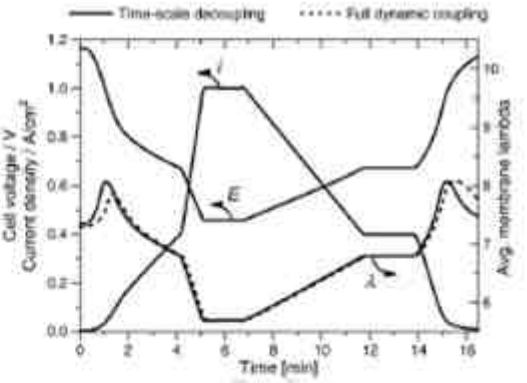

Fig. 4. Imposed load profile and current and average membrane lambda response for a generic load profile of 1000 s. Multi-scale simulations with decoupled time scales (solid lines, steady-state cell-level model) and full dynamic coupling (broken lines, dynamic cell-level model) are compared. Simulation parameters are $p = 3$ bar, $T = 80$ °C, constant dewpoint humidification (anode 80 °C, cathode 64 °C).

run, therefore meeting the demand of real-time capability. For the fully dynamic case, computational time is 45 min, with a considerable slow-down during strong gradients in the load profile due to the decreasing time stepsize of the cell-level solver.

Fig. 5 shows spatiotemporally resolved current density and water flux (color-coded) versus system time and position along the fuel cell channel simulated for full dynamic coupling. Both current density and water flux are quite inhomogeneous and strongly vary along the load profile. Further discussion is beyond the scope of the present paper.

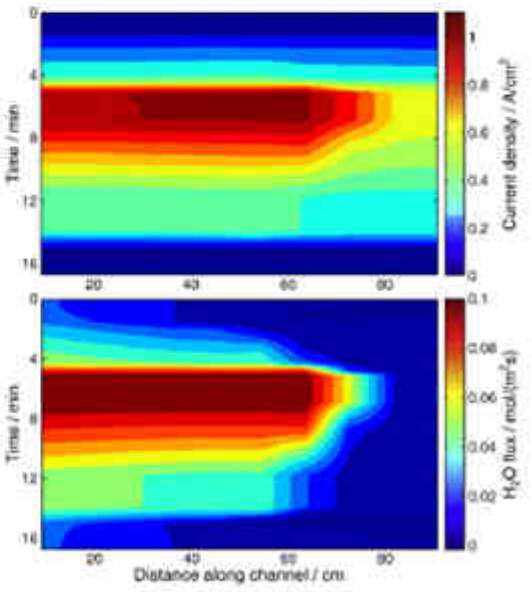

Fig. 5. Current density (a) and water flux through the MEA from anode to cathode (b) versus spatial position along the fuel cell channel and system time along the load profile shown in Fig. 4 (full dynamic coupling). Simulation parameters are $p = 3$ bar, $T = 80$ °C, constant dewpoint humidification (anode 80 °C, cathode 64 °C).

Please cite this article as: M.P. Eschenbach, et al., Multi-scale simulation of fuel cells: From the cell to the system, Solid State Ion. (2010), doi:10.1016/j.ssi.2010.06.041

The multi-scale approach gives a detailed insight into cell-level properties that are usually not available in system-level models. This has a number of advantages. For example, it is known from segmented-cell measurements [17] that fuel or oxygen starvation locally occurs at much higher voltages than what would be expected from global cell data. Only a control strategy based on spatially resolved models is sensitive towards local starvation or local membrane drying. Physically-based cell-level models also provide a basis for integration of micro-scale mechanisms, including electrode degradation or gas permeation. The latter has to be dealt with on the system-level regarding the control strategy of, for example, anode recirculation. Finally, model validation against experimental data can be extended to a much more detailed level since more data can be used for comparison (e. g., impedance measurements or outlet humidity sensors).

6. Conclusions

We have presented a computational approach for integrating detailed physically-based fuel cell models into system-level simulations with the commercial software tool SIMULINK. This allows to make critical cell information (e.g., local membrane water management in PEFCs) available on the system-level, which can be used for visualizing cell properties or for control purposes. Furthermore, the use of two independent numerical solvers allows the decoupling of time scales which increases computational speed by a factor of around four in comparison to full dynamic coupling. The approach will be used in future studies on PEFC-based fuel cell vehicles and SOFC-based hybrid power plants.

Acknowledgements

The authors thank Dr. Norbert Wagner and Alexander Bauder (DLR Stuttgart) for their support on impedance interpretation and test bench operation, respectively.

References

[1] S.B. Adler, W.G. Bessler, in: W. Vielstich, H. Yokokawa, H.A. Gasteiger (Eds.), Handbook of Fuel Cells–Fundamentals, Technology and Applications, Vol. 5, John Wiley & Sons, Chichester, UK, 2009, p. 441.
[2] M. Vogler, A. Bieberle-Hütter, L.J. Gauckler, J. Warnatz, W.G. Bessler, J. Electrochem. Soc. 156 (2008) B663.
[3] A.A. Franco, P. Schott, C. Jallut, B. Maschke, Fuel Cells 7 (2007) 99.
[4] A.Z. Weber, J. Newman, J. Electrochem. Soc. 151 (2004) A311.
[5] W.G. Bessler, S. Gewies, J. Electrochem. Soc. 154 (2007) B548.
[6] M. Eikerling, J. Electrochem. Soc. 153 (2006) E58.
[7] P. Mock, S.A. Schmid, J. Power Sources 190 (2009) 133.
[8] P. Schott, P. Baurens, J. Power Sources 156 (2006) 85.
[9] E. Leucht, K.A. Friedrich, Modelling of tubular SOFC in hybrid power plant systems – cell and stack modelling, *8th European Solid Oxide Fuel Cell Forum*, Lucerne, Switzerland, 2008, p. A0214.
[10] [illegible] Q1
[11] C. Graf, K.A. Friedrich, A. Weiß, N. Bärtolow, J. Fuel Cell Sci. Technol. 3 (2006) 403.
[12] W.G. Bessler, S. Gewies, M. Vogler, Electrochim. Acta 53 (2007) 1782.
[13] F. Meier, G. Eigenberger, Electrochim. Acta 49 (2004) 1731.
[14] J. Pukrushpan, A. Stefanopoulou, H. Peng, Control of Fuel Cell Systems, Springer, London, 2005.
[15] N. Wagner, Impedance Spectroscopy. Theory, Experiment and Applications, John Wiley & Sons, Hoboken, New Jersey, 2005, pp. 479–537.
[16] P. Deuflhard, E. Hairer, J. Zugck, Num. Math. 51 (1987) 501.
[17] W.G. Bessler, S. Gewies, C. Willich, G. Schiller and K.A. Friedrich, Fuel Cells, 2009, [illegible] Q2

Please cite this article as: M.P. Eichenbach, et al., Multi-scale simulation of fuel cells: From the cell to the system, Solid State Ion. (2010), doi:10.1016/j.ssi.2010.06.041

ECS Transactions, 25 (35) 275-292 (2010)
10.1149/1.3414025 ©The Electrochemical Society

CO Induced Reconstruction of Pt_xCo_y Electrocatalytic Nanoparticles in a PEM Fuel Cell Anode under transportation Operating Conditions

Seng Kian Cheah[1], Olivier Lemaire[1], Patrick Gélin[2] and Alejandro A. Franco[1],

[1]Commissariat à l'Energie Atomique (CEA)
DRT/LITEN/Département Transports et Hydrogène/
Laboratoire des Composants Piles à Combustible, Electrolyseurs et de Modélisation
(LCPEM)
17, Rue des Martyrs – 38054 Grenoble cedex 9 (France)
[2]Institut de Recherches sur la Catalyse et l'Environnement de Lyon (IRCELYON), UMR 5256
2, Avenue Albert Einstein – 69626 Villeurbanne cedex (France)
Corresponding author: seng-kian.cheah@cea.fr

In this paper, based on a multiscale modelling framework, we focus on understanding the impact of CO adsorption on the intrinsic stability properties of Pt_xCo_y nanoparticles under PEMFC anode operating conditions. First, CO adsorption effect on Pt_xCo_y has been studied by using Monte Carlo (MC) simulation. Then, the MC results are coupled with an *ab initio* based kinetic model to simulate the effect of CO poisoning on the activity and durability of the Pt_xCo_y nanoparticles as HOR catalysts. The results are compared with simulations carried out with pure Pt, where potential self-oscillatory behaviour is detected and experimentally confirmed. The Pt_xCo_y HOR activity and stability reveals to be strongly dependent on the nanoparticle size and composition. For some nanoparticle sizes, simulations show that PtCo nanoparticles provide better CO tolerance than Pt_3Co. CO adsorption on PtCo slows down Co dissolution in short-term operation. However, this effect is overcome by the increase of the anode potential due to CO adsorption. Thus, CO adsorption enhances Co dissolution in long-term operation. Due to this Co dissolution, the HOR activity of PtCo degrades faster than Pt_3Co in long-term operation.

Introduction

Polymer Electrolyte Membrane Fuel Cells (PEMFC) are considered as good candidates to replace internal combustion engines for stationary and transportation applications, especially for light-duty vehicles (1). PEMFC have in particular the advantages of higher conversion efficiency and low emissions. Due to low operating temperature and high sensitivity of the platinum catalysts to impurities, PEMFC require high purity hydrogen and air/oxygen feed to the anode and cathode sides respectively. However, the main hydrogen sources are reforming of various kinds of hydrocarbons. Impurities are thus inevitably present and further purification is necessary. In particular, carbon monoxide (CO) is one of the main pollutants in hydrogen and it is well known that Pt-based PEMFC performance rapidly decreases with some ppm of CO in hydrogen (2). **Fig. 1** illustrates the effect of different CO concentrations in the H_2 feed stream on short-term single PEMFC voltage (3).

Some mitigating solutions are currently used to limit the CO impact on performance: high temperature operation (4), air bleeding (2, 5), multi-metallic catalysts (6-11) etc. Moreover,

with the membrane, catalyst undoubtedly accounts for the PEMFC high cost (1). In this context, replacement of the platinum by multi-metallic catalysts is currently a promising pathway. They allow a significant decrease of costs and an improvement of the anodic hydrogen pollutant tolerance. That is why bimetallic catalysts with higher CO tolerance have been intensively studied during the last years. In particular, PtRu is commercially used thanks to its high CO tolerance (12, 13). However, Ru is also quite expensive and has to be replaced by another cheaper alternative in the effort to reduce the cost of fuel cells. Therefore, Watanabe *et al.* have proposed the non-precious transition metals as the alloying metals with Pt (6, 7).

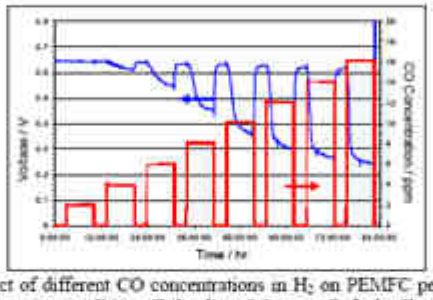

Figure 1. Effect of different CO concentrations in H_2 on PEMFC performance under steady-state operating conditions (Pt loading: 0.5 mg.cm^{-2}; fuel cell temperature: 70°C; anode and cathode pressure: 0.15 MPa; anode and cathode relative humidity: 60%; current density: 0.6 A.cm^{-2}).

The CO tolerance mechanisms of the Pt-M catalysts (where M is a non-precious transition metal) have been intensively studied. In general, two mechanisms are proposed by the scientific community:

- Bifunctional effect. The adsorbed CO is oxidized by the spill-over of adsorbed -OH produced through water dissociation promoted by the alloying metals (14).
- Ligand effect/electronic effect. The alloying metals decrease the Fermi level of Pt 5d band. As a result, the back donation of electron to the $2\pi^*$ band of CO is reduced, so that the bonding of CO to Pt is weakened. A weaker bonding will result in lower CO coverage or higher mobility of CO, thus enough free sites are available for H_2 oxidation reaction (7, 9).

The stability properties of the bimetallic catalysts are crucial to maintain the CO tolerance property in the long-term PEMFC operation. It is well known that under high potential and acidic environment, which is the case in general PEMFC operating conditions, the alloying metals tend to dissolve from the catalysts (15-17). Due to these degradation phenomena, the positive effects of alloying are reduced and the catalysts will eventually operate similar to a pure Pt catalyst. Moreover, it has also been shown that the adsorption of gas molecule on the surface of bimetallic catalysts may induce surface reconstruction phenomena (18-20). For example, in the case of PtRu, Pt tends to segregate at the surface of particles when no species are adsorbed on the surface. When CO is adsorbed, a reverse segregation of Ru at the surface is observed (21).

To our knowledge, hitherto the stability properties of Pt_xCo_y under CO adsorption and the influences on performance of fuel cell anode have never been studied. Therefore, in this work, Monte Carlo (MC) simulation has been used to understand the possible CO induced surface reconstruction on the catalysts. In parallel, a multiscale kinetic model has first been developed to describe the instantaneous reaction of CO and H_2 on pure Pt catalyst in the anode, and has been validated by half cell experiments. The model has then been adapted to the case of the bimetallic catalysts and correlated to their degradation. By coupling the two approaches, the time evolution of the catalyst performance under influence of CO adsorption has been evaluated.

Theoretical Approach

Global Modelling Algorithm

In our previous publications, the MC approach and the multiscale *ab initio*/irreversible thermodynamic-based kinetic approach were coupled to describe the time evolution of Pt_xCo_y catalysts activity towards the oxygen reduction reaction in the PEMFC cathode (17). In this work, the same approaches have been used and adapted to the reactions that occur in the PEMFC anode. Firstly, the influence of CO on the catalyst particles nanostructure is accounted for by using the MC Metropolis algorithm (17). The Monte Carlo approach is used to calculate the atomic organization from the kinetically calculated instantaneous $X^F_{Co}(t)$ and total number of particle atoms, $N_t(t)$ in the nanoparticle. This information is used to obtain the instantaneous surface composition of Co, $X^S_{Co}(t)$. Instantaneous coupling of these two approaches will allow the prediction of time evolution of experimental observables (e.g. PEMFC anode potential at fixed current). A schematic diagram of this methodology is described in **Fig 2**.

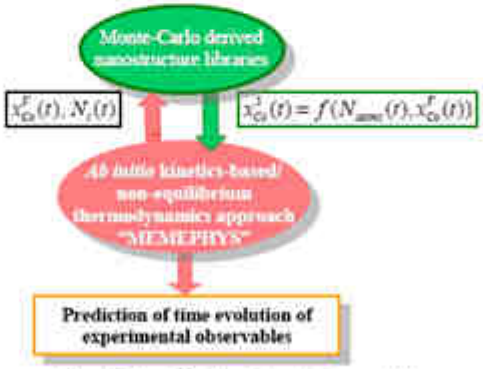

Figure 2. Instantaneous coupling of Monte Carlo and multiscale modelling approaches that allows the prediction of time evolution of fuel cells experimental observables for Pt_xCo_y under the influence of CO in H_2.

Monte Carlo Algorithm

As described in our previous publication (17), Pt_xCo_y catalysts were simulated with number of atoms in a particle corresponding to the "magic numbers" 38, 201, 586,….. Indeed, with these numbers of atoms, the catalysts are the most stable in a truncated octahedron structure. By using this predefined structure, the complex and lengthy procedures in the MC simulation can be simplified. Sutton-Chen multiatomic potential was applied in the annealing MC method to simulate the pseudo-equilibrium atomic repartition of each structure (17). This potential provides the total nanoparticle energy U as the addition of terms that describes the two-body repulsive interaction between the atoms i and j separated by a distance r_{ij}, and of many-body cohesion terms associated with atom i:

$$U = \sum_{i}^{N_{atoms}} \left[\frac{1}{2} \varepsilon^{AB} \sum_{j \neq i}^{N_{atoms}} \left(\frac{\sigma^{AB}}{r_{ij}} \right)^{n^{AB}} - c^{A} \varepsilon^{A} \sqrt{\sum_{j \neq i}^{N_{atoms}} \left(\frac{\sigma^{AB}}{r_{ij}} \right)^{m^{AB}}} \right] \quad [1]$$

In **Eq. [1]**, ε^{AB} is the so-called energy parameter, σ^{AB} is the lattice constant, c is a dimensionless parameter, and n and m are positive integers with n>m.

Our MC algorithm is based on exchanging two different randomly chosen atoms. The trial acceptance probability of the exchange-resulting configuration is based on the standard Metropolis algorithm. If the energy of the new configuration is smaller than the one of the old configuration, the trial is always accepted. In the opposite case, the trial is accepted only if the probability P is greater than a random number chosen between 0 and 1:

$$P = \exp\left(\frac{-\Delta U}{k_B T} \right) \geq random \quad [2]$$

Temperature being indirectly implicated in the nanoparticle energy minimization, we choose to impose an annealing cooling schedule. The initial temperature, cooling schedule, and total simulation length are the three important parameters of a simulated annealing optimization. All the MC simulations presented in this paper have been performed by starting at 900 K with the following cooling schedule:

$$T(i) = \frac{1}{2}(900 - 100)\left[1 + \cos\left(\frac{i\pi}{N_{Steps}} \right) \right] + 100 \quad [3]$$

with $T(i)$ the temperature as a function of the trial step i, N_{steps} the total number of simulation steps necessary to reach the minimum of the global energy. As explained above, MC simulations are performed on truncated octahedrons previously relaxed using the multiatomic Sutton–Chen potential for random distributions of platinum and cobalt atoms. The relaxed inter-atomic lengths depend on the considered nanoparticle size. Nanoparticles simulated are considered to be the optimum structure of Pt_xCo_y catalyst under vacuum.

In order to study the influence of CO adsorption, nanoparticles obtained with the above mentioned procedures were further simulated. The same procedures as above were applied.

However, the annealing was not applied and temperature was fixed at 353 K, which is a typical PEMFC operating temperature. Besides, the total energy U of the system now includes the adsorption energy of CO on the surface atoms:

$$U = \sum_{i}^{N_{atoms}} \left[\frac{1}{2} \varepsilon^{AB} \sum_{j \neq i}^{N_{atoms}} \left(\frac{\sigma^{AB}}{r_{ij}} \right)^{n^{AB}} - c^{A} \varepsilon^{A} \sqrt{\sum_{j \neq i}^{N_{atoms}} \left(\frac{\sigma^{AB}}{r_{ij}} \right)^{m^{AB}}} \right] + xE_{ads}^{Pt} + yE_{ads}^{Co} \qquad [4]$$

x and y are the numbers of Pt and Co atoms with adsorbed CO on the surface of the particle. Table I gives the values of the different parameters. E_{ads}^{m} is the CO adsorption energy on the respective metal where m is Pt or Co. The values of E_{ads}^{m} were obtained from Christoffersen *et al.* (21).

Table I. Platinum, cobalt and Pt-Co cluster parameters used in the Sutton-Chen potential and the CO adsorption energies.

	σ^{AB} (x 10 nm)	ε^{AB} (10^{-2} eV)	c	m	n	E_{ads}^{m} (eV)
Platinum	3.92	1.9833	34.408	8	10	-1.46
Cobalt	3.54	1.5566	39.432	6	9	-1.19
Pt-Co	3.73	1.7570		7	9.5	

Ab initio Kinetics-based/non-equilibrium Thermodynamics Approach

In our global kinetic model, called MEMEPHYS and being developed at CEA during the last 8 years, the experimental observables (e.g. anode potential evolution at fixed current) are simulated from a combination of physical, chemical, and electrochemical models at different scales. Generally, MEMEPHYS model can be separated into three scales: nanoscale, microscale and cell level (Fig. 3). At the cell level, input parameters such as current density, temperature and properties of reactant gases are introduced as input data. In this work, the cell level consists of the anode, i.e., a half cell. This input data is used in the microscale to simulate the transport properties of different species such as the H_2 or CO molecules. The results from microscale then instantaneously affect the nanoscale parameters, where elementary chemical and electrochemical reactions rates are described in relation to a non-equilibrium thermodynamics description of the electrochemical double layer (interface between the catalyst and the electrolyte) (22).

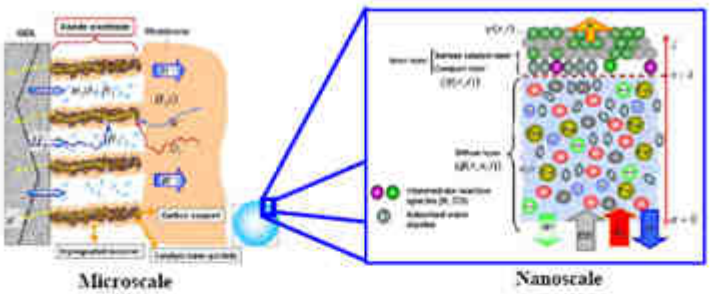

Figure 3. Schematic diagram of micro- and nano-scales of the kinetic model. Diffusion phenomena are modelled in the microscale. The results obtained are used to simulate instantaneously the nanoscale, which is based on the electrochemical double layer model.

Nanoscale: Compact Layer Model. By defining $\psi(r, t)$ as the potential at the catalyst, and $\phi(L, t)$ as the potential at the interface between the compact layer and the diffuse layer. The potential drop through the compact layer is denoted as the surface potential, $\eta_F(t)$:

$$\eta_F(t) = \psi(r, t) - \phi(L, t) \quad [5]$$

The calculation of $\eta_F(t)$ was already described in our previous publications (22, 23). It results from the superposition of the electrostatic potential drop across the compact layer, $\Delta\phi_1$, and the ad-layer dipolar moment induced potential drop, $\Delta\phi_2$:

$$\Delta\phi_1 = -\frac{\sigma}{\varepsilon_{CL}} d > 0 \quad [6]$$

$$\Delta\phi_2 = \frac{\Gamma^{Pt} + \Gamma^{Co}}{\varepsilon_{DL}} \quad [7]$$

where σ is the catalyst surface charge density, Γ the dipolar surface charge density, ε_{CL} and ε_{DL} the electric permittivity of the compact and diffuse layers respectively. Γ is calculated by using the dipolar moment of water molecule, μ_{H_2O} and the number of water molecules for which the hydrogen end is pointing towards the electrode ($\vec{n}^m$) or away from the electrode surface ($\overleftarrow{n}^m$). m stands for Pt or Co. CO dipolar moment contribution to Γ is assumed to be negligible, as it is one order of magnitude lower than for the water molecule.

$$\Gamma^m = \mu_{H_2O}(\vec{n}^m - \overleftarrow{n}^m) \quad [8]$$

By defining

$$A = \frac{\xi[3]}{2\pi\varepsilon_{DL}} \quad [9]$$

$$a_M = 2e^{\frac{-\Delta G^{\circ}_{ads,M}}{RT}} \quad [10]$$

$$X = \frac{\mu\sigma}{k_B T\varepsilon_{CL}} + \frac{A\mu^2}{k_B T d^3}(\vec{\theta} - \overleftarrow{\theta}) \quad [11]$$

we can show that the surface potential $\eta_F(t)$ will be (17):

$$\eta_F(t) = -\frac{\sigma.d}{\varepsilon_{CL}} - \frac{(a_{Co}\theta^{Co} + a_{Pt}\theta^{Pt}).n^{max}.\Theta_{H_2O}.\mu.\sinh[X]}{\varepsilon_{DL}} \quad [12]$$

and

$$\vec{\theta} - \overleftarrow{\theta} = \frac{\vec{n} - \overleftarrow{n}}{n^* + \vec{n} + \overleftarrow{n}} = \frac{-\sinh[X]}{\frac{n^*}{\Theta_{H_2O}(n^{Co}.a^{Co} + n^{Pt}.a^{Pt})} + \cosh[X]} \quad [13]$$

where n^* is the addition of number of free sites and occupied sites by reaction intermediates per unit of area. By using equations [11] and [13] we have:

$$\frac{\sinh[X]}{\frac{1}{\Theta_{H_2O}}\frac{(\theta^{Co} + \theta^{Co}_{ad}) + (\theta^{Pt} + \theta^{Pt}_{ad})}{\theta^{Co}.a_{Co} + \theta^{Pt}.a_{Pt}} + \cosh[X]} = \frac{d^3}{A\mu\varepsilon_{CL}}\sigma - \frac{k_B T d^3}{A\mu^2}X \quad [14]$$

Eq [14] is the transcendental equation that can be used to determine X and it has a single solution for every σ value. The value of θ^M is determined from

$$\theta^M = \frac{1 - \theta^M_{ad}}{1 + \Theta_{H_2O}.a_M \cosh[X]} \quad [15]$$

and

$$\theta^{Pt} + \theta^{Co} + \theta^{Pt}_{ad} + \theta^{Co}_{ad} + \vec{\theta} + \overleftarrow{\theta} = 1 \quad [16]$$

where θ^M_{ad} is the total coverage of all reaction intermediates for Pt and Co (M=Pt or Co).

Ab initio-based Kinetic Model. In our model, the hydrogen oxidation reaction (HOR) in the anode is described by using the Tafel–Heyrovsky–Volmer three steps reactions model (22, 24-26).

$$H_2 + 2s \leftrightarrow 2Hs \quad \text{(Tafel)} \qquad [17]$$

$$H_2 + s \leftrightarrow Hs + H^+ + e^- \quad \text{(Heyrovsky)} \qquad [18]$$

$$Hs \leftrightarrow s + H^+ + e^- \quad \text{(Volmer)} \qquad [19]$$

The rate of these reactions are expressed as below by assuming that the adsorbed species are not interacting with each other

$$v_{Taf} = k_{Taf}\theta_s^2 C_{H_2}(L,t) - k_{-Taf}\theta_{Hs}^2 \qquad [20]$$

$$v_{Hey} = k_{Hey}\theta_s C_{H_2}(L,t)e^{(1-\alpha_{Hey})f\eta_F(t)} - k_{-Hey}\theta_{Hs}C_{H^+}(L,t)e^{(-\alpha_{Hey})f\eta_F(t)} \qquad [21]$$

$$v_{Vol} = k_{Vol}\theta_{Hs}e^{(1-\alpha_{Vol})f\eta_F(t)} - k_{-Vol}\theta_s C_{H^+}(L,t)e^{(-\alpha_{Vol})f\eta_F(t)} \qquad [22]$$

The HOR is assumed to take place on Pt sites of the bimetallic catalyst only. Alloying of the Pt and Co is assumed to not affecting the reaction constants. Thus, θ_s is the coverage of Pt free sites.

On the other hand, the CO reaction with the bimetallic catalyst is described by using a two steps reaction (27, 28):

$$CO + s^M \rightarrow CO - s^M \quad \text{(COad)} \qquad [23]$$

$$CO - s^M + H_2O \rightarrow 2H^+ + s^M + CO_2 + 2e^- \quad \text{(COOR)} \qquad [24]$$

and the corresponding reaction rates are determined by:

$$v_{COad} = k_{COad}\theta_s^M C_{CO}(L,t)e^{\frac{\omega\theta_{CO}^M}{RT}} \qquad [25]$$

$$v_{COOR} = k_{COOR}\theta_{CO}^M \Theta_{H_2O}e^{2(1-\alpha_{COOR})f\eta_F(t)} \qquad [26]$$

where ω is the CO-CO interaction parameter (28).

Besides that reaction of external species with the bimetallic catalyst, the degradation reaction of the catalyst, i.e. Co dissolution, was also considered:

$$Co \rightarrow Co^{2+} + 2e^- \quad \text{(CoOR)} \qquad [27]$$

with the following reaction rate (17):

$$v_{CoOR} = k_{CoOR}\theta_s^{Co}e^{2(1-\alpha_{CoOR})f\eta_F(t)}$$

In the model, the reaction rate is normalized to the catalyst surface area (the unit is thus mol.m^{-2}.s^{-1}). The rate constant is determined by using the Eyring's equation (29):

$$k^{\circ} = \frac{k_B T}{h} e^{\frac{-\Delta G}{RT}} = \frac{k_B T}{h} e^{\frac{\Delta S}{T}} e^{\frac{-\Delta H}{RT}} \quad [28]$$

The Gibbs' free energies in [28] were obtained from *ab initio* data. The Gibbs' energy of HOR is considered to be independent of the composition of the bimetallic catalyst. However, it is well known that the interaction of CO on Pt changes from pure Pt to bimetallic catalyst and, the composition of the bimetallic catalysts gives different CO tolerance characters (6, 8, 9, 12). Thus, we propose that the Gibbs' energies of COad and COOR on Pt are functions of the bimetallic catalysts composition (surface or volumetric) as a first approximation. Besides, Co oxidation Gibbs' energy is also a function of Co composition (17). The Gibbs' energies are written as:

$$\Delta G_{COad\_Pt} = [1 - x^{V}_{Co}(t)].\Delta G^{\circ}_{COad\_Pt} \quad [29]$$

$$\Delta G_{COOR\_Pt} = \left[\frac{1}{1 - \left(\frac{x^{V}_{Co}(t)}{2}\right)}\right] \Delta G^{\circ}_{COOR\_Pt} \quad [30]$$

$$\Delta G_{CoOR} = \left[\frac{x^{s}_{Co}(t)}{x^{V}_{Co}(t_o)}\right] \Delta G^{\circ}_{CoOR} - RT \ln C^{\circ}_{CoOR} \quad [31]$$

By using the reaction rates of the corresponding reactions, the flow of reactants and products to and from the compact layer can be determined. At the same time, the evolution of the catalyst surface charge density can be calculated based on:

$$\frac{d\sigma}{dt} = \frac{I(t)}{S_{Catalyst}(t)} + J_{Far}(t) \quad [32]$$

where $I(t)$ is the nominal current, $S_{catalyst}(t)$ the instantaneous active catalyst surface area and

$$J_{Far}(t) = \nu_{Hey} + \nu_{Vol} + 2\nu_{COOR\_Pt} + 2\nu_{COOR\_Co} + 2\nu_{CoOR} \quad [33]$$

Diffuse layer model. In this part, we describe the transport of the electrically charged species (H^+, Co^{2+}) and electrically neutral species (CO, H_2 and CO_2) in the diffuse layer and the coupling with the compact layer model. This allows the calculation of the time-dependent species concentrations at the compact layer (x = L, cf. **Fig 3**). The diffuse layer model is based on the diffusion and migration transport of the reaction species coupled with the electric field generated by the resulting charge distribution. All species mentioned above including FIX^- (sulfonate group of Nafion®) and water, are considered as punctual, so the inter-particle electrical interaction is neglected. The solvatation and convection by water are not considered.

The flow for the electrically neutral species, for example H_2, is assumed to be given by Fick's law of diffusion and the mass balance leads to

$$\frac{\partial C_{H_2}}{\partial t} = -\nabla \cdot \vec{J}_{H_2} = -\nabla \cdot (-D_{H_2} \nabla C_{H_2}) = D_{H_2} \nabla^2 C_{H_2} \qquad [34]$$

where we assume that the diffusion coefficient D_{H2} is constant.

For the case of the electrically charged species, for example H^+, the diffusion coefficient in the medium is also supposed to be independent of the concentration. In a similar way that in the H_2 case, combining the flow related to the Fick's diffusional force to the electrical force, with the mass balance, we obtain the equation representing the H^+ concentration (Nernst–Planck equation):

$$\begin{aligned} \frac{\partial C_{H^+}}{\partial t} &= -\nabla \cdot \vec{J}_{H^+} = -\nabla \cdot (-D_{H^+} \nabla C_{H^+} - fD_{H^+} C_{H^+} \nabla \phi) \\ &= D_{H^+} \nabla^2 C_{H^+} + fD_{H^+} \nabla C_{H^+} \nabla \phi + fD_{H^+} \nabla C_{H^+} \nabla^2 \phi \end{aligned} \qquad [35]$$

where $\phi(x,t)$ is the electric potential in the electrolyte, which is calculated from the Poisson's equation:

$$\frac{F}{\varepsilon_{CL}} (C_{H^+} + 2C_{Co^{2+}} - C_{FIX}) = -\nabla^2 \phi \qquad [36]$$

where the sulfonate groups concentration C_{FIX} is assumed to be constant. These sulfonate sites are supposed to be located outside of the compact layer and not to affect its structure. Equations [35] and [36] are introduced because at the nanoscopic scale (near the electrode surface where the electron transfer takes place) electroneutrality cannot be assumed and because there is not any supporting electrolyte (the conductivity of protons in the Nafion® is not infinite). Far from the compact layer, the system becomes electroneutral.

The following boundary conditions are used to solve the differential equations. The bulk electrolyte is located at $x = 0$, where $C_{H^+} + C_{Co^{2+}} = C_{FIX}$ and the concentration of H_2 and CO at x = 0 are calculated by using Henry's law by assuming Nafion® behaves like water. The scalar potential $\phi(x = 0) = 0$. At x = L, the boundary conditions are calculated by using the reaction rate:

$$J_{H_2}(L,t) = -(\nu_{Taf} + \nu_{HOR}) \qquad [37]$$

$$J_{CO}(L,t) = -(\nu_{COad\_Pt} + \nu_{COad\_Co}) \qquad [38]$$

$$J_{CO_2}(L,t) = \nu_{COOR\_Pt} + \nu_{COOR\_Co} \qquad [39]$$

(negative when it is consumed and positive when it is produced)

$$J_{H^+}(L,t) = v_{Re} + v_{Tr} + 2v_{CO2\_Pt} + 2v_{CO2\_Co} \quad [40]$$

$$J_{CO^-}(L,t) = v_{CO2} \quad [41]$$

The boundary condition for Eq. [36] is given by $\frac{\partial \phi(L,t)}{\partial x} = -\frac{\sigma}{\varepsilon_{CL}}$, where σ is obtained from Eq. [32]. Then, Eq. [36] allows calculation of $\phi(L,t)$, which, using Eq. [5], allows calculation of the electronic potential $\psi(t)$ in the catalyst.

Experimental

Electrochemical Characterization: Half Cell Experiment

A 8 mm diameter of an Elat gas diffusion electrode (GDE) from BASF was used to perform the experiments. The Pt catalyst loading was 0.5 mg/cm^2. By using hot pressing method, a Nafion® NRE 212 CS membrane was bonded on the GDE at 150°C and 4 MPa to form the half membrane electrode assembly (MEA). The MEA was then placed in the sample holder and immersed in 0.5 M of H_2SO_4 liquid electrolyte with the membrane facing the electrolyte and the GDL in contact with the gold grid current collector to be the working electrode.

A three electrodes system was set up with a Pt mesh as the counter electrode and a $Hg/HgSO_4$ reference electrode. The three electrodes system was connected to a Bio-logic VMP2 potentiostat. The electrolyte was de-aerated by continuous bubbling of nitrogen gas. A galvanostatic experiment was carried out at 20 mA while a mixture of H_2 and CO gases was fed to the working electrode. The experiments were carried out with 15, 30 and 45 ppm of CO.

Results and Discussions

Monte Carlo Simulation

We have simulated the Pt_xCo_y bimetallic catalyst particles using the annealing Monte Carlo method. By considering that the catalyst is under CO rich environment, we assumed that the catalyst was under full coverage of CO. The results of simulation are shown in **Fig 4**.

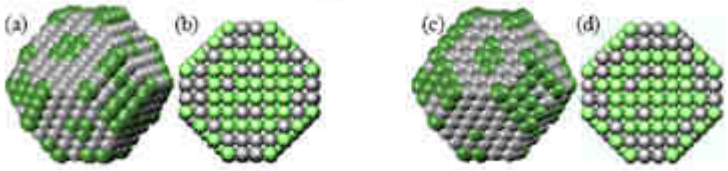

Figure 4. Simulated PtCo nanoparticle with the influence of CO in full view (a) and cut view (b); without the influence of CO in full view (c) and cut view (d). The green atoms represent Co and the grey atoms represent Pt.

The simulation results show that the CO adsorption does not induce big reverse segregation as observed in the case of PtRu where the Ru atoms are clearly being "pulled out" from the core of the catalyst (21). Particles with different composition and number of atoms (using the magic number) were simulated and the same results were observed. It shows that the particles in which more Pt is segregated at the surface are rather stable. Therefore, the number of available Pt sites is only proportional to the composition and particle size regardless of the CO coverage (17). Consequently, the data obtained with the MC simulation can be coupled with the kinetic model to simulate the time evolution of the catalysts.

Ab initio-based Kinetic Model

The developed kinetic model is easily tuneable to adapt to different sizes and compositions of Pt_xCo_y catalysts. Besides, we are able to simulate the response of the catalysts in the context of a half cell. Simulations have been carried out on Pt as it is the conventional effective fuel catalyst. Then, the performance of Pt_3Co and PtCo are evaluated in particular because the former has a Co-core and Pt-shell structure while the latter has a rather homogeneous distribution of Pt and Co atoms. These specific structures are believed to be affecting the CO tolerance and stability properties of the particles. Besides, these two compositions are commercially available as opposed to other compositions.

Initially, simulations of the half cell anodic response under CO poisoning effect have been performed on pure Pt catalyst. The particles radius of Pt catalysts has been predetermined to be 2 nm and the half cell is operating at 298 K. The results shown in **Fig 5** have been plotted as polarization curves. It is clear that the pure Pt catalysts are seriously poisoned by CO. These results are well consistent with the well known poisoning effect of CO on pure Pt catalyst.

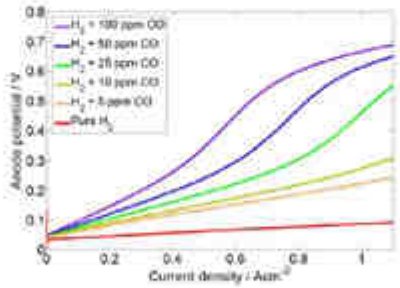

Figure 5. Anodic polarization curve of a half cell loaded with pure Pt catalysts with radius of 2 nm under the influence of different CO concentrations.

However, when the potential of the half cell with pure Pt catalyst was simulated in galvanostatic conditions, a self-oscillatory behaviour was observed. As shown in **Fig 6**, the anode potential oscillates in the range of 0.18 V – 0.7 V under a constant current of 20 mA (10 mA.cm^{-2}) when H_2 contains from 30 to 100 ppm of CO. Rather constant amplitude was observed after the onset of oscillations, which was earlier for higher CO concentration. In the case of 16 ppm of CO, the anode potential increases but the poisoning effect is not strong enough to reach oscillation. Without CO in H_2, oscillation was not observed. **Fig 6 (b)** is a

detailed view of the results with 30 ppm CO. It shows that the potential increases gradually from 0.18 V up to 0.7 V, and then drops abruptly down to 0.18 V in a periodical way.

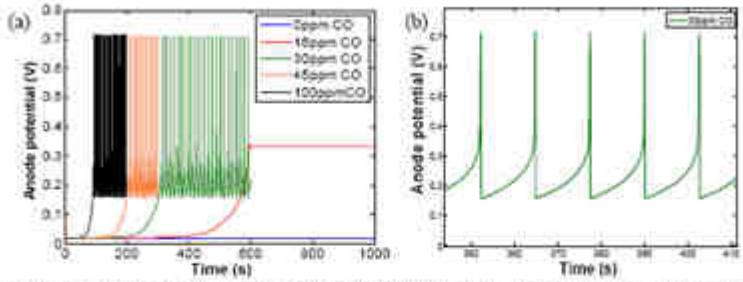

Figure 6. **(a)** Simulation results of potential of anodic half-cell with pure Pt catalyst under constant current of 20 mA (40 mA.cm^{-2}) for different CO concentrations. (b) Detailed view of (a) for 30 ppm CO in H_2.

Experiments on half cells under similar conditions were carried out in order to confirm the simulation results. The experiment results are shown in **Fig 7**. Qualitatively, they are in good agreement with our simulation results. As seen in **Fig 7 (a)**, like in simulation results (**Fig. 6 (a)**) the potential self-oscillations start earlier for higher CO concentration (30). The detailed behaviour of self-oscillations is observed in **Fig 7 (b)**, where periodic gradual potential increase was followed by abrupt potential drop. The potential self-oscillatory behaviour under the poisoning effect of CO has only been reported elsewhere for bimetallic catalysts (31-33). Although Zhang *et al.* mentioned the possibility of total recovery of Pt catalyst performance after CO poisoning, this was done by stopping the supply of CO to the catalyst (34). This potential self-oscillatory behaviour is thus reported here for the first time.

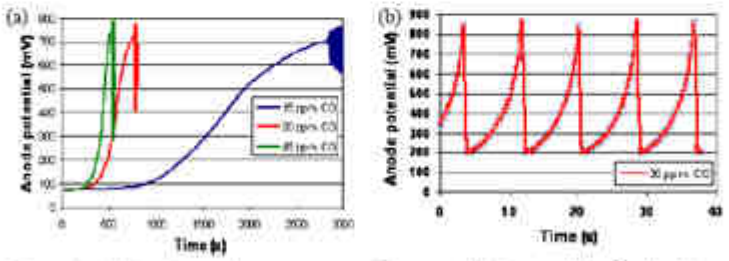

Figure 7. (a) Experimental measurements of the potential of an anodic half-cell with pure Pt catalyst with different concentrations of CO in H_2 under constant current of 40 mA.cm^{-2}. (b) Detailed view of (a) for 30 ppm of CO in H_2.

The phenomenon of potential self-oscillations can be explained by considering reactions **[23]** and **[24]**. The increase of anode potential is due to the gradual poisoning of CO on the Pt catalysts (reaction **[23]**). As a consequence, the availability of free sites for H_2 oxidation to sustain the same electrical current is consistently decreased. Therefore, the anode

overpotential increases continuously to enhance the HOR rate to compensate the loss of reaction sites. From **Eq [25]**, it is clear that the adsorption rate of CO is proportional to its concentration. Higher CO concentration then means higher poisoning rates. Thus, the onset of oscillation is the earliest for the highest CO concentration. The abrupt potential drop is due to the fast kinetics of CO electrooxidation following the reaction **[24]**. A fast electrooxidation of adsorbed CO resumes the free sites for HOR which decreases again the anode overpotential abruptly down to initial potential.

Simulations were also carried out on Pt_3Co bimetallic catalysts. The polarization curves are shown in **Fig 8**. Compared to pure Pt catalyst, the anode overpotential of Pt_3Co does not exhibit big increment under H_2 + CO. According to our model, this is due to the decrease of CO adsorption Gibbs' energy as a result of Co existence in the bimetallic. The presence of Co reduces the adsorption energy of CO on Pt sites thus the coverage of CO is also reduced. Therefore, the decrease in free sites that bring to increase of overpotential due to CO adsorption does not occur on Pt_3Co catalyst as for the case of pure Pt.

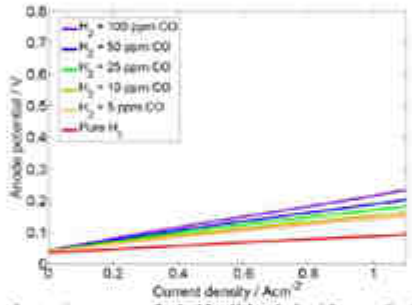

Figure 8. Anodic polarization curve of a half cell loaded with pure Pt_3Co catalysts with radius of 2 nm under the influence of different CO concentrations.

Performances with PtCo and Pt_3Co catalysts and H_2 + 10 ppm CO under galvanostatic condition were compared. The preset current was 0.5 $A.cm^{-2}$ and the catalysts particle size was 2 nm. The results in **Fig 9** show that the anode potential for Pt_3Co is constant whereas a gradual anode potential increase is observed for PtCo catalyst. These observations are attributed to the difference of stability between Pt_3Co and PtCo catalysts. For Pt_3Co, MC simulation shows that the particle has a Pt skin structure. Therefore, Co atoms are "protected" from dissolution into the electrolyte as a result of oxidation. In contrast to this, PtCo catalyst has surface Co atoms which can be oxidized easily. Thus, the performance of PtCo is degrading and the anode overpotential is increasing with time due to the loss of Co atoms. Although the performance of Pt_3Co is stable (Co dissolution is negligible) with particle size of 2 nm, Co dissolution could be observed when the Pt_xCo_y particle size is less than 1.5 nm.

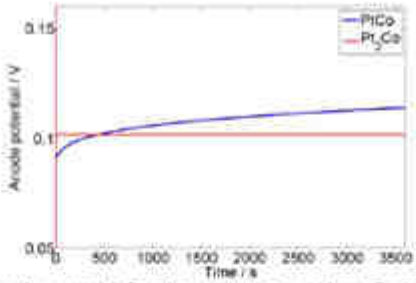

Figure 9. Simulated anode potential for PtCo and Pt_3Co catalysts for H_2 + 10 ppm CO under 0.5 $A.cm^{-2}$ constant current.

PtCo catalysts were further investigated to understand the influence of CO concentration in H_2 on the Co dissolution. As explained before, the Co dissolution is a crucial phenomenon that increases the anode overpotential thus degrading the performance. Therefore, Co dissolution needs to be limited. As seen in **Fig 10 (a)**, Co dissolution is lower for higher CO concentration in the short term. Nonetheless, an opposite behaviour was observed for a longer duration. The amount of Co dissolved from the PtCo catalyst increases with the CO concentration as shown in **Fig 10 (b)**. These opposite behaviours can be explained by considering the CO coverage and overpotential increase due to CO coverage. At the beginning, CO is adsorbed on the catalyst and slows down the Co dissolution. This effect is more pronounced for higher CO concentration, as the CO coverage on the catalyst is higher. Thus, Co dissolution is lower for higher CO concentration. However, the anode overpotential increases at the same time due to the higher CO coverage (as explained before in the case of pure Pt). The high anode overpotential will promote Co dissolution and this effect will become stronger than that of CO coverage after a certain time. This means that high CO concentration will eventually promote Co dissolution in long term.

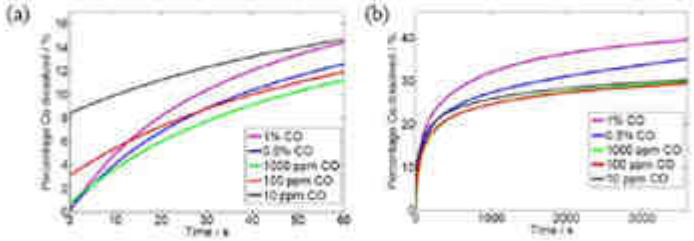

Figure 10. Percentage of Co dissolved from PtCo catalyst versus operation time with H_2 + CO mixtures, under 0.5 $A.cm^{-2}$ constant current . (a) Simulated results for the first 60 s. (b) Simulated results for the long run.

Conclusions

We have studied the impact of CO adsorption on the intrinsic stability properties of Pt_xCo_y nanoparticles under PEMFC anode operating conditions. First, Monte Carlo (MC) simulation has been applied to study the CO adsorption effect on Pt_xCo_y nanostructure. Then, the MC results are coupled with an *ab initio* based kinetic model to simulate the effect of CO poisoning on the activity and durability of the Pt_xCo_y nanoparticles as HOR catalysts. The results are compared with simulations carried out with pure Pt, where potential self-oscillatory behaviour is detected and experimentally confirmed. The Pt_xCo_y HOR activity and stability reveals to be strongly dependent on the nanoparticle size and composition. For some nanoparticle sizes, simulations show that PtCo nanoparticles provide better CO tolerance than Pt_3Co. CO adsorption on PtCo slows down Co dissolution in short-term operation. However, CO adsorption increases the anode potential and enhances Co dissolution in long-term operation. Due to this Co dissolution, the HOR activity of PtCo degrades faster than Pt_3Co in long-term operation.

Acknowledgements

This work was partially funded by the French Research Agency (ANR) through the program PAN-H and within the context of the POLIMPAC project. The authors gratefully acknowledge Nicolas Guillet from LCPEM for his help for experiments with half cells.

Appendix

Table II. Parameters used in kinetic simulation

Parameters	Units	Values	References
$\Delta G^{0}_{COad\_Pt}$	$Jmol^{-1}$	-25444	(28)
ω_Pt	$Jmol^{-1}$	$4.097x10^{4}$	(28)
$\Delta G^{0}_{COOR\_Pt}$	$Jmol^{-1}$	-19687	(28)
α_{COOR_Pt}	-	0.85	(28)
$\Delta G^{0}_{COad\_Co}$	$Jmol^{-1}$	-21444	Fitted
ω_Co	$Jmol^{-1}$	$3.977x10^{4}$	Fitted
$\Delta G^{0}_{COOR\_Co}$	$Jmol^{-1}$	-12687	Fitted
α_{COOR_Co}	-	0.85	Fitted
ΔH^{0}_{CoOR}	$Jmol^{-1}$	-17368	(17)
ΔS^{0}_{CoOR}	$Jmol^{-1}K^{-1}$	123	(17)
α_{CoOR}	-	0.85	(17)
C^{0}_{CoOR}	-	0.1	(17)

The others parameters used in the simulation can be found in our previous publications (17, 22, 28).

Reference List

(1) Marcinkoski J., Kopasz J.P.,and Benjamin T.G. *Int J Hydrogen Energy* **33**, 3894 (2008).
(2) Gottesfeld S., Pafford J. *J Electrochem Soc* **135**, 2651 (1988).
(3) CEA technical report, POLIMPAC project, ANR-PAN'H, 2008.
(4) Li Q.F., He R.H., Gao J.A., Jensen J.O.,and Bjerrum N.J. *Journal of The Electrochemical Society* **150**, A1599-A1605 (2003).
(5) Baschuk J.J., Li X.G. *International Journal of Energy Research* **27**, 1095 (2003).
(6) Watanabe M., Igarashi H.,and Fujino T. *Electrochemistry* **67**, 1194 (1999).
(7) Watanabe M., Zhu Y.M., Igarashi H.,and Uchida H. *Electrochemistry* **68**, 244 (2000).
(8) Uchida H., Izumi K., Aoki K.,and Watanabe M. *Physical Chemistry Chemical Physics* **11**, 1771 (2009).
(9) Igarashi H., Fujino T., Zhu Y.M., Uchida H.,and Watanabe M. *Physical Chemistry Chemical Physics* **3**, 306 (2001).
(10) Shimodaira Y., Tanaka T., Miura T., Kudo A.,and Kobayashi H. *The Journal of Physical Chemistry C* **111**, 272 (2006).
(11) Christoffersen E., Liu P., Ruban A., Skriver H.L.,and Nørskov J.K. *J Catal* **199**, 123 (2001).
(12) Iorοi T., Akita T., Yamazaki S.i., Siroma Z., Fujiwara N.,and Yasuda K. *Electrochim Acta* **52**, 491 (2006).
(13) Russell A.E., Ball S.C., Maniguet S.,and Thompsett D. *J Power Sources* **171**, 72 (2007).
(14) Pereira L.G., Paganin V.A.,and Ticianelli E.A. *Electrochim Acta* **54**, 1992 (2009).
(15) Antolini E., Salgado J.R.C.,and Gonzalez E.R. *J Power Sources* **160**, 957 (2006).
(16) Yu P., Pemberton M.,and Plasse P. *J Power Sources* **144**, 11 (2005).
(17) Franco A.A., Passot S., Fugier P., Anglade C., Billy E., Guetaz L., et al. *J Electrochem Soc* **156**, B410 (2009).
(18) Khanra B.C., Menon M. *International Journal of Modern Physics B* **13**, 59 (1999).
(19) Tao F., Grass M.E., Zhang Y., Butcher D.R., Renzas J.R., Liu Z., et al. *Science* **322**, 932 (2008).
(20) Mu R., Fu Q., Liu H., Tan D., Zhai R.,and Bao X. *Appl Surf Sci* **255**, 7296 (2009).
(21) Christoffersen E., Stoltze P.,and Nørskov J.K. *Surf Sci* **505**, 200 (2002).
(22) Franco A.A., Schott P., Jallut C.,and Maschke B. *J Electrochem Soc* **153**, A1053 (2006).
(23) Franco A.A., Schott P., Jallut C.,and Maschke B. *Fuel Cells* **7**, 99 (2007).
(24) Harrington D.A., Conway B.E. *Electrochim Acta* **32**, 1703 (1987).
(25) Harrington D.A., Conway B.E. *Journal of Electroanalytical Chemistry* **221**, 1 (1987).
(26) Bai L., Harrington D.A.,and Conway B.E. *Electrochim Acta* **32**, 1713 (1987).
(27) Springer T.E., Rockward T., Zawodzinski T.A.,and Gottesfeld S. *J Electrochem Soc* **148**, A11 (2001).
(28) Franco A.A., Guinard M., Barthe B.,and Lemaire O. *Electrochimica Acta* **54**, 5267 (2009).
(29) H.Eyring *J Chem Phys* **107**, (1935).
(30) Lemaire O., Guillet N., Franco A.A. Dispositif de détermination de la concentration en monoxyde de carbone et procédé. FR patent (2008).
(31) Lu H., Rihko-Struckmann L., Hanke-Rauschenbach R.,and Sundmacher K. *Topics in Catalysis* **51**, 89 (2008).
(32) Murthy M., Esayian M., Hobson A., MacKenzie S., Lee W.K.,and Van Zee J.W. *J Electrochem Soc* **148**, A1141-A1147 (2001).

(33) Carrette L.P.L., Friedrich K.A., Huber M.,and Stimming U. *Physical Chemistry Chemical Physics* **3**, 320 (2001).
(34) Zhang J.X., Thampan T.,and Datta R. *J Electrochem Soc* **149**, A765-A772 (2002).

ECS Transactions, 25 (35) 259-273 (2010)
10.1149/1.3414024 ©The Electrochemical Society

Modeling Chemical Degradation of a Polymer Electrolyte Membrane and its Impact on Fuel Cell Performance

Romain Coulon[a,b*], Wolfgang G. Bessler[b] and Alejandro A. Franco[a]

[a] CEA, LITEN, DTH, Laboratoire des Composants pour Piles à Combustible et Electrolyseurs, et de Modélisation (LCPEM), 17, Rue des Martyrs, 38054 Grenoble cedex 9, France
[b] German Aerospace Center (DLR), Institute of Technical Thermodynamics, Pfaffenwaldring 38-40, 70569 Stuttgart, Germany
*E-mail: romain.coulon1@cea.fr

We present here an elementary kinetic model of the electrochemical phenomena occurring in a polymer electrolyte membrane fuel cell (PEFC). Chemical degradation of the Nafion® membrane is described through a combination of OH radical formation via Fenton's reaction and a radical mechanism of side chain decomposition. At the electrodes, the model is coupled to a description of the hydrogen oxidation reaction, the oxygen reduction reaction, and the hydrogen peroxide formation reaction at the anodic side. We establish a first feedback between the evolution of structural properties of the membrane and its transport parameters (i.e., proton conductivity) for a fully humidified fuel cell. We assess the influence of the chemical membrane degradation on the cell performance and on macroscopic properties of the membrane (i.e., sulfonate site concentration).

Introduction

One of the major issues of the application of low-temperature fuel cells like polymer electrolyte membrane fuel cells (PEFC) under automotive conditions is the limited durability. The decrease of performance of a cell is due to a number of physicochemical effects, like carbon-support corrosion, platinum oxidation and dissolution, Ostwald's ripening, poisoning through local adsorption of pollutants, or regarding the ionomer, mechanical and chemical degradation [1-5]. All these phenomena act at the same time during the operation of a PEMFC. This makes it difficult to estimate the impact of each of them on the reduction of cell potential over time [6], which also strongly depends on operating conditions and materials. Indeed, in some cases, the degradation of the membrane was identified to be the dominant mechanism for performance loss [7].

Modeling and simulation

Global assumptions

During the operation of a PEFC, water transport is an important issue, causing the drying of the anode and, if the water evacuation is not sufficient at the cathode, the flooding of it [8]. Both phenomena are involved in the decay of the cell potential. As here our problem is to see the impact of the chemical degradation of the membrane on the decay of cell potential, we are starting our modeling from a point where a steady-state can be assumed for the water in the membrane (the transient phase of flooding the electrode with liquid water is not taken into account) [9, 10]. To be in agreement with experiments previously done at CEA [10], we assume an isothermal fuel cell, fed with pure fully humidified hydrogen and oxygen. Finally we consider that the excess of water produced at the cathode is directly evacuated through the gas diffusion layer (GDL) without any further resistance.

Model organization

Figure 1 presents the global organization of our model. It is divided into 2 interdependent parts: the anodic region only exposed to hydrogen (reaction "1"), the anodic region exposed to both hydrogen and oxygen, the latter resulting of the cross-over phenomena from cathode to anode (reaction "2"), and the cathode operating with pure oxygen. The reaction "1" considers the occurring of the hydrogen oxidation reduction (HOR). The reaction "2" takes into account the formation of hydrogen peroxide, as a result of potential-independent reactions between hydrogen and oxygen. The two phenomena are occurring at the same place on the electrode on a competitive way and occur at the same time during the work of the fuel cell, so that the further balance equation will take into account the both reactions. That implies that every parameters accounting for the reaction "1" will be the same as those for reaction "2".

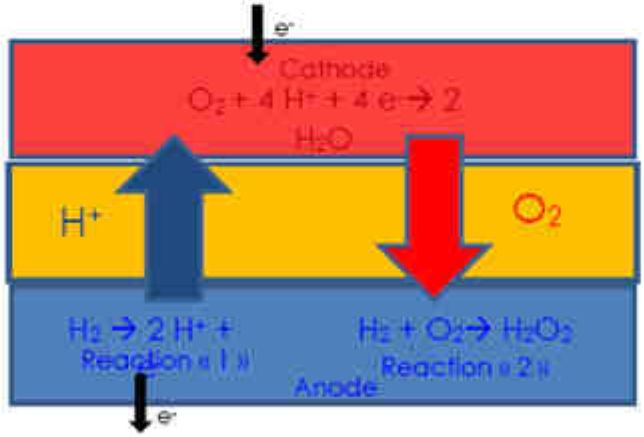

Figure 1. Global architecture of our membrane electrode assembly model.

Electrode models

The chosen electrode morphology is similar to that presented in Ref. [1, 10]: Carbon support (and Pt) networks are considered embedded in a hydrated ionomer medium (Nafion® phase). These structures also include nano/micropores, allowing the gas transport to the active site of the electrode. This is certainly a simple representation of the multi-scale complexity of an electrode, but it allows to capture the elementary processes taking place in the MEA and to describe, on a physical basis, the coupling between them.

The multiscale electrochemical models of the anode and the cathode are based on the work of Franco *et al.* and have been described in detail previously [10, 11]. In summary, within a continuum framework, each electrode submodel is designed to describe coupled physicochemical phenomena at different geometrical scales: a microscale transport phenomena description of reactants (H_2 and O_2) and charges (protons and electrons) through the electrode and the membrane thickness (no cross-over of H_2 is considered) and a spatially distributed microscale model of the reactant diffusion through the hydrated Nafion® ionomer layer covering the Pt/C networks, coupled to a 1D nanoscale mechanistic description of the catalyst electrolyte interface at the electrode (non equilibrium description of the electrochemical double layer). The nanoscale models consist of a compact layer submodel describing in a detailed way the competitive adsorption of the intermediate reaction species and the parasite water molecules on the catalyst surface, and of a diffuse layer submodel in the electrolyte, constituted of protons and spatially fixed counter-ions (sulfonate sites) [1-6, 9-11]. Moreover we consider the presence of water peroxide in the bulk as well.

Elementary kinetic mechanisms at the electrodes

The chemical and electrochemical reactions are described here with the PEFC elementary kinetic modeling approach already introduced by Franco *et al.* in [1-6, 9-11] where, adsorption, desorption, surface and charge-transfer reactions (dependent on the surface potential across the compact layer) are individually resolved. Intermediate species are described via their surface coverages,

$$\theta_z + \theta_{inter} + \vec{\theta} + \overleftarrow{\theta} = 1 \qquad [1]$$

where θ_z is the catalyst surface coverage by the free sites, θ_{inter} is the surface coverage by the reaction intermediates, and $\vec{\theta}$ and $\overleftarrow{\theta}$ the surface coverage by parasitically adsorbed water molecules with dipolar moment opposed (up) and directed (down) to the platinum layer. Note that all the coverages are defined at the compact layer level, thus a physical-based description of the electrochemical interface is provided, taking into account the coupling between the double layer structure and the electrochemical reactions [11].

In the anode "1", the HOR is described according to the elementary kinetic Tafel-Heyrovsky-Volmer model [10, 11],

$$H_2 + 2\,(s) \rightleftharpoons 2\,H(s)\ (Tafel) \qquad [2]$$

$$(s) + H_2 \rightleftharpoons H(s) + H^+ + e^- \text{ (Heyrovsky)} \quad [3]$$
$$H(s) \rightleftharpoons (s) + H^+ + e^- \text{ (Volmer)} \quad [4]$$

In the anode "2" the production of H_2O_2 is described through a three-step potential-independent mechanism [12],

$$O_2 + (s) \rightleftharpoons O_2(s) \text{ (a)} \quad [5]$$
$$O_2(s) + H(s) \rightleftharpoons HO_2(s) + (s) \text{ (b)} \quad [6]$$
$$HO_2(s) + H(s) \rightleftharpoons H_2O_2 + (s) \text{ (c)} \quad [7]$$

In the cathode to describe the ORR, we apply the following elementary mechanism [1-6, 9-11],

$$O_2 + H^+ + e^- + (s) \rightleftharpoons O_2H(s) \text{ } (ORR_1) \quad [8]$$
$$O_2H(s) + H_2O + 2(s) \rightleftharpoons O_2H(s) \text{ } (ORR_2) \quad [9]$$
$$OH(s) + H^+ + e^- \rightleftharpoons H_2O + (s) \text{ } (ORR_3) \quad [10]$$

The rates of these elementary steps are calculated using standard mass-action kinetics with surface potential-dependent rate coefficients for charge-transfer reactions, as described previously [10, 11]. For each intermediate, a balance equation is set up that describes the temporal evolution of the surface coverage.

Membrane model

Oxygen permeation model

In the Nafion membrane oxygen transport is assumed to be governed by Fickian diffusion [9, 10]

$$\frac{\partial C_{O_2}}{\partial t} = -\nabla_z \cdot \vec{J}_{O_2} = -\nabla_z \cdot (-D_{O_2} \nabla_z C_{O_2}) \quad [11]$$

where C_{O_2} and D_{O_2} are respectively the concentration and the diffusion coefficient of the hydrogen and the oxygen.

By assuming at the cathode side an equilibrated absorption of O_2 in hydrated Nafion, the concentrations at $z = 0$ are given by Henry's laws [9, 10].

$$C_{O_2}(z = 0, t) = \frac{p_{O_2}}{H_{O_2}} \quad [12]$$

where H_{O2} is the Henry's coefficients.

Expression of the conductivity

In order to take into account a feedback between the evolution of the structure of Nafion® and its transport properties, we particularly focus on the proton conductivity.

Commonly in the literature, an empirical equation is used as an expression for the proton conductivity $\sigma_{H^+}(t)$ [13]. In order to take into account the structural evolution, an expression has to be derived that depends on physical and structural parameters of the membrane. We extended the approach of Choi et al., with combined the Nernst-Einstein theory and the Einstein-Smoluchowski relation [13].

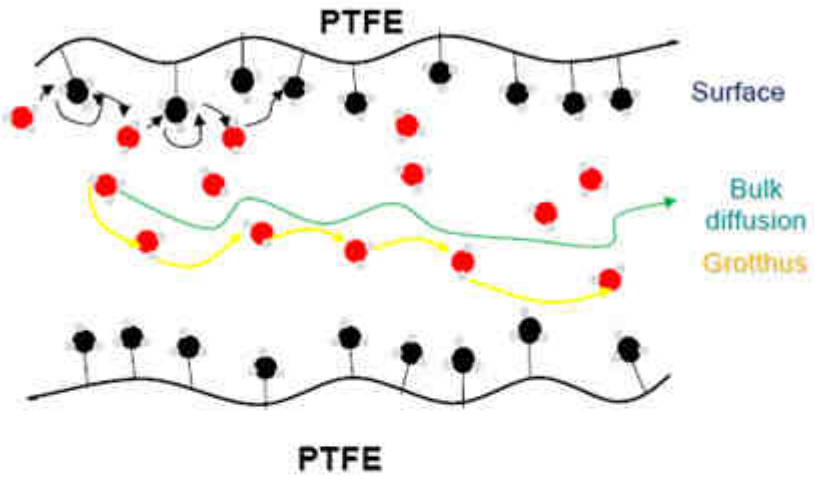

Figure 2. Schematic representation of a Nafion® pore with proton transport.

The conductivity is expressed as the sum of three contributions (Fig. 2): The bulk diffusion of protons, the diffusion via a proton hoping mechanism (Grotthus mechanism) and the surface diffusion in a hydration shell in the vicinity of the sulfonated groups. The proton conductivity is thus expressed as

$$\sigma_{w^-} = \frac{\varepsilon_i}{\tau}\left[\frac{F^2}{RT}\left(D^*_{H^+} \cdot C^*_{H^+} + D^0_{H^+} \cdot C_{H^+} + D^{\pm}_{H^+} \cdot C_{H^+}\right)\right] \qquad [13]$$

where ε/τ is the ratio between porosity and tortuosity, D_i are the diffusion coefficients and C_i are the concentration of protons, either in the "bulk" (middle of the pore) or at the surface of the pore. ε/τ shows the dependence between the structure and the conductivity. It was shown that

$$\varepsilon_i = \frac{\lambda}{\lambda + r} \qquad [14]$$

where

$$r = \frac{\overline{V_0}}{\overline{V_{H_2O}}} \quad [15]$$

and

$$\overline{V_0} = \frac{EW(t)}{\rho_{NAFION}} \quad [16]$$

where $\overline{V_i}$ is the molar volume of water and Nafion®, λ the local number of water molecules persulfonate site and $EW(t)$ the equivalent weight of the membrane. $EW(t)$ is defined by $EW = m^{dry}_{Nafion} / n_{SO3^-}$; knowing the evolution of dry Nafion® weight and the amount of sulfonated groups in the membrane, Equations [13-16] allow to calculate the evolution of the $EW(t)$ and thus the evolution of membrane resistance calculated with [10]

$$R(t) = \frac{e_{electrode}}{S_{electrode} \cdot \sigma_{H^+}(t)}. \quad [17]$$

This value is then used to calculate the electrostatic potentials of the cathode and anode electrolyte bulk. By assuming electroneutrality in the electrolyte, the proton transport is governed by Ohm's law and thus

$$\phi^{cathode}_{bulk}(t) = \phi^{anode}_{bulk}(t) - R(t) \cdot I_{total} \quad [18]$$

Membrane chemical degradation model

In our approach, we consider that the only chemical degradation occurring in the membrane is due to the radical-induced cutting of side chains. The global mechanism we assume for this reaction is [14]

$$HOOC - R(-S) + HO\cdot \rightleftharpoons HOOC - R + A\ (DEG) \quad [19]$$

where R represents a back bone chain, S a side chain and A the molecule which results from cutting the side chain (i.e., perfluoro(3-oxa-5-methyl)pentane-1-sulfonic-5-carboxylic diacid). The evolution of the concentration of sulfonated groups will depend on the concentration of hydroxide radicals, the former concentration of side chains and the degradation constant k_{DEG} following

$$\frac{dC_{SO_3}}{dt} = -k_{DEG} \cdot C_{SO_3} \cdot C_{HO\cdot} = -v_{DEG} \quad [20]$$

Hydroxyl radicals are formed via the decomposition of hydrogen peroxide through the so-called Fenton's reactions,

$$H_2O_2 + Fe^{2+} \rightleftharpoons Fe^{3+} + HO\cdot + HO^- \text{ (F1)} \quad [21]$$
$$H_2O_2 + Fe^{3+} \rightleftharpoons Fe^{2+} + HOO\cdot + H^+ \text{ (F2)} \quad [22]$$
$$HOO\cdot + Fe^{3+} \rightleftharpoons Fe^{2+} + O_2 + H^+ \text{ (F3)} \quad [23]$$
$$H_2O_2 + HO\cdot \rightleftharpoons H_2O + HOO\cdot \text{ (F4)} \quad [24]$$
$$HO\cdot + Fe^{2+} \rightleftharpoons Fe^{3+} + HO^- \text{ (F5)} \quad [25]$$

The time-dependent concentrations of the different intermediates and reaction products are given by the following system of differential equations (so-called rate equations),

$$\frac{dC_{H_2O_2}}{dt} = v_c - v_{F1} - v_{F2} \quad [26]$$
$$\frac{dC_{Fe^{2+}}}{dt} = -v_{F1} + v_{F2} + v_{F3} - v_{F5} \quad [27]$$
$$\frac{dC_{Fe^{3+}}}{dt} = v_{F1} - v_{F2} - v_{F3} + v_{F5} \quad [28]$$
$$\frac{dC_{HO\cdot}}{dt} = v_{F1} - v_{F4} - v_{F5} - v_{DEG} \quad [29]$$
$$\frac{dC_{HOO\cdot}}{dt} = v_{F2} - v_{F3} \quad [30]$$

with

$$v_{F1} = k_{F1} \cdot C_{H_2O_2} \cdot C_{Fe^{2+}} \quad [31]$$
$$v_{F2} = k_{F2} \cdot C_{H_2O_2} \cdot C_{Fe^{3+}} \quad [32]$$
$$v_{F3} = k_{F3} \cdot C_{HOO\cdot} \cdot C_{Fe^{3+}} \quad [33]$$
$$v_{F4} = k_{F4} \cdot C_{H_2O_2} \cdot C_{HO\cdot} \quad [34]$$
$$v_{F5} = k_{F1} \cdot C_{HO\cdot} \cdot C_{Fe^{2+}} \quad [35]$$

These expressions allow the calculation of the side chain concentration over time and thus, the evolution of conductivity. Moreover, due to the direct time-dependent coupling of membrane degradation model and membrane conductivity model with the electrode nanoscale models, the decrease of cell potential during the operation of the cell can be simulated.

Simulation methodology

All simulations presented in this paper were carried out in the MEMEPHYS code, being developed at CEA from 8 years ago [1-6, 9-11], and programmed into a hybrid in-house environment combining Matlab-Simulink®, Comsol Multiphysics® and C language. All model parameters associated with the membrane and with the operational conditions are given in Table I and Table II.

k_a, k_b, k_c and k_{DEG} were approximating using the optimisation toolbox of Matlab-Simulink®, fitted after inhouse measurements of membrane resistance during the work of a PEM fuel cell.

TABLE I: Default parameters and operating conditions used for the simulations.

Parameters	Symbol	Value
Temperature	T	353 K
Pressure anode	P_{anode}	$1.5 \cdot 10^5$ Pa
Pressure cathode	$P_{cathode}$	$1.5 \cdot 10^5$ Pa
Surface electrode	$S_{electrode}$	2.1 cm²
Membrane thickness (default)	$e_{membrane}$	25 µm
Water content	λ	14

TABLE II: Kinetics Parameters used for the simulations.

Parameters	Value	Ref.
k_a	10^{-8} m³·mol⁻¹·s⁻¹	Estimated
k_b	10^{-3} m⁻²·mol·s⁻¹	Estimated
k_c	10^{-2} m·s⁻¹	Estimated
k_{DEG}	100	Estimated
k_{F1}	$63 \cdot 10^{-3}$ m³·mol⁻¹·s⁻¹	[15]
k_{F2}	$2.3 \cdot 10^{-6}$ m³·mol⁻¹·s⁻¹	[16]
k_{F3}	$3.3e \cdot 10^{2}$ m³·mol⁻¹·s⁻¹	[17]
k_{F4}	$3.3e \cdot 10^{4}$ m³·mol⁻¹·s⁻¹	[18]
k_{F5}	$3.2e \cdot 10^{5}$ m³·mol⁻¹·s⁻¹	[19]

Results and discussion

Impact of membrane degradation on cell performance

In Fig. 3, we compare the polarization curves of a fuel cell under the conditions defined in Table I. We can observe that the influence of the membrane degradation on the decay of potential is negligible until t = 1000 hr. For longer operating times, the impact of membrane degradation on the performance becomes pronounced. Fig. 4 shows the temporal evolution of the cell potential at several given currents. We observe a strong influence of this value on the cell potential for currents above 0.5 A. This shows how operating conditions influence degradation behavior.

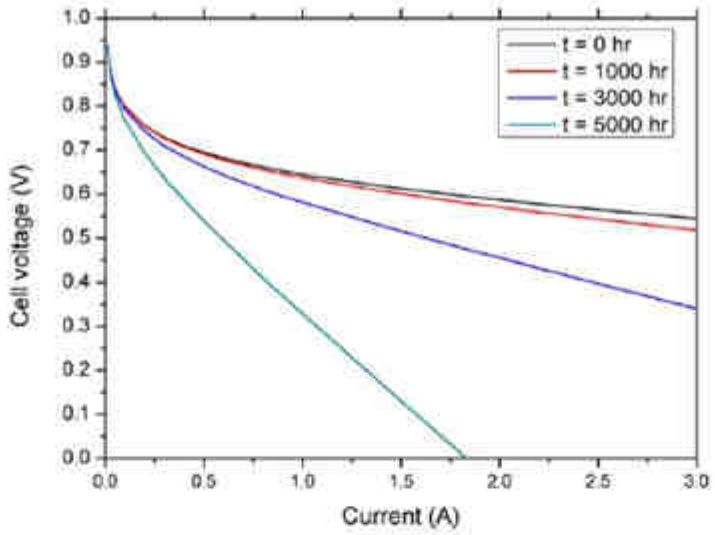

Figure 3. Predicted polarization curves for different simulated operation times

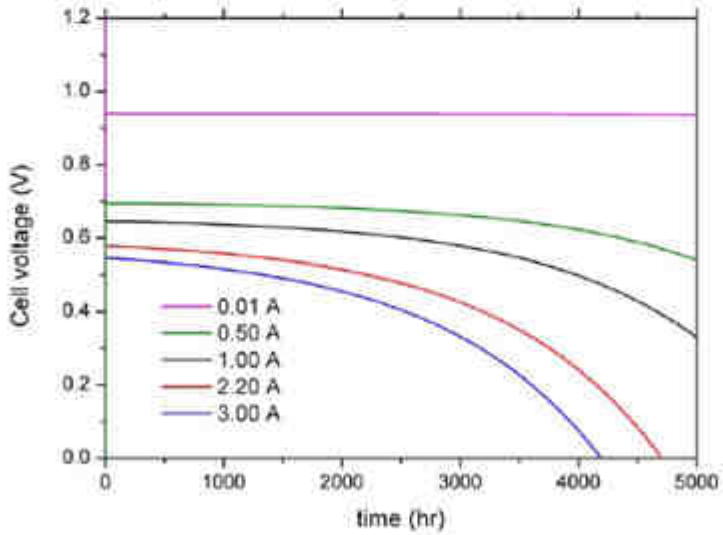

Figure 4. Simulated temporal evolution of the cell potential for different currents.

Impact of membrane degradation on membrane conductivity

The evolution of the membrane conductivity versus time is shown in Fig. 5 for different currents. The membrane conductivity is continuously decreasing over time. The slope of the curve is decreasing as well, suggesting that the conductivity would reach a constant value at the end of the life of the cell. Fig. 6 shows the same data plotted as membrane conductivity versus current. Both plots show that the increase of membrane resistance with time is only little dependent on current.

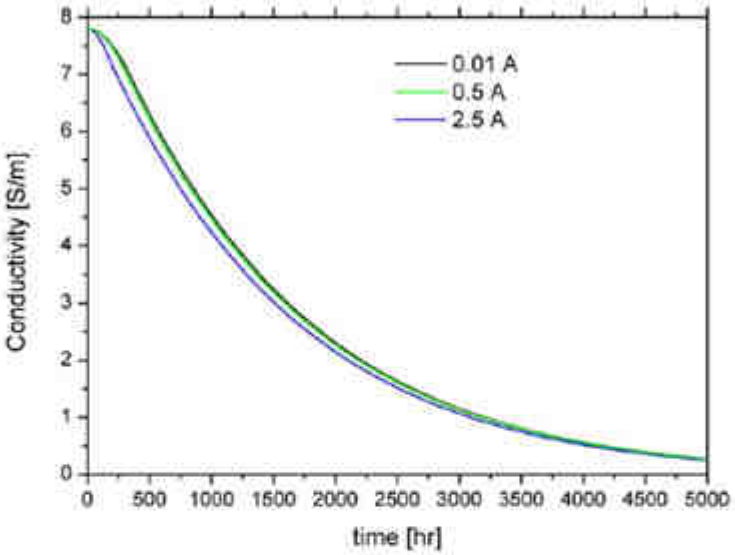

Figure 5. Evolution of the membrane conductivity over time

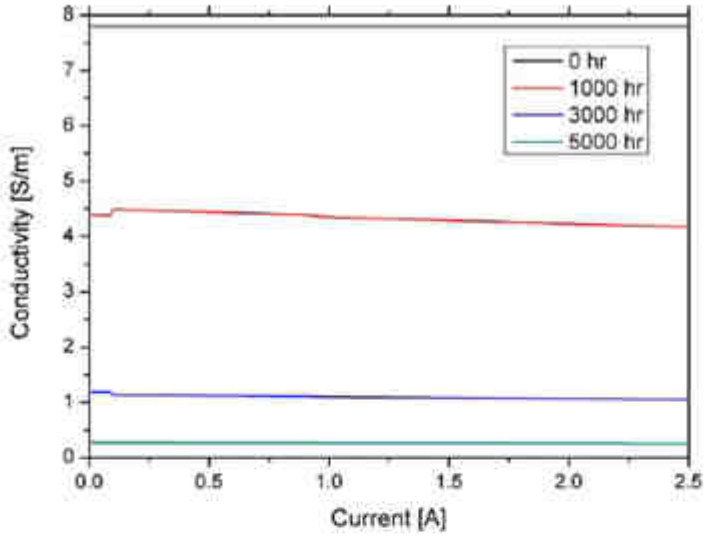

Figure 6. Evolution of membrane conductivity with current.

Influence of membrane thickness on the membrane degradation

Fig. 7 shows the membrane conductivity plotted versus time for different membrane thicknesses of 25, 50 and 100 µm. We observe an only little impact of the thickness on the conductivity. Therefore, material properties stay largely unchanged from a thin membrane to a thick membrane. Fig. 8 shows an enlargement of the last 1,000 hr for the Fig. 7. We observe here that the conductivity of the thicker membrane remains better than that one of the others membranes. Fig. 9 shows the concentration of sulfonic acid groups in the membrane over time. Here we observe that for the 100 µm case, the concentration is higher, which means the degradation is smaller. These findings lead to the conclusion that even if a thin membrane has a smaller resistance due to its little thickness, it is slightly more sensible to degradation.

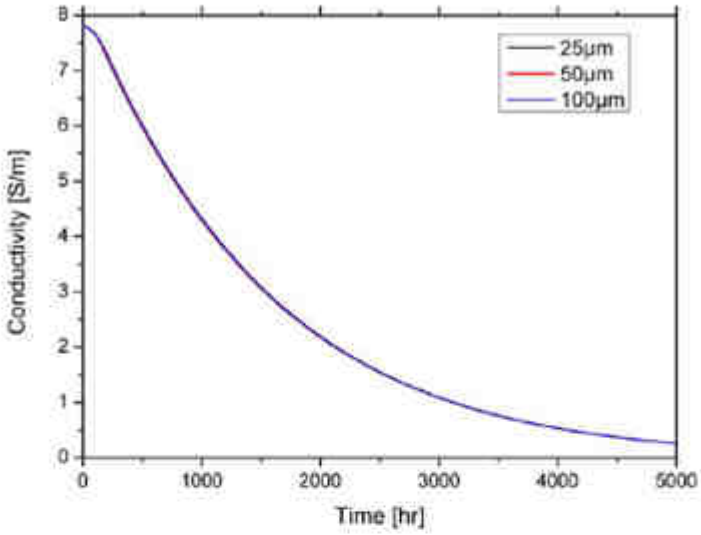

Figure 7. Membrane conductivity evolution for several membrane thicknesses.

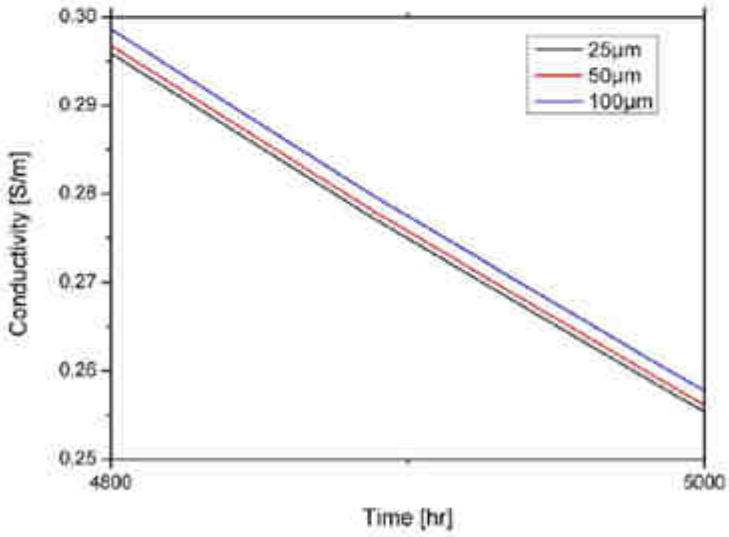

Figure 8. Enlargement of the 1,000 last hours of the Fig. 7.

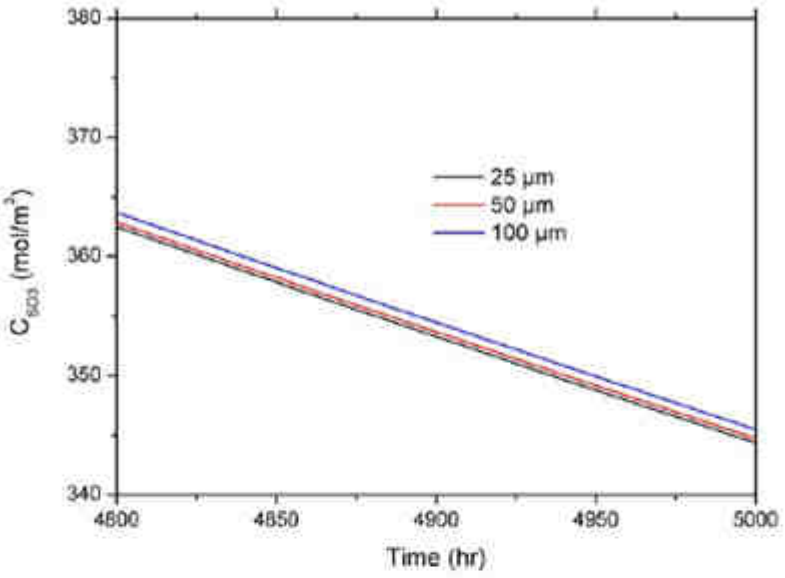

Figure 9. SO_3 concentration for the last 200 hr of the simulations.

Outlook

Further development of the model is underway. Firstly, the cross-over model we used, a common application of the Fick's law, does not take into account the structural modification of the nanostructure of the membrane (a loss of matter would cause an increase of H_2 and O_2 permeation). Secondly, the model is currently designed for a fully-hydrated membrane under fuel-starvated conditions. A further step will be a 1D discretization of the membrane in the perpendicular direction to the electrodes. Lastly, we will validate our model with *in situ* and *ex situ* experiments and couple it with other degradation mechanisms which have already been developed and validated, such as carbon corrosion and catalyst dissolution [1-4].

Conclusions

We have presented a multi-scale elementary-kinetic model, following the approach proposed by Franco *et al* in [1-4], that allows to predict the long-time polymer electrolyte membrane degradation in fuel cells. Here we have focused on the impact of membrane degradation on the cell potential for several nominal currents. Chemical degradation of the Nafion® membrane is described through a combination of OH radical formation via Fenton's reaction and a radical mechanism of side chain decomposition. At the electrodes, the model is coupled to a description of the hydrogen oxidation reaction, the oxygen reduction reaction, and the hydrogen

peroxide formation reaction at the anodic side. This is to our knowledge the first model taking into account a feedback between polymer electrolyte membrane structural evolution and cell potential degradation. The degradation of the membrane has a pronounced influence on the fuel cell for operating times above 1000 hr. The actual operating conditions (electrical current) and membrane thickness have only minor influence on the increase of the specific membrane resistance.

Acknowledgments

This work is funded by the European Commission through the program PCRD 7, within the context of the project "DECODE".

References

1. Franco, A.A. and M. Gerard, *Multiscale Model of Carbon Corrosion in a PEFC: Coupling with Electrocatalysis and Impact on Performance Degradation.* Journal of the Electrochemical Society, 2008. **155**(4): p. 18.
2. Franco, A.A., et al., *Impact of carbon monoxide on PEFC catalyst carbon support degradation under current-cycled operating conditions* Electrochimica Acta, 2009. **54**(22).
3. Franco, A.A., et al., *Transient Multi-Scale Modeling of PtxCoy Catalysts Degradation in PEFC Environments.* ECS Transactions, 2008. **13**(17).
4. Franco, A.A., et al., *PtxCoy Catalysts Degradation in PEFC Environments: Mechanistic Insights.* Journal of the Electrochemical Society, 2009. **156**(3).
5. Franco, A.A. and M. Tembely, *Transient Multiscale Modeling of Aging Mechanisms in a PEFC Cathode.* Journal of the Electrochemical Society, 2007. **154**(7): p. 12.
6. Franco, A.A., et al., *Multi-scale Modeling-based Prediction of PEM Fuel Cells MEA Durability under Automotive Operating Conditions* ECS Transactions, 2009. **54**(22).
7. Schmittinger, W. and A. Vahidi, *A review of the main parameters influencing long-term performance and durability of PEM fuel cells.* Journal of Power Sources, 2008. **180**.
8. Wang, Y. and C. Wang, *Transient analysis of polymer electrolyte fuel cells.* Electrochimica Acta, 2005. **50**(6).
9. Franco, A.A., *A Physical Multiscale Model of the Electrochemical Dynamics in a Polymer Electrolyte Fuel Cell,* PhD Thesis, 2005, Université Claude Bernard: Lyon-1.
10. Franco, A.A., et al., *A Multi-Scale Dynamic Mechanistic Model for the Transient Analysis of PEFCs.* Fuel Cells, 2007. 7(2).
11. Franco, A.A., et al., *A Dynamic Mechanistic Model of an Electrochemical Interface* Journal of the Electrochemical Society, 2006. **153**.
12. Chen, C. and T. Fuller, *Modeling of H_2O_2 formation in PEMFCs.* Electrochimica Acta, 2009. **54**(16).
13. Choi, P., N.H. Jalani, and R. Datta, *Thermodynamics and Proton Transport in Nafion II. Proton Diffusion Mechanisms and Conductivity.* Journal of the Electrochemical Society, 2005. **152**(3): p. 8.

14. Xie, T. and C.A. Hayden, *A kinetic model for the chemical degradation of perfluorinated sulfonic acid ionomers: Weak end groups versus side chain cleavage.* Polymer, 2007. **48**: p. 10.
15. Gallard, H., J.D. Laat, and B. Legube, *Influence du pH sur la vitesse d'oxydation de composès organiques par FeII/H2O2. Mécanismes reactionnels et modélisation.* New Journal of Chemistry, 1998. **22**(3).
16. Lin, S. and M.D. Gurol, *Catalytic decomposition of hydrogen peroxide on iron oxide: kinetics, mechanism and implications.* Environmental Science and Technology, 1998. **32**.
17. Haber, F. and J. Weiss, *The catalytic decomposition of hydrogen peroxide by iron salts.* Proc. R. Soc. Ser., 1934. **T27**.
18. Christensen, H., K. Sehested, and H. Corfitzen, *Reactions of hydroxyl radicals with hydrogen peroxide at ambient and elevated temperatures.* Journal of Physical Chemistry, 1982. **86**.
19. Buxton, G.V., et al., *Critical review of rate constants for reactions of hydrated electrons, hydrogen atoms and hydroxyl radicals (OH/O−) in aqueous solution.* Journal of Physical Chemistry, 1988. **17**(2).

Journal of The Electrochemical Society, 157 (6) B943-B951 (2010)
0013-4651/2010/157(6)/B943/9/$28.00 © The Electrochemical Society

Pt_xCo_y Catalysts Degradation in PEFC Environments: Mechanistic Insights

II. Preparation and Characterization of Particles with Homogeneous Composition

Pascal Fugier,[a,*] Sylvain Passot,[a] Christelle Anglade,[a] Laure Guétaz,[b] Nicolas Guillet,[b] Eric De Vito,[b] Sophie Mailley,[c] and Alejandro A. Franco[a,*,z]

[a]Laboratoire des Technologies des Surfaces, Département des Technologies des Nanomatériaux, [b]Laboratoire des Composants pour Piles à Combustibles et de Modélisation, Département de l'Electricité et de l'Hydrogène pour les Transports, and [c]Laboratoire des Batteries Avancées, Département de l'Electricité et de l'Hydrogène pour les Transports, Commissariat à l'Energie Atomique et aux Energies Alternatives/Centre de Grenoble LITEN, 38054 Grenoble Cedex 9, France

In this paper, we present experimental results on the preparation and the electrochemical characterization of Pt_xCo_y electrocatalytic particles with homogeneous composition, modeled by Franco et al. [*J. Electrochem. Soc.*, 154, B410 (2008)]. Preparation is made through the direct liquid injection metallorganic chemical vapor deposition technique previously developed at CEA, and electrochemical analysis is carried out by using a rotating disk electrode and membrane-assembled gas diffusion electrode. Degradation structural changes are characterized by using transmission electron microscopy, X-ray diffraction, and X-ray photoelectron spectroscopy. Optimal Co compositions are identified for better oxygen reduction reaction activity and durability, validating the modeling studies.

Manuscript submitted September 4, 2009; revised manuscript received March 15, 2010. Published May 3, 2010.

The specific activity and stability of polymer electrolyte fuel cell (PEFC) electrodes can be improved by alloying Pt with some transition metals (e.g., Co, Ni, and V). These electrodes therefore achieve lower overall Pt loadings compared to pure Pt-based electrodes. In our previous paper,[1] we have proposed a multiscale kinetic model describing the oxygen reduction reaction (ORR) activity and degradation of Pt_xCo_y nanoparticles in PEFC environments. This model provides mechanistic insights on the impact of the nanostructure and operating conditions on the Pt_xCo_y nanoparticles durability. On the basis of ab initio data, we identify favorable pathways of the ORR on Pt_xCo_y nanoparticles and of the competitive Pt–Co dissolution in acidic media. The derived ab initio-based kinetics is coupled to a description of the atomic reorganization at the nanoparticle level as a function of the cumulated Pt and Co mass losses. This nanoscale model is coupled with a transport macroscale model of charges and O_2 through a PEFC cathode, and sensitivity simulations to several operation conditions and initial compositions/morphologies are performed. Two kinds of particles are simulated:

1. Annealed Pt_xCo_y nanoparticles (representative of complete alloys) by using the Monte Carlo method.
2. Homogeneous Pt_xCo_y particles, i.e., with the surface composition equal to the volume composition (representative of bulk-truncated structures or incomplete alloys).

In this paper, we focus on the preparation and the electrochemical characterization of the second kind of Pt_xCo_y particles. The goal here is not to prepare highly active and stable electrocatalytic system but to prepare model electrodes with structures/morphologies that can be compared with the Pt_xCo_y homogeneous particles that we modeled in Ref. 1.

Preparation methods for pure Pt or Pt-based electrocatalysts are generally aqueous methods using various reducing agents. The conventional method consists in depositing Pt on carbon and then Co on Pt/C.[2-4] For example, Xiong and Manthiram synthesized Pt-M (M = Fe, Co, Ni, and Cu) catalysts by using a commercial Pt catalyst supported on carbon black.[2] Two other synthesis methods are presented in Ref. 5 and 6. Li et al. developed a method for the synthesis of Pt-Co based on the preparation of a Co/C composite support followed by removing the excess Co in a H_2SO_4 solution.[7]

Other methods based on surface technologies have also been studied such as the chemical vapor deposition (CVD) process. Chemical deposition processes used for the formation of thin films or supported nanoparticles are based on chemical reactions between inorganic or organic metal-containing species, leading to the formation of a thin layer on an appropriate substrate. All these processes are one-step processes, in general, simpler and less expensive than physical deposition processes. They are commonly used for the production of various coatings (metals, oxides, and composites), the main advantage being that they allow an easy scaling up to large size systems and a conformal coverage of complex shapes. The chemical reactions used in CVD are numerous and include thermal decomposition (pyrolysis), reduction, hydrolysis, and oxidation, which can be used either singly or in combination. These reactions can be activated by several methods, the most important one being thermal activation and plasma activation. Depending on the applications and specifications, the reactants (precursors) have to be correctly chosen from the following general groups: halides, carbonyls, metallorganics (MO_x), and hybrids.

In our group at CEA, a modified CVD method, the metallorganic chemical vapor deposition (MOCVD) process, has been developed to prepare PEFC electrodes directly on a gas diffusion layer (GDL) support.[8,9] MOs are compounds in which the atom of a metallic element is bound to one or more carbon atoms of an organic hydrocarbon group. Most of the elements used in MOCVD are from the IIa, IIb, IIIb, IVb, Vb, and VIb groups.

In an MOCVD process, thin films or nanoparticles are formed on a surface from the thermal decomposition of the gaseous precursor molecules. The total pressure used in the gas phase is generally a low pressure, in the range of a few Torrs.

Precursors for MOCVD should, in general, have an evaporation rate that is high enough, stable, and constant in time. The precursor molecule should be chemically and thermally stable during the transport through the gas phase to the surface. The precursor should be

1. Relatively easy to synthesize.
2. Not be dangerous and should not produce dangerous products.
3. Must be soluble and stable in a suitable solvent without formation of precipitates (in a droplet-derived deposition process).

* Electrochemical Society Active Member.
z E-mail: pascal.fugier@cea.fr; alejandro.franco@cea.fr

Classical MOCVD processes are based on the evaporation of solid MO precursors and meet the problem of irreproducibility of vapor generation and transport, thus making the growth process and consequently the films properties less reproducible. Due to these reasons, new liquid delivery systems have been introduced a few years ago to overcome the problem of thermal stability of some complexes such as the pulsed liquid injection metallorganic chemical vapor deposition (PLI-MOCVD) process or the direct liquid injection metallorganic chemical vapor deposition (DLI-MOCVD) process.[10-12] The main advantages of these liquid delivery systems are:

1. A single precursor mixture can be used for multi component systems.
2. Very high growth rates can be obtained.
3. Precursors (solid or liquid) can be kept at low temperature and atmospheric pressure.
4. Only small amounts of materials (a few microliters) are volatilized.

The evaporation of precursors with low vapor pressure even under atmospheric pressure is possible. In PLI-MOCVD, the solution is injected directly by a microvalve. The injector injects microdoses (a few microliters) of an organic solution containing a dissolved mixture or a pure MO liquid precursor. After flash evaporation, the resulting vapor mixture is transported by gas toward the heated substrate. The frequency, the opening time, and the solution concentration are the main parameters controlling the growth rate. To date, on the basis of this liquid delivery system, high quality noble metal nanoparticles or oxide films have been obtained in our institute.[13] This method is very versatile and is thus suitable for in situ deposition of thin films or complex systems such as metal/oxide composites, carbon nanotube, nanoparticles, and multilayers.

In this paper, we discuss the structural and electrochemical properties of model Pt_xCo_y PEFC cathodes made using the DLI-MOCVD process depositing on a carbon support Pt and Co at the same time. Results are reported for cathodes operated under different operating conditions and operating times. This compliments our modeling work on Pt_xCo_y-based nanoparticles already published in Ref. 1 and 14.

The paper is organized as follows. First, we present the experimental preparation of the cathodes and characterization setups. Second, we discuss the characterization results regarding the activity and stability properties according to the Pt_xCo_y nanostructure, in connection with our previously published modeling results. Finally, we conclude and indicate further directions in our research.

Experimental

Preparation of the Pt_xCo_y electrocatalysts.— Pt_xCo_y electrocatalysts were prepared using the DLI-MOCVD method developed at CEA. For the deposition of the bimetallic electrocatalysts in the reactor, dimethyl(1,5-cyclooctadiene) platinum(II) [$Pt^{II}(Me_2cod)$, Strem] and cobalt(III) acetylacetonate [$Co^{III}(acac)_3$, Strem] were used as precursors. All precursors are soluble in toluene (Aldrich) for the used concentrations (<0.03 M). Simultaneous liquid injection was done to obtain bulk-truncated or incomplete Pt_xCo_y alloys. The Pt_xCo_y ratio is controlled by the precursor concentration. The precursor solutions were pushed by nitrogen. The solvent was then evaporated and cracked by thermal effect and oxidative atmosphere (O_2 80%, N_2 20%). Both precursors were also decomposed by the temperature and gas pressure inside the reactor (Fig. 1). Pt_xCo_y electrocatalysts were formed at 350°C on a GDL (ELAT LT1400W, E-Tek BASF) playing the role of microporous carbon catalyst support.[a] No ionomer impregnation was applied after the catalyst elaboration to avoid ionomer poisoning effects on the catalysts' electrochemical behavior during the experimental tests.

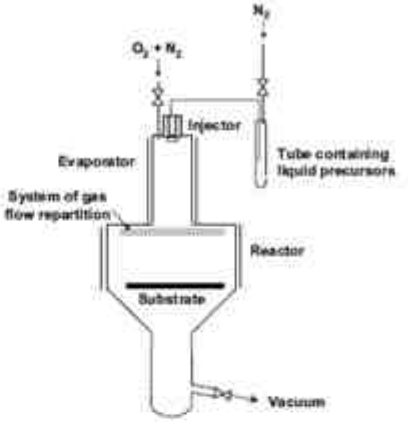

Figure 1. Schematic diagram of the DLI-MOCVD process reactor.

Structural and chemical characterization methods.— The metal loadings in the fresh samples were measured by inductively coupled plasma atomic emission spectroscopy (ICPAES). The morphology and the particle size distribution were observed by electron microscopy [transmission electron microscopy (TEM) and field-emission gun scanning electron microscopy (FEGSEM)]. Observations of the GDL support surface after deposition were performed using a LEO 1530 FEGSEM coupled with an energy-dispersive X-ray spectrometry (EDXS) analysis. TEM images and EDXS analyses were also realized using a JEOL 2000 FX microscope. The particle structures were observed by high resolution transmission electron microscopy (HRTEM) using a JEOL 4000 EX microscope. The X-ray diffraction (XRD) patterns were obtained from a Bruker D5000 diffractometer. The surface of the nanoparticles was characterized by X-ray photoelectron spectroscopy (XPS). The XPS device used in this study consisted of an SSI S-Probe spectrometer equipped with a monochromatized Al Kα source. The pass energy was chosen to be 50 eV while the energy resolution was kept at 850 meV.

Chemical leaching was carried out (24 h, H_2SO_4 0.5 M, 50°C) on the pure Pt catalyst and on the three Pt_xCo_y catalysts to distinguish the dissolution induced by the acidic media from the one induced by the potential cycling. Then, platinum and cobalt were also dosed by ICPAES.

Electrochemical characterization methods.— Our materials were characterized by two electrochemical methods. Rotating disk electrode (RDE) experiments were used first because of their easy implementation and because they allowed us to characterize the catalysts in the most severe conditions of stability. Half-cell experiments were used for fine testing the most interesting materials under conditions closer to the fuel cell environment. Both RDE experiments and half-cell experiments were carried out directly on gas

[a] The DLI-MOCVD reactor is a tool dedicated for preparing Pt-Co catalysts. In our catalysts preparation, we have implemented precursors with high purity level (99.9%) and high quality solvents typically used in microelectronics. Based on ICP characterizations, we have not observed any presence of impurities on the fresh catalysts and on the GDL support.

diffusion electrodes (GDEs) (GDE = GDL + catalyst deposit). All the electrochemical experiments were carried out at room temperature in a 0.5 M H_2SO_4 electrolyte.

Ex situ characterizations: RDE performance experiments.— The cell used for the RDE experiments is constituted by a classical three-electrode system with a working electrode consisting of a glassy carbon disk (Sigradur Grade G) supporting our substrate. The counter electrode is a reversible hydrogen electrode (RHE). Before the tests, 1 μL of ethanol was put on the GDE and rinsed with deionized water. The electrochemical three-electrode cell was connected to a digital potentiostat (Autolab PGSTAT30), with an RHE as a reference electrode.

The linear sweep voltampeorometry was used to allow the determination of the "electroactive catalyst surface area" (ECSA) (or at least, the H^+ adsorption properties on the catalysts) (under nitrogen bubbling) and to quantify the properties of our catalysts regarding the ORR (under oxygen bubbling). The effective electroactivity of the Pt_xCo_y regarding ORR was determined from voltammetry experiments (2 mV s^{-1}) between 1 and 0.4 V_{RHE}. Before each voltammetry, the electrode was kept for 1 min at a potential of 1 V_{RHE} to ensure a reproducible electrocatalytic surface state. During all the experiments, the N_2 or O_2 concentration was kept constant at its saturation value by permanent gas bubbling. The RDE angular rotation rate ω was varied in the 200–900 rpm range. Levich approach is used to calculate the current limited by the convective transport (voltammetry sigmoidal wave height or Levich current)

$$I_L(\omega) = 0.620 \times n \times F \times A_g \times D^{2/3} \times \upsilon^{-1/6} \times C_0 \times \omega^{1/2} = B \times C_0 \times \omega^{1/2} \quad [1]$$

where n is the number of electrons transferred in the ORR, F is the Faraday constant, A_g the is the geometric area of the RDE, D is the O_2 diffusion coefficient, υ is the kinematic viscosity of the electrolyte, C_0 is the O_2 concentration in solution at the bulk level just outside the nanoscopic diffusion layer developed on the catalyst nanoparticle surface (see our atomistic-based nanoscale model in Ref. 1, 14, and 15), and B is the Levich coefficient. The electrode steady-state current $j(E,\omega)$ (A m^{-2} geometric) at a given electrode potential E and angular rotation rate ω is given by the following equation

$$\frac{1}{j(E,\omega)} = \frac{1}{j_k} + \frac{1}{j_L(\omega)} = \frac{1}{j_k} + \frac{1}{nB\omega^{1/2}} \quad [2]$$

where j_k is the cathodic activation current density at a potential E and $j_L(\omega)$ is the transport-limited current density in the voltammogram (A m^{-2} geometric) derived from Eq. 1.

The RDE voltammogram results presented in this paper display current densities corrected ($j_{corrected}$) by the diffusion in solution using the classical Levich method (for high ORR Butler–Volmer overpotentials, i.e., for $E > 0.8$ V_{RHE})

$$j_{corrected} = \frac{j_L(\omega) \times j(E,\omega)}{j_L(\omega) - j(E,\omega)} \quad [3]$$

Ex situ characterizations: RDE aging test.— Our RDE aging test is analogous to Colón-Mercado and Popov's accelerated durability test[16] where they used a three-electrode system with a Hg/Hg_2SO_4 electrode as the reference electrode. Our aging experiments were carried out at $I = 0$ A (open circuit) for 7 days (160 h) at 60°C in H_2SO_4/0.5 M saturated O_2 electrolyte and using a saturated calomel electrode as a reference electrode connected to an EGG Par 273 digital potentiostat. The same electrochemical characterizations as described above were done before and after aging.

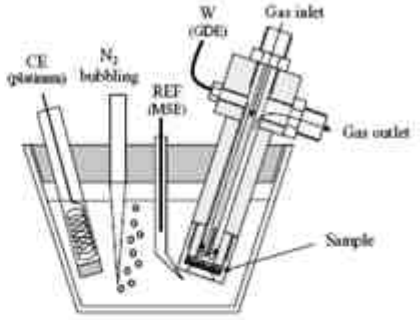

Figure 2. Representation of the three-electrode device for GDE testing (half-cell).

In situ characterizations: half cell performance experiments.— A GDE (14 mm diameter disk) and a Nafion NRE 212 CS membrane (DuPont) were directly bonded together by a hot-pressing process (10 MPa at 150°C for 2 min and 30 s). The obtained membrane electrode assembly (MEA) was inserted in the sample holder with the GDL facing up[17] (Fig. 2). The membrane is then in contact with the liquid electrolyte (0.50 cm^2) while the same surface area of the GDL is fed with the reactive gas. A gold grid provides the electrical contacts and a polytetrafluoroethylene (PTFE) gasket set on the membrane side ensured the tightness of the device.

A three-electrode, two-compartment setup containing 40 mL of H_2SO_4 solution with continuous nitrogen bubbling was used. A platinum mesh was used as a counter electrode, and the reference electrode was in mercury sulfate (mercury sulfate electrode Hg/Hg_2SO_4/0.5 M H_2SO_4 radiometer). Electrochemical experiments were conducted with a digital Bio-logic VMP2 potentiostat. Polarization curves were captured following this test scheme: While the oxygen flow was set at 2 mL h^{-1}, six voltammetry cycles from 0.05 to 1.15 V_{RHE} at 20 mV s^{-1} and one voltammetry cycle at 5 mV s^{-1} were performed.

Results and Discussion

Microstructural characterization results on fresh electrodes and aged electrodes.— Atomic Pt/Co volumetric ratios were calculated from ICPAES measurements and compared to EDXS results (Table I). Our DLI-MOCVD process allowed us to obtain very low metal loadings (<100 μg/cm^2), making possible materials economies and decreasing cost for possible technology commercialization.

Microstructural characterizations.— Figure 3 shows the FEGSEM images of the four fresh materials prepared by DLI-MOCVD. Atomic ratios were estimated by EDXS. On the pure Pt electrode,

Table I. Compositions of the prepared Pt_xCo_y model electrodes.

	Pt ICPAES loadings (μg/cm²)	Co ICPAES loadings (μg/cm²)	Pt/Co ratio calculated from ICPAES values	EDXS (Pt_{x+1}/Co_{y+1})
Pt	61	0	100/0	
Pt_3Co	39	9.3	72/28	76/24
PtCo	68	17	55/45	61/39
$PtCo_3$	29	42	17/83	23/77

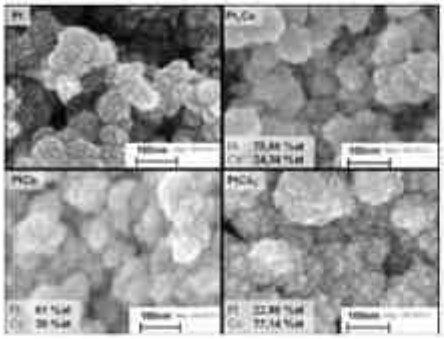

Figure 3. FEGSEM images of the four Pt_xCo_y materials prepared by DLI-MOCVD.

nanoparticles are well-defined and the carbon support is still visible between them. When cobalt is added to platinum, depending on the Pt/Co ratio, the aspect is closer to pure platinum or to pure cobalt, the latter growing with a "cauliflower" aspect, probably due to cobalt oxide.

Figure 4 reports the coupled microtome EDXS analysis of the Pt and Co contents inside the GDL. The deposit is present only in the first 5 μm in the GDL thickness with a nonhomogeneous distribution. There is a "crust" at the GDL surface level with a composition close to the expected atomic Pt-Co ratio. However, in depth, the Pt loading appears to be higher.

HRTEM images of Pt_3Co (Fig. 5a) show particle size of around 7–10 nm. The nanoparticles do not have any specific shape. Furthermore, an amorphous oxide layer seems to be present on the nanoparticles (Fig. 5b).

Figure 6 presents the morphology change after the electrochemical aging described in the Electrochemical operation and postaging results section. Before aging, the catalyst particles present a homogeneous distribution. After degradation, the electrode appears to be more porous (higher roughness at the GDL surface), in agreement with our modeling results in Ref. 1 and 14 where the Pt dissolution rate is predicted to be considerably lower than the Co dissolution rate when the two materials coexist at the catalyst (the Pt dissolution rate increases as the Co content at the particle level decreases) and the homogeneous catalyst become more and more like a skeleton-structured particle (the transition element dissolves leaving "holes" in a Pt matrix, like a "French emmental cheese").

XRD structure characterization of the fresh materials.— XRD characterizations provide information about the catalyst crystallographic structure. The diffractograms of all the fresh materials are presented in Fig. 7. The first narrow peak corresponds to the PTFE and the second peak to graphitic carbon, both materials constitutes the GDL. Pure Pt, Pt_3Co, and PtCo diffractograms show the main peaks of the face-centered cubic (fcc) Pt structure. The diffractogram of Pt_3Co also shows a slight shift to higher angles indicating Co insertion inside the Pt crystal lattice. The cobalt atomic fraction alloyed with platinum is calculated from Vegard's law for lattice parameters between a pure fcc platinum and a pure hexagonal close-packed (hcp) cobalt

$$x_{sample}^{Co} = \left(\frac{a_{sample} - a_{Pt,fcc}}{a_{Co,hcp}\sqrt{2} - a_{Pt,fcc}} \right) \quad [4]$$

Where a_{sample}, $a_{Pt,fcc}$, and $a_{Co,hcp}$ are the lattice parameters of the sample (3.895 nm), the pure fcc platinum (3.923 nm), and the pure hcp cobalt (2.506 nm). We find that only about 8% of cobalt is

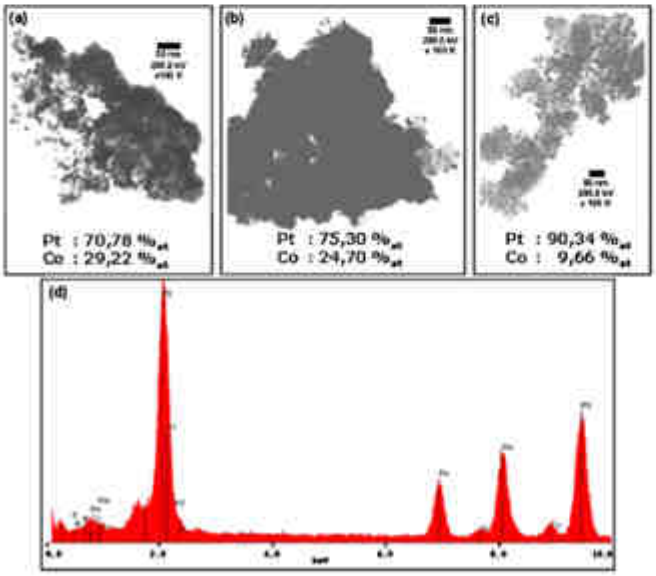

Figure 4. (Color online) [(a), (b), and (c)] EDXS results on fresh Pt_3Co catalysts presented with their associated TEM images. The spectrum (d) corresponds to the image (b). The Cu element appears because of the TEM grid.

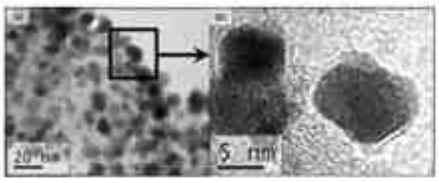

Figure 5. HRTEM images of Pt_xCo nanoparticles elaborated by DLI-MOCVD on a GDL support.

alloyed with platinum in the fresh Pt_xCo sample. The result is analogous for the fresh PtCo sample. The diffractogram of fresh $PtCo_3$ does not show the same main peaks. The peaks of the platinum pattern are lost within the GDL background signals.

These characterization results provide a signature of homogeneous composition (bulk truncated or incomplete alloy) inside these catalysts.[1,14]

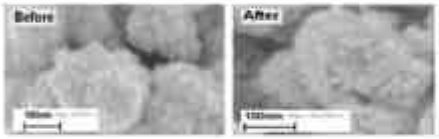

Figure 6. FEGSEM images of the Pt_xCo material elaborated by DLI-MOCVD before and after aging.

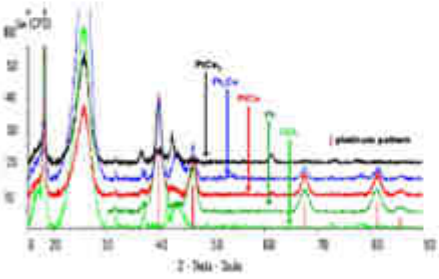

Figure 7. (Color online) XRD spectra of the Pt_xCo_y materials deposited on the GDL by DLI-MOCVD.

XPS surface characterization of the fresh electrodes.— The formation of an oxide layer on the Pt_xCo_y particles should be strongly favored with respect to the conditions of preparation and the oxidation state of the cobalt precursor. This hypothesis is confirmed by the XPS analyses: metallic cobalt (778–778.5 eV)[16,21] is not detected on fresh Pt_xCo_y samples. Instead, a wide peak appears at 781 eV (Fig. 8a), showing the presence of a thick layer of Co oxides (~781 eV).[22,23] However, the abrasion of this oxide layer leads to the apparition of a peak at 778.9 eV (considering the calculated sputtering yields of Pt, Co, and O elements for 500 eV Ar ions,[24] preferential abrasion of oxygen is negligible) (Fig. 8b). This result is coherent with our expectations and our model, which assumes initial oxide coverage in Ref. 1 and 14, as is the case for Pt_3Co in Ref. 25.

XPS surface characterization of the aged electrodes.— XPS analysis on aged electrodes showed unambiguously that the Co disappears from the nanoparticle composition after RDE aging experiments, regardless of their initial composition. Figure 9 compares the survey spectra recorded before and after aging for the $PtCo_3$ sample. After electrochemical aging, no Co peak (around 780 eV) is visible.

As presented in our previous paper,[14] the intensity of the XPS Pt signal after aging depends on the initial composition. For pure Pt, the signal intensity is smaller meaning less metal is visible on the surface after than before. For the three bimetallic catalysts, because of the Co dissolution and of its disappearance from the surface, the Pt signal intensity is greater after than before.

In addition, the XPS analysis after abrasion confirms the hypothesis of a homogeneous profile (bulk-truncated structure or incomplete alloy) in the particles.

Figure 10 shows the O 1s spectra for the three bimetallic materials. Before aging (Fig. 10a-c), two contributions are measured, and after aging, only one is measured (Fig. 10d). Considering Fig. 10, the Co is totally dissolved and no signal is observed. This information confirms that on fresh materials, the Co is oxidized (the peak at 530 eV, which corresponds to oxygen bonded to cobalt disappears when the cobalt peaks disappear).

Electrochemical operation and post-aging results.— Chemical leaching.— By dosing the Pt and Co dissolved in the acid solution and by comparing these results with the initial loading values, we are able to determine the quantity of catalyst dissolved from the carbon support. The Pt dissolution is inferior to 1% in the four cases. For the three Pt_xCo_y catalysts, the Co quantity dissolved is close to 50% (Pt_3Co: 58%, PtCo: 54%, and $PtCo_3$: 49%). Our analysis shows that metal dissolution is caused by two different effects: acidic media and potential cycling. Thus, even for an initially well-alloyed material, chemical leaching can possibly take place in the PEFC environment that can lead to an electrode enriched in Pt on the surface before polarization. This phenomenon, occurring without polarization, is not explicitly accounted for in our model in Ref. 1 and 14 (focused on understanding the material degradation under polarization conditions, including open-circuit voltage conditions, i.e., zero total current) but has been recently modeled by ourselves in Ref. 26.

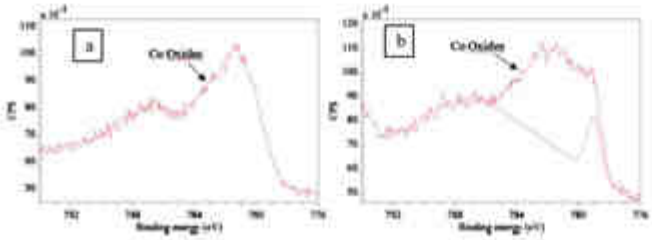

Figure 8. (Color online) XPS spectra of $Co_{2p\ 3/2}$ (a) before and (b) after Ar sputtering ($P_{Ar} = 2.10^{-7}$ mbar, 2kV) the $PtCo_3$ sample surface.

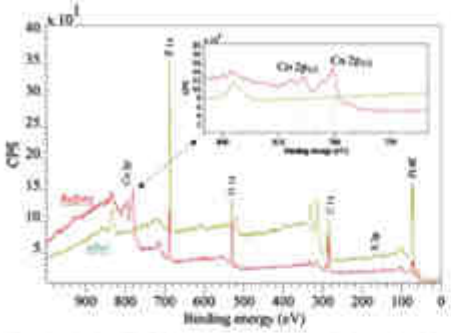

Figure 9. (Color online) XPS survey spectra of the $PtCo_3$ sample, before (green) and after (red) aging.

Ex situ characterizations: RDE performance experiments.— Figure 11 shows cyclic voltamperograms at the beginning of life (BoL) and after the aging of the four tested electrocatalysts. At the BoL, these Pt_xCo_y materials exhibit very different effective ECSA lower to the pure Pt catalyst (Fig. 12a).

The ECSA were calculated by measuring the peak area in the voltammograms and using the following equation

$$ECSA_{Hupd} = \frac{Q_H}{q_H} = \frac{A_H/\nu}{q_H} \quad [5]$$

where A_H is the hydrogen peak desorption area (C V s^{-1}), ν is the scan rate (mV s^{-1}), and q_H is the adsorption charge per cm^2 of platinum on a smooth Pt electrode [assumed to be 210 $\mu C/cm^2$ for a hydrogen monolayer on Pt(111)[27-29]].

We emphasize that this methodology to determine the ECSA based on Eq. 5 only provides a relative comparison of the materials. Rigorously speaking, the "210" value in Eq. 5, derived from an "on-top" adsorption on Pt atoms is unjustified with the Pt_xCo_y catalysts (H^+ can adsorb simultaneously on-top and in bridge between Pt and Co atoms at the Pt_xCo_y catalyst surface and, thus, in a different way compared to pure Pt surfaces). Detailed density functional theory (DFT) studies on adsorption properties of H^+ on Pt_xM_y surfaces are ongoing in our group and are the subject of an ongoing publication.[30]

In the zone of adsorption/desorption, some hydrogen was situated between 0.05 and 0.4 V_{RHE}, three different peaks appeared for all of the considered bimetallic electrodes. These peaks are representative of the adsorption of H^+ on the (110), (111), and (100) crystallographic faces of the platinum and they are very marked (according to Paulus et al.,[31] the insertion of a transition metal leads to poor definition of these peaks). This can indicate that the surface of the particles is Pt-rich.

Figure 12b presents the current densities regarding the ORR as function of the Pt loading for the four tested materials. The current densities provided by the different systems can be ranked as Pt_3Co > $PtCo$ > Pt > $PtCo_3$. We emphasize here that the pure Pt catalyst does not provide the highest current, in contrast to what it could be expected from the ECSA measurement in Fig. 12a. This clearly illustrates that H_{upd} is not an appropriate technique to evaluate the ECSA of the Pt_xCo_y catalysts, as only accounts for H^+ adsorption on Pt sites and as ORR elementary mechanisms on Pt_xCo_y involve both Pt and Co sites.[1,14]

Ex situ characterizations: RDE aging test.— Figure 11 also shows the four cyclic voltamperometries after electrochemical aging of the DLI-MOCVD electrodes at a high fixed potential (low current conditions) in the presence of O_2. The highest current density loss is measured for the pure Pt catalyst (Fig. 13), and Pt_3Co results to be the most stable material, in agreement with our modeling predictions in Ref. 1 and 14. Pt_3Co and $PtCo$ GDE are both still better than pure Pt GDE after aging, in agreement with our model results for short electrode operation time[1] (for longer times, ~12 days, according to our model, the Pt_3Co and $PtCo$ performances could become lower than pure Pt).

The $PtCo_3$ electrocatalyst has the lowest current density among the four materials, and it shows the higher degradation of the three

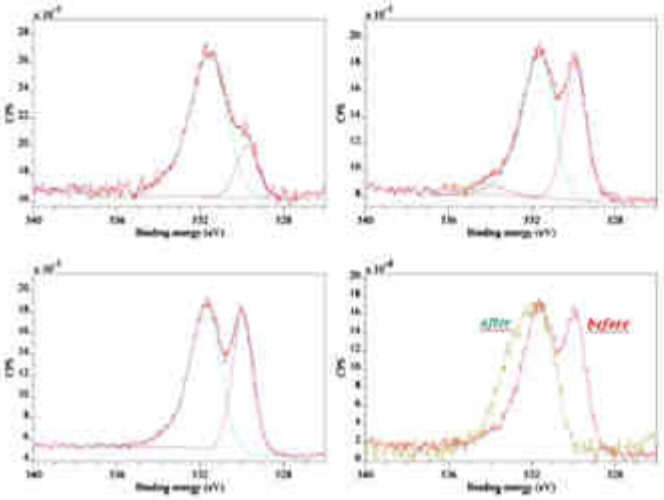

Figure 10. (Color online) [(a), (b), and (c)] XPS oxygen 1s spectra for the three bimetallic electrocatalysts and (d) superposition of the spectra of the PtCo material before and after electrochemical aging.

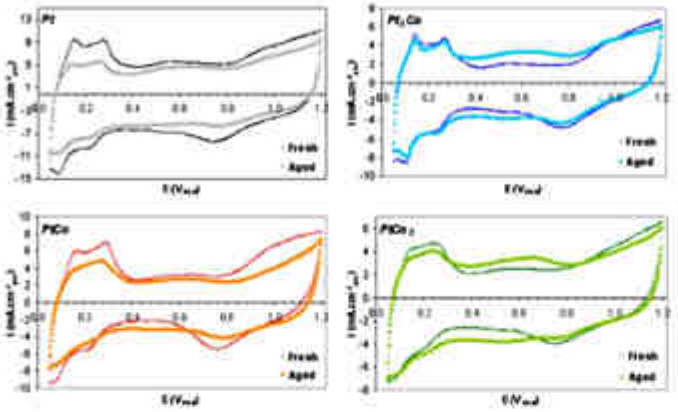

Figure 11. (Color online) Cyclic voltammograms for the four materials elaborated by DLI-MOCVD, before and after aging at a potential of 0.85 V_{RHE} during 160 h. Nitrogen bubbling, H_2SO_4 0.5 M, 100 mV/s, 900 rpm.

bimetallic materials, in agreement with our modeling predictions in Ref. 1 where we demonstrated, on the basis of ab initio-based elementary kinetics, that the Co dissolution rate is higher (more thermodynamically favorable in acidic media) than the Pt dissolution rate and that the Co dissolution rate is higher for higher Co volume contents. This explains why the stability decreases as the Co volume content increases (i.e., Pt_3Co > PtCo > $PtCo_3$, ranking built here on the basis of the "current loss" signature).

In situ characterizations: half cell performance experiments.— As in RDE experiments, cyclic voltammetry was used here to evaluate the ECSA of the catalysts. In this case, the ECSA are calculated from the hydrogen desorption peak area and from the carbon oxide (CO) stripping peak area. The voltammograms recorded in 0.5 M H_2SO_4 at 298 K and 20 mV s^{-1} scan rate after CO adsorption on pure Pt and illustrate the charges corresponding to desorption of H_{upd} (Q_H) and CO (Q_{CO}). The CO stripping ECSA is calculated from Eq. 5 with q_R = 420 $\mu C/cm^2$ representing the charges required to oxidize a monolayer of CO on a Pt electrode.[26,32] As for the H_{upd} methodology, we emphasize that this method only provides a relative comparison of the materials. Detailed DFT studies on the adsorption properties of CO (for the three compositions of PtCo) surfaces are ongoing in our group and are the subject of a future publication.[26,33]

From the calculated values reported in Table II, one can note the quite good agreement of the results obtained by the two methods. It also appears that the values of the roughness factor S_{ad}/S_{geo} (cm^2 Pt/cm^2) are very low compared to typical values reported on MEAs (200–300 cm^2 Pt/cm^2).[34] However, the Pt specific surface area A_{Pt} (m^2/gPt) is of the same order of magnitude such as MEAs, typically 50–80 m^2/gPt.[34]

The relatively high Pt ECSA suggests that the catalyst layer is very thin (in agreement with the microtome analysis discussed in the Microstructural characterization results on fresh electrodes and aged electrodes section) and that a great part of the particles are electrochemically active.

Cyclic voltammetry experiments under O_2 were performed on each sample, prepared and tested in the same conditions to facilitate a direct comparison of the performance of the various catalysts.

Electrochemical impedance spectroscopy (EIS) measurements were also performed on the samples at four current densities: 0.1, 2, 10, and 20 $mA\ cm^{-2}$, applying a 0.2 $mA\ cm^{-2}$ amplitude sinus signal from 10 kHz to 0.2 Hz. Oxygen reduction current curves are presented in Fig. 14. The potentials are corrected for the ohmic loss with the values of the electrolyte resistance, R_Ω (cf. Fig. 16) previously determined by EIS measurements. A semilogarithmic representation (Tafel plot) is given in Fig. 15 showing that the linear evolution of the potential is the same for the three bimetallic catalysts. The slopes are close to 130 mV dec^{-1} whereas it comes near to 120 mV dec^{-1} for pure Pt.[35]

The reduction current of the different catalysts at 0.9 V_{RHE} are given in Table III. Oxygen reduction current corrected with the Pt loading shows similar values for the three PtCo catalysts. These values are closely twice more than for the pure Pt catalyst, showing the improvement on the ORR activity induced by the presence of Co, as already demonstrated with our model.[1,14] Evolutions of the transfer resistance for oxygen reduction vs current density, determined by impedance spectroscopy, are given in Fig. 16.

From these figures, it can be concluded that the best performances are given by the highest Pt-loaded bimetallic samples, in agreement with our modeled polarization curves in Ref. 1 and 14.

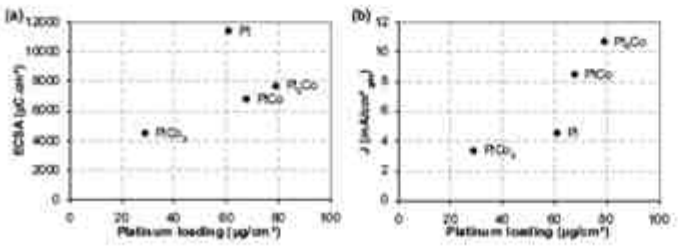

Figure 12. (a) ECSA and (b) current density measured at a potential of 0.85 V_{RHE} plotted as function of Pt loadings for the four prepared materials.

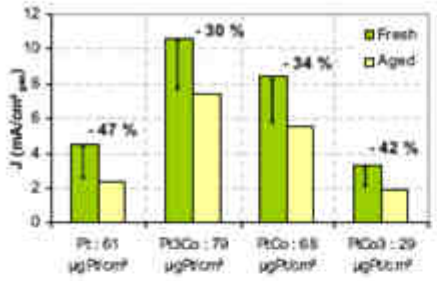

Figure 13. (Color online) Experimental aging results (using Levich equation) for Pt_xCo_y and elaborated by DLI-MOCVD and aged at 0 A during 160 h. The current densities presented here were measured at a potential of 0.85 V_{RHE}.

Table II. ECSA and platinum surface area of the prepared catalysts calculated by hydrogen adsorption (Hupd) and CO stripping voltammograms.

	ECA_{Hupd}		ECA_{CO}	
Catalyst	S_{cat}/S_{geo} (cm^2_{Pt}/cm^2)	A_{Pt} (m^2/g_{Pt})	S_{cat}/S_{geo} (cm^2_{Pt}/cm^2)	A_{Pt} (m^2/g_{Pt})
Pt	20	29	23	34
Pt_3Co	28	40	29	43
PtCo	25	37	27	40
$PtCo_3$	15	22	16	24

Compared to these catalysts, pure Pt shows a 30–40 mV shift toward the anodic potential. Then, the low Pt loaded bimetallic sample curve is still further shifted of approximately 40 mV. The following activity rank can be built, in excellent agreement with our previously published modeling results: PtCo > Pt_3Co > Pt > $PtCo_3$. According to our model, the surface accumulation of HO_2 species is higher for $PtCo_3$ compared to Pt_3Co because of the higher Co surface composition; thus, $PtCo_3$ has a lower overall ORR activity. The number of possible surface transfers of ad-oxygenated species from Pt to Co is maximum at a surface composition of 50–50%, and this explains why homogeneous PtCo offers better ORR activity.[1]

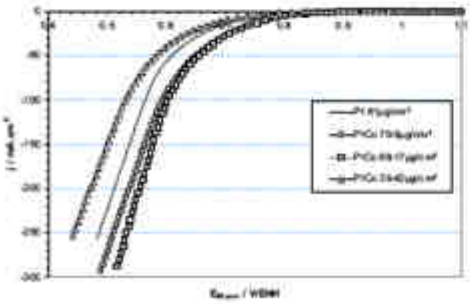

Figure 14. (Color online) i_R-corrected voltammograms (0.5 M H_2SO_4, 25°C, sweep rate of 20 mV s^{-1}). Oxygen reduction current density vs applied potential.

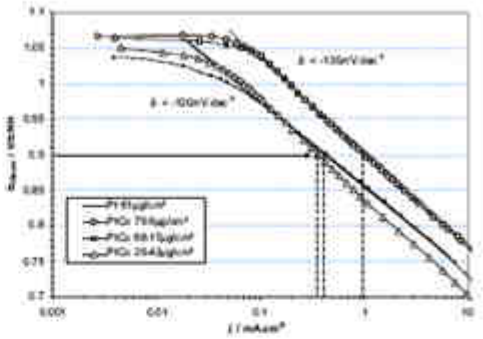

Figure 15. (Color online) Semilogarithmic representation (Tafel plot) of the i_R-corrected oxygen reduction current.

Table III. Reduction current of the different catalysts at 0.9 V_{RHE}.

	Pt	Pt_3Co	PtCo	$PtCo_3$
J_{geo} at 0.9 V(µA/cm²)	418	1057	1057	360
J_m at 0.9 V(A/g_{Pt})	6.8	13.4	15.5	12.4
J_S at 0.9 V(µA/cm^2_{Pt})	19	37	41	23

Conclusions

In this paper, we report the experimental results on the preparation and the electrochemical characterization of Pt_xCo_y electrocatalytic particles with homogeneous composition, which we previously modeled in Ref. 1 and 14. We demonstrate that DLI-MOCVD elaborated Pt_xCo_y catalysts supported on a GDL substrate are interesting model systems to understand the electroactivity and stability properties of Pt_xCo_y bulk-truncated or incomplete alloy structures. Electrochemical analysis of the samples has been carried out by using RDE and half-cell experiments. Fresh catalysts and structural changes were characterized by using TEM, XRD, and XPS. An optimal Co composition is identified for better ORR activity and catalyst durability, validating our previously published multiscale model results with kinetic parameters fully obtained by using ab initio DFT data.

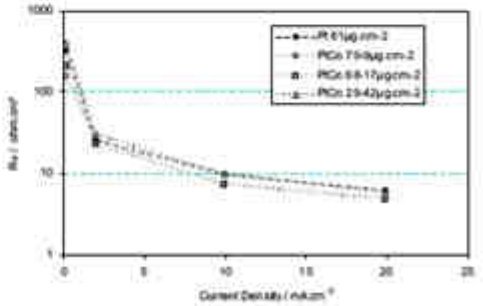

Figure 16. (Color online) Evolution of the transfer resistance for oxygen reduction obtained by impedance spectroscopy vs current density.

These results provide a first indication on the performance and durability of catalysts elaborated by DLI-MOCVD in conditions close to a PEFC cathode. Even if we noted degradation of the Pt_xCo_y under the RDE aging experiments, the Co element apparently slows down the mobility of the Pt on the carbon support, therefore decreasing the electrochemical ripening phenomena.[7] Furthermore, the degree of graphitization of the GDL support possibly plays a role on the activity and stability properties of the prepared catalysts, and this will be the focus of further studies in our group.

Moreover, DLI-MOCVD method can reveal an interesting catalyst preparation technique to achieve ultralow catalyst loadings for PEFC cathodes. To prepare electrochemically stable Pt_xCo_y catalysts, this technique could be combined with thermal annealing ($T > 400°C$) but other carbon supports than GDLs (not thermically stable at $T > 400°C$) should be used. More generally, the preparation of model electrodes and a combined experimental electrochemistry/modeling approach provide interesting insights on the understanding of the Pt_xCo_y electrocatalyst nanostructure impact on their activity and stability properties. Within this context, in an incoming paper[26] we are reporting the preparation of particles with a nanostructure similar to the Monte Carlo-based one modeled in Ref. 1.

Acknowledgments

This work was funded by the ANR PAN-H (French National Research Agency) within the context of the OPTICAT project.

Commissariat à l'Energie Atomique et aux Energies Alternatives assisted in meeting the publication costs of this article.

References

1. A. A. Franco, S. Pauwe, C. Anglade, E. Billy, L. Guetaz, N. Guillet, E. De Vito, P. Pegere, and S. Mailley, *J. Electrochem. Soc.*, 156, B410 (2009).
2. L. Xiong and A. Manthiram, *J. Electrochem. Soc.*, 152, A697 (2005).
3. F. Yu, M. Pocherton, and P. Plaine, *J. Power Sources*, 144, 11 (2005).
4. S. Koh, C. Yu, P. Ma, I. B. Srivastava, and P. Strasser, *J. Power Sources*, 172, 30 (2007).
5. X. Li, B. B. Colón-Mercado, G. Wu, J.-W. Lee, and B. N. Popov, *Electrochem. Solid-State Lett.*, 10, B201 (2007).
6. S. C. Zignani, E. Antolini, and E. R. Gonzalez, *J. Power Sources*, 182, 83 (2008).
7. S. Theilon, F. Sanchette, S. Velanga, E. Godon, J. Bucardt, and H. Guillon, WO Pat. 2002/070130 (2002).
8. S. Mailley, P. Capron, S. Theilon, and T. Krebs, WO Pat. WO 2007/088292 A1 (2007).
9. S. Mailley, F. Sanchette, S. Theilon, and E Ennoure, WO Pat. 2007/088291 (2007).
10. J. P. Sounenc, R. Mesbr, F. Weiss, O. Thomas, and A. Abrutis, French Pat. 93-08838 (1993) and extended European Pat. FR94/000858 (1994).
11. F. Febres, J. P. Senateur, F. Weiss, R. Madar, and A. Abrutis, *J. Phys. IV*, C5, 1079 (1995).
12. J. P. Senateur, F. Febres, S. Pignard, F. Weiss, A. Abrutis, V. Bigelyte, A. Teiserskis, Z. Saltyte, and R. Vengalis, *J. Alloys Compd.*, 251, 288 (1997).
13. S. Theilon, F. Sanchette, and J. Bucardt, Abstract 87, The Electrochemical Society Meeting Abstracts, Vol. 501, Quebec City, Canada, May 15–20, 2005.
14. A. A. Franco, S. Pauwe, C. Anglade, E. Billy, L. Guetaz, N. Guillet, E. De Vito, P. Pegere, and S. Mailley, *ECS Trans.*, 13(17), 29 (2008).
15. A. A. Franco, P. Schott, C. Jallut, and B. Maschke, *J. Electrochem. Soc.*, 153, A1053 (2006).
16. B. B. Colón-Mercado and B. N. Popov, *J. Power Sources*, 155, 253 (2006).
17. N. Guillet, L. Roué, S. Marcotte, D. Villers, J. P. Dodelet, N. Ghaboo, and S. Tat Vu, *J. Appl. Electrochem.*, 36, 863 (2006).
18. N. S. McIntyre and M. G. Cook, *Anal. Chem.*, 47, 2208 (1975).
19. I. Alstrup, I. Chorkendorff, R. Candia, B. S. Clausen, and H. Topsoe, *J. Catal.*, 77, 397 (1982).
20. S. L. T. Andersson and R. F. Howe, *J. Phys. Chem.*, 93, 4913 (1989).
21. A. B. Mandale, S. Badrinarayanan, S. K. Date, and A. P. B. Sinha, *J. Electron Spectrosc. Relat. Phenom.*, 33, 61 (1984).
22. M. Ohn and K. Hirokawa, *J. Electron Spectrosc. Relat. Phenom.*, 8, 475 (1976).
23. B. J. Tan, K. J. Klabunde, and P. M. A. Sherwood, *J. Am. Chem. Soc.*, 113, 855 (1991).
24. M. P. Seah, *Thin Solid Films*, 81, 279 (1981).
25. U. Bardi, B. C. Beard, and P. N. Ross, *J. Catal.*, 124, 22 (1990).
26. A. A. Franco, Abstract 3016, The Electrochemical Society Meeting Abstracts, Vol. 902, Vienna, Austria, Oct 4–9, 2009.
27. J. Wu, X. Z. Yuan, H. Wang, M. Blanco, J. J. Martin, and J. Zhang, *Int. J. Hydrogen Energy*, 33, 1735 (2008).
28. T. Vidakovic, M. Christov, and K. Sundmacher, *Electrochim. Acta*, 52, 5606 (2007).
29. A. Lasia, *J. Electroanal. Chem.*, 562, 23 (2004).
30. R. Ferreira de Morais, D. Loffreda, P. Sautet, and A. A. Franco, *ECS Trans.*, 25(34), 167 (2010).
31. U. A. Paulus, A. Wokaun, G. G. Scherer, T. J. Schmidt, V. Stamenkovic, N. M. Markovic, and P. N. Ross, *Electrochim. Acta*, 47, 3787 (2002).
32. H. Gasteiger, N. Markovic, P. Ross, and E. Cairns, *J. Phys. Chem.*, 98, 617 (1994).
33. S. K. Cheah, E. Gélin, O. Lemaire, and A. A. Franco, *ECS Trans.*, 25(35), 273 (2010).
34. H. A. Gasteiger, S. S. Kocha, B. Sompalli, and F. T. Wagner, *Appl. Catal., B*, 56, 9 (2005).
35. http://www.eud.gov/energyinformationadministration/pdf/021207-aEIW6D4823267.PDF, last accessed September 3, 2009.
36. E. Quesnel, F. Pagère, R. Bouchetalle, A. A. Franco, E. Pauthe-Vargnes, L. Guetaz, O. Secondy, and V. Muffato, In preparation.

Journal of The Electrochemical Society, **156** (3) B410-B424 (2009)
0013-4651/2009/156(3)/B410/15/$25.00 © The Electrochemical Society

Pt_xCo_y Catalysts Degradation in PEFC Environments: Mechanistic Insights

I. Multiscale Modeling

Alejandro A. Franco,[a,b,z] Sylvain Passot,[b] Pascal Fugier,[b] Christelle Anglade,[b] Emmanuel Billy,[b] Laure Guétaz,[a] Nicolas Guillet,[a] Eric De Vito,[a] and Sophie Mailley[c]

Commissariat à l'Energie Atomique (CEA)/DRT/LITEN, [a]Département de Technologies de l'Hydrogène, Laboratoire des Composants PEM, [b]Département des Technologies des NanoMatériaux, Laboratoire des Technologies des Surfaces, [c]Département des Technologies des NanoMatériaux, Laboratoire des Composants pour l'Energie, 38000 Grenoble, France

In this article, we focus on the understanding of the Pt_xCo_y electrocatalysts degradation in polymer electrolyte fuel cell (PEFC) environments. A multiscale atomistic/kinetic model is derived providing mechanistic insights on the impact of the nanostructure and operating conditions on Pt_xCo_y nanoparticles durability. On the basis of ab initio (AI) data, we identify favorable pathways of the oxygen reduction reaction (ORR) on Pt_xCo_y nanoparticles and of the competitive Pt–Co dissolution in acidic media. The derived AI kinetics is coupled to a description of the atomic reorganization at the nanoparticle level as a function of the cumulated Pt and Co mass losses. This nanoscale model is coupled with a transport microscale model of charges and O_2 through a PEFC cathode, and simulation sensitivity studies to operating conditions and initial composition/morphologies are performed and complemented by microstructural and electrochemical characterizations carried out on aging direct liquid injection metallorganic chemical vapor deposition elaborated model electrodes detailed in our experimental companion paper.
© 2009 The Electrochemical Society. [DOI: 10.1149/1.3058048] All rights reserved.

Manuscript submitted July 16, 2008; revised manuscript received November 24, 2008. Published January 20, 2009.

Low-temperature acidic polymer electrolyte fuel cells (PEFCs) represent an environmentally friendly technology and are attracting considerable interest as a means for producing electricity by direct electrochemical conversion of hydrogen and oxygen into water. There are, however, severe shortcomings of the present technologies that need to be overcome to make low-temperature PEFCs more economically attractive. Platinum has the highest catalytic activity for the cathodic oxygen reduction reaction (ORR) of any of the pure metals[1] and constitutes the state-of-the-art catalyst for PEFC electrodes. However, due to the ORR kinetic limitations, the cathodic potential losses amount to 0.3–0.4 V under typical PEFC operating conditions. In order to increase the ORR global rate, current PEFC cathodes achieve uniform and highly dispersed Pt loadings [high-surface-area platinum particles ($\sim$50 m^2/g)] by using high surface area ($\sim$250 to 750 m^2/g) carbon supports (carbon black with a high degree of graphitic character). Despite these progresses on improving ORR rate, typical Pt loadings still remain high and costly for large-scale electrode commercialization.

Another shortcoming of Pt-based catalysts is their instability. Although Pt nanoparticles are very stable in acid electrolytes at low electrode Butler–Volmer potentials, considerable dissolution of Pt takes place under PEFC cathode operating conditions representative of automotive applications (e.g., dynamical potential cycles passing through 0.90–1.1 V vs normal hydrogen electrode).[2] Thus, operating PEFC in these potentials, in both steady-state and drive-cycle conditions, produces extensive catalyst oxidation, dissolution, and redistribution of the Pt atoms,[3] leading to the reduction of the specific catalytic surface area and to the loss of the electrochemical activity.[4,5] These spatiotemporal changes translate into the long-term cell potential degradation, and PEFC lifetime can be limited to 300–500 h under some specific power drive-cycle operating conditions representative of automotive applications.[6]

Alternatively, it has been shown that the activity and stability of PEFC electrodes can be improved by alloying Pt with some transition metals (e.g., Co, Ni, V, ...); these electrodes also achieve lower global Pt loadings compared to pure Pt-based electrodes. Among these Pt alloys, Pt–Co nanomaterials have been widely studied as promising alternative catalysts for PEFC applications, showing enhanced ORR activity and better stability than pure Pt materials.[7-9] Because composition combinatorial methods for improving Pt_xCo_y activity and stability have had limited success, several studies have been dedicated to the understanding of the Pt–Co nanostructure impact on its activity and stability properties.

Stamenkovic et al.[10] reported experiments showing the atomistic organization effects on Pt_xCo_y activity. The authors compared the electrochemical activity of extended surfaces obtained only from sputtering to Pt-skin surfaces obtained by sputtering/annealing cycles under ultrahigh-vacuum; sputtered/annealed surfaces were found to show better electrochemical activities. Watanabe et al.[11] studied the ORR activity and the durability in acidic media of ordered [face-centered tetragonal (fct) structure] and disordered [face-centered cubic (fcc) structure] Pt-Co alloys. The fcc a structure has been found to be more stable than the fct structure, both having the same composition.

On the basis of ab initio (AI) electronic structure calculations, Rogues et al.[12] explained ORR enhancement on Pt_3Co surfaces by a positive shift of the onset Butler–Volmer potential for forming OH_{ads} on the alloy compared to a pure Pt-catalyst surface, thereby allowing O_2 to adsorb at higher potentials and reducing the overpotential for O_2 reduction. These authors also showed that the ORR activity clearly depends on the surface composition and structure; in this sense, they studied the effect of cobalt concentration alloyed with platinum.[13] They concluded that alloying more Co with Pt could also reduce the ORR overpotential.

Regarding durability aspects, Ball et al.[5,9] as well as Colón-Mercado and Popov,[14] studied the long-term aging impact on the Pt_xCo_y specific activity and on morphology (30,000 potential cycles in a PEFC for Ball et al.; 480 h in accelerated durability test cell and 1600 h in a PEFC for Colón-Mercado and Popov). Following Colón-Mercado and Popov,[14] Pt atoms seem to be less dissolved from Pt_xCo_y electrodes than from pure Pt-based electrodes.

According to Antolini et al. the coordination of Co with Pt atoms could also affect the performance and durability.[15] Yu et al.[16] studied Pt_3Co/C aging (2400 potential cycles) impact on their activity in a PEFC and found that dissolved Co ions do not affect the membrane conductivity.

Zignani et al.[17] studied the stability and durability of in-house PtCo/C and pure Pt/C catalysts under various operation conditions

* Electrochemical Society Active Member.
[z] E-mail: alejandro.franco@cea.fr

in a half-cell. After constant potential operation (0.8 V) during 30 h, the authors concluded that PtCo/C remain more active than Pt/C. the influence of Co loss on the PtCo/C ORR activity was believed to be negligible. Moreover, thermal treatment at 550 °C has been found to increase the mean particle size for both catalysts and promote a Co surface enrichment in PtCo/C. The authors proposed that a high amount of surface Co and its oxides hinders molecular oxygen to reach the Pt active sites and the ORR activity is considerably lower than that of pure Pt.

Detailed Pt_xCo_y degradation mechanisms are still less known. Only a few papers are devoted to the study of the long-term (>300 h) durability.[8,9,14] Deep theoretical understanding of electrocatalysis is crucial to provide a rigorous physically based interpretation of experimental observables. Because of the advances in the quantum electronic structure theory and the increase in computer power and software, bimetallic catalysts can now be routinely addressed by AI electronic structure calculations yielding atomistic insight into the fundamental factors underlying their reactivity and stability. Ma and Balbuena,[18] Wang and Balbuena,[19] Gu and Balbuena,[20] Seminario and Balbuena,[21] and Balbuena et al.[22] reported many theoretical studies related to ORR activity and Pt_xCo_y morphologies. The authors studied ORR intermediates adsorption on different Pt-Co structures, identified thermodynamically favorable pathways for the ORR and for the metals oxidation/dissolution, and analyzed the platinum segregation to the surface.

Greeley and Norskov estimated trends in the thermodynamics of binary surface alloy dissolution in acidic media from density functional theory (DFT) calculations.[23] For the surface alloys, the change in the dissolution Butler–Volmer potential for solute metal atoms compared to pure/metallic solute was calculated for Pt_xCo_y catalysts: it was found that Pt atoms are more stable in a Pt = solute/Co = host system compared to pure Pt bulk. In contrast, Co atoms are more unstable in a Co = solute/Pt = host system compared to pure Co bulk. Furthermore, the authors analyzed the dissolution of Pt "skin" layers from Pt_3Co bulk alloys, and the skins were found to be stabilized compared to pure Pt.

According to Greeley and Norskov,[23] water splitting and hydroxyl adsorption can also modify these surface alloys dissolution thermodynamics. We can conclude from this result that the stability properties of nanostructured catalysts (e.g., facility to oxidize) can be strongly affected by the electrochemical reactions of interest in PEFC environments, thus, the hydrogen oxidation reaction or the ORR. Even structure and inter-atomic distance can just change after gas exposure[24] or liquid adsorption (this is the so-called reconstruction phenomena). In this sense, we can refer, for example, to the work reported by Zhu et al.[25] These authors investigated the effect of hydrogen chemisorption on the surface composition of bimetallic Pt-Rh catalytic clusters using molecular dynamics calculations. They found that surface segregation is dramatically altered by hydrogen chemisorption: in the absence of hydrogen, the cluster surfaces are Pt-rich, but in the presence of hydrogen, the cluster surfaces can be Rh rich. This "reversing segregation phenomenon" has been experimentally demonstrated by Savargaonkar et al. on the basis of nuclear magnetic resonance studies.[26]

In our opinion, there is a great value in exploring and creating theoretical tools to enable quantitative interpretation and prediction of fundamental chemistry and electrochemistry into PEFC engineering practice. This requires modeling at appropriate length/time scales and creating bridges between such scales with reasonable computational effort, as well as a better communication between theory and experiments. Within this sense, in an attempt to provide a physically based description of the electrochemical phenomena in PEFC environments, in our group we have developed a multiscale mechanistic model of the PEFC membrane electrode assembly (MEA) Pt-based electrocatalysis, based on a nonequilibrium thermodynamics approach,[27,28] allowing atomistic and macroscopics approaches to link.[29,30] The model couples microscale transport descriptions of reactants and charges with a spatially distributed description of the nanoscale electrochemical Pt/hydrated Nafion interface in the presence of electrochemical reactions.[31] This model includes a description of coupled electrochemical aging processes in a PEFC MEA, including cathodic Pt oxidation/dissolution/ripening,[29,32] Pt^{2+} diffusion/migration/recrystallization in ionomer and cathodic carbon corrosion.[33,34] From its strong nonlinear structure, our approach describes the feedback between performance and intrinsic MEA aging processes, analyzes MEA response sensitivity to operating conditions, initial Pt/C/Nafion loadings, and temporal evolution of the electrocatalytic activity. In this way, the model allows MEA durability prediction within a physical-based mechanistic framework.

In this article we focus on extending this approach for Pt_xCo_y catalytic nanoparticles in order to provide mechanistic insight on the role of the atomic compositional and nanomorphological effects on the activity and the stability of these materials in PEFC environments.[35] Our companion paper[36] reports in-house model electrodes elaboration using direct liquid injection metal organic chemical vapor deposition (DLI-MOCVD) process, and all the characterizations associated (structural, morphological, and electrochemical properties, under different operating conditions and operating times) used to support and validate the theoretical developments described in the present paper.[35]

This article is organized as follows. First, we present our Pt_xCo_y model description and the postulated coupled mechanisms used to explain the nanostructural effects on activity and stability. Second, we discuss some simulation results triggering the discussions published in our experimentally dedicated companion paper (activity and stability studies as function of the nanostructure). Finally, we conclude and indicate further directions in our modeling research.

Theoretical approach

Global model structure.— In principle, degradation of bimetallic nanocatalysts could occur through three main phenomena: metals dissolution and particles coarsening[22] and carbon-support corrosion-driven particle detachment.[34] These mechanisms have been largely studied in the case of pure Pt in PEFC cathode environments, but not as much for bimetallic catalyst such as Pt_xCo_y; it is believed that addition of cobalt atoms in platinum particles stabilize platinum against its dissolution,[23] and particle coarsening is believed to be less important because of the initial large size (compared to pure Pt) of the bimetallic catalysts.[9] The possible role of alloying metals as a "coarsening stopper" was also already mentioned by Glass et al.[37] in the context of electrochemical investigations of Pt-Cr alloys in phosphoric acid. Thus, in our model, in a first approximation, we assume that only metals dissolution impacts the cathode performance degradation.

The Pt_xCo_y degradation model proposed in this paper is supported on an AD/irreversible thermodynamics-based kinetic approach used to describe the ORR and the Co and Pt atoms oxidation/dissolution leading to the decrease with time of the specific catalytic surface area) and to calculate the temporal behavior of the experimental observables (electrode potential). The proposed kinetic approach depends on the instantaneous Pt_xCo_y particles surface composition, and thus, it is necessary to account for a description of the instantaneous Pt_xCo_y nanostructure during operation in the PEFC environment.

Several descriptions are possible for the particles structure: crystallographic structures, core-shell structure, homogeneous structure, etc. For the simulations shown in this paper, we assume two possible morphologies (Fig. 1). The first one represents the catalysts elaborated and tested by Ball et al.[9] and by ourselves:[35,36] a homogeneous atomic Co concentration profile inside the particles assuming no Pt surface segregation, the so-called skeleton-structured catalyst mentioned by Stamenkovic et al.,[10] i.e., with

$$x^S_{Co}(t) = x^V_{Co}(t) \quad [1]$$

where $x^S_{Co}(t)$ is the instantaneous Co surface composition and $x^V_{Co}(t)$ is the instantaneous Co content in the nanoparticle (both surface and volume compositions being fractions of 1).

Figure 1. (Color online) Two approaches used in this paper to predict the instantaneous Pt_xCo_y cluster nanostructure during their degradation.

The second assumed morphology represents more the structure of the sputtered/annealed materials also discussed by Stamenkovic et al.[19] In this case, the atomic Co concentration profile inside the nanoparticles is obtained from Monte Carlo calculations. The Monte Carlo approach is used to calculate the atomic organization from the kinetically calculated instantaneous $x^E_{Co}(t)$ and the total number of atoms $N_{atoms}(t)$ in the nanoparticle.

The instantaneous atomic Co surface composition is given by the function

$$x^E_{Co}(t) = f[N_{atoms}(t), x^E_{Co}(t)] \quad [2]$$

We underline that for the calculation results presented in this paper, in a first approximation, both nanoparticles are assumed to be fcc structures. However, we emphasize that the modeling procedure proposed in our approach can be extended to other sets of structures.

The kinetic part of our model includes a description of the nanoscale Pt_xCo_y catalyst/electrolyte electrochemical interfacial phenomena under nonequilibrium conditions. Because in PEFC environments it seems unreasonable to ignore the role of the structure of the electrochemical double layer on the kinetics, here we develop an extension of our previously published transient irreversible thermodynamics model of a pore Pt/hydrated Nafion interface.[31,32] The model here is constituted first of all of a compact layer, which describes the competitive adsorption of ORR intermediate reaction species on both Co and Pt sites, the Co and Pt oxidation/dissolution, and the specific water molecules adsorption. Second, the model considers a diffuse layer submodel, which describes the transport by diffusion and electromigration of the ionic species close to the catalyst, participating in the electrochemical reactions and coupled with the electric field generated by the charge distribution of H^+, Pt^{2+}, Co^{2+}, and sulfonate groups FIX^- (Fig. 2). The nanoscale coordinate inside the diffuse layer of some nanometers thickness is noted by x, and the Pt_xCo_y /hydrated Nafion interface is supposed to be flat and located at $x = L$. The electrochemical phenomena occurring at the compact layer level are described on the basis of AI data available in the literature, as detailed later in this paper.[17,28,31,32]

The nanoscale interfacial model is coupled to a spatially distributed microscale model of the oxygen diffusion through the hydrated ionomer solution film ("impregnated" Nafion layer) and the microscale transport phenomena description of H^+, Co^{2+}, and Pt^{2+} through the membrane-cathode assembly (Fig. 3). We note by z the microscale coordinate in the thickness of the "impregnated" Nafion layer in the cathode (for microscale coordinates, see Ref. 28); the interfacial nanoscale model is located at the microscale point $z = e_{Pt}$.

For simplicity reasons, in this paper we restrict ourselves to the case of an isothermal PEFC cathode fed with pure oxygen fully saturated with water vapor. In these conditions, it does not appear necessary to take into account the pore phase flooding by liquid water and the gas diffusion layer (GDL) of a typical PEFC,[28] and the Nafion medium conductivity can be supposed to be constant.

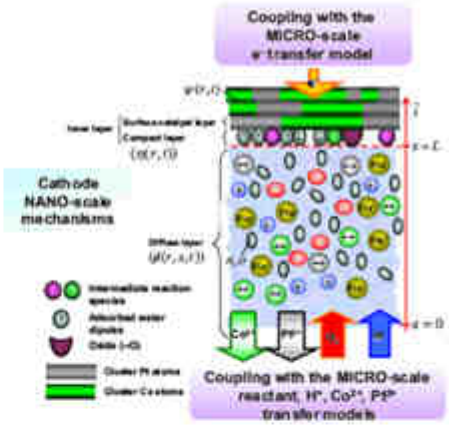

Figure 2. (Color online) Nonequilibrium thermodynamics model of the Pt_xCo_y/electrolyte interface.

Particles nanostructure modeling.— Homogeneous structural approach.— To model the homogeneous Pt_xCo_y structures we assume a random organization of Pt–Co atoms inside the nanoparticle. After aging and cobalt loss, this organization can be related to a Pt-skeleton structure evoked above.

Truncated octahedron structural approach.— A nanoparticle or atomic aggregate is constituted by more or less ordered atoms that can be assimilated to spheres.[34] From an energetic viewpoint, the assembly of these spheres cannot form a spherical shape (as typically assumed in PEFC models) but a polyhedron characterized by external facets. Considering a fcc structure, the associated characteristic polyhedron is a truncated octahedron. Truncated octahedron structures can only exist for specific numbers of atoms, the so-called magic numbers: 38, 201, 586,....[35] It is important to note that the smaller are the nanoparticles, the larger are their surface/volume ratios (Fig. 4).

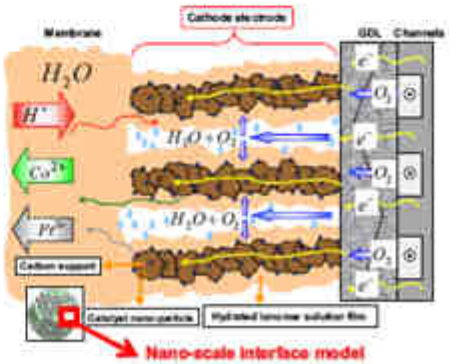

Figure 3. (Color online) Nonequilibrium thermodynamics model of the microscale phenomena in the Pt_xCo_y-based PEFC cathode.

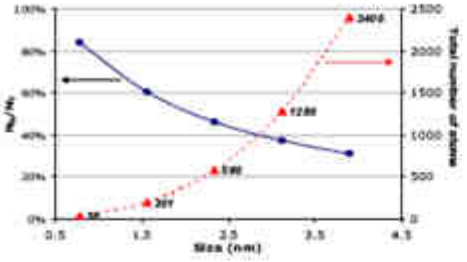

Figure 4. (Color online) Number of surface atoms over number of total atoms and total atoms number, as a function of the nanoparticle size.

Our second adopted structural approach consists in calculating Pt_xCo_y nanoparticles pseudo-equilibrated atomic repartition for truncated octahedron structures. For each nanoparticle size (corresponding to a number of atoms), we carry out simulations with several atomic cobalt volume compositions. Surface and volume repartitions are used to build a library that is coupled with the kinetic part of our model discussed in the next section.

In order to simulate the pseudo-equilibrated atomic repartition at each truncated octahedron structure, we use the annealing Monte Carlo method applied to a Sutton–Chen multiatomic potential.[39-42] This potential provides the total nanoparticle energy as the addition of terms describing the two-body repulsive interaction between the atoms i and j separated by a distance r_{ij}, and of many-body cohesion terms associated with atom i

$$U = \sum_{i}^{N_{atoms}} \left[\frac{1}{2} \varepsilon^{AB} \sum_{j \neq i}^{N_{atoms}} \left(\frac{\sigma^{AB}}{r_{ij}} \right)^{n^{AB}} - c^A \varepsilon^A \sqrt{\sum_{j \neq i}^{N_{atoms}} \left(\frac{\sigma^{AB}}{r_{ij}} \right)^{m^{AB}}} \right] \quad [3]$$

In Eq. 3 ε^{AB} is the so-called energy parameter, σ^{AB} is the lattice constant, c is a dimensionless parameter, and n and m are positive integers with $n > m$ (Table I). The three parameters ε^{AB}, σ^{AB}, and c are determined by the equilibrium lattice parameters and lattice energy of a fcc crystal. The type of fcc crystal structure is determined by m and n.

Our Monte Carlo algorithm is based on exchanging two different randomly chosen atoms. The probability of the trial acceptance of the exchanging-resulted configuration is based on the standard Metropolis algorithm.[43] If the energy of the configuration is smaller than the energy of the old configuration, the trial is always accepted. If this difference of energies is positive, then the trial is accepted only if the probability P is greater than a random number chosen between 0 and 1

$$P = \exp\left(\frac{-\Delta U}{k_B T} \right) \geq \text{random} \quad [4]$$

Temperature being indirectly implicated in the nanoparticle energy minimization, we choose to impose an annealing cooling schedule. The initial temperature, cooling schedule, and total simulation length are the three important parameters of a simulated annealing optimization.[44] All the Monte Carlo simulations presented in this paper have been performed by starting at 900 K with the cooling schedule (temperature evolution as a function of the trial step l)[45]

$$T(l) = \frac{1}{2}(900 - 100)\left[1 + \cos\left(\frac{l \cdot \pi}{N_{steps}} \right) \right] + 100 \quad [5]$$

with N_{steps} being the total number of simulation steps necessary to reach the global energy minimum.

Monte Carlo simulations are performed on truncated octahedrons previously relaxed using the multiatomic Sutton-Chen potential for random distributions of platinum and cobalt atoms. The relaxed inter-atomic lengths depend on the considered nanoparticle size.

Table I. Platinum, cobalt, and Pt–Co cluster parameters used in the Sutton–Chen potential.

	σ^{AB} (× 10 nm)	ε^{AB} (10^{-2} eV)	c	m	n
Platinum	3.92	1.9833	34.408	8	10
Cobalt	3.54	1.5566	39.432	6	9
Pt–Co	3.73	1.7570		7	9.5

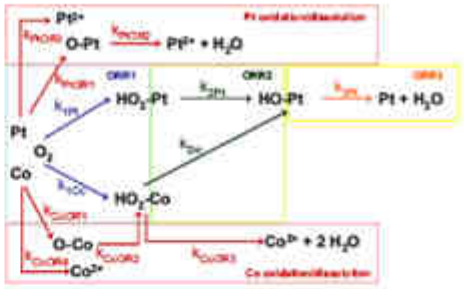

Figure 5. (Color online) Ab initio-adopted ORR steps coupled with Pt and Co oxidation/dissolution reactions.

Ab initio-based kinetics modeling.—*Kinetics.*— In our work, we assume for the ORR a mechanism something different from the one classically adopted in literature for pure Pt (the so-called parallel direct/indirect pathway, as speculated for the first time by Wroblowa et al.[46] and discussed later by Yeager[47]): we consider here series/parallel elementary reaction steps describing the intermediates formation and dissociation on both platinum and cobalt sites[27,28] (Fig. 5). As discussed in our previous paper,[27] H_2O_2 is assumed to be a product that can be formed and not an intermediate of the water formation; thus, we do not describe here H_2O_2 formation.

We assume here that molecular oxygen can react with both platinum and cobalt atoms. According to Balbuena et al.,[19] cobalt atoms are more thermodynamically favorable to enhance the on-top HO_2–Co formation than platinum. However, platinum is thermodynamically more favorable than cobalt for the HO–Pt formation. Thus, we suppose that HO–Co intermediate is not formed on cobalt sites. Moreover, an electroless surface diffusion of the first oxygenated intermediate HO_2 from cobalt to platinum sites is introduced as well as the following HO_2 reduction into HO–Pt. The assumption in our model of surface diffusion (mobility) of species from Co sites to Pt sites is fully consistent with thermodynamic requirements: this surface diffusion process is a key mechanism in the majority of electrochemical reactions (e.g., Ref. 48) and largely recognized in the standard physical electrochemistry literature. Because an intermediate surface diffusion coefficient is difficult to be evaluated on the basis of DFT calculations (it will depend not only on the catalyst surface nanostructure, but also on the instantaneous coverage of the intermediates), we choose, as a first step in this paper, to propose a mean field (MF) model. Within this MF approach, intermediates surface diffusion is assumed to be much faster than the electrochemical reaction rates and, thus positions of individual adsorbates become irrelevant. In this case, it is sufficient to specify the surface configuration at a specific time in terms of effective surface coverages on both Co and Pt sites.

Adding to these five ORR reactions, we also describe four reactions related to the cobalt oxidation/dissolution and three related to the platinum oxidation/dissolution. On the basis of these discussions, we can say for platinum and cobalt

$$\theta^{Co} + \theta^{Co}_{O} + \theta^{Co}_{HO_2} + \theta^{\vec{Co}} + \theta^{\overleftarrow{Co}} = 1 \quad [6]$$

$$\theta^{Pt} + \theta^{Pt}_{HO_2} + \theta^{Pt}_{O} + \theta^{Pt}_{HO} + \theta^{\vec{Pt}} + \theta^{\overleftarrow{Pt}} = 1 \quad [7]$$

where θ^M are the on-top surface coverage by free sites on M sites (M = Co or Pt) or by adsorbed ORR intermediates or oxides. $\vec{\theta}$ (respectively, $\overleftarrow{\theta}$) are the covering fractions with water dipoles oriented toward the catalyst (respectively, opposed).

By calculating the Gibbs energies ΔG on the basis of available AI data (before degradation, at time t_0)[20] for the elementary reactions assumed in this mechanism, we find that all the ORR steps are spontaneous (negative Gibbs energies).

For the "ORR1" reaction part in Fig. 5, we have $\Delta G_{1Pt} > \Delta G_{1Co}$ which means that the reaction is more favorable on cobalt than on platinum.[19,21] ORR1 part reaction rates are written as

$$O_2 + H^+ + e^- + Co \rightarrow HO_2Co \quad (1Co) \quad [8]$$

$$v_{1Co} = k_{1Co}\theta^{Co}C_H(L,t)C_{O_2}(L,t)e^{-\alpha_{1Co}f\eta(t)} \quad [9]$$

$$O_2 + H^+ + e^- + Pt \rightarrow HO_2Pt \quad (1Pt) \quad [10]$$

$$v_{1Pt} = k_{1Pt}\theta^{Pt}C_H(L,t)C_{O_2}(L,t)e^{-\alpha_{1Pt}f\eta(t)} \quad [11]$$

where α are the electronic transfer coefficients and $f = F/RT$ (η is the Frumkin potential introduced in our previous papers for pure platinum.[21,28] Its adaptation to the case of bimetallic electrocatalysts is developed in the next section. $C_H(L,t)$ and $C_{O_2}(L,t)$ are the protons concentration and the oxygen concentration at the interface $x = L$ both calculated by the diffuse layer transport equations (given below). However, they have to be activities rather than concentrations

$$a_i = \gamma_i \cdot \frac{C_i}{C^\circ} \quad [12]$$

In diluted solutions (as assumed here), the activity coefficient γ_i is near to 1 and the reference concentration C° is, by convention, equal to 1 mol m^{-3}. Thus, we assimilate here the activities to (dimensionless) concentrations.

Regarding the ORR2 reaction part, we adopt a mechanism describing the reduction of the intermediate HO_2 into HO from cobalt to platinum sites ($\Delta G_{2Pt} = -5.207 \times 10^4$ J/mol) in order to favor oxide formation on cobalt and reduction of the HO intermediate into water on platinum sites (ORR3 reaction part). The ORR2 reaction part also concerns the reduction of HO_2 into HO but on platinum sites alone ($\Delta G_{2Pt} = -5.848 \times 10^4$ J/mol). The ORR2 reaction rates are given by

$$HO_2Co + H_2O + 3Pt \rightarrow 3HOPt + Co \quad (2m) \quad [13]$$

$$v_{2m} = k_{2m}\theta^{Co}_{HO_2}\Theta_{H_2O}(\theta^{Pt})^3 \quad [14]$$

$$HO_2Pt + H_2O + 2Pt \rightarrow 3HOPt \quad (2Pt) \quad [15]$$

$$v_{2Pt} = k_{2Pt}\theta^{Pt}_{HO_2}\Theta_{H_2O}(\theta^{Pt})^2 \quad [16]$$

where Θ_{H_2O} is the water activity in the hydrated Nafion matrix.*

* In order to describe the PEFC operation with reactants not fully vapor saturated, Θ_{H_2O} can be calculated through a model describing water transport in the Nafion and in the pore phases.[29]

Furthermore, by computing the Gibbs energy of the ORR3 reaction part on Pt and on Co, it is more negative on platinum: thus, in a first approximation, we do not describe HO intermediate reduction on cobalt. The associated reaction rate is given by

$$HOPt + H^+ + e^- \rightarrow H_2O + Pt \quad (ORR3) \quad [17]$$

$$v_{3Pt} = k_{3Pt}\theta^{Pt}_{HO}C_H(L,t)e^{-\alpha_{3Pt}f\eta(t)} \quad [18]$$

The oxidation/dissolution of cobalt sites is assumed to be given by

$$Co + H_2O \rightarrow OCo + 2H^+ + 2e^- \quad (CoOR1) \quad [19]$$

$$v_{CoOR1} = k_{CoOR1}\theta^{Co}\Theta_{H_2O}e^{-2(1-\alpha_{CoOR1})f\eta(t)} \quad [20]$$

$$OCo + H_2O \rightarrow HO_2Co + H^+ + e^- \quad (CoOR2) \quad [21]$$

$$v_{CoOR2} = k_{CoOR2}\theta^{Co}_{O}\Theta_{H_2O}e^{-(1-\alpha_{CoOR2})f\eta(t)} \quad [22]$$

$$HO_2Co + 3H^+ + e^- \rightarrow Co^{2+} + 2H_2O \quad (CoOR3) \quad [23]$$

$$v_{CoOR3} = k_{CoOR3}\theta^{Co}_{HO_2}[C_H(L,t)]^2 e^{-\alpha_{CoOR3}f\eta(t)} \quad [24]$$

$$Co \rightarrow Co^{2+} + 2e^- \quad (CoOR4) \quad [25]$$

$$v_{CoOR4} = k_{CoOR4}\theta^{Co}e^{-2(1-\alpha_{CoOR4})f\eta(t)} \quad [26]$$

where CoOR2 and CoOR3 reaction steps account by the coupling between oxidation/dissolution of cobalt and the ORR (through the production/consummation of the ORR intermediate HO_2).

According to Greeley and Norskov AI studies,[23] a host of cobalt atoms could stabilize solute platinum atoms by shifting their Butler-Volmer dissolution potential to more positive values. However, as in our model we are describing Co dissolution (atomic Co content decreases with operation time) platinum oxidation/dissolution is expected to occur with time-increasing reaction rates (i.e., platinum stability decreases when the Co content decreases)

$$Pt + H_2O \rightarrow OPt + 2H^+ + 2e^- \quad (PtOR1) \quad [27]$$

$$v_{PtOR1} = k_{PtOR1}\theta^{Pt}\Theta_{H_2O}e^{-2(1-\alpha_{PtOR1})f\eta(t)} \quad [28]$$

$$OPt + 2H^+ \rightarrow Pt^{2+} + H_2O \quad (PtOR2) \quad [29]$$

$$v_{PtOR2} = k_{PtOR2}\theta^{Pt}_{O}[C_H(L,t)]^2 \quad [30]$$

$$Pt \rightarrow Pt^{2+} + 2e^- \quad (PtOR3) \quad [31]$$

$$v_{PtOR3} = k_{PtOR3}\theta^{Pt}e^{-2(1-\alpha_{PtOR3})f\eta(t)} \quad [32]$$

All the reaction rates are written in mol m^{-2} s^{-1} unit, which corresponds to the unit of the kinetic parameter. Normalized rate parameter k° (s^{-1} units) is estimated from the Eyring equation[42,58]

$$k^\circ = \frac{k_B T}{h} e^{-\Delta S^\circ/RT} = \frac{k_B T}{h} e^{\Delta S^\circ_{ref}/R} e^{-\Delta H^\circ/RT} \quad [33]$$

In order to write the reaction rates in appropriate units, k° is divided by the initial catalyst surface area and the Avogadro number.

Furthermore, because of the degradation of the Pt_xCo_y nanoparticles, the surface properties (e.g., surface Pt/Co atomic ratio, electronic structure, etc.) are expected to evolve with time. As the Gibbs energy differences ΔG in Eq. 33 are strongly dependent on the catalyst nanostructure (i.e., its electronic structure), they will also evolve with operation time because of the degradation. In order to account for these time/structural dependences, in a first approximation, the Gibbs energy differences are written as a function of the instantaneous atomic cobalt (surface or volumetric) compositions, according to the expressions presented in Table II (see Appendix A) (Gibbs energy differences at time t_0 are calculated from available AI literature data in Ref. 19 and 20, where individual Gibbs energies for reactants and products are reported). As it is still a challenge for

Table II. First-order approximation for the Gibbs energies (ΔG°): thermodynamic values of fresh materials).

Effects on ORR	Effects on oxidation/dissolution
$\Delta G_{1Co} = \frac{s^{sat}_{Co}(t)}{s^{sat}_{Co}(t_0)}\Delta G^\circ_{1Co}$	$\Delta G_{Co(OH)2} = \frac{s^{sat}_{Co}(t)}{s^{sat}_{Co}(t_0)}\Delta G^\circ_{Co(OH)2} - RT\ln C_{Co(OH)2}$
$\Delta G_{1Pt} = \left[1 - \frac{s^{sat}_{Co}(t)}{s^{sat}_{Co}(t_0)}\right]\Delta G^\circ_{1Pt}$	$\Delta G_{CoOH} = \left[1 - \frac{s^{sat}_{Co}(t)}{s^{sat}_{Co}(t_0)}\right]\Delta G^\circ_{CoOH} - RT\ln C_{CoOH}$
$\Delta G_{2e} = N_{neighbor}\Delta G^\circ_{2e}$	$\Delta G_{Pt(OH)2} = \left[1 - \frac{s^{sat}_{Co}(t)}{s^{sat}_{Co}(t_0)}\right]\Delta G^\circ_{Pt(OH)2}$
Appendix B	$\Delta G_{PtOH} = \left[1 - \frac{s^{sat}_{Co}(t)}{s^{sat}_{Co}(t_0)}\right]\Delta G^\circ_{PtOH} - RT\ln C^\circ_{PtOH}$

atomistic (DFT-based) approaches doing calculations taking into account simultaneously all kinds of intermediates, electric field, water and degradation, these approximations allow us closing the gap between the available AI data and the impact of the degradation on the instantaneous reactivity.

Moreover, the instantaneous surface coverages by the three intermediates adsorbed on platinum or cobalt are calculated from the balance equations indicated in Table III [$s^{max\,Pt}$ and $s^{max\,Co}$ denote fractions of s^{max}, the maximum number of sites on the electrocatalytic surface[74] (see Appendix C)].

The molar flux of O_2, H^+, Co^{2+}, and Pt^{2+} at $x = L$ are calculated from the kinetic rates

$$J_{O_2}(x = L) = -(v_{1Co} + v_{1Pt}) \quad [34]$$

$$J_{H^+}(x = L) = -(v_{1Co} + v_{1Pt} + v_{2Pt} - 2v_{Co(OH)2} - v_{CoOH2} + 3v_{CoOH2} - 2v_{Pt(OH)2} + 2v_{Pt(OH)2}) \quad [35]$$

$$J_{Co^{2+}}(x = L) = v_{Co(OH)2} + v_{CoOH2} \quad [36]$$

$$J_{Pt^{2+}}(x = L) = v_{Pt(OH)2} + v_{Pt(OH)2} \quad [37]$$

The faradaic current on Co sites is given by

$$J^{Co}_{Fdc} = -F(v_{1Co} - 2v_{Co(OH)2} - v_{CoOH2} + v_{CoOH2} - 2v_{CoOH2}) \quad [38]$$

and on Pt sites

$$J^{Pt}_{Fdc} = -F(v_{1Pt} + v_{2Pt} - 2v_{Pt(OH)2} - 2v_{Pt(OH)2}) \quad [39]$$

However, by assuming from a macroscopic viewpoint that the charge surface density σ is the same on platinum and on cobalt, the total faradaic current is given by

$$J_{Fdc}(t) = J^{Pt}_{Fdc}(t) + J^{Co}_{Fdc}(t) \quad [40]$$

The charge surface density σ is related to the faradaic current through the charge conservation law

$$-\frac{d\sigma(t)}{dt} = \frac{I(t)}{S_{catalyst}(t)} + J_{Fdc}(t) \quad [41]$$

where $I(t)$ is the nominal current demanded to the cathode and $S_{catalyst}(t)$ is the instantaneous catalyst surface area.

Frumkin potential.— Following our previous work,[19] the Frumkin potential (or electrostatic potential drop through the electrochemical inner layer) can be written as the addition of two contributions

$$\eta(t) = \Delta\varphi_1(t) + \Delta\varphi_2(t) \quad [42]$$

where

$$\Delta\varphi_1(t) = \frac{-\sigma(t)}{\varepsilon_{CL}}d \quad [43]$$

and

$$\Delta\varphi_2(t) = \frac{\Gamma}{\varepsilon_{DL}} = \frac{\mu(\vec{n} - \vec{n})}{\varepsilon_{DL}} \quad [44]$$

where d is the thickness of a water molecule, ε_{CL} the electric permittivity in the compact layer and ε_{DL} in the diffuse layer, μ the dipolar moment of a water molecule, Γ the dipolar surface density within the compact layer.[75] $\vec{n}$ (respectively, $\vec{n}$) is the number of dipoles per unit of area directed (respectively, opposed) toward the electrocatalytic surface.

In contrast to the charge surface density σ, the dipolar surface density Γ is assumed to be different on surface Co and Pt sites. In fact, the affinity of Co and Pt to adsorb water molecules is not the same, as already shown by AI calculations.[23] Thus, for Γ we have

$$\Gamma = \Gamma^{Pt} + \Gamma^{Co} \quad [45]$$

with

$$\Gamma^{Pt} = \mu(\vec{n}^{Pt} - \vec{n}^{Pt}) \quad [46]$$

and

$$\Gamma^{Co} = \mu(\vec{n}^{Co} - \vec{n}^{Co}) \quad [47]$$

The number of sites with adsorbed water dipoles are obtained from the following mass action laws (M = Co or Pt)

$$\vec{n}^M = n^M\Theta_{H_2O}e^{(-\Delta\vec{G}^0_M/RT)} \quad [48]$$

$$\vec{n}^M = n^M\Theta_{H_2O}e^{(-\Delta\vec{G}^0_M/RT)} \quad [49]$$

As on a pure Pt surface,[72] the Gibbs free energy related to the water adsorption on the Pt–Co surface results from three contributions

$$\Delta G^0 = \Delta G^0_c + \Delta G^0_e + \Delta G^0_i \quad [50]$$

where ΔG^0_c is the chemical adsorption energy, ΔG^0_e is the electrostatic energy corresponding to the work of the field created by the charge of the metallic phase to carry a dipole from infinity to the electrode surface, and ΔG^0_i is the interdipolar interaction energy. We can demonstrate[76] that

$$\Delta G^{\vec{n}}_e = \mp\mu\frac{\Delta\phi(x = L,t)}{2\varepsilon} \quad [51]$$

$$\Delta G^{\vec{n}}_i = \mp\frac{A_1\mu^2}{\varepsilon^3}(\vec{n} - \vec{n}) \quad [52]$$

Table III. Surface coverage calculations.

Surface coverage on Co	Surface coverage on Pt
$\frac{s^{max\,Co}d\theta^{Co}_{H_2O}}{N_A\ dt} = v_{1Co} - v_{2e} + v_{Co(OH)2} - v_{CoOH2}$	$\frac{s^{max\,Pt}d\theta^{Pt}_{H_2O}}{N_A\ dt} = v_{1Pt} - v_{2Pt}$
$\frac{s^{max\,Co}d\theta^{Co}_{O}}{N_A\ dt} = v_{CoOH2} - v_{Co(OH)2}$	$\frac{s^{max\,Pt}d\theta^{Pt}_{OH}}{N_A\ dt} = 3v_{2Pt} + 3v_{1Pt} - v_{1Pt}$
	$\frac{s^{max\,Pt}d\theta^{Pt}_{O}}{N_A\ dt} = v_{Pt(OH)2} - v_{Pt(OH)2}$

where $\vec{\theta}$ (respectively, $\overleftarrow{\theta}$) are the covering fraction with dipoles oriented toward the electro-catalytic surface (respectively, opposed). $A = \xi(3)/2\pi\varepsilon_{PEL}$ and ξ designs the Riemann's ζ function.

Similarly to the pure Pt case, ΔG_{ads}^0 concerns the electrostatic interaction of water molecules adsorbed on the surface. However, in the case of the Pt-Co surface, water molecules adsorbed on Pt sites also interact with water molecules adsorbed on Co sites. Then, we have

$$\vec{\theta} - \overleftarrow{\theta} = (\vec{\theta}^{Co} + \vec{\theta}^{Pt}) - (\overleftarrow{\theta}^{Co} + \overleftarrow{\theta}^{Pt}) \quad [53]$$

By defining

$$\sigma_M = 2e^{-A\mu^2/k_BT}\sigma^{eq} \quad [54]$$

and

$$X = \frac{\mu\sigma}{k_BT\varepsilon_{CL}} + \frac{A\mu^2}{k_BTd^2}(\vec{\theta} - \overleftarrow{\theta}) \quad [55]$$

Eq. 48 and 49 become

$$\vec{n}^M = n^M\Theta_{M,0}e^{-\frac{\mu\sigma}{2}} \quad [56]$$

$$\overleftarrow{n}^M = n^M\Theta_{M,0}e^{+\frac{\mu\sigma}{2}} \quad [57]$$

and the difference is analogous for cobalt and platinum

$$\vec{n}^M - \overleftarrow{n}^M = -n^M\Theta_{M,0}\sigma_M\sinh[X] \quad [58]$$

Then, the Frumkin potential $\eta(t)$ becomes

$$\eta(t) = -\frac{\sigma d}{\varepsilon_{CL}} - \frac{\{x_{Co}^2(t)\sigma_{Co}\theta^{Co} + [1 - x_{Co}^2(t)]\sigma_{Pt}\theta^{Pt}\}n^M\Theta_{M,0}\sigma_M\sinh[X]}{\varepsilon_{PEL}} \quad [59]$$

This potential is written in terms of X, which is the single solution of a transcendental equation for each value of $\sigma(t)$. Using the number of dipoles adsorbed on the nanoparticle surface per unit of area, we obtain

$$\vec{n} - \overleftarrow{n} = (\vec{n}^{Co} + \vec{n}^{Pt}) - (\overleftarrow{n}^{Co} + \overleftarrow{n}^{Pt}) \quad [60]$$

and

$$\vec{n} + \overleftarrow{n} = \vec{n}^{Co} + \overleftarrow{n}^{Pt} + \vec{n}^{Co} + \overleftarrow{n}^{Pt} \quad [61]$$

then

$$\vec{\theta} - \overleftarrow{\theta} = \frac{\vec{n} - \overleftarrow{n}}{n^* + \vec{n} + \overleftarrow{n}} = \frac{-\sinh[X]}{[n^*/\Theta_{M,0}(n^{Co}\sigma_{Co} + n^{Pt}\sigma_{Pt})] + \cosh[X]} \quad [62]$$

where n^* is the addition of the number of free sites and of the number of sites covered by the intermediate reaction species per unit of area.

By using Eq. 55, we have

$$\vec{\theta} - \overleftarrow{\theta} = \frac{k_BTd^2}{A\mu^2}X - \frac{d^2}{A\mu\varepsilon_{CL}}\sigma \quad [63]$$

And then, from Eq. 62 and 63, the transcendental equation is

$$\frac{\sinh[X]}{\frac{1}{\Theta_{M,0}}\frac{(x_{Co}(t)(\theta^{Co} + \theta_{ads}^{Co}) + (1 - x_{Co}(t))(\theta^{Pt} + \theta_{ads}^{Pt}))}{(x_{Co}(t)\theta^{Co}\sigma_{Co} + (1 - x_{Co}(t))\theta^{Pt}\sigma_{Pt})} + \cosh[X]} = \frac{d^2}{A\mu\varepsilon_{CL}}\sigma - \frac{k_BTd^2}{A\mu^2}X \quad [64]$$

The value of θ^M (M = Co or Pt) is given by

$$\theta^M = \frac{1 - \theta_{ads}^M}{1 + \Theta_{M,0}\sigma_M\cosh[X]} \quad [65]$$

The surface coverages of dipoles on platinum and on cobalt ($\vec{\theta}^M$,$\overleftarrow{\theta}^M$) are obtained from Eq. 6 and 7.

Nanoparticles equivalent size temporal evolution.— In our model, each nanoparticle (homogeneous or fcc) is associated to a sphere in which the nanoparticle is inscribed. It is the radius of this sphere that we use to define the instantaneous nanoparticle equivalent radius $r(t)$. By extending our previous approach on pure Pt,[32] this radius is given by the solution of the differential equation

$$\frac{dr(t)}{dt} = k_dA_d\upsilon_{H_2PtCl_6}c_{Pt}^*\left\{\frac{-E_{d,a}}{RT} + \frac{2\upsilon_{Pt}\gamma_{Pt/ionO}}{RT}\left(\frac{1}{r(t)}\right)\right\} - \upsilon_{PtCo}j_{Co,d}(t,L) - \upsilon_{Pt,0}j_{Pt,0}(t,L) \quad [66]$$

where A_d is a pre-exponential factor, k_d is a rate constant, $\upsilon_{Pt,0}$ and υ_{PtCo} are the molar volumes of pure platinum and pure cobalt nanoparticles and υ_{PtCo} is the molar volume of the Pt-Co nanoparticle defined as $\upsilon_{PtCo} = (1/2)(\upsilon_{Pt,0} + \upsilon_{PtCo})$.[34] $E_{d,a}$ is the activation energy of a particle of infinite size, $\upsilon_{Pt,0}$ is a proportionality coefficient and γ the cluster/hydrated Nafion interfacial energy. In Eq. 66, the first term on the right is related to the particle surface energy minimization.[32] Furthermore, it is possible to add a term accounting for the electrochemical Ostwald ripening (we recall that as a first step approach, no redeposition of Co or Pt atoms is assumed here).

Total electrode catalyst surface area is directly calculated from the particles instantaneous radius

$$S_{catalyst}(t) = S_{catalyst}^{ini}\left[\frac{r(t)}{r(t=0)}\right]^2 \quad [67]$$

where $S_{catalyst}^{ini}$ is the initial catalyst surface area and $r(t = 0)$ the initial equivalent particle radius. Fresh catalyst surface area and particle radius are inputs of the model.

Reactant transfer in the hydrated Nafion film.— According to the nonequilibrium thermodynamics, the flux of the electrically neutral O_2 in the hydrated Nafion film within the cathode (cf. Fig. 3) is assumed to be given by the Fick's law of diffusion and the mass balance leads to

$$\frac{\partial C_{O_2}}{\partial t} = -\nabla_z\overrightarrow{J_{O_2}} = -\nabla_z(-D_{O_2}\nabla_zC_{O_2}) = D_{O_2}\nabla_z^2C_{O_2} \quad [68]$$

where we assume that the diffusion coefficient D_{O_2} is constant. The boundary conditions of Eq. 68 are given by Eq. 34 at $z = L$ (i.e., $z = e_{PEL}$, see Ref. 20), and by

$$C_{O_2}(z=0,t) = \frac{P_{O2}}{5.08 \times 10^6 \times \exp(-498/T)} \quad [69]$$

where the oxygen partial pressure p_{O_2} is given by

$$p_{O_2} = P_{cathode} - p_{sat} \quad [70]$$

where $P_{cathode}$ is the cathode total pressure, equal to 1.5 bar for all the simulation results discussed in this paper.

Ionic transfer in the electrolyte.— The one-dimensional-diffuse layer submodel (cf. Fig. 2) describes the transport by diffusion and electromigration of the electrically charged species close to the catalyst, participating in the electrochemical reactions and coupled with

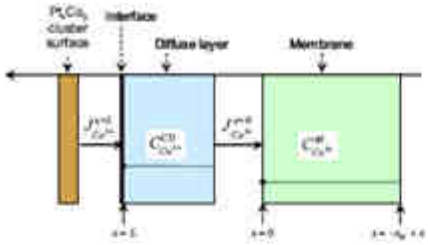

Figure 6. (Color online) Finite element method used to describe the transport of cobalt ions within the electrolyte.

the electric field generated by the charge distribution of H^+, Co^{2+}, and Pt^{2+}. As a first approximation, all species are considered as punctual, so the interparticle electrical interaction is neglected. The solvation and convection by water are not considered. For H^+, Co^{2+}, and Pt^{2+}, the diffusion coefficients in the hydrated Nafion phase are also assumed to be independent of the concentrations. The H^+ concentration at $x = L$ is calculated as in our previous papers.[31,32,34] Concentrations of Co^{2+} and Pt^{2+} in the diffuse layer and in the membrane are calculated using the finite element method (Fig. 6). Ionic molar fluxes are governed by the Nernst–Planck equations

$$\frac{\partial C_{M^{2+}}}{\partial t} = -\nabla_x J^x_{M^{2+}} = -\nabla_x(-D_{M^{2+}}\nabla_x C_{M^{2+}} - 2(D_{M^{2+}}C_{M^{2+}}\nabla_x\phi)) \quad [71]$$

(M = Co or Pt) where $D_{M^{2+}}$ is the diffusion coefficient of M^{2+}.[23]

Moreover, as confirmed by experiments reported in several papers,[9] in contrast to Pt^{2+}, we assume here that Co^{2+} is not redeposited as metallic cobalt within the ionomer. Thus, only platinum ions are assumed to precipitate within the membrane[34] by reacting with hydrogen from the anode

$$Pt^{2+} + H_2 \rightarrow Pt + 2H^+ \quad [72]$$

$$v_{recryst} = k_{recryst}C^{sat}_{Pt^{2+}}(l)C_{H_2}(l) \quad [73]$$

where $k_{recryst}$ is the recrystallization rate parameter and C_{H_2} is the hydrogen concentration in the membrane. This model allows simulating a spatially dependent Pt crystallites concentration, which is observed to be a function of the oxygen and hydrogen pressures, respectively, in the cathode and in the anode (detailed electrocatalysis for the last one is not accounted here).[33]

Simulation Results

Monte Carlo simulations have been carried out by means of an in-house code developed within a Matlab environment. Kinetics simulations have been performed by using an in-house developed code within a Matlab/Simulink environment by using the commercial Simulink solver ode15s with variable integration time step. This code has been run in a computer with an Intel processor 2.8 Ghz, 1.24 Gb of RAM.

Monte Carlo simulation results.— Monte Carlo simulations on fcc morphologies provide information about surface atomic composition, subsurface composition and their dependence on size and on global cobalt atomic composition. All this information allows us to build a good first understanding about atomic organization in a particle and its evolution when material is lost.

Nanoparticle size effect.— Depending on the global atomic composition, the particle size has or does not have an influence on the nanoparticle surface composition. In the case of no surface segregation, surface atoms seem to have preferential positions [vertex, edge, (111) facet, or (100) facet]. Cobalt seems to prefer (111) facets (Fig. 7a). Moreover, x^s_{Co} increases as the nanoparticle size decreases (e.g., from 1.6 to 0.8 nm). Thus, cobalt surface composition seems to decrease slowly with the size.

In the case when surface segregation occurs, the surface is mostly constituted of the element that segregates (platinum in Fig. 7b).

Cobalt volume composition.— According to Ma and Balbuena,[18] surface segregation is primarily determined by the surface energy and the atomic size. This is the physical explanation. However, surface segregation could also be understood by statistical concepts. Indeed, our Monte Carlo simulation (Fig. 8) show that surface composition is strongly dependent on global volume composition. Thus, for compositions far from 50/50, the surface is mainly composed of atoms which are in the majority.

Thus, for $Pt_{75}Co_{25}$, it is platinum which preferentially segregates to the surface but for $Pt_{25}Co_{75}$, it is cobalt which preferentially segregates to the surface. When the surface top layer is enriched in one element, the second layer is enriched in the other element. This suggests the formation of percolated Pt-rich and Co-rich regions, which agrees with recently published high-resolution transmission electron microscopy (TEM) characterizations.[36]

Coupling with the kinetic model.— For implementing the Monte Carlo simulation/multiscale model coupling, kinetic rates need, as input, the instantaneous nanoparticle surface composition. However, because of computational limitations, direct coupled Monte Carlo-kinetics simulations are not possible at the present in our group. Thus, we choose to simulate only particles in a pseudo-transient state; thus, we simulate only fcc structure nanoparticles with a magic number of atoms. Finally, we obtain a library of particle structures with different sizes and volume compositions. Cobalt surface composition is interpolated from a three-dimensional surface function (Fig. 9). The insertion of this interpolation function within the kinetics model emulates the atomic reorganization in the particle occurring during the degradation.

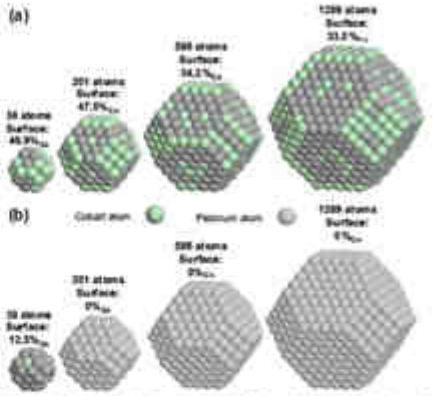

Figure 7. (Color online) Nanoparticles of Pt_xCo_y after Monte Carlo simulations for four different sizes (respectively, 0.8, 1.6, 2.3, 3.1 nm): (a) $Pt_{50}Co_{50}$ and (b) $Pt_{25}Co_{75}$.

ORR activity simulations results.— Homogeneous profile simulations.— Figure 10a shows modeling simulation results before long-term aging of the instantaneous activity of pure Pt compared to different homogeneous Pt_xCo_y catalysts. Activity of the different systems can be ranked as $PtCo > Pt_3Co > Pt > PtCo_3$, in excellent qualitative agreement with in-house experiments carried out in a

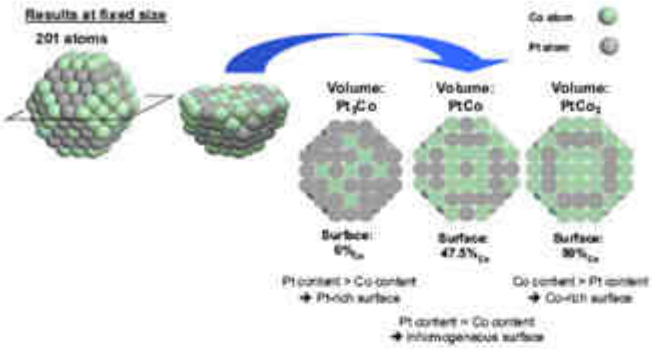

Figure 8. (Color online) Cut views of nanoparticles of 201 atoms (1.6 nm) after Monte Carlo simulations for three different atomic compositions. $PtCo_3$ is expected to be more unstable because it has more Co atoms at the surface.

half-cell (Fig. 10b with Pt and Pt_xCo_y elaborated by DLI-MOCVD process (details of elaboration and half-cell test are provided in Ref. 35 and 36).[1] These results can be explained as it follows. In our kinetic model, the first part of the ORR concerns both Pt and Co sites (cf. Eq 8 and 10): O_2 reduction forming adsorbed HO_2 on both Pt and Co sites. The kinetic rate k_{1Co} in Eq. 9, decreases when the Co surface composition $z^S_{Co}(t)$ decreases (see Table II). In contrast to this, k_{1Pt} (cf. Eq. 11) increases when the Co surface composition $z^S_{Co}(t)$ decreases. That means that surface accumulation of HO_2 is higher for $PtCo_3$ compared to Pt_3Co (because of the higher Co surface composition, assuming a small cluster), and thus, $PtCo_3$ has a lower overall activity.

Furthermore, the rate associated to the step (2 m) (cf. Eq. 13) is strongly dependent on the number of surface Pt–Co neighbors, with a maximum for a 50–50% surface composition (the number of possible surface transfers from Co to Pt is maximum at a surface composition of 50-50%), as it is described in Appendix B. This fact also explains why PtCo offers the better activity. The third part of the ORR concerns only Pt sites (cf. Eq. 17): electrochemical reduction of HO into H_2O. Thus, the associated step rate does not depend on the Pt–Co surface composition and then does not affect the calculated activity ranking.

Homogeneous profile vs Monte Carlo profile.— In Fig. 11, we compare the simulated polarization curves of the homogeneous and the Monte Carlo profiles for Pt_3Co and PtCo nanoparticles: both homogeneous nanoparticles show better instantaneous ORR activity (before long-term aging) than the Monte Carlo ones. These simulation results could seem in disagreement with Stamenkovic et al. experiments[18] in which they concluded that sputtered/annealed extended surfaces show better activities than simple sputtered extended surfaces. However, we emphasize here that our simulations concern nanoparticles and not extended bulk surfaces. Furthermore, in our model, we assume that only the topmost surface layer has an impact on ORR activity through different adsorption sites available on this surface: ORR activity of extended surfaces is believed to be also dependent on metal sublayers electronic properties.[32,33,43] These inputs are now being included in our model in order to be able to evaluate the scale effects (extended surface vs nanoparticle) on ORR activity and to compare our results with Stamenkovic et al.[18] experiments as well as incoming in-house experiments (see the Conclusion section).

[1] It is known that in ex-chemical PEFC fed with hydrogen and oxygen fully saturated with water (100% relative humidity), liquid water formation (water flooding) is considerably high at the electrodes level. In these conditions, interfacial electrochemistry can be treated as an electrode/liquid electrolyte interfaces.[42] Thus, the comparison between our simulations (for a fully hydrated PEFC cathode/PEM) and the half-cell experiments (with liquid electrolyte) is justified and pertinent.

Stability simulation results.— Homogeneous profile.— Figure 12 shows modeling results for homogeneous Pt_xCo_y aging vs Pt aging for two constant demanded current densities. For low currents (0.1 A/cm^2, Fig. 12a) our model predicts a potential "collapse" after 4.9×10^7 s for PtCo, after 5.9×10^7 s for Pt_3Co, and after 4.6×10^7 s for Pt. PtCo degradation is faster than Pt_3Co but slower than Pt. The observed potential failure occurs when the cathode catalyst surface area (driven by the temporal evolution of the catalyst dissolution) becomes too small to ensure the demanded current. Low current durability simulations can be summarized by Pt_3Co > PtCo > Pt > $PtCo_3$.

For intermediate currents (0.5 A/cm^2, Fig. 12b), our model predicts a potential collapse after 4×10^7 s for PtCo and after 6×10^7 s for Pt_3Co ($PtCo_3$ is not represented on this graph because of its predicted very fast degradation). PtCo degradation is now faster than pure Pt, which underlines the fact that durability trends are strongly dependent on the PEFC operating conditions. These durability rankings are explained as follows. Co dissolution rate is higher than Pt dissolution rate, and the Co dissolution rate is higher for higher Co volume contents (cf. Reactions 23 and 25). This explains why in the two durability rankings (for low and intermediate current) the durability decreases as the Co volume content increases (i.e., Pt_3Co > PtCo > $PtCo_3$). The change of position in the ranking for Pt is explained because Pt durability itself increases as the nominal current increases, as previously reported by us in Ref. 32 and in agreement with experimental knowledge.[39]

Cobalt dissolution is strongly related to the demanded current density (or applied potential). This fact is illustrated through the Fig. 13 simulation results on homogeneous Pt_xCo_y dissolved amount of

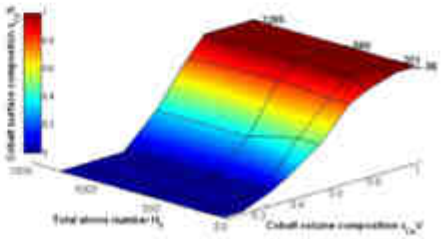

Figure 9. (Color online) Monte Carlo results compiled for cobalt surface composition interpolation from cobalt volume composition and total atoms number. When cobalt surface composition is equal to 0 (respectively, 1) no cobalt (respectively, platinum) is present in the surface.

cobalt increases as the current decreases. Calculated Pt dissolution rate (not shown here) is considerably lower than the Co dissolution rate (the Pt dissolution rate increases as the Co content at the nanoparticle level decreases) and the homogeneous nanoparticles become more and more like a skeleton-structured nanoparticle (the transition element dissolves leaving "holes" in a Pt matrix, like a "French emmental cheese"), exactly as speculated by Stamenkovic et al.[49]

In Fig. 14a, we show the simulated impact of the current density on the HO surface coverage on Pt sites. For the three materials, HO surface coverages on Pt sites show a maximum. Surface coverage by the adsorbed HO intermediate on Pt alone is higher than on Pt sites of Pt_3Co_1 catalyst because of the higher probability to adsorb HO on Pt for Pt alone than for Pt_3Co_1. PtCo and $PtCo_3$ plots show very similar behaviors with a maximum comprised between 1 and 1.5 A/cm^2. PtCo degradation is too strong at high current densities; the curve cannot be plotted for these current densities. Surface coverage by adsorbed intermediate O–Pt is also plotted (Fig. 14b) in the function of current densities. The four materials show a higher O–Pt coverage at low current densities (high potential).

Figure 15 presents the simulated impact of three dissolved hydrogen concentrations inside the membrane on the predicted cathode potential temporal evolution. Higher concentrations of dissolved hydrogen induce more ionic platinum precipitation within the membrane, and then a smaller PEFC cathode durability.

Homogeneous profile vs Monte Carlo profile.— In Fig. 16, we show the simulated temporal evolution of the potential for different constant current densities for Pt_3Co homogeneous and Monte Carlo profiles. The calculated effect of the current density on the durability is plotted in Fig. 17, which shows a bell-shaped curve suggesting that an "optimal" current density inducing a maximal durability exists. This predicted shape is explained as follows. Lower currents favor bimetallic dissolution. Then, catalyst surface area decreases faster as the current decreases: durability decreases as the current density decreases. At higher currents, dissolution is slower; however, because the demanded current is higher, failure potential is reached faster as the current increases, and durability decreases again as the current increases.

These durability simulation results for both homogeneous and Monte Carlo–derived profiles, are consistent with the loss of Pt–M/C catalysts in PEFC experimentally speculated to be attributed to the excess basemetal deposited onto the carbon support, the incomplete alloying of the transition element to Pt, and the thermodynamically instability of the transition metal under PEFC potentials in electrolytes.

Conclusion

On the basis of a multiscale theoretical approach, in this paper we focused on the understanding of the degradation mechanisms of Pt_xCo_y electrocatalytic nanoparticles in PEFC operating conditions. We have proposed a mechanistic model describing the ORR on aging Pt_xCo_y electrocatalytic nanoparticles in a PEFC environment. The proposed model extends our previous approaches describing the

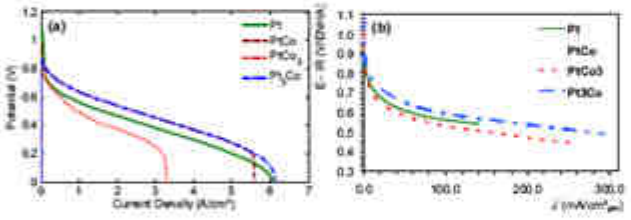

Figure 10. (Color online) (a) Instantaneous polarization curves obtained from multiscale model simulations for Pt_xCo_y and Pt. Morphological assumptions: initial particles size: 2 nm; initial catalyst surface area: 0.01 m^2; homogeneous profile. (b) Experimental activity results for Pt_xCo_y and Pt elaborated by DLI-MOCVD and tested in a half-cell.

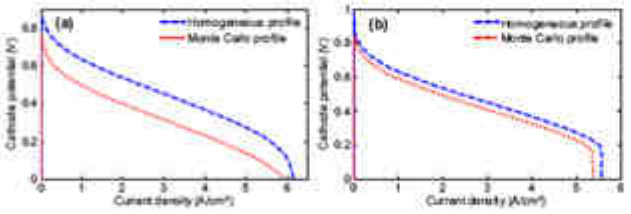

Figure 11. (Color online) Polarization curves obtained from the model simulations. Morphological assumptions: initial particles size: 1.5 nm; initial catalyst surface area: 0.01 m^2; homogeneous profile vs Monte Carlo profile (a) Pt_3Co and (b) PtCo.

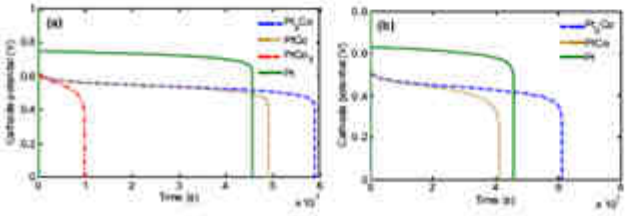

Figure 12. (Color online) Model durability simulation results for Pt_xCo_y and Pt at a constant demanded current density. Morphological assumptions: initial particles size: 2 nm; initial catalyst surface area: 0.01 m^2; homogeneous profile: (a) 0.1 A/cm^2 and (b) 0.5 A/cm^2.

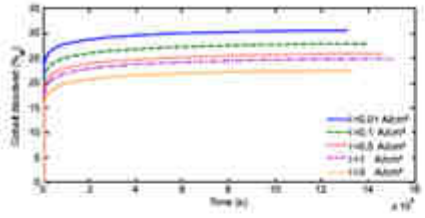

Figure 13. (Color online) Predicted percentage of dissolved Co for the Pt_3Co catalyst as function of the operating time and at different nominal currents. Morphological assumptions: initial particles size: 3.5 nm; initial catalyst surface area: 0.01 m^2; homogeneous profile.

aging of a Pt/electrolyte interface coupled to the ORR.[29,32] On the basis of literature AI data accounting for first atomic layer effects, we identified favorable pathways of the ORR on Pt_xCo_y nanoparticles and of the competitive Pt-Co oxidation/dissolution in acidic media. The derived AI-based kinetics has been coupled to a description of the atomic nanoparticle reorganization (segregation, surface energy minimization) as function of the simulated Pt and Co mass losses: the time-evolution of the Pt-Co surface and volume ratios at the nanoparticle level was simulated according to homogeneous and Monte Carlo-based structural models. The interfacial model has been coupled with a continuum microscale model of the charges and O_2 transports through the PEFC cathode thickness.

By describing the feedback between the instantaneous performance and the intrinsic catalyst degradation process, the resulting

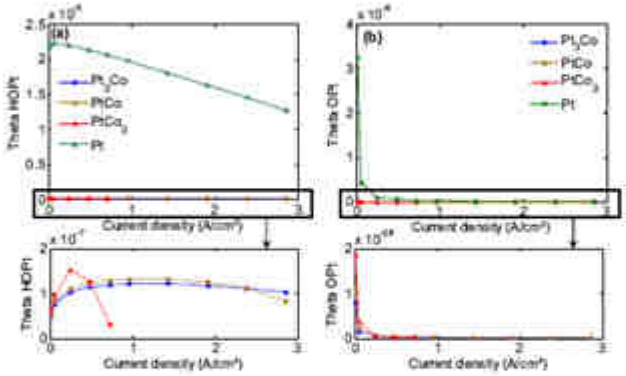

Figure 14. (Color online) OH and O surface coverages on platinum sites for Pt_3Co after 1000 s aging. Morphological assumptions: homogeneous profile, initial particles size: 2 nm; initial catalyst surface area: 0.01 m^2. (a) HO–Pt, (b) O–Pt.

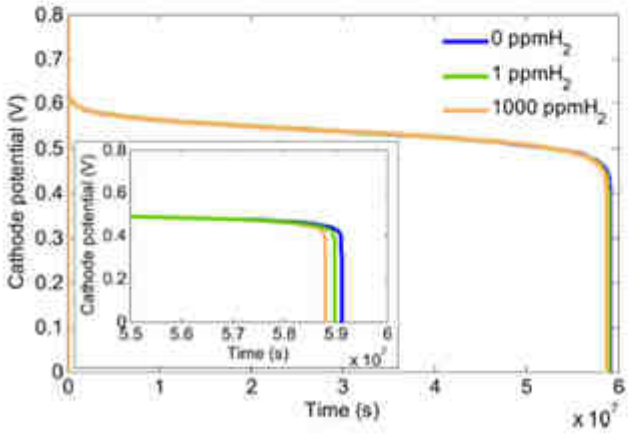

Figure 15. (Color online) Predicted effect of the dissolved hydrogen concentration in the membrane on the cathode potential temporal evolution for Pt_3Co. Morphological assumptions: homogeneous profile, initial particles size: 2 nm; initial catalyst surface area: 0.01 m^2.

multiscale model analyses the sensitivity of the cathode response to the operating conditions, initial compositions, nanostructure, and temporal evolution of the ORR activity.

The model leads with both instantaneous performance and durability prediction for different Pt_xCo_y atomic compositions, and allows accounting for the impact of the PEFC cathode polarization on the nanoparticle structure. Despite that only atomic first layer effects on electronic structure are accounted in the model, simulations results on homogeneous Pt_xCo_y show excellent agreement with half-cell experiments carried out on DLI-MOCVD electrodes.[36] At intermediate currents, activity of the different systems can be ranked as

$$PtCo > Pt_3Co > Pt > PtCo_3$$

This result clearly highlights the existence of an optimal Co content at the nanoparticle level providing the best performance.

Regarding durability simulations, we obtain for low currents (0.1 A/cm^2)

$$Pt_3Co > PtCo > Pt > PtCo_3$$

and for intermediate currents (0.5 A/cm^2)

$$Pt_3Co > Pt > PtCo > PtCo_3$$

which underlines the strong degradation dependence on electrode operating conditions, and that the nanoparticles with a high Co content are more unstable.

We highlight here that the activity/durability rankings are not only dependent on the assumed operating conditions and the initial composition of the nanoparticle, but also on the assumed nanoparticle structure (homogeneous or Monte Carlo-based) and the initial size.

Further theoretical developments are necessary to complement our studies:

1. We are now developing a model module describing both recommunication (reverse segregation phenomena without polarization) and electrochemical Ostwald's ripening of the bimetallic clusters that will be coupled to the other considered phenomena.
2. Second atomic layer effects on electronic structure are being included in the model, and effects on clusters degradation will be explored.
3. It will be interesting to explore the transient behavior of bigger clusters (5–20 nm); efforts are occurring in our group to reduce computational limitations.

In our companion paper,[36] we discuss the pertinence of our simulation results by comparison to dedicated experiments carried out on DLI-MOCVD-elaborated model electrodes by using a rotating disk electrode and half-cells, and where degradation structural changes have been characterized by using TEM, X-ray diffraction, and X-ray photoelectron spectroscopy.

Acknowledgments

This work was founded by the ANR PAN-H (French National Research Agency) within the context of the OPTICAT project.

Commissariat à l'Energie Atomique assisted in meeting the publication costs of this article.

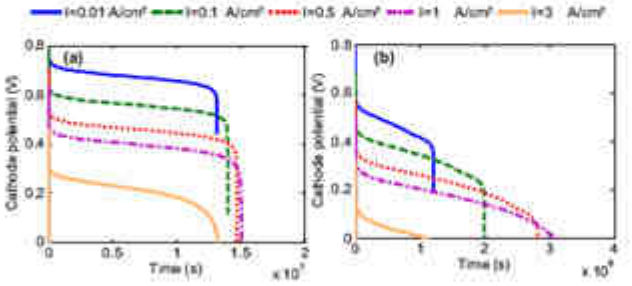

Figure 16. (Color online) Model-based predicted cathode potential degradation for Pt_3Co. Morphological assumptions: initial particles size: 1.5 nm; initial catalyst surface area: 0.01 m^2. (a) Homogeneous profile and (b) Monte Carlo profile.

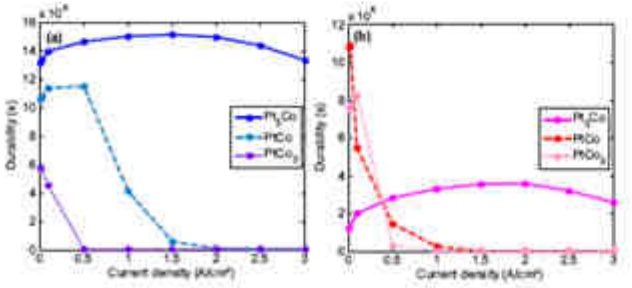

Figure 17. (Color online) Model-based predicted durability for Pt_3Co. Morphological assumptions: initial particles size: 1.5 nm; initial catalyst surface area: 0.01 m^2. (a) Homogeneous profile, (b) Monte Carlo profile.

Table A-I. Gibbs energies used for the kinetic rates (ΔG^0; thermodynamic values of fresh materials) (adjusted from Ref. 19 and 20).

	ΔG^0 (J/mol)
1Co	-5.470×10^4
1Pt	-5.089×10^4
2m	-5.207×10^4
2Pt	-5.848×10^4
3Pt	-9.513×10^4
CoOR1	2.242×10^5
CoOR2	1.133×10^5
CoOR3	-7.008×10^4
CoOR4	2.133×10^5
PtOR1	2.170×10^5
PtOR2	4.300×10^4
PtOR3	2.664×10^5

Table A-II. Empirical corrective factor (fitted).

	Corrective factor C
CoOR3	10^{-10}
CoOR4	10^{-1}
PtOR3	10^{-5}

Appendix A
Gibbs Energies Used for the Kinetic Rates

Gibbs energies used for the kinetic rates (Table A-I) are fitted from AI calculated data available in the literature.[19,20] This fit is found to be necessary because available AI data do not correspond to realistic systems but to absolute systems (e.g., extended surfaces, temperature of 0 K, vacuum conditions). Some of the used Gibbs energies include an empirical corrective factor (Table A-II) independent of the composition.

Appendix B
Neighbors Number Definition

The number of surface Pt$_x$Co neighbors as function of the Co surface composition can be written as

$$N_{neighbors} = \mathrm{floor}\left[\frac{s_{Co}^2(x)}{s_{Co}^2 k_s} - 0.5\right] \qquad [B\text{-}1]$$

where size represents the cardinal size function.

Appendix C
n^{max}, *Maximal Quantity of Free Sites per Unit Area*

For a monometallic electrocatalyst, n^{max} is constant and represents the maximal quantity of free sites per unit area of metallic phase

$$n^{max} = \frac{1}{d} \qquad [C\text{-}1]$$

For a bimetallic electrocatalyst, n^{max} is also constant and can be written as the addition of the two contributions

$$n^{max} = n^{max,Co} + n^{max,Pt} \qquad [C\text{-}2]$$

where $n^{max,M}$ represents the fraction of maximal quantity of free sites per unit area of M

$$n^{max,Co} = s_{Co}^2(x) n^{max} \qquad [C\text{-}3]$$

$$n^{max,Pt} = [1 - s_{Co}^2(x)] n^{max} \qquad [C\text{-}4]$$

Appendix D
Parameters

In Table D-I, we indicate the main parameters values used in the model simulations shown in this paper. For the other parameters values used in these simulations, refer to our previous publications.[32,34]

Table D-I. Parameters values chosen for the simulations shown in this paper.

	Units	Ref.
$S_{electrode} = 2.1 \times 10^{-4}$	m^2	Measured and 34 and 32
$e_M = 25 \times 10^{-9}$	m	Measured and 34
$L = 5 \times 10^{-5}$ (estimated from the model)	m	27, 28, and 32
$e_{PS} = 10^{-5}$	m	34 and 32
$\Delta G_C^{ref} = 1$ (M = Co or Pt)	J mol^{-1}	27, 31, 28, and 29
$\alpha_M = 2\exp(-\Delta G_C^{ref}/RT)$	dimensionless	This work
$D_{Co^{2+}} = 3.8 \times 10^{-16}$	m^2/s	53 and this work
$D_{H^+} = 1 \times 10^{-27}$	m^2/s	32 and this work
$\rho_{Co} = 8900$	kg/m^3	51
$\rho_{Pt} = 21450$	kg/m^3	51
All $\alpha = 0.5$	dimensionless	This work
$E_{ref,d} = 4RT$	J mol^{-1}	32
$A_d = \frac{1}{2^{\alpha_{max}} N_A} \frac{k_B T}{h}$	mol m^{-2} s^{-1}	This work
$k_d = 10^{-3}$	mol m^{-2} s^{-1}	This work
$\alpha_{Ox} = 1$	dimensionless	32
$\chi = 0.5$	J m^{-2}	32
$v_{mPt} = 9.1 \times 10^{-6}$		
$v_{mCo} = 6.6 \times 10^{-6}$	m^3 mol^{-1}	51
$k_{europt} = 10^{10}$	mol m^{-2} s^{-1}	This work

List of Symbols

Constants

$d = 2 \times 10^{-10}$	compact layer thickness, m
$F = 96485$	Faraday constant, C mol^{-1}
$h = 6.626068 \times 10^{-34}$	Planck constant, m^2 kg s^{-1}
$k_B = 1.380 \times 10^{-23}$	Boltzmann constant, J K^{-1}
$N_A = 6.022 \times 10^{23}$	Avogadro number, mol^{-1}
$R = 8.314$	ideal gas constant, J K^{-1} mol^{-1}
$v_{mPt} = 9.1 \times 10^{-6}$	platinum molar volume, m^3 mol^{-1}
$v_{mCo} = 6.6 \times 10^{-6}$	cobalt molar volume, m^3 mol^{-1}
$\varepsilon_0 = 8.854 \times 10^{-12}$	electric permittivity of vacuum, C^2 N^{-1} m^{-2}
$\mu = 0.617 \times 10^{-30}$	dipolar moment of a water molecule, C m

Latin

$\alpha = 2\exp(-\Delta G_C^{ref}/RT)$	
$A = s[O_2^*]^{\gamma_{Ox}}$	
$f_i(\theta_i)$	
$= \Sigma_{j=0}^{m} (1/j!)\theta_i^j$ $(\theta_i > 1)$	Flowers function, $[[O_2^*] = 1.20]$
A_d	pre-exponential factor, mol m^{-2} s^{-1}
s	dimensionless parameter in the multicationic Ising-Chen potential
C_{O_2}	oxygen concentration, mol m^{-3}
C_{H^+}	proton concentration, mol m^{-3}
$C_{Co^{2+}}$	Pt^{2+} concentration, mol m^{-3}
$C_{Co^{2+}}$	Co^{2+} concentration, mol m^{-3}
D_{O_2}	oxygen diffusion coefficient in Nafion, m^2 s^{-1}
$D_{Pt^{2+}}$	Pt^{2+} diffusion coefficient in Nafion, m^2 s^{-1}
$D_{Co^{2+}}$	Co^{2+} diffusion coefficient in Nafion, m^2 s^{-1}
e_M	membrane thickness, m
e_{PS}	microscale impregnated Nafion/water layer thickness, m
E_{act}	activation energy of a platinum-cobalt particle of cobalt size, J mol^{-1}
$f = F/RT$	
I	total electric current demanded to the cathode, A

J_{O_2} oxygen molar flux in Nafion, mol s^{-1} m^{-2}
J_{H^+} protons molar flux in Nafion, mol s^{-1} m^{-2}
$J_{M^{n+}}$ M^{n+} molar flux in Nafion, mol s^{-1} m^{-2} (M = Co or Pt)
i^{M}_{Faci} faradaic current through the M sites associated to the electrochemical reaction steps, A m^{-2} (M = Co or Pt)
I_{Fact} total faradaic current associated to the electrochemical reaction steps on both Co and Pt sites, A m^{-2}
k_i standard reaction rate parameter, mol s^{-1} m^{-2}
L diffuse layer thickness, m
m positive integer number in the multiatomic Ising-Chen potential
n positive integer number in the multiatomic Ising-Chen potential
n^{gas} surficial quantity of free sites per unit of area of catalyst phase, m^{-2}
n^{Me^0} surficial quantity of free sites per unit of area of M-based catalyst surface (M = Co or Pt), m^{-2}
n^{M} number of free sites per unit of area of M-based catalyst surface, m^{-2} (M = Co or Pt)
N_{atom} total number of atoms in one nanoparticle
N_{step} number of steps performed during an annealing Monte Carlo simulation
$N_{neighbour}$ mean number of platinum atoms close to one cobalt atom (neighbour number)
P probability of a trial to be accepted (annealing Monte Carlo simulation method)
$P_{mixture}$ cathodic total pressure, Pa
P_{O_2} cathodic oxygen partial pressure, Pa
P_{sat} saturated water vapor partial pressure, Pa
r mean radius of Pt-Co nanoparticles, m
r_{ij} distance between atom i and atom j
S^{real}_{atom} initial total catalytic surface area, m^2
S_{atom} total catalytic surface area, m^2
T absolute temperature, K
U total energy of a nanoparticle atomic system calculated with the Ising-Chen potential

$v_{alloy} = (1/2)$
$\times (v_{Co} + v_{Pt})$ platinum-cobalt alloy molar volume, m^3 mol^{-1}
v_i electrochemical reaction rates, mol s^{-1} m^{-2}
x^s_{Co} surface atomic cobalt composition
x_{Co} atomic cobalt composition in the nanoparticle volume
ΔG Gibbs energy, J mol^{-1}
$\Delta G^{ads}_{H_2O}$ water chemical adsorption energy, J mol^{-1}
$\Delta G^{ele}_{H_2O}$ adsorbed water electrostatic energy, J mol^{-1}
$\Delta G^{int}_{H_2O}$ water interphase interaction energy, J mol^{-1}
ΔG^{r}_{MR} Gibbs energy of a reaction MR, J mol^{-1}
ΔH^{r}_{MR} enthalpy of a reaction MR, J mol^{-1}
ΔS^{r}_{MR} entropy of a reaction MR, J mol^{-1}

Greek

α elementary reaction step electronic number coefficients
α_{Me} proportionality coefficient in the nanoparticle equivalent size temporal evolution submodel
γ_i activity coefficient
Γ interfacial dipolar surface density, Debye m^{-2}
Γ^M interfacial dipolar surface density on M sites, Debye m^{-2} (M = Co or Pt)
ε_{CL} electric permittivity in the compact layer, C^2 J^{-1} m^{-1}
ε_{DL} electric permittivity in the diffuse layer (electrolyte phase), C^2 J^{-1} m^{-1}
ε^{M} energy parameter in the multiatomic Ising-Chen potential, eV
η electrostatic potential difference between the catalyst and the electrolyte phases (through the compact layer), V
θ^{Ox}_{M} covering fraction of dipoles oriented toward the M sites (M = Co or Pt)
θ^{Red}_{M} covering fraction of dipoles opposed to the M sites (M = Co or Pt)
θ^{M} covering fraction of free M sites (M = Co or Pt)
θ^{M}_{O} covering fraction of the intermediate reaction species, O-M (M = Co or Pt)
$\theta^{M}_{HO_2}$ covering fraction of the intermediate reaction species HO_2-M (M = Co or Pt)
θ^{Pt}_{HO} covering fraction of the intermediate reaction species HO-Pt
Θ_{H_2O} diffuse layer and bulk water activity
ρ charge density on the catalyst surface, C m^{-2}
σ^{M} lattice constant in the multiatomic Ising-Chen potential, Å
ϕ electrostatic potential in the electrolyte phase, V
χ platinum-cobalt/Nafion interfacial tension, J m^{-2}
ψ electrostatic potential in the platinum-cobalt/C medium, V

Acronyms

GDL gas diffusion layer
IM impregnated nafion/water film

References

1. J. K. Nørskov, J. Rossmeisl, A. Logadottir, L. Lindqvist, J. R. Kitchin, T. Bligaard, and H. Jonsson, *J. Phys. Chem. B*, 108, 17886 (2004).
2. X. Wang, H. Kumar, and D. J. Myers, *Electrochem. Solid-State Lett.*, 9, A225 (2006).
3. H. Xu, R. Kunz, and J. M. Fenton, *Electrochem. Solid-State Lett.*, 10, B1 (2007).
4. E. Yeziels, A. Tzinguelis, T. Akin, T. Ioiou, and Z. Siroma, *Phys. Chem. Chem. Phys.*, 8, 746 (2006).
5. F. J. Fernández and Y. Shao-Horn, *Electrochem. Solid-State Lett.*, 10, B60 (2007).
6. S. Escribano, R. Jamard, A. Morin, S. Solan, and L. Guetaz, in *Proceedings of 16th World Hydrogen Energy Conference*, Lyon, June 13–16, 2006, Paper no. 519.583 (on CD) (2006).
7. S. C. Ball, S. L. Hudson, B. Theobald, and D. Thompsett, 210th ECS Meeting, Abstract no. 0572.
8. S. C. Ball, S. L. Hudson, B. E. Theobald, and D. Thompsett, *ECS Trans.*, 11(1), 1267 (2007).
9. S. C. Ball, S. L. Hudson, J. Hin Leung, A. E. Russell, D. Thompsett, and B. E. Theobald, *ECS Trans.*, 11(1), 1247 (2007).
10. V. R. Stamenkovic, B. S. Mun, M. Arenz, K. J. J. Mayrhofer, C. A. Lucas, G. Wang, P. N. Ross, and N. M. Markovic, *Nature Mater.*, 6, 241 (2007).
11. M. Watanabe, K. Tsurumi, K. Hayakawa, T. Nakamura, and F. Sonobuel, *J. Electrochem. Soc.*, 141, 2659 (1994).
12. J. Roques, A. B. Anderson, V. S. Murthi, and S. Mukerjee, *J. Electrochem. Soc.*, 152, E393 (2005).
13. J. Roques and A. B. Anderson, *Surf. Sci.*, 581, 105 (2005).
14. B. K. Colón-Mercado and B. N. Popov, *J. Power Sources*, 155(2), 253 (2006).
15. E. Antolini, J. R. C. Salgado, and E. R. Gonzalez, *J. Power Sources*, 160, 957 (2006).
16. P. Yu, M. Pemberton, and P. Plasse, *J. Power Sources*, 144, 11 (2005).
17. S. C. Zignani, E. Antolini, and E. R. Gonzalez, *J. Power Sources*, 182, 83 (2008).
18. T. Ma and P. D. Beltrame, *Surf. Sci.*, 602, 197 (2008).
19. Y. Wang and P. B. Balbuena, *J. Phys. Chem. B*, 109, 18902 (2005).
20. Z. Gu and P. B. Balbuena, *J. Phys. Chem. A*, 110, 9743 (2006).
21. J. M. Svetanoto and P. B. Balbuena, *Chem. Phys. Lett.*, 419, 275 (2005).
22. P. B. Balbuena, D. Altomare, Y. Vadlamani, S. Bingi, L. A. Agapito, and J. M. Seminario, *J. Phys. Chem. A*, 108, 6378 (2004).
23. J. Greeley and J. K. Nørskov, *Electrochim. Acta*, 52, 5829 (2007).
24. R. Chenitz, D. de Caro, B. Chandut, P. Lecante, and E. Sarrack, *New J. Chem.*, 25, 525 (2001).
25. L. Zhu, R. Wang, T. E. King, and A. E. DePristo, *J. Catal.*, 167, 406 (1997).
26. N. Savargaonkar, B. C. Khanra, M. Pruski, and T. S. King, *J. Catal.*, 163, 277 (1996).
27. A. A. Franco, Ph.D. Thesis, Université Claude Bernard Lyon-I, France, no. 2007LYO10239 (2007); http://tel.archives-ouvertes.fr/tel-00111908/fr/.
28. A. A. Franco, F. Schott, C. Jallut, and B. Maschke, *Fuel Cells*, 7, 99 (2007).
29. A. A. Franco, *ECS Trans.*, 6(30), 1 (2007).
30. A. A. Franco, F. Schott, C. Jallut, and F. M. Maschke, Abstract 1296, The Electrochemical Society Meeting Abstracts, Vol. 2003-1, Quebec, Canada, May 15–20, 2003.
31. A. A. Franco, F. Schott, C. Jallut, and B. Maschke, *J. Electrochem. Soc.*, 153, A1053 (2006).
32. A. A. Franco and M. Tembely, *J. Electrochem. Soc.*, 154, B712 (2007).
33. M. Gerard, Master Research 2 project Diploma (2007).
34. A. A. Franco and M. Gerard, *J. Electrochem. Soc.*, 155, B367 (2008).
35. A. A. Franco, S. Passot, C. Angleda, E. Billy, L. Guetaz, N. Guillet, E. De Vito, S. Maillet, and P. Tingaut, *ECS Trans.*, 13(15), 35 (2008).
36. A. A. Franco, S. Passot, C. Angleda, E. Billy, L. Guetaz, N. Guillet, E. De Vito, S. Maillet, and P. Tingaut, *J. Electrochem. Soc.*, In preparation.
37. J. T. Glass, G. L. Cahen, Jr., G. E. Stoner, and E. J. Taylor, *J. Electrochem. Soc.*, 134, 58 (1987).
38. A. Perez, P. Melinon, I. Lerond, and P.-F. Brevet, *Les Nanosciences. Nanochimie, gaz et nanophysique, Agrégats et colloïdes*, Chap. 7, Ed. Belin, Paris (2004).
39. A. P. Sutton and J. Chen, *Philos. Mag. Lett.*, 61, 139 (1990).
40. R. Rafii-Tabar and A. P. Sutton, *Philos. Mag. Lett.*, 63, 217 (1991).
41. G. E. Ramírez Caballero and P. B. Balbuena, *Mol. Simul.*, 32, 297 (2006).
42. Y. H. Chui and K. Y. Chan, *Chem. Phys. Lett.*, 408, 49 (2005).
43. N. Metropolis, A. W. Rosenbluth, M. N. Rosenbluth, A. H. Teller, and E. Teller, *J. Chem. Phys.*, 21, 1087 (1953).
44. F. Calvo and P. Labastie, *Eur. J. Phys.*, 26, 523 (2005).
45. R. T. Lobo, Simulated Annealing Cooling Schedules, http://fcaysys.nsfcel.gov/lobo/sa/sa1.html.
46. B. S. Wickham, Y. C. Fan, and G. Hammerly, *J. Electroanal. Chem. Interfacial Electrochem.*, 69, 195 (1976).
47. E. Yeager, *J. Mol. Catal.*, 5, 20 (1986).
48. T. E. Shubina and M. T. M. Koper, *Electrochim. Commun.*, 8, 703 (2006).
49. H. Eyring, *J. Chem. Phys.*, 3, 107 (1935).
50. W. E. K. Wynne-Jones and H. Eyring, *J. Chem. Phys.*, 3, 492 (1935).
51. *CRC Handbook of Chemistry and Physics*, 66th ed., Chemical Rubber Company, Cleveland (1985).

52. W. Sun, *Acta Mater.*, 53, 3129 (2005).
53. A. Dolan, M. Tabuba, E. Nomi, and M. Ghorbani, *Mater. Chem. Phys.*, 102, 135 (2007).
54. P. J. Ferreira, G. J. la O', Y. Shao-Horn, D. Morgan, R. Makharia, S. Kocha, and H. A. Gasteiger, *J. Electrochem. Soc.*, 152, A2256 (2005).
55. H. Liu, J. Zhang, F. D. Coms, W. Gu, B. Litteer, and H. A. Gasteiger, *ECS Trans.*, 3(1), 493 (2006).
56. S. Chen, P. J. Ferreira, W. Sheng, N. Yabuuchi, L. F. Allard, and Y. Shao-Horn, *J. Am. Chem. Soc.*, 130, 13818 (2008).
57. M. Shao, P. Liu, J. Zhang, and R. Adzic, *J. Phys. Chem. B*, 111, 6772 (2007).
58. R. M. Darling and J. P. Meyers, *J. Electrochem. Soc.*, 150, A1523 (2003).

Electrochimica Acta 54 (2009) 5267–5279

Contents lists available at ScienceDirect

Electrochimica Acta

journal homepage: www.elsevier.com/locate/electacta

Impact of carbon monoxide on PEFC catalyst carbon support degradation under current-cycled operating conditions

Alejandro A. Franco*, Magalie Guinard, Benoit Barthe, Olivier Lemaire

Commissariat à l'Energie Atomique (CEA), DRT/LITEN/Département de Transport et Hydrogène/Laboratoire des Composants Piles à combustible et Electrolyseurs et de Modélisation (LCPEM) - 17, Rue des Martyrs – 38054 Grenoble cedex 9, France

ARTICLE INFO

Article history:
Received 6 November 2008
Received in revised form 1 April 2009
Accepted 2 April 2009
Available online 9 April 2009

Keywords:
PEFC aging
CO poisoning
Carbon corrosion
Current-cycling
Multiscale modeling

ABSTRACT

It is well known that, even at ppm levels, the presence of CO in a PEFC anode feed stream has a significant impact on the MEA performance. Numerous work on short-term CO impact on PEFC performance under steady-state current demands has been carried out. However, to the best of our knowledge, the impact of long-term (i.e., >600 h) CO contamination on intrinsic Pt and C support aging (Pt oxidation/dissolution/ripening, C oxidation, ...) under current-cycled operating conditions has never been explored. In this paper, on the basis of a combined theoretical and experimental approach, we investigate the long-term CO effect on PEFC performance and degradation. Firstly, on the basis of our previously published PEFC materials degradation models, we suggest that anodic CO poisoning could be used to mitigate the cathodic carbon-catalyst-support corrosion phenomena and thus to enhance the MEA durability. Secondly, endurance experiments are performed on single fuel cells with current-cycled protocols representative of transport applications. The impact of CO on electrochemical transient response shows a reasonable agreement with simulated behaviors, and it is experimentally demonstrated that the impact of CO on the cell potential degradation rate is strongly dependent on the current-cycle mode.

1. Introduction

In recent years, low-temperature PEFCs have attracted much attention and research efforts due to their potential as a clean and silent power source for many applications: traction of vehicles (by replacing the thermal generators by electric motors), portable devices, and stationary production of electricity. This has resulted in tremendous technological progress, such as the introduction of thin per-fluorinated ionomer membranes and improvements to electrode structures which can increase the catalyst utilization (and thus decrease the precious catalyst loadings). However, in order to be competitive in the most attractive markets, the PEFC technologies need further improvement, particularly in terms of cost, reliability and durability.

One of the major sources of hydrogen fuel for PEFCs is expected to consist of hydrocarbon reforming. Currently, the main studied methods of hydrocarbon reforming are steam reforming, partial oxidation and auto-reforming [1]. Regardless of what procedure is applied, the presence of impurities in hydrogen fuel is unavoidable, and the supply of hydrogen obtained by the reforming of alcohols or hydrocarbons to PEFCs requires an extensive gas clean-up process [2–4]. Feed stream impurities, mainly CO, H_2S, NH_3, organic sulfur–carbon, and carbon–hydrogen compounds can cause significant PEFC performance degradation, as well as permanent membrane damage [5].

In particular, it is well accepted in the scientific community that the presence of CO in the anode feed stream can have a major impact on Pt-based PEFC performance through the poisoning of the anodic catalyst. Numerous studies have been devoted to understanding the short-term (about 10 h) CO impact on the Pt-based PEFC electrochemical response as a function of different steady-state operation parameters, such as current, temperature and reactant pressure [6–9].

Moreover, it is well known that the addition of a small amount (0.5–1%) of O_2 or air in the anode feed stream (O_2/air bleeding) is effective in mitigating the CO poisoning of the PEFC anode [10,11] because O_2 oxidizes CO adsorbed on the Pt catalyst [12–14]. Chen et al. and Du et al. have experimentally determined the optimum quantity of oxygen or air which can be added as a function of the CO concentration to enhance PEFC performance [12,14]. Several PEFC mathematical models accounting for O_2 bleeding have also been reported by several groups [15–18].

Abbreviations: COR, carbon oxidation reaction; GDL, gas diffusion layer; HOR, hydrogen oxidation reaction; MEA, membrane electrodes assembly; ORR, oxygen reduction reaction; PEFC, polymer electrolyte fuel cell; HR-TEM, high resolution-transmission electron microscopy; SEM, scanning electron microscopy; CCM, catalyst coated membrane; NHE, normal hydrogen electrode; XPS, X-ray photoelectron spectroscopy; FTIR, fourier transformed infrared spectroscopy.

* Corresponding author.
E-mail address: alejandro.franco@cea.fr (A.A. Franco).

0013-4686/$ – see front matter © 2009 Elsevier Ltd. All rights reserved.
doi:10.1016/j.electacta.2009.04.008

Nomenclature

a	$2\exp\left(-\Delta G_C^0/RT\right)$
A	$\zeta[3]/2\pi r_{DL}\left(\zeta(i2)=\sum_{p=1}^{\infty}\frac{1}{p^{i2}}(i2>1)\right.$ $\left.-\text{Riemman's function}-,\ \zeta[3]\cong 1.20\right)$
C_i	hydrogen, oxygen or carbon monoxide concentration (mol m^{-3})
C_{SO_3}	Nafion® sulfonate groups concentration (mol m^{-3})
D_i	diffusion coefficient of hydrogen, oxygen or carbon monoxide in hydrated Nafion® (m^2 s^{-1})
d	compact layer thickness (m)
e_M	membrane thickness (m)
e_{IH}	on-catalyst water/ionomer layer thickness (m)
f	F/RT
$F=96{,}485$	Faraday's constant (C mol^{-1})
I_{ext}	current demanded by the external load (A)
I_{total}	total current (A)
I_C	carbon corrosion (reverse) current (A)
j_i	hydrogen, oxygen or carbon monoxide molar flux in hydrated Nafion® (mol s^{-1} m^{-2})
j_{Far}^{Anode}	anodic Faradaic current (A)
k_i	kinetic rate parameter (mol s^{-1})
$k_B=1.380\times10^{-23}$	Boltzmann's constant (J K^{-1})
L	diffuse layer thickness (m)
Γ^{max}	maximal quantity of free sites per unit of area of electro-active phase (m^{-2})
$N_A=6.022\times10^{23}$	Avogadro's number (mol^{-1})
$R=8.314$	ideal gas constant (J K^{-1} mol^{-1})
m_{Pt}^i	anode or cathode platinum mass (kg)
p_{sat}	water saturation pressure (Pa)
P_{Anode}	anode total pressure (Pa)
$P_{Cathode}$	cathode total pressure (Pa)
p_i	hydrogen, oxygen or carbon monoxide partial pressure in the pore phase (Pa)
T	absolute temperature (K)
v_i	electrochemical reaction rate (mol s^{-1} m^{-2})

Greek letters

ε_{H_2O}	water surface fraction on the electroactive catalyst surface
α	elementary reaction step electronic transfer coefficient
y_{CO}	anode CO content (ppm)
ε_{CL}	electric permittivity in the inner layer (C^2 J^{-1} m^{-1})
ε_{DL}	electric permittivity in the diffuse layer (electrolyte phase) (C^2 J^{-1} m^{-1})
ϕ	electrostatic potential in the electrolyte phase (V)
γ_{Pt}^{Anode}	anode platinum surface area (m^2)
θ	electrostatic potential difference between the Pt or C and the electrolyte phases (through the compact layer) (V)
$\mu=0.617\times10^{-29}$	dipolar moment of a water molecule (C m)
$\tilde{\theta}$	covering fraction of dipoles opposed to the electro-active phase
$\bar{\theta}$	covering fraction of dipoles oriented towards the electro-active phase
θ_*	covering fraction of free sites
θ_i	covering fraction of the intermediate reaction species
σ	electronic surface density at the Pt level (C m^{-2})
ω	surface CO–CO molecular interaction parameter (J mol^{-1})
ψ	electrostatic potential in the Pt and C phases (V)

The numerous experimental and modeling efforts, discussed above, have been on the short-term CO impact on PEFC performance under steady-state current demands. To the best of our knowledge, the impact of long-term (i.e., >600 h) CO contamination on PEFC behavior under current-cycled operating conditions inducing severe intrinsic PEFC material aging (Pt oxidation/dissolution/ripening, C oxidation, ...), has never been explored.

As discussed by us in previous papers [19–21], several experimental studies have indicated that the cathodic carbon catalyst-support corrosion is exacerbated by the presence of O_2 in the anode [22]. It has been shown that the presence of O_2 in the anode induces a reverse proton current between the electrodes, driving the cathode carbon oxidation (Fig. 1a). This can result in a significant decrease of the cathode thickness, and thus a degradation of the PEFC performance: a dramatic catalyst active surface area loss can be also induced by this cathode carbon corrosion phenomenon [23–25]. In contrast, the anode thickness did not appear to change. According to Tang et al., after a shut down operation, air can gradually diffuse into the anode side through an open anode exhaust port, creating an oxygen/hydrogen boundary [26]. It is also believed that misdistribution or local interruptions in the anode hydrogen supply (the so-called fuel starvation phenomenon) improves O_2 permeation from the cathode into the anode [27]. According to Fuller and Gray [28], as well as Darling and Jayne [29], the formation of liquid water drops in the anodic channel could also locally block the hydrogen access to the electrode. In-line direct gas mass spectroscopy analysis has successfully detected intermittent CO_2 emission peaks in exhausted gas from the cathode, indicating that carbon corrosion especially occurs during the load cycle in the PEFC [27,30,31].

In successive previous papers [19,21,32,33] we have summarized our multiscale modeling research on materials degradation mechanisms in PEFCs. We have proposed a model describing mechanistically the feedback between the instantaneous MEA performance and the intrinsic aging processes allowing the prediction of the PEFC single cell potential evolution and the MEA durability.

More precisely, the cathode carbon corrosion phenomena has been addressed in [19,21]: a cathode submodel describing the microscale transport of reactants and charges through the electrode and impregnated ionomer layer has been coupled with a non-equilibrium thermodynamics description of the nanoscale electrochemical interface phenomena [34] occurring on both Pt and corroding C. The model allows the investigation of the cumulative effect of the partial exposure of the anode catalyst to O_2 (induced by membrane crossover or fuel starvation) on transient PEFC performance, as well as the catalytic role of the cathodic Pt on the C microstructure degradation. In particular, the model accounts for the Pt "detachment" from the C support, a C corrosion-driven Pt coarsening mechanism (Fig. 1b, not to be confused with the electrochemically driven Ostwald's ripening mechanism [32]) and the increase of the "contact resistance" between the electrode and the GDL during degradation. The proposed model captures the sensitivity of the MEA response to the operating conditions (nominal current, reactant-gas pressure, temperature, ...), to the composition (Pt, C, Nafion® loadings) and to the evolution of the electrochemical activity from the C corrosion mechanism. It predicts the time degradation of the electrochemical activity on a

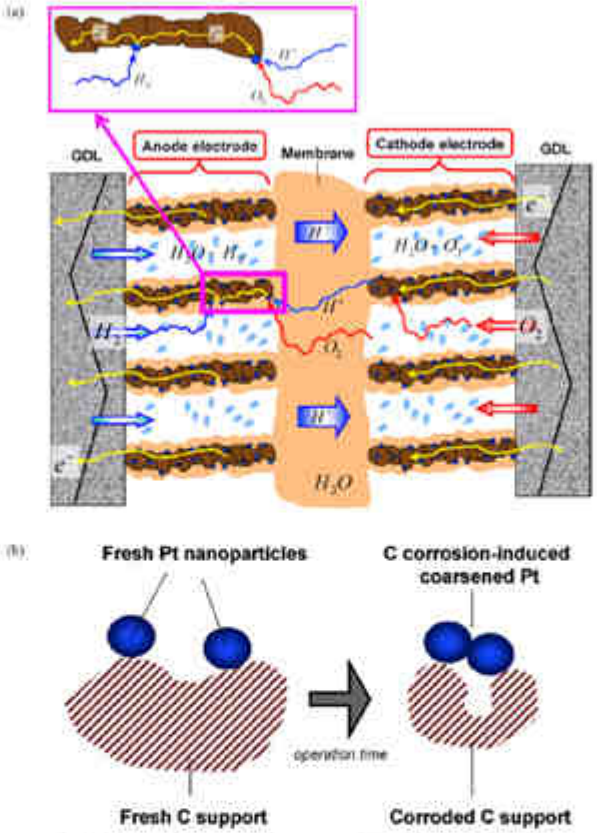

Fig. 1. (a) Local anode ORR enhancement under PEFC current-cycling operation (fuel starvation conditions). (b) Induced cathode carbon corrosion and resulting Pt nanoparticles coarsening.

mechanistic basis, and allows analysis of the impact of the electrodes initial morphological properties on durability, as well as the influence of time on impedance spectra patterns. This approach is very powerful, and, through the coupling with other material degradation models [32,33], provides insights on the interplay between the different aging phenomena. The use of infinite dimensional Bond Graph theory has made this multiscale model hierarchical and modular, so that it is reusable in other electrochemical contexts and it can be easily coupled to other physicochemical phenomena.

In this paper, we use a combined theoretical and experimental approach to investigate the impact of the presence of CO in the anode feed stream of a PEFC on the MEA long-term (at least 600 h) performance degradation, under current-cycled operation representative of transport application conditions. The aim here is to provide some insight on the competition between these two degradation mechanisms.

This paper is organized as follows. Firstly, we describe our modeling approach and extend our previous published theoretical work by accounting simultaneously for anode CO poisoning and cathode carbon catalyst-support corrosion. We also present simulation results. In this part, the modeling description is only focused on the CO-related phenomena as the other mechanisms taken into account are the same as in [19]. Secondly, we describe the experimental protocols used and discuss the results on the basis of the mechanistic insights provided by the model. Finally, we conclude and indicate further directions in order to complement our theoretical/experimental investigation.

2. Modeling

2.1. Global model description

The model discussed in this paper extends our previously published work on PEFC carbon catalyst-support degradation modeling [19]. As operation with and without CO is independent of the humidification conditions, we consider the case of an isothermal fuel cell fed with hydrogen and oxygen fully saturated with water vapor (Fig. 2) and we assume that the membrane and electrodes

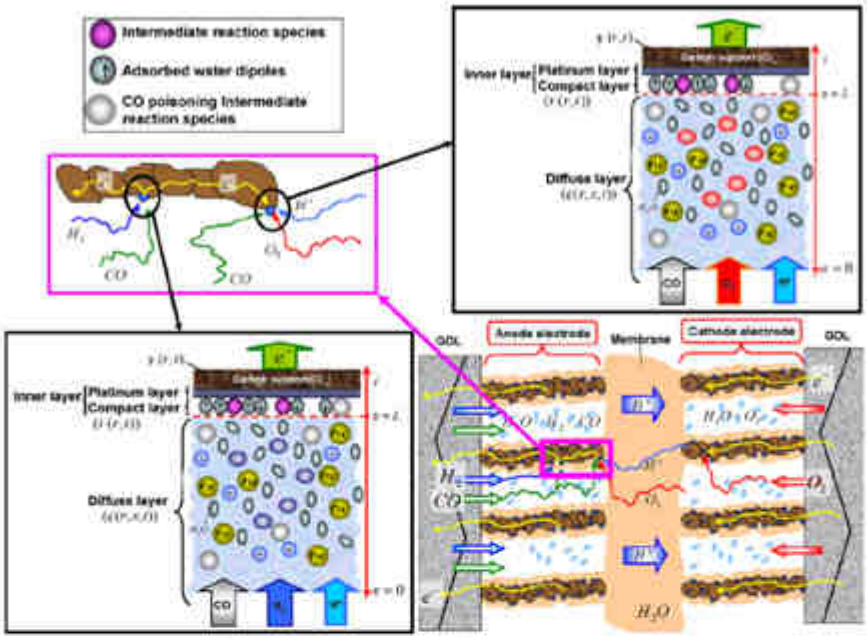

Fig. 2. Our multiscale mechanistic model of PEFC cathode degradation in the presence of CO in the anode (anodic nanoscale models are detailed; for the cathodic nanoscale models refer to [19]).

are already fully humidified at the simulated operation time $t = 0$ s (PEFC starting operation time). It must be noted that these conditions allow reasonable calculation times with relevant qualitative results. In particular, it is not necessary to take into account the transient pore phase flooding by liquid water in the electrode [35]: in fact, the chemical potential of water is the same in the pore and ionomer phases, inducing equilibrium conditions and thus no transients. The additional water production in the cathode is assumed to be evacuated through the liquid phase with zero thermodynamic resistance (no chemical potential gradient). These comments are extensible to the water description in the GDL. As we consider pure feeding gases (no nitrogen), hydrogen and oxygen pressure drops in the pore phases are neglected. The CO_2 produced in the cell is assumed to add negligible pressure (there is no accumulation of CO_2 in the anode or in the cathode; CO_2 diffuses through the GDL and is evacuated by the channels).

As in our PEFC carbon corrosion model in [19], oxygen crossover transients are not taken into account. In the simulations discussed in this paper, cathode carbon catalyst-support corrosion (and the induced Pt nanoparticles coarsening and detachment) is assumed to be the main aging mechanism inducing PEFC performance degradation. The anodic carbon oxidation and the oxidation/dissolution/electrochemical ripening of Pt nanoparticles (described in our previous papers [19,32,33]) are not considered here (full couplings with these mechanisms are now being implemented in our group and are published elsewhere [36]).

Our global model mathematical organization is presented in Fig. 3. The model consists of four interacting parts: the anode region operating with hydrogen and CO (called anode "1"), the anode region exposed to crossover oxygen and CO (anode "2"), the cathode Pt/ionomer interface (cathode "1") and the cathode C/ionomer interface (cathode "2"). The pair anode "1"/cathode "1" constitutes the direct fuel cell, and the pair anode "2"/cathode "2" constitutes the reverse fuel cell. The explanation of why this separation in four interacting parts is justified has been already reported by us in [19]. Local catalyst regions where both H_2 and O_2 coexist, producing $OH^\bullet$ and $OOH^\bullet$ radicals attacking the membrane, are not described in this model.

In cathode "1", only the ORR is assumed to occur, while in cathode "2" the COR is the only electrochemical reaction taking place. These two electrode models interact, e.g., through the description

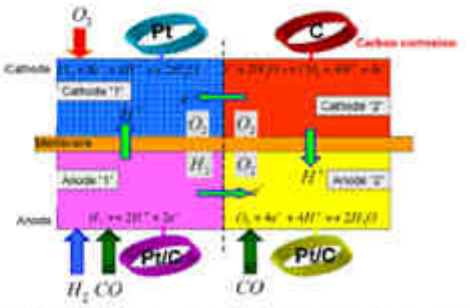

Fig. 3. Our model mathematical organization taking into account the presence of CO in the anode (local "face to face" MEA cut view).

of the Pt coarsening in cathode "1" driven by the carbon degradation occurring in cathode "2" (cf. Fig. 1b and [19–21]).

In the anode, we account for two different sets of electrochemical reactions: the HOR coupled to the CO adsorption/electrooxidation on pure Pt and the ORR coupled to the CO adsorption/electrooxidation on pure Pt. As shown in Fig. 3, electrons produced by the COR (reverse current $\bar{i}$) in cathode "2", are consumed by the ORR in cathode "1"; the protons produced are consumed by the ORR occurring in anode "2" (this favors the COR in cathode "2"). The total current flowing into the cathodic platinum phase is the sum of the external load current and the C corrosion-related reverse current. As in [19], the cathodic electrostatic potential ψ_C is assumed to be the same for the platinum and carbon phases (i.e., the same for both cathodes). The anodic electrostatic potential ψ_A is also assumed to be the same for the two anodes (excellent electronic conductivity is assumed between the two anode regions).

The multiscale character of our approach is illustrated in Fig. 2. The model couples:

- Spatially distributed nanoscale dynamic models describing the detailed electrochemical processes, including transient double layer effects, in the Pt-electrolyte interface (anode "1", anode "2" and cathode "1") and C–electrolyte interface (cathode "2") (a non-equilibrium thermodynamics approach supported on first-principles based elementary electrokinetic pathways [19,35,36]).
- A description of microscale transport phenomena of protons through the MEA [19].
- Spatially distributed microscale models of the reactant diffusion through the on-catalyst impregnated hydrated-Nafion® layer in the electrodes (H_2, CO and O_2 in the anode, O_2 in the cathode) (anode H_2 and cathode O_2 diffusion equations are the same as in [19] and are not recalled here).
- A 1-D steady-state description of the O_2 crossover through the membrane.

As in our previous papers, we note r, the microscale coordinate in the thickness of the electrodes and z, the microscale coordinate for reactant diffusion in the thickness of the impregnated hydrated-Nafion® layer. The interfacial nanoscale model is located at the micro-scale point $z = \eta_{ltr}$ [19], and the nanoscale coordinate inside the diffuse layer is noted by x (Fig. 2). The Pt–electrolyte and C–electrolyte interfaces are assumed to be flat and located at $x = L$ [19]. Only the nanoscale models corresponding to anode "1" and anode "2" are shown in Fig. 2: the nanoscale models of cathode "1" and cathode "2" are the same as in [19] and are not recalled here.

2.2. Anode submodel description

Despite the fact that the electrooxidation mechanism of CO and hydrogen in the PEFC anode appears to be agreed upon and well known, the adsorption of CO on Pt reveals to be very complex, especially at the low temperatures typically encountered in a PEFC where it is a function of both potential and CO concentration [37]. It is accepted that CO oxidation and adsorption occur on the (1 0 0) and (1 1 0) sites of Pt catalysts in an acid electrolyte. According to Dhar et al. [38], the adsorption of CO in an H_2 environment involves CO linearly bonded to Pt, and seems to obey Temkin's isotherm as the CO coverage appears to be a function of the anode potential as well as concentration in addition to the temperature and catalyst structure. Furthermore, Dhar et al. show that through the adsorbed CO–CO interaction parameter, the adsorption isotherm is strongly dependent on the surface conditions of the Pt surface: this creates a difficulty in broadly applying experimental or theoretical results.

Some experiments indicate that CO oxidation occurs on Pt(1 1 1) at approximately 0.6 V/NHE with a peak at 0.8 V/NHE [39,40]. Rotating disk electrode experiments, in which CO is replenished on the Pt surface, increase the potential at which CO is oxidized to 0.9 V/NHE [41]. *In situ* FTIR [42,43] as well as nuclear magnetic resonance spectroscopy experiments [44] show multiple binding sites for CO on Pt (linear CO_{ads_L}, bridged CO_{ads_B} and reduced CHO_{ads}), with the relative occupancy of the sites dependent on both the coverage and the electrode potential. Different oxidation behaviors are observed for different populations of the three CO_{ads} species, suggesting that different oxidation reaction pathways are associated with the different CO_{ads} states on the Pt catalyst, but the details are still not entirely clear. In order to provide insights to the elementary mechanisms behind the CO catalyst contamination process, *ab initio* electronic structure calculations have been largely used for Pt and binary alloy catalysts [45]. Atomistic models describing adsorption and electrooxidation of CO, including the effects of nanocatalyst composition and morphology (terraces, clusters, pseudomorphic layers, skinned metals, ...) are now available [46,47]. However, atomistic studies usually neglect the impact of the hydrogen chemisorption and oxidation on the CO mechanisms. Application of atomistic-resolved methods for modeling the electrochemical processes in a PEFC-like environment remains a major challenge: description of the coupling between chemistry and the electric field at the atomic scale is not an easy task. Some tentative steps in this direction have already been reported [45], but under unrealistic (zero absolute temperature) or very restricted (low Butler–Volmer overpotential, or a system close to equilibrium) PEFC operating conditions. Furthermore, there are still unresolved issues with *ab initio* methods, such as the geometry of the adsorbed species, the correct assignments of different vibrational modes of the adsorbed molecules on the surface, and multiple adsorbate lateral interactions.

The focus in this paper is placed on appraising synergies between anode CO contamination and cathode C corrosion, which can be achieved in a qualitative sense. Thus, in our nanoscale compact layer model in anode "1", we couple our multi-step HOR mechanistic description in [19] with simple Springer et al.'s mechanism [48] describing the CO poisoning of the catalyst (*CO Adsorption Reaction*) and its electrooxidation (*CO ElectroOxidation Reaction*) through two elementary steps:

$$CO + s \rightarrow COs \quad (COAR_1) \tag{1}$$

$$COs + H_2O \rightarrow CO_2 + 2H^+ + 2e^- + s \quad (COEOR_1) \tag{2}$$

Thus, we have, for the coverage at the compact layer level:

$$\theta_s + \theta_H + \theta_{CO} + \vec{\theta} + \overleftarrow{\theta} = 1 \tag{3}$$

where θ_s represents the free site coverage, θ_H and θ_{CO} are the on-top Pt surface coverage by adsorbed H and adsorbed CO, and $\vec{\theta}$ (respectively $\overleftarrow{\theta}$) are the covering fractions of water dipoles oriented towards the catalyst (respectively opposed). The reaction rates associated with the elementary steps (1) and (2) are written as:

$$v_{COAR_1} = k_{COAR_1}\theta_S C_{CO}(L,t)e^{-\omega\theta_{CO}/RT} \tag{4}$$

$$v_{COEOR_1} = k_{COEOR_1}\theta_{COS}\theta_{H_2O}e^{2(1-\alpha)F\eta_{Anode-1}(t)} \tag{5}$$

where ω is the adsorbed CO–CO molecule interaction parameter (the total activation energy is assumed to be corrected by a CO surface coverage dependent linear relation [18]), $C_{CO}(L,t)$ is the CO concentration at the interface $x = L$ calculated by a transport equation through the microscale impregnated hydrated ionomer layer (see the following), θ_{H_2O} is the water activity in the Nafion® electrolyte, $\eta_{Anode-1}(t)$ is the interfacial electrostatic potential drop through the anode "1" compact layer introduced in our previous

papers for pure platinum [19,34,35], $\eta_{Anode\text{-}1}(t)$ is given by:

$$\eta_{Anode\text{-}1}(t) = \psi_{Anode\text{-}1}(t) - \phi_{Anode\text{-}1}(x = L, t) = -\frac{\sigma_{Anode\text{-}1}(t)d}{\varepsilon_{CL}} - \frac{\alpha n^{max}\theta_{Pt}(t)\theta_{H_2O,l}\sinh[X(t)]}{\sigma_{CL}} \quad (6)$$

where $\psi_{Anode\text{-}1}(t)$ is the electrostatic potential in the anode "1" catalyst phase and $\phi_{Anode\text{-}1}(L,t)$ is the electrostatic potential in the anode "1" hydrated Nafion® phase, which is just outside the adsorbates layer on the catalyst with charge surface density $\sigma_{Anode\text{-}1}(t)$. $X(t)$ in Eq. (6) is given by the solution of the transcendental equation:

$$\frac{\alpha\sinh[X(t)]}{(1/\theta_{H_2O}) + ((\theta_H + \theta_{CO})/\theta_*)(1/\theta_{H_2O}) + \alpha\cosh[X(t)]} = \frac{d^2}{\varepsilon_{CL}A_{ll}}\sigma_{Anode\text{-}1}(t) - \frac{k_B T d^2}{A_{ll} F^2}X(t) \quad (7)$$

where the different parameters are defined in [19,35]. θ_* is given by:

$$\theta_* = \frac{1 - \theta_H - \theta_{CO}}{1 + \theta_{H_2O}\alpha\cosh[X(t)]} \quad (8)$$

where the calculation of θ_H is given in [19] and where θ_{CO} is given by the solution of the balance equation:

$$\frac{n^{max}}{N_A}\frac{d\theta_{CO}}{dt} = r_{COAR_1} - r_{COOR_1} \quad (9)$$

The charge surface density $\sigma_{Anode\text{-}1}(t)$ is related to the Faradaic current

$$j_{Far}^{Anode\text{-}1}(t) = F\left(r_{HET} + r_{VOL} + 2r_{COOR_1}\right) \quad (10)$$

(definitions of r_{HET} and r_{VOL} are detailed in [19]) through the charge conservation law

$$-\frac{d\sigma_{Anode\text{-}1}(t)}{dt} = \frac{j_{total}(t)}{\gamma_{Pt}^{Anode\text{-}1}} + j_{Far}^{Anode\text{-}1}(t) \quad (11)$$

$j_{total}(t)$ is given by:

$$j_{ext}(t) + \bar{j}(t) = j_{Total}(t) \quad (12)$$

where $j_{ext}(t)$ is the external load current (the input of the model), and $\bar{j}(t)$ is the reverse current produced by the cathode carbon oxidation reaction (see [19] for details).

$\gamma_{Pt}^{Anode\text{-}1}$ is the anode "1" catalyst surface area given by:

$$\gamma_{Pt}^{Anode\text{-}1} = \gamma_{Pt}^{Anode} - \gamma_{Pt}^{Anode\text{-}2} \quad (13)$$

where the platinum surface area exposed to oxygen $\gamma_{Pt}^{Anode\text{-}2}$ is assumed, for simplicity, to be constant[1] (the assumed values of γ_{Pt}^{Anode} and $\gamma_{Pt}^{Anode\text{-}2}$ for the results shown in this paper are the same as in [19]).

In the nanoscale compact layer model in anode "2", we couple a multi-step ORR mechanistic description [19,49] with the CO adsorption and the surface reaction between CO and O species (*CO Oxidation Reaction*). Furthermore, on the basis of experimental PEFC tests, it has been suggested that the oxygen permeating across the membrane from the cathode side can also appreciably affect the anode Butler–Volmer potential by providing another route for CO oxidation [6]. One explanation proposed for this is that CO is oxidized by O_2 via a non-electrochemical Pt surface redox mechanism, for instance:

$$O_2 + 2Pt \rightarrow 2(Pt\text{–}O) \quad (14)$$

[1] A detailed O_2 crossover transport model can be used here to calculate $\gamma_{Pt}^{Anode\text{-}2}$ in a transient way capturing the fact that the fuel starvation conditions are favored at high currents.

Table 1
Parameter values used in the numerical simulations (the parameters not indicated have the same values as in [19]).

	Geometrical or physicochemical parameter value	Unit	Reference
Anode "1"	$\gamma_{Pt}^{Anode} = 0.020$ $i_{0_{ref}}^{Anode} = 10^{-9}$	m^2 $m^2\,s^{-1}$	Estimated and [19] This work
	$n_2 = 0.5$ $\alpha = 20,870$ $k_{COR_1} = 1$	dimensionless $J\,mol^{-1}$ $m\,s^{-1}$	[37] [37] Fitted from ex situ FTIR experiments [58]
	$k_{COOR_1} = 10^{-8}$	$mol\,m^2\,s^{-1}$	[37]
	$k_{OAR_1} = 10^{-10}$ $k_{COAR_1} = 10$	$m\,s^{-1}$	[37]
Anode "2"	$k_{COR_2} = 1$ $k_{-COR_2} = 0$	$mol\,m^2\,s^{-1}$	Fitted from ex situ FTIR experiments [58]
	$k_{COOR_2} = 10^{-8}$ $k_{COOR_2} = 10^{-4}$		
	$\sigma_{dl}^{Anode} = 1.21$	ng	This work

$$(Pt\text{–}O) + (Pt\text{–}CO) \rightarrow 2Pt + CO_2 \quad (15)$$

Another suggested pathway is that adsorbed O reacts first with adsorbed H to form adsorbed OH according to the following reaction [50]:

$$(Pt\text{–}O) + (Pt\text{–}H) \rightarrow (Pt\text{–}OH) + Pt \quad (16)$$

which further reacts electrochemically with surface CO through the reaction:

$$(Pt\text{–}OH) + (Pt\text{–}CO) \rightarrow 2Pt + CO_2 + H^+ + e^- \quad (17)$$

In contrast to this, in our model we have

$$O_2 + H^+ + e^- + s \rightarrow O_2Hs \quad (ORR_1) \quad (18)$$

$$O_2Hs + H_2O + 2s \rightarrow 3OHs \quad (ORR_2) \quad (19)$$

$$OHs + H^+ + e^- \rightarrow H_2O + s \quad (ORR_3) \quad (20)$$

$$O_2 + 2s \rightarrow 2Os \quad (OAR_1) \quad (21)$$

$$CO + s \rightarrow COs \quad (COAR_2) \quad (22)$$

$$Os + COs \rightarrow CO_2 + 2s \quad (COOR_1) \quad (23)$$

Thus, for the coverage at the anode "2" compact layer level we have:

$$\theta_* + \theta_{O_2H} + \theta_{OH} + \theta_O + \theta_{CO} + \tilde{\theta} + \bar{\theta} = 1 \quad (24)$$

where θ_{O_2H}, θ_{OH} and θ_O are the on-top Pt surface coverage by adsorbed intermediates.

The reaction rates associated to the elementary steps (18)–(23) are written as:

$$r_{ORR_1} = k_{ORR_1}\theta_*(C_{H^+}(L,t)C_{O_2}(L,t)e^{-n_2\beta\eta_{Anode\text{-}2}(t)} - k_{-ORR_1}\theta_{O_2H}e^{(1-n_2)\beta\eta_{Anode\text{-}2}(t)} \quad (25)$$

$$r_{ORR_2} = k_{ORR_2}\theta_{O_2Hs}\theta_{H_2O}\theta_*^2 - k_{-ORR_2}\theta_{OHs}^2 \quad (26)$$

$$r_{ORR_3} = k_{ORR_3}\theta_{OHs}C_{H^+}(L,t)e^{-n_2\beta\eta_{Anode\text{-}2}(t)} - k_{-ORR_3}\theta_*\theta_{H_2O}e^{(1-n_2)\beta\eta_{Anode\text{-}2}(t)} \quad (27)$$

$$r_{OAR_1} = k_{OAR_1}\theta_*^2 C_{O_2}(L,t) - k_{-OAR_1}\theta_O^2 \quad (28)$$

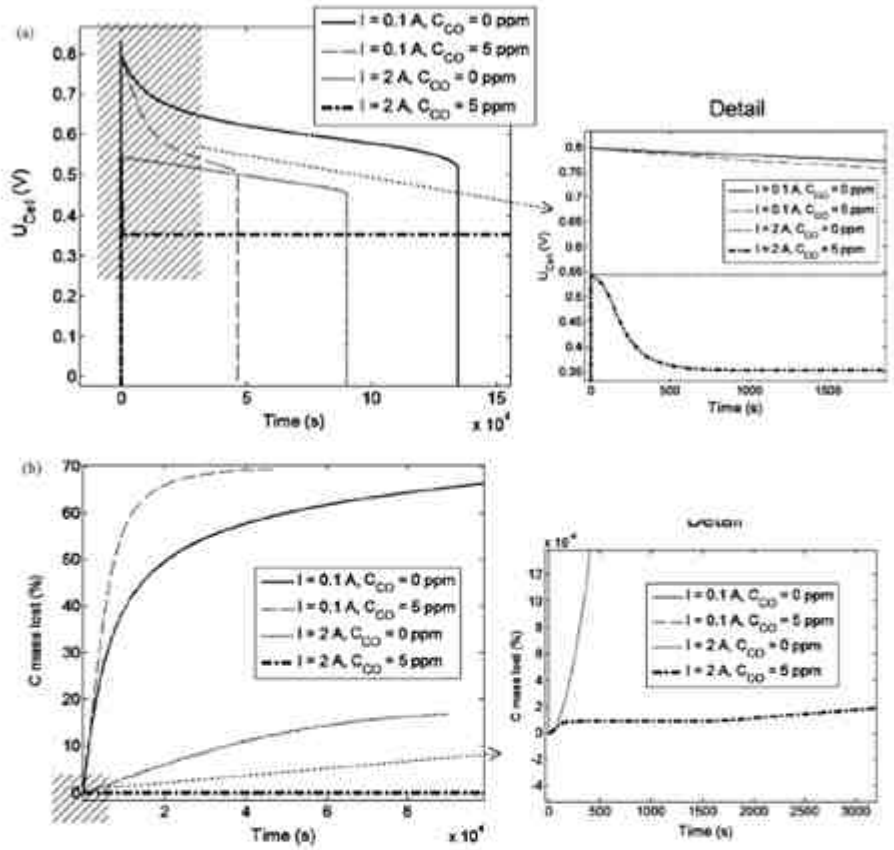

Fig. 4. (a) Simulated temporal evolution of the cell potential at two different currents and two different anodic CO concentrations. (b) Associated cumulative carbon mass loss.

$$r_{COAR_2} = k_{COAR_2}\theta_1 C_{CO}(\bar{L},t)\, e^{-\frac{\alpha F\eta}{RT}} \tag{29}$$

$$r_{COOR_1} = k_{COOR_1}\theta_O\theta_{CO} \tag{30}$$

$\eta_{Anode\text{-}2}(t)$ is calculated from an equation analogous to (6) with X given by:

$$\frac{\alpha \sinh[X(t)]}{(1/\Theta_{H_2O}) + (\theta_{O_2H} + \theta_{OH} + \theta_O + \theta_{CO}/\theta_S)(1/\Theta_{H_2O}) + \alpha\cosh[X(t)]} = \frac{d^2}{\varepsilon_{Cl}A_{\Delta L}}\sigma_{Anode\text{-}2}(t) - \frac{k_B T d^2}{A_{\Delta L}^2}X(t) \tag{31}$$

where θ_S and the intermediates coverage are given by the solution of:

$$\theta_S = \frac{1-\theta_{O_2H}-\theta_{OH}-\theta_O-\theta_{CO}}{1+\Theta_{H_2O}\cosh[X(t)]} \tag{32}$$

$$\frac{\eta^{max}}{N_A}\frac{d\theta_{O_2H}}{dt} = r_{OBR_1} - r_{OBR_2} \tag{33}$$

$$\frac{\eta^{max}}{N_A}\frac{d\theta_{OH}}{dt} = 3r_{OBR_2} - r_{OBR_1} \tag{34}$$

$$\frac{\eta^{max}}{N_A}\frac{d\theta_O}{dt} = 2r_{OAR_1} - r_{COOR_1} \tag{35}$$

$$\frac{\eta^{max}}{N_A}\frac{d\theta_{CO}}{dt} = r_{COAR_2} - r_{COOR_1} \tag{36}$$

The charge surface density $\sigma_{Anode\text{-}2}(t)$ is related to the Faradaic current:

$$j_{Fad}^{Anode\text{-}2}(t) = -F(r_{OBR_1} + r_{OBR_2}) \tag{37}$$

through the charge conservation law:

$$\frac{d\sigma_{Anode\text{-}2}(t)}{dt} = \frac{j_{total}(t)}{\gamma_{Pt}^{Anode\text{-}2}} + j_{Fad}^{Anode\text{-}2}(t) \tag{38}$$

Proton transfer and electrostatic potential behavior through the diffuse layer (polarization layer effects) in both anodes are accounted as detailed in [19].

At the microscale, the CO transport in the hydrated Nafion® phase in both anodes is described by a single-diffusion equation:

$$\frac{\partial C_{CO}}{\partial t} = -\nabla_z \cdot \vec{J}_{CO} = -\nabla_z \cdot (-D_{CO}\cdot\nabla_z C_{CO}) \tag{39}$$

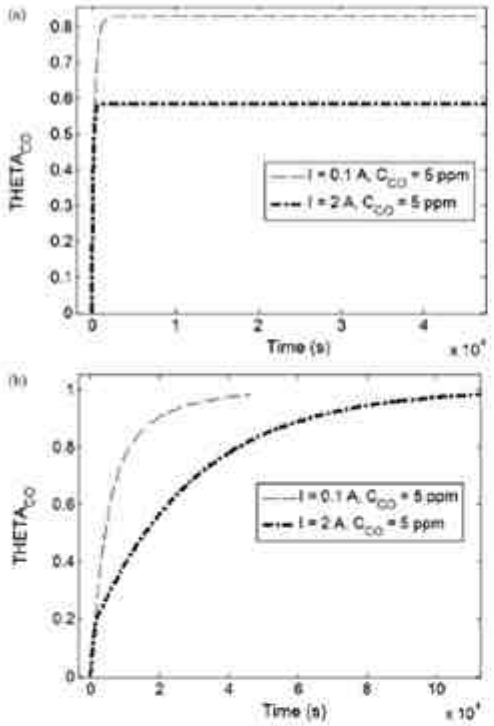

Fig. 5. (a) Simulated temporal evolution of the CO coverage in the anode "1" compact layer. (b) Simulated temporal evolution of the CO coverage in the anode "2" compact layer.

where we assume that the diffusion coefficient D_{CO} is constant. At $z=0$ the CO concentration is given by Henry's law of hydrogen adsorption with Nafion® behaving as liquid water [51]:

$$C_{CO}(x=0,t) = p_{CO} \times \left[9.5 \times 10^6 \times \exp\left(1300\left(\frac{1}{T}-\frac{1}{298}\right)\right)\right] \quad (40)$$

p_{CO} is the CO-gas partial pressure in the pore phase given by:

$$p_{CO} = 10^{-6} \chi_{CO} P_{Anode} \quad (41)$$

where χ_{CO} is the CO content (in ppm) of the H_2 feed stream. At the compact layer level (of both anode "1" and anode "2") ($x=L$ & $z=e_{pc}$), the boundary condition for Eq. (39) is:

$$j_{CO}(x=L,t) = -r_{COAR_1} - r_{COAR_2} \quad (42)$$

In contrast to [19] we assume here that the H_2 partial pressure in the pore phase is given by:

$$p_{H_2} = P_{Anode} - p_{sat} \quad (43)$$

thus, the anodic crossover O_2 is assumed to be always dissolved in the hydrated Nafion® phase. By assuming no accumulation of O_2 in the membrane and in the anode "2" Nafion®, the effective O_2 concentration at $x=L$ ($\equiv z=e_{pc}$) in anode "2" is calculated from:

$$C_{O_2}(x=L)^{Anode\text{-}2} = \Omega(I)\left[\frac{P_{Cathode}-p_{sat}}{H_{O_2}} - \frac{e_M}{D_{O_2}} j_{O_2}(x=L,t)\right] \quad (44)$$

where D_{O_2} is the oxygen diffusion through the hydrated Nafion®, $j_{O_2}(x=L,t)$ is the O_2 molar flux at $x=L$ related to the O_2 consumption kinetic rates:

$$j_{O_2}(x=L,t) = -(r_{OAR_1} - r_{OAR_2}) \quad (45)$$

and

$$\Omega(I) = \left[\frac{4}{4-I_{crit}}\right] \quad (46)$$

which is an empirical equation taking into account the fact that the fuel starvation conditions (O_2 concentration in anode "2") are favored at high currents.[2]

All simulation results presented in this paper are obtained by coupling the anode "1" and anode "2" models with the cathode "1", cathode "2" and membrane multiscale models detailed in [19,21] in the mathematical way which is described in those papers.

2.2. Numerical predictions

In Table 1 we indicate the main parameter values used in the model simulations shown in this paper. The other parameter values and the used simulation software are identical to our previous publications [19,21]. We recall that our modeling framework allows simulating the evolution of a large variety of state variables, such as the single anodic $\psi_A(t)$ and cathodic $\psi_C(t)$ potentials, the reverse current and the carbon mass loss [19].

In Fig. 4(a) we show the evolution of the cell potential ($U_{cell}(t) = \psi_C(t) - \psi_A(t)$) predicted by the model at fixed operating currents (I = 0.1 and 2 A) with and without 5 ppm of CO in the H_2 stream.

Fig. 4(b) represents the associated evolution of cumulative cathode carbon mass loss for a cell operating with and without 5 ppm of CO in the anode. In Fig. 5(a) and (b) we show the calculated transient response of the CO coverages at anodes "1" and "2".

In Fig. 4(a) we can observe that for high currents (I = 2 A), at short-term operation, the presence of CO strongly reduces the cell potential – increases the anode potential – (anode "1" poisoning predominates, cf. Fig. 5(a)), but the durability (long-term) appears to be improved compared to the situation without CO (the long-term cell potential evolution is dominated by the C corrosion-induced cathodic potential evolution, cf. Fig. 10 in [19]). The corresponding evolution of the cumulative cathode carbon mass loss clearly highlights the decrease of the cathodic carbon corrosion due to the reactivity of the crossover O_2 with the CO at the anode level. In contrast to this interesting behavior, at lower currents (I = 0.1 A), the operation with CO provides a lower durability than the operation without CO because the CO poisoning mechanism in both anodes predominates (Fig. 5).

3. Experimental

3.1. Experimental tools and protocols

In this part, we describe the MEA and the equipment used for the experimental tests, and we detail the applied current-cycled protocols.

3.1.1. MEA

In this study, we have used the standard MEA of our laboratory which have been extensively used and electrochemically characterized in previous studies [52,53]. The 25 cm² MEAs (CCM-type) were based on a Nafion® NRE212CS membrane (50 μm thickness)

[2] In order to account for the transient hydrogen starvation, here we can also use a fully mechanistic description of these phenomena.

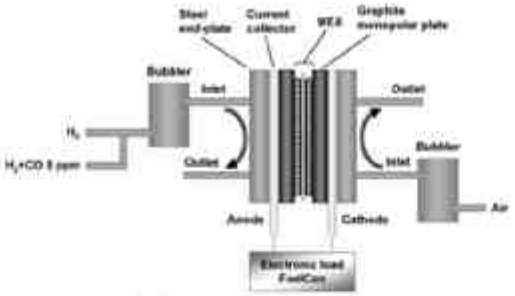

Fig. 6. Scheme of the MEA test management.

from DuPont. Anode and cathode catalyst layers, as well as carbon felt gas diffusion layers (H2315-T10A from Freudenberg), have been deposited on the membrane. The platinum catalyst loadings were 0.19 ± 0.01 and 0.25 ± 0.01 mg cm^{-2} on the anode and cathode sides, respectively (*Pt/C* powder from BASF). A Teflon®/carbon based microporous layer was deposited on the gas diffusion layers. The MEAs were hot pressed under 3.5×10^6 Pa, at 130 °C for 3.5 min. Gas tightness was ensured by using silicone gaskets from Silfox.

3.1.2. Single fuel cell and test station

The single fuel cell used for all experiments was made of steel end-plates, gilt copper current collectors and graphite monopolar plates. A classical design with one single gas channel was chosen for the monopolar plates.

All experiments were performed using an automatic test station from FuelCon (Fig. 6). The humidification of the fuel cell was ensured by bubblers with optimized sizing. All gas lines between the humidifiers and the fuel cell were overheated (typically 15 °C above the temperature of the bubblers) to avoid condensation. The current-cycling of the fuel cell was performed using an electronic load from FuelCon.

The test station was supplied by high purity gases from Air Products (H_2 and H_2 + CO 5 ppm). Specific filters ensured the high quality of the compressed air.

3.1.3. Test protocols

All experiments were performed under the same temperature and pressure conditions. The temperature of the cell was fixed at 70 °C, the pressures for the anode and cathode sides were 1.6×10^5 Pa, and the anode and cathode-relative humidities were 60%. Gases were supplied to the fuel cell in a counter-flow scheme.

The fuel cell was first conditioned under constant current (0.8 A cm^{-2}), with stoichiometries of 1.2 and 2 (anode and cathode, respectively), for 16 h with pure hydrogen and air. The conditioning phase was followed by the current cycle itself. The first 22 h of the current-cycle phase were always performed under pure hydrogen and air, before introducing CO. Two current-cycle protocols were applied in this work (Fig. 7):

Protocol 1 (called $0/i_{max}$): 30 min phase with current density set to 0 A cm^{-2}, followed by a 30 min phase with current density set to 0.54 A cm^{-2}.

Protocol 2 (called i_{min}/i_{max}): 30 min phase with current density set to 0.108 A cm^{-2}, followed by a 30 min phase with current density set to 0.54 A cm^{-2}.

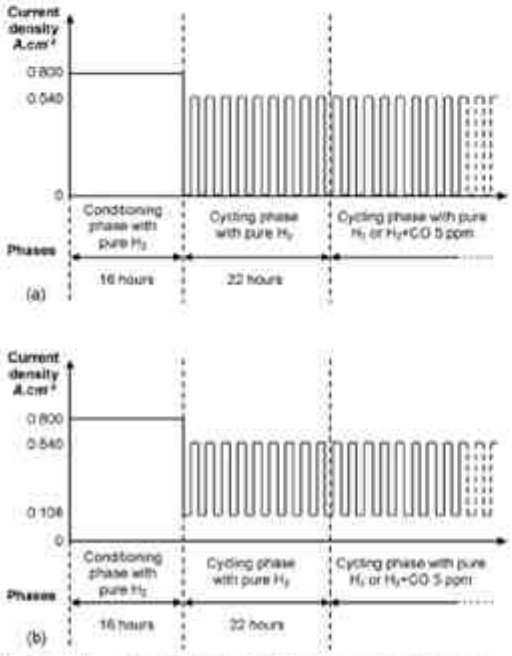

Fig. 7. (a) $0/i_{max}$ experimental protocol and (b) i_{min}/i_{max} experimental protocol.

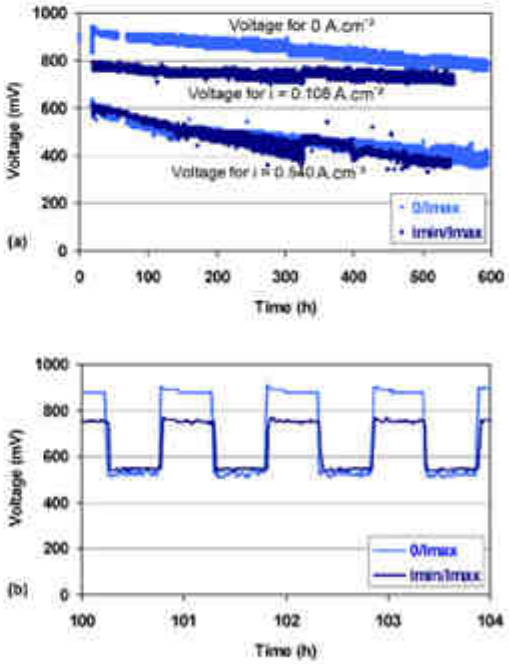

Fig. 8. (a) Performance degradation for $0/i_{max}$ and i_{min}/i_{max} current-cycle protocols under pure hydrogen. (b) Detail of voltage evolution for $0/i_{max}$ and i_{min}/i_{max} current-cycle protocols under pure hydrogen.

Table 2
Values of the voltage and degradation rates for $0/I_{max}$ and I_{min}/I_{max} protocols under pure H_2.

$0/I_{max}$				I_{min}/I_{max}			
Current density ($A\,cm^{-2}$)	Initial value voltage (mV)	Final value voltage (mV)	Degradation rate ($mV\,h^{-1}$)	Current density ($A\,cm^{-2}$)	Initial value voltage (mV)	Final value voltage (mV)	Degradation rate ($mV\,h^{-1}$)
0	880	780	0.17	0.108	700	720	0.13
0.540	620	300	0.40	0.540	610	360	0.46

The first current cycle is typically used as a simplified cycle to test the PEFC for transport applications [54] compared to complex cyclic current profile [55]. To increase the hydrogen starvation and its impact on cathodic carbon corrosion, we decided to modify only one parameter: the minimal current. This second current cycle corresponds to protocol 2. The flow rates were set automatically according to the current densities and to the stoichiometries (1.2 for the anode and 2 for the cathode). For the current density $0\,A\,cm^{-2}$ (in protocol 1), the flow rates were fixed to the same value as for $0.108\,A\,cm^{-2}$ (in protocol 2). For comparison, both current-cycle protocols were also performed under pure hydrogen.

Voltage–current polarization curves were measured to compare performance before and after the I_{min}/I_{max} current-cycle protocol under pure H_2 and H_2 + CO 5 ppm. These polarization curves were acquired by sweeping current densities with steps of $0.02\,A\,cm^{-2}$ for 30 s.

4. Results and discussion

In this subsection, we describe the experimental results of PEFC degradation under pure H_2 and H_2 + CO. Interpretation of some of these results is based on the previously discussed modeling results.

4.1. Degradation under pure H_2

The degradation of the PEFC performance under the two current-cycle protocols without CO is shown in Fig. 8(a). For the I_{min}/I_{max} protocol, a break can be observed at 325 h which is due to an interruption of the test station. Nevertheless, the performance decrease is linear and this allows the measurement of a degradation rate, which remains constant for the duration of the experiment. Table 2 gives, for each protocol, the values of the initial and final voltages and the degradation rates for the two current densities. An example of the voltage evolution is shown in Fig. 8(b) between 100 and 104 h. The voltage response is fairly constant for a given current density. The general behaviors are the same for the two protocols, which indicates, in a first approximation, similar degradation mechanisms.

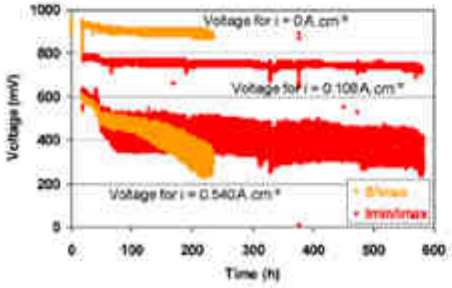

Fig. 8. Performance degradation for $0/I_{max}$ and I_{min}/I_{max} current-cycle protocols under H_2 + CO.

4.2. Degradation under H_2 + CO

The degradation of the PEFC performance under H_2 + CO 5 ppm is shown in Fig. 9. For the two protocols, in the presence of CO, we can observe that the performance degradation depends strongly on

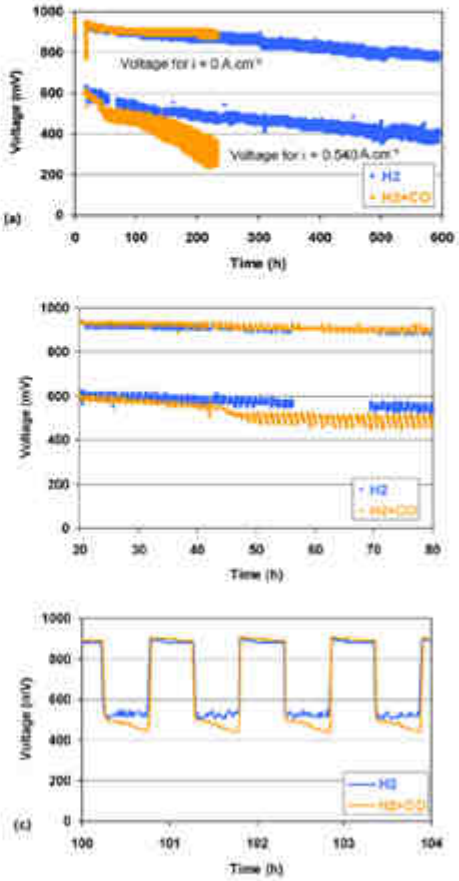

Fig. 10. (a) Performance degradation for $0/I_{max}$ current-cycle protocol under pure hydrogen and H_2 + CO 5 ppm. (b) Impact of the introduction of CO on the performance for $0/I_{max}$ current-cycle protocol. (c) Detail of the voltage evolution for $0/I_{max}$ current-cycle protocol under pure H_2 and H_2 + CO.

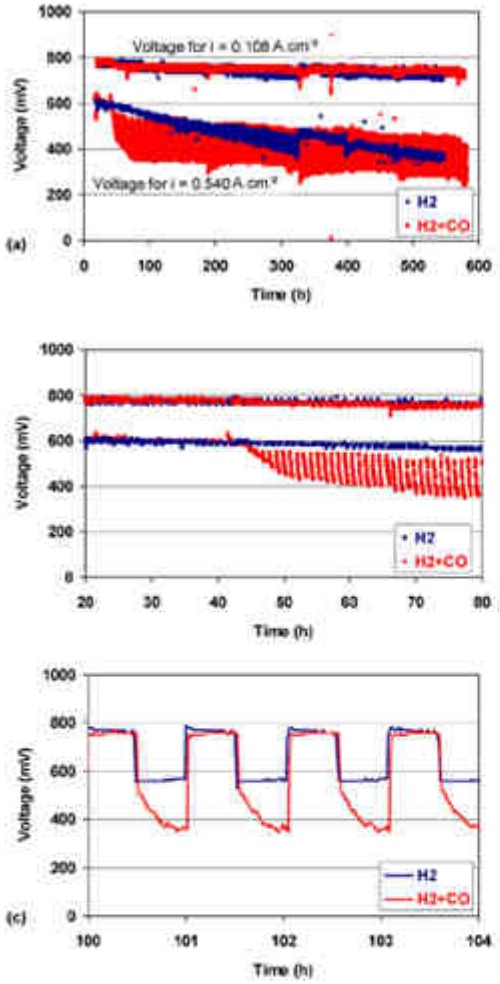

Fig. 11. (a) Performance degradation for I_{min}/I_{max} current-cycle protocol under pure hydrogen and H_2 + CO. (b) Impact of the introduction of CO on performance for I_{min}/I_{max} current-cycle protocol. (c) Detail of the voltage evolution for I_{min}/I_{max} current-cycle protocol under pure H_2 and H_2 + CO.

the characteristics of the current-cycle protocol, which was not the case under pure H_2 (Fig. 8(a)).

4.2.1. With $0/I_{max}$ protocol

The degradation of the PEFC performance under the $0/I_{max}$ current-cycle protocol with and without CO is shown in Fig. 10. In the presence of CO, the performances of the fuel cell decreases rapidly and continuously. The voltage decrease is mainly due to the contamination of the Pt catalyst, as has been described in the literature [6–9]. Fig. 10(b) provides the impact to the voltage of the introduction of CO. The mean voltage at I_{max} drops rapidly by about 70 mV. The voltage at $I = 0\ A\,cm^{-2}$ is not impacted. The details of the voltage evolution are shown in Fig. 10(c). The slight voltage decrease for $I = 0\ A\,cm^{-2}$ is equivalent under pure and polluted hydrogen. In contrast, for $I = 0.54\ A\,cm^{-2}$, the voltage remains constant under pure hydrogen, and decreases under H_2 + CO. This variation explains the amplitude of the voltage curve for I_{max} with CO in Fig. 10(a).

4.2.2. With I_{min}/I_{max} protocol

Fig. 11(a) shows the degradation of the PEFC performance under the I_{min}/I_{max} current-cycle protocol with and without CO. As was observed for the $0/I_{max}$ protocol, the performance is clearly impacted by CO contamination. With CO, the mean voltage drops in 550 h from 470 to 340 mV. During the pollution phase, it can be observed that the degradation rate (0.24 mV h^{-1}) under H_2 + CO 5 ppm is lower than the degradation rate under pure hydrogen (0.45 mV h^{-1}). After about 500 h, mean voltage values are the same and we can observe a crossing. In other words, experimental results under I_{min}/I_{max} current-cycled operating conditions show that the CO anode contamination produces a strong short-term performance degradation, but it slows down the long-term performance degradation, confirming the modeling prediction discussed in Section 2.

We can also see in Fig. 12 that the performance of the MEA with CO is equivalent to the performance without CO at the end of the experiment. Again, at the time of the introduction of CO (Fig. 11(b)), the mean voltage at I_{max} drops in a few hours by about 100 mV, while the voltage at I_{min} does not vary. Details of the voltage are shown in Fig. 11(c). It can be observed that the evolution of voltage is completely different at $I = 0.108\ A\,cm^{-2}$ and $I = 0.54\ A\,cm^{-2}$. In particular, at I_{max} under H_2 + CO, the voltage decreases strongly during each 30 min step.

Fig. 13 shows the simulated cell potential evolution under an I_{min}/I_{max} cycled-current operation, for the conditions described in Section 2. These calculations show similar behavior as in experimental results. At short-time scales, in the absence of CO, the cell potential appears to be roughly constant during the $I = I_{max}$ phases, while in the presence of CO the cell potential decreases very quickly with time. This short-time scale potential decrease is explained through the gradual anodic potential increase as a consequence of the CO adsorption kinetics. This kind of behavior overlaps the long-time scale potential degradation. In the absence of CO at short-time scales, the cell potential is recovered very rapidly during $I_{min} \rightarrow I_{max}$ and $I_{max} \rightarrow I_{min}$ current transitions (in this case, cell potential degradation is only significant at long-time scales).

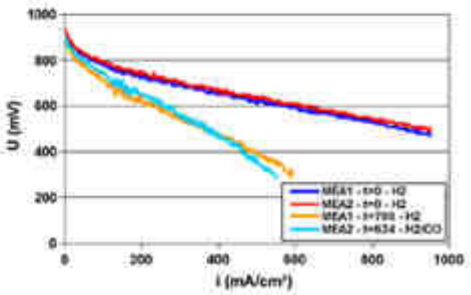

Fig. 12. Polarization curves before and after I_{min}/I_{max} current cycle, under pure H_2 and H_2 + CO.

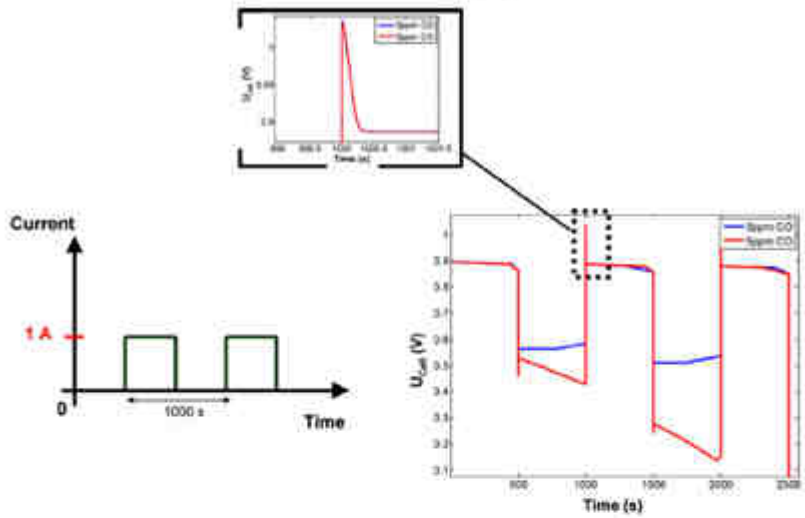

Fig. 13. Simulated cell potential response under current-cycled conditions with an H_2 + CO anode.

5. Conclusions

On the basis of a combined theoretical and experimental approach, we have investigated the impact of the injection of CO in the anode feed stream of a PEFC on the MEA long-term (at least 600 h) performance degradation, under current-cycled operation representative of transport application conditions.

First of all, on the basis of our previously published multi-scale mechanistic models describing the feedback between the instantaneous PEFC performance and its materials degradation, we proposed a mechanism describing the transient behavior of a PEFC MEA in the presence of CO at the anode, and accounting at the same time for the carbon catalyst-support corrosion phenomena in the cathode. Numerical simulations suggest that under specific operating conditions, CO injection in the anode feed stream could be used to mitigate carbon catalyst-support corrosion of the cathode electrode under current-cycled operating conditions. This interesting feature is here explained by the anodic reactivity between the CO and the membrane crossover O_2, the last one being the "driving force" of the cathode → anode proton pumping effect believed to be the mechanism responsible for the cathode carbon catalyst-support corrosion.

In parallel, experiments have been carried out showing results in qualitative agreement with theoretical behaviors, and demonstrating that the CO effect on the cell potential degradation is strongly dependent on the current-cycle mode. In particular, we discuss the impact of two endurance tests on the PEFC performance degradation, under both pure H_2 (and air in the cathode side) and H_2 + 5 ppm CO (and air in the cathode side):

30 min phase with the current density set to 0 A cm^{-2}, followed by a 30 min phase with the current density set to 0.54 A cm^{-2} (protocol $0/i_{max}$).
30 min phase with the current density set to 0.108 A cm^{-2}, followed by a 30 min phase with the current density set to 0.54 A cm^{-2} (protocol i_{min}/i_{max}).

The short- and long-term degradation of the PEFC performance under the $0/i_{max}$ protocol is stronger under H_2 + CO than under pure H_2 operation. In these conditions, the anode Pt-catalyst CO contamination is the main mechanism contributing to the performance degradation. In contrast, the long-term degradation of the PEFC performance under the i_{min}/i_{max} protocol is lower under H_2 + CO compared to pure H_2 operation: i_{min}/i_{max} protocols are expected to induce more fuel starvation than $0/i_{max}$ protocols and thus a more significant cumulative anodic O_2 concentration which can react with CO. This synergy between O_2 and CO reduces both the CO poisoning on the anode side and the O_2-driven proton pumping effect responsible for the cathodic carbon catalyst-support corrosion: we have recently filed a patent describing this carbon corrosion mitigation method which constitutes in our opinion an interesting example on the use of modeling as a tool for proposing technical innovations in engineering practice [56]. Furthermore, it can be noted that the anodic CO injection can also reduce PEM chemical attack induced by the $OOH^{\bullet}$ and $OH^{\bullet}$ radicals formed by coexistence of H_2 and O_2 on some anodic Pt sites, as explained by us elsewhere [57].

To complete these results, it is interesting to perform microstructural (e.g., SEM, HR-TEM) and chemical (e.g., XPS) characterizations on fresh and aged MEAs (with and without CO) in order to provide deeper insights on these behaviors: our first results by using these techniques are published elsewhere [58].

From a more technological perspective, in order to minimize the impact of the presence of CO in H_2 on PEFC performance under i_{min}/i_{max} cycle operation, the use of CO-tolerant catalysts (e.g., Pt-Ru, Pt-Sn, ...) on the anode side could be envisaged.

On the basis of these interesting results, this work could be extended to more complex current cycles, representative of different PEFC applications. In particular, we have shown that, even if in the short-term, CO strongly impacts the performance, it can improve the long-term durability of the PEFC. This could allow the use of a less purified and thus cheaper H_2 feed in the PEFC.

Acknowledgments

This work was funded by the French Research Agency (ANR) through the program PAN-H and within the context of the POLIMPAC project. We also thank Margaret A. Gabriel (CEA-Grenoble) for her English assistance during the preparation of this paper.

References

[1] T. Nejat Veziroglu, F. Barbir, Emerging Technologies Series, UNIDO, Vienna, 1998.
[2] D. Dalle Nogare, P. Baggio, C. Tomasi, L. Mutri, P. Canu, Chem. Eng. Sci. 62 (2007) 5418.
[3] H.A. Stewart, J.L. Heck, Chem. Ing. Progress 65 (1969) 78.
[4] T. Saitou, K. Sugiyama, J. Alloys Compd. 231 (1995) 865.
[5] X. Cheng, Z. Shi, N. Glass, L. Zhang, J. Zhang, D. Song, Z.-S. Liu, H. Wang, J. Shen, J. Power Sources 165 (2007) 739.
[6] J. Zhang, T. Thampan, R. Datta, J. Electrochem. Soc. 149 (2002) A765.
[7] J. Divisek, H.-F. Oetjen, V. Peinecke, V.M. Schmidt, U. Stimming, Electrochim. Acta 43 (1998) 3811.
[8] S.J. Lee, S. Mukerjee, E.A. Ticianelli, J. Mc Breen, Electrochim. Acta 44 (1999) 3283.
[9] K. Narusawa, M. Hayashida, Y. Kamiya, H. Roppongi, D. Kurashima, K. Wakabayashi, JSAE Rev. 24 (2003) 41.
[10] S. Gottesfeld, J. Pafford, J. Electrochem. Soc. 135 (1988) 2651.
[11] J.W. Bauman, T.A. Zawodzinski Jr., S. Gottesfeld, in: S. Gottesfeld, T.F. Fuller (Eds.), Proton Conducting Membrane Fuel Cells II, PV 98-27, The Electrochemical Society Proceedings Series, Pennington, NJ, 1997, p. 136.
[12] C.-C. Chen, C.-C. Chung, H.-H. Lin, Y.-Y. Yan, J. Fuel Cell Sci. Tech. 5 (2008) 014501.
[13] F.A. Uribe, J.A. Valerio, F.H. Garzon, T.A. Zawodzinski, Electrochem. Solid-State Lett. 7 (2004) A376.
[14] B. Du, R. Pollard, J.F. Elter, 210th ECS Meeting, Abstract #644, 2006.
[15] A.A. Shah, P.C. Sui, G.-S. Kim, S. Ye, J. Power Sources 166 (2007) 1.
[16] G. Karimi, X. Li, J. Power Sources 159 (2006) 943.
[17] N. Zamel, X. Li, Int. J. Hydrogen Energy 33 (2008) 1335.
[18] J.J. Baschuk, X. Li, Int. J. Hydrogen Energy 27 (2003) 1095.
[19] A.A. Franco, M. Gerard, J. Electrochem. Soc. 155 (2008) B367.
[20] A.A. Franco, M. Gerard, 213th ECS Meeting 801, 2008, p. 1160.
[21] A.A. Franco, M. Gerard, M. Guinard, B. Barthe, O. Lemaire, ECS Trans. 3 (15) (2008) 35.
[22] C.A. Reiser, L. Bregoli, T.W. Patterson, J.S. Yi, D. Yang, M.L. Perry, T.D. Jarvi, Electrochem. Solid-State Lett. 8 (2005) A273.
[23] Y. Shao, G. Yin, Y. Gao, J. Power Sources 171 (2007) 558.
[24] X. Yu, S. Ye, J. Power Sources 172 (2007) 145.
[25] C. Grolleau, C. Coutanceau, F. Pierre, J.M. Leger, Electrochim. Acta 53 (2008) 7157.
[26] H. Tang, Z. Qi, M. Ramani, J.F. Elter, J. Power Sources 158 (2006) 1306.
[27] Y. Fujii, S. Tsushima, K. Teranishi, K. Kawata, T. Nanjo, S. Hirai, ECS Trans. 3 (2006) 735.
[28] T.F. Fuller, G. Gray, ECS Trans. 1 (2006) 345.
[29] R.M. Darling, D. Jayne, ECS Trans. 11 (2007) 975.
[30] W.R. Baumgartner, E. Wallnöfer, T. Schaffer, J.O. Besenhard, V. Hacker, V. Peinecke, P. Prenninger, ECS Trans. 3 (2006) 811.
[31] S. Maass, F. Finsterwalder, G. Frank, R. Hartmann, C. Merten, J. Power Sources 176 (2008) 444.
[32] A.A. Franco, M. Tembely, J. Electrochem. Soc. 154 (2007) B712.
[33] A.A. Franco, ECS Trans. 6 (2007) 1.
[34] A.A. Franco, P. Schott, C. Jallut, B. Maschke, J. Electrochem. Soc. 153 (2006) A1053.
[35] A.A. Franco, P. Schott, C. Jallut, B. Maschke, From Fundamentals to Systems, Fuel Cells 7 (2007) 99.
[36] A.A. Franco, R. Ferreira de Morais, S.-K. Cheah, Abstract in 215th Meeting of the Electrochemical Society, San Francisco, May 24–29, 2009.
[37] J.J. Baschuk, X. Li, Int. J. Energy Res. 25 (2001) 695.
[38] H.P. Dhar, L.G. Christner, A.K. Kush, J. Electrochem. Soc. 134 (1987) 3021.
[39] Z. Jusys, R.J. Behm, J. Phys. Chem. B 105 (2001) 10874.
[40] H.A. Gasteiger, N. Markovic, J.P.N. Ross, E.J. Cairns, J. Phys. Chem. 98 (1994) 617.
[41] H.A. Gasteiger, N.M. Markovic, J.P.N. Ross, J. Phys. Chem. 99 (1995) 8290.
[42] L. Dubau, F. Hahn, C. Coutanceau, J.-M. Leger, C. Lamy, J. Electroanal. Chem. 554–555 (2003) 407.
[43] A. Lopez-Cudero, A. Cuesta, C. Gutierrez, J. Electroanal. Chem. 579 (2005) 1.
[44] B.M. Rush, J.A. Reimer, E.J. Cairns, J. Electrochem. Soc. 148 (2001) A137.
[45] E. Christoffersen, P. Liu, A. Ruban, H.L. Skriver, J.K. Nørskov, J. Catal. 199 (2001) 123.
[46] B. Andreaus, M. Eikerling, J. Electroanal. Chem. 607 (2007) 121.
[47] T.H.M. Housmans, C.G.M. Hermse, M.T.M. Koper, J. Electroanal. Chem. 607 (2007) 69.
[48] T. Springer, T. Zawodzinski, S. Gottesfeld, in: S. Srinivasan, J. McBreen, A.C. Khandkar, V.C. Tilak (Eds.), Electrode Materials and Processes for Energy Conversion and Storage, PV 97-13, The Electrochemical Society Proceedings Series, Pennington, NJ, 1997, p. 15.
[49] Y. Wang, P.B. Balbuena, J. Phys. Chem. B 108 (2004) 4376.
[50] N.M. Markovic, C.A. Lucas, B.N. Grgur, P.N. Ross, J. Phys. Chem. 103 (1999) 9616.
[51] J. Winkelmann, Landolt-Börnstein—Group IV Physical Chemistry, Numerical Data and Functional Relationships in Science and Technology: Gases in Gases, Liquids and their Mixtures, Springer, Berlin, Heidelberg, 2007.
[52] S. Escribano, R. Jamard, A. Morin, S. Solan, L. Guetaz, Proceedings of the 16th World Hydrogen Energy Conference, Paper no. 519-583 (in conference CD), Association Française de l'Hydrogène, 2006.
[53] CEA technical report, DVD-AME project, ANR-PAN'H, 2008.
[54] C. Bonnet, S. Didierjean, N. Guillet, S. Besse, T. Colinart, P. Carré, J. Power Sources 182 (2008) 441.
[55] D. Liu, S. Case, J. Power Sources 162 (2006) 521.
[56] A.A. Franco, O. Lemaire, S. Escribano, "Method for mitigating the carbon corrosion and the polymer electrolyte membrane degradation in a PEFC", FR patent EN 08 50875 (2008).
[57] A.A. Franco, S. Escribano, O. Lemaire, Abstract in 215th Electrochemical Society Meeting, San Francisco, May 24–29, 2009.
[58] A.A. Franco, B. Barthe, O. Lemaire, Abstract in 215th ECS Meeting, May 24–29, 2009.

Journal of The Electrochemical Society, 156 (2) B225-B233 (2009)
0013-4651/2008/156(2)/B225/9/$25.00 © The Electrochemical Society

Diffuse Charge Effects in Fuel Cell Membranes

P. Maarten Biesheuvel,[a,b,z] Alejandro A. Franco,[c,*] and Martin Z. Bazant[d,e,*]

[a]Department of Environmental Technology, Wageningen University, Wageningen, The Netherlands
[b]Materials Innovation Institute, Delft, The Netherlands
[c]Commissariat à l'Energie Atomique/DRT/LITEN/Département des Technologies de l'Hydrogène/Laboratoire de Composants PEM, 38000 Grenoble, France
[d]Department of Chemical Engineering and Mathematics, Massachusetts Institute of Technology, Cambridge, Massachusetts 02139, USA
[e]UMR Gulliver 7083, ESPCI-CNRS, 75005 Paris, France

It is commonly assumed that electrolyte membranes in fuel cells are electrically neutral, except in unsteady situations, when the double-layer capacitance is heuristically included in equivalent circuit calculations. Indeed, the standard model for electron transfer kinetics at the membrane/electrode interface is the Butler–Volmer equation, where the interfacial overpotential is based on the total potential difference between the electrode and bulk electrolyte. Here, we develop an analytical theory for a solid-state proton-conducting membrane that accounts for diffuse charge in the electrostatic polarization layers and illustrate its use for a steady-state hydrogen concentration cell. The theory predicts that the total membrane charge is nonzero, except at a certain hydrogen pressure, which is a thermodynamic constant of the fuel cell membrane. Diffuse layer polarization introduces the Frumkin correction for reaction rates, where the overpotential is based on the potential difference across only the compact (Stern) part of the polarization layer. In the Helmholtz limit of a relatively thin diffuse layer, we recover well-known results for a neutral membrane; otherwise, we predict significant effects of diffuse charge on the electron-transfer rate. Our analysis also takes into account the excluded volume of solvated protons, moving in a uniform charge density of fixed anions.

Manuscript submitted July 15, 2008; revised manuscript received October 2, 2008. Published December 9, 2008.

One of the key elements in electrochemical processes is the transfer of electrical charge across the electrode-electrolyte interface. The kinetics of this reaction is commonly described by the Butler–Volmer (BV) equation, which is formulated as the difference between an anodic and a cathodic reaction rate. These reaction rates depend on the concentrations of the participating atoms and ions and on the interfacial overpotential, which describes the influence of the step in potential of the electron when going from the electrode into the electrolyte phase and vice versa.[1-5] The overpotential is typically defined as the potential drop across the entire double layer, between the electrode and the neutral bulk electrolyte, relative to the equilibrium state, where the net Faradaic current is zero. As emphasized long ago by Frumkin,[6] it is more accurate to evaluate the concentrations where the reaction actually occurs, at the hypothetical "outer Helmholtz plane" or "pre-electrode plane," which is the distance of closest approach to the electrode for a solvated ion, separated from the electrolyte bulk by the polarization layer ("diffuse layer" or "space-charge region"); see Fig. 1a.[2,7-11] This introduces the so-called Frumkin correction to the BV equation, where the overpotential is based on the potential step from metal to the reaction plane, across only the charge-*free* compact layer (the "Stern layer," "compact layer," or "inner layer"), and not including the diffuse layer. In describing reaction rates, the compact layer is commonly described as a flat, uncharged, uniform dielectric film on the electrode. With this approach, the Frumkin correction has been included in a few general models of thin electrochemical cells, for example, by Itskovich et al.[11] and Kornyshev and Vorotyntsev,[12,13] who also included ion volume constraints for a solid electrolyte with a single mobile ion, and by Bonnefont et al.,[5] Bazant et al.,[14] and Chu and Bazant.[15]

In models of fuel cells, diffuse charge is almost always neglected and the ion-conducting membrane is assumed to be electrically neutral. Indeed, for fuel cell modeling including diffuse charge, we are only aware of the work by Franco et al.,[10,16] where Frumkin-corrected electron transfer equations are used, within the framework of transition state theory, to describe the elementary electrochemical reaction mechanisms under transient conditions in polyelectrolyte membrane fuel cell (PEFC) environments. Their nanoscale interfacial model postulates an inner layer formed by dynamically competing surface-adsorbed water molecules and electrochemical intermediate reaction species, which modify the effective water dipolar density and the dynamic evolution of the generated electric potential drop between the metal and the electrolytic phase (i.e., the Frumkin potential across the Stern layer). The inner-layer model is coupled to the standard Poisson-Nernst-Planck (PNP) diffuse-layer model for the diffusion and electro-migration of protons in the presence of fixed counterions representing the PEFC Nafion sulfonate groups. Numerical solutions of this model have shown that diffuse-layer effects are essential to describe time-dependent degradation processes in fuel cells.[17-20] In the present article, we develop a simpler analytical model to predict some basic effects of diffuse charge during steady-state operation.

Interestingly, it is sometimes argued (Ref. 20, p. 13989; Ref. 21, p. 1410) that the relevance of the Frumkin correction must be small because the ion concentrations in polymer electrolytes (such as Nafion) are high. Similarly, Wang et al.[22] (p. A1734) argue that "the term $c_{H^+}/c_{H^+,*}$ [the Frumkin correction] can be approximated by unity because the proton concentration is fixed in acid ionomers, [and] high in acid liquid media, and thus essentially constant during the hydrogen oxidation reaction." These arguments are often used to support neglecting the diffuse part of the double layer and thus replacing the potential difference of the compact (Stern) part by the full potential difference from metal to bulk electrolyte. However, as we will argue, even at high ion concentrations, there can still be a significant potential difference (and proton concentration gradient) in the diffuse part of the polarization layer, which affects reaction rates; as a result, diffuse-charge effects can be important even in solid electrolytes. Similar conclusions have been reached by Franco et al.[10,16] on the basis of nanoscale modeling of PEFCs and by Bazant et al.[14] and Chu and Bazant[15] through analysis of a general mathematical model for binary electrochemical cells. Aromatic calculations also highlight the importance for accounting for diffuse layer effects for a more accurate prediction of the energetics in general interfacial electrochemical processes.[23]

The goal of the present contribution is to derive simple analytical expressions for the voltage and power generated by a fuel cell in steady state, taking into account diffuse charge in the membrane. The physical insights and general formulas resulting from this approach are intended to complement the more detailed time-dependent numerical models of fuel cells described elsewhere (e.g., by Franco et al.[10,16] and references therein). To keep matters as

* Electrochemical Society Active Member.
[z] E-mail: maarten.biesheuvel@wur.nl

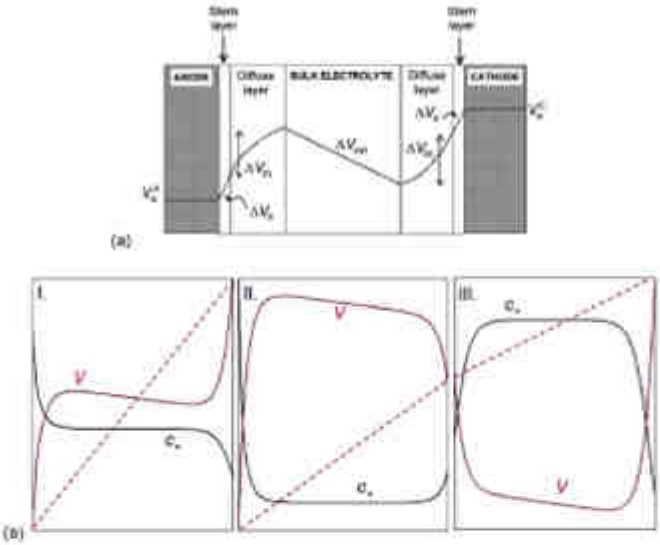

Figure 1. (Color online) (a) Schematic representation of the electrostatic potential profile in the fuel cell membrane. In this representation, there is an excess of protons in the anodic polarization layer and a deficit on the cathodic side. (b) As in (a), but for three cases: I, as in (a); II, with an excess of protons on both sides; and III, with a deficit of protons on both sides. The dashed lines show the electrical voltage increase through the external circuit.

simple as possible, we analyze a planar proton-conducting polyelectrolyte membrane with fixed negative charge.[24] Our analysis is based on two types of mean-field, continuum models for proton transport, where either positive point charges or solvated protons of a nonzero size move in a uniform background density of immobile anions.[11-13] The membrane model is completed by Frumkin-corrected BV reaction kinetics for the charge transfer from the metal catalyst across a uniform Stern layer to the reaction plane. Although this general model already incorporates a number of complicated physical effects, it remains simple enough for mathematical analysis of various limiting cases. In the context of fuel cell modeling, one aspect is the inclusion of ion volume constraints in the description of the polarization layer and the charge transfer rate.

To illustrate the use of the analytical membrane model, we apply it to the simplest case of a fuel cell where the only reactive gas-phase species is hydrogen. In such a "concentration cell," it is a difference in hydrogen concentration between the anodic and cathodic compartments that drives the electrical current.[25] This allows us to neglect other processes, such as the catalytic conversion of gaseous oxygen, and to consider only the Tafel–Heyrovsky–Volmer reaction mechanism for the conversion of molecular hydrogen into protons and electrons at each electrode.[16,22,23] As a first approximation, we neglect the Heyrovsky reaction step, which is a mixed reaction of simultaneous atomic hydrogen adsorption and proton formation. Transport limitations in the gas phases, nonisothermal operation, and the nonzero thickness of the electrode reaction region (and the mass transport therein[26]) are also neglected, as well as water transport for the case of PEFCs.[27] Although we consider the adsorption/desorption equilibrium of hydrogen onto the catalyst, we neglect a diffusional limitation for the adsorbed hydrogen atoms on the catalyst surface. In summary, we consider as possible rate-limiting steps the ad-/desorption of hydrogen, the electrochemical conversion of hydrogen atoms into protons (and vice versa), as well as the ohmic transport of electrons and ions through the external circuit and the electrolyte membrane, respectively. Although our analysis is performed for a hydrogen concentration cell, it can easily be extended to other types of fuel cells or electrochemical systems, and its conclusions about diffuse-charge effects on reaction rates should have broad applicability.

Theory

As explained above, we illustrate the modeling of diffuse charge in a fuel cell membrane via the example of an electrochemical hydrogen concentration cell, where the only mobile and reactive ion in the electrolyte phase is the proton. At the cathode, the proton can react with an electron to form a neutral adsorbed hydrogen atom (Volmer reaction step) that can diffuse over the catalytic surface, combine with a second hydrogen atom, and desorb as molecular hydrogen (Tafel reaction step). We assume that the adsorbed hydrogen atoms are at equilibrium with the hydrogen molecules. For simplicity, we neglect a possible limitation in the catalytic surface concentration of sites for protons to adsorb to (i.e., we set the adsorption site vacancy concentration θ_v to unity[15]). At the anode, we have the reverse situation.

Ohmic laws.— According to Ohm's law, the generated electrical voltage, V, is given by

$$V = V_{C,M} - V_{A,M} = iR_{ext} \quad [1]$$

with i is current, R_{ext} is the external resistance, and $V_{C,M}$ and $V_{A,M}$ are the electrical potentials in the metallic phase of the cathode and anode, respectively. In the electrolyte bulk phase (membrane), we also assume Ohm's law[17]

$$\Delta V_{elyt} = V_{A,b} - V_{C,b} = iR_{elyt} \quad [2]$$

where b stands for the electrolyte bulk phase, just beyond the polarization layer (outer, or Volta, potential), and where the electrolyte resistance is given for a planar membrane by

$$R_{dyn} = \frac{L}{A\sigma} \quad [3]$$

where L is the thickness, A is the area, and σ is the ionic conductivity of the membrane. Assuming that protons are the only charge-carrying ions, σ is given by

$$\sigma = Dc_+\frac{z^2}{kT} \quad [4]$$

where D is the proton diffusion coefficient and c_+ is the bulk proton concentration.

BV equation.— The BV equation including the Frumkin correction describes the electronic current at the electrode-electrolyte interface as the sum of a cathodic and an anodic reaction[2,13,19]

$$i = -k_R c_O \exp(-\alpha_R f\Delta V_s) + k_O c_R \exp(\alpha_O f\Delta V_s) \quad [5]$$

where k_R and k_O are reaction rate constants, c_O and c_R are concentrations at the reaction plane of the ion in the oxidized (O) and reduced (R) state, and ΔV_s is the Stern potential difference, defined as the difference in potential between the metal phase (the electrode), $V_{j,M}$, and the potential at the reaction plane, V_r, thus $\Delta V_s = V_{j,M} - V_r$. The sum of the transfer coefficients α_R and α_O equals unity; f equals F/RT, or e/k_BT. We stress that if diffuse charge were neglected, as in most fuel cell models, the Stern potential drop ΔV_s would be replaced by the total voltage drop across the full double layer, from the metal to the neutral bulk phase.

The representation of Eq. 5 considers both the oxidant and reductant to be species present in the electrolyte phase (typical for an electrochemical reaction in a polar solvent, such as water). However, in fuel cells, one of the species that participates in the electrochemical reaction is typically uncharged and derives from an adjacent phase (such as the hydrogen atoms that are surface adsorbed to a catalytically active surface), and it is a standard approximation to set its concentration near the site of the electrochemical reaction equal to the reactant concentration c_O or c_R in Eq. 5. As discussed below, Eq. 5 also assumes an ideal dilute solution, which can be relaxed more generally by replacing concentrations with chemical activities. Further on, we consider corrections due to excluded volume of the reacting species in the electrolyte phase.

The sign of the current i in Eq. 5 is defined to be negative at the cathode (i.e., negative in the direction for reduction, $O^+ + e^- \rightarrow R$). Implementing in Eq. 5 the proton for O, the adsorbed hydrogen atom for R, and assuming that the electron transfer coefficients are given by $\alpha_O = \alpha_R = 1/2$, we obtain the Volmer reaction rate for the electrochemical conversion of hydrogen

$$i = -k_R c_{H^+} \exp\left(-\frac{1}{2}f\Delta V_s\right) + k_O c_{H_{ads}} \exp\left(\frac{1}{2}f\Delta V_s\right) \quad [6]$$

We can relate the concentration of adsorbed hydrogen atoms $c_{H_{ads}}$ to the gas-phase hydrogen pressure p_{H_2} according to the Tafel reaction step[20]

$$i = k_{ad}p_{H_2} - k_{des}c_{H_{ads}}^2 \quad [7]$$

We now make two simplifications: (i) Assuming that the ad/desorption of hydrogen gas in Eq. 7 is fast compared to the faradaic reactions at both electrodes in Eq. 6, the adsorbed hydrogen atom is in equilibrium with the molecular hydrogen, and we can replace $c_{H_{ads}}$ in Eq. 6 by $\sqrt{k_{ad}/k_{des}}\cdot p_{H_2}$ and define $k_j = k_O\cdot\sqrt{k_{ad}/k_{des}}$; (ii) For thin double layers and non-negligible bulk ion concentrations, it is common to assume local electrochemical equilibrium, or a constant electrochemical potential, in the diffuse layers in the electrolyte. Ignoring volume constraints for a dilute solution, this allows us to relate the concentration of protons at the reaction plane, c_H, to the proton concentration in the bulk of the electrolyte phase, c_+, according to a Boltzmann distribution

$$c_H = c_+\exp(-f\Delta V_{DL}) \quad [8]$$

where the potential difference across the diffuse part of the double layer is ΔV_{DL}, which is $V_r - V_b$. In the bulk electrolyte phase, the proton concentration is approximately constant and at a value of c_+, which equals the concentration of the background, fixed, negative charge. This has previously been shown by Franco *et al.*[10] by solving the full PNP equations for the transport of protons in Nafion, a polyelectrolyte membrane, where the thickness of the polarization layer was found to be between 1 and 5 nm for the anode and cathode diffuse layers in a PEFC. The nearly uniform bulk proton concentration due to fixed anions is a crucial difference between solid and liquid electrolytes, which eliminates diffusion limitations and nonequilibrium space-charge formation;[15] instead, bulk transport is dominated by electromigration and the diffuse layers typically remain in equilibrium. With these two simplifications, Eq. 6 takes the form

$$i = -k_j\left\{\overline{\sqrt{p^+}}\exp\left(-f\Delta V_{DL} - \frac{1}{2}f\Delta V_s\right) - \overline{\sqrt{p_{H_2}}}\exp\left(\frac{1}{2}f\Delta V_s\right)\right\} \quad [9]$$

where

$$\overline{\sqrt{p^+}} = c_+\frac{k_R}{k_j} \quad [10]$$

The critical fuel pressure p^+ is a thermodynamic constant of the fuel cell membrane at given temperature, and k_j is a kinetic constant dependent on structural details of the electrode.

Structure of the polarization layers.— Let us discuss the structure of the Stern and diffuse layer in more detail. Directly next to the electrode is the charge-free Stern layer, across which the potential decay is ΔV_s, which is separated by the reaction plane from the diffuse layer (or "space-charge region"), across which the potential drop is $\Delta V_{DL} = V_r - V_b$, where DL stands for diffuse layer. The reaction plane is located within the electrolyte phase, and is the closest interface to where the reacting ions and atoms that are in the electrolyte phase are assumed to be able to approach the metallic phase. The reaction plane is often denoted as the "outer Helmholtz plane" or "Stern plane." (We can also interpret it as the typical distance over which the electron can tunnel from electrode into the electrolyte; Ref. 2, p. 130). In the diffuse layer, both the proton concentration and the electric potential rapidly change. For ideal Boltzmann–Coulomb statistics based on Eq. 5, the structure of the diffuse layer is described by the Poisson–Boltzmann (PB) equation, which amounts to a mean-field approximation for pointlike ions. However, many modified theories are available that incorporate correlations or excluded volume effects.[20,29]

To relate the potential drop over the Stern layer ΔV_s to the charge stored in the diffuse layer, q (in charge/area), we consider continuity of the electrical displacement at the reaction plane, assuming a constant electric field in the Stern layer, to obtain

$$q = -\varepsilon\frac{\Delta V_s}{\lambda_s} \quad [11]$$

which is identical to the calculation of the nonpolar contribution $\Delta\varphi_1$ to the overall Frumkin potential difference, given in Franco *et al.*[8] This is a standard approximation, which (via Gauss' law) relates the Stern voltage drop to the normal electric field at the inner edge of the diffuse layer, by modeling the Stern layer as a thin, planar, dielectric film. Equation 11 provides a boundary condition for the electrostatic potential whenever diffuse charge is considered.[8,14,20] In Eq. 11, the parameter λ_s is an effective width for the Stern layer, equal to its true width times the permittivity ratio of the electrolyte to the Stern layer, and ε is the permittivity of the electrolyte, which relates to κ, the inverse Debye length, and to c_+, the background number concentration of negative charge, according to $\kappa^2 = 2c_+e^2/(\varepsilon k_BT)$. For our purposes, Eq. 11 amounts to the as-

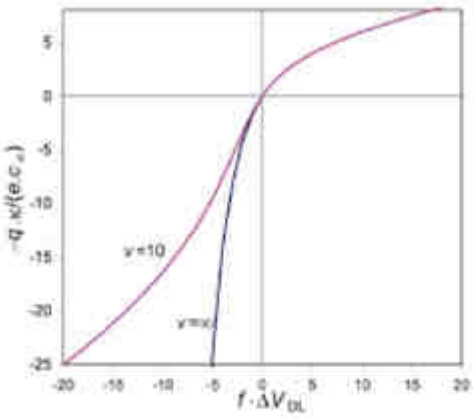

Figure 2. (Color online) Surface charge density q of the polarization layer as a function of diffuse-layer potential difference ΔV_{DL} according to the modified one-dimensional planar PB model with fixed anions and mobile cations, as function of volume parameter v, which is the inverse volume fraction of protons in the bulk phase.

sumption of a constant Stern-layer capacitance, which can be relaxed and extended in various ways, as discussed in Ref. 14 and 16.

To calculate the total charge (per unit area) stored in each diffuse layer, q, we must consider the detailed structure of these layers, including the concentration of fixed counter charge, and we require a model for the electrostatic potential. For an ideal, dilute solution in equilibrium, the standard model is based on PB theory, which is a mean-field approximation for pointlike ions, as noted above. In the simplest case of a symmetric binary electrolyte, Gouy's solution to the PB equation yields Chapman's well-known formula

$$q = -4ec_\infty\kappa^{-1}\sinh\left(\frac{1}{2}f\Delta V_{DL}\right) \qquad [12]$$

but this is not suitable for a solid electrolyte, with only one mobile species. Instead, we must solve the PB equation for mobile protons, and for anions which are fixed (to a good approximation for most proton-conducting membranes), which results in $2fd^2V/dx^2 = \kappa^2[1 - \exp(-fV)]$. For this case, an analytical formula for the charge density is available, given by[17]

$$q = -2\,\mathrm{sgn}(\Delta V_{DL})ec_\infty\kappa^{-1}\sqrt{\exp(-f\Delta V_{DL}) + f\Delta V_{DL} - 1} \qquad [13]$$

where sgn stands for "sign of" [i.e., $\mathrm{sgn}(x) = x/|x|$]. For very negative values of ΔV_{DL}, Eq. 12 and 13 coincide, but for $f\Delta V_{DL}$ close to zero, q as predicted by Eq. 13 is a factor of $\sqrt{2}$ smaller than according to Eq. 12. Because cation expulsion is not considered in Eq. 13, it is more realistic for a solid electrolyte. While for a binary liquid electrolyte, Eq. 12 is symmetric and exponentially diverging in ΔV_{DL}, for a solid electrolyte with only one mobile ion and for $\Delta V_{DL} > 0$ the charge density q as predicted by Eq. 13 grows much more slowly, following a square-root dependence on ΔV_{DL}, which is due to the finite maximum charge density set by the anions (see Fig. 2). Interestingly, analogous models of ionic volume constraints in a binary electrolyte[25] or molten salt[26] yield the same square-root scaling at both large positive or negative voltage, because in all these cases, the diffuse layer has asymptotically uniform charge density set by the maximum density of counterions. For a solid electrolyte, the strong asymmetry of the total charge density with voltage is a very interesting aspect of polarization layers that have fixed background charge, whose role in fuel cell membranes has not previously been discussed.

One assumption behind Eq. 13 is that the protons in the electrolyte are point charges. However, the finite volume of the protons can be taken into account in various ways, while maintaining the mean-field approximation, following the classical theory of steric effects in a binary electrolyte.[26,27,25] The simplest approach is based on a Langmuir lattice isotherm, where the controlling parameter, v, is the number of available sites per proton ($v > 1$) in the quasi-neutral bulk phase. Equivalently, the parameter $\phi_\infty = 1/v$ is the volume fraction occupied by protons in bulk (analogous to the parameter ν defined in Ref. 28). For a model of a solid electrolyte with one mobile ion of finite size, Iskovich et al. derived a modified form of the charge-voltage relation[17]

$$q = -2\,\mathrm{sgn}(\Delta V_{DL})ec_\infty\kappa^{-1} \times\sqrt{f\Delta V_{DL} + v\ln[1 + v^{-1}\{\exp(-f\Delta V_{DL}) - 1\}]} \qquad [14]$$

which reduces to Eq. 13 for very large v. The volume constraint on the proton concentration leads to the same square-root asymptotic scaling of the total charge with diffuse-layer voltage for a positively charged diffuse layer ($\Delta V_{DL} < 0$), as that noted above for a negatively charged diffuse layer ($\Delta V_{DL} > 0$), because in both limits the charge density becomes saturated at finite limiting values. In Fig. 2, we give results for q vs ΔV_{DL} using Eq. 13 (when v is set to infinity) and using Eq. 14 (setting $v = 10$), where these general trends are apparent.

Steady-state electrical potential profiles.— Figure 1a shows a schematic representation of the potential profiles in the electrochemical cell model. Here, an example is given with an excess of protons in the anode polarization layer, related to the fact that the diffuse layer potential difference ΔV_{DL} is negative [ΔV_{DL} being the difference in potential at the Stern plane (reaction plane) relative to the value in the bulk electrolyte]. On the cathode side, we have a deficit of protons and $\Delta V_{DL} > 0$. Because we assume local equilibrium in the double layer, the Stern layer potential difference ΔV_S always has the same sign as the diffuse-layer potential difference because the electric displacement is continuous at the Stern plane. Though we expect this approximation to have broad applicability for fuel cell membranes, it is important to note that at a large enough current, or for a too weak diffuse-layer field, local equilibrium can be violated, which can cause "charge inversion" in the diffuse layer, as has recently been predicted using a similar mean-field model for biological membranes transmitting ionic current.[24]

In our model of a fuel cell membrane, the magnitudes of $\Delta V_{DL,i}$ and $\Delta V_{S,i}$ are coupled through Eq. 11 in combination with either Eq. 12, 13, or 14. The electric potential decreases through the bulk of the electrolyte (thus, $\Delta V_{elyt} = V_{A,b} - V_{C,b} > 0$), which is a required condition for the protons to spontaneously migrate in the electric field through the bulk electrolyte. Similarly, the external potential difference $\Delta V_{ext} = V_{m,C} - V_{m,A}$ must be positive for the electrons to flow spontaneously through the external circuit and do work. Now it is important to realize that though ΔV_{ext} and ΔV_{elyt} must always be positive, the polarization layer potential differences $\Delta V_{DL,i}$ and $\Delta V_{S,i}$ do not necessarily have the signs as depicted in Fig. 1a, with the associated excess of protons on the anode side and a proton deficit on the cathode side. Actually, we can have the situation that both layers have a deficit of protons, or both have a proton excess (see cases II and III in Fig. 1b). This situation, for instance, occurs when the current is low and both gas-phase pressures (at the anode side and at the cathode side) are above p^* (resulting in an excess of protons on both sides), or when both gas-phase pressures are below p^* (resulting in a proton deficit on both sides). However, other parameter settings are also possible to give these "symmetric" situations.

The case of a proton deficit on the anode side, and an excess on the cathode side, is impossible within our model. This can be concluded from the fact that the potential must be continuous through

the entire circuit (see Eq. 29 below) and that ΔV_{elyt} and ΔV_{ext} must always be positive. Roughly speaking, the two polarization layers (each consisting of a diffuse part plus a Stern part) must "rectify" the potential mismatch created in the system by the bulk proton transport and the external electron transport. Therefore, the two polarization layers must compensate for the total potential drop ΔV_{elyt} plus ΔV_{ext}. This is most effectively done when having an excess of protons on the anode side and a deficit on the cathode side, but Kirchoff's rule of zero total voltage drop around a current loop (Eq. 29) can also be respected in a system where there is an excess of protons on both sides, or a deficit of protons on both sides, as illustrated in Fig. 1b.

We stress again that, in the present model, the excess proton charge on the anodic side is not constrained in any way to exactly compensate the proton charge deficit on the cathodic side. The total diffuse charge on the membrane (number of mobile proton minus the number of fixed anions) though generally small (compared to the total number of ions) typically is nonzero. This violation of the traditional assumption of overall electroneutrality of the membrane, due to unbalanced diffuse charge produced by the faradaic reactions, has been explicitly noted and quantified in models of binary electrochemical thin films[14] while in the context of fuel cell membranes is implicitly included in the model of Ref. 10.

Influence of ion volume constraints on the electrochemical charge transfer rate.— A fundamental question that has received little attention in the electrochemical literature is the manner in which nonideal solution behavior at an interface affects faradaic reaction rates, going beyond the BV equation (Eq. 5). For example, above we have accounted for volume constraints in the solid electrolyte at equilibrium following a classical lattice-gas model, but there are two basic ways that such entropic considerations should also influence the reaction rate: (*i*) the ion concentration at the reaction (Stern) plane, relative to the bulk, is altered by steric effects in the diffuse layer, and (*ii*) the reaction kinetics may be directly affected by volume constraints on the reactants and activated complexes, thus modifying the local BV equation (Eq. 5).

Effect (*i*) follows from the equilibrium theory for the polarization layer given by Eq. 11 and 14. Using a lattice-based model of volume constraints, the equilibrium distribution (Eq. 8) must be modified by adding to the ideal chemical potential an excess term given by $\mu^{\mathrm{ex}} = -\ln(1-\phi)$, where $\phi = c/(c_{\mathrm{ref}})$ is the excluded volume.[27,28,32,33] The approximation of constant electrochemical potential then yields the proton concentration at the reaction plane, to be used in Eq. 6

$$c_{\mathrm{H}^+} = c_{+}\frac{1-\phi}{1-\phi_{+}}\exp(-f\Delta V_{\mathrm{DL}}) = c_{+}\frac{\nu\exp(-f\Delta V_{\mathrm{DL}})}{\nu-1+\exp(-f\Delta V_{\mathrm{DL}})} \qquad [15]$$

which resembles a Fermi–Dirac distribution and reduces to the Boltzmann distribution (Eq. 8) in the limit $\nu \to \infty$. In the opposite limit $\nu \to 1$, the proton concentration at the Stern plane approaches the value in bulk (i.e., $c_{\mathrm{H}^+} \to c_{+}$) because volume constraints are so strong that protons remain at a nearly uniform concentration of "close packing" across the entire membrane.

Effect (*ii*) can be included in various ways. A general approach, consistent with the treatment of the bulk, is to express reaction rates in terms of differences in chemical potential for the reaction complex, as it undergoes stochastic transitions in a landscape of excess chemical potential (relative to an ideal gas). Such a theoretical framework is developed in Ref. 35 and applied there to various examples of surface adsorption and electrochemical reactions in concentrated solutions. One example can be found in Ref. 36, where the intercalation reaction in a rechargeable battery cathode is driven by changes in chemical potential, which include contributions from differences in enthalpy, entropy, and concentration gradients, in a general lattice-based phase-field model.

Here, we apply the more familiar approach to describe volume constraints in reactions, similar to Langmuir-isotherm models for specific adsorption of ions on electrodes,[1] although we focus on the reverse situation, where volume constraints arise only in the electrolyte phase, consistent with our electrolyte membrane model, and not for the adsorbed neutral hydrogen atoms on the catalyst surface. As in standard models of heterogeneous catalysis, the reaction plane is conceptually divided into a lattice of sites, where both occupied and unoccupied sites are considered as reacting species. The true reaction $\mathrm{O} + e^- \rightarrow R$ occurring in a concentrated solution is thus replaced by the approximate dilute-solution reaction, $\mathrm{O} + e^- + \mathrm{S} \rightarrow R$, where S is a vacant site for the ion O in the oxidized state. This reduces the oxidation reaction rate by a factor $1-\phi$, which is the available volume fraction in the reaction plane for new protons resulting from oxidation of hydrogen. We ignore volume constraints in the reverse reaction rate [except for effect (*i*) above] by assuming that the occupancy of adsorbed neutral hydrogen atoms on the catalyst surface remains small enough not to hinder the reduction of protons.

Including these two effects in the BV equation (Eq. 6) results in

$$i = -(1-\phi)\left(k_{\mathrm{f}}\frac{c_{+}}{1-\phi_{+}}\exp\left(-f\Delta V_{\mathrm{DL}} - \frac{1}{2}f\Delta V_{\mathrm{s}}\right) - k_{\mathrm{r}}\sqrt{p_{\mathrm{H}_2}}\exp\left(\frac{1}{2}f\Delta V_{\mathrm{s}}\right)\right) \qquad [16]$$

which can be simplified to

$$i = -k_{\mathrm{f}}(1-\phi)\left(\sqrt{p^*}\exp\left(-f\Delta V_{\mathrm{DL}} - \frac{1}{2}f\Delta V_{\mathrm{s}}\right) - \sqrt{p_{\mathrm{H}_2}}\exp\left(\frac{1}{2}f\Delta V_{\mathrm{s}}\right)\right) \qquad [17]$$

where we assume infinitely fast hydrogen ad-/desorption (the Tafel reaction step) and where the critical pressure p^* is slightly modified via $\sqrt{p^*} = c_{+}/(1-\phi_{+}) \cdot k_{\mathrm{r}}/k_{\mathrm{f}}$. In summary, when proton volume constraints are incorporated in the membrane model, we suggest that Eq. 9 is modified by a prefactor $1-\phi$, where ϕ follows from $\phi = c_{\mathrm{H}^+}/(c_{\mathrm{ref}})$ with c_{H^+} from Eq. 15, and by the replacement of the constant c_{+} by $c_{+}/(1-\phi_{+})$. Furthermore, ΔV_{DL} and ΔV_{s} are no longer related to each other through Eq. 11 and 13, but require Eq. 11 and 14.

Results and Discussion

In this section, numerical results are presented for the concentration cell model, and simple analytical results are derived for several limits. The critical hydrogen pressure p^* defined above is the same at both electrodes because it is a thermodynamic parameter for the membrane electrolyte material. First, we derive simple formulas for an ideal, dilute membrane, and then we consider effects of volume constraints at high proton concentrations.

Analytical solution for $p_{\mathrm{H}_2,A} = p_{\mathrm{H}_2,C}$.— We begin by considering the equilibrium situation, where the gas-phase hydrogen pressure p_{H_2} is equal on both sides of the membrane, and no current flows. Setting $i = 0$ in Eq. 9, we obtain

$$\sqrt{p^*}\exp(-f\Delta V_{\mathrm{DL}}) = \sqrt{p_{\mathrm{H}_2}}\exp(f\Delta V_{\mathrm{s}}) \qquad [18]$$

which, using Eq. 11 and 13, yields the nonlinear relation

$$f\Delta V_{\mathrm{s}} = \mathrm{sgn}(\Delta V_{\mathrm{DL}})\lambda\sqrt{\exp(-f\Delta V_{\mathrm{DL}}) + f\Delta V_{\mathrm{DL}} - 1} \sim \frac{1}{\sqrt{2}}\lambda\left[f\Delta V_{\mathrm{DL}} - \frac{1}{6}(f\Delta V_{\mathrm{DL}})^3 + \cdots\right] \qquad [19]$$

which can be solved iteratively. Following Ref. 9, 14, and 32, we have introduced the dimensionless parameter $\lambda = \lambda_{\mathrm{s}}/\kappa$, the ratio of the effective Stern-layer thickness to the diffuse-layer thickness, because this allows us to analyze the limits of large and small polarization effects. Note that combination of Eq. 11 with Eq. 12, 13, or 14 results in a relation between ΔV_{s} and ΔV_{DL} which only depends

on δ and f and does not require values for κ or c_∞.

For a sufficiently high gas-phase hydrogen pressure some of the hydrogen molecules will be converted into excess protons residing in the electrolyte (with the electrons stored on the surface of the metal phase). As the gas-phase pressure is decreased, below a certain p_{H_2} there is no longer an excess of protons in the material, but instead a proton deficit will develop (i.e., the polarization layers become negatively charged). Let us first find the value of p_{H_2} for which the total excess proton charge in the electrolyte is zero (i.e., the gas phase pressure for which the electrolyte membrane is uncharged). In this case, $q = 0$, thus also ΔV_{EL}, as well as ΔV_S. Inserting $\Delta V_{EL} = \Delta V_S = 0$ in Eq. 18, we obtain the result that $p_{H_2} = p^*$. Therefore, at an applied hydrogen pressure of p^*, the membrane has zero total charge. At this special pressure, no molecules are taken up or released by the material; thus, it is meaningful to view p^* as a thermodynamic property of the electrolyte material, in equilibrium with hydrogen gas.

For any other gas conditions, the total charge on the electrolyte will generally be nonzero, in contrast to traditional membrane models assuming electroneutrality. The total charge can be cumbersome to calculate analytically, but close to $p_{H_2} = p^*$ we can use the linearization of ΔV_S vs ΔV_{DL} as given by Eq. 19. Together with Eq. 11 this results in

$$q = ec_\infty\kappa^{-1}(\lambda + \sqrt{2}I^{-1}\ln\frac{p_{H_2}}{p^*} \qquad [20]$$

which shows that for $p_{H_2} > p^*$ the electrolyte will become positively charged (containing an excess of protons in both polarization layers), and vice versa for $p_{H_2} < p^*$. Equation 20 suggests that physical parameters of the electrolyte material, such as p^* or λ, can be inferred from experimental measurements of stored charge vs applied pressure, in equilibrium.

The above analysis shows that when diffuse-layer polarization is included in the membrane model, it can naturally describe the total proton charge stored in the polarization layers, even at equilibrium (e.g., as function of the gas-phase hydrogen pressure). In contrast, when diffuse-layer effects are omitted, polarization charge is absent from the model and assumed to be zero. Indeed, it is commonly believed that the stored charge in the membrane (via its differential capacity C_{EL}) is only relevant for dynamical modeling of fuel cells via resistor-capacitor (RC) circuit models. We stress, however, that the standard BV approach does not give a rationale for the existence or relevance of C_{EL}, and its widespread use in empirical RC models for transients in fuel cells is thus theoretically inconsistent. Instead, the Frumkin-corrected BV equation naturally includes the polarization layer capacity C_{EL}, and shows that C_{EL} is not only important for transients, but also for stationary operation, and even for equilibrium.

Simplified model for very high kinetic rates.— Next we consider a concentration cell operating in a steady state, with $p_{H_2,A} > p_{H_2,C}$. In the case that the electrochemical kinetics are very fast (as well as the hydrogen ad-/desorption step), the equilibrium Eq. 18 is valid at both electrodes, and together with Eq. 1, 2, and 29 (to be discussed further on), we obtain for the cell voltage vs current i the well-known expression

$$V = V_0 - iR_{ohm} \qquad [21]$$

where the ideal Nernstian cell voltage V_0 is given by

$$V_0 = \frac{1}{2f}\ln\frac{p_{H_2,A}}{p_{H_2,C}} \qquad [22]$$

The generated electrical power $(P = iV)$ is then straightforwardly derived from Eq. 1 and 21. As Eq. 21 shows, for infinitely fast kinetics, the details of charge stored in the polarization layers, as described by Eq. 19, are irrelevant. In this respect, the present model behaves as expected.

Simplified model for electrochemical kinetic rates very high.— Next we consider the case where the electrochemical step (Volmer) is still very fast (i.e., at equilibrium), but a limited rate for the hydrogen ad-/desorption (Tafel) is considered. The electrochemical reaction equilibria follow from Eq. 6, assuming that both the oxidation and reduction rates are much larger than the current i, and thus equal to one another. This determines the total double-layer voltage on each electrode

$$\Delta V_T = \frac{1}{2f}\ln\left(\frac{p^*}{c_{H_3O^+}^2}\frac{k_{adsj}}{k_{desj}}\right) \qquad [23]$$

where $\Delta V_T = \Delta V_S + \Delta V_{DL}$. In this case, Eq. 21 is modified to

$$V = \frac{1}{2f}\ln\left(\frac{k_{adsC}k_{adsA}p_{H_2,A} - i}{k_{adsA}k_{adsC}p_{H_2,C} + i}\right) - iR_{elyt} \qquad [24]$$

For a very small current i [due to a high value of R_{ext} (i.e., close to an open circuit)], or a high value for k_{adsA} and k_{adsC}, Eq. 24 reduces to Eq. 21 and 22. For a very low external resistance R_{ext} (close to a short circuit), $V \to 0$ and the (maximum) current i is obtained iteratively from Eq. 24. Setting $R_{elyt} = 0$ and $k_{adsA} = k_{adsC}$ we obtain a simple analytical result for the maximum current, $i_{max} = 1/2 \cdot k_{ads}(p_{H_2,A}+p_{H_2,C})$, which is an example of a "reaction-limited current," also predicted in some regimes for binary electrochemical thin films.[8,10]

Thus, when only the electrolyte resistance and the hydrogen ad-/desorption kinetics are important, the details of the polarization layers are unimportant for steady-state behavior. Clearly, for diffuse layer effects to play a role in the steady state, the electrochemical reaction must be at least partially rate limiting, which we consider next. For simplicity, we will assume hereafter that the hydrogen ad-/desorption reaction (Tafel reaction step) is always at equilibrium, so that we can use Eq. 9 for both the anode and the cathode. At the end of this section, we will include volume effects and will replace Eq. 9 by Eq. 17.

Helmholtz and GC limits.— In the general situation where electrochemical reactions are at least partially rate limiting, simple analytical results are possible in two interesting limits, namely, where the effective Stern layer thickness λ_S is either much larger or much smaller than the diffuse-layer thickness κ^{-1}. In the former "Helmholtz limit," $\delta \to \infty$ and $\Delta V_S \gg \Delta V_{EL}$, and the Stern layer carries the total double-layer voltage and diffuse-layer polarization is zero. In the latter "Gouy-Chapman (GC) limit," $\delta \to 0$ and $\Delta V_S \ll \Delta V_{EL}$, and the Stern potential difference can be set to zero. These asymptotic limits based on the parameter δ were introduced in Ref. 14 in the context of modeling binary-electrolyte thin films; here, we develop a similar analysis for a fuel cell membrane.

Combining Eqs. 2, 9, and 29 and setting $\Delta V_{EL,j} = 0$ results for the Helmholtz limit in an explicit expression for the generated voltage V versus the current i given by

$$V = V_0 - \left\{\frac{2}{f}\operatorname{arcsinh}\frac{i}{2k_A\sqrt[4]{p^*p_{H_2,A}}} + iR_{elyt} + \frac{2}{f}\operatorname{arcsinh}\frac{i}{2k_C\sqrt[4]{p^*p_{H_2,C}}}\right\} \qquad [25]$$

This formula resembles standard expressions from fuel-cell models assuming a neutral membrane and BV kinetics, if we identify $k_j\sqrt[4]{p^*p_{H_2,j}}$ as the exchange current density i^*. Indeed, in standard BV fuel cell modeling,[4,27-44] the ideal voltage V_0 is reduced (as in Eq. 25) by subtracting the ohmic drop across the electrolyte, iR_{elyt}, and the surface overpotential $\eta_j = 2/f \cdot \operatorname{arcsinh}(i/2i^*)$ for each electrode. In all of these fuel cell models, the Tafel and Heyrovsky reaction steps are neglected, just as in the present model. For low currents i, Eq. 25 simplifies to

$$V = V_0 - i \cdot [(fk_A\sqrt[4]{p^*p_{H_2,A}})^{-1} + R_{elyt} + (fk_C\sqrt[4]{p^*p_{H_2,C}})^{-1}] \quad [26]$$

which has the familiar form of two "charge-transfer resistances" in series with the electrolyte bulk resistance, R_{elyt}. The charge-transfer resistance in Eq. 26 scales with hydrogen pressure to power −1/4 (see also Table III in Ref. 42).

The analysis shows that the state-of-the-art BV models in literature can be identified as the Helmholtz limit ($\delta \to \infty$) of our more complete model, resulting in Eq. 25. This identification makes it possible to systematically extend the state-of-the-art approach to BV modeling to allow for nonzero membrane charge by taking finite values of δ instead of implicitly assuming $\delta \to \infty$.

Departures from electroneutrality are most important in the GC limit, $\delta = 0$; thus, this limit is convenient to quantify maximum effects of diffuse charge using our model. Assuming $\Delta V_{\delta} = 0$ in Eq. 9, we obtain an explicit expression for the generated voltage V as function of the current i given by

$$V = V_0 - \left\{ f^{-1} \ln\left(\frac{k_A\sqrt{p_{H_2,A}}}{k_A\sqrt{p_{H_2,A}} - i} \right) + iR_{elyt} + f^{-1} \ln\left(\frac{k_C\sqrt{p_{H_2,C}} + i}{k_C\sqrt{p_{H_2,C}}} \right) \right\} \quad [27]$$

which has different nonlinear, surface-overpotential contributions compared to the opposite limit of an uncharged membrane in Eq. 25. For small currents i, Eq. 27 simplifies to

$$V = V_0 - i \cdot [(fk_A\sqrt{p_{H_2,A}})^{-1} + R_{elyt} + (fk_C\sqrt{p_{H_2,C}})^{-1}] \quad [28]$$

Thus, in the GC limit, we have, just as in the Helmholtz limit, an analytical expression for the linearized current-voltage relation, which corresponds to a "resistances-in-series" model, but with very different expressions for the charge transfer resistance (i.e., compare Eq. 26 to Eq. 28). An interesting point is that the GC limit does not reduce to the same expression as for the Helmholtz limit, even though both limits are independent of details of the polarization layer. This difference is due to the fact that in the GC limit the concentration of ions (protons) in the charge-transfer reaction is evaluated at the Stern reaction plane, while in the Helmholtz limit bulk-phase values are used. Interestingly, the two expressions given above are equally valid for the case of fixed countercharge (as in a solid electrolyte) as for the situation that the counterchange is mobile (as for aqueous solution). It must finally be noted that when Eq. 27 is used outside the fuel cell range (where $0 < V < V_0$), it will diverge at two limiting currents which are $i_{max} = -k_C\sqrt{p_{H_2,C}}$ and $i_{max} = k_A\sqrt{p_{H_2,A}}$.

Electrochemical reactions partially rate limiting—numerical calculations.— To illustrate the behavior of the model in general situations, between the limits analyzed above, we obtain numerical solutions. The complete model is based on Eq. 1, 2, 9, and 19, where Eq. 9 and 19 are evaluated on both the anode and cathode. Equation 9 for the cathode requires an additional minus sign. The model is completed with an overall potential constraint, given by

$$\Delta V_{S,A} + \Delta V_{DL,A} + \Delta V_{elyt} - \Delta V_{DL,C} - \Delta V_{S,C} + \Delta V_{ext} = 0 \quad [29]$$

where ΔV_{ext} is equal to the generated voltage V as used in the above equations. This set of equations is a self-consistent one-dimensional steady-state model, including diffuse-layer effects (but without volume constraints for the protons), in which the hydrogen atom on the catalytic surface is considered to be at equilibrium with the bulk gas phase. In this model, both charge-transfer limitations and bulk-transport limitations within the membrane are considered.

Unless otherwise stated, the parameter settings are $\delta = 1$, $\nu = \infty$, and $p^* = 10^{-6}$ bar in the examples below. For the electrochemical kinetic constants, we will generally assume $k_f = k = k_A = k_C$ (with dimension A/bar$^{1/2}$). At the anode side the hydrogen pressure is set to $p_{H_2,A} = 1$ bar, while it is 1 pbar at the cathode ($p_{H_2,C} = 10^{-12}$ bar). The temperature is $T = 800$ K, and thus the factor f is equal to $F/RT = 14.51$ V^{-1}. The open-circuit cell voltage is $V_0 = 1/(2f)\ln(p_{H_2,A}/p_{H_2,C}) \sim 952$ mV.

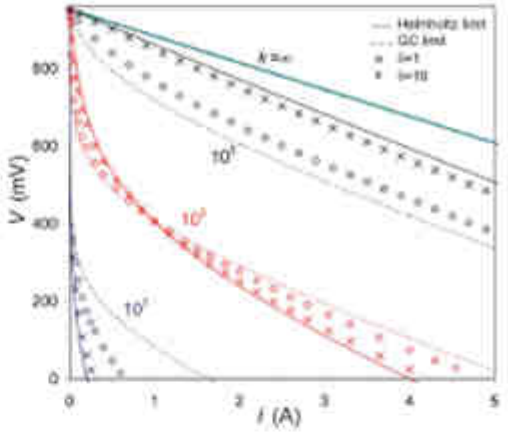

Figure 3. (Color online) Generated voltage V vs current i in a hydrogen concentration cell with a proton-conducting membrane. Parameter values are discussed in the text. k is the kinetic rate constant of both the anode and cathode charge-transfer reaction (with dimension A/bar$^{1/2}$). The case "$k = \infty$" represents absence of kinetic limitation. Symbols represent the numerical model (x: $\delta = 10$; ○: $\delta = 1$), while solid and dashed lines give the Helmholtz and GC limits, respectively.

Though the exact values for the chosen parameter are not very relevant for the objective of the paper (which is to explain the structure of a fuel cell model that includes diffuse-charge effects), we have taken realistic parameter settings: $T = 800$ K is typical for a high-temperature solid-state fuel cell, $V_0 \sim 1$ V is a typical value for an open-circuit voltage, and $p_{H_2,A} = 1$ bar represents atmospheric conditions for the hydrogen gas on the anode side ($p_{H_2,C}$ follows automatically from $p_{H_2,A}$ and V_0). The electrolyte resistance is chosen arbitrary at $R_{elyt} = 68.9$ mΩ, a value that can always be achieved by changing the membrane area or thickness (as long as we can assume that the diffuse layers remain thin). The kinetic rate constant k is varied such that we go from the limit of the purely ohmic transport dominated regime, to parameter settings where the kinetics are rate limiting.

Comparison of full theory with the Helmholtz and GC limits.— We now show that the simple analytical formulas derived above tend to bound the numerical solutions of the complete model and thus may suffice for use in many practical situations. In Fig. 3, we present results for the full theory (symbols are as follows: ○: $\delta = 1$, x: $\delta = 10$) and compare to predictions of the Helmholtz and GC limits, given by Eq. 25 and 27 (solid and dashed lines, respectively). In the limit where kinetic limitations are absent (i.e., $k = \infty$), all models reduce to the simple expression given by Eq. 21, with V decreasing linearly with current i. When finite values are used for the kinetic rate constant, very interesting differences develop between the three approaches. At a relatively high kinetic constant of $k = 10^1$ A/bar$^{1/2}$, we observe that the Helmholtz limit gives the highest prediction for V, after which the numerical results for $\delta = 10$ and 1 follow, with the GC limit giving the lowest prediction for generated voltage V. However, for a value of the kinetic constant which is reduced to $k = 10^0$ A/bar$^{1/2}$, this behavior is significantly modified. The region where $V_H > V_{\delta=10} > V_{\delta=1} > V_{GC}$ is limited from current zero to a current of $i \sim 1$ A. Beyond $i \sim 1$ A, the

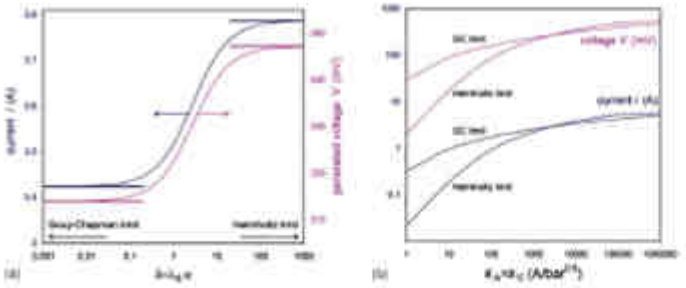

Figure 4. (Color online) Influence of h, the ratio of Nernst layer thickness λ_N to the diffuse-layer thickness, κ^{-1}, on concentration-cell current i and voltage V. (a) Continuous curves are based on full calculations; the Helmholtz limit is based on Eq. 25, and the GC limit on Eq. 27. $k_A = k_C = 10^4$ A/bar$^{1/2}$. (b) Results for i and V in the GC and Helmholtz limit as a function of $k_A = k_C$.

performance sequence is exactly reversed, with V_{GC} higher than predictions of the other calculations. At even lower values of k, the transition point (the value of i above which the GC limit predicts the highest performance) rapidly shifts to zero current (e.g., at $k = 10$ A/bar$^{1/2}$ it is located around $i \sim 0.01$ A). Figure 3 furthermore shows that for the present parameter settings, the Helmholtz limit rather well approximates the exact results if $h \gg 10$, whereas the GC limit closely follows the exact results for $h \ll 1$ (except for $k = 10$ A/bar$^{1/2}$ for a current beyond $i \sim 0.2$ A).

In Fig. 4, we analyze the influence of the parameter h in more detail. For one particular condition given by $k_A = k_C = 10^4$ A/bar$^{1/2}$ and $R_{int} = 91.6$ mΩ, we give in Fig. 4a results for current i and generated voltage V as function of h. In this case, both the current i and the concentration cell voltage V increase with increasing h, while both i and V level off both at very low and very high h. Furthermore, Fig. 4 shows that the limiting expressions are valid (for this calculation) for $h < 0.1$ (for the GC limit) and for $h > 100$ (for the Helmholtz limit).

In Fig. 4b, we only analyze the Helmholtz and GC limits and show the influence of the kinetic constant on the prediction of the two limiting expressions. As already observed in Fig. 3, the ratio $\alpha = (i_{GC}/i_H \sim V_{GC}/V_H)$ is a strong function of k, starting significantly above unity at low k (e.g., $\alpha \sim 15$ at $k = 1$ A/bar$^{1/2}$). Thus, at $k = 1$ A/bar$^{1/2}$, we have in the GC-limit currents and voltages that are ~15 times higher than in the Helmholtz limit. Increasing k, α decreases, and we have $\alpha = 1$ for $k \sim 3000$ A/bar$^{1/2}$, after which α decreases further to reach a minimum value of ~0.82 at $k = 10^5$ A/bar$^{1/2}$. Thus at $k = 10^5$ A/bar$^{1/2}$, predictions for the Helmholtz limit are ~23% above those for the GC limit. With further increasing k, α increases again, finally to reach unity for $k \to \infty$.

Influence of ion volume constraints on reaction rate.— Finally, we analyze the effect of ion volume constraints on the structure of the polarization layer, the electrochemical reaction rate, and concentration-cell performance. In Fig. 5, we show the influence of $v = 1/\phi_\infty$, where v is the number of potential sites per proton (at the proton bulk concentration), on the voltage difference over the Stern and polarization layer, ΔV_S and ΔV_{DL}, for $\Delta V_T = \Delta V_S + \Delta V_{DL} = -10$ ($h = 1$), based on Eq. 11 and 14, while Fig. 6 shows the resulting effect on the cathodic and anodic current (for $k_A = k_C = 1$ A/bar$^{1/2}$). As Fig. 5 shows, for a given ΔV_T, the influence of volume constraints on the Stern and polarization potential differences, as well as on the resulting electrochemical charge transfer rate, can be very large. Whereas without volume constraints, ΔV_S and ΔV_{DL} are about equal in magnitude, when volume constraints are turned on the ratio $\Delta V_{DL}/\Delta V_S$ becomes very large. Simultaneously, the charge transfer rate goes to zero when v goes from infinity to unity.

However, if we run the full concentration cell model (for $k_A = k_C = 10^4$ A/bar$^{1/2}$), we find that at the parameter settings of Fig. 3 there is not such a pronounced influence of volume constraints on cell performance: if we reduce v from $v = 200$ (almost no volume constraints) to $v = 2$ (very significant volume constraints), the generated voltage decreases by a maximum of ~90 mV (namely, at high current, $i \sim 6$ A); see Fig. 6. To increase the influence of volume constraints, we reduce the kinetic rate of the anodic reaction (the anode being the electrode where the protons are typically in excess, which is thus the electrode where volume constraints become most apparent). Reducing k_A by a factor of 10^2 has only a small influence on the generated voltage when $v = 200$, but has a very significant influence when $v = 2$. Now we have a much increased difference in generated voltage between the case of $v = 200$ and 2, namely, up to 260 mV (at $i = 4$ A). Reducing k_A by a further factor of 10^2 results in a difference in generated voltage between the $v = 200$ and 2 case of 270 mV at $i \sim 0.2$ A. In conclu-

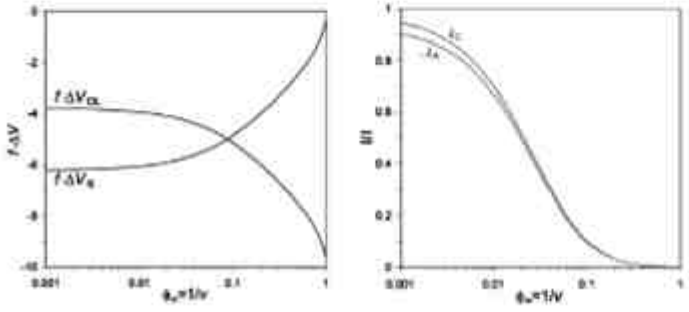

Figure 5. Influence of proton volume constraints on the structure of the polarization layer and the resulting electrochemical reaction rates ($h = 1$, $f\Delta V_T = -10$, $k_A = k_C = 1$ A/bar$^{1/2}$, ρ_{fix} and ρ^+ as in Fig. 3).

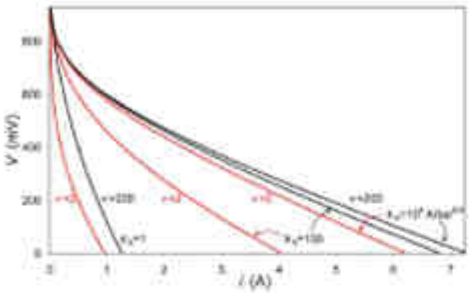

Figure 6. (Color online) Influence of proton volume constraints on the generated cell voltage V as function of current I (k = 1, k_C = 10^3 A/bar$^{3/2}$, R_{ohm} = 68.9 mΩ).

sion, although volume constraints do not have as large an impact in the concentration cell model as they do in a sub-calculation for a polarization layer with fixed ΔV_p, volume constraints can significantly influence predicted cell performance, reducing the generated voltage at a given current, compared to dilute-solution theory.

Conclusions

We have developed simple, general models for diffuse-charge effects in fuel cell membranes and applied them to the case of a steady-state concentration cell. This approach goes beyond the standard model, based on the BV equation for the electron charge transfer rate across a neutral membrane, while remaining analytically tractable and physically transparent. At equilibrium, we present an analytical expression for the proton charge in the polarization layer as a function of hydrogen pressure. In the Helmholtz limit of a very low polarization layer thickness relative to the Stern layer thickness, the state-of-the-art representation of the BV equation for a neutral membrane is recovered, but corrections due to nonzero diffuse charge can also be calculated. In the Helmholtz limit, as well as in the opposite GC limit, simple analytical expressions are obtained for generated voltage as function of current. For the first time in fuel cell modeling, to our knowledge, ion volume constraints are also included in the model via a modified PB equation for the polarization layer and a modified equation for the charge transfer rate. Compared to dilute-solution PB theory, the concentrated solution model predicts a substantially modified structure of the polarization layer and a reduction in the generated cell voltage due to an increased crowding of finite-sized ions.

Acknowledgments

This research was carried out under project no. MC3.05236 in the framework of the Strategic Research Programme of the Materials Innovation Institute in The Netherlands (www.m2i.nl). We thank W. G. Bessler (DLR Stuttgart, Germany), G. J. M. Janssen (ECN Petten, the Netherlands) and K. M. B. Jansen (Delft University of Technology) for very useful discussions during preparation of this manuscript. MZB thanks ESPCI for hospitality and support through the Paris Sciences Chair.

The Massachusetts Institute of Technology and CEA-Grenoble assisted in meeting the publication costs of this article.

References

1. J. O. Bockris and A. K. N. Reddy, *Modern Electrochemistry*, Plenum, New York (1970).
2. A. J. Bard and L. R. Faulkner, *Electrochemical Methods*, John Wiley & Sons, Hoboken, NJ (2001).
3. J. S. Newman, *Electrochemical Systems*, Prentice-Hall, Englewood Cliffs, NJ (1973).
4. R. O'Hayre, S.-W. Cha, W. Colella, and F. B. Prinz, *Fuel Cell Fundamentals*, John Wiley & Sons, Hoboken, NJ (2006).
5. W. G. Bessler, S. Gewies, and M. Vogler, *Electrochim. Acta*, 53, 1782 (2007).
6. A. Frumkin, *Z. Phys. Chem. Abt. A.*, 164, 121 (1933).
7. R. Parsons, *Adv. Electrochem. Electrochem. Eng.*, 1, 1 (1961).
8. B. B. Damaskin, V. A. Safonov, and N. V. Fedorovich, *J. Electroanal. Chem.*, 349, 1 (1993).
9. A. Bonnefont, F. Argoul, and M. Z. Bazant, *J. Electroanal. Chem.*, 500, 52 (2001).
10. A. A. Franco, P. Schott, C. Jallut, and B. Maschke, *Fuel Cells*, 7, 99 (2007).
11. E. M. Itskovich, A. A. Kornyshev, and M. A. Vorotyntsev, *Phys. Status Solidi A*, 39, 229 (1977).
12. A. A. Kornyshev and M. A. Vorotyntsev, *Electrochim. Acta*, 23, 267 (1978).
13. A. A. Kornyshev and M. A. Vorotyntsev, *Electrochim. Acta*, 26, 303 (1981).
14. M. Z. Bazant, K. T. Chu, and B. J. Bayly, *SIAM J. Appl. Math.*, 65, 1463 (2005).
15. K. T. Chu and M. Z. Bazant, *SIAM J. Appl. Math.*, 65, 1485 (2005).
16. A. A. Franco, P. Schott, C. Jallut, and B. Maschke, *J. Electrochem. Soc.*, 153, A1053 (2006).
17. A. A. Franco and M. Gerard, *J. Electrochem. Soc.*, 155, B367 (2008).
18. A. A. Franco, *ECS Trans.*, 6(30), 1 (2007).
19. A. A. Franco and M. Tembely, *J. Electrochem. Soc.*, 154, B712 (2007).
20. S. Chen and A. Kucernak, *J. Phys. Chem. B*, 108, 13984 (2004).
21. M. R. Gennero de Chialvo and A. C. Chialvo, *Phys. Chem. Chem. Phys.*, 6, 4038 (2004).
22. J. X. Wang, T. E. Springer, and R. R. Adzic, *J. Electrochem. Soc.*, 153, A1732 (2006).
23. C. D. Taylor, S. A. Wasileski, J.-S. Filhol, and M. Neurock, *Phys. Rev. B*, 73, 165402 (2006).
24. M. N. M. K. R. Leung, and D. Y. C. Leung, *Fuel Cells*, 7, 240 (2007).
25. K. C. Neyerlin, W. Gu, J. Jorne, and H. A. Gasteiger, *J. Electrochem. Soc.*, 154, B631 (2007).
26. P. Jansen, G. Lindbergh, and G. Sundholm, *J. Electrochem. Soc.*, 149, A437 (2002).
27. M. Eikerling, *J. Electrochem. Soc.*, 153, E58 (2006).
28. M. S. Kilic, M. Z. Bazant, and A. Ajdari, *Phys. Rev. E*, 75, 021502 (2007).
29. P. M. Biesheuvel and M. van Soestbergen, *J. Colloid Interface Sci.*, 316, 490 (2007).
30. M. Z. Bazant, K. Thornton, and A. Ajdari, *Phys. Rev. E*, 70, 021506 (2004).
31. A. A. Kornyshev, *J. Phys. Chem. B*, 111, 5545 (2007).
32. J. J. Bikerman, *Philos. Mag.*, 33, 384 (1942).
33. V. Freise, *Z. Elektrochem.*, 56, 822 (1952).
34. D. Lauren, G. J. Monson, M. Z. Bazant, and J. F. Jensen, *Eur. Phys. J. E*, Accepted.
35. M. Z. Bazant, D. Lauren, and K. Solomon, To be published.
36. G. Singh, G. Cedar, and M. Z. Bazant, *Electrochim. Acta*, 53, 7599 (2008).
37. C. Y. Wang, *Chem. Rev. (Washington, D.C.)*, 104, 4727 (2004).
38. L. Pisani and G. Murgia, *J. Electrochem. Soc.*, 154, B703 (2007).
39. W. G. Bessler, J. Warnatz, and D. G. Goodwin, *Solid State Ionics*, 177, 3371 (2007).
40. H. Ju and C.-Y. Wang, *J. Electrochem. Soc.*, 151, A1954 (2004).
41. R. F. Mann, J. C. Amphlett, M. A. I. Hooper, H. M. Jensen, B. A. Peppley, and P. R. Roberge, *J. Power Sources*, 86, 173 (2000).
42. D. M. Bernardi and M. W. Verbrugge, *J. Electrochem. Soc.*, 139, 2477 (1992).
43. G. Murgia, L. Pisani, M. Valentini, and B. D'Aguanno, *J. Electrochem. Soc.*, 149, A31 (2002).
44. S. Kakac, A. Pramuanjaroenkij, and X. Y. Zhou, *Int. J. Hydrogen Energy*, 32, 761 (2007).

Journal of The Electrochemical Society, 155 (4) B367-B384 (2008)
0013-4651/2008/155(4)/B367/18/$23.00 © The Electrochemical Society

Multiscale Model of Carbon Corrosion in a PEFC: Coupling with Electrocatalysis and Impact on Performance Degradation

Alejandro A. Franco[*,z] and Mathias Gerard

Commissariat à l'Energie Atomique, DRT/LITEN/Département de Technologies de l'Hydrogène/Laboratoire de Composants PEM (LCPEM), 38000 Grenoble, France

In this paper we propose a mechanistic model describing the coupling between the polymer electrolyte fuel cell (PEFC) membrane electrodes assembly (MEA) electrocatalysis and the cathode carbon catalyst-support corrosion. The electrocatalysis description includes our previously introduced irreversible thermodynamics microscale models of the electrochemical reactions (hydrogen oxidation reaction/oxygen reduction reaction) coupled with the catalyst/ionomer interface double layer phenomena. Physically, the model describes the feedback between the instantaneous performance and the intrinsic cathode carbon oxidation process. It allows exploring the impact of the operating conditions (nominal current, reactant gas pressures, temperature, etc.) and the initial electrodes compositions (carbon and platinum loadings) on the PEFC MEA durability. Some numerical simulations show agreement with experimental knowledge already reported in literature, in particular, when the anode chamber is partially exposed to oxygen (induced by polymer electrolyte membrane crossover or fuel starvation), cathode thickness decrease and cell potential decay are predicted. Furthermore, we found that cathode damage increases as platinum loading increases and as platinum nanoparticles size decreases. Moreover, carbon corrosion favors the platinum coarsening; competition between carbon oxidation reaction and electrocatalytic mechanisms is investigated. Simulations also suggest that an "optimal" external load current inducing a "maximal" durability exists. The sensitivities of the electrochemical impedance spectra to the operating conditions and simulated operation time are also provided.

Manuscript submitted October 10, 2007; revised manuscript received December 21, 2007.
Available electronically February 20, 2008.

In order to reach large-scale development and commercialization of low-temperature polymer electrolyte fuel cells (PEFCs), it seems crucial to elucidate membrane electrodes assembly (MEA) degradation mechanisms to help improve both PEFC electrochemical performance and durability and reduce manufacturing cost. Under realistic operation conditions, severe MEA nano-microstructural deterioration is observed inducing the cell voltage degradation.[1,2] In particular, electrode platinum/carbon (Pt/C) damages are attributed to several coupled physicochemical phenomena, such as the oxidation/dissolution of the platinum, the transport of dissolved platinum in the Nafion phase, platinum coarsening, and Nafion degradation.[2,3]

In order to decrease the total Pt-based PEFC efficiency lost due to the high thermodynamic overpotential of the oxygen reduction reaction (ORR), current PEFC cathode electrodes achieve uniform and highly dispersed Pt loadings [high-surface-area Pt particles (~ 80 m^2/g)] by using high-surface-area (~ 100–1500 m^2/g) carbon supports [carbon black (CB) with a high degree of graphitic character, such as Vulcan XC-72, Black Pearls BP 2000, etc.]. These CB supports consist mostly of near-spherical particles of 50 nm diam, that aggregate forming agglomerates of ~ 250 nm diam.[4]

It is largely recognized that CB corrosion also has a major impact on MEA performance degradation. CB supports are thermodynamically unstable at typical cathode operating conditions [the equilibrium Butler–Volmer potential for carbon oxidation to carbon dioxide is a ~ 0.2 V vs reference hydrogen electrode (RHE) at 25°C[5]]. Despite that carbon corrosion reaction reveals to be quite slow at common PEFC operating temperatures (<120°C) with a steady nonzero current demand, severe CB structure damage has been observed after a PEFC power-cycled and start-up/shutdown operation representative of automotive applications.[10-16] In-line direct gas mass spectroscopy analysis successfully detected intermittent peaks of carbon dioxide emission in exhausted gas from the cathode, indicating that carbon corrosion occurs during load cycle in the PEFC.[17,18]

Several experimental studies implied that this degradation is due to the presence of oxygen (O_2) in the anode. Reiser et al.[13] have used two different experimental setups exacerbating the cathode carbon corrosion phenomena: (*i*) two single cells electrically connected in parallel, where the electrodes of one of the cells were exposed to stagnant air and (*ii*) a single cell with two segmented gas flows on the anode, where in one of them oxygen flow was introduced.

In both experimental setups, the authors show that the presence of the oxygen in the anode induces a reverse current between the electrodes increasing the cathode carbon oxidation, which manifests as a significant decrease in the thickness of the cathode and cell performance. In contrast, the anode thickness appeared to be unchanged.

A similar parallel cell setup has been used by Tang et al.[11] highlighting the dramatic catalyst active surface area loss induced by this cathode carbon corrosion phenomenon. According to the same authors, after the shutdown operation, if the anode exhaust port is not closed, air can gradually diffuse into the anode side, creating an oxygen/hydrogen boundary. It is also believed that maldistribution or anode local interruption of hydrogen supply (the so-called fuel starvation phenomenon) improves oxygen permeation from the cathode into the anode.[20]

According to Fuller and Gray,[21] as well as Darling and Jayne,[22] formation of liquid water drops in the anodic channel could also locally block the hydrogen access to the electrode. The corrosion problems of CB in PEFCs have stimulated enormous interest in looking for alternative catalyst supports, such as carbon nanotubes (CNTs).[23] In particular, a multiwalled CNT was found to improve corrosion resistance in acidic liquid electrolytes over Vulcan XC-72.[24]

Many ex situ experiments have been carried out in order to elucidate the kinetics and the mechanisms that control the carbon catalyst-support oxidation in acidic media. However, this process remains poorly understood, maybe due to the complex surface structure of carbon supports that could present pollutants or surface oxides (such as phenols, quinones, lactones, carboxylic acids, etc.), generated by the CB fabrication methods.[5,25,26] It is assumed that the oxidation mechanism in acidic media occurs through the two-step mechanism

$$C + H_2O \leftrightarrow C\text{-}O_{ads} + 2H^+ + 2e^- \quad [1]$$

$$C\text{-}O_{ads} + H_2O \leftrightarrow CO_2 + 2H^+ + 2e^- \quad [2]$$

where O_{ads} is an oxidation intermediate specie.

* Electrochemical Society Active Member.
z E-mail: alejandro.franco@cea.fr

It is believed that supported platinum catalyzes (accelerates) this carbon oxidation reaction (COR). Ex situ potentiostatic hold tests (1.2 V vs RHE applied) have been carried out by Ball et al. in order to study the carbon and platinum stability.[9] The authors showed that at 80°C the percentage of carbon corroded increases with its specific surface area and that increasing the temperature increases the carbon surface oxidation. Moreover, the carbon is oxidized at lower potentials in the presence of platinum, and the higher the mass fraction of platinum is, the higher the production rate of CO_2 is.

Furthermore, following the experiments carried out by Stevens et al.,[29] both the decrease of the platinum nanoparticle size and the increase of the carbon initial surface area led to the increase of the carbon corrosion. The authors also showed that carbon degradation increases as the humidity of the electrochemical environment increases. Additionally, according to Roen et al., carbon corrosion is found to increase by increasing the supported platinum loading.[30]

In PEFC environments, COR mechanism could be strongly affected by the presence of ionomer, solvent (water in both gas and liquid phases), and catalyst, which can modify the carbon stability properties. Maass et al. have recently reported experiments accounting for the PEFC environment: carbon corrosion rates were found to be higher under dynamic operation and to strongly depend on electrode history.[31] The authors highlight the complexity of the COR in the PEFC environment and the necessity of the development of mathematical models to provide more insight. Furthermore, in an operating PEFC, carbon catalyst-support oxidation is expected to be strongly coupled with other aging mechanisms: interpretation of the experimental observations becomes difficult, and thus, analysis through mathematical modeling becomes crucial.

Different modeling approaches allowing simulating PEFC performances have been developed during the last 20 years.[32,33] However, at present, too little modeling work addressing PEFC degradation has been reported.

Reiser et al. have proposed a one-dimensional static model devoted to the calculation of the PEFC electrode/electrolyte electropotential profiles when the anode is partially exposed to air, in order to define the conditions that could be favorable for the cathode carbon oxidation.[17] By using a numerical finite element method, the authors solve a Poisson equation coupled with a conservation equation of the electric charges and a classic Butler–Volmer description of the global hydrogen oxidation reaction (HOR) and ORR.

A similar model has been recently proposed by Meyers and Darling.[34] The model describes how a maldistribution of hydrogen across the fuel electrode can induce both oxygen permeation from the cathode to the anode and cathode carbon corrosion in the fuel starved region. Implications of this reverse current mechanism are explored by simulating a cell with a nonuniform distribution of hydrogen along the fuel channel in both steady-state and transient operation. The mathematical model is a one-dimensional (1D) representation taking into account the reactants transported in the channels and the Butler–Volmer equations.

Fuller and Gray[23] proposed a two-dimensional extension of these models to calculate the electric-potential profile under conditions of partial hydrogen coverage in the anode. Computational fluid dynamics model versions describing carbon corrosion in a PEFC has been also recently proposed.[35]

One common feature of these models is that they describe which operating conditions affect carbon corrosion but do not describe the impact of carbon corrosion on instantaneous performance (any prediction of the transient behavior of the PEFC MEA, such as cell potential degradation, is provided). The instantaneous feedback between performance and aging is not taken into account. Furthermore, the role of the catalyst in the carbon corrosion is not explored (platinum and carbon are treated as a unique single phase). These models do not predict the impact of the initial catalyst and carbon loadings on the PEFC durability.

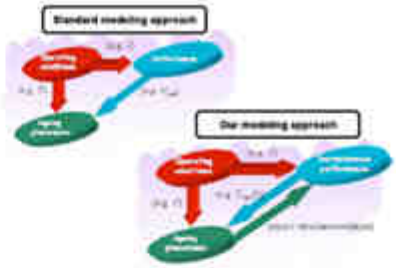

Figure 1. (Color online) Principles behind the standard modeling approach and our modeling approach of aging mechanisms in PEFC environment.

Another common feature is that electrochemistry is described statically: electrochemical reactions are described globally, and the coupling between them and the double-layer phenomena is not taken into account.

In an attempt to provide an engineering tool to suggest guidelines for improving PEFC performance and durability, in this paper we propose a mechanistic model of carbon-catalyst-support corrosion in PEFC environments, including detailed electrochemistry and an explicit description of the instantaneous feedback between performance and the aging carbon catalyst-support process (Fig. 1). The model is suitable for integration in a more global multiscale MEA model and is developed on the basis of an irreversible thermodynamics approach of PEFC electrochemistry previously proposed by us.[5,36,40] The work here complements our recently proposed transient mechanistic model of platinum oxidation-dissolution-electrochemical ripening in the PEFC cathode.[5]

In this paper, we investigate the cumulative effect of the partial exposure of the anode catalyst to oxygen on the transient PEFC performance. The aim here is to provide some insight into the competition between the platinum interface reactions and the cathodic carbon oxidation.

This paper is organized as follows. In the next section, we present the main physical assumptions of our model. Global mathematical structure is also discussed. In the HOR and ORR section, we describe the catalyst anode and cathode models. In the COR section, the cathode carbon oxidation model is provided, followed by a section on membrane models. Then, we discuss some numerical simulation experiments [static operating conditions and dynamic simulation of electrochemical impedance spectra (EIS)], focusing on the sensitivity of the simulated cell response to the nominal current, temperature, pressure, platinum and carbon loading, and PEFC operation time. Finally, we conclude and propose some future work directions in order to improve our model.

Main Assumptions

Global physicochemical hypothesis.— Water transfer phenomenon is a mandatory issue that has been addressed in several low-temperature PEFC models.[41] As a first approximation in our model, we consider the case of an isothermal fuel cell fed with pure oxygen and hydrogen fully saturated with water vapor (to be in agreement with experiments now occurring in our group). In particular, we assume that the polymer electrolyte membrane (PEM) and electrodes are already fully humidified at the simulated operation time $t = 0$ s (PEFC starting operation time). In these conditions, it is not necessary to take into account the transient pore phase flooding by liquid water in the electrode;[36,37] in fact, chemical potential of water becomes the same in pore and ionomer phases, inducing equilibrium conditions and thus no transients. The additional water production in the cathode is assumed to be evacuated through the liquid phase

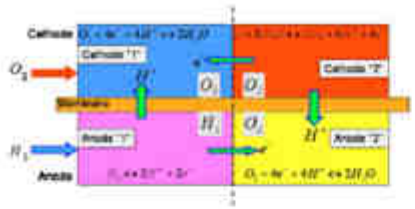

Figure 2. (Color online) Model organization.

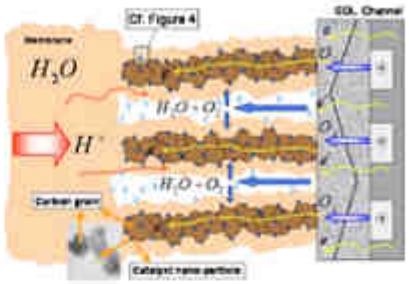

Figure 3. (Color online) Cathode microscale models.

with zero thermodynamic resistance (no chemical potential gradient). These comments are extensive to water description in the gas diffusion layer (GDL). Pressure drop is supposed to be negligible in the GDL and the pore phase, and the additional water production is assumed to be evacuated through the liquid phase.

As we consider pure feeding gases (no nitrogen), hydrogen and oxygen pressure drops in the pore phases are neglected.[24] Produced CO_2 pressure is regarded to be negligible [there is no accumulation of CO_2 in the cathode; the CO_2 diffuse through the GDL, and is evacuated by the channels (cf. COR section)].

In this first step model, oxygen crossover transients are not taken into account. The anodic carbon oxidation and the oxidation-dissolution-electrochemical ripening of Pt nanoparticles are not considered here.

Global model organization.— Our global model organization is presented in Fig. 2. The model consists of four interacting parts: the anode region operating with hydrogen (anode 1), the anode region exposed to oxygen (anode 2), the cathode Pt/ionomer interface (cathode 1), and the cathode C/interface (cathode 2). The couple anode 1/cathode 1 constitutes the direct fuel cell, and the couple anode 2/cathode 2, the reverse one.

In cathode 1, only the ORR is assumed to occur. In cathode 2, the COR is the only electrochemical reaction taking place. These two electrode models interact, e.g., as in the description of the platinum coarsening in cathode 1 driven by the carbon degradation occurring in cathode 2 (see COR section).

In the anode, we account for two different electrochemical reactions: the HOR and the ORR. As shown in Fig. 2, electrons produced by the COR (reverse current $\bar{I}$) in cathode 2, are consumed by the ORR in cathode 1; the protons produced are consumed by the ORR occurring in anode 2 (this favors the COR in cathode 2). Then, the total current entering in the cathodic platinum phase is the addition of the external load current and the reverse current.

The cathodic electrostatic potential ϕ_C is assumed to be the same for platinum and carbon phases (i.e., the same for both cathodes). The anodic electrostatic potential ϕ_A is assumed to be the same for the two anodes (excellent electronic conductivity is assumed between the two anode regions).

Modeled electrode morphology.— The electrode morphology adopted here is similar to that previously introduced in Ref. 37: carbon agglomerate networks (and supported Pt) are assumed to be embedded in a hydrated ionomer medium (the so-called impregnated Nafion phase in our previous papers) (Fig. 3). These structures also include nano/micropores, allowing the reactant gas transport. Obviously, this is a simplistic representation of the high-level complexity of the electrode morphology. However, it allows one to capture the elementary processes taking place in the MEA and to describe, on a physical basis, the coupling between them.

Within a continuum framework, each electrode submodel is designed to describe coupled physicochemical phenomena taking place at different geometrical scales: a microscale transport phenomena description of reactants (H_2/O_2) and charges (protons and electrons) through the electrodes and the membrane thickness, and a spatially distributed microscale model of the reactant diffusion through the hydrated Nafion ionomer layer covering the Pt/C networks, are coupled to a 1D nanoscale mechanistic description of the catalyst-electrolyte interface (anodes 1 and 2, cathode 1) and of the carbon-electrolyte interface (cathode 2) (Fig. 4).

The nanoscale models in anodes 1 and 2 and cathode 1 are similar to those introduced in our previous papers:[25-28] they consist of a compact layer submodel describing the competitive adsorption of the intermediate reaction species and the parasite water molecules on the catalyst surface, and of a diffuse layer submodel in the electrolyte, constituted of protons and spatially fixed counterions (sulfonate sites). The nanoscale model of the C/ionomer interface (cathode 2) is also shown in Fig. 4. Because of the highly complex nature of the C interface, we account here only for the inner layer describing the competitive adsorption of C oxides and water molecules (see COR section).

We note z as the microscale coordinate in the thickness of the impregnated Nafion layer. The interfacial nanoscale model is located at the microscale point $z = e_m$, and the nanoscale coordinate inside the diffuse layers of some nanometers thickness is noted by x. The Nafion/Pt and Nafion/C interfaces are supposed to be flat and located at $z = L$.

Adopted cathodic carbon structure.— In order to simulate the temporal evolution of the cathode thickness (cf. COR section), we account for high carbon surface area/volume ratio by representing the carbon phase as a two-dimensional Sierpinski's carpet projected in the cathode thickness direction (Fig. 5).

The total volume occupied by carbon $V_C(t)$ is given by

$$V_C(t) = S_{\text{electrode}}\left(\frac{8}{9}\right)^n E_{\text{cathode}}(t) = \frac{m_C(t)}{\rho_C} \qquad [3]$$

where n is the Sierpinski's fractal order, $S_{\text{electrode}}$ the electrode geometrical area, $E_{\text{cathode}}(t)$ the (time-dependent) cathode thickness, ρ_C the carbon density, and $m_C(t)$ the instantaneous carbon mass constituting the cathode.

The internal total carbon surface area $\gamma_C(t)$ is

$$\gamma_C(t) = \sqrt{S_{\text{electrode}}}\frac{4}{5}\left[\left(\frac{8}{3}\right)^n - 1\right]E_{\text{cathode}}(t) \qquad [4]$$

By assuming an initial cathodic carbon mass $m_C(t = 0) = 1.05$ mg, $S_{\text{electrode}} = 2.1$ cm^2, [an initial cathode thickness $E_{\text{cathode}}(t = 0) = 15$ μm (cf. Tables I and II)] and using Eq. 3, the fractal order is $n = 16.28$; this value is adopted for the calculations presented in this paper. By using Eq. 4 with these parameter values, the specific carbon surface area in the cathode is $S^C_{\text{specific}} = 1420$ m^2 g^{-1}, in quantitative agreement with experimental measurements.[6] Equation 3 also implies that if we increase the initial carbon mass, the initial cathode thickness $E_{\text{cathode}}(t = 0)$ is increased.

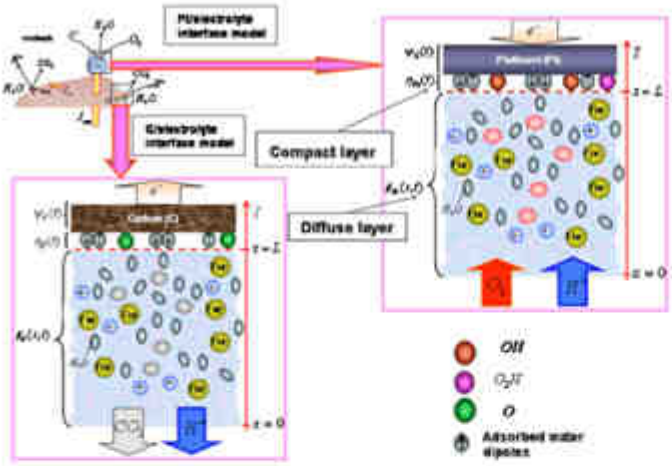

Figure 4. (Color online) Cathode nanoscale models.

HOR and ORR: Anodes 1 and 2 and Cathode 1 Models

These models are similar to those already introduced in our previous papers. We underline here how they couple with the cathode 2 model discussed in the COR section.

Mesoscale mechanisms.— In the anode pore phase, the hydrogen and oxygen partial pressures (p_{H_2}, p_{O_2}) are assumed to obey

$$P_{anode} = p_{sat} + p_{H_2} + p_{O_2}^{anode} \quad [5]$$

where p_{sat} is the water saturation pressure (cf. Table I). In a first approximation, we assume a linear relation between anode hydrogen and oxygen partial pressures and total anode pressure, according to*

$$p_{H_2} = K_\phi(P_{anode} - p_{sat}) \quad [6]$$

$$p_{O_2}^{anode} = (1 - K_\phi)(P_{anode} - p_{sat}) \quad [7]$$

where K_ϕ is a dimensionless constant comprised between 0 and 1 (cf. Table II).

The anodic platinum surface area γ_{Pt}^{anode} is assumed to be partially exposed to oxygen. The platinum surface area γ_{Pt}^{anode1} exposed to hydrogen is given by

$$\gamma_{Pt}^{anode\,1} = K_{S2H}\gamma_{Pt}^{anode} \quad [8]$$

where K_{S2H} is a coefficient comprised between 0 and 1 (cf. Table II). The platinum surface area γ_{Pt}^{anode2} exposed to oxygen is given by

$$\gamma_{Pt}^{anode\,2} = (1 - K_{S2H})\gamma_{Pt}^{anode} \quad [9]$$

In the cathode pore phase, the oxygen partial pressure p_{O_2} is assumed to obey

$$P_{cathode} = p_{sat} + p_{O_2}^{cathode} \quad [10]$$

In the impregnated Nafion layers hydrogen and oxygen transport is assumed to be governed by diffusion[36,37]

$$\frac{\partial C_i}{\partial t} = -\nabla_\perp \cdot J_i = -\nabla_\perp \cdot (-D_i \nabla_\perp C_i) \quad [11]$$

where C_i and D_i are, respectively, the concentration and the diffusion coefficient of the hydrogen (anode 1) and oxygen (anode 2 and cathode 1).

By assuming equilibrated absorption of H_2 and O_2 in hydrated Nafion, we have at $z = 0$ (Henry's laws)[36,37]

$$C_{H_2}(z = 0, t) = \frac{p_{H_2}}{H_{H_2}} \quad [12]$$

$$C_{O_2}(z = 0, t) = \frac{p_{O_2}}{H_{O_2}} \text{ (valuable for both anode 2 and cathode 1)} \quad [13]$$

where H_{H_2} and H_{O_2} are the Henry's coefficients given in Table I.

The fluxes $J_i(i; z = e_{pl})$ are given by the kinetics at the compact layer level, as described in the following section.

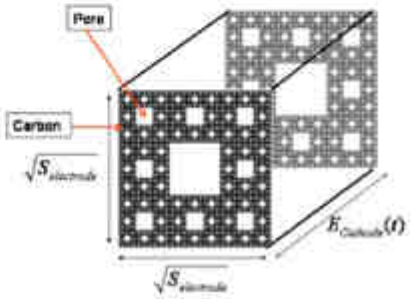

Figure 5. (Color online) Modeled cathode carbon phase morphology.

* In a more complete model, these parameters could be calculated by describing the transient oxygen permeation through the PEM.

Table I. Parameters values used in the numerical simulations.

	Geometrical or physicochemical parameter value	Unit	References
Anode	$\gamma_{\text{Pt}}^{\text{anode}} = 0.0147$	m^2	Estimated
Cathode 1	$\gamma_{\text{Pt}}^{\text{cathode}}(t = 0) = 0.0587$	m^2	Estimated
Cathode 2	$\gamma_C(t = 0) = 0.0147$	m^2	Estimated
Cathode 2	$S^C_{\text{specific}} = 1420$	$m^2\ g^{-1}$	Estimated and 9
Cathode 1	$S^{\text{Pt}}_{\text{specific}} = 130$	$m^2\ g^{-1}$	Estimated
	$E_M = 25 \times 10^{-6}$	m	Measured
	$e_{\text{PE}} = 10^{-6}$	m	Estimated 5-7 and 36-40
	$E_{\text{cathode}}(t = 0) = 15 \times 10^{-6}$	m	Measured
	$E_{\text{channel}} = 1 \times 10^{-3}$	m	Measured
	$E_{\text{GDL}} = 200 \times 10^{-6}$	m	Measured
	$S_{\text{electrode}} = 2.1 \times 10^{-4}$	m^2	Measured
	$d = 2 \times 10^{-10}$	m	5-7 and 36-40
	$L = 5.10^{-10}$	m	Calculated 5
	$n = 16.28$	—	Calculated (Eq. 4)
	$C_{\text{fix}} = 1200$	mol m^{-3}	36-38
Anode 1	$\alpha_{\text{Ha}} = \alpha_{\text{Ha}} = 0.5$		Fitted
Anode 2	$\alpha_{\text{ORR1}} = \alpha_{\text{ORR1}} = 0.5$	—	Fitted
Cathode 1	$\alpha_1 = \alpha_1 = 0.5$	—	Fitted
Cathode 2	$\alpha_{C1} = 0.11\ \alpha_{C2} = 0.1$	—	Fitted
Anode 1	$k_{\text{Ha}} = 10^{-7}\ k_{\text{Ha}} = 10^{-6}$	m s^{-1}	This work and 5-7 and 36-40
	$k_{-\text{Ha}} = 10^{-6}\ k_{-\text{Ha}} = 10^{-5}$		
	$k_{-\text{Ha}} = 10^{-3}\ k_{\text{Ha}} = 10^{-2}$	mol $m^{-2}\ s^{-1}$	This work and 5-7 and 36-40
Anode 2	$k_{\text{ORR1}} = 10^{2}$	$m^4\ mol^{-1}\ s^{-1}$	Fitted
	$k_{-\text{ORR1}} = 10^{-5}$	mol $m^{-2}\ s^{-1}$	Fitted
	$k_{\text{ORR2}} = 10^{2}\ k_{-\text{ORR2}} = 10^{-1}$		
	$k_{-\text{ORR1}} = 10^{-5}$		
	$k_{\text{ORR1}} = 10^{2}$	m s^{-1}	Fitted
Cathode 1	$k_1 = 10^{-2}$	$m^4\ mol^{-1}\ s^{-1}$	This work and 5-7 and 36-40
	$k_{-1} = 1.3 \times 10^{-1}\ k_2 = 10^{-1}\ k_{-2} = 10^{-4}\ k_{-3} = 10^{-4}$	mol $m^{-2}\ s^{-1}$	Fitted
	$k_3 = 10^{3}$	m s^{-1}	Fitted
Cathode 2	$k_{C1} = k^0_{C1} \exp(-\Delta G^C_1/RT)$	mol $m^{-2}\ s^{-1}$	Fitted
	$k_{C1} = k^0_{C1} \exp(-\Delta G^C_1/RT)$		
	$k_{-C1} = k^0_{-C1} \exp(-\Delta G^C_2/RT)$	$m^4\ mol^{-1}\ s^{-1}$	Fitted
	$k_{-C2} = k^0_{-C2} \exp(-\Delta G^C_2/RT)$	$m^3\ mol^{-2}\ s^{-1}$	Fitted
	$k^0_{C1} = 1 \times 10^{-10}$	mol $m^{-2}\ s^{-1}$	Fitted
	$k^0_{C2} = 1 \times 10^{-25}$		
	$k^0_{-C1} = 1 \times 10^{-30}$	$m^4\ mol^{-1}\ s^{-1}$	Fitted
	$k^0_{-C2} = 1 \times 10^{-55}$	$m^3\ mol^{-2}\ s^{-1}$	Fitted
	$\Delta G^C_1 = 6 \times 10^4\ \Delta G^C_2 = 1 \times 10^5$	J mol^{-1}	Fitted
	$\Delta G^C_2 = 6 \times 10^4\ \Delta G^C_2 = 1 \times 10^5$		
	$\varepsilon^{\text{anode}}_{\text{PE}} = 4 \times \varepsilon_0$	C $V^{-1}\ m^{-1}$	5
	$\varepsilon^{\text{cathode}}_{\text{PE}} = 4 \times \varepsilon_0$	C $V^{-1}\ m^{-1}$	36 and 37
	$\varepsilon_{\text{PE}} = 20 \times \varepsilon_0$	C $V^{-1}\ m^{-1}$	36 and 37
	(the same value in both electrodes)		
	$\Delta G^0_C = 1$	J mol^{-1}	5-7, 36, and 37
	(the same value in both electrodes)		
	$\Theta_{H_2O} = 1.435 + 0.0022\lambda - \frac{2.75}{\lambda} - 0.13 \ln \lambda$	—	53
	$D_{H_2} = 2.97 \times 10^{-10} \times T \times 10^{-[1.19(6.28(T_0 - 0.0333)(293 - T^{0.5})T_0 \cdot 308)+3}$	$m^2\ s^{-1}$	5 and 37
	$D_{O_2} = 3.92 \times 10^{-14} \exp(0.025 \times T)$	$m^2\ s^{-1}$	5 and 37
	$D_{H_2O} = 3.1 \times 10^{-7} \times \exp(-2768/T)$	$m^2\ s^{-1}$	5 and 37
	$D_{CO_2} = 0.193 \times 10^{-4}$	$m^2\ s^{-1}$	50
	$C_{CO_2}(t = 0) = 0$	mol m^{-3}	Assumed
	$Q_m = Q_{\text{max}} = 2 \times 10^{-6}$	$m^3\ s^{-1}$	Assumed
	$\rho_C = 2267$	kg m^{-3}	36
	$M_C = 12.011 \times 10^{-3}$	kg mol^{-1}	36
	$\rho_{\text{PE}} = 2147.0$	kg m^{-3}	36
	$P_{\text{sat}} = 10^{-5} \times \exp[23.1961 - [3816.44/(T - 46.13)]]$	Pa	5-7 and 36-40
	$H_{H_2} = 1.09 \times 10^6 \exp(77/T)$	Pa $m^3\ mol^{-1}$	38
	$H_{O_2} = 5.08 \times 10^6 \exp(-498/T)$	Pa $m^3\ mol^{-1}$	5
	$Ew = (0.46\lambda - 0.25)\exp\left[-1190\left(\frac{1}{T} - \frac{1}{298.15}\right)\right]$	S m^{-1}	53
	$\beta = 4$		Assumed
	$K_E = 10^{-2}$	Ω	Assumed

Table II. Default parameters and operating conditions used for the simulations.

Default operating parameter value
$I_{ext} = 0.01$ A
$T = 353$ K
$P_{cathode} = 1.5 \times 10^5$ Pa
$P_{anode} = 1.5 \times 10^5$ Pa
$m_C(t=0) = 1.05$ mg
$W_{Pt} = 40\%$
$s_{Pt} = 1$ nm
$S_{electrode} = 2.1$ cm^2
$m_{Pt}^{anode} = 0.21$ mg
$m_{Pt}^{cathode} = 0.42$ mg
$e_M = 25$ μm
$\lambda = 14$
$K_{1/h} = 0.9$
$K_{\theta} = 0.9$

Nanoscale mechanisms.— The nanoscale models describe the interfacial electrochemical phenomena taking place in anodes 1 and 2 as well as in cathode 2 (cf. Fig. 5). According to our approach,[5,6,34,40] in the compact layer we have

$$\theta_s + \theta_{inter} + \tilde{\theta} + \bar{\theta} = 1 \quad [14]$$

where θ_s is the catalyst surface coverage by the free sites, θ_{inter} is the surface coverage by the reaction intermediates, and $\tilde{\theta}$ and $\bar{\theta}$ the surface coverage by parasite adsorbed water molecules with dipolar moment opposed (up) and directed (down) to the platinum layer. Note that all the coverages are defined at the compact layer level: a simple physically based description of the electrochemical interface is provided, taking into account the coupling between the double layer structure and the electrochemical reactions.

In anode 1, we describe the HOR according to the Tafel–Heyrovsky–Volmer reaction model[39]

$$H_2 + 2s \leftrightarrow 2Hs \quad \text{(Tafel)} \quad [15]$$

$$s + H_2 \leftrightarrow Hs + H^+ + e^- \quad \text{(Heyrovsky)} \quad [16]$$

$$Hs \leftrightarrow s + H^+ + e^- \quad \text{(Volmer)} \quad [17]$$

In anode 2 and cathode 1, for the ORR description, we assume the mechanism[5,36,41]

$$O_2 + H^+ + e^- + s \leftrightarrow O_2Hs \quad (ORR_1) \quad [18]$$

$$O_2Hs + H_2O + 2s \leftrightarrow 3OHs \quad (ORR_2) \quad [19]$$

$$OHs + H^+ + e^- \leftrightarrow H_2O + s \quad (ORR_3) \quad [20]$$

The rates of these elementary steps can be written for the HOR as[39]

$$v_{Taf} = k_{Taf}\theta_s^2 C_{H_2}(L,t) - k_{-Taf}\theta_{Hs}^2 \quad [21]$$

$$v_{Heyr} = k_{Heyr}\theta_s C_{H_2}(L,t)e^{(1-\alpha_{Heyr})f\eta(t)} - k_{-Heyr}\theta_{Hs}C_{H^+}(L,t)e^{-\alpha_{Heyr}f\eta(t)} \quad [22]$$

$$v_{Vol} = k_{Vol}\theta_{Hs}e^{(1-\alpha_{Vol})f\eta(t)} - k_{-Vol}\theta_s C_{H^+}(L,t)e^{-\alpha_{Vol}f\eta(t)} \quad [23]$$

and for the ORR in cathode 1[5,37]

$$v_1 = k_1\theta_s C_{H^+}(L,t)C_{O_2}(L,t)e^{-\alpha_1 f\eta(t)} - k_{-1}\theta_{O_2Hs}e^{(1-\alpha_1)f\eta(t)} \quad [24]$$

$$v_2 = k_2\theta_{O_2Hs}\theta_{H_2O}\theta_s^2 - k_{-2}\theta_{OHs}^3 \quad [25]$$

$$v_3 = k_3\theta_{OHs}C_{H^+}(L,t)e^{-\alpha_3 f\eta(t)} - k_{-3}\theta_s\theta_{H_2O}e^{(1-\alpha_3)f\eta(t)} \quad [26]$$

and, respectively, $\tilde{v}_1$, $\tilde{v}_2$, and $\tilde{v}_3$ for the ORR in anode 2 with kinetic parameter values being not necessarily the same as in Eq. 24-26.

In the previous kinetic equations, $C_{H_2}(L,t)$ is the hydrogen concentration at $x = L$, $C_{O_2}(L,t)$ the oxygen concentration in cathode 1 or in anode 2, $C_{H^+}(L,t)$ the proton concentration, and θ_{Hs}, θ_{O_2Hs} and θ_{OHs} are the surface coverages by adsorbed intermediates. $f = F/RT$, α_i denotes the electronic transfer factors, k_i are the standard rate constants, and $\eta(t)$ is the electrostatic potential drop through the compact layer, defined as[36,38]

$$\eta(t) = \Psi(t) - \phi(x = L,t) \quad [27]$$

where $\Psi(t)$ is the electrostatic potential in the catalyst phase and $\phi(L,t)$ is the electrostatic potential in the Nafion phase just outside the water layer adsorbed on the catalyst with charge surface density $\sigma(t)$. $\eta(t)$ is given by

$$\eta(t) = \Delta\varphi_1 + \Delta\varphi_2 = -\frac{\sigma(t)d}{\varepsilon_{CL}} - \frac{cn^{max}\theta_s(t)\Theta_{H_2O,\mu}\sinh[X(t)]}{\varepsilon_{DL}} \quad [28]$$

where $\Delta\varphi_1$ is the electrostatic potential drop related to the thickness of the adsorbed water layer, $\Delta\varphi_2$ is the potential drop related to the dipolar nature of these molecules, where d is the "effective thickness" of the compact layer (e.g., this layer could consist of several water layers), $a = 2\exp(-\Delta G_C^0/RT)$, ε_{CL} is the electric permittivity of the compact layer, and ε_{DL} is the electric permittivity of the diffuse layer. We have demonstrated that $X(t)$ in Eq. 28 is given by the solution of the transcendental equation[38]

$$(a\sinh[X])\Big/\left(\frac{1}{\Theta_{H_2O}} + \frac{\theta_{inter}}{\theta_s}\frac{1}{\Theta_{H_2O}} + a\cosh[X]\right) = \frac{d^2}{\varepsilon_{DL}\lambda\mu}\sigma - \frac{kTd^2}{\lambda\mu^2}X \quad [29]$$

The value of θ_{Hs} (anode 1) and the values of θ_{OHs} and θ_{OHs} (anode 2 and cathode 2) are given by the solution of the balance equations

$$\frac{n^{max}}{N_A}\frac{d\theta_{Hs}}{dt} = -v_{Vol} + v_{Heyr} + 2v_{Taf} \quad \text{(for anode 1)} \quad [30]$$

$$\frac{n^{max}}{N_A}\frac{d\theta_{O_2Hs}}{dt} = v_1 - v_2 \quad \text{(for anode 2 and cathode 1)} \quad [31]$$

$$\frac{n^{max}}{N_A}\frac{d\theta_{OHs}}{dt} = 2v_2 - v_3 \quad \text{(for anode 2 and cathode 1)} \quad [32]$$

For the surface coverage by dipoles directed toward the electrode, we have[5,37,38]

$$\tilde{\theta} = \left(\frac{a}{2}e^{-X}\right)\Big/\left(\frac{1}{\Theta_{H_2O}} + \frac{\theta_{inter}}{\theta_s}\frac{1}{\Theta_{H_2O}} + a\cosh[X]\right) \quad [33]$$

and for the opposed ones, we have

$$\bar{\theta} = \left(\frac{a}{2}e^{X}\right)\Big/\left(\frac{1}{\Theta_{H_2O}} + \frac{\theta_{inter}}{\theta_s}\frac{1}{\Theta_{H_2O}} + a\cosh[X]\right) \quad [34]$$

θ_s is given by[5,37,38]

$$\theta_s = \frac{1 - \theta_{inter}}{1 + \Theta_{H_2O}a\cosh[X]} \quad [35]$$

The diffuse layer models describe the proton diffusion/electromigration transport (in the nanometric neighborhood of the Pt/C particles), coupled with the electric field generated by the resulting charge distribution. All species are considered as punctual, and the interparticle electrical interaction and water solvatation are neglected. The proton-driving equations are given by

$$\frac{\partial C_{H^+}}{\partial t} = -\nabla_x \vec{J}_{H^+} = -\nabla_x(-D_{H^+}\nabla_x C_{H^+} - fD_{H^+}C_{H^+}\nabla_x\phi) \quad [36]$$

and the electrostatic potential in the diffuse layer by the Poisson's equation as

$$\frac{F}{\varepsilon_{DL}}(C_{H^+} - C_{Ex^-}) = -\nabla_x^2\phi \quad [37]$$

where $\phi(x,t)$ is the electrical potential in the electrolyte phase, and C_{Ex^-} the concentration of the spatially immobile anions modelling the Nafion sulfonate sites.[38]

For the anode 1 diffuse layer model, the boundary conditions are given by

$$J_{H^+}^{\text{anode }1}(x = L) = v_{\text{Hmp}} + v_{\text{Vol}} \quad [38]$$

$$C_{H^+}^{\text{anode }1}(x = 0) = C_{Ex^-} \quad [39]$$

$$\phi_{\text{anode }1}(x = 0) = \phi_{\text{anode }1}^{\text{bulk}} = 0 \text{ (reference potential)} \quad [40]$$

$$E_{\text{anode }1}(x = L) = \frac{\sigma_{\text{anode }1}(t)}{\varepsilon_{DL}} \quad [41]$$

where $\sigma(t)$ is obtained as explained in the following section. This diffuse layer model allows calculating $C_{H^+}(L,t)$ and $\phi(L,t)$. Following the procedure described in Ref. 36-40, the combination of Eq. 27-29 gives $\phi_{Pt}|_{\text{anode}}$, the electrostatic potential in the anode Pt/C phase.

For the cathode 1 ORR, we have

$$J_{H^+}^{\text{cathode }1}(x = L) = -(v_L + v_3) \quad [42]$$

$$C_{H^+}^{\text{cathode }1}(x = 0) = C_{Ex^-} \quad [43]$$

$$\phi_{\text{cathode }1}(x = 0) = \phi_{\text{cathode }1}^{\text{bulk}} \quad [44]$$

$$E_{\text{cathode }1}(x = L) = \frac{\sigma_{\text{cathode }1}(t)}{\varepsilon_{DL}} \quad [45]$$

Again, in cathode 1, this diffuse layer model allows calculating $C_{H^+}(L,t)$ and $\phi(L,t)$. The combination of Eq. 27-29 gives $\phi_{Pt}|_{\text{cathode}}$, the electrostatic potential in the cathode Pt and C phases.

For the anode 2 ORR, we write

$$J_{H^+}^{\text{anode }2}(x = L) = -(\bar{v}_1 + \bar{v}_3) \quad [46]$$

$$C_{H^+}^{\text{anode }2}(x = 0) = C_{Ex^-} \quad [47]$$

$$\phi_{\text{anode }2}(x = L) = \phi_{Pt}|_{\text{anode}} - \eta_{\text{anode }2} \quad [48]$$

$$E_{\text{anode }2}(x = L) = \frac{\sigma_{\text{anode }2}(t)}{\varepsilon_{DL}} \quad [49]$$

The anode 2 diffuse layer model allows calculating $C_{H^+}(L,t)$ for kinetics Eq. 24 and 26, as well as $\phi(x = 0,t)$ as described in the section on membrane models.

The charge density $\sigma_2(t)$ is calculated by the conservation law at the catalyst/electrolyte interface surface[5,36-38] as

$$J_{Pt}^{\text{anode }1}(t) - J_{Ne}^{\text{anode }1}(t) = -\frac{\partial\sigma_{\text{anode }1}(t)}{\partial t} \quad [50]$$

for anode 1 where

$$J_{Ne}^{\text{anode }1}(t) = F(v_{\text{Hmp}} + v_{\text{Vol}}) \quad [51]$$

$$J_{Pt}^{\text{anode }1}(t) = \frac{I_{\text{load}}(t)}{\gamma_{Pt}^{\text{anode }1}} \quad [52]$$

where $\gamma_{Pt}^{\text{anode }1}$ is given by Eq. 8 and $I_{\text{load}}(t)$ by

$$I_{\text{ext}}(t) + \bar{I}(t) = I_{\text{load}}(t) \quad [53]$$

where $I_{\text{ext}}(t)$ is the external load current (the input of the model), and $\bar{I}(t)$ is the reverse current produced by the carbon oxidation (cf. next section).

For cathode 1, we have

$$J_{Pt}^{\text{cathode}}(t) - J_{Ne}^{\text{cathode }1}(t) = \frac{\partial\sigma_{\text{cathode }1}(t)}{\partial t} \quad [54]$$

where

$$J_{Ne}^{\text{cathode }1}(t) = -F(v_L + v_3) \quad [55]$$

$$J_{Pt}^{\text{cathode}}(t) = \frac{I_{\text{load}}(t)}{\gamma_{Pt}^{\text{cathode}}(t)} \quad [56]$$

where $\gamma_{Pt}^{\text{cathode}}(t)$ is the surface of the platinum interface in cathode 1 (cf. next section).

Finally, for the anode 2 ORR, we have

$$J_{Pt}^{\text{anode }2}(t) - J_{Ne}^{\text{anode }2}(t) = \frac{\partial\sigma_{\text{anode }2}(t)}{\partial t} \quad [57]$$

where

$$J_{Ne}^{\text{anode }2}(t) = -F(\bar{v}_1 + \bar{v}_3) \quad [58]$$

$$J_{Pt}^{\text{anode }2}(t) = \frac{\bar{I}(t)}{\gamma_{Pt}^{\text{anode }2}} \quad [59]$$

with $\gamma_{Pt}^{\text{anode }2}$ given by Eq. 9.

The boundary conditions to coupling with the microscale transport description of the reactants (Eq. 11) in the impregnated Nafion are

$$J_{H_2}(L,t) = -(v_{\text{Hmp}} + v_{\text{Vol}}) \quad [60]$$

for anode 1 and

$$J_{O_2}^{\text{I}}(L,t) = -v_L \text{ (or } -\bar{v}_1) \quad [61]$$

for cathode 1 (anode 2).

On the basis of Eq. 27 and 28, the anode 1 and cathode 1 nanoscale models calculate the electrostatic potential in the Pt phase $\phi_{Pt}(t)$ for both electrodes; thus, the cell potential is given by $U_{\text{cell}}(t) = \phi_{Pt}(t)|_{\text{cathode}} - \phi_{Pt}(t)|_{\text{anode}}$.

Carbon Oxidation Reaction: The Cathode 2 Model

The cathode 2 model describes the COR mechanism taking place on the carbon catalyst support surface area represented by the fractal geometry (cf. Fig. 5). The model also describes the temporal evolution of the cathode thickness, as well as the COR-driven Pt coarsening and the augmentation of the GDL/cathode contact resistance.

Mechanisms.— In an analogous way to anode 1 and cathode 1, here we introduce a compact layer model describing the carbon oxidation mechanism (cf. Fig. 4). In a first approximation, the carbon oxidation is modeled by the two-step mechanism in Eq. 1 and 2 with an O intermediate specie. In this compact layer, we have the global equation

$$\theta_* + \theta_{\text{O}} + \tilde{\theta} + \bar{\theta} = 1 \quad [62]$$

The reaction rates are, respectively, for v_{C1} and v_{C2}

$$v_{C1} = k_{C1}\Theta_{H_2O}a_C(t)e^{2(1-\alpha_{C1}(t))\eta_{\text{anode}}(t)}k_{-C1}C_{H^+}^2\theta_{\text{O}}e^{-2\alpha_{C1}(t)\eta_{\text{anode}}(t)} \quad [63]$$

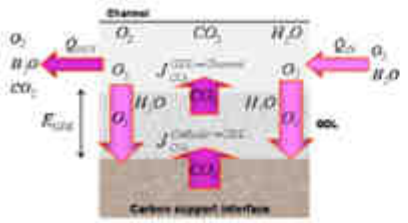

Figure 6. (Color online) Carbon dioxide transfers through the cathode GDL and chamber.

$$v_{C2} = k_{C2}\theta_O\theta_{Ni,0}e^{2(1-\alpha_{C2})\eta_{cath}(t)} - k_{-C2}C_{H^+}^2 C_{CO_2}^{cathode}(t)e^{-2\alpha_{C2}\eta_{cath}(t)} \quad [64]$$

where k_i are the standard rate parameters (cf. Table I), C_{H^+} is the proton concentration [supposed to be the same as in the bulk ($C_{H^+} = C_{H,b}$)], $C_{CO_2}^{cathode}(t)$ is the CO_2 concentration in the cathode, and θ_O is the surface coverage by the absorbed monoatomic oxygen on the carbon interface surface given by the solution of the balance equation

$$\frac{d\theta_O}{dt} = \frac{N_A}{n^{free}}(v_{C1} - v_{C2}) \quad [65]$$

In Eq. 63, $a_C(t)$ is the carbon pure phase activity,[b] and is given by[47]

$$a_C(t) = \frac{m_C(t=0) - m_C^{lost}(t)}{m_C(t=0)} \quad [66]$$

with $m_C(t=0)$ the initial carbon mass in the cathode and $m_C^{lost}(t)$ the cumulated lost carbon mass given by

$$m_C^{lost} = \int_0^t v_{C2}(t)M_C\gamma_C(t)dt \quad [67]$$

where M_C is the carbon molar mass.

The concentration of CO_2 in the cathode is given by the balance equation

$$\frac{dC_{CO_2}^{cathode}}{dt} = f_{CO_2}^{carbon-GDL}\gamma_C(t) - f_{CO_2}^{GDL-channel}S_{electrode} \quad [68]$$

where $f_{CO_2}^{cathode-GDL}$ is the CO_2 molar flux from the cathode to the GDL, given by

$$f_{CO_2}^{cathode-GDL} = +v_{C2} \quad [69]$$

$f_{CO_2}^{GDL-channel}$ is the CO_2 molar flux from the GDL to the cathode chamber (channel), given by

$$f_{CO_2}^{GDL-channel} = -D_{CO_2}\nabla C_{CO_2}^{GDL} \quad [70]$$

where D_{CO_2} is the diffusion coefficient of CO_2 into the GDL. As is shown in Fig. 6, expression 70 can be written as

$$f_{CO_2}^{GDL-channel} = \frac{D_{CO_2}(C_{CO_2}^{cathode} - C_{CO_2}^{channel})}{E_{GDL}} \quad [71]$$

where $C_{CO_2}^{channel}$ is the CO_2 concentration in the cathodic chamber given by

$$\frac{dC_{CO_2}^{channel}}{dt}S_{electrode}E_{channel} = Q_{in}C_{CO_2}^{in} - Q_{out}C_{CO_2}^{channel} + f_{CO_2}^{GDL-channel}S_{electrode} \quad [72]$$

where Q_{in} and Q_{out} are, respectively, the inlet and outlet gas flow in the cathode channel, $C_{CO_2}^{in}$ is the CO_2 concentration in the oxygen inlet flow gas, $C_{CO_2}^{channel}$ the CO_2 concentration in the channel, and $E_{channel}$ the cathode channel thickness.

The C/electrolyte interfacial potential in Eq. 63 and 64 is given by

$$\eta_{cath}(t) = \phi_C(t) - \phi_C(x = L, t) \quad [73]$$

where the electrostatic potential in the carbon phase is known [$\phi_C(t) = \phi_{pl}(t)$ is assumed], and the electrostatic potential at the compact layer level is assumed to be the same as in the bulk [$\phi_C(x = L, t) = \phi_C^{bulk}(t)$, calculated as explained later, in the section on membrane models]. The current produced by the COR is

$$I(t) = F_{tot}^{cathode-2}(t)\gamma_C(t) = 2F(v_{C1} + v_{C2})\gamma_C(t) \quad [74]$$

which constitutes the input for Eq. 53 and 59.

The different coverages are

$$\tilde{\theta} = \left(\frac{a}{2}e^{X}\right) \Big/ \left(\frac{1}{\Theta_{Pt,0}} + \frac{\theta_O}{\theta_s}\frac{1}{\Theta_{Ni,0}} + a\cosh[X]\right) \quad [75]$$

$$\tilde{\theta} = \left(\frac{a}{2}e^{X}\right) \Big/ \left(\frac{1}{\Theta_{Ni,0}} + \frac{\theta_O}{\theta_s}\frac{1}{\Theta_{Ni,0}} + a\cosh[X]\right) \quad [76]$$

with the same transcendental equation calculating X as in the other electrodes (cf. Eq. 29), with $\sigma(t)$ provided by the solution of

$$\Delta\varphi_1(t) = \sigma(t)\frac{d}{\varepsilon_{CL}} = \eta_{cath}(t) - \Delta\varphi_2(t) = \eta_{cath}(t) - \frac{n^{ads}\mu_s(\tilde{\theta} - \tilde{\theta}_0)}{e_{ox}} \quad [77]$$

COR induced degradation mechanisms.— In our model, we assume three phenomena to be directly linked with the COR: the decrease of the cathode electrode thickness [$E_{cathode}(t)$], the decrease of the platinum surface area of the cathode [$\gamma_{Pt}^{cathode}(t)$], and the increase of the cathode/GDL contact resistance [$R_C(t)$].

Cathode thickness temporal evolution.— From Eq. 3, we derive a linear relation between the cathode thickness $E_{cathode}(t)$ and the lost carbon mass $m_C^{lost}(t)$

$$E_{cathode}(t) = \frac{1}{\rho_C S_{electrode}(8.9)^{1/2}}[m_C(t=0) - m_C^{lost}(t)] \quad [78]$$

The total cathode carbon surface area $\gamma_C(t)$ decreases following Eq. 4.

COR-driven platinum coarsening.— Under operating PEFC conditions, the platinum oxidation/dissolution,[46] the electrochemical Ostwald's ripening,[7,8] and the platinum coarsening driven by the COR cathode degradation,[9] contribute to decrease the platinum surface area.

In the model in this paper, we take into account only the platinum coarsening (the two other mechanisms being already implemented in our previous model[47]). This mechanism is assumed to be driven by the decrease of the cathode thickness: when the carbon support degrades, the platinum nanoparticles coarsening is favored

[b] An activity of 1 means that carbon phase is pure, and an activity of 0 means that the carbon phase is not present in any amount. In fact, we imagine carbon as a pure solid phase at $t = 0$ (activity equal to 1). Then, during carbon oxidation, complex surface oxides (impurities, represented in our model with the intermediate species O) appear, affecting the energetics of the system and the ability of the carbon to react and decreasing its activity with time. Obviously, Eq. 66 constitutes only a first approximation model (activities depend not only on composition, but also on pressure and temperature).

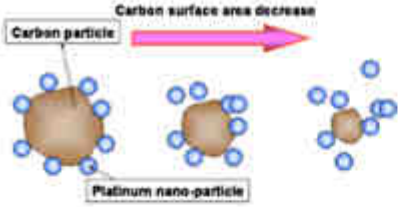

Figure 7. (Color online) Cathodic COR-driven Pt coarsening mechanism.

and they can detach from the carbon support becoming useless.[44,46] Both processes contribute to the active surface area decrease (Fig. 7).

In a first approximation, we assume the mathematical relation for the platinum surface area of cathode 1 [$\gamma_{Pt}^{cathode}(t)$]

$$\gamma_{Pt}^{cathode}(t) = \gamma_{Pt}^{cathode}(t=0)\left(\frac{E_{cathode}(t)}{E_{cathode}(t=0)}\right)^{\beta} \quad [79]$$

where β is a dimensionless positive constant, $E_{cathode}(t=0)$ the initial thickness of the cathode electrode, and $\gamma_{Pt}^{cathode}(t=0)$ is the initial surface area of platinum in cathode 1 given by

$$\gamma_{Pt}^{cathode}(t=0) = \frac{3m_{Pt}}{r_{Pt}\rho_{Pt}} \quad [80]$$

where m_{Pt} is the platinum total mass in the cathode, r_{Pt} is the radius of the platinum nanoparticles (spherical representation),[5] and ρ_{Pt} is the platinum density.

Time-dependent contact resistance.— $R_C(t)$ denotes the time-dependent contact resistance between the cathode electrode and the GDL (Fig. 8). When the cathode is not damaged (no carbon degradation), we assume to have $R_C(t=0) = 0$, and the electrostatic potential in the electrode carbon phase ϕ_C and the one on the current collector $\tilde{\phi}_C$ are the same. However, when the carbon layer is damaged, the electric connectivity among the electrode, the GDL,[47] and the current collector is degraded and then $R_C(t)$ increases.[15,47,48]

In a first approximation, we assume that $R_C(t)$ is a function of $E_{cathode}(t)$ according to

$$R_C(t) = K_R\left(1 - \frac{E_{cathode}(t)}{E_{cathode}(t=0)}\right) \quad [81]$$

where K_R is a positive constant (cf. Table I).

The measured cathode potential becomes

$$\tilde{\phi}_C(t) = \phi_C(t) - R_C(t)I_{load}(t) \quad [82]$$

Remark. In a first approximation, the impregnated Nafion thickness is assumed to be constant. Actually, because the carbon thickness decreases, the Nafion thickness may increase (if Nafion chemical degradation is not significant), increasing even more the reactant transport resistances and the impact on MEA performance degradation rate.

Membrane Models and Exchanged Currents

The membrane is considered impermeable to gases; only protons and water transfer through it. By assuming the electroneutrality in the electrolyte phase, the proton transport is governed by Ohm's law. For the two couples, anode 1/cathode 1 and anode 2/cathode 2, we have

$$\phi_{cathode}^{bulk}(t) = \phi_{anode}^{bulk}(t) - R_{membrane}i_{ far}(t) \quad [83]$$

where $\phi_{cathode}^{bulk}$ and ϕ_{anode}^{bulk} are the electrostatic potentials of the cathode and anode electrolyte bulk ($x = 0$). ϕ_{anode}^{bulk} for anode 2 is calculated by combining Eq. 48 and A-9 (cf. Appendix A). Furthermore, $i_{far}(t) = I_{load}(t)$ for the direct cell (anode 1/cathode 1) and $i_{far}(t) = -\tilde{I}(t)$ for the reverse cell (anode 2/cathode 2).

In Eq. 83, $R_{membrane}$ is the membrane resistance given by[37]

$$R_{membrane} = \frac{E_M}{S_{electrode}\sigma_H(\lambda, T)} \quad [84]$$

where E_M is the membrane thickness, $\sigma_H(\lambda, T)$ the protonic conductivity, and λ the local number of water molecules per sulfonate site (cf. Table I).

Numerical Experiments

Software and parameters.— We have solved our model numerically by means of an in-house code developed within a Simulink/Matlab environment. Discretization of the equations describing the reactants diffusion through the Nafion phase has been directly performed by using Simulink: five grid points have been used for the impregnated layer models. Solutions of the diffuse layer transport equations are analytically approximated as described in Appendix A.

For the simulations shown in this paper, we have chosen the set of physicochemical and geometrical parameters given in Table I. The orders of magnitude of some of the involved parameters is our model are known (e.g., electrical permittivity ε_{CD}), others are estimated [e.g., $\gamma_C(t=0)$] or measured (e.g., $S_{electrode}$). Electrokinetics parameters are obtained following the procedure in Ref. 36: calculated observables (e.g., potential) are fitted with experimental values under well-known operating conditions [e.g., predicted open-circuit voltage (OCV) value obeys Nernstian behavior under equilibrium conditions (i.e., at $I = 0$ A)]. Results shown in all figures in this paper are obtained in the conditions detailed in Table II, unless stated otherwise. The numerical code allows the analysis of the dynamic behavior of the different state variables for different simulated operation times (t_{OT}), including the electrode electronic potentials $\phi_A(t)$ and $\phi_C(t)$ and the cell potential $U_{cell}(t)$, in response to a static or dynamic current demand $I_{load}(t)$ at given temperature T, pressures P_{anode} and $P_{cathode}$, and initial platinum, Nafion, and carbon loadings. Also, the model allows analyzing the temporal evolution of the reverse current $\tilde{I}$, the CO_2 concentration, the cathode electrode thickness [$E_{cathode}(t)$], the cumulated carbon mass loss, and the platinum surface area.

Electrochemical impedance spectroscopy diagrams are also calculated for different t_{OT} and operating conditions. These transient simulations are carried out by following the numerical method previously introduced by us in the context of PEFC modeling:[15,36,40] the calculation is performed by controlling the current in the time domain with subsequent fast Fourier transformation. For the determination of the impedances, as in real experiments, a small sinusoidal signal (1% of the nominal current) is superimposed on the fixed (dc) current level $\bar{I}_{load}$ in order to obtain a linear response of the potentials. This is performed for frequencies ranging from 10^{-2} to 10^{6} Hz in the anticlockwise direction. As in our previous models, prior to starting the simulation of the periodic signal response, the pseudo-steady-state is calculated.

We underline that the full coupled model (i.e., including anode 1, cathode 1, anode 2, and cathode 2) is solved here. Simulations have been carried out on a computer with an Intel Pentium 4 processor 2.8 GHz, 1.24 Gb of RAM, using the commercial Simulink solver ode15s with variable integration time step. The approximate calculation running time for a simulated operation time of 10^6 s is 15 s. Calculation time (including the calculation of the pseudostationary state) of an EIS with 40 frequency points is ~1 min.

[a] In a first approximation, and in contrast to our work in Ref. 5-7, this radius is assumed to be constant here.

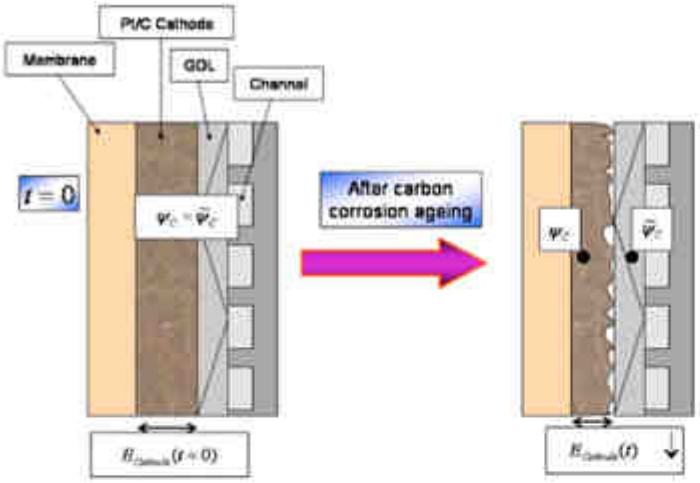

Figure 8. (Color online) COR-driven cathode/GDL contact resistance increase.

Numerical simulations.— Impact of the COR-driven degradation mechanisms on the performance temporal evolution.— In Fig. 9, we compare the polarization curves obtained without and with cathode carbon oxidation for three different simulated operation times (the calculation without the coupling with the COR corresponds to the case $t_{OT} = 0$ s).

For the shorter simulated operation times ($t_{OT} = 0$ and $t_{OT} = 10^4$ s), the cell potential shape agrees with typical experimental cell polarization curves. At $t_{OT} = 10^4$ s, the OCV potential appears to be lower because of the simultaneous presence of hydrogen and oxygen in the anode chamber.

For longer simulated operation times ($t_{OT} = 10^5$ and $t_{OT} = 10^6$ s), the aging impact on performance reveals higher potential at OCV and low-current potential (no considerable impact is observed for intermediate and high operating currents). This behavior agrees with experimental observations[9] and theoretical results discussed later in this paper (cf. Fig. 16).

On the basis of these results, we underline here that carbon oxidation could be another explanation of the experimentally observed PEFC OCV degradation under power cycling conditions, which some authors attribute to the presence of H_2O_2 in the cathode (resulting from H_2 membrane crossover from the anode).[10]

Figure 10 shows the simulated long-term behavior of the anode, cathode, and cell potential, for two static nominal currents. First, we note that ϕ_C and U_{cell} decrease with time because of the COR-driven degradation mechanisms [by not taking into account the COR description, the model calculates time-invariant potentials (not shown here)]. When the cathode carbon phase is degraded, the cathode thickness and the platinum surface area $\gamma_{Pt}^{cathode}$ decrease with time (Fig. 11a and b), the latter following the platinum coarsening mechanism (cf. Eq. 70). Thus, the current density at the platinum level $J_{Pt}^{cathode}$ increases, despite the corrosion current I decline shown in Fig. 12 (this current decreases because carbon mass decreases). In fact, there exists a competition between the COR rate, inducing the $J_{Pt}^{cathode}$ decrease, and the COR-driven platinum coarsening, inducing

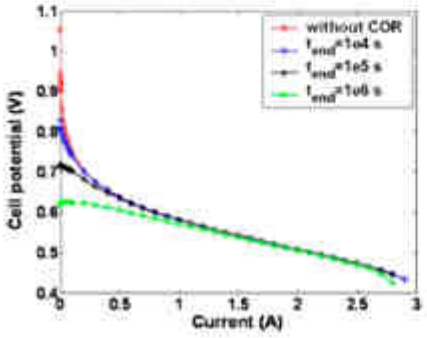

Figure 9. (Color online) Predicted polarization curves for different simulated operation times.

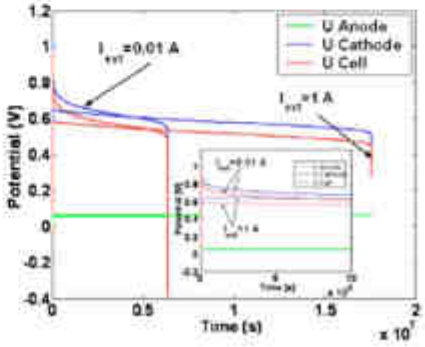

Figure 10. (Color online) Simulated temporal evolution of the electrodes and cell potentials.

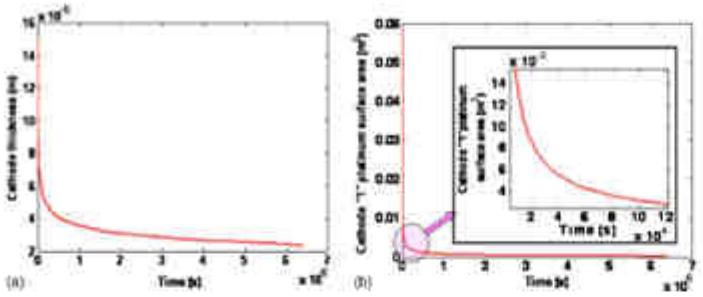

Figure 11. (Color online) (a) Simulated temporal evolution of the cathode thickness and (b) simulated temporal evolution of the cathode platinum area.

the $r_{Pt}^{cathode}$ increase. Prediction of cathode thickness and corrosion current decays has been already reported in experimental literature.[11,31]

For both nominal currents in Fig. 10, at a given simulated operation time (>1000 h), the simulated cathodic potential decreases dramatically. This potential failure occurs when the cathode platinum surface area $\gamma_{Pt}^{cathode}$ (driven by the temporal evolution of the cathode thickness) becomes too small to ensure the demanded current I_{ext}.

The predicted "potential collapse" operation times probably overestimate the durability of typical PEFC because, in the model discussed here, we do not include coupling with other degradation mechanisms. Our previous model in Ref. 5-7 can be coupled to the model here in order to explore the competition between the different aging mechanisms, as we propose for future work[69] (cf. Conclusion section).

The temporal evolution of the cumulative carbon mass loss and the CO_2 concentration in the cathode layer $C_{CO_2}^{cathode}$ at $I_{ext} = 0.01$ A are provided in Fig. 13. The predicted behavior is governed by the carbon corrosion reaction rates (cf. Eq. 63 and 64). The cumulative carbon mass loss increases with time, but the slope decreases because of the platinum surface area decrease (cf. discussion of Fig. 2B). The transient CO_2 concentration behavior is in qualitative agreement with some in-line measurements reported in literature.[18]

The calculated effect of the external nominal current I_{ext} on the MEA durability [cell potential "failure time" (cf. Fig. 10)] is plotted in Fig. 14, which shows a bell-shaped curve suggesting that an "optimal" external current inducing a maximal durability exists. The predicted shape is explained as follows. Lower currents favor COR-driven Pt coarsening (COR is favored). Then, $\gamma_{Pt}^{cathode}$ decreases faster as the current decreases: durability decreases as the nominal current decreases. At higher currents, COR-driven Pt coarsening is slower; however, because the demanded current is higher, failure potential is reached faster as the current increases, and durability decreases again as the current increases.

As shown in Fig. 15, the model captures the effect of the simulated operation time on the EIS pattern. At $I_{ext} = 0.1$ A, for short simulated operation times, EIS consists of a high-frequency capaci-

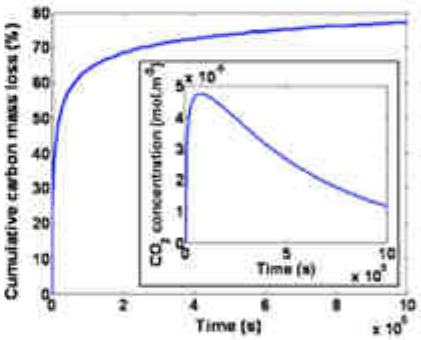

Figure 13. (Color online) Simulated cumulative carbon mass loss and carbon dioxide concentration in the cathode.

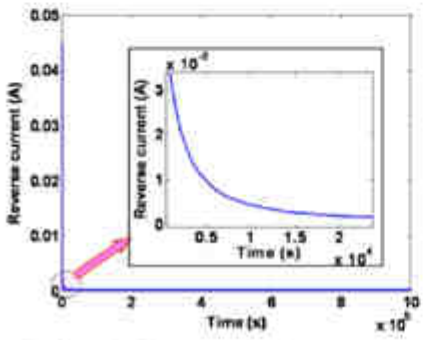

Figure 12. (Color online) Simulated time-dependent reverse current.

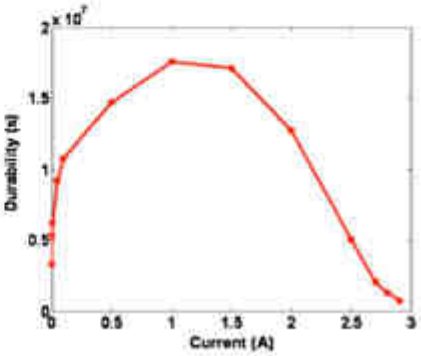

Figure 14. (Color online) Calculated durability (time when "potential failure" occurs) as a function of the external nominal current.

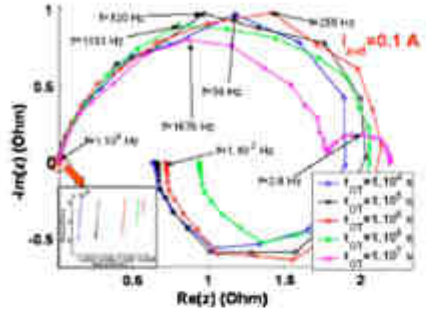

Figure 15. (Color online) EIS sensitivity to the simulated operation time.

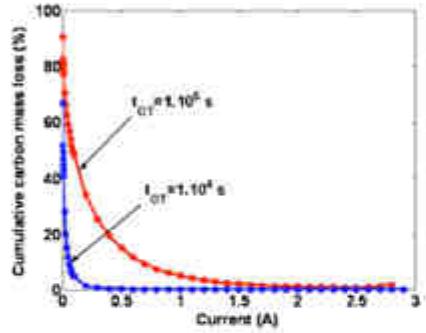

Figure 16. (Color online) Impact of the nominal external current on the cumulative carbon mass loss for two simulated operation times.

tive and of a low-frequency inductive loop, in agreement with experimentally observed patterns.[30] The low-frequency inductive loop is related to the competition between intermediates species on the catalytic surface,[7] and its size decreases with simulated operation time (because $J_{Pt}^{cathode}$ increases). Furthermore, the high-frequency capacitive arc diameter, also linked to interfacial electrochemical phenomena, looks less sensitive to short operating times.

The degradation impact is more significant when the simulated operation time is longer. We can see that the inductive loop becomes a capacitive loop at $t = 1 \times 10^7$ s, as already reported,[18] and the high-frequency loop diameter decreases considerably.

The increase of the amplitude of the low-frequency capacitive loop is associated with the increase of the oxygen transport limitation through the microscale Nafion layer because of the COR-driven rise of $J_{Pt}^{cathode}$.

Moreover, we can see that the high-frequency resistance increases with time. Because in our simulations the membrane resistance remains unchanged (no ionomer degradation mechanisms included), this behavior is due to the $R_C(t)$ increase originated by the COR.

Impact of the operating conditions on the degradation.— In Fig. 16, we show the impact of the external current I_{ext} on the cumulative carbon mass loss [defined as $m_C^{\%} = [m_C^{lost}/m_C(t=0)] \times 100$], for two simulated operation times. It can be observed that when the current increases, the cathodic potential decreases and then the COR becomes slower (cf. Fig. 9); lost carbon mass is higher at lower currents, in agreement with ex situ experimental behaviors.[8] This suggests that, to mitigate cathode carbon oxidation during start-up/shutdown H_2 flow experiments, it seems better to operate the MEA at intermediate/high current values.

Figures 17 and 18 illustrate the effect of the external current I_{ext} on the EIS shape for two simulated operation times. At $t_{OT} = 10^5$ s, the impact of the carbon corrosion on performance is not yet significant and the EIS sensitivity to the nominal current is analogous to the tendency already reported by us by simulating a MEA without describing the aging phenomena[6,17,34,40] (Fig. 17a-c). At low currents, the EIS high-frequency capacitive arc diameter decreases with the demanded current and the inductive loop de-

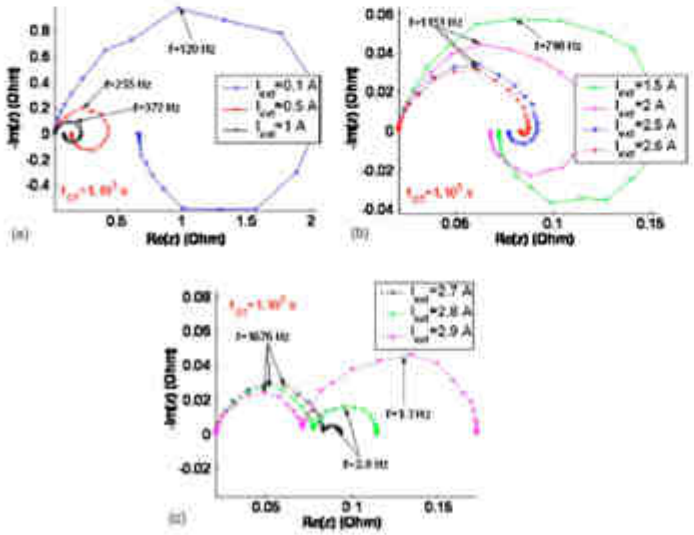

Figure 17. (Color online) Simulated impact of the nominal external current on the EIS pattern at $t_{OT} = 10^5$ s.

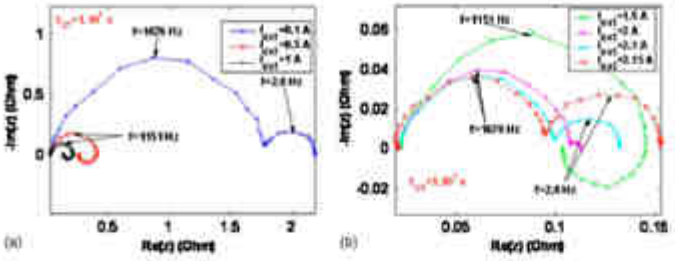

Figure 18. (Color online) Simulated impact of the nominal external current on the EIS pattern at $t_{OT} = 10^5$ s.

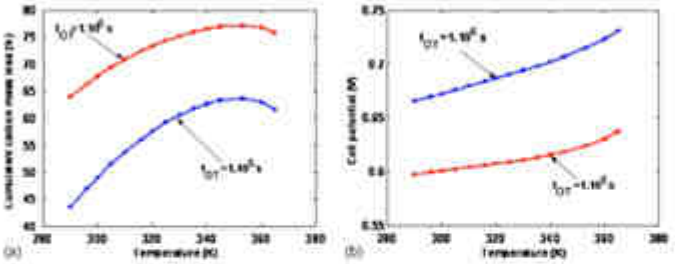

Figure 19. (Color online) (a) Simulated impact of the temperature on the cumulative carbon mass loss and (b) simulated impact of the temperature on the cell potential.

creases. At a sufficiently high current, a low-frequency capacitive loop related to the oxygen transport limitation through the micrometer-scale hydrated Nafion layer appears. As expected, the magnitude of this low-capacitive arc increases as the nominal current increases.

At $t_{OT} = 1 \times 10^5$ s, the COR-driven degradation is quite significant at $I_{ext} = 0.1$ A, which translates as the presence of a low-frequency capacitive loop (not observed for the same current at $t_{OT} = 10^5$ s) (Fig. 18a). However, for intermediate currents ($I_{ext} = 0.5$ and 1 A) the EIS shapes are qualitative and quantitative similar to the ones calculated at $t_{OT} = 10^5$ s because COR impact on performance decreases with current. At higher currents (Fig. 18b), despite that COR process and the driven platinum coarsening are slower, the available platinum surface area becomes too low to ensure the demanded external current. Then, transport limitation low-frequency capacitive arcs appear at lower currents than in the $t_{OT} = 10^5$ s case.

Figure 19 shows the impact of the temperature on the cumulated carbon mass loss and on the performance, for two simulated operation times. As expected from the experimental knowledge, the cathode damage increases with the temperature, up to $T \sim 355$ K; the temperature favors the COR (cf. Table I). For higher temperatures, however, cumulated carbon mass loss slightly decreases; this interesting feature occurs because the remaining $\gamma_{Pt}^{cathode}$ at a given simulated operation time decreases with temperature (COR-driven Pt coarsening is faster as temperature increases), slowing down the carbon corrosion process (cf. discussion of Fig. 2B).

Figures 20 and 21 show the simulated temperature impact on EIS at $I_{ext} = 0.1$ A, for two different operation simulated times ($t_{OT} = 10^5$ and $t_{OT} = 10^5$ s). In both cases, because the hydrated Nafion proton conductivity increases with the temperature (cf. Table I), the high-frequency resistance shifts toward the Nyquist's plan origin.

The predicted sensitivity of the capacitive and inductive loop sizes is related to the temperature-dependent mathematical expressions used to describe the electrochemical reactions, the carbon oxidation mechanism, and the reactant transports. It can be observed that at $t_{OT} = 10^5$ s, the amplitude of the high-frequency capacitive arc is slightly bigger at the highest temperature (Fig. 20).

Otherwise, at $t_{OT} = 10^5$ s, the impact of the COR-driven degradation is significant (cf. Fig. 11a): the amplitude of the high-frequency arc is smaller at the highest temperature (Fig. 21). As shown in Fig. 21, the COR also contributes to decrease the amplitude of these low-frequency inductive arcs. These loops are masked, for a sufficiently high temperature, by a low-frequency capacitive loop, with an amplitude increasing with temperature. In fact, temperature favors the COR-driven platinum coarsening and again, this leads to the decreasing of $\gamma_{Pt}^{cathode}$ and to the increasing of $J_{Pt}^{cathode}$. The increase of this current density leads to early hydrogen and oxygen limitation and manifests as a bigger low-frequency arc amplitude at the highest temperature.

In Fig. 22, we focus on the reactant pressures impact on the cumulated lost carbon mass at two simulated operation times (we assume $P_{anode} = P_{cathode}$). The lost carbon mass increases when the

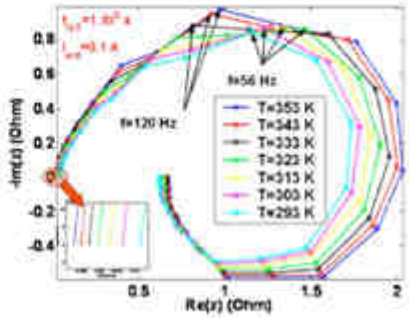

Figure 20. (Color online) Simulated impact of the temperature on the EIS pattern at $t_{OT} = 10^5$ s.

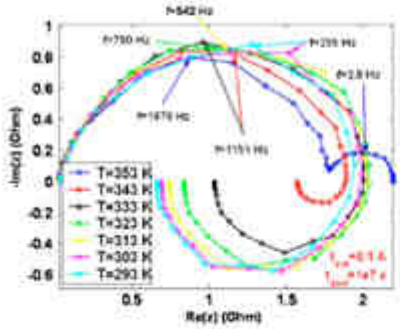

Figure 21. (Color online) Simulated impact of the temperature on the EIS pattern at $t_{OT} = 10^7$ s.

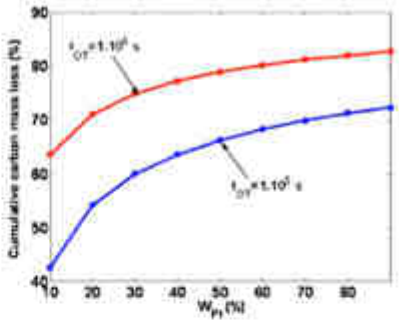

Figure 24. (Color online) Simulated impact of the cathode Pt mass ratio on the cumulative carbon mass loss for two simulated operation times.

anode and cathode pressures are increased together; this is because the increase of the oxygen concentration in the anode side, which improves the cathode COR mechanism, as shown in Fig. 23a. As expected, the cell potential decreases when the oxygen concentration in the anode increases, as shown in Fig. 23b.

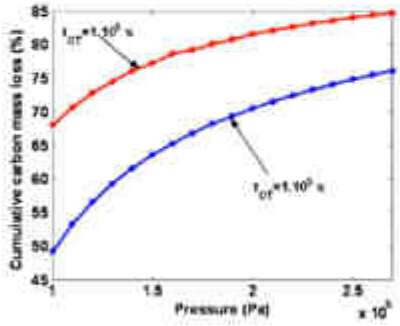

Figure 22. (Color online) Simulated impact of the reactant pressure on the cumulative carbon mass loss (anode and cathode pressures assumed to be the same).

Impact of initial Pt/C loadings and cathode structural properties on COR degradation.— As shown in Fig. 24, the model captures the impact of the initial cathodic platinum mass ratio W_{Pt} on the cumulated carbon mass loss, for two simulated operation times. Increasing the platinum mass in the cathode considerably increases the carbon support damage, in agreement with some experimental results.[39] Hence, it is clear that the cathodic ORR (cathode 1) plays a major role on the COR (cathode 2), by directly consuming the electrons produced by the fuel reaction (the cathode platinum "catalyzes" the carbon corrosion).

The slopes of these curves decrease as the initial W_{Pt} increases; this is because $\tau_{Pt}^{cathode}$ decreases during the simulated PEFC operation, and then, COR is slowed down (cf. Fig. 20).

The impact of W_{Pt} on EIS is provided at two simulated operation times in Fig. 25a and b. At $t_{OT} = 10^5$ s, the impact of platinum loading reveals small (EIS shapes are similar for the three platinum loadings). For $t_{OT} = 10^7$ s, the increase of the initial platinum loading accelerates the carbon damage (low-frequency capacitive arcs increase with the initial platinum loading). In fact, the decrease of the platinum loading delays the COR impact on the PEFC MEA performances.

In Fig. 26, we show the influence of the initial carbon mass on the cumulated carbon mass loss at $t_{OT} = 10^5$ s, for three cathodic platinum mass ratios. It is not surprising to observe that the increase of the initial carbon mass leads to the increase of the cathode damage, because of the increase of the platinum loading (platinum mass ratio Pt/C kept constant).

In contrast to this, in Fig. 27 we show that if we keep constant the initial platinum loading when the carbon mass is increased, then the cathode carbon damage appears to be decreased.

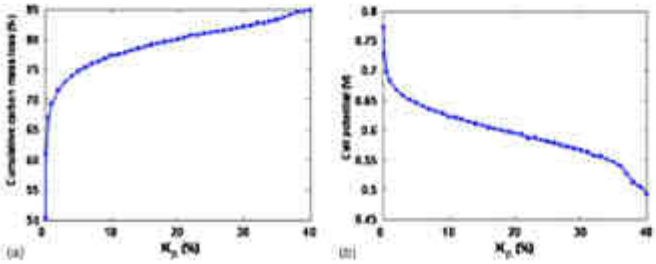

Figure 23. (Color online) (a) Simulated impact of the percentage of oxygen in the anode on the cumulative carbon mass loss and (b) simulated impact of the percentage of oxygen in the anode on the cell potential.

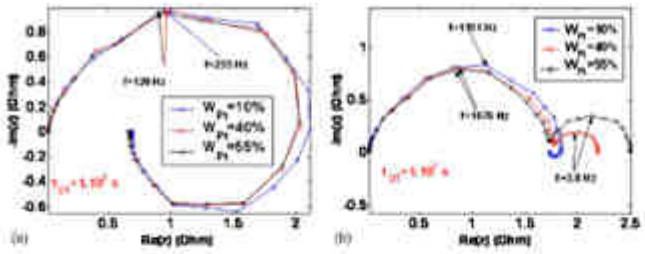

Figure 25. (Color online) Simulated impact of the cathode Pt mass ratio on the EIS shape for two simulated operation times.

Figure 28 illustrates the calculated impact of the platinum nanoparticle radius on the cumulative carbon mass loss for two simulated operation times (in contrast to our previous model in Ref. 5-7, this radius is time invariant here). It can be observed that increasing the radius (decreasing $S_{Pt}^{cathode}/V_{Pt}^{cathode}$) reduces the cumulative carbon mass loss. This is because $J_{Pt}^{cathode}$ decreases as the radius increases, and then the COR appears to be less catalyzed by the platinum. This theoretical behavior is in agreement with the experimental tendencies provided by Stevens et al.[29] and by Adjemian.[71]

The above analysis means that a mechanism such as the electrochemical Ostwald's ripening [contributing to the mean radius increase with time (cf. Fig. 3 and 10 in Ref. 5)] will contribute to slowing down the COR process.

Figure 29 shows the simulated EIS sensitivity to the platinum nanoparticle radius for two simulated operation times. We emphasize that for the shorter operation time ($t_{OT} = 10^5$ s), the radius does not considerably impact the EIS pattern. At $t_{OT} = 10^7$ s, a low-frequency capacitive arc associated with the increase of $J_{Pt}^{cathode}$ and the oxygen transport limitation appears for the smaller radius considered in the calculations. This also illustrates that performance degradation is faster for small catalyst nanoparticle radius, in agreement with results discussed in Fig. 28.

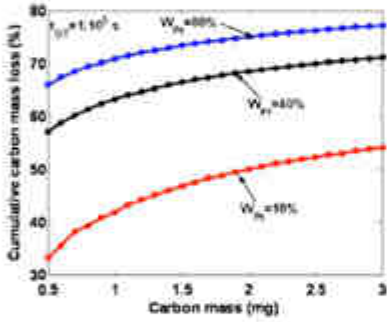

Figure 26. (Color online) Simulated impact of the initial cathode carbon mass on the cumulative carbon loss for three Pt mass ratios ($t_{OT} = 10^7$ s).

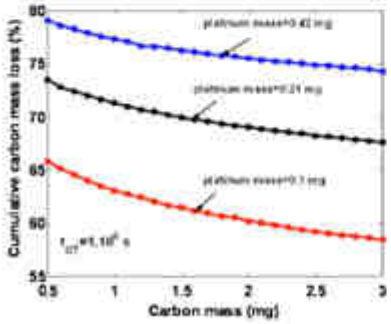

Figure 27. (Color online) Simulated impact of the initial cathode carbon mass on the cumulative carbon loss for three initial Pt loadings ($t_{OT} = 10^6$ s).

Conclusion

In this work, we have proposed a first-step model describing the coupling between the cathode carbon catalyst-support corrosion and the electrocatalysis phenomena taking place in a PEFC MEA, operating with fully hydrated reactant gases. The electrocatalysis description includes our previously introduced irreversible thermodynamics models of the electrochemical reactions on Pt (HOR/ORR) coupled with the Pt/ionomer interface double-layer structure.

The proposed model describes, mechanistically, the feedback between the instantaneous MEA performance and the intrinsic cathode

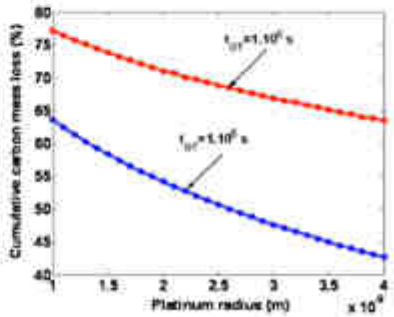

Figure 28. (Color online) Simulated impact of the Pt grain radius on the cumulative carbon mass loss for two operation times.

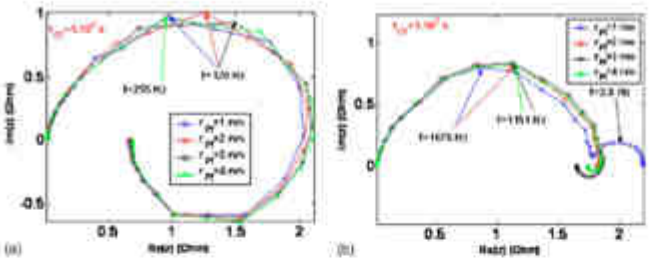

Figure 29. (Color online) Simulated impact of the Pt grain radius on the EIS patterns for two operation times.

carbon oxidation process. In each time step, both the effect of the performance on aging and the effect of aging on the performance are described.

Because of its continuum character, the model could be easily integrated into a more global multiscale model of PEFC response; in our opinion, this is interesting for PEFC engineering practice. The proposed model explicitly represents the different physicochemical phenomena as nonlinear submodels in interaction (modular character) and allows one to study the impact of the operating conditions (nominal current, reactant gas pressures, temperature, etc.) and the initial electrode compositions (carbon and platinum loadings) on the PEFC MEA instantaneous performance and durability.

Numerical simulations have been performed in an in-house computational code (Matlab/Simulink), showing qualitative agreement with already reported experimental behaviors and allowing one to gain a deeper understanding of the governing processes. In particular, the model captures the impact of the simulated operation time on the EIS patterns (temporal multiscale character). The simulations also suggest some other interesting features not yet observed experimentally, such as the existence of an "optimal" external current inducing a maximal durability. Dedicated ex situ (half cells) and in situ (monocells) experiments are now occurring in our group in order to validate these model predictions.

Moreover, further theoretical developments are necessary to improve our model. Ab initio quantum-chemical electronic structure calculations are envisaged in order to better understand the carbon oxidation mechanisms (more thermodynamically favorable pathways, oxidative species, etc.) and to estimate the electrokinetic parameter values with atomistic resolution. We emphasize that we are describing here the electrochemical reactions taking place at the compact-layer level. Thus, our kinetic parameter values cannot be directly compared to the values reported in current mechanistic models, where the electrostatic correction of the activation energy in an electrochemical reaction step is assumed to be given by the electrode potential (defined as $\varphi_s - \phi^{\text{bulk}}$). Furthermore, from its modular character, the model could be easily coupled with a mechanistic description of the other competing aging phenomena (e.g., coupled oxidation, dissolution, and ripening, taken into account elsewhere,[5] or the ionomer chemical degradation).

Additionally, water transfer is a major task in low-temperature PEFCs operating without fully hydrated reactants. It has been demonstrated in particular that the rate of cathode carbon corrosion during cold-start/hot-stop cycling of a PEFC is strongly influenced by reactants relative humidity.[24] In order to extend our model application domain, we plan to couple this model with an irreversible thermodynamics description of the water transfer through the MEA thickness.[33,34]

At the present state, the model is supported on spatial averages of microstructural transport properties (e.g., diffusion coefficient of reactants through the ionomer phase) and on mathematical relations describing cathode/GDL contact resistance evolution and COR-driven Pt coarsening. However, cathode mass transport properties are expected to change during the MEA degradation. In the future, we plan to support the transport phenomenological relations and the COR-driven aging descriptions assumed in the model with microscale resolved mechanisms accounting for the aging-induced morphological structure changes.

Commissariat à l'Energie Atomique (CEA) assisted in meeting the publication costs of this article.

Appendix A: Diffuse Layer Ionic Transport Approximation

For the calculations shown in this paper, in a first approximation, we assume that proton transfer occurring in the nanoscale diffuse layer is quasistationary. By neglecting the temporal term in Eq. 36, we obtain

$$\nabla \cdot \vec{J}_{H^+} = 0 \qquad [A\text{-}1]$$

with $\vec{J}_{H^+}^{\text{anode}} = +\vec{J}_{H^+}^{\text{bulk}}\vec{n}$ for the anode and $\vec{J}_{H^+}^{\text{cathode}} = -\vec{J}_{H^+}^{\text{bulk}}\vec{n}$ for the cathode ($\vec{n}$ being the surface normal to the catalyst).

In the cathode, we have at $x = L$

$$J_{H^+}(x = L) = D_{H^+}\left(\frac{\partial C_{H^+}}{\partial x} + fC_{H^+}\frac{\partial \phi}{\partial x}\right)\vec{n} \qquad [A\text{-}2]$$

and by rearranging terms

$$\frac{J_{H^+}(x = L)}{D_{H^+}} = e^{f\phi}\frac{\partial\left(C_{H^+}e^{f\phi}\right)}{\partial x} \qquad [A\text{-}3]$$

The proton concentration at $x = L$ is given by

$$C_{H^+}(x = L) = e^{f(\phi(L))}\left[C_{H^+}(x = 0)e^{f(\phi(0))} + \frac{J_{H^+}(x = L)I_{\text{integral}}}{D_{H^+}}\right] \qquad [A\text{-}4]$$

with

$$I_{\text{integral}} = \int_0^L e^{f\phi(x)}dx \qquad [A\text{-}5]$$

where $\phi(x)$ is the electrostatic potential in the electrolyte that can be calculated by the Poisson's equation (Eq. 37). This potential can be approximated by

$$\phi(x) = \frac{(E(x = L))}{\Delta L^2}x^2 + \phi_{\text{cathode}}^{\text{bulk}} \qquad [A\text{-}6]$$

which reproduces, quite well, the numerical solution of coupled partial differential Eq. 36 and 37 obtained by the finite-element method.[35,36]

Then, I_{integral} becomes

$$I_{\text{integral}} = \frac{e^{\beta}}{4(\alpha)^{3/2}}\int_0^{-\alpha^2} e^{-(x+\alpha)}\sqrt{-x}\,dx = \frac{e^{\beta}}{4(\alpha)^{3/2}}\left[\sqrt{\pi}\left(\frac{1}{2},\alpha^2\right)\right] \qquad [A\text{-}7]$$

with $\alpha = f|E(x = L)|\Delta L^2$ and $\beta = f\phi^{\text{bulk}}$, and where $\gamma(a,x)$ is the incomplete gamma function. For the anode case, mathematical expressions are similar and we can show that

$$C_{H^+}(x = L) = e^{f(\phi(L))}\left[C_{H^+}(x = 0)e^{f(\phi(0))} - \frac{J_{H^+}(x = L)I_{\text{integral}}}{D_{H^+}}\right] \qquad [A\text{-}8]$$

with

$$\phi(x) = -\frac{|E(x = L)|}{4L^2}x^2 + \phi_{\text{anode}}^{\text{bulk}} \qquad [A\text{-}9]$$

and

$$\Gamma_{oxygen} = \frac{e^0}{\theta \omega l^{+n}} \left[\nu \left(\frac{1}{\lambda} \omega l^{+} \right) \right] \quad [A\text{-}10]$$

List of Symbols

C_{H^+}	proton concentration, mol m^{-3}
C_i	hydrogen or oxygen concentration, mol m^{-3}
C_{fix}	charged fixed sites concentration (sulfonates of Nafion), mol m^{-3}
d	compact layer thickness, m
$D_{CO_2,i}$	diffusion coefficient of CO_2 in the GDL, m^2 s^{-1}
D_i	diffusion coefficient of hydrogen or oxygen in hydrated Nafion, m^2 s^{-1}
D_{H^+}	diffusion coefficient of protons in hydrated Nafion, m^2 s^{-1}
$L_{cathode}$	cathode layer thickness, m
L_{GDL}	gas diffusion layer thickness, m
$L_{channel}$	channel thickness, m
ε_{ion}	impregnated hydrated Nafion layer thickness, m
δ_M	membrane thickness, m
E	electric field, N C^{-1}
f	F/RT, C J^{-1}
F	Faraday's constant, 96,485 C mol^{-1}
I_{HC}	protonic conductivity, S m^{-1}
I_{out}	current demanded by the external load, A
I	crossover current produced by the carbon oxidation reaction, A
I_{cell}	total current crossing the direct fuel cell, A
I_{loc}	local electronic current density at the electrochemical interface (Pt/Celectrolyte -anodic 1 and 2-, Pt/electrolyte -cathode 1-, Celectrolyte -cathode 2-), A m^{-2}
J_i	hydrogen or oxygen molar flux in hydrated Nafion, mol s^{-1} m^{-2}
J_{H^+}	proton molar flux in hydrated Nafion, mol s^{-1} m^{-2}
J_{CO_2}	CO_2 molar flux in the cathode or in the gas diffusion layer, mol s^{-1} m^{-2}
k_1	electronic standard rate constant, m s^{-1}
K_{ion}	fraction of the total anode platinum surface area exposed to hydrogen (anode 1)
K_H	contact resistance constant (cathode), Ω
L	diffuse layer thickness, m
m_C	cathode carbon mass, kg
M_C	carbon molar mass, kg mol^{-1}
m_{Pt}	anode or cathode platinum mass, kg
n	fractal order
n^{max}	maximal quantity of free sites per unit of area of electroactive phase, m^{-2}
N_A	Avogadro's number, 6.022×10^{23} mol^{-1}
P_{sat}	water saturation pressure, Pa
$P_{cathode}$	cathode total pressure, Pa
P_{anode}	anode total pressure, Pa
P_i	hydrogen or oxygen partial pressure in the pore phase, Pa
Q_i	inlet or outlet gas flow in the cathode channel, m^3 s^{-1}
R	ideal gas constant, 8.3143 J K^{-1} mol^{-1}
R_C	cathode/gas diffusion layer contact resistance, Ω
r_{Pt}	platinum nanoparticle radius, m
$S_{membrane}$	geometric surface of the membrane-electrodes assembly, m^2
$S_{specific}$	specific platinum or carbon surface area, m^2 g^{-1}
T	absolute temperature, K
t_{cell}	simulated operation time, s
V_C	total volume occupied by carbon in the cathode, m^3
v_i	electrochemical reaction rate, mol s^{-1} m^{-2}
W_{Pt}	cathode platinum mass ratio, % Pt/C

Greek Symbols

α	elementary reaction step electronic transfer coefficient
β	cathode thickness evolution law constant
γ_i	platinum or carbon surface area, m^2
ΔG_a^0	dipolar chemical adsorption energy, J mol^{-1}
ΔG_r^0	carbon oxidation reaction chemical activation energy, J mol^{-1}
ε_0	electric permittivity of vacuum, 8.854×10^{-12} C^2 J^{-1} m^{-1}
ε_{13}	electric permittivity in the inner layer, C^2 J^{-1} m^{-1}
ε_{24}	electric permittivity in the diffuse layer (electrolyte phase), C^2 J^{-1} m^{-1}
η	electrostatic potential difference between the electroactive and the electrolyte phases (through the compact layer), V
θ	covering fraction of dipoles opposed to the electroactive phase
$\tilde{\theta}$	covering fraction of dipoles oriented toward the electroactive phase
θ_0	covering fraction of free sites
θ_{OH}	covering fraction of the intermediate reaction species Hx
θ_{OHx}	covering fraction of the intermediate reaction species OHx
θ_{COx}	covering fraction of the intermediate reaction species O_2Hx
θ_O	covering fraction of the intermediate reaction species O
θ_{H_2O}	water surface fraction on the electroactive catalyst surface
λ	number of water molecules per sulfonate site
μ	dipolar moment of a water molecule, 0.617×10^{-29} C m
ρ_i	platinum or carbon density, kg m^{-3}
σ	electronic surface density, C m^{-2}
ϕ	electrostatic potential in the electrolyte phase, V
$\tilde{\phi}$	electrostatic potential in the electroactive phase (Pt and C), V

References

1. S. D. Knights, K. M. Colbow, J. St-Pierre, and D. P. Wilkinson, *J. Power Sources*, 127, 127 (2004).
2. Z. Luo, D. Li, H. Tang, M. Pan, and R. Ruan, *Int. J. Hydrogen Energy*, 31, 1831 (2006).
3. Y. Shao, G. Yin, and Y. Gao, *J. Power Sources*, 171, 558 (2007).
4. P. J. Ferreira, G. J. la O', Y. Shao-Horn, D. Morgan, R. Makharia, S. Kocha, and H. A. Gasteiger, *J. Electrochem. Soc.*, 152, A2256 (2005).
5. A. A. Franco and M. Tembely, *J. Electrochem. Soc.*, 154, B712 (2007).
6. A. A. Franco, Abstract 934, The Electrochemical Society Meeting Abstracts, Vol. 2007-1, Chicago, IL, May 6–11, 2007.
7. A. A. Franco, *ECS Trans.*, 6(10), 1 (2007).
8. A. L. Dicks, *J. Power Sources*, 156, 128 (2006).
9. S. C. Ball, S. L. Hodgson, D. Thompsett, and B. Theobald, *J. Power Sources*, 171, 18 (2007).
10. K. Tsuneishi, K. Kawata, S. Tanikawa, and S. Hirai, *Electrochem. Solid-State Lett.*, 9, A473 (2006).
11. H. Tang, Z. Qi, M. Ramani, and J. F. Elter, *J. Power Sources*, 158, 1306 (2006).
12. M. L. Perry, T. W. Patterson, and C. Reiser, *ECS Trans.*, 3(1), 783 (2006).
13. J. Li, P. He, K. Wang, M. Duvas, and S. Yi, *ECS Trans.*, 3(1), 743 (2006).
14. M. F. Mathias, R. Makharia, H. A. Gasteiger, J. J. Conley, T. J. Fuller, C. J. Gittleman, S. S. Kocha, D. P. Miller, C. K. Mittelsteadt, T. Xie, S. G. Yan, and P. T. Yu, *Interface (Netherlands)*, 14, 24 (2005).
15. C. A. Reiser, L. Bregoli, T. W. Patterson, J. S. Yi, D. Tang, M. L. Perry, and T. D. Jarvi, *Electrochem. Solid-State Lett.*, 8, A273 (2005).
16. R. Wakabayashi, D. Constantin, X. François, F. Harel, M.-C. Pera, D. Hissel, and J.-M. Kauffmann, *Int. J. Hydrogen Energy*, 32, 4323 (2007).
17. Y. Fujii, S. Tanikawa, K. Tsuneishi, K. Kawata, T. Nonaka, and S. Hirai, *ECS Trans.*, 3(1), 735 (2006).
18. W. R. Baumgartner, E. Wallnöfer, T. Schaffer, J. O. Besenhard, V. Hacker, V. Peinecke, and P. Prenninger, *ECS Trans.*, 3(1), 811 (2006).
19. W. R. Baumgartner, Oral Communication presented at the CARISMA, European Coordinated Action Workshop on Degradation Issues for MEAs (CP-4), Grenoble, July 5–6, 2007.
20. T. W. Patterson and R. M. Darling, *Electrochem. Solid-State Lett.*, 4, A182 (2001).
21. T. E. Fuller and G. Gray, *ECS Trans.*, 1(8), 345 (2006).
22. R. M. Darling and D. Jayne, *ECS Trans.*, 11(1), 973 (2007).
23. L. Li and Y. Xing, *J. Electrochem. Soc.*, 153, A1823 (2006).
24. X. Wang, W. Li, Z. Chen, M. Waje, and Y. Yan, *J. Power Sources*, 158, 154 (2006).
25. S. C. Ball, *CARISMA European Coordinated Action Workshop on Electrocatalysts for Low Temperature PEFC*, Paris May 15–16, 2007.
26. M. Dweiri, P. Atanassov, I. Xie, and G. Rice, *ECS Trans.*, 1(8), 41 (2006).
27. X. Yu and S. Ye, *J. Power Sources*, 172, 133 (2007).
28. Y. Shao, G. Yin, and Y. Gao, *J. Power Sources*, 171, 558 (2007).
29. D. A. Stevens, M. T. Hicks, G. M. Haugen, and J. R. Dahn, *J. Electrochem. Soc.*, 152, A2309 (2005).
30. L. M. Roen, C. H. Paik, and T. D. Jarvi, *Electrochem. Solid-State Lett.*, 7, A19 (2004).
31. I. Mann, F. Finsterwalder, G. Frank, R. Hartmann, and C. Merten, *J. Power Sources*, 176, 444 (2007).
32. A. Brylewski, *Int. J. Hydrogen Energy*, 30, 1181 (2005).
33. C. Y. Wang, *Chem. Rev. (Washington, D.C.)*, 104, 4727 (2004).
34. J. P. Meyers and R. M. Darling, *J. Electrochem. Soc.*, 153, A1432 (2006).
35. S. Kumar, Abstract 559, The Electrochemical Society Meeting Abstracts, Vol. MA2006-02, Cancun, Mexico, Oct. 29–Nov. 3, 2006.
36. A. A. Franco, PhD. thesis, Université Claude Bernard, Lyon-1 France, no. 2007LYO10239 (2007), http://tel.archives-ouvertes.fr/tel-00189888/
37. A. A. Franco, F. Schott, C. Jallut, and B. Maschke, *Fuel Cells*, 7, 99 (2007).
38. A. A. Franco, F. Schott, C. Jallut, and B. Maschke, *J. Electrochem. Soc.*, 153, A1053 (2006).
39. A. A. Franco, F. Schott, C. Jallut, and B. M. Maschke, Abstract 1296, The Electrochemical Society Meeting Abstracts, Vol. MA2006-02, Québec City, Canada, May 15–20, 2006.
40. A. A. Franco, P. Schott, C. Jallut, and B. M. Maschke, in *Proceedings of the 3rd European PEFC Forum*, Paper B063, Lucerne, July 4–8, 2005.
41. Y. Wang and C. Wang, *Electrochim. Acta*, 50, 1307 (2005).
42. A. Damjanovic, D. B. Sepa, and M. V. Vojnovic, *Electrochim. Acta*, 24, 887 (1979).
43. D. Kondepudi and I. Prigogine, *Modern Thermodynamics: From Heat Engines to Dissipative Structures*, Wiley, New York (1998).
44. T. Toda, H. Uchida, and M. Watanabe, *Electrochim. Acta*, 52, 2997 (2007).
45. J. Wang, G. Yin, Y. Shao, S. Zhang, Z. Wang, and Y. Gao, *J. Power Sources*, 171, 331 (2007).
46. M. Sugimu, G. Xin, and T. Ohsaka, *ECS Trans.*, 3(1), 607 (2006).

47. C. He, J. Desai, G. Brown, and S. Bollepalli, *Interface (Netherlands)*, **14**, 41 (2005).
48. M. E. Debe, A. Schmoeckel, S. Hendricks, G. Vernstrom, G. Haugen, and R. Atanasoski, *ECS Trans.*, **1**(6), 51 (2006).
49. A. A. Franco, Oral Communications presented at the 3rd Annual International Conference on Fuel Cells Durability and Performance 2007, Miami, FL, Nov. 15–16, 2007.
50. R. B. Bird, W. E. Stewart, and E. N. Lightfoot, *Transport Phenomena*, Wiley, New York (1960).
51. E. Adiprasito, Oral Communication presented at the CARISMA, European Coordinated Action Workshop on Degradation Issues for MEAs (CP3-4), Grenoble July 3–5, 2007.
52. B. Du, R. Pollard, M. Ramani, P. Gasteiger, and J. F. Elter, *ECS Trans.*, **5**(1), 271 (2007).
53. F. Meier and G. Eigenberger, *Electrochim. Acta*, **49**, 1731 (2004).
54. H. Kuhn, A. Wokaun, and G. G. Scherer, *Electrochim. Acta*, **52**, 2322 (2007).

Journal of The Electrochemical Society, **154** (7) B712-B723 (2007)
0013-4651/2007/154(7)/B712/12/$20.00 © The Electrochemical Society

Transient Multiscale Modeling of Aging Mechanisms in a PEFC Cathode

Alejandro A. Franco* and **Monroa Tembely**

Commissariat à l'Energie Atomique, Direction de la Recherche Technologique/Laboratoire d'Innovation pour les Technologies Nouvelles et les Nano Matériaux/Département des Technologies de l'Hydrogène/Laboratoire de Composants PEM, 38000 Grenoble Cedex, France

In this paper we propose a mechanistic model of the electrochemical processes in a polymer electrolyte fuel cell cathode, focusing on aging phenomena. The proposed model is based on a nonequilibrium thermodynamics approach previously developed by us, describing the transient response to current perturbations of an electrochemical double layer at the catalyst/Nafion-electrolyte interface. It describes the internal dynamics of the electrochemical double layer, taking into account the coupling between the transport of protons and Pt^{2+} in the diffuse layer, as well as the carbon-supported Pt coarsening, the Pt oxidation, the oxygen reduction reaction, and the water dipoles adsorption in the inner layer. This continuous nanoscale interfacial model is coupled with a microscale model of the oxygen transport through the impregnated Nafion layer and is designed to be coupled with a continuous microscale model of electron, proton, and Pt^{2+} transports through the membrane-cathode assembly thickness. The model allows analysis of cathodic potential sensitivity to the operating conditions, the initial Pt loading, and to the temporal evolution of the electrochemical activity from aging mechanisms. In particular, the influence of simulated time on the impedance spectra pattern is studied.

Manuscript submitted September 19, 2006; revised manuscript received February 13, 2007. Available electronically May 23, 2007.

Electrode durability in state-of-the-art polymer electrolyte fuel cells (PEFCs) is one of the main shortcomings limiting the large-scale development and commercialization of this zero-emission power technology. It is largely observed that the microstructural properties of Pt and Pt-alloy electrodes evolve during the membrane-electrodes assembly (MEA) operation,[1-10] limiting the PEFC lifetime to 300–500 h under some power drive-cycle operating conditions representative of automotive applications.[4] For example, extensive catalytic grain coarsening and redistribution is observed after steady-state and drive-cycle conditions, leading to reduction of the specific catalytic surface area and to loss of the electrochemical activity.[1,5] Furthermore, platinum recrystallization within the Nafion membrane after operation has been also reported.[1,2,5] These spatiotemporal microstructural changes are strongly dependent on the electrode operating conditions and translate into cell potential degradation.[1-10]

Because of the strong coupling between different physicochemical phenomena, interpretation of these experimental observations is difficult, and analysis through mathematical modeling becomes crucial in order to establish microstructure-performance relationships, to elucidate MEA degradation and failure mechanisms, and to help improve both PEFC electrochemical performance and durability.

Analogies with electrical circuit models are often used in order to give some interpretation of the PEFC transient operation, such as in electrochemical impedance spectroscopy (EIS).[11-21] However, these models are not predictive because their impedance parameters have to be fitted at each PEFC operation point. Some authors[14-21] derive analytical expressions of the impedances as functions of the nominal current and reactant concentrations, assuming some simple electrochemical mechanisms within the electrodes, but analytical computations of complex impedances become impossible for more complicated mechanisms. From the fact that their parameters are temporally constant, these models cannot be used in order to predict the temporal evolution of polarization curves and EIS performed on an aging PEFC.

Monte Carlo and ab initio quantum-chemical electronic structure approaches are used in order to investigate some specific aging processes in the PEFC environment.[22-24] However, because of the short time scales regarded, real-time coupling of these atomistic models with continuous descriptions of transport phenomena in a fuel cell still remains out of reach.

Darling and Meyers have proposed an interesting model of the platinum oxidation/dissolution in an acid medium, suitable for continuous PEFC modeling at the component level.[25,26] By using empirical Butler-Volmer equations written in terms of the electrode potential, the authors calculate the carbon-supported platinum surface coverage by oxides. Oxide adsorption is implicitly supposed to take place in the bulk, just outside the catalyst/Nafion interfacial electrochemical double layer. Thus, the coupling with intermediate reaction species of the oxygen reduction reaction (ORR) and the parasite water adsorption on the catalyst surface, expected in realistic PEFC environments,[27,28] is not taken into account.

In a recent paper[29] we proposed a dynamic mechanistic model of an electrochemical interface using an irreversible thermodynamics approach which is easily integrable within a more global, multiscale model, describing transport phenomena in a PEFC MEA.[30-53] This continuous model describes the dynamical behavior of a zero-dimensional inner layer, formed by surface-adsorbed water molecules and electrochemical intermediate reaction species which modify the effective water dipolar density, and the generated electric potential drop between the electronic conductor and the electrolytic phases, coupled with a one-dimensional (1D) diffuse layer submodel in the electrolyte, composed of spatially moving protons driven by diffusion/migration and fixed counterions representing Nafion sulfonates. As an example of application, in that paper we have presented the case of the hydrogen oxidation reaction.

In an attempt to provide an engineering tool allowing the MEA microstructure to be linked with both performance and durability, in this paper we extend the nanoscale model in Ref. 29 to a PEFC cathode. The proposed model describes the internal dynamics of the electrochemical double layer, taking into account the coupling between the transport of protons and Pt^{2+} in the diffuse layer, as well as carbon-supported Pt coarsening, Pt oxidation, the ORR, and the water dipoles adsorption in the inner layer. This continuous nanoscale interfacial model is coupled with a microscale model of the oxygen transport through the impregnated Nafion layer, and is designed to be coupled with a continuous transport micro-scale model of electrons, Pt^{2+}, and protons through the MEA thickness.

The paper is organized as follows. First we present the main geometrical and physical assumptions of our model, indicating its localization into our continuous multiscale approach, briefly recalled in Appendixes A and B.[30-53] In the following section we describe the nanoscale model. We then discuss some numerical experiments, focusing on the sensitivity of the simulated cathode to the cell working conditions (given by nominal current, temperature, oxygen pressure, and initial electrode Pt loading) and time. Finally, we conclude and propose some future work directions in order to improve our model.

* E-mail: alejandro.franco@cea.fr

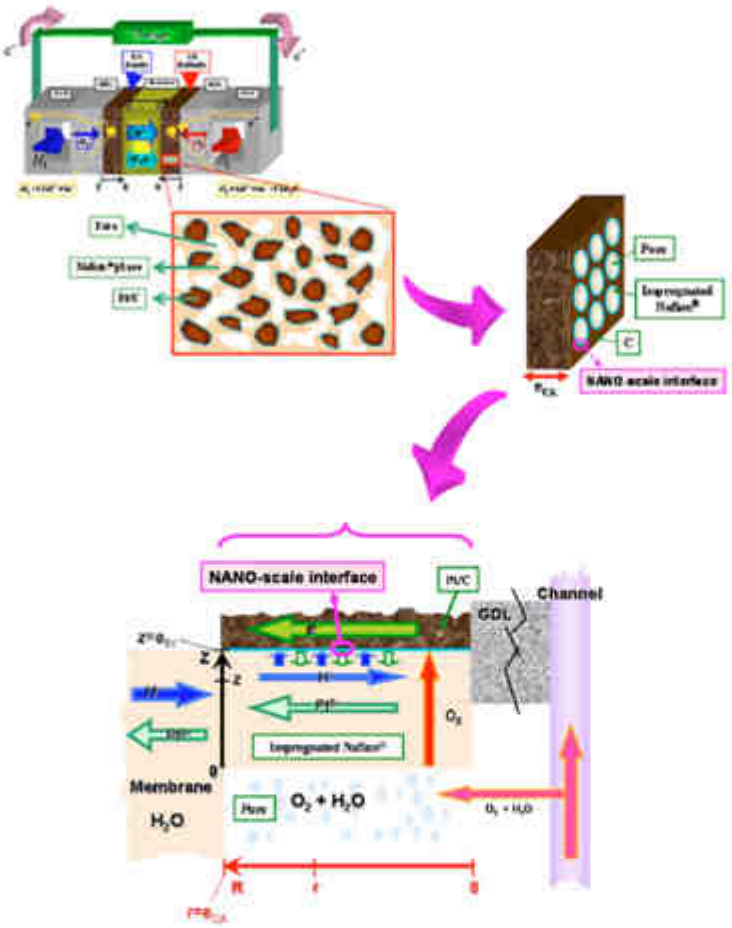

Figure 1. (Color online) Microscale models of the PEFC cathode and situation of the nanoscale model discussed in this paper.[9,32]

Main Assumptions

Figure 1 shows our multiscale model resulting from the coupling of three different geometrical scales:[33] the spatially distributed microscale model of the oxygen diffusion through the on-catalyst impregnated Nafion layer (cf. Appendix A), the microscale transport phenomena description of protons and Pt^{2+} through the membrane-cathode assembly thickness (cf. Appendix B), and the spatially distributed nanoscale dynamic model of the Pt/C-Nafion interface coupled to Pt aging mechanisms, described in the following section. We denote r the microscale coordinate in the thickness of the cathode active layer and z the microscale coordinate in the thickness of the impregnated Nafion layer. The interfacial nanoscale model is located at the microscale point $z = e_{pt}$, and the nanoscale coordinate inside the diffuse layer of some nanometers thickness is noted by x (Fig. 2). The Nafion/Pt layer interface is supposed to be flat and located at $x = L$.[29,30]

For simplicity reasons, in this paper we restrict ourselves to the case of an isothermal PEFC cathode fed with pure oxygen fully saturated with water vapor. In these conditions it does not appear necessary to take into account the pore phase flooding by liquid

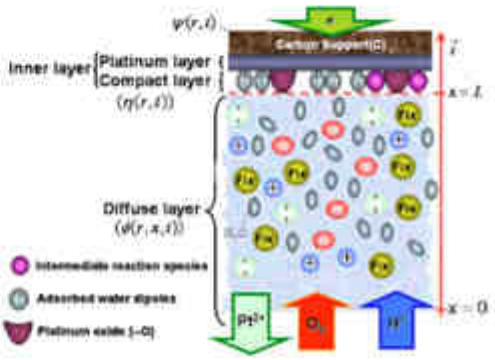

Figure 2. (Color online) The cathodic nanoscale model constituted of a carbon-supported platinum layer, an inner layer, and a diffuse layer.

water and the gas diffusion layer of a typical PEFC,[30,33-35] and the Nafion phase conductivity can be supposed to be constant (cf. Appendix B).

As discussed by us elsewhere,[32,36-38] our approach has been designed in a modular way so that it can be easily coupled with other physicochemical phenomena (water transport, nitrogen diffusion, thermal transfer, pollutants,...).

The Nanoscale Model

The nanoscale model is constituted of an inner and a diffuse layer submodel (cf. Fig. 2). It describes the temporal behavior of the Pt/C/Nafion electrochemical interface. Degradation mechanisms taken into account lead to the decrease with time of the specific catalytic surface area $\gamma(r,t)$ (defined here as the catalyst/Nafion interface area per unit of electrode volume[29,30,32,33]). Under the spherical grains hypothesis, we have in a first approximation

$$\gamma(r,t) = \frac{3}{r_{\mathrm{Pt}}(r,t)} \frac{1}{g_{\mathrm{Pt}}} \left(\frac{w_{\mathrm{Pt}}(r,t)}{c_{\mathrm{CA}}} \right) \quad [1]$$

where $r_{\mathrm{Pt}}(r,t)$ is the average platinum grain radius at each microscale point r (or at each mesh within a spatial discretization according the direction R, cf. Fig. 1), and $w_{\mathrm{Pt}}(r,t)$ is the local carbon-supported platinum mass loading per unit of MEA surface. These quantities are respectively computed through a platinum grain-coarsening submodel and an oxidation/dissolution submodel describing the carbon-supported platinum mass loss, as detailed in the following.

The inner layer submodel.— In this paper, the inner layer model proposed by us in Ref. 29 is split into two parts: a carbon-supported platinum layer submodel which describes the coarsening of platinum grains according to an electrochemical Ostwald's ripening process,[40,41] and a compact layer submodel describing the adsorption of ORR intermediates, platinum oxide, and water dipoles on the hypothetical flat catalyst surface at $x = L$ resulting from Eq. 1 (cf. Fig. 2). Because of its modular character, the model structure and the couplings here are independent of the complexity of the used submodels.

The carbon-supported platinum layer submodel: calculation of $r_{\mathrm{Pt}}(r,t)$.— In the carbon-supported platinum layer submodel, an Ostwald's ripening process is mathematically described, allowing calculation of the temporal evolution of the mean carbon-supported platinum grain radius. As a first approximation, we assume that the platinum grain coarsening is controlled both by dissolution and deposition. Following Sun,[42] we assume the hypothetical surface-energy-driven reaction

$$\mathrm{M(Pt)} \underset{k_{\mathrm{g}}}{\overset{k_{\mathrm{d}}}{\rightleftharpoons}} \mathrm{M(Pt^{z+})} + z e^- \quad [2]$$

where M(Pt) represents a Pt monomer in a grain of radius r_{Pt} diluting in the hydrated Nafion phase, and $\mathrm{M(Pt^{z+})}$ the diluted monomer depositing on the grain (Fig. 3). We associate with this reaction the kinetic parameters k_{d} and k_{g}, respectively, the rate constants of surface-energy-driven dissolution, and deposition at temperature T. We emphasize that electrons in Eq. 2 are supposed to be exchanged between grains through the carbon support and do not participate in the electrochemical reactions described in the following section. Then, even under open-circuit conditions, where the outer current is zero, ions are exchanged laterally between the grains via the electrolyte, and a parallel electronic current runs through the carbon support.[40]

We can write k_{d} as the Boltzmann factor

$$k_{\mathrm{d}} = A_{\mathrm{d}} \exp\left(-\frac{E_{\mathrm{d}}}{RT} \right) \quad [3]$$

where E_{d} is the apparent activation energy for the hypothetical dissolution (J/mol) and A_{d} a pre-exponential factor. When an infinite size grain transforms to a grain of radius r_{Pt}, the molar Gibbs free energy of M(Pt) increases, and this leads to a reduction of the apparent dissolution activation energy, which can be written as

$$E_{\mathrm{d},\infty} - E_{\mathrm{d}} = -\Delta E_{\mathrm{d}} = \alpha_{\mathrm{c,Pt}} \Delta G_{\mathrm{Pt}} \quad [4]$$

where $E_{\mathrm{d},\infty}$ is the activation energy of a grain of infinite size, and

$$\Delta G_{\mathrm{Pt}} = \frac{2\chi v_{\mathrm{Pt}}}{r_{\mathrm{Pt}}(r,t)} \quad [5]$$

where χ and v_{Pt} are the Pt/Nafion interfacial energy and the molar volume of platinum grains, respectively. Following Sun, we have supposed here that the variation of the molar free energy is proportional to the variation of the activation energy (this is analogous to the assumption currently adopted for electrochemical reactions when one writes Butler-Volmer equations). Thus the dissolution flux is

$$j_{\mathrm{d}} = k_{\mathrm{d}} = A_{\mathrm{d}} \exp\left(-\frac{E_{\mathrm{d},\infty}}{RT} + \frac{\alpha_{\mathrm{c,Pt}} 2\chi v_{\mathrm{Pt}}}{RT} \frac{1}{r_{\mathrm{Pt}}(r,t)} \right) \quad [6]$$

The deposition flux is supposed to be given by

$$j_{\mathrm{g}} = k_{\mathrm{g}} C_{\mathrm{Pt^{z+}}}(r, x = L, t) \quad [7]$$

where $C_{\mathrm{Pt^{z+}}}(r, x = L, t)$ is the platinum ion concentration in the Nafion phase, computed by the diffuse layer model. Finally, the average grain radius variation rate can be written as

$$\frac{dr_{\mathrm{Pt}}}{dt} = (j_{\mathrm{g}} - j_{\mathrm{d}}) v_{\mathrm{Pt}} \quad [8]$$

allowing, by numerical integration, calculating $r_{\mathrm{Pt}}(r,t)$ in Eq. 1.

The compact layer submodel.— The compact layer is formed by the ORR intermediate reaction species, the Pt oxides, and the water molecules adsorbed on the time-dependent hypothetical flat surface located at $x = L$ (cf. Fig. 2). Thus, on that surface, we have

$$1 = \theta_* + \theta_{\mathrm{inter}} + \theta_{\mathrm{O}} + \vec{\theta} + \overleftarrow{\theta} = \theta_* + \theta^{\mathrm{I}} + \vec{\theta} + \overleftarrow{\theta} \quad [9]$$

where θ_* is the surface coverage by free sites, θ_{inter} the surface coverage by the ORR intermediates, θ_{O} the surface coverage by monoatomic oxygen of platinum oxide, and $\vec{\theta}$ and $\overleftarrow{\theta}$ the surface coverage by adsorbed water molecules with dipolar moment opposed («up») and directed («down») to the platinum layer (two-state hypothesis[29,44,45]).

In our model, an interfacial electrostatic potential difference between the catalyst and the hydrated Nafion phase (cf. Fig. 2) governs the development of the set of electrochemical reactions steps on the hypothetical flat surface with a charge surface density $\sigma(r,t)$. As in Ref. 29, this potential difference is denoted by $\eta(r,t)$ and it is a function of time according to

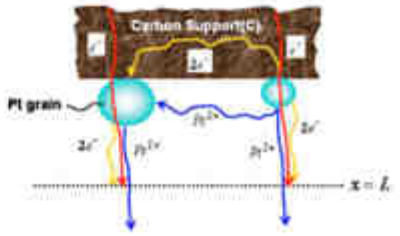

Figure 3. (Color online) Schematic representation of the Pt grain coarsening controlled both by dissolution and deposition within the Pt layer submodel. In this submodel, electrons and Pt^{z+} are exchanged between grains (electrochemical Ostwald's ripening) and between the platinum and the compact layer through the hypothetical interface at $x = L$ (the red arrows represent electrons coming from the external load).

$$\eta(r,t) = \phi(r,t) - \phi(r,L,t) \quad [10]$$

where $\phi(r,t)$ is the electrostatic potential in the catalyst phase and $\phi(r,L,t)$ is the electrostatic potential in the Nafion phase just outside the water layer adsorbed on the flat surface.[29,49,50]

In order to describe mathematically the ORR, we assume a mechanism constituted by three reaction steps[30,51,52]

$$O_2 + H^+ + e^- + s \rightleftharpoons O_2Hs \quad [11]$$

$$O_2Hs + H_2O + 2s \rightleftharpoons 3\ OHs \quad [12]$$

$$OHs + H^+ + e^- \rightleftharpoons H_2O + s \quad [13]$$

where s is a free site on the flat, time-dependent surface. Neglecting the interaction between the adsorbed intermediates and between the intermediates and the water molecules, (Langmuir's behavior[53]), the rates of these elementary steps can be written as

$$v_1 = k_1\theta_s C_{H^+}(r,L,t)C_{O_2}(r,L,t)e^{\alpha_1 f\eta(r,t)} - k_{-1}\theta_{O_2Hs}e^{(1-\alpha_1)f\eta(r,t)} \quad [14]$$

$$v_2 = k_2\theta_{O_2Hs}\Theta_{H_2O}\theta_s^2 - k_{-2}\theta_{OHs}^2 \quad [15]$$

$$v_3 = k_3\theta_{OHs}C_{H^+}(r,L,t)e^{\alpha_3 f\eta(r,t)} - k_{-3}\theta_s\Theta_{H_2O}e^{(1-\alpha_3)f\eta(r,t)} \quad [16]$$

where $C_{O_2}(r,L,t)$ is the oxygen concentration and $C_{H^+}(r,L,t)$ is the proton concentration at $x = L$ (cf. Fig. 2), both calculated by the diffuse layer Eq. 33 and 34. θ_{O_2Hs} and θ_{OHs} are the surface coverage by adsorbed ORR intermediates, Θ_{H_2O} the water activity in the Nafion matrix,[a] α_1 and α_3 the electronic transfer coefficients, and $f = F/RT$.

We model the platinum oxidation/dissolution using the reaction mechanism proposed by Darling and Meyers[25,28]

$$s \rightleftharpoons Pt^{2+} + 2e^- \quad \text{(Electrochemical platinum dissolution)}[b] \quad [17]$$

$$s + H_2O \rightleftharpoons Os + 2H^+ + 2e^- \quad \text{(electrochemical platinum oxide formation)} \quad [18]$$

$$Os + 2H^+ \rightleftharpoons Pt^{2+} + H_2O \quad \text{(chemical dissolution of the platinum oxide)} \quad [19]$$

where Os represents the platinum oxide. Therefore the platinum mass loss becomes from steps 17 and 19.

Again, neglecting the interaction between the adsorbed intermediates and between the intermediates and the water molecules, the rates of the different reaction steps are given by

$$w_1 = b_1\theta_s e^{(1-\beta_1)f\eta(r,t)} - b_{-1}C_{Pt^{2+}}(r,L,t)e^{-\beta_1 f\eta(r,t)} \quad [20]$$

$$w_2 = b_2\theta_s\Theta_{H_2O}e^{(1-\beta_2)f\eta(r,t)} - b_{-2}\theta_{Os}C_{H^+}(r,L,t)^2 e^{-\beta_2 f\eta(r,t)} \quad [21]$$

$$w_3 = b_3\theta_{Os}C_{H^+}(r,L,t)^2 - b_{-3}C_{Pt^{2+}}(r,L,t)\Theta_{H_2O} \quad [22]$$

where $C_{Pt^{2+}}(r,L,t)$ is the dissolved platinum concentration calculated from Eq. 35, b_i and b_{-i} are the rate constants for each step, and β_i the electronic transfer coefficients.

The compact layer submodel also describes the evolution of the surface dipolar density, which depends on the water adsorption on the flat surface, coupled with the intermediate electrochemical species through Eq. 9. This submodel allows calculation of the resulting electric potential drop $\eta(r,t)$ in Eq. 10. As discussed in Ref. 29, according to the superposition principle of electrodynamics, $\eta(r,t)$ can also be written as the sum of the drop related to the thickness of the adsorbed water layer ($\Delta\varphi_1$), and the drop related to the dipolar nature of these molecules ($\Delta\varphi_2$). Both contributions are functions of the charge surface density $\sigma(r,t)$, which is calculated by the charge conservation law at the platinum layer/Nafion interface, as detailed in the following parts. Using a mean field approximation, we show that $\eta(r,t)$ is given by

$$\eta(r,t) = \Delta\varphi_1 + \Delta\varphi_2 = -\frac{\sigma(r,t)d}{\varepsilon_{CL}} - \frac{\alpha n_s\Theta_{H_2O}\mu\ \sinh[X(r,t)]}{\varepsilon_{CL}} \quad [23]$$

where $\alpha = 2\exp(-\Delta G_2^0/RT)$, $n_s = \theta_s n^{max}$, ε_{CL} is the electric permittivity of the compact layer, and ε_{DL} is the electric permittivity of the diffuse layer. In a similar way to the anodic case in Ref. 29, we can demonstrate that $X(r,t)$ in Eq. 23 is given by the solution of the transcendental equation

$$\frac{\alpha\ \sinh[X]}{\dfrac{1}{\Theta_{H_2O}} + \dfrac{\theta^s}{\theta_s}\dfrac{1}{\Theta_{H_2O}} + \alpha\cosh[X]} = \frac{d^3}{\varepsilon_{CO}A\mu}\sigma - \frac{kTd^3}{A\mu^2}X \quad [24]$$

For the surface coverage by dipoles directed toward the platinum layer, we have

$$\tilde{\theta} = \frac{(\alpha/2)e^X}{\dfrac{1}{\Theta_{H_2O}} + \dfrac{\theta^s}{\theta_s}\dfrac{1}{\Theta_{H_2O}} + \alpha\cosh[X]} \quad [25]$$

For the opposed ones, we have

$$\tilde{\theta} = \frac{(\alpha/2)e^X}{\dfrac{1}{\Theta_{H_2O}} + \dfrac{\theta^s}{\theta_s}\dfrac{1}{\Theta_{H_2O}} + \alpha\cosh[X]} \quad [26]$$

Then θ_s and n_s can be calculated from

$$\theta_s = \frac{n_s}{n^{max}} = \frac{1}{\dfrac{1}{\Theta_{H_2O}} + \dfrac{\theta^s}{\theta_s}\dfrac{1}{\Theta_{H_2O}} + \alpha\cosh[X]} = \frac{1-\theta^s}{1+\alpha\Theta_{H_2O}\cosh[X]} \quad [27]$$

The covering fractions θ_{O_2Hs}, θ_{OHs}, and θ_s are obtained by solving the following balance equations

$$\frac{n^{max}d\theta_{O_2Hs}}{N_A\ dt} = v_1 - v_2 \quad [28]$$

$$\frac{n^{max}d\theta_{OHs}}{N_A\ dt} = 3v_2 - v_3 \quad [29]$$

$$\frac{n^{max}d\theta_s}{N_A\ dt} = w_2 - w_3 \quad [30]$$

The charge density $\sigma(r,t)$ in Eq. 23 and 24 is calculated from the current density conservation at the platinum layer/Nafion phase interface according to

$$J(r,t) + J_{PEFC}(r,t) = -\frac{\partial\sigma(r,t)}{\partial t} \quad [31]$$

where

$$J_{PEFC}(r,t) = -F[v_1 + v_3 - 2(w_1 + w_2)] \quad [32]$$

and $J(r,t)$ is the local electronic current density traversing the platinum layer and computed by the microscale electronic model recalled in Appendix B.

[a] In order to describe the PEFC operation with reactants not fully vapor saturated, Θ_{H_2O} can be calculated through a model describing water transport in the Nafion and in the pore phases.[50]

[b] In a first approximation, we suppose that only the more external Pt atoms of the grains are active for the ORR.

The diffuse layer submodel.— The 1D-diffuse layer submodel describes the transport by diffusion and migration of species close to the catalyst phase (platinum layer), participating in the electrochemical reactions and coupled with the electric field generated by the charge distribution of H^+ and Pt^{2+} (cf. Fig. 2). All species are considered as punctual (diluted solution theory),[29,34,49] so the interparticle electrical interaction is neglected. The solvation and convection by water are not considered. According to the nonequilibrium thermodynamics, the fluxes of the electrically neutral O_2 are assumed to be given by the Fick's law of diffusion and the mass balance leads to

$$\frac{\partial C_{O_2}}{\partial t} = -\nabla_x \cdot \vec{J}_{O_2} = -\nabla_x \cdot (-D_{O_2}\nabla_x C_{O_2}) = D_{O_2}\nabla_x^2 C_{O_2} \quad [33]$$

where we assume that the diffusion coefficient D_{O_2} is constant.

In the case of the electrically charged species H^+ and Pt^{2+}, the diffusion coefficients in the hydrated Nafion are also supposed independent of the concentration. Combining the flux related to the Fick's diffusion force and to the electrical force, with the mass balance, we obtain the equations representing the H^+ and the Pt^{2+} concentration (Nernst-Planck equations)

$$\frac{\partial C_{H^+}}{\partial t} = -\nabla_x \cdot \vec{J}_{H^+} = -\nabla_x \cdot (-D_{H^+}\nabla_x C_{H^+} - fD_{H^+}C_{H^+}\nabla_x\phi) \quad [34]$$

$$\frac{\partial C_{Pt^{2+}}}{\partial t} = -\nabla_x \cdot \vec{J}_{Pt^{2+}} = -\nabla_x \cdot (-D_{Pt^{2+}}\nabla_x C_{Pt^{2+}} - 2fD_{Pt^{2+}}C_{Pt^{2+}}\nabla_x\phi) \quad [35]$$

where $\phi(r,x,t)$ is the electrical potential in the electrolyte, which is calculated from the Poisson's equation

$$\frac{F}{\varepsilon_{DL}}(C_{H^+} + 2C_{Pt^{2+}} - C_{Pt0}) = -\nabla_x^2\phi \quad [36]$$

Equations 34-36 are introduced because at the nanoscale (near the electrified surface where the electron transfer takes place) electroneutrality cannot be assumed, and because there is not any supporting electrolyte (the conductivity of H^+ and Pt^{2+} in the hydrated Nafion medium is not infinite).

The boundary condition for Eq. 33 at $x = L$ is given by

$$J_{O_2}(r,x = L,t) = -v_1 \quad [37]$$

At $x = 0$, the boundary condition for Eq. 33 is calculated by the microscale diffusion model through the hydrated Nafion microscale layer recalled in Appendix A.

The boundary conditions for Eq. 34 and 35 at $x = L$ are deduced from the electrochemical reactions in the inner layer

$$J_{H^+}(r,x = L,t) = -(v_1 + v_3) + 2(v_2 - v_3) \quad [38]$$

$$J_{Pt^{2+}}(r,x = L,t) = v_3 + v_2 \quad [39]$$

In a first approximation, we assume electroneutrality in the bulk ($x = 0$) as well as a low concentration of dissolved platinum

$$C_{H^+}(r,x = 0,t) + 2C_{Pt^{2+}}(r,x = 0,t) - C_{Pt0} \sim 0 \quad \text{(electroneutrality condition)} \quad [40]$$

$$\text{with } C_{Pt^{2+}}(r,x = 0,t) \sim 0 \quad [41]$$

$$\text{and then } C_{H^+}(r,x = 0,t) \sim C_{Pt0} \quad [42]$$

We deduce the boundary condition of Eq. 36 at $x = L$ from the Gauss theorem applied around the inner layer[29,30,32]

$$\frac{\partial\phi}{\partial x}(r,L,t) = -\frac{\sigma(r,t)}{\varepsilon_{CL}} \quad [43]$$

where $\sigma(>0)$ is computed from Eq. 31.

Furthermore, $\phi(r,x = 0,t)$ is computed from the proton microscale model through the cathode thickness, as explained in the following section and in Appendix B.

Finally, from Eq. 1, we can calculate the temporal evolution of the specific catalytic surface area $\gamma(r,t)$ due to both oxidation/dissolution and Pt coarsening, through the expression

$$\gamma(r,t) = \frac{5}{\tau_{Pt}(r,t)}\frac{1}{\rho_{Pt}}\left(\frac{w_{Pt}(t=0)}{\varepsilon_{CL}} - M_{Pt}C_{Pt^{2+}}(r,x = L,t)\right) \quad [44]$$

where M_{Pt} is the platinum molar mass.

Numerical Simulations

Fixing as a reference $\phi(r,x = 0,t) = 0$ in the anode side,[30,32] $\phi(r,x = 0,t)$ in the cathode side can be calculated from the ionic microscale model described in Appendix B (cf. Eq. B-3 and B-4). In this paper we show numerical simulation results from a one-mesh discretization through the cathode thickness. In this case, we have[30,31]

$$\phi(x = 0,t) = -\frac{\varepsilon_M I(t)}{S_{MEA}\sigma_{H^+}} \quad [45]$$

where S_{MEA} is the geometrical surface of the MEA and σ_{H^+} is the Nafion protonic conductivity (depending on temperature and water content, cf. Appendix B). Equation 45 constitutes the boundary condition at $x = 0$ for Eq. 36 which calculates $\phi(L,t)$. Finally, using Eq. 10, we can calculate the cathode electrostatic potential $\psi(t)$.

The local nanoscale current density in Eq. 31 is given by (cf. Ref. 29, 30, and 32 and Appendix B)

$$j(t) = \frac{I(t)}{\varepsilon_{CL}S_{MEA}}\frac{1}{\gamma(t)} \quad [46]$$

Computational code and parameters.— The model is simulated by means of an in-house numerical code developed by coupling three commercial software systems: Simulink (describing particularly the boundary conditions at $x = 0$ and at $x = L$ of the nanoscale model), Femlab (describing the ionic transport phenomena in the nanoscale diffuse layer), and all are integrated in Matlab. Simulations have been performed on a computer with an Intel Pentium 4 processor, 2 GHZ, 1 Gb of RAM, using the solver ode15s with a variable integration time step. Finite element discretization of the equations describing the ionic transport in the diffuse layer has been performed using Femlab programming facilities (15 grid points have been used).[a] Discretization of the equations describing the oxygen diffusion through the Nafion phase has been directly performed by using Simulink (five grid points have been used for both the diffuse and the impregnated layer models). For the simulations shown here, we have chosen the set of physicochemical parameters given in Table I.

From the decomposition of the model into parts based on mechanistic models and their explicit coupling, it becomes easily interpretable and adaptable to different model assumptions and working conditions. Thus, the numerical code allows the analysis of stationary and dynamic behavior of the different state variables (θ^1,σ ...) and the cathode electrostatic potential $\psi(t)$ in response to a current demand $I(t)$ at given temperature T and pressure $P_{cathode}$.

In this section we present some illustrative simulation results of the steady-state and transient responses of the cathode, focusing on their sensitivity to some working conditions, electrode composition (platinum/Nafion loading), and simulated time. We specially focus

[a] Using Femlab programming facilities, the ionic diffuse layer model is exported to the Simulink environment as an S-function block.

Table I. Parameters values chosen for the simulations showed in this paper.

		Units	References
Parameters	$w_{Pt}(t=0) = 0.5$ mg cm^{-2}	mg cm^{-2}	This work
	$\epsilon_M = 50 \times 10^{-6}$	m	This work
	$\epsilon_{Pt} = 10^{-9}$	m	Ref. 70 and this work
	$\epsilon_{Ck} = 15 \times 10^{-6}$	m	This work
	$\delta_{MEA} = 2.1 \times 10^{-4}$	m^2	This work
	$C_{TPX} = 1200$	mol m^{-3}	29, 30, and 32-35
	$\alpha_1 = \alpha_3 = 0.5$ $\beta_1 = \beta_2 = 0.5$ $\alpha_{Ox} = 1$	Dimensionless	This work
	$\varepsilon_{H} = 6 \times \varepsilon_0$; $\varepsilon_{TK} = 20 \times \varepsilon_0$	C V^{-1} m^{-1}	29, 30, 32-35, and 49
	$k_1 = 10^{-2}$ $k_{-2} = 10^{-14}$ $k_3 = 10^{-10}$	m^4 mol^{-1} s^{-1}	This work
	$k_{-1} = 1.3 \times 10^{-2}$ $k_2 = 10^{-2}$ $k_{-3} = 10^{-6}$	Mol m^{-2} s^{-1}	This work
	$k_{-2} = 10^{-6}$ $k_{-3} = 10^{-6}$ $k_3 = 10^{-10}$ $k_3 = 10^{-14}$		
	$k_3 = 10^3$ $k_{-3} = 10^{-14}$ $k_{-3} = 10^{-22}$	m s^{-1}	This work
	$A_d = 3.3 \times 10^{-11}$	mol m^{-2} s^{-1}	This work
	$k_d = 2.97 \times 10^2$	(mol/m^2 s)/(mol/m^3)	This work
	$r_{Pt}(t=0) = 3 \times 10^{-9}$	m	1 and 71
	$E_{a,d} = 48T$	J mol^{-1}	This work
	$\chi = 0.5$	J m^{-2}	This work
	$\Delta G_c^0 = 1$	kJ mol^{-1}	29, 30, and 32-35
	$n^{max} = 1/d^2$	sites m^{-2}	29, 30, and 32-35
	$k = 14$	Molecules sulfonate site^{-1}	30, 32, 35, and 60
	$m_{H_2O} = 1$	Dimensionless	This work
	$D_{H^+} = 2.97 \times 10^{-14} \times T \times 10^{-(1.31(203-T_c)+0.09(203-T_c)^2/(T+105)_K)}$	m^2 s^{-1}	30 and 32-35
	$D_{HO_2^-} = 1 \times 10^{-7}$	m^2 s^{-1}	Ref. 1 and This work
	$D_{O_2} = 3.1 \times 10^{-7} \times \exp(-2768/T)$	m^2 s^{-1}	30, 32-35, and 60
	$L = 5 \times 10^{-5}$ (estimated from the model)	m	30, 32-35, and 60

on the EIS response, calculated by simulation in the time domain and subsequent fast Fourier transformation (numerical approach used previously in Ref. 29, 30, 32-34, 53, and 54). For the determination of the ac impedance shown here, a sufficiently small sinusoidal signal (e.g., 10% of the nominal current) is superimposed on the fixed (dc) current level $\bar{I}$ in order to obtain a linear response of the potential $\psi(t)$. This is performed for frequencies ranging from 10^{-2} to 10^6 Hz in anticlockwise direction. Prior to starting the simulation of the periodic signal response, the pseudo-steady-state is calculated (state at short times compared to the full simulated lifetime of the electrode).

Some sensitivity studies to operating conditions at a given simulated time.— In Fig. 4 we show the calculated potential η and the resulting cathodic electrostatic potential ψ as a function of the nominal current, at the simulated operating time $t = 10^4$ s. The cathodic potential shape agrees with current experimental cell polarization curves (at low currents, the global cell potential is essentially determined by the cathodic one, as generally accepted in PEFC literature, and according to the predictions obtained with our anodic model).[29,30,32,34] At high currents, because of the oxygen transport limitation through the microscale impregnated Nafion layer, the ψ curve slope changes.

Figures 5 and 6 show the sensitivity of the different covering fractions to the nominal current at the operating time $t = 10^4$ s. We can see that the increment of the nominal current leads to the diminution of the platinum oxide coverage (Fig. 5). For the chosen Pt oxidation/dissolution kinetic parameters in Table I, the calculated platinum oxide coverage values ($\sim 10^{-10}$) are very small. Parameter fitting is required with dedicated experiments under development by us.

Because η is negative, the covering fraction of dipoles opposed to the platinum layer is higher than the directed one.[29,30,32] The increase in nominal current leads to the diminution of these covering fractions, leaving more sites to be occupied by the reaction intermediates. Then, the coverage by ORR intermediates increases with nominal current, as shown in Fig. 6. Moreover, the model captures the effect of nominal current on EIS (Fig. 7 and 8). Calculated spectra patterns are in good agreement with typical experimental results in PEFC environments.[30,32,57,61] The arc diameter results

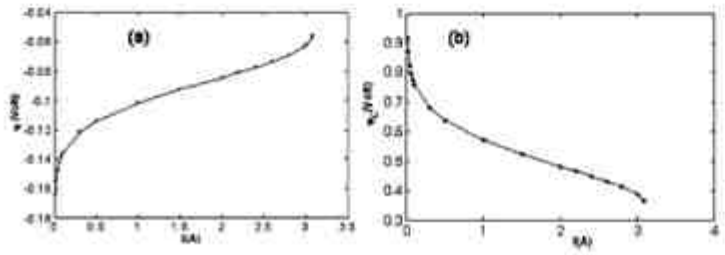

Figure 4. Potential drop through the inner layer (a) and cathodic electrostatic potential (b) as function of the nominal current ($P_{Cathode} = 1.5$ bar, $T = 353$ K, simulated time $= 10^4$ s).

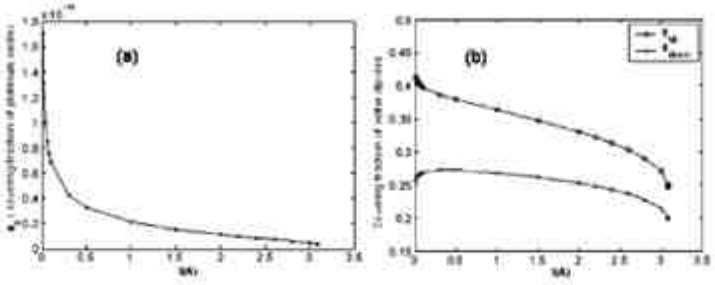

Figure 5. Covering fraction of platinum oxide (a) and covering fraction of water dipoles (b) as a function of the nominal current ($P_{Cathode}$ = 1.5 bar, T = 353 K, simulated time = 10^4 s).

from the coupling between the different phenomena taken into account in our model (Pt grain coarsening, intermediate adsorption, protons, oxygen, and dissolved platinum transport, etc.). At low currents, EIS is constituted of a capacitive and of a low-frequency inductive loop, in agreement with already reported experimental results.[55,61] The low-frequency inductive loop is related to the competition between intermediates on the catalytic surface,[62,63] and its size decreases as the nominal current increases. In addition, the high frequency capacitive arc diameter decreases with the demanded current. For a sufficiently high current, a low-frequency capacitive loop related to the oxygen transport through the microscale Nafion layer appears. At high currents the magnitude of the low-capacitive arc increases with the increase of the nominal current, because of the oxygen diffusion limitation through the microscale Nafion layer. We can see also in Fig. 7 and 8 that the membrane resistance remains unchanged because we have assumed a constant water content inside the Nafion phase (this is consistent with experimental EIS performed on a cell operating with fully hydrated reactants, as reported in Ref. 30, 32, and 60).

Figure 9 shows the simulated EIS temperature sensitivity, for different nominal currents, at $t = 10^4$ s. In all the cases, because the hydrated Nafion phase proton conductivity increases with temperature (cf. Eq. 53, Appendix B), the high-frequency intersection point with the real axe shifts toward the Nyquist's plan origin. The predicted sensitivity of the capacitive and inductive loops sizes is related to the temperature-dependent mathematical expressions used to describe the electrochemical reactions and the Pt grain coarsening rate as well as the oxygen diffusion coefficient. At I = 0.5 A we note that the low-frequency inductive arc diameter is smaller at the highest temperature. Otherwise, at I = 1 A the inductive loop is not greater at 353 K, and a low-frequency capacitive arc appears. Also, it can be observed that for all current levels the size of the high-frequency capacitive arc is smaller at the highest temperature. This is explained by the improvement of the electrochemical reactions with temperature. However, low-frequency capacitive arcs are bigger at the highest temperature. We emphasize that this is not contradictory with already published experimental and theoretical results (cf. Ref. 30, 32, and 60), where temperature increase leads to the decrease of the low-frequency capacitive arc magnitude: the EIS plots here have to be analyzed in terms of the aging processes taken into account in this model. In fact, temperature favors both Pt oxidation/dissolution and coarsening, which, according to Eq. 1, leads to a decreasing specific catalytic area γ and to an increase of the local nanoscale current density J (cf. Eq. 46). Then, the increase of J leads to an early oxygen transport limitation and a bigger low-frequency arc magnitude at the highest temperature. Even though simulated time is the same for both 313 and 353 K EIS, the simulated cathode at 353 K is more aged.

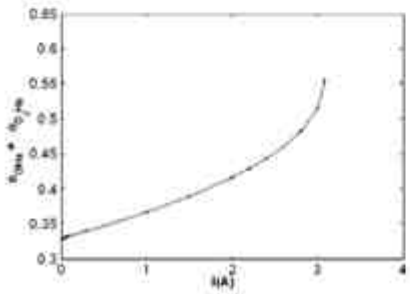

Figure 6. Covering fraction of ORR intermediates as function of the nominal current ($P_{Cathode}$ = 1.5 bar, T = 353 K, simulated time = 10^4 s).

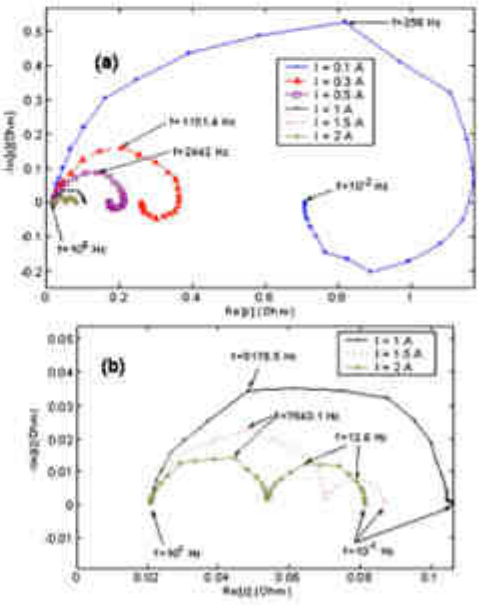

Figure 7. (Color online) Simulated cathode-membrane EIS sensitivity to the nominal current (a) and detail (b) ($P_{Cathode}$ = 1.5 bar, T = 353 K, simulated time = 10^4 s).

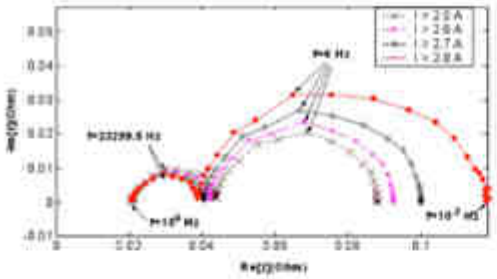

Figure 8. (Color online) Simulated cathode-membrane EIS sensitivity to the nominal current ($P_{Cathode}$ = 1.5 bar, T = 353 K, simulated time = 10^4 s).

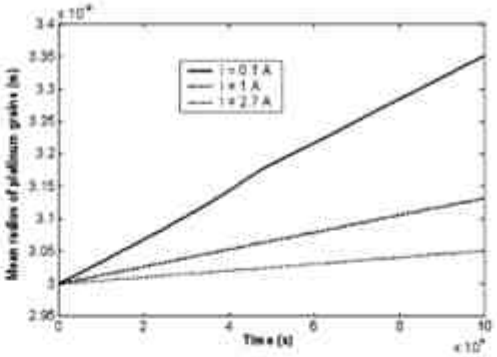

Figure 10. Simulated temporal evolution of the mean Pt grain radius for different nominal currents ($P_{Cathode}$ = 1.5 bar, T = 353 K).

Simulated temporal evolution of the cathode response.—Figure 10 displays the calculated time evolution of the *average* platinum grain radius for three nominal currents. These curves show that the coarsening rate increases with the electrode potential (which decreases with current). The effect of the same nominal currents on the simulated temporal evolution of the specific catalytic surface area, computed from Eq. 1, is provided in Fig. 11. As pointed out previously, the calculated decreasing trend is due to both Pt oxidation/dissolution and coarsening and is in qualitative agreement with experimental tendencies in literature.[12]

Furthermore, the model captures the cathode durability sensitivity to Pt and Nafion initial loadings. As illustrative examples, in Fig. 12 and 13 we present the simulated temporal evolution of the electrostatic cathode potential ϕ at I = 0.1 A and at I = 3 A, for three initial platinum loadings multiples of $w_{Pt}(t=0)$ = 0.5 mg cm^{-2}. At I = 0.1 A, the cathode degradation rate decreases with decreasing initial platinum loading. Otherwise, Fig. 13 (I = 3 A) reveals lower degradation rates, in consistence with the γ degradation rate dependence with nominal current in Fig. 11. Furthermore, the required initial platinum loading for minimal degradation rate is comprised between $5w_{Pt}(t=0)$ and $w_{Pt}(t=0)$. This feature, interesting in our opinion for engineering purposes, needs to be validated by experimental studies in progress in our group.

In Fig. 14 we show simulations of the cathodic potential as a function of the operating time at two nominal currents. It can be seen that the potential decays dramatically from a given operating time. This potential "collapse" is experimentally observed in some cells after long time operation (stationary or cycled nominal currents[2]) and is sometimes attributed to the membrane pin-holing.[24] However, our simulations indicate that this behavior can also be expected in the absence of membrane deterioration (Nafion aging is not taken into account in our model). As explained previously, because of the Pt aging mechanisms, J increases and γ decreases with time, until not enough Pt is available to ensure the demanded nominal current I. From a given operating time, the potential decays faster as a consequence of the oxygen impoverishment at the nanoscale compact layer (J increases dramatically).

The simulated time evolutions of the EIS pattern for three nominal currents are shown in Fig. 15-17, emphasizing the temporal multiscale character of the model. In the three cases it is noted that a long simulated operating time strongly affects the EIS shape.

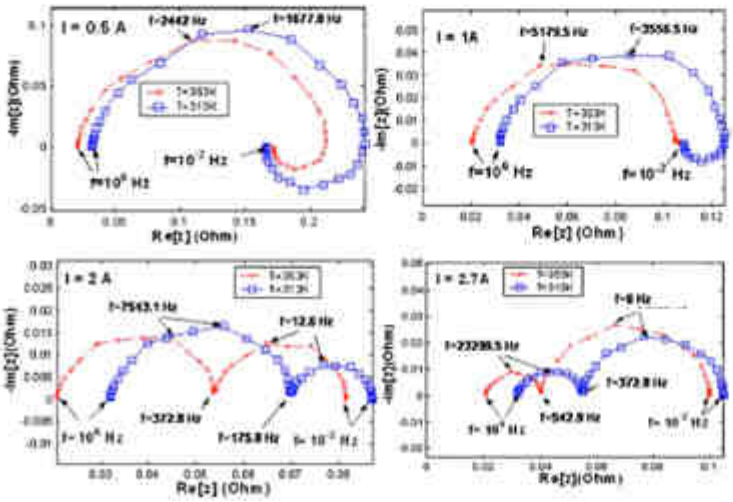

Figure 9. (Color online) Simulated cathode-membrane EIS sensitivity to the temperature and the nominal current ($P_{Cathode}$ = 1.5 bar, simulated time = 10^4 s).

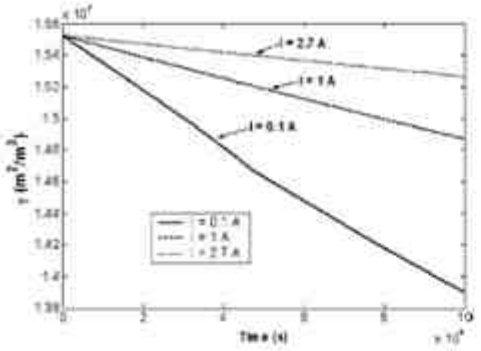

Figure 11. Simulated temporal evolution of the specific catalytic surface area for different nominal currents ($P_{Cathode}$ = 1.5 bar, T = 353 K).

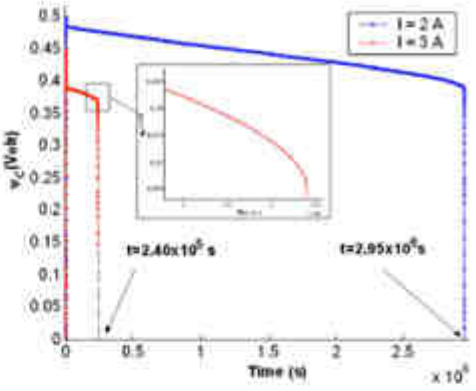

Figure 14. (Color online) Simulated long temporal evolution of the cathodic electrostatic potential for two nominal currents ($P_{Cathode}$ = 1.5 bar, T = 353 K).

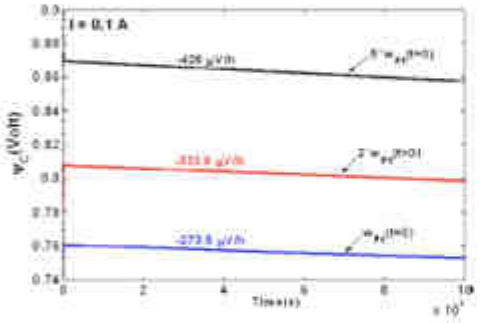

Figure 12. (Color online) Simulated temporal evolution of the cathodic electrostatic potential at I = 0.1 A for different initial Pt loadings ($P_{Cathode}$ = 1.5 bar, T = 353 K) (the fast transients at very early times correspond to the numerical initialization of the model).

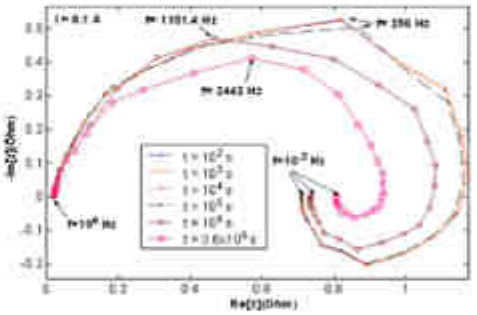

Figure 15. (Color online) Simulated temporal evolution of the cathode-membrane EIS at I = 0.1 A ($P_{Cathode}$ = 1.5 bar, T = 353 K).

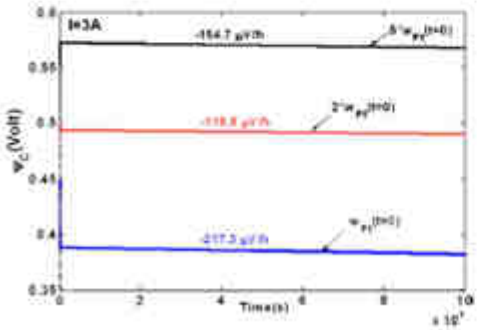

Figure 13. (Color online) Simulated temporal evolution of the cathodic electrostatic potential at I = 3 A for different initial Pt loadings ($P_{Cathode}$ = 1.5 bar, T = 353 K).

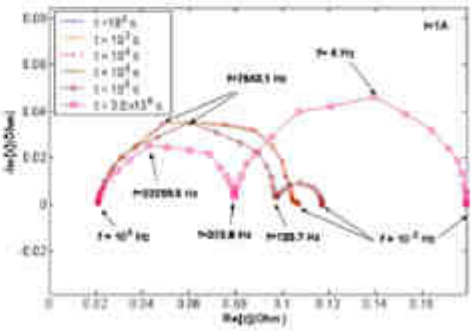

Figure 16. (Color online) Simulated temporal evolution of the cathode-membrane EIS at I = 1 A ($P_{Cathode}$ = 1.5 bar, T = 353 K).

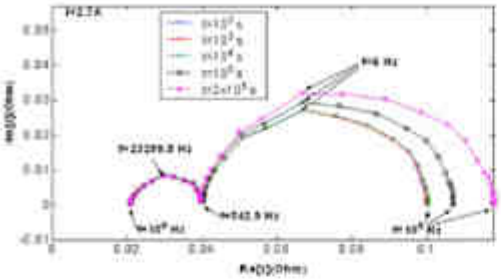

Figure 17. (Color online) Simulated temporal evolution of the cathode-membrane EIS at $I = 2.7$ A ($P_{Cathode} = 1.5$ bar, $T = 353$ K).

1. At $\bar{I} = 0.1$ A (Fig. 15), both the capacitive and inductive arc diameters decrease with time, and frequencies shift again, due to the decreasing γ (increasing J), we find here a similar behavior to that observed in Fig. 7 for low nominal currents.

2. At $\bar{I} = 1$ A (Fig. 16), the high-frequency arc diameter decreases with time and the low-frequency capacitive arc increases.

3. At $\bar{I} = 2.7$ A (Fig. 17), we have a very small variation of the high-frequency arc diameter, while the low-frequency arc amplitude increases; this behavior agrees with the EIS sensitivity to high nominal currents in Fig. 8, where oxygen transport limitation becomes important (again, even if $\bar{I}$ is fixed for all the simulated times in Fig. 17, J increases with time).

Conclusions

Based on an irreversible thermodynamics description, in this paper we propose a mechanistic model for the transient simulation of a PEFC cathode. As a first step, the model carries out a coupling of aging phenomena with a nanoscale model proposed recently by us,[28] describing an electrochemical Pt/Nafion interface in the presence of electrochemical reactions. The proposed model describes the internal dynamics of the electrochemical double layer, taking into account the coupling between the transport of protons and Pt^{2+} in the diffuse layer, as well as the carbon-supported Pt coarsening, the Pt oxidation, the ORR, and the water dipoles adsorption in the inner layer. This continuous nanoscale interfacial model is coupled with a microscale model of the oxygen transport through the impregnated Nafion layer and is designed to be coupled with a continuous transport microscale model of electrons, Pt^{2+}, and protons through the MEA thickness.

The numerical model was implemented in a Matlab-Simulink/Femlab environment. The model represents explicitly the different physical phenomena as nonlinear submodels in interaction (cf. Bond Graph network theory[30,36-38,65]). It is hence modular and captures the sensitivity of the electrode response to the operating conditions (nominal current, reactant-gas pressure, temperature), to the composition (platinum/Nafion loading), and to the temporal evolution of the electrochemical activity from aging mechanisms. In particular, the influence of time on impedance spectra pattern can be simulated. Some of the numerical results obtained are in qualitative agreement with some previously reported experimental and theoretical results. Furthermore, we start now the conception of an experimental setup (three electrodes EIS, following the Khun et al. approach[66,67]) in an in-house dedicated PEFC bench in order to perform the parameter identification of our model and to validate some results, such as the predicted durability dependence on initial Pt loading.

From a theoretical point of view, further model sophistication is necessary. We are now working in the extension of this model in order to include anodic electrochemical Ostwald's ripening, ionic platinum reduction from hydrogen crossover within the membrane,[1] membrane and carbon support degradation,[31,66-68] and water-transport effects.[56] We will also analyze the simulated cell response to cycled-current experiments representative of automotive applications.[1,2,33]

Commissariat à l'Energie Atomique assisted in meeting the publication costs of this article.

Appendix A
Microscale Oxygen Transport Model

As we consider pure feeding oxygen (no nitrogen), oxygen pressure drop in the pore phase is neglected (cf. Fig. 1). Then, oxygen partial pressure is given by

$$P_{O_2} = P_{cathode} - P_{sat} \quad [A-1]$$

where the saturated water pressure P_{sat} is as a function of temperature according to[39]

$$P_{sat} = 10^{-4} \times \exp\left(23.1961 - \frac{3816.44}{T - 46.13}\right) \quad [A-2]$$

The oxygen transport in the thickness of the impregnated Nafion layer is supposed to be given by the diffusion equation

$$\frac{\partial C_{O_2}}{\partial t} = -\nabla_x \cdot \vec{J}_{O_2} = -\nabla_x \cdot \left(-D_{O_2} \nabla_x C_{O_2}\right) = D_{O_2} \nabla_x^2 C_{O_2} \quad [A-3]$$

with the boundary condition given by Henry's relation[39]

$$C_{O_2}(x, z = 0, t) = \frac{P_{O_2}}{5.08 \times 10^6 \times \exp(-498/T)} \quad [A-4]$$

The oxygen flux at $z = e_{pc}$ is calculated by the diffuse layer submodel; continuity of fluxes is written at the interface between the two scales of modeling

$$J_{O_2}(x, z = e_{pc}, t) = J_{O_2}(x, z = 0, t) \quad [A-5]$$

where $J_{O_2}(x, z = e_{pc}, t)$ is the input flux for the microscale model, and $J_{O_2}(x, z = 0, t)$ is the output flux computed by the nanoscale model.

Remark.— Because in our model we suppose that feeding oxygen is saturated with water, we can consider that in the cathode the additional water production is evacuated through the liquid phase.[39] This liquid phase may occupy a fraction of the pore phase, but as we assume an electrode working with pure oxygen, it does not significantly affect the oxygen concentration in the active layer. Furthermore, the pressure drop through the gas diffusion layer is supposed to be negligible.

Appendix B
Microscale Charges Transport Models

The membrane model.— The membrane is considered to be quasi-homogeneous, impermeable to gases, and only protons and water are supposed to transfer within it. At the microscale the electroneutrality in the Nafion phase can be assumed[28,30,63,69] and the proton transport is governed by an Ohm's relation. The local protonic current within the membrane is given by

$$i_M(x,t) = -S_{MEA}\sigma_M \nabla_x \phi(x,t) \quad [B-1]$$

where $\phi(x,t)$ is the local ionic electrostatic potential in the Nafion phase and σ_M is the protonic conductivity given by[39]

$$\sigma_M = (0.46\lambda - 0.25)e^{-1300(1/T - 1/298.15)} \quad [B-2]$$

In this equation, $\lambda(x,t)$ is the local number of water molecules per sulfonate site and T is the local temperature. Assuming no accumulation of protons, the conservation law gives

$$\nabla_x \cdot \left(\frac{i_M(x,t)}{S_{MEA}}\right) = 0 \quad [B-3]$$

As in the context of this work feeding gases are fully saturated with vapor, λ is close to 14 water molecules per sulfonate site[28,39] and the membrane conductivity can be supposed constant.

The electrode microscale electric model.— As in the membrane model case, at the microscale the electroneutrality in the Nafion phase can be assumed because we are far from the electrified surface (platinum layer). Then, we have no proton accumulation, $C_{H^+} = C_{FIX}$, and its transport within the electrode is also governed by Eq. B-1. The conservation law gives

$$\nabla_x \cdot \left(\frac{i_M(x,t)}{S_{MEA}}\right) = S_M(x,t) \quad [B-4]$$

where $S_M(x,t)$ is the local consumption of protons given by the distributed term

$$S_M(x,t) = \beta(x,t)\gamma(t) \quad [B-5]$$

The local electronic current in the carbon phase at the microscale can be written as

$$\zeta_e(x,t) = -S_{\text{MEA}}\sigma_e\nabla_x\phi(x,t) \quad [B\text{-}6]$$

where $\phi(x,t)$ is the local electronic electrical potential, computed by the macroscale submodels, and σ_e, is the electronic conductivity. Neglecting electronic accumulation, the local consummation is calculated from the conservation law of the electrons:

$$\nabla_x\cdot\left(\frac{i_e(x,t)}{S_{\text{MEA}}}\right) = S_e(x,t) \quad [B\text{-}7]$$

where

$$S_e(x,t) = \beta(x,t)\gamma(x) \quad [B\text{-}8]$$

The boundary conditions for Eq. B-7 are

$$\zeta_e(x = x_{\text{CL}},t) = 0 \quad [B\text{-}9]$$

$$\zeta_e(x = 0,t) = I(t) \quad [B\text{-}10]$$

where $I(t)$ is the global current delivered by the fuel cell.

Remark.— As a first approximation, we have supposed a negligible Pt^{2+} concentration at the microscale (cf. Eq. 40-42). This assumption cannot be maintained if one describes Pt crystallization within the membrane. In this case, a coupling through Nernst-Planck-Poisson equations appears between protons and Pt^{2+} transports, as in the diffuse layer case, but with a source term describing a spatially dependent reaction between Pt^{2+} and crossover H_2.[28]

List of Symbols

α	$=2\exp(-\Delta G^{\ddagger}_{ads}/RT)$
A	$=([\Gamma])^2\pi r_{\text{Pt}}[(\Omega=\sum_{i=1}^{\infty}1/i^2\ (\Omega>1)$
	Riemann's function $=\frac{\pi^2}{6}\ ]=1.20]$
A_{ad}	pre-exponential factor for the platinum deposition rate, mol m^{-2} s^{-1}
b_i	standard rate reaction constants
C_{FIX^-}	charged fixed sites concentration (sulfonates of Nafion), mol m^{-3}
C_{H^+}	proton concentration, mol m^{-3}
C_{O_2}	oxygen concentration, mol m^{-3}
$C_{\text{Pt}^{2+}}$	Pt^{2+} concentration, mol m^{-3}
d	$=2\times10^{-10}$; thickness of a water molecule, m
D_{H^+}	proton diffusion coefficient in Nafion, m^2 s^{-1}
D_{O_2}	oxygen diffusion coefficient in Nafion, m^2 s^{-1}
$D_{\text{Pt}^{2+}}$	Pt^{2+} diffusion coefficient in Nafion, m^2 s^{-1}
e_{CL}	electrode thickness, m
e_{DL}	microscale impregnated Nafion layer thickness, m
e_{M}	membrane thickness, m
$E_{\text{act},\gamma}$	activation energy of a platinum grain of infinite size, J mol^{-1}
f	$=F/RT$
F	Faraday's constant, 96,485 C mol^{-1}
k_{e^-}	electronic conductivity in the Pt/C phase, S m^{-1}
k_{H^+}	protonic conductivity, S m^{-1}
j	local electronic current density traversing the platinum layer (microscale model), A m^{-2}
$j_{\text{Pt}^{2+}}$	faradaic current associated to the electrochemical reactions, A m^{-2}
J_{H^+}	molar flux of protons in Nafion, mol s^{-1} m^{-2}
J_{O_2}	molar flux of oxygen in Nafion, mol s^{-1} m^{-2}
$J_{\text{Pt}^{2+}}$	molar flux of Pt^{2+} in Nafion, mol s^{-1} m^{-2}
k	$=1.380\times10^{-23}$; Boltzmann's constant, J K^{-1}
k_{d}	deposition kinetic constant, mol m^{-2} s^{-1}
k_{p}	dissolution kinetic constant, m s^{-1}
k_i	standard rate reaction constants
I	total current demanded to the fuel cell, A
L	diffuse layer thickness, m
M_{Pt}	$=195.60\times10^{-3}$; platinum molar mass, kg mol^{-1}
n^{max}	maximal quantity of free sites per unit of area of catalyst phase, m^{-2}
n_s	number of free sites per unit of area of catalyst phase, m^{-2}
N_{A}	$=6.022\times10^{23}$; Avogadro's number, mol^{-1}
P_{cathode}	cathode total pressure, Pa
P_{O_2}	oxygen partial pressure in the pore phase, Pa
P_{sat}	saturated water pressure, Pa
r	coordinate according to the electrode thickness
r_{Pt}	mean radius of platinum grains on carbon support, m
R	$=8.314$; ideal gas constant, J K^{-1} mol^{-1}
S_{MEA}	geometric surface of the MEA, m^2
T	absolute temperature, K
w_i	electrochemical reaction rates, mol s^{-1} m^{-2}
w_{Pt}	local platinum mass loading per unit of MEA surface, kg m^{-2}
x	coordinate according to the diffuse layer (macroscale model)
z	coordinate according to the microscale impregnated Nafion layer

Greek

α	elementary reaction step electronic transfer coefficient
α_{Ads}	proportionality coefficient between the free surface energy and the activation energy of Ostwald's platinum dissolution (platinum layer)
β	elementary reaction step electronic transfer coefficient
γ	specific catalytic surface area, m^2/m^2
Γ	interfacial dipolar surface density, Debye m^{-2}
$\Delta G^{\ddagger}_{\text{ads}}$	dipolar chemical adsorption energy, J mol^{-1}
ΔG_{Pt}	molar Gibbs free energy change by platinum conversing, J mol^{-1}
ε_{CL}	electric permittivity in the compact layer, C^2 J^{-1} m^{-1}
ε_{DL}	electric permittivity in the diffuse layer (electrolyte phase), C^2 J^{-1} m^{-1}
ε_0	$=8.854\times10^{-12}$; electric permittivity of vacuum, C^2 N^{-1} m^{-2}
η	electronic potential difference between the catalyst and the electrolyte phases (through the inner layer), V
θ	covering fraction of dipoles oriented toward the platinum layer
$\bar{\theta}$	covering fraction of dipoles opposed to the platinum layer
θ'	$=\theta_{\text{OH}_2}+\theta_{\text{O}_2\text{H}}+\theta_{\text{H}}$
θ_{f}	covering fraction of free sites
θ_{O}	covering fraction of the monoatomic oxygen of the PtO
θ_{OH}	covering fraction of the intermediate reaction specie, OHs
$\theta_{\text{O}_2\text{H}}$	covering fraction of the intermediate reaction specie O_2Hs
$\Theta_{\text{H}_2\text{O}}$	water activity
λ	water content in the Nafion phase (number of water molecules per sulfonate site)
μ	$=0.617\times10^{-29}$; dipolar moment of a water molecule, C m
ν_i	electrochemical reaction rates, mol s^{-1} m^{-2}
ν_{Pt}	$=9.1\times10^{-6}$; platinum molar volume, m^3 mol^{-1}
ρ_{Pt}	$=2.147\times10^{4}$; carbon-supported platinum density, kg m^3
σ	charge density on the catalyst surface, C m^{-2}
ϕ	electronic potential in the electrolyte phase, V
χ	platinum/Nafion interfacial tension, J/m^2
ψ	electronic potential in the Pt/C phase, V

References

1. F. J. Ferreira, G. F. Ju Gr, Y. Shao-Horn, D. Morgan, R. Makharia, S. Kocha, and H. A. Gasteiger, *J. Electrochem. Soc.*, 152, A2256 (2005).
2. S. Escribano, R. Ismaïl, A. Morin, S. Solan, and L. Guetaz, in *Proceedings of the 16th World Hydrogen Energy Conference*, Paper no. 519–580 (in conference CD), Association Française de l'Hydrogène, CEA, Shell Hydrogen, Air Liquide, Total, Renault, IFP, Institut Français du Pétrole, Gaz de France, SNECMA (2006).
3. J. Xie, D. L. Wood III, K. L. More, P. Atanassov, and R. L. Borup, *J. Electrochem. Soc.*, 152(5), A1011 (2005).
4. K. Yasuda, A. Taniguchi, T. Akita, T. Ioroi, and Z. Siroma, *Phys. Chem. Chem. Phys.*, 8, 746 (2006).
5. M. E. van der Geyet, N. J. Dangerfield, and D. A. Harrington, *J. Electroanal. Chem.*, 420, 89 (1997).
6. M. Azzaroual, B. Rousseau, P. Fleyssinet, and J. B. Duran, *Geochim. Cosmochim. Acta*, 48, 4433 (2001).
7. D. Liu and S. Case, *J. Power Sources*, 162, 521 (2006).
8. R. L. Borup, J. R. Davey, F. H. Garzon, D. L. Wood, and M. A. Inbody, *J. Power Sources*, 163, 76 (2006).
9. M. E. Feldgun, J. O. Zerbino, H. R. de Taccone, and A. J. Arvia, *J. Electrochem. Soc.*, 126, 592 (1979).
10. D. D. Macdonald, *Electrochim. Acta*, 51, 1376 (2006).
11. J. R. Macdonald, *Solid State Ionics*, 176, 1961 (2005).
12. A. G. Hombaston, L. Gonzalez, M. A. Rubio, W. Agila, E. Villanueva, D. Gervasi, E. Chaneto, R. Moreno, and J. R. Inaudis, *J. Power Sources*, 151, 25 (2005).
13. J.-D. Kim, Y.-I. Park, K. Kobayashi, M. Nagai, and M. Kunimatsu, *Solid State Ionics*, 140, 313 (2001).
14. J.-P. Diard, N. Glandut, B. Le Gorrec, and C. Montella, *J. Electrochem. Soc.*, 151, A2193 (2004).
15. M. Eikerling and A. A. Kornyshev, *J. Electroanal. Chem.*, 475, 107 (1999).
16. F. Berthier, J.-P. Diard, and R. Michel, *J. Electroanal. Chem.*, 510, 1 (2001).
17. D. D. Macdonald, E. Sikora, and G. Engelhardt, *Electrochim. Acta*, 43, 87 (1998).
18. J. R. Macdonald, in *Impedance Spectroscopy, Emphasizing Solid Material and Systems*, John Wiley & Sons, New York (1987).
19. S. P. Jiang, J. G. Love, and S. P. S. Badwal, *Key Eng. Mater.*, 125, 81 (1997).
20. S. Wallwoven, M. Bautista, Y. Bultel, and J.-P. Diard, 14ème Forum sur les Impédances Electrochimiques, Paris, Jan 14, 2002, pp. 221–230, CNRS (2002).
21. D. A. Harrington, *J. Electroanal. Chem.*, 420, 101 (1997).
22. A. Parthesius, *J. Membr Sci.*, 278, 269 (2006).
23. A. Parthesius, Ph.D. Thesis, Universität Stuttgart, Germany (2004).
24. R. M. Darling and J. P. Meyers, *J. Electrochem. Soc.*, 150, A1523 (2003).
25. R. M. Darling and J. P. Meyers, *J. Electrochem. Soc.*, 152, A242 (2005).
26. T. Jacob, W. Goddard, and M. Scheffler, Abstract P19 of Workshop of Computational Electrochemistry, Santorini, Sept 26–29, 2004.
27. S. S. Jang, B. V. Merinov, T. Jacob, and W. A. Goddard III, in *International Conference on Solid State Ionics-13*, Abstract P698, International Solid State Ionics (2005).
28. A. A. Franco, P. Schott, C. Jallut, and B. Maschke, *J. Electrochem. Soc.*, 153,

A1053 (2000).
30. A. A. Franco, P. Schott, C. Jallut, and B. Maschke, *Fuel Cells: From Fundamentals to Systems*, Vol. 7, pp. 99–117, Wiley-VCH, New York, (2007).
31. A. A. Franco, Abstract 954, The Electrochemical Society Meeting Abstracts, Vol. 2007-1, Chicago, IL, May 6–11, 2007.
32. A. A. Franco, Ph.D. Thesis, Université Claude Bernard Lyon 1, France (2005), http://tel.archives-ouvertes.fr/tel-00010968/en/
33. A. A. Franco, P. Schott, C. Jallut, and B. M. Maschke, Abstract 1286, The Electrochemical Society Meeting Abstracts, Vol. 2005-1, Québec, Canada, May 15–20, 2005.
34. A. A. Franco, P. Schott, C. Jallut, and B. M. Maschke, in *Proceedings of the 3rd European PEFC Forum*, Lucerne, July 4–8, 2005, Paper B063 (in conference CD), Swiss Federal Office of Energy (2005).
35. L. Gerbaut, Ph.D. Thesis, Institut National Polytechnique de Grenoble, Grenoble, France (1998) (http://www.ensieg.inpg.fr/LEG/en/ENV)
36. A. A. Franco, P. Schott, C. Jallut, and B. Maschke, in *Proceedings of the 5th MATHMOD Conference*, I. Troch and F. Breitenecker, Editors, ARG ESTM Report no. 30, Vienna University of Technology, p. 93, and in conference CD (2006).
37. A. A. Franco, C. Jallut, and B. Maschke, *Mathematical and Computer Modeling of Dynamical Systems*, Submitted (2006).
38. A. A. Franco, P. Schott, C. Jallut, and B. Maschke, *A Multiscale Dynamic Model of a PEFC Electrode*, e-STA (e-sciences), http://www.sciences.fr/e-sta, no. 3 (2005).
39. A. A. Franco, P. Schott, C. Jallut, and B. Maschke, in *Proceedings of the JIMACS 2005*, Lyon, Sept 5–9, 2005, GDR MACS (2005) (in conference CD).
40. A. Schneider, J. Baig, D. Gryaznov, J. Maier, and W. Sitte, *J. Phys. Chem. B*, **110**, 12274 (2006).
41. I. M. Lifshitz and V. V. Slyozov, *J. Phys. Chem. Solids*, **19**, 35 (1961).
42. C. Wagner, *Z. Elektrochem.*, **65**, 581 (1961).
43. W. Sun, *Acta Mater.*, **53**, 3329 (2005).
44. N. F. Mott and R. J. Watts-Tobin, *Electrochim. Acta*, **4**, 79 (1961).
45. J. O'M. Bockris and K. T. Jeng, *Adv. Colloid Interface Sci.*, **33**, 1 (1990).
46. J. O'M. Bockris and M. A. Habib, *Electrochim. Acta*, **22**, 41 (1977).
47. X. Guo and H. S. White, *J. Electroanal. Chem.*, **389**, 13 (1995).
48. V. P. Zhdanov and B. Kasemo, *Appl. Surf. Sci.*, **219**, 256 (2003).
49. J. O'M. Bockris, and S. U. M. Khan, in *Surface Electrochemistry: A Molecular Level Approach*, Plenum Press, New York (1993).
50. A. Damjanovic and V. Brusic, *Electrochim. Acta*, **12**, 615 (1967).
51. D. B. Sepa, M. V. Vojnovic, and A. Damjanovic, *Electrochim. Acta*, **26**, 781 (1981).
52. N. M. Markovic and P. N. Ross, Jr., *Surf. Sci. Rep.*, **45**, 117 (2002).
53. W. G. Bessler, *Solid State Ionics*, **176**, 997 (2005).
54. D. G. Goodwin, in *Proceedings of the 9th International Symposium on Solid Oxide Fuel Cells (SOFC-IX)*, S. C. Singhal and J. Mizusaki, Editors, PV 2005-07, pp. 689–707, The Electrochemical Society Proceedings Series, Pennington, NJ (2005).
55. H. Kuhn, R. Andersen, A. Wokaun, and G. G. Scherer, *Electrochim. Acta*, **51**, 1622 (2006).
56. H. Kuhn, R. Andersen, A. Wokaun, and G. G. Scherer, in *Proceedings of the 3rd European PEFC Forum*, Paper B076 (in conference CD), Swiss Federal Office of Energy (2005).
57. T. Biloul, L. Gerbaut, O. Antoine, P. Osil, and R. Durand, *J. Electroanal. Chem.*, **527**, 143 (2002).
58. O. Antoine, Y. Bultel, and R. Durand, *J. Electroanal. Chem.*, **499**, 85 (2001).
59. T. A. Anthony and A. M. Svensson, Abstract 0043, The Electrochemical Society Meeting Abstracts, Vol. 2006-2, Cancun, Mexico, Oct 29–Nov 3, 2006.
60. A. A. Franco, P. Schott, C. Jallut, and B. Maschke, in *Proceedings of the 16th World Hydrogen Energy Conference*, Paper 372 Association Française de l'Hydrogène, CEA, Shell Hydrogen, Air Liquide, Total, Renault, HF, Institut Français du Pétrole, Gaz de France, SNECMA (2006) (in conference CD).
61. A. A. Franco, M. Tembely, C. Jallut, and B. Maschke, in *Proceedings of the II Jornadas Iberoamericanas de Pilas de Combustible e Hidrogeno*, Buenos Aires, July 24–26, 2006, Red Iberoamericana de Pilas de Combustible e Hidrogeno (in conference CD).
62. I. Epelboin, M. Keddam, and J. C. Lestrade, *Faraday Discuss. Chem. Soc.*, **56**, 264 (1973).
63. C. Gabrielli, *Identification of Electrochemical Processes by Frequency Response Analysis*, Solartron Instrumentation Group, Ref. No. 004/83 (Farnborough, England) pp. 16–20 (1987).
64. J. Yu, T. Matsuura, Y. Yoshikawa, M. N. Islam, and M. Hori, *Electrochem. Solid-State Lett.*, **8**, A156 (2005).
65. P. C. Biesterfeld, *Physical Systems Theory in Terms of Bond Graphs*, Ph.D Thesis, University of Twente, The Netherlands (1984).
66. D. A. Stevens, M. T. Hicks, G. M. Haugen, and J. R. Dahn, *J. Electrochem. Soc.*, **152**, A2309 (2005).
67. J. F. Meyers and R. M. Darling, *J. Electrochem. Soc.*, **153**, A1432 (2006).
68. V. O. Mittal, H. R. Kunz, and J. M. Fenton, *J. Electrochem. Soc.*, **153**, A1755 (2006).
69. F. Meier and G. Eigenberger, *Electrochim. Acta*, **49**, 1731 (2004).
70. M. Inaba, M. Ueo, I. Maruyama, A. Tasaka, K. Kinoshita, and Z. Ogumi, *J. Electroanal. Chem.*, **417**, 105 (1996).
71. S. Escribano, Ph.D. Thesis, Institut National Polytechnique de Grenoble, Grenoble, France (1995), http://www.ensieg.inpg.fr/LEG/en/ENV.

DOI: 10.1002/fuce.200500204

A Multi-Scale Dynamic Mechanistic Model for the Transient Analysis of PEFCs

A. A. Franco[1]*, P. Schott[1], C. Jallut[2], and B. Maschke[2]

[1] Commissariat de l'Energie Atomique, DRT/LITEN/DTH/Laboratoire d'Essais et Validations de Composants H_2-Piles à Combustible, 17, Rue des Martyrs, FR-38000 Grenoble, France

[2] Laboratoire d'Automatique et de Génie des Procédés, LAGEP UMR CNRS, FR-5007 Université Lyon-1, 43 Bd du 11 Novembre 1918, FR-69622 Villeurbanne cedex, France

Received July 5, 2005; accepted May 23, 2006

Abstract

Electrochemical impedance spectroscopy is an experimental technique widely used for the transient analysis of PEFCs. Experimental results are usually analyzed using equivalent circuit models, which have to be fitted to each operation point and do not offer direct access to the internal physical parameters of the electrodes.

In this paper, a multiscale mechanistic Membrane-Electrode Assembly model is proposed, based on irreversible thermodynamics and electrodynamics, and dependent on the internal physical parameters, such as the effective catalyst surface, the electrical permittivity of the materials, the reaction kinetics, and the diffusion coefficients of the reactant species.

This model results from the coupling of a microscale transport phenomena description through the electrode and the electrolyte thickness, a spatially distributed microscale model of the reactant diffusion through the Nafion® layer covering the Pt/C particles, and a spatially distributed nanoscale description of the Nafion®-Pt/C interface. This interfacial model is based on an internal description of the double layer dynamics, coupling the transport phenomena in the diffuse layer with the electrochemical reactions and water adsorption in the inner layer.

The system dynamics can be simulated and are dependent on the current, the temperature, the reactant pressures, and the Pt/Nafion® loadings on the electrodes. The first simulations carried out are in good qualitative agreement with experimental results, giving access to the contributions of the different phenomena and to the sensitivity of the operating conditions.

Keywords: Electrochemical Double Layer, Electrochemical Impedance Spectroscopy, Irreversible Thermodynamics, Multiscale Modeling, Polymer Electrolyte Fuel Cell

1 Introduction

Electrochemical impedance spectroscopy (EIS) is a widely used experimental technique for the transient analysis of physical phenomena in Polymer Electrolyte Fuel Cell (PEFC) environments [1–16]. Experimental results are usually analyzed using analogy circuit models, which do not offer direct access to the internal physical parameters of the electrodes. In these models, charge transfer is typically represented by ideal resistors and mass transport by complex impedances. The interfacial accumulation of intermediate reaction species and the electrochemical double layer at the catalyst/electrolyte interface are represented by uncoupled capacitive elements (the adsorption of intermediates is supposed to be taking place in the bulk) [6–7, 16–22].

One drawback of this approach is that these models are not predictive and their parameters have to be fitted for each working point (given by the nominal current, temperature, and reactant species concentration). It is known from experiment that the character of EIS spectra strongly depends on these working conditions and on the electrode composition [23], e.g., EIS spectra are arc shaped with a diameter depending on the nominal current. Also, due to the fact that the AC circuit components are a global linear representation of the nanoscopic physical mechanisms involved, an analogous circuit involving three or more circuit elements can often be arranged in various ways and still produce similar impedance responses [24–27].

Analytical expressions of the impedances as functions of the nominal current and reactant concentration can also be derived, assuming some simple electrochemical mechanisms

* Corresponding author, alejandro.franco@cea.fr

in the electrode, but analytical computations of complex impedances are impossible for more complicated mechanisms [18, 20–21].

In this work, a dynamic numerical model of a Membrane-Electrode Assembly (MEA) is proposed, based on non-equilibrium thermodynamics and electrodynamics [21, 28–29]. The model is composed of anode, cathode, and electrolyte mechanistic sub-models. The model computes, dynamically, the potential difference between the two electrodes in response to a time dependent current demand $I(t)$. A Fast Fourier Transform on the input and output signals allows the simulation of the EIS experiments.

Typically, PEFC electrodes are volumetric and are formed from catalyst/electronic conductor particles (called the metal phase) immersed in an ionic conductor medium (called the electrolyte phase) and a void fraction (called the pore phase) (Figure 1) [30, 31]. This ionic conductor contains spatially fixed and negatively charged sulfonate sites (in this case Nafion®). The electrodes, which are several micrometers thick, are separated by a 20 to 100 micrometer electrolyte phase. The particles that constitute the metal phase (Pt/C) have a typical diameter of 100 nanometers and are presumed to be uniformly distributed in the electrode volume, as well as homogeneously covered with the impregnated electrolyte layer of 10^{-7} m maximum thickness [32].

An electrochemical double layer, several nanometers thick, is formed in the vicinity of the metal phase (Figure 2). As discussed by Franco et al. [33], it is composed of a diffuse layer and an inner layer. The diffuse layer consists of moving ions, counter-ions from the electrolyte phase, and of water molecules. The inner layer is formed from adsorbed water molecules at the surface of the metal phase, and intermediate reaction species.

Therefore, three very different geometrical scales are involved, so, the electrochemical cell is represented by a multiscale model, as illustrated in Figure 1. It is noted that R is the microscopic thickness coordinate of the active layer (the same axis is used for both the anode and the cathode). In addition, it is noted that Z is the microscopic thickness coordinate for the impregnated Nafion® layer. The interfacial double layer is placed at the microscopic point $z = e_{Nf}$. X is the nanoscopic coordinate in this double layer. The multiscale model results from the coupling of a microscale transport phenomena description through the electrode and the electrolyte thickness, a spatially distributed microscale model of the reactant diffusion through the Nafion® layer, and a spatially distributed nanoscale dynamic model of the Pt/C-electrolyte

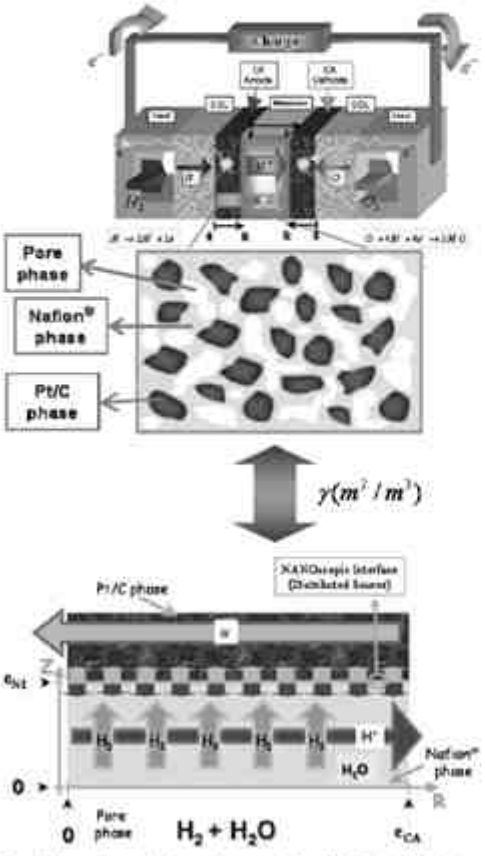

Fig. 1 Electrode morphology and geometrical model. The Nafion® phase can be seen as an "effective Nafion®/water phase".

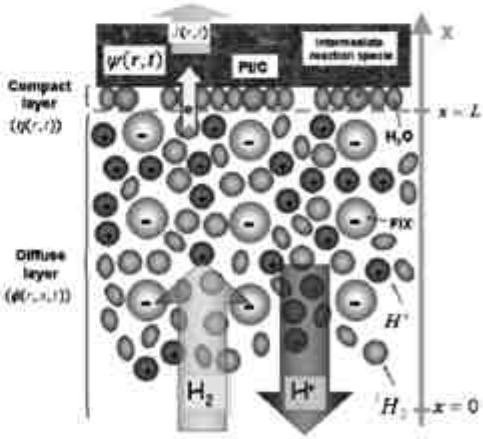

Fig. 2 Schematic representation of the nanoscale interface (electrochemical double layer). Example of the anodic case: the hydrogen species arrives to the inner layer where the electron transfer reaction takes place. The proton species is produced at $x = L$ and evacuated through $x = 0$ (source: [33]).

interface, as introduced by Franco et al. [33]. The nanoscale description is based on a dynamic model of the electrochemical double layer structure, coupled with the electrochemical reactions (Figure 2). To the best of our knowledge, this is the first time that such a nanoscale description has been coupled to microscale transport phenomena models, in order to simulate the MEA transient response.

As explained elsewhere, the multiscale model, using infinite-dimensional Bond Graph theory [34–35], is designed in a modular way so that it is suitable for use in other contexts (CO poisoning, ageing mechanisms) [23, 36–39].

2 The Microscale Models

In the first step of the work presented here, the case of isothermal fuel cells fed with pure hydrogen and oxygen fully saturated with water vapour is considered. Under these conditions, it appears that it is not necessary to take into account the gas diffusion layers of a typical fuel cell [40].

As discussed in Section 1, the model has been designed in a modular way, so it will be possible, in a second step, to extend it by coupling with other phenomena (water transport, nitrogen diffusion, thermal transfer, etc.).

2.1 The Membrane Model

The membrane is considered to be impermeable to gases, only protons and water transfer through it.

As will be shown in Section 4.2, at the microscale, electroneutrality in the electrolyte phase can be assumed, and proton transport is governed by Ohm's law. The local protonic current in the membrane is given by

$$i_{H^+}(r,t) = -S_{electrode}\sigma_{H^+}\nabla_r\phi(r,t) \tag{1}$$

where $S_{electrode}$ is the geometric surface of the MEA, $\phi(r,t)$ is the local protonic electrical potential in the Nafion® phase, and σ_{H^+} is the protonic conductivity given by [41]

$$\sigma_{H^+} = (0.46\lambda - 0.25)e^{\left[-1300\left(\frac{1}{T}-\frac{1}{303}\right)\right]} \tag{2}$$

In this equation, λ is the local number of water molecules per sulfonate site and T is the local temperature. Assuming no accumulation of protons, the conservation law gives

$$\nabla_r\left(\frac{i_{H^+}(r,t)}{S_{electrode}}\right) = 0 \tag{3}$$

In the context of this work, the feed gases are fully saturated with vapour and the membrane conductivity is presumed to be constant (under these conditions λ is close to 14 water molecules per sulfonate site [40]). Experimental results confirm that the electro-osmotic flux is not sufficient to significantly dry out the anode.

2.2 The Electrode Models

Since pure feed gases (no nitrogen) are considered, the hydrogen and oxygen pressure drops in the pore phases are neglected. The gas partial pressures are

$$p_{H_2} = P_{anode} - p_{sat} \tag{4}$$

$$p_{O_2} = P_{cathode} - p_{sat} \tag{5}$$

where p_{sat}, the saturated water pressure, is given as a function of temperature [23, 40]

$$p_{sat} = 10^{-5}\times\exp\left(23.1961 - \frac{3816.44}{T-46.13}\right) \tag{6}$$

Gas transport in the thickness of the impregnated Nafion® layers is assumed to be represented by diffusion equations for both H_2 and O_2 (denoted by index i)

$$\frac{\partial C_i}{\partial t} = -\nabla_x\vec{f}_i = -\nabla_x(-D_i\nabla_x C_i) = D_i\nabla_x^2 C_i \tag{7}$$

with the following boundary conditions

$$C_{H_2}(z=0,t) = \frac{P_{H_2}}{1.09\times10^6\times\exp(77/T)}$$

(Henry's Law for the anodic case [40]) (8)

$$C_{O_2}(z=0,t) = \frac{P_{O_2}}{5.08\times10^6\times\exp(-498/T)}$$

(Henry's Law for the cathodic case [40]) (9)

The hydrogen and oxygen fluxes at $z = e_{NI}$ are given by the nanoscale sub-models (Section 3). The continuity of fluxes at the interface between the two modelling scales is written as

$$J_i(r,z=e_{NI},t) = J_i(r,x=0,t) \tag{10}$$

where $J_i(r,z=e_{NI},t)$ is the input flux for the microscopic scale model and $J_i(r,x=0,t)$ is the output flux computed for the nanoscopic scale model.

At the microscale, the electroneutrality of the Nafion® phase can be assumed, since it is far from the electrified surface (Pt/C particles surface) (Section 4.2). Therefore, there is no proton accumulation and $C_{H^+} = C_{RX}$, where C_{RX} is the counter-ion concentration (sulfonate site concentration). So proton transport in the electrodes is also governed by Eq. (1). The law of conservation gives

$$\nabla_r\left(\frac{i_{H^+}(r,t)}{S_{electrode}}\right) = S_{H^+}(r,t) \tag{11}$$

where $S_{H^+}(r,t)$ is the local production (anode) or consumption (cathode) of protons. The production and consumption of these species is given by the distributed source

$$S_{H^+}(r,t) = j(r,t)\gamma \tag{12}$$

where γ is the specific contact area between the catalyst and electrolyte (in $m^2\ m^{-3}$) and $j(r,t)$ is the current density (in $A\ m^{-3}$), equal to the local electronic current (Eq. (15)).

Remark 1: In this model, since it is assumed that the feed gases are saturated with water, it is thought that the additional water production at the cathode is evacuated through the liquid phase. This liquid phase may occupy a fraction of the pore phase, but since the case considered is of an electrode working with pure oxygen it doesn't significantly affect the oxygen concentration in the active layer. Any pressure drop through the gas diffusion layer is assumed to be negligible.

The local electronic current in the carbon phase at the microscale can be expressed as

$$i_e(r,t) = -S_{electrode}\,\nabla_r\varphi(r,t) \tag{13}$$

where $\varphi(r,t)$ is the local electronic electrical potential, computed by the nanoscale sub-models (Section 3), and g_e is the electronic conductivity. Neglecting electronic accumulation, the local production (anode) or consumption (cathode) of electrons is computed from the conservation law:

$$\nabla_r\left(\frac{i_e(r,t)}{S_{electrode}}\right) = S_e(r,t) \tag{14}$$

where

$$\int(r,t)_\Gamma = S_e(r,t) \tag{15}$$

The boundary conditions for Eq. (14) are

$$i_e(r = e_{CL},t) = 0 \tag{16}$$

$$i_e(r = 0,t) = I(t) \tag{17}$$

where $I(t)$ is the global current delivered by the fuel cell.

3 The Nanoscale Models

The nanoscale models allow the computation of the boundary conditions and sources terms for the microscale models (transport of gases through the impregnated Nafion® layer, proton and electron transport through the electrode thickness).

3.1 The Diffuse Layer Models

The diffuse layer models are based on transport by the diffusion and migration (at nanometre lengths from the Pt/C particles) of the reactant species coupled with the electric field generated by the resulting charge distribution (Figure 2). All species are considered as punctual (diluted solution theory) [42], so interparticle electrical interaction is neglected. Solvatation and convection by water are not considered.

According to non-equilibrium thermodynamics, the fluxes of the electrically neutral species H_2 and O_2 are assumed to be given by Fick's law of diffusion and the mass balance leads to:

$$\frac{\partial C_i}{\partial t} = -\nabla_x f_i = -\nabla_x\left(-D_i\nabla_x C_i\right) = D_i\nabla_x^2 C_i \tag{18}$$

where the diffusion coefficient, D_i, is assumed to be constant.

In the case of the electrically charged species H^+, the diffusion coefficient in the medium is also assumed to be independent of the concentration. Combining the flux related to Fick's diffusional force and the electrical force, with the mass balance, an equation representing the proton concentration is obtained (Nernst-Planck equation):

$$\frac{\partial C_{H^+}}{\partial t} = -\nabla_x f_{H^+} = -\nabla_x\left(-D_{H^+}\nabla_x C_{H^+} - fD_{H^+}C_{H^+}\nabla_x\phi\right) = \\ = D_{H^+}\nabla_x^2 C_{H^+} + fD_{H^+}\nabla_x C_{H^+}\nabla_x\phi + fD_{H^+}C_{H^+}\nabla_x^2\phi \tag{19}$$

where $\phi(r,x,t)$ is the electrical potential in the electrolyte, which is calculated from the Poisson's equation:

$$\frac{F}{\varepsilon_{DL}}\left(C_{H^+} - C_{FIX}\right) = -\nabla_x^2\phi \tag{20}$$

Remark 2: Magnetic effects are neglected in Eq. (20) (because the frequency range of interest is lower than 1 MHz [23, 43, 44]). C_{FIX}, in Eq. (20), is assumed to be constant, to enable it to correspond with the experimental conditions. These counter-ions are thought to be located outside the inner layer and do not affect its structure [23, 33].

Remark 3: It is important to note that Eq. (19) and (20) are introduced because, at the nanoscale (near the electrified surface where electron transfer takes place), electroneutrality cannot be assumed, and because there is no supporting electrolyte (proton conductivity in Nafion® is not infinite).

The concentrations, $C_{H^+}(r,0,t)$ and $C_i(r,0,t)$, and the scalar potential, $\phi(r,0,t)$, are coupled with the microscale models (Section 2, Eq. (7) and (10)).

Eq. (18), (19), and (20) are coupled at $x = L$ to the interfacial inner layer model (Section 3.2). This inner layer model computes $f_{H^+}(r,L,t)$ and $f_i(r,L,t)$ (boundary conditions for Eq. (19) and Eq. (19)) and gives an algebraic relation between $\phi(r,L,t)$ and $\partial\phi(r,L,t)/\partial x$ (boundary condition for Eq. (20)).

3.2 The Inner Layer Models

The inner layer is formed by adsorbed water molecules and intermediate reaction species at the surface of the catalyst phase [23, 33, 42, 45–47]. In this work, this layer is modelled according to a continuum framework, based on non-equilibrium thermodynamics and electrodynamics, introduced and discussed by Franco et al. [33].

The water molecules behave like punctual electric dipoles and generate an interfacial potential discontinuity, which allows electron transfer between the electrolyte phase and the catalyst phase. The model describes the evolution of the surface dipolar density, which depends on the adsorption of water and of intermediate electrochemical species. It allows the calculation of the resulting electric potential drop between the two phases, known as the "Frumkin overpotential"[1] and

[1] *Note that this definition of "overpotential" [48] differs from that usually used in the context of electrochemical cell modelling, where it is referred to as the "global" potential loss of the cell [49–57].*

denoted by $\eta(r,t)$. In addition, it permits the development of a set of electrochemical reaction steps on the metallic surface with an electronic surface density of $\sigma(r,t)$ (Figure 3). It is a function of time, as described according to

$$\eta(r,t) = \varphi(r,t) - \phi(r,L,t) \tag{21}$$

where $\phi(r,L,t)$ is the electric potential in the electrolyte just outside the water layer adsorbed on the catalyst surface and $\varphi(r,t)$ is the electric potential in the metallic phase.

According to the superposition principle of electrodynamics, $\eta(r,t)$ is also given by the sum of the drop related to the thickness of the adsorbed water layer ($\Delta\varphi_1$) and the drop related to the dipolar nature of these molecules ($\Delta\varphi_2$). The next two subsections show how these two contributions are related to the electronic surface density $\sigma(r,t)$ in the Pt/C phase. This density is calculated by the charge conservation law at the metal/electrolyte interface (see Sections 3.2.2–3.2.4).

In this Section, an expression for the electrostatic potential difference, $\eta(r,t)$, will be derived from a model of the inner layer, describing interfacial water adsorption, which is based on the hypothesis of two possible dipolar orientations of the water molecules, i.e., hydrogen-end towards and opposed to the metal surface. This simple two-state assumption is similar to the original Mott and Watts-Tobin model [58]. It can be seen as a particular case of statistical multistate models and is a first step towards the consideration of more complex models, as presented for instance in [59–64]. The structure and couplings of the model are independent of the complexity of the water adsorption sub-model used (the structure of the model remains the same if the water adsorption sub-model is changed, because only the computation of the dipolar density Γ (cf. Eq. (27)) is affected).

3.2.1 Calculation of $\Delta\varphi_1$

According to Gauss's theorem [44–45], $\sigma(r,t)$ can be expressed as a function of $-\partial\phi/\partial x(r,L,t)$, the electric field at the metal/electrolyte interface (remember that $-\partial\phi/\partial x(r,L,t)$ is the boundary condition for Eq. (20)). Assuming a linear relation between the displacement vectors, $\vec{D}_i$, and the electric field in the diffuse and inner layers, the following is obtained (box number 1 in Figure 3):

$$\left\|\frac{\vec{D}_{Pt/C}(r,L,t)}{\varepsilon_{DL}}\right\| = \left\|\frac{\vec{D}_{CL}(r,L,t)}{\varepsilon_{CL}}\right\| \tag{22}$$

where the continuity of the electric field through the water layer is used [33] (considered as punctual dipoles), ε_{DL} is the electrical permittivity of the electrolyte phase, and ε_{CL} is the electric permittivity of the adsorbed water layer [23, 33, 42] (believed to be independent of temperature). According to Gauss's theorem, the following occurs for the anodic case (box number 2 in Figure 3):

$$-\left\|\vec{D}_{CL}(r,L,t)\right\| + \left\|\vec{D}_{Pt/C}(r,t)\right\| = \sigma(r,t) \tag{23}$$

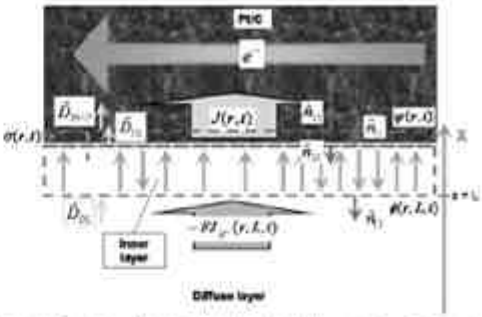

Fig. 3 Calculation of the interfacial electric field: application of Gauss's theorem in the vicinity of the Pt/C phase.

The Pt/C phase is considered as a perfect electronic conductor in the direction perpendicular to the electrode thickness (electrons go out according to the electronic flux through the electrode thickness), giving $\left\|\vec{D}_{Pt/C}(r,t)\right\| = 0$ and

$$\left\|\frac{\vec{D}_{CL}(r,L,t)}{\varepsilon_{CL}}\right\| = \left\|\frac{\partial\phi}{\partial x}(r,L,t)\right\| = -\frac{\sigma(r,t)}{\varepsilon_{CL}} \tag{24}$$

For anodic and cathodic reaction $\varphi(r,t) - \phi(r,L,t) > 0$ and $\varphi(r,t) - \phi(r,L,t) < 0$, respectively, and due to the small thickness, d, of the water layer, the potential drop through the compact layer can be approximated to:

$$\Delta\varphi_{1a} = -\frac{\sigma(r,t)}{\varepsilon_{CL}}d > 0 \text{ (anodic)};\ \Delta\varphi_{1c} = -\frac{\sigma(r,t)}{\varepsilon_{CL}}d < 0 \text{ (cathodic)} \tag{25}$$

3.2.2 Calculation of $\Delta\varphi_2$

Since the water layer is considered to be a layer of punctual dipoles, the interfacial potential drop, $\Delta\varphi_2$, is given by [33, 43]:

$$\Delta\varphi_2 = \frac{\Gamma(r,t)}{\varepsilon_{DL}} \tag{26}$$

where Γ is the dipolar surface density (in debye m^{-2}). To find an expression for Γ as a function of $\sigma(r,t)$, the 2-states hypothesis is used (Figure 4). $\vec{n}$ ($\vec{n}$) is the number of dipoles per unit of area directed[2] (or opposed) towards the electrode. Hence the dipolar surface density is:

$$\Gamma = \mu(\vec{n} - \overleftarrow{n}) \tag{27}$$

where μ is the dipolar moment of a water molecule. The oriented adsorption of a water molecule is described by the equilibrium reactions:

$$H_2O + s \leftrightarrow \overrightarrow{H_2O} - s \text{ and } H_2O + s \leftrightarrow \overleftarrow{H_2O} - s \tag{28}$$

[2] Hydrogen-end towards the metal.

where s is an adsorption site on the electrode surface. The application of the mass action laws gives

$$\frac{\vec{n}}{n_s\theta_{H_2O}} = \vec{k} = e^{-\frac{\vec{\Delta G^0}}{RT}} \text{ and } \frac{\vec{n}}{n_s\theta_{ads}} = \overleftarrow{k} = e^{-\frac{\overleftarrow{\Delta G^0}}{RT}} \quad (29)$$

where n_s is the number of free sites per unit area, θ_{H_2O} is the volume fraction of free water molecules (assumed to be constant and conserved on the surface)[3], and ΔG^0 is the Gibbs free energy of the Eq. (28). This energy results from three contributions, according to Eq. (30):

$$\Delta G^0 = \Delta G_c^0 + \Delta G_e^0 + \Delta G_i^0 \quad (30)$$

where

- ΔG_c^0 is the chemical adsorption energy (which is assumed to be constant and independent of the dipole orientation)
- ΔG_e^0 is the electrostatic energy, corresponding to the work of the field created by the charge of the metallic phase to carry a dipole from infinity to the catalyst surface
- ΔG_i^0 is the inter-dipole interaction energy

The electrostatic energies for the two opposing dipolar orientations are:

$$\vec{\Delta G_e^0} = +\mu\frac{\partial\phi}{\partial x}(r,L,t) \text{ and } \overleftarrow{\Delta G_e^0} = -\mu\frac{\partial\phi}{\partial x}(r,L,t) \quad (31)$$

where the potential reference is taken as being equal to zero at infinity [23, 28, 33].

The free energies, ΔG_i^0, can be evaluated as follows (Figure 4). First, a dipole 2, already adsorbed, is considered, e.g., oriented towards the electrode. Then, a water molecule 1 is considered, oriented in the same way, adsorbing at the electrode surface (with coordinates x and y). The work required

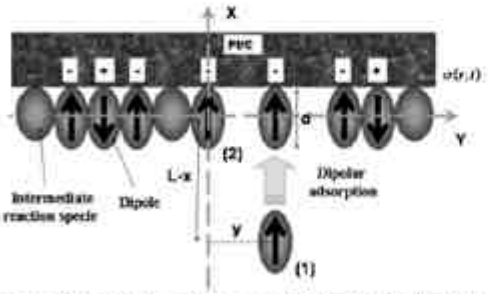

Fig. 4 Orientation of the adsorbed water dipoles and calculation of the interdipolar interaction energy.

[3] *The model has been designed in a modular way [23, 33, 36–39] and it can easily be coupled to other physical phenomena, like water transport in the Nafion® and in the pore phases. Due to its modular character, the structure of the model is independent of the complexity of the water sub-model used (the structure of the model remains the same if other water sub-model is used, only the computation of the water activity, Θ_{H_2O} and λ (cf. Eq. (2)) are affected).*

to move the water molecule from infinity to the catalyst surface is calculated using

$$W_{dipole/dipole} = \int_{-\infty}^{L} F_x dx \quad (32)$$

where

$$F_x = \frac{\mu^2}{4\pi\varepsilon_{DL}}\left[\frac{15(L-x)^5}{((L-x)^2+y^2)^{7/2}} - \frac{9(L-x)}{((L-x)^2+y^2)^{5/2}}\right] \quad (33)$$

which is the force on dipole 1 in the field of dipole 2 [44].

It is presumed that the adsorbing dipole is very slightly deviated in the Y direction by the dipole already adsorbed. Therefore, the integral Eq. (32) can be calculated in the X direction only:

$$W_{dipole/dipole} = \frac{\mu^2}{4\pi\varepsilon_{DL}}\frac{1}{y^3} \quad (34)$$

where it is assumed (to a first approximation) that ε_{DL} is independent of x [23, 33, 42]. If the water molecule adsorbs on an electrode covered with dipoles all oriented in its direction, the Gibbs energy received by the molecule is the sum of the effect of every adsorbed dipole (assuming that dipole number j is placed in position jd on the Y axis):

$$W_{\rightarrow} = 2\times\sum_{j=1}^{\infty}\frac{\mu^2}{4\pi\varepsilon_{DL}}\frac{1}{(jd)^3} = \frac{\mu^2}{2\pi\varepsilon_{DL}d^3}\sum_{j=1}^{\infty}\frac{1}{j^3} = \frac{\mu^2\zeta[3]}{2\pi\varepsilon_{DL}d^3} = \frac{\mu^2 A}{d^3} \quad (35)$$

where ζ defines Riemann's Zeta function[40] (the factor 2 comes from the necessity to take into account the dipoles adsorbed on both sides of the molecule considered) with $A = \zeta[3]/2\pi\varepsilon_{DL}$. In a similar way, for the case of dipoles oriented towards the electrolyte, the Gibbs energy experienced by the molecule is:

$$W_{\leftarrow} = -\frac{\mu^2 A}{d^3} \quad (36)$$

If the two orientations coexist, the fraction covered with dipoles oriented towards the electrode is indicated by $\vec{\theta}$, with the opposing fraction being $\overleftarrow{\theta}$:

$$\vec{\theta} = \frac{\vec{n}}{n^{max}} = \frac{\vec{n}}{n^* + \vec{n} + \overleftarrow{n}} \text{ and } \overleftarrow{\theta} = \frac{\overleftarrow{n}}{n^{max}} = \frac{\overleftarrow{n}}{n^* + \vec{n} + \overleftarrow{n}} \quad (37)$$

where n^{max} is the maximal quantity of free sites per unit area (represented in Figure 5 as spheres, showing three possible ways of packaging) and where n^* is the sum of the number of free sites, n_s, and the sites covered by an intermediate reaction species (see Sections 3.2.3 and 3.2.4) per unit area. Averaging the interaction of a given dipole with the other dipoles (mean field approximation), the total work of adsorption under dipolar interaction is then:

$$\vec{W} = \vec{\Delta G_i^0} = \frac{A\mu^2}{d^3}(\vec{\theta} - \overleftarrow{\theta}) \text{ and } \overleftarrow{W} = \overleftarrow{\Delta G_i^0} = -\frac{A\mu^2}{d^3}(\vec{\theta} - \overleftarrow{\theta}) \quad (38)$$

[4] $\zeta(\Omega) = \sum_{j=1}^{\infty}\frac{1}{j^{\Omega}}(\Omega > 1), \zeta[3] \approx 1.20$

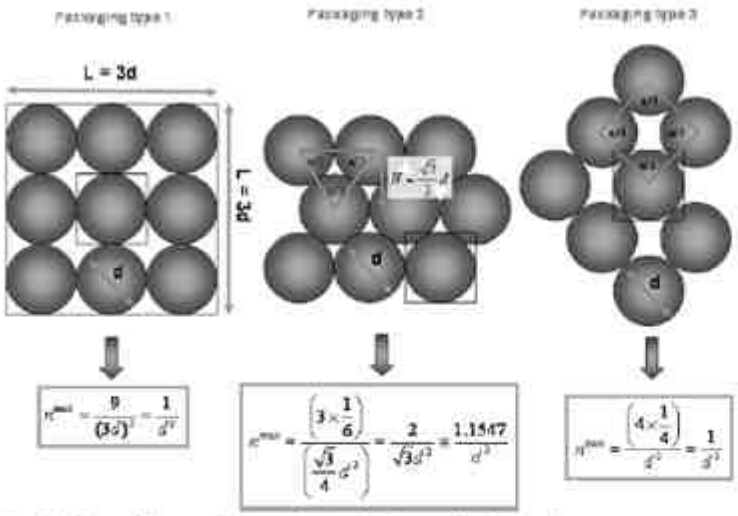

Fig. 5 Calculation of the maximal quantity of free sites by three possible sphere packaging.

According to (37), the following can be written

$$\tilde{\theta} - \bar{\theta} = \frac{\tilde{n} - \bar{n}}{n^* + \tilde{n} + \bar{n}} \tag{39}$$

Defining

$$X = \frac{\mu\sigma}{kT\varepsilon_{CL}} + \frac{A\mu^2}{kT\delta^3}(\tilde{\theta} - \bar{\theta}) \text{ and } a = 2r^{\frac{n_d^2}{n_s}} \tag{40}$$

and the equations in (29) become

$$\tilde{n} = n_s\Theta_{H_2O}\frac{a}{2}e^{-X} \text{ and } \bar{n} = n_s\Theta_{H_2O}\frac{a}{2}e^{X} \tag{41}$$

and Eq. (40) becomes

$$\frac{a\,Sinh[X]}{\frac{n^*}{n_s\Theta_{H_2O}} + a\,Cosh[X]} = \kappa\sigma - \zeta X,$$

$$\text{with } \kappa = \frac{\delta^3}{\varepsilon_{CL}A\mu} \text{ and } \zeta = \frac{kT\delta^3}{A\mu^2} \tag{42}$$

This transcendental equation in X allows the computation of $\tilde{\theta} - \bar{\theta}$ and consequently $\tilde{n} - \bar{n}$. It has a single solution for a given value of $\sigma(r,t)$. Considering Eqs. (26) and (27) the subsequent equation is obtained

$$\Delta\varphi_2 = -\frac{an_s\Theta_{H_2O}\mu Sinh[X(r,t)]}{\varepsilon_{DL}} \tag{43}$$

Finally, $\eta(r,t)$ can be written as

$$\eta(r,t) = \Delta\varphi_1 + \Delta\varphi_2 = -\frac{\sigma(r,t)d}{\varepsilon_{CL}} - \frac{an_s\Theta_{H_2O}\mu Sinh[X(r,t)]}{\varepsilon_{DL}} \tag{44}$$

The calculation of the number of free sites per unit of area, n_s, and its coupling with the electrochemical reactions are presented in the subsequent Sections 3.2.3 and 3.2.4.

$\sigma(r,t)$ is calculated from the law of conservation of charge, at the catalyst/electrolyte interface [33, 43-44] (Figure 3):

$$j(r,t) - j_{Far,A}(r,t) = -\frac{\partial\sigma(r,t)}{\partial t} \text{ (anode)} \tag{45}$$

$$j(r,t) - j_{Far,C}(r,t) = \frac{\partial\sigma(r,t)}{\partial t} \text{ (cathode)} \tag{46}$$

where $j_{Far,A}(r,t)$ and $j_{Far,C}(r,t)$ are the faradaic current densities, given by the electrochemical reactions rates (Sections 3.2.3 and 3.2.4). $j(r,t)$ is calculated from the microscale electron transport model (Eqs. (13)-(15)).

3.2.3 *Coupling of the Inner Layer Model with the Electrochemical Reaction at the Anode*

A Tafel-Heyrovsky-Volmer three step reaction model is considered for hydrogen oxidation, in order to calculate the temporal variation of n^* (and so of n_s) used in the anodic inner layer model. This reaction mechanism is well known [23, 33, 65-67]:

$$H_2 + 2s \leftrightarrow 2Hs \text{ (Tafel)} \tag{47}$$

$$s + H_2 \leftrightarrow Hs + H^+ + e^- \text{ (Heyrovsky)} \tag{48}$$

$$Hs \leftrightarrow s + H^+ + e^- \text{ (Volmer)} \tag{49}$$

The rates of these elementary steps can be described as [33]:

$$v_{TAF} = k_{TAF}\theta_s^2 C_H(r,L,t) - k_{-TAF}\theta_H^2 \tag{50}$$

$$v_{HEY} = k_{HEY}\theta_s C_H(r,L,t)e^{(1-\alpha_{HEY})f\eta(r,t)} - k_{-HEY}\theta_H C_{H^+}(r,L,t)e^{-\alpha_{HEY}f\eta(r,t)} \tag{51}$$

$$v_{VOL} = k_{VOL}\theta_H e^{(1-\alpha_{VOL})f\eta(r,t)} - k_{-VOL}\theta_s C_{H^+}(r,L,t)e^{-\alpha_{VOL}f\eta(r,t)} \tag{52}$$

where $C_H(r,L,t)$ is the hydrogen concentration and $C_{H^+}(r,L,t)$ is the proton concentration at $z = L$ (Figure 2), both calculated by the diffuse layer Eqs. (18) and (19). θ_s is the surface coverage of free sites, and θ_H is the surface coverage of adsorbed monatomic hydrogen. k_i and k_{-i} are the standard electronic rate constants for each step, $f = F/RT$ and α denote the Frumkin electron transfer factors [33, 48].

The boundary condition for Eq. (18) at $z = L$ for the anode is

$$j_H(r,L,t) = -(v_{TAF} + v_{HEY}) \tag{53}$$

(negative because hydrogen is consumed). For Eq. (19)

$$j_{H^+}(r,L,t) = (v_{HEY} + v_{VOL}) = \frac{j_{ext,A}(r,t)}{F} \tag{54}$$

(positive because protons are produced).

In the following, θ_s and θ_H are computed. Recall that the interfacial electrostatic potential difference, $\eta(r,t)$, appearing in Eqs. (50)-(52) is a function of the electronic density, $\sigma(r,t)$ (Eq. (44)). The value of θ_H is given by the solution of the balanced equation

$$\frac{n^{max}}{N_A}\frac{d\theta_H}{dt} = -v_{VOL} + v_{HEY} + 2v_{TAF} \tag{55}$$

where N_A is Avogadro's number. According to the definition of $n^* = n_s + n_H$ and using $\theta_i = n_i/n^{max}$, Eq. (42) becomes

$$\frac{a\sinh[X]}{\frac{1}{\theta_{H_2O}} + \frac{\theta_H}{\theta_s}\frac{1}{\theta_{H_2O}} + a\cosh[X]} = \kappa\sigma - \zeta X \tag{56}$$

The surface coverage for dipoles directed towards the metal phase is

$$\vec{\theta} = \frac{\frac{a}{2}e^{-X}}{\frac{1}{\theta_{H_2O}} + \frac{\theta_H}{\theta_s}\frac{1}{\theta_{H_2O}} + a\cosh[X]} \tag{57}$$

and for those in the opposite direction is

$$\overleftarrow{\theta} = \frac{\frac{a}{2}e^{X}}{\frac{1}{\theta_{H_2O}} + \frac{\theta_H}{\theta_s}\frac{1}{\theta_{H_2O}} + a\cosh[X]} \tag{58}$$

Finally coupling Eqs. (55) and (56) and remembering that

$$\theta_s + \theta_H + \vec{\theta} + \overleftarrow{\theta} = 1 \tag{59}$$

it can be demonstrated that θ_s can be computed from

$$\theta_s = \frac{1-\theta_H}{1+\theta_{H_2O}a\cosh[X]} \tag{60}$$

and n_s, required in Eq. (44), is given by

$$n_s = \theta_s n^{max} \tag{61}$$

3.2.4 Coupling of the Inner Layer Model with the Electrochemical Reaction at the Cathode

The oxygen reduction mechanism at the cathode is not well understood [7, 18, 23, 68–72]. In this work, a Damjanovic three step reaction model is assumed, in order to calculate the temporal variation of n^* (and so of n_s) used in the cathodic inner layer model. This mechanism consists of three reaction steps [18, 23, 70]:

$$O_2 + H^+ + e^- + s \leftrightarrow O_2Hs \text{ (Dmj 1)} \tag{62}$$

$$O_2Hs + H_2O + 2s \leftrightarrow 3OHs \text{ (Dmj 2)} \tag{63}$$

$$OHs + H^+ + e^- \leftrightarrow H_2O + s \text{ (Dmj 3)} \tag{64}$$

The rates of these elementary steps can be described as [23]:

$$v_1 = k_1\theta_s C_{H^+}(r,L,t)C_{O_2}(r,L,t)e^{-\alpha_1 f\eta(r,t)} - k_{-1}\theta_{O_2H}e^{(1-\alpha_1)f\eta(r,t)} \tag{65}$$

$$v_2 = k_2\theta_{O_2H}\theta_{H_2O}\theta_s^2 - k_{-2}\theta_{OH}^3 \tag{66}$$

$$v_3 = k_3\theta_{OH}C_{H^+}(r,L,t)e^{-\alpha_3 f\eta(r,t)} - k_{-3}\theta_s\theta_{H_2O}e^{(1-\alpha_3)f\eta(r,t)} \tag{67}$$

where $C_{O_2}(r,L,t)$ is the oxygen concentration and $C_{H^+}(r,L,t)$ is the cathodic proton concentration at $z = L$ (Figure 2), both calculated by the diffuse layer Eq. (18) and (19). $\theta_{O_2H_2}$ and θ_{OH_3} are the surface coverages by adsorbed intermediates.

The boundary condition for Eq. (18), at $z = L$ in the cathode, is

$$j_{O_2}(r,L,t) = -v_{Dmj1} \tag{68}$$

(negative because oxygen is consumed). For Eq. (19) the following is obtained

$$j_{H^+}(r,L,t) = -(v_{Dmj1} + v_{Dmj3}) = -\frac{j_{ext,C}(r,t)}{F} \tag{69}$$

(negative because protons are consumed).

The values of $\theta_{O_2H_2}$ and θ_{OH_3} are given by the solutions of the balanced equations:

$$\frac{n^{max}}{N_A}\frac{d\theta_{O_2H_2}}{dt} = v_1 - v_2 \tag{70}$$

$$\frac{n^{max}}{N_A}\frac{d\theta_{OH_3}}{dt} = 3v_2 - v_3 \tag{71}$$

In a similar way to the anodic case, it can demonstrate that Eq. (42) becomes

$$\frac{a\mathrm{Sinh}[X]}{\frac{1}{\theta_{H,O}}+\frac{\theta_{O,Pt}}{\theta_{Pt}}\frac{1}{\theta_{H,O}}+\frac{\theta_{Naf}}{\theta_{Pt}}\frac{1}{\theta_{H,O}}+a\mathrm{Cosh}[X]}=\lambda\sigma-\zeta X \tag{72}$$

For the surface coverage with dipoles directed towards the electrode,

$$\vec{\theta}=\frac{\frac{s}{2}e^{-X}}{\frac{1}{\theta_{H,O}}+\frac{\theta_{O,Pt}}{\theta_{Pt}}\frac{1}{\theta_{H,O}}+\frac{\theta_{Naf}}{\theta_{Pt}}\frac{1}{\theta_{H,O}}+a\mathrm{Cosh}[X]} \tag{73}$$

and for the opposed ones,

$$\overleftarrow{\theta}=\frac{\frac{s}{2}e^{X}}{\frac{1}{\theta_{H,O}}+\frac{\theta_{O,Pt}}{\theta_{Pt}}\frac{1}{\theta_{H,O}}+\frac{\theta_{Naf}}{\theta_{Pt}}\frac{1}{\theta_{H,O}}+a\mathrm{Cosh}[X]} \tag{74}$$

Then θ_g and n_g can be calculated from

$$\frac{n_g}{n^{max}}=\theta_g=\frac{1}{1+\frac{\theta_{O,Pt}}{\theta_{Pt}}+\frac{\theta_{Naf}}{\theta_{Pt}}+\theta_{H_2O}a\mathrm{Cosh}[X]}=\frac{1-\theta_{CO_2Pt}-\theta_{OHPt}}{1+\theta_{H_2O}a\mathrm{Cosh}[X]} \tag{75}$$

3.3 Fuel Cell Potential Calculation

The boundary condition for Eq. (20), at $x = L$, is given by $\partial\phi(r,L,t)/\partial x$, which is calculated from $\sigma(r,t)$ (obtained from Eq. (45) or (46)) and using Eq. (24). The boundary condition at $x = 0$ is fixed at $\phi(r,0,t) = 0$ for the anode (reference electrostatic potential) and is calculated from the microscale proton model for the cathode.

Eq. (20) allows the calculation of $\phi(r,L,t)$, which, using Eq. (21), enables the calculation of the electronic potential $\varphi(r,t)$ for each particular electrode. Finally, the fuel cell potential is given by the difference

$$U_{cell}(t)=\varphi_C(r=0,t)-\varphi_A(r=0,t) \tag{76}$$

4 Numerical Simulations

A code has been developed to solve the problem numerically by coupling three software packages: Simulink® (describing the boundary conditions in $x = 0$, $x = L$, and the interconnection between the different partial differential equations), Femlab® (describing the transport phenomena in the nanoscale diffuse layer model and in the microscale models, using the finite element method), all integrated with Matlab®. The simulations were performed using a microcomputer with an Intel® Pentium® 4 2 GHZ processor, 1 GB of RAM. The set of physico-chemical parameters given in Table 1 were chosen for the simulations shown here.

The numerical code allows the analysis of the stationary and dynamic behaviour of the different state variables (for example, $C_H(r,x,t)$, $\sigma(r,t)$, etc.), the electrode electronic potentials, $\varphi(r,t)$, and the fuel cell potential, $U_{cell}(t)$, in response to a current demand, $I(t)$, at a given temperature, T, and pressure, P_{anode} and $P_{cathode}$. From the decomposition of the model into parts based on first-principle models and their explicit coupling, it becomes easy to interpret and adapt the model to different model assumptions and working conditions. In this section, some results of the steady-state and transient response of the simulated MEA are shown, and the sensitivity to some working conditions and electrode composition are studied (platinum/Nafion® loading). This is particularly focussed on the EIS response, calculated by simulation in the time domain with subsequent Fast Fourier Transformation. Previously, this approach has been shown in the context of solid oxide fuel cells [73–74] and polymer electrolyte fuel cells [23, 28–29, 33]. To determine the AC impedance shown here, a sufficiently small sinusoidal signal (e.g., 15 mA) is superimposed on the fixed (DC) current level, I, in order to obtain a linear response for the fuel cell potential, $U_{cell}(t)$. This is done for frequencies ranging from 0.01 Hz to 10^6 Hz, in an anti-clockwise direction. The steady-state is calculated, prior to starting the simulation of the periodic signal response. The time of calculation for an impedance spectrum with 40 frequency points is approximately 50 minutes.

Table 1 Parameters values used in the numerical simulations.

Parameters	Units	References
$\gamma = 5.39\times10^{5}$	$m^2\,m^{-3}$	This work
$r_{Pt} = 50\times10^{-9}$	m	This work
$r_{Nf} = 10^{-9}$	m	This work and [32]
$r_{CA} = 15\times10^{-9}$	m	This work
$S_{Nafion/Pt} = 2.1\times10^{-4}$	m^2	This work
$C_{DL} = 1,200$	$mol\,m^{-3}$	[16, 23, 33, 40, 75–77]
$\theta_{H_2O}=\theta_{SO_3^-}=0.5$, $a_1=0.8$, $a_2=0.99$	Without dimension	This work
$\kappa_{Cl^-,mob}=6\times\varepsilon_0$	$C\,V^{-1}\,m^{-1}$	[42]
$\kappa_{Cl^-,partout}=4\times\varepsilon_0$	$C\,V^{-1}\,m^{-1}$	[42]
$\varepsilon_{DL}=20\times\varepsilon_0$ (the same value in both electrodes)	$C\,V^{-1}\,m^{-1}$	[42]
$\Delta G^0_C=1$ (the same value in both electrodes)	$kJ\,mol^{-1}$	[23]
$k_{ORR}=10^{-3}$, $k_{HOR}=10^{-4}$, $k_{-ORR}=10^{-4}$, $k_{-HOR}=10^{-3}$, $k_3=10^8$	$m\,s^{-1}$	This work and [18, 23, 33, 40, 65–67]
$k_{-2,ORR}=10^{-5}$, $k_{HOR}=10^{-3}$, $k_{-1}=10^{-6}k_2=10^8$, $k_{-2}=10^{-6}k_{-3}=1$	$mol\,m^{-2}\,s^{-1}$	This work and [23, 33, 65–67]
$k_3=10^4$	$m^4\,mol^{-1}\,s^{-1}$	This work
$\lambda=14$ (the same value in both electrodes)	Water molecules / sulfonate site	[23, 40]
$\Theta_{H_2O}=1.833+0.0022\lambda-\frac{2.75}{\lambda}-0.13\ln\lambda$	Without dimension	[43]
$D_{H^+}=2.97\times10^{-10}\times T$	$m^2\,s^{-1}$	[78]
$\times10^{\left[\frac{\text{(volume of saturated wet)}}{\text{(volume of dry)}}-1\right]\times2}$		
$D_{O_2}=3.92\times10^{-14}\times\exp(0.025\times T)$	$m^2\,s^{-1}$	[23, 31, 35]
$D_{H_2}=3.1\times10^{-7}\times\exp(-2700/T)$	$m^2\,s^{-1}$	[40]
$L=10^{-6}$	m	Discussion Section 4.2 and [33]

4.1 Sensitivity Study to Working Conditions: Some Multiscale MEA Model Simulation Results

In Figure 6, the simulated polarisation curves for three different Pt/Nafion® loadings are shown and are compared

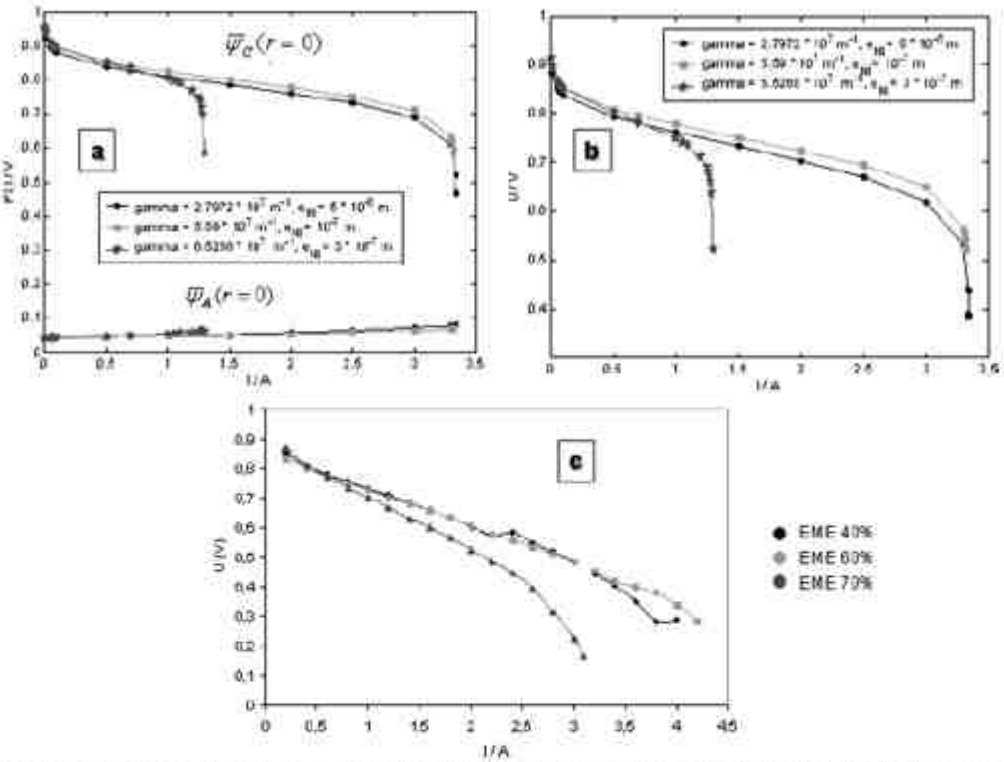

Fig. 6 Steady-state anodic and cathodic electronic potentials (a) and resulting polarisation curves (b) for three different Pt/Nafion® loadings. Experimental results (c) for three different mass ratios (Pt/Nafion®). $P_{anode} = P_{cathode} = 1.5$ bar, $T = 353$ K.

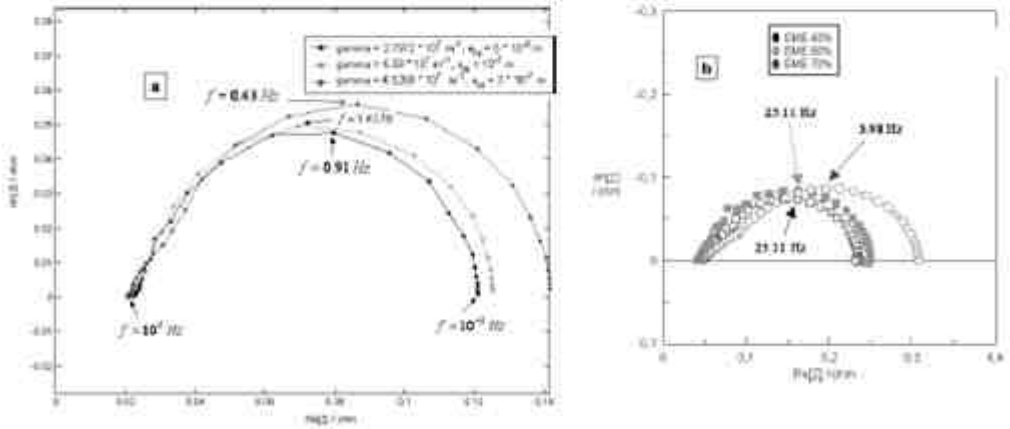

Fig. 7 Simulated EIS (a) for three different Pt/Nafion® loadings. Experimental EIS (b) for three different mass ratios (Pt on Nafion). $I = 0.2$ A, $P_{anode} = P_{cathode} = 1.5$ bar, $T = 353$ K.

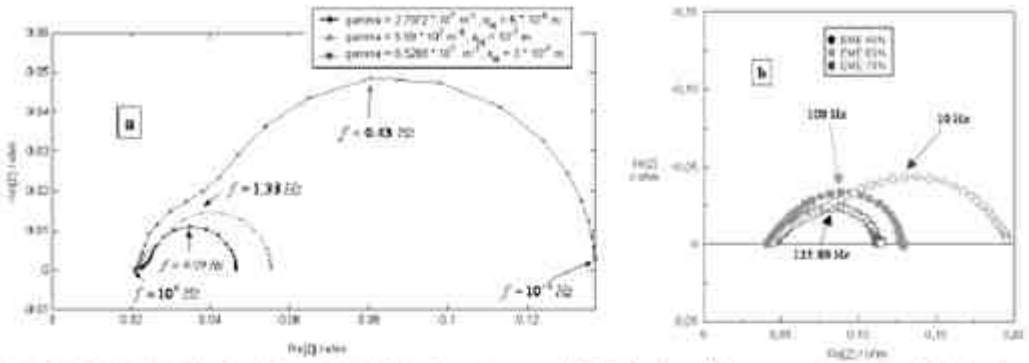

Fig. 8 Simulated EIS (a) for three different Pt/Nafion® loadings. Experimental EIS (b) for three different mass ratios (Pt on Nafion). $I = 1$ A, $P_{anode} = P_{cathode} = 1.5$ bar, $T = 353$ K.

with experimental results also recorded here. These experiments were performed on a test bench working with a single PEFC with $S_{electrode} = 2.1$ cm^2, fed with fully vapour saturated pure hydrogen and oxygen, and warmed by resistance films, as discussed in [23]. It can be seen that when the electrodes are overloaded with Nafion®, the limiting current drops because of reactant transport limitations. Therefore, an explanation of the tendencies of the experimental results shown in Figure 6c can be proposed, where the polarisation curves for three Pt/Nafion® mass ratios are shown. The parameter identification of the model is under development [23].

The simulated EIS for two nominal current values are shown in Figure 7 and 8. They are qualitatively compared with experimental results for the same three electrode composition discussed in Figure 6. These arcs result from the coupling of all the phenomena taken into account in the model: the anodic and cathodic intermediates species, and proton and reactant transport.

At high currents, the increase in the Pt/Nafion® ratio produces an increase in the amplitude of the low frequency arc (as a consequence of the increase in the reactant transport limitation). This explains the experimental observations in Figure 7b and 8b. The development of *in-situ* measurements of the separated anodic and cathodic spectra commences, following a technique proposed by Khun et al. [6–7], to facilitate the parameter identification work.

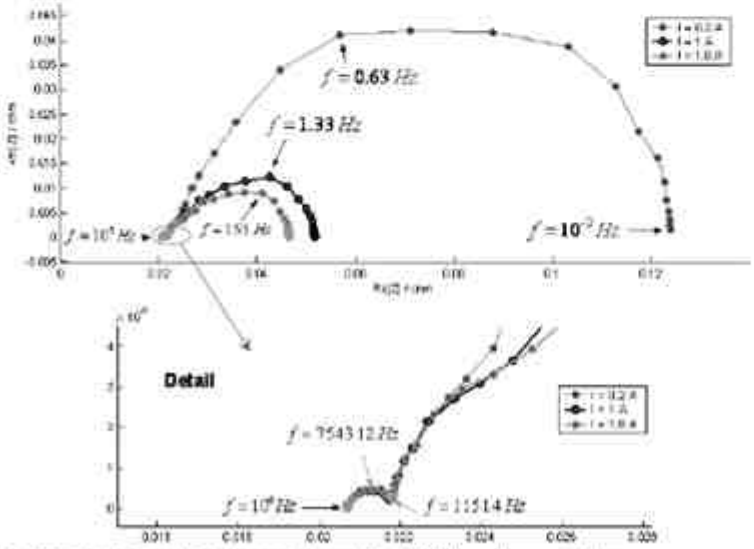

Fig. 9 Simulated EIS sensitivity to the nominal current. $T = 353$ K, $P_{anode} = P_{cathode} = 1.5$ bar.

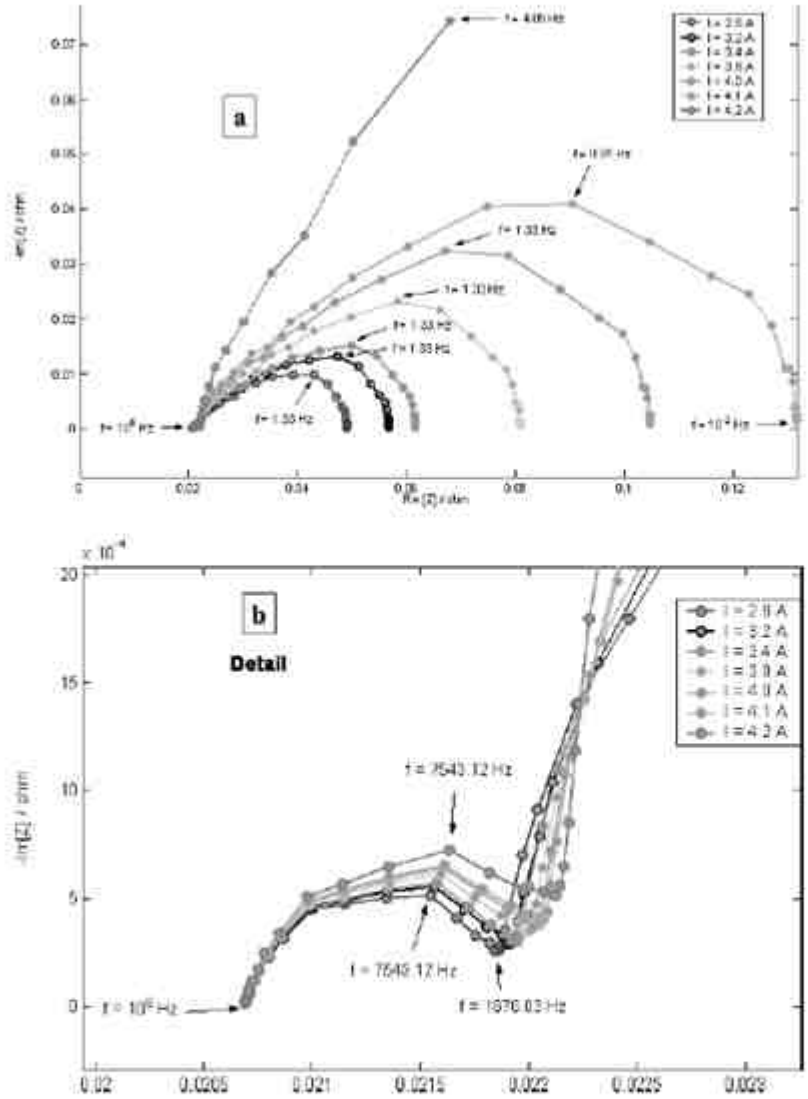

Fig. 10 Simulated EIS sensitivity to the nominal current (a) and detail for high frequencies (b). T = 353 K, $P_{anode} = P_{cathode}$ = 1.5 bar.

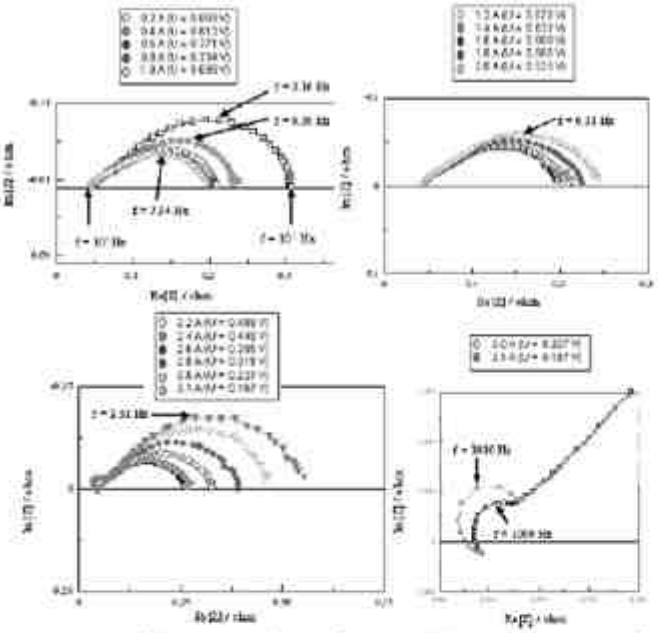

Fig. 11 Experimental EIS sensitivity to the nominal current. EME 70%, $P_{anode} = P_{cathode} = 1.5$ bar, $T = 353$ K.

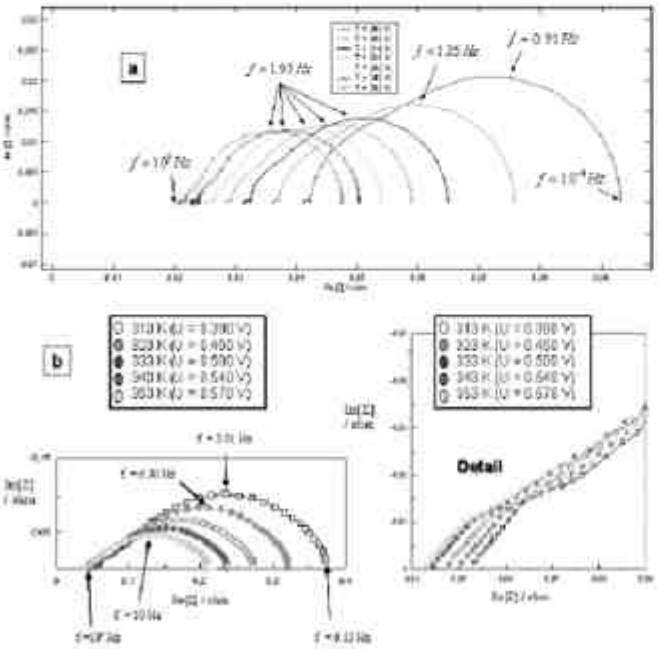

Fig. 12 Simulated EIS sensitivity (a) to the cell temperature, $I = 1$ A, $P_{anode} = P_{cathode} = 1.5$ bar. Experimental SIE sensitivity (b), EME 70%, $I = 2$ A, $P_{anode} = P_{cathode} = 1.5$ bar.

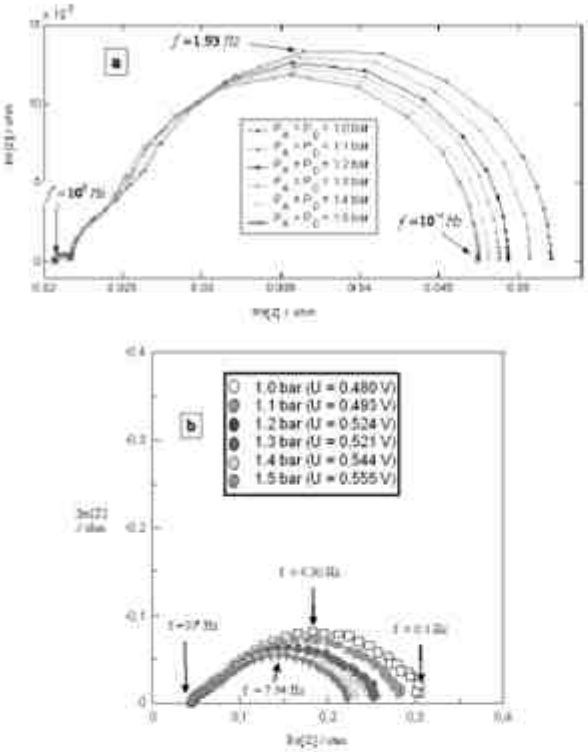

Fig. 13. Simulated EIS sensitivity to the total anodic and cathodic pressures (a), $I = 1$ A, $T = 353$ K. Experimental sensitivity (b), EME 70%, $I = 2$ A, $T = 353$ K.

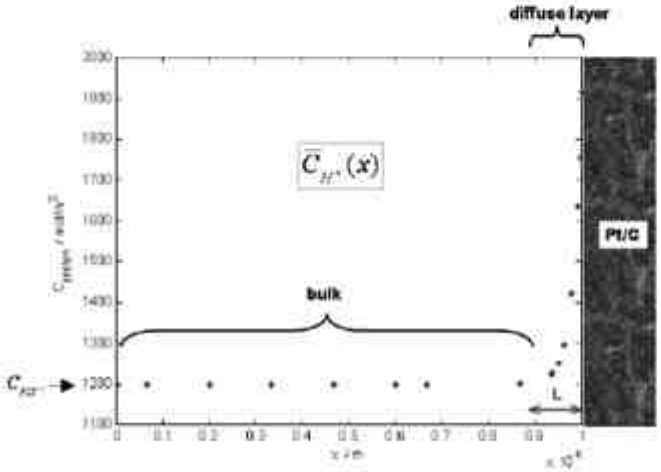

Fig. 14. Stationary proton concentration profile in the Nafion® phase. The Pt/C phase is located at $x = 10^{-4}$ m, $I = 0.1$ A, $T = 353$ K, $P_{anode} = 1.5$ bar.

As shown in Figure 9 and 10, the model is able to calculate the influence of the nominal current, I, on the EIS. These spectra are composed of a small arc, for frequencies higher than 1,150 Hz, and a larger arc for low frequencies.

In Figure 9, it is shown that an increase in the current demanded, from 0.2 to 1.8 A, leads to the diminution of the large arc (up to a limit arc) and to an increase of the top frequency (the small arc is less sensitive). This behaviour can be explained by the increase in the Frumkin potential difference with an increase in the nominal current, as explained by Franco [23].

When the current demanded is increased up to 2.6 A, the amplitude of the large arc increases (the amplitude of the smaller one also increases, but with less sensitivity). This second regime can be explained by reactant transport limitation in the cathode (inflexion point in the cathodic electronic potential curve in Figure 6). These simulations are confirmed by experimental results (Figure 11).

In Figure 12a, the simulated EIS for different cell temperatures are shown. It can be observed that the amplitude of the large arc diminishes when the temperature increases. This is linked to its influence on the reactant diffusion coefficients and electrochemistry. The spectrum shifts to the left, due to the increase in the proton conductivity (Eq. (2)). The use of Eq. (2) overestimates the shift. However, the qualitative trend is in good qualitative agreement with experimental results (Figure 12b).

In Figure 13a, the simulated EIS for different anodic and cathodic pressures are illustrated. The amplitude of the large arc diminishes when the pressure increases. This also seems to be in good qualitative agreement with the experimental results.

4.2 Sensitivity Study to Working Conditions: Some Nanoscale Model Simulation Results

Figure 14 shows the computed stationary proton concentration profile in the vicinity of the anodic Pt/C phase for a given nominal current. It shows that electroneutrality is reached at a distance of 1 nm from the Pt/C phase. Therefore, the value of L can be adjusted for the simulations, $L = 10^{-9}$ m (this value is independent of the nominal current and depends only on the sulfonate concentration and temperature, as discussed elsewhere [23]). This justifies considering only the migration force for proton transport at the microscale (Eq. (1)), in agreement with current assumptions in the literature [55].

Figure 15 shows the stationary electrostatic ionic potential profile of the Nafion® in the vicinity of the anodic Pt/C phase, for the same nominal current. By analyzing Figure 14 and 15, it is observed that, in contrast to the microscale proton transport where the only thermodynamic force is the electrical one, at the nanoscale diffuse layer, protons move against the electrostatic potential because of the diffusional driving force (protons are produced on the catalyst surface). For the cathodic case, the discussion is analogous: the concentration and potential profiles are both opposite to the anodic case [23].

The model also allows further analysis of the different contributions to the EIS. In the following, an EIS, performed on the anodic nanoscale model, is discussed. This calculation was performed setting $\gamma = 10^8$, $S_{electrode} = 20 \times 10^{-4} m^2$, $I/S_{electrode} = 1.5 A cm^{-2}$, with the kinetic parameters given in [33], and fixing $C_{H_2}(t = 0, x = 0, t) = C_{H_2}(z = 0, t)$ (Eq. (8)). Reactant transport through the microscale impregnated Nafion® phase is neglected, in order to study the nanoscale model sensitivity. The reactant concentration was observed to be approximately constant within the diffuse layer (because of the small thickness).

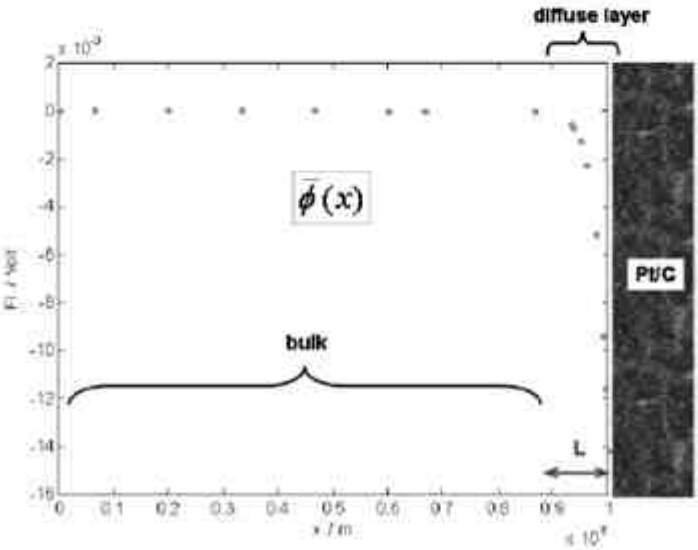

Fig. 15 Electrostatic ionic potential profile in the Nafion® phase. The Pt/C phase is located at $x = 10^{-9}$ m. $I = 0.1$ A, $T = 353$ K, $P_{anode} = 1.5$ bar.

The contributions of the inner and diffuse layers on the global double layer dynamics were studied, Figure 16. The diameters of the EIS arcs obtained are linked to the reaction kinetics and double layer effect (accumulation and transport of the ions in the diffuse layer and the behaviour of the inner layer) (Figure 2). The high frequency limit for all spectra is close to zero, since, in these simulations, only localised transport phenomena are taken into account (in the Nafion® layer surrounding the Pt/C particles).

The comparison between the EIS curves, Figure 16, shows that the coupled phenomena taken into account in this model have a significant effect on the

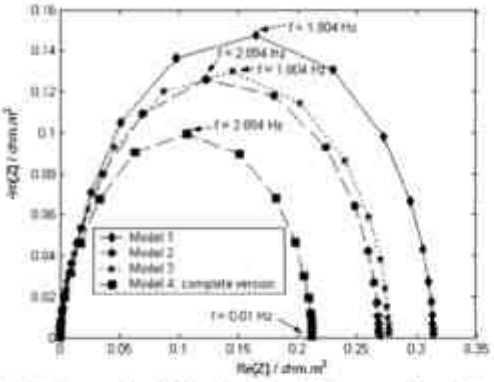

Fig. 16 Nanoscale model for the anode. SE (parameters from [33]) 1), calculated without proton concentration changes in the diffuse layer and without the second term in Eq. (44); nanoscale model 2), calculation performed neglecting proton transport in the diffuse layer and including the complete Eq. (44); nanoscale model 3), calculated with proton transport in the diffuse layer and without the second term in Eq. (44); nanoscale model 4), all coupled phenomena considered. $T = 318$ K, $P_{H_2} = 1.5$ bar.

computed nanoscale impedance spectra. The solid-line spectrum is calculated without considering proton concentration changes in the diffuse layer and without considering the second term in Eq. (42) (which introduces coupling between $\eta(r, t)$, the dipolar layer structure, and the electrochemical kinetics). Proton transport in the diffuse layer is neglected but the complete Eq. (44) is taken into account when obtaining the dashed line spectrum. The dotted-line spectrum corresponds to the case where proton transport phenomena are considered in the diffuse layer, without the second term in Eq. (44). Finally, the dash-dot-line spectrum corresponds to the situation when all the coupled phenomena are considered. The diameter of the spectrum is reduced significantly.

Some others sensitivity studies of the nanoscale models can be found in [23, 33].

5 Concluding Remarks

A continuum mechanistic model for the simulation of the dynamics of a PEFC MEA has been proposed, based on a non-equilibrium thermodynamics/electrodynamics description. As three very different geometrical scales are involved, the MEA is represented by a multiscale model. A microscale transport phenomena description, through the electrode and the membrane thickness, and a spatially distributed microscale model of reactant diffusion through the Nafion® layer covering Pt/C particles, are coupled to a spatially distributed nanoscale description of the catalyst-electrolyte interface, without going up to molecular dynamics approaches (as discussed in [33, 78]). This model focuses on a mechanistic description of the electrochemical double layer, formed at this interface in the presence of electrochemical reactions.

The nanoscale model is composed firstly of a 0-D *inner layer* sub-model, constituted by surface-adsorbed water molecules, where an electrochemical electron-transfer reaction takes place. The adsorption of intermediate reaction species affects the water layer structure.

This inner layer model describes the dynamic evolution of the resulting dipolar density and the generated electrical potential drop between the catalyst and the electrolytic phases.

Secondly, the nanoscale model is composed of a 1-D *diffuse layer* sub-model in the electrolyte composed of spatially moving ions (protons) and fixed counter-ions (sulfonate sites). The ionic transport description takes into account diffusion and electric field effects. At the interface, the total current is given by the reaction kinetics, depending on the interfacial electrostatic potential difference and coupled with the inner layer model.

The multiscale model was implemented in a Matlab®/Simulink®/Femlab® environment.

The model is able to predict the influence of the working conditions (nominal current, reactant pressures, cell temperature) and electrode composition on the characteristics of the impedance spectra. The model also allows the evaluation of the contribution of the different layers (diffuse and inner layers) and physical phenomena (diffusion, electric migration) at the nanoscale, and shows that all of these contributions are significant.

The simulated MEA impedance diagrams are in qualitative agreement with experimental results [23]. Parameter identification for the model was then begun.

Using distributed-parameter Bond Graph theory, the model was designed in a modular way [23, 36–39]. It is based on first-principles modelling and represents explicitly the different physical phenomena as non-linear interacting submodels. Hence, it is reusable and it is possible to extend it by coupling with other phenomena (ageing mechanisms, water transport, nitrogen diffusion, thermal transfer, etc.) [79]. Also, the proposed model, even if directly linked to a practical example in this paper, could be extended to model other types of electrochemical cells (Pb-acid batteries, Li-ion batteries, etc.) [57].

List of Symbols

Latin Letters

$a = 2\exp(-\Delta G_C^0/RT)$	
T	Absolute temperature / K
P_{anode}	Anode total pressure / Pa
$N_A = 6.022 \times 10^{23}$	Avogadro's number / mol^{-1}
$k = 1.380 \times 10^{-23}$	Boltzmann constant / J K^{-1}
$P_{cathode}$	Cathode total pressure / Pa
C_{FIX}	Charged fixed sites concentration (sulfonates of Nafion®) / mol m^{-3}
D_j	Diffusion coefficient of hydrogen or oxygen in Nafion® / m^2 s^{-1}

D_{H^+}	Diffusion coefficient of protons in Nafion® / $m^2 s^{-1}$
ΔG_C^0	Dipolar chemical adsorption energy / $J mol^{-1}$
ΔG_E^0	Dipolar electrostatic adsorption energy / $J mol^{-1}$
ΔG_I^0	Dipolar interaction adsorption energy / $J mol^{-1}$
$\vec{D}$	Displacement vector / $C m^{-2}$
v_i	Electrochemical reaction rate / $mol s^{-1} m^{-2}$
δ_{ef}	Electronic conductivity in the Pt/C phase / $\Omega^{-1} m^{-1}$
k_i	Electronic standard rate constant / $m s^{-1}$
$f = F/RT$	
I_{Fa}	Faradaic current / $A m^{-2}$
$F = 96,485$	Faraday's constant / $C mol^{-1}$
$S_{electrode}$	Geometric surface of the Membrane-Electrode Assembly / m^2
ΔG^0	Gibb's free energy for the dipolar adsorption / $J mol^{-1}$
C_i	Hydrogen or oxygen concentration / $mol m^{-3}$
p_i	Hydrogen or oxygen partial pressure in the pore phase / Pa
R	Ideal gas constant (8.314 $J K^{-1} mol^{-1}$)
j	Local electronic current density at the surface of the Pt/C phase (nanoscopic model) / $A m^{-2}$
n^{max}	Maximal quantity of free sites per unit area of the metallic phase / m^{-2}
J_{H_2}	Molar flux of hydrogen in Nafion® / $mol s^{-1} m^{-2}$
J_{H^+}	Molar flux for the protons in Nafion® / $mol s^{-1} m^{-2}$
$\vec{n}$	Number of dipoles opposed to the metallic phase per unit area / m^{-2}
$\overleftarrow{n}$	Number of dipoles directed towards the metallic phase per unit area / m^{-2}
n_*	Number of free sites per unit area of the metallic phase / m^{-2}
n_{H_2}	Number of sites covered by the intermediate reaction species H_2 per unit area of the metallic phase / m^{-2}
$n_{O_2H_2}$	Number of sites covered by the intermediate reaction species O_2H_2 per unit area of the metallic phase / m^{-2}
n_{OH_2}	Number of sites covered by the intermediate reaction species OH_2 per unit area of the metallic phase / m^{-2}
C_{H^+}	Proton concentration / $mol m^{-3}$
δ_{H^+}	Proton conductivity / $S m^{-1}$
P_{sat}	Saturated water pressure
n^*	Sum of free sites and sites covered by intermediate reaction species per unit area of the metallic phase / m^{-2}
d	Thickness of a water molecule (2×10^{-10} m)
I	Total current demanded by the fuel cell / A

Greek Letters

$\vec{\theta}$	Covering fraction of dipoles opposed to the metallic phase
$\overleftarrow{\theta}$	Covering fraction of dipoles oriented towards the metallic phase
θ_*	Covering fraction of free sites
θ_{H_2}	Covering fraction of the intermediate reaction species H_2
θ_{OH_2}	Covering fraction of the intermediate reaction species OH_2
$\theta_{O_2H_2}$	Covering fraction of the intermediate reaction species O_2H_2
μ	Dipolar moment of a water molecule (0.617×10^{-29} C m)
ε_0	Electric permittivity of a vacuum ($8.854 \times 10^{-12} C^2 N^{-1} m^{-2}$)
ε_{CL}	Electric permittivity in the inner layer / $C^2 J^{-1} m^{-1}$
ε_{DL}	Electric permittivity in the diffuse layer (electrolyte phase) / $C^2 J^{-1} m^{-1}$
ψ	Electric potential in the metallic phase (Pt/C) / V
ϕ	Electric potential in the electrolyte phase / V
σ	Electronic surface density / $C m^{-2}$
α	Elementary reaction step, Frumkin electronic transfer coefficient
Γ	Interfacial dipolar surface density / debye m^{-2}
λ	Local number of water molecules per sulfonate site
η	Potential difference at the metal/electrolyte interface (through the inner layer) / V
γ	Specific active surface area / $m^2 m^{-3}$
θ_{H_2O}	Surface fraction of water on the catalyst surface

Abbreviations

AC	Alternating current
CA	Active layer
DC	Direct current
EIS	Electrochemical impedance spectroscopy
GDL	Gas diffusion layer
MEA	Membrane-electrode assembly
NI	Impregnated Nafion®
PEFC	Polymer electrolyte fuel cell

References

[1] M. Ciureanu, S. D. Mikhailenko, S. Kaliaguin, *Catalysis Today* **2003**, *82*, 195.
[2] Z. Xie, S. Holdcroft, *Journal of Electroanalytical Chemistry* **2004**, *568*, 247.
[3] T. J. P. Freire, E. Gonzalez, *Journal of Electroanalytical Chemistry* **2001**, *503*, 57.
[4] A. G. Hombrados, L. Gonzalez, M. A. Rubio, W. Agila, E. Villanueva, D. Guinea, E. Chinarro, B. Moreno, J. R. Jurado, *Journal of Power Sources* **2005**, *151*, 25.
[5] J.-D. Kim, Y.-I. Park, K. Kobayashi, M. Nagai, M. Kunimatsu, *Solid State Ionics* **2001**, *140*, 313.
[6] H. Kuhn, B. Andreaus, A. Wokaun, G. G. Scherer, *Electrochimica Acta* **2006**, *51*, 1622.
[7] H. Kuhn, B. Andreaus, A. Wokaun, G. G. Scherer in *Proceedings of 3rd European PEFC Forum*, (Ed. Ulf Bossel), Luzern, Switzerland, **2005**, paper B076.
[8] J.-P. Diard, N. Glandut, B. Le Gorrec, C. Montella, *Journal of The Electrochemical Society* **2004**, *151 (12)*, A2193.
[9] G. Li, P. G. Pickup, *Journal of The Electrochemical Society* **2003**, *150 (11)*, C745.
[10] T. E. Springer, T. A. Zawodzinski, M. S. Wilson, S. Gottesfeld, *J. Electrochem. Soc.* **1996**, *143 (2)*, 587.
[11] I. A. Schneider, H. Kuhn, A. Wokaun, G. G. Scherer, *Journal of The Electrochemical Society* **2005**, *152 (10)*, A2092.
[12] F. Jaouen, G. Lindbergh, K. Wiezell, *Journal of The Electrochemical Society* **2003**, *150 (12)*, A1711.
[13] B. Andreaus, A. J. McEvoy, G. G. Scherer, *Electrochimica Acta* **2002**, *47*, 2223.
[14] V. A. Paganin, C. L. F. Oliveira, E. A. Ticianelli, T. E. Springer, E. R. Gonzalez, *Electrochimica Acta* **1998**, *43 (24)*, 3761.
[15] E. Antolini, L. Giorgi, A. Pozio, E. Passalacqua, *Journal of Power Sources* **1999**, *77*, 136.
[16] W. Friede, *PhD Thesis* INPL, France, **2003**.
[17] Y. Bultel, L. Genies, O. Antoine, P. Ozil, R. Durand, *J. Electroanal. Chem.* **2002**, *527*, 143.
[18] O. Antoine, Y. Bultel, R. Durand, *J. Electroanal. Chem.* **2001**, *499*, 85.
[19] M. Eikerling, A. A. Kornyshev, *J. Electroanal. Chem.* **1999**, *475*, 107.
[20] F. Jaouen, G. Lindbergh, *Journal of The Electrochemical Society* **2003**, *150 (12)*, A1699.
[21] S. Walkiewicz, M. Bautista, Y. Bultel, J.-P. Diard, *14ème Forum sur les Impédances Electrochimiques*, Paris, **2002**.
[22] J. P. Diard, B. Le Gorrec, C. Montella in *Cinétique électrochimique, Méthodes*, Editions Hermann, Grenoble, **1996**.
[23] A. A. Franco, *PhD Thesis*, Université Claude Bernard, Lyon, France, **2005**.
[24] F. Berthier, J.-P. Diard, R. Michel, *Journal of Electroanalytical Chemistry* **2001**, *510*, 1.
[25] D. D. Macdonald, E. Sikora, G. Engelhardt, *Electrochim. Acta* **1998**, *43*, 87.
[26] J. R. Macdonald in *Impedance Spectroscopy, Emphasizing Solid Material and Systems*, (Ed. J. R. Macdonald), John Wiley & Sons, New York, **1987**.
[27] S. P. Jiang, J. G. Love, S. P. S. Badwal, *Key Engineering Materials* **1997**, *125*, 81.
[28] A. A. Franco, P. Schott, C. Jallut, B. M. Maschke, orally presented at *207th Meeting of the Electrochemical Society*, Québec, Canada, **2005**.
[29] A. A. Franco, P. Schott, C. Jallut, B. M. Maschke in *Proc. 3rd European PEFC Forum*, (Eds. Ulf Bossel), Luzern, Switzerland, **2005**, paper B063.
[30] M. Eikerling, A. A. Kornyshev, A. Kulikovsky, *The Fuel Cell Review*, December 2004-January 2005.
[31] S. Escribano, *PhD Thesis*, INPG, Grenoble, France, **1995**.
[32] M. Inaba, M. Uno, J. Maruyama, A. Tasaka, K. Katakura, Z. Ogumi, *Journal of Electroanalytical Chemistry* **1996**, *417*, 105.
[33] A. A. Franco, P. Schott, C. Jallut, B. Maschke, *Journal of the Electrochemical Society* **2006**, *153 (6)*, A1053.
[34] A. J. Van der Schaft, B. M. Maschke in *Advanced topics in control systems theory*, (Ed. F. Lamnabhi-Lagarrigue, A. Lovia, E. Panteley), Springer, London, **2005**, pp. 115.
[35] D. Eberard, L. Lefèvre, B. M. Maschke, *Proceedings International Conference PhysCon 2005*, Petersburg, Russia, **2005**, pp. 543.
[36] A. A. Franco, P. Schott, C. Jallut, B. Maschke in *Proceedings of the 5th MATHMOD Conference*, Vienna, Austria, **2006**, paper 103.
[37] A. A. Franco, P. Schott, C. Jallut, B. Maschke, can be found under http://www.see.asso.fr/.
[38] A. A. Franco, orally presented at *Solid State Ionics Conference*, Baden-Baden, Germany, **2005**.
[39] A. A. Franco, P. Schott, C. Jallut, B. Maschke, *Proceedings of the JDMACS 2005*, Lyon, France, **2005**, paper 87.
[40] L. Gerbaux, *PhD Thesis*, INP6, Grenoble, France, **1996**.
[41] F. Meier, G. Eigenberger, *Electrochimica Acta* **2004**, *49*, 1731.
[42] J. O'M. Bockris, S. U. M. Khan in *Surface Electrochemistry: a molecular level approach*, Plenum Press, New York, **1993**.
[43] J. D. Jackson in *Classical Electrodynamics*, John Wiley & Sons Inc., New York, **1962**.
[44] W. Panofsky, M. Phillips in *Classical Electricity and Magnetism*, 2nd Edition, Addison – Wesley Publishing Company Inc., New York, **1962**.
[45] H. Girault in *Electrochimie physique et analytique*, Presses Polytechniques et Universitaires Romandes, Lausanne, **2001**.
[46] J. S. Newman in *Electrochemical Systems*, 2nd Edition, Prentice Hall Englewood Cliffs, New York, **1991**.
[47] F. Scholz in *Electroanalytical Methods*, 1st Edition (Ed. F. Scholz), Springer, Berlin, **2002**.
[48] V. P. Zhdanov, B. Kasemo, *Applied Surface Science* **2003**, *219*, 256.
[49] J. C. Amphlett, R. F. Mann, B. A. Peppley, P. R. Roberge, A. Rodrigues, *Journal of Power Sources* **1996**, *64*, 183.
[50] Y. Wang, C.-Y. Wang, *Electrochimica Acta* **2005**, *50*, 1307.

[51] P. R. Pathapati, X. Xue, J. Tang, *Renewable Energy* **2005**, *30*, 1.
[52] N. P. Siegel, M. W. Ellis, D. J. Nelson, M. R. von Spakovsky, *Journal of Power Sources* **2004**, *128*, 173.
[53] P. Costamagna, *Chemical Engineering Science* **2001**, *56*, 323.
[54] P. Costamagna, S. Srinivasan, *Journal of Power Sources* **2001**, *102*, 242.
[55] N. P. Siegel, M. W. Ellis, D. J. Nelson, M. R. von Spakovsky, *Journal of Power Sources* **2003**, *115*, 81.
[56] K. W. Lum, J. J. McGuirk, *Journal of Power Sources* **2005**, *143*, 103.
[57] S. S. Zhang, K. Xu, T. R. Jow, *Electrochim. Acta* **2004**, *49*, 1057.
[58] N. F. Mott, R. J. Watts-Tobin, *Electrochim. Acta* **1961**, *4*, 79.
[59] J. O'M. Bockris, K. T. Jeng, *Advances in Colloid and Interface Science* **1990**, *33*, 1.
[60] J. O'M. Bockris, M. A. Habib, *Electrochim. Acta* **1977**, *22*, 41.
[61] S. L. Marshall, B. E. Conway, *J. Electroanal. Chem.* **1992**, *337*, 1.
[62] S. L. Marshall, B. E. Conway, *J. Electroanal. Chem.* **1992**, *337*, 19.
[63] S. L. Marshall, B. E. Conway, *J. Electroanal. Chem.* **1992**, *337*, 45.
[64] R. Guidelli in, A. F. Silva, *Trends in Interficial Electrochemistry*, Reidel, Dordrecht, **1986**.
[65] D. A. Harrington, B. E. Conway, *Electrochim. Acta* **1987**, *32*, 1703.
[66] L. Bai, D. A. Harrington, B. E. Conway, *Electrochim. Acta* **1987**, *32*, 1713.
[67] D. A. Harrington, B. E. Conway, *J. Electroanal. Chem.* **1987**, *221*, 1.
[68] V. Rai, M. Aryanpour, A. Dhanda, S. Walch, H. Pitsch, presented at 207th Joint International Meeting of The Electrochemical Society, Quebec City, Canada, **2005**.
[69] T. Jacob, W. Goddard, M. Scheffler, *Calculations on the Cathode Reaction in PEM-Fuel Cells*, Computational Electrochemistry Workshop: on the application of atomistic computer simulation method in interfacial electrochemistry, Santorini, Greece, **2004**, paper P19.
[70] A. Damjanovic, V. Brusic, *Electrochimica Acta* **1967**, *12*, 615.
[71] D. B. Sepa, M. V. Vojnovic, A. Damjanovic, *Electrochimica Acta* **1981**, *26* (6), 781.
[72] N. M. Markovic, P. N. Ross Jr., *Surface Science Reports* **2002**, *45*, 117.
[73] W. G. Bessler, *Solid State Ionics* **2005**, *176*, 997.
[74] D. G. Goodwin, *Proceedings of the Ninth international symposium on solid oxide fuel cells (SOFC-IX)*, (Eds. S. C. Singhal, J. Mizusaki), Quebec City, Canada, **2005**, pp. 699.
[75] D. M. Bernardi, M. W. Verbrugge, *Journal of the Electrochemical Society* **1992**, *139* (9), 2477.
[76] G. Maggio, V. Recupero, L. Pino, *J. Power Sources* **2001**, *101*, 275.
[77] T. Berning, D. M. Lu, N. Djilali, *J. Power Sources* **2002**, *106*, 284.
[78] X. Gao, H. S. White, *Journal of Electroanalytical Chemistry* **1995**, *389*, 13.
[79] R. M. Darling, J. P. Meyers, *Journal of the Electrochemical Society* **2003**, *150* (11), A1523.

Journal of The Electrochemical Society, 153 (6) A1053-A1061 (2006)
0013-4651/2006/153(6)/A1053/9/$20.00 © The Electrochemical Society

A Dynamic Mechanistic Model of an Electrochemical Interface

Alejandro A. Franco,[a,z] Pascal Schott,[a] Christian Jallut,[b] and Bernhard Maschke[b]

[a]*Commissariat à l'Energie Atomique, DRT/LITEN/DTH/Laboratoire d'Essais et Validations de Composants H_2-Piles à Combustible, 38000 Grenoble, France*
[b]*Laboratoire d'Automatique et de Génie des Procédés, LAGEP UMR CNRS, ESCPE, F-69622 Villeurbanne Cedex, France*

We propose a dynamic mechanistic model, based on nonequilibrium thermodynamics and electrodynamics, describing the transient response to current perturbations of an electrochemical double layer at the metal/electrolyte interface in the presence of electrochemical reactions. As an example of application, we have simulated the hydrogen oxidation reaction taking place in a polymer electrolyte fuel cell anode. The model is composed of (*i*) a 0-D *inner layer* submodel describing the composition of the metallic phase surface where water and reactant can be adsorbed, and the generated electric potential difference between the metal and the electrolyte phases; and (*ii*) a 1-D *diffuse layer* submodel in the electrolyte constituted by spatially moving ions and counterions, describing the ionic transport by migration–diffusion, based on the coupling of a Nernst–Planck's equation with a Poisson's equation. At the interface, the reaction kinetics depending on the potential difference is coupled with the inner-layer model through the charge conservation law. The numerical model allows dynamic simulation of the evolution of the local electric potentials (ionic and electronic) and concentrations inside the interface, and the influence of the working conditions on the impedance spectra characteristics.
 [DOI: 10.1149/1.2188353]

Manuscript submitted June 2, 2005; revised manuscript received February 1, 2006. Available electronically April 13, 2006. This was in part Paper 1206 presented at the Quebec City, Canada, Meeting of the Society, May 15–20, 2005.

Electrochemical impedance spectroscopy (EIS) is a widely used experimental technique for transient analysis of the behavior of electrodes in electrochemical devices (such as fuel cells, batteries, or cells used in the experimental setups for the characterization of catalysts). Experimental results are usually analyzed using analogical ac linear circuit models in order to correlate these results to some relevant physical and chemical phenomena.[1-18] In these models, charge transfer is typically represented by ideal resistors and mass transport by complex impedances. The interfacial accumulation of intermediate reaction species and the electrochemical double layer at the metal (for instance, the catalyst)/electrolyte interface are represented by capacitive elements.[19-23]

The parameters of these models have to be fitted at each electrode working point (given by the nominal current, the temperature, and the reactant species concentration).[1-18,20,21] For instance in the case of polymer electrolyte fuel cell (PEFC) electrodes,[22] it is experimentally known that the character of EIS spectra strongly depends on these working conditions.[10,20,21,23,24]

Other authors[4] derive analytical expressions of the impedances as functions of the nominal current and reactant concentration, assuming some simple electrochemical mechanisms in the electrode. Analytical computations of complex impedances become impossible for more complicated mechanisms.

In the analogical models, the interfacial double layer is represented by a capacitance connected in parallel to the resistances and capacitances representing the electrochemical reactions[25] (in the context of PEFCs, see, for instance, Ref. 4, 9, 19-21, and 26). In the interfacial double layer, however, highly complex and coupled phenomena take place which have been largely studied in the absence of electrochemical reactions. The classical Gouy–Chapman–Stern theory provides a description of the *diffuse layer* structure under conditions of thermodynamic equilibrium.[12,14,17,18] The compact or *inner layer*, formed by the water dipolar adsorption on the electrode surface, has been also modeled using equilibrium models based on statistical mechanics. Watts-Tobin was the first to propose a two-state model to describe water adsorption on an Hg electrode surface.[27] Numerous improvements and modifications of this model have been proposed in the past four decades using multistate models,[28] molecular dynamics (MD), and Monte-Carlo (MC) techniques.[11,29] In situ experimental IR spectroscopy demonstrates that the solvent structure is clearly more complex than suggested by discrete-state statistical models.[13] In consequence, the MD and MC approaches have been used with increasing frequency to investigate the structure of liquids at hard surfaces. However, simulation results obtained from these approaches depend strongly on the chosen internal water structure and the chosen interaction potential, as discussed in Ref. 33. MD and MC techniques have also been recently used to simulate the electrochemical reactions in PEFCs.[34,35] However, coupling of such models with continuous models of the transport phenomena in a fuel cell still remain out of reach. The main objective of this paper is to propose a model that can be easily extrapolated and integrated into a more global, multiscale model describing transport phenomena through a membrane electrodes assembly (MEA) of a PEFC.[22,24,36-38] The model consists of a continuous macroscopic mechanistic dynamic model, describing the internal behavior of an electrochemical interface between electronic (electrode) and an ionic (electrolyte) phases in response to current perturbation. The proposed model of the electrochemical interface is composed of the coupled models of the inner layer structure, the intermediate reaction species, and the transport phenomena in the diffuse layer. Finally, this allows the dynamic response of the electrostatic potential $\psi(t)$ in the electrode to be calculated as a function of the demanded current $I(t)$. Access to internal parameters like local concentrations or ionic potential is provided in order to allow analysis of the simulated (EIS) experiments.

In this work we focus on the case of PEFC electrodes Nafion/Pt–C interfaces[39] with negligible curvature compared to the thickness of the electrochemical double layer, typically some nanometers. In this way, we can consider a monodimensional geometry and implement our model according to a cartesian space variable x, perpendicular to the metallic phase (Fig. 1a) located at $x = L$.

The following section introduces our inner layer model, describing first the evolution of the surface water dipolar density and the resulting electric potential drop between the metal and the electrolyte, depending on the electronic current perturbation. Water molecules are modeled like punctual electric dipoles which modulate the electrochemical kinetic reaction equations.[25,26,37] Hydrogen is supposed to be oxidized inside the inner layer through the adsorption of intermediate reaction species, giving an electrically charged proton and an electron. In order to show how the concentration of these species couples with the model of the water adsorption, we implement as an example the hydrogen oxidation reaction (HOR). We then describe the diffuse layer model coupled with the inner layer model in order to calculate the interfacial proton and hydrogen concentrations. We suppose the absence of a supporting electrolyte to be in correspondence with some practical situations (for instance, PEFC electrodes[23,24,36-38,40,41]) and the presence of spatially fixed

[z]E-mail: alejandro.franco@cea.fr

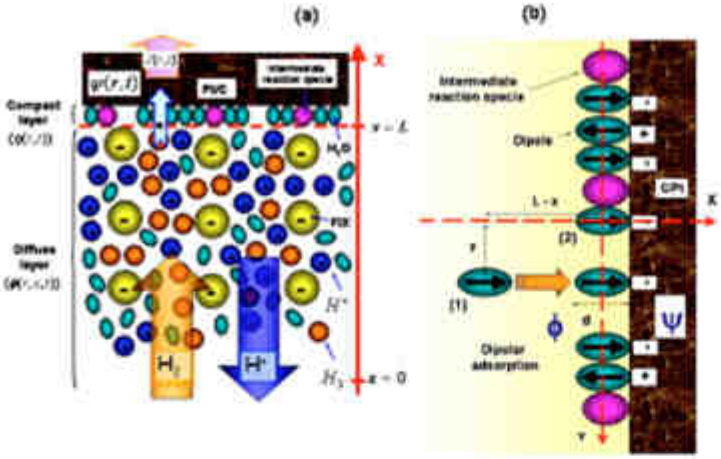

Figure 1. (a) A schematic representation of the nanoscopic interface model (anodic case). The reactant species (hydrogen) arrives to the inner layer where the electron-transfer reaction takes place. Protons are produced at $x = L$ and evacuated through $x = 0$. (b) Intermediate reaction species and dipolar water adsorption on the Pt surface (orientation of the adsorbed water dipoles and calculation of the interdipolar interaction energy).

counterions FIX^- (such as the sulfonate groups in Nafion[22,24,26,28]). Partial differential equations describe reactants transport (H_2 and H^+) by diffusion and electric migration. These equations allow calculation of the local spatiotemporal evolution of the concentrations and the electric potentials.

Finally, simulations of the stationary and transient responses are carried out and presented. In particular, the sensitivity of calculated impedance spectra to some physical parameters and operating conditions is studied. The contributions of the different phenomena are discussed.

The Inner Layer Model: Water Adsorption Submodel

In our model, an interfacial potential difference between the electrolyte and the metal (Fig. 1) governs the development of a set of electrochemical reaction steps on the metallic surface (see the following section), with an electronic surface density σ. This potential drop is denoted by $\eta(t)$ and it is a function of time according to[9]

$$\eta(t) = \phi(t) - \phi(L,t) \qquad [1]$$

where $\phi(L,t)$ is the electrostatic potential in the electrolyte just outside the water layer adsorbed on the metal surface, and $\phi(t)$ is the electrostatic potential in the metallic phase. $\phi(t)$ is calculated as the sum of the potential $\phi(L,t)$ and of $\eta(t)$.

In order to calculate $\eta(t)$, we develop in this section a model describing the interfacial water adsorption coupled with electrochemical reaction intermediates. In this model, for the sake of simplicity, the water is assumed to be adsorbed according to two dipolar orientations: hydrogen end toward and opposed to the metal surface. This simple two-state assumption is similar to the original Watts–Tobin model.[29] It can be seen as a particular case of statistical multistate models and is a first step toward the consideration of more complex models presented, for instance, in Ref. 30 and 43-47. The model structure and the couplings of our model are independent of the complexity of the used water adsorption submodel. The structure of our model remains the same if one changes the water adsorption submodel, because only the computation of the dipolar density Γ (cf. Eq. 5) is affected.

According to the superposition principle, $\eta(t)$ is the sum of the potential drop related to the thickness of the adsorbed water layer ($\Delta\phi_1$) and the drop related to the dipolar surface density ($\Delta\phi_2$). In the next two subsections we show how these two contributions are related to the electronic surface density σ on the metal phase. This density is obtained from the charge conservation law at the electrode/electrolyte interface. This is detailed later when the inner layer model is coupled both with the equation of conservation of charge and the reaction kinetics.

Electrostatic potential drop $\Delta\phi_1$.— According to Gauss' theorem, we can express σ as a function of $-\partial\phi/\partial x(L,t)$, the electric field in the metal/electrolyte interface (Fig. 2). Assuming a linear relation between the displacement vectors D_i in the diffuse and inner layers and the electric field, one obtains

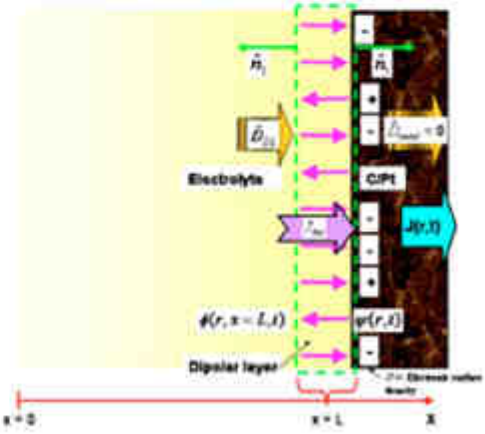

Figure 2. Calculation of the interfacial electric field. Application of the Gauss theorem in the vicinity of the metallic phase (PEC in the case of a PEFC electrode). r denotes the microscopic coordinate of the multiscale model where the model presented in this paper has been integrated.[12,24,26-28]

[9]This potential drop is not an experimentally measurable quantity.[42]

$$\left\|\frac{\mathbf{D}_{\varepsilon 2}(L,t)}{\varepsilon_{\mathrm{DL}}}\right\| = \left\|\frac{\mathbf{D}_{\varepsilon 2}(L,t)}{\varepsilon_{\mathrm{CL}}}\right\| = \left\|\frac{\partial\phi}{\partial x}(L,t)\right\| = -\frac{\sigma}{\varepsilon_{\mathrm{CL}}} \quad [2]$$

where we have used the continuity of the electric field through the water layer[40,49] and supposed that the metallic phase is a perfect electronic conductor. In this expression $\varepsilon_{\mathrm{DL}}$ is the electrical permittivity of the electrolyte phase and $\varepsilon_{\mathrm{CL}}$ is electric permittivity of the adsorbed water layer[4,50] (supposed to be independent of temperature). For an anodic reaction ($\phi - \phi_e > 0$, and due to the small thickness d of the water layer, the potential drop can be approximated by

$$\Delta\phi_1 = \frac{\sigma}{\varepsilon_{\mathrm{CL}}} d > 0 \quad [3]$$

Electrostatic potential drop $\Delta\phi_2$.— If the water layer is considered as a layer of punctual dipoles, the electrostatic potential drop $\Delta\phi_2$ is given by[48,49]

$$\Delta\phi_2 = \frac{\Gamma}{\varepsilon_{\mathrm{DL}}} \quad [4]$$

where Γ is the dipolar surface density (in Debye/nm^2). To find the expression of Γ as a function of σ, we use the two-state hypothesis (Fig. 1b): we call $\vec{n}$ (respectively $\vec{n}$) the number of dipoles per unit of area directed[4] (respectively opposed) toward the electrode. Hence the dipolar surface density is

$$\Gamma = \mu(\vec{n} - \overleftarrow{n}) \quad [5]$$

where μ is the dipolar moment of a water molecule. We describe the oriented adsorption of the water molecules through the equilibrated reactions

$$H_2O + s \leftrightarrow H_2\vec{O} - s \quad \text{and} \quad H_2O + s \leftrightarrow H_2\overleftarrow{O} - s \quad [6]$$

where s is an adsorption site on the electrode surface. Application of the laws of mass action gives

$$\frac{\vec{n}}{n_s\theta_{H_2O}} = \vec{K} = e^{-\Delta\vec{G}^0/RT} \quad \text{and} \quad \frac{\overleftarrow{n}}{n_s\theta_{H_2O}} = \overleftarrow{K} = e^{-\Delta\overleftarrow{G}^0/RT} \quad [7]$$

where n_s is the number of free sites per unit of area, θ_{H_2O} is the volume fraction of the free water molecules (assumed to be constant and conserved on the surface), and ΔG^0 the Gibbs' free energy of the Reaction 6. This energy results from three contributions, according to Eq. 8

$$\Delta G^0 = \Delta G_C^0 + \Delta G_e^0 + \Delta G_i^0 \quad [8]$$

where ΔG_C^0 is the chemical adsorption energy (which is assumed to be constant and independent of the dipole orientation), ΔG_e^0 is the electrostatic energy corresponding to the work of the field created by the charge of the metallic phase to carry a dipole from infinity to the electrode surface, and ΔG_i^0 is the interdipolar interaction energy. The electrostatic energies for the two opposite dipolar orientations are, respectively

$$\Delta\vec{G}_e^0 = +\mu\frac{\partial\phi}{\partial x}(L,t) \quad \text{and} \quad \Delta\overleftarrow{G}_e^0 = -\mu\frac{\partial\phi}{\partial x}(L,t) \quad [9]$$

where the potential reference is taken equal to zero at infinity.[22,24]

The free energies ΔG_i^0 can be evaluated as follows (Fig. 1b): let us consider a dipole 2 already adsorbed, oriented toward the electrode. For example, let us now consider a water molecule 1 oriented in the same way, adsorbing on the electrode surface (with coordinates x and y). We calculate the work supplied to carry the water molecule from the infinity to the electrode surface through

[4] Hydrogen and toward the metal.

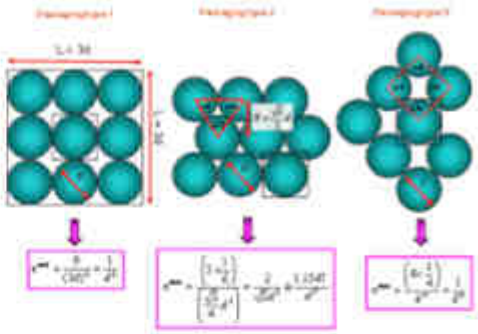

Figure 3. Calculation of the maximal quantity of free sites by two possible sphere packagings.

$$W_{\text{dipole/dipole}} = \int_{-\infty}^{x} F_y dx \quad [10]$$

where

$$F_y = \frac{\mu^2}{4\pi\varepsilon_{\mathrm{DL}}}\left[\frac{15(L-x)^3}{[(L-x)^2+y^2]^{7/2}} - \frac{9(L-x)}{[(L-x)^2+y^2]^{5/2}}\right] \quad [11]$$

which is the force on dipole 1 in the field of dipole 2.[48] We suppose that the adsorbing dipole is very slightly deviated according to the direction Y by the one already adsorbed, so we can calculate the integral (Eq. 10) only in the X direction

$$W_{\text{dipole/dipole}} = \frac{\mu^2}{4\pi\varepsilon_{\mathrm{DL}}}\frac{1}{y^3} \quad [12]$$

where we have supposed that $\varepsilon_{\mathrm{DL}}$ is independent of x. If now the water molecule is adsorbing on an electrode covered with dipoles all oriented toward this one, the Gibbs' energy received by the molecule is the sum of the works provided by every adsorbed dipole (we suppose that the dipole number j is placed in the position jd on the Y axis)

$$W_{\leftarrow} = 2 \times \sum_{j=1}^{\infty}\frac{\mu^2}{4\pi\varepsilon_{\mathrm{DL}}}\frac{1}{(jd)^3} = \frac{\mu^2}{2\pi\varepsilon_{\mathrm{DL}}d^3}\sum_{j=1}^{\infty}\frac{1}{j^3} = \frac{\mu^2\zeta[3]}{2\pi\varepsilon_{\mathrm{DL}}d^3} = \frac{\mu^2 A}{d^3} \quad [13]$$

where ζ designs the Riemann's zeta function[9] (the factor 2 comes from the necessity to take into account the dipoles adsorbed on both sides of the considered molecule) with $A = \zeta[3]/2\pi\varepsilon_{\mathrm{DL}}$. In a similar way, for the case of dipoles oriented toward the electrolyte, the Gibbs' energy received by the molecule is

$$W_{\rightarrow} = -\frac{\mu^2 A}{d^3} \quad [14]$$

If the two orientations coexist, we will indicate by $\vec{\theta}$ (respectively $\overleftarrow{\theta}$) the covering fraction with dipoles oriented toward the electrode (respectively opposed). We have then

$$\vec{\theta} = \frac{\vec{n}}{n^{\max}} = \frac{\vec{n}}{n^* + \vec{n} + \overleftarrow{n}} \quad \text{and} \quad \overleftarrow{\theta} = \frac{\overleftarrow{n}}{n^{\max}} = \frac{\overleftarrow{n}}{n^* + \vec{n} + \overleftarrow{n}} \quad [15]$$

where $n^{\max}$ is the maximal quantity of free sites per unit of area (represented in Fig. 3 as spheres, showing three possible ways of

[9] $\zeta(x) = \sum_{n=1}^{\infty} 1/n^x$ ($x > 1$), $\zeta[3] \approx 1.20$

packaging), and where n^* is the sum of the number of free sites and sites covered by an intermediate species of reaction (see the following section) per unit of area. Averaging the interaction of a given dipole with the others (mean field approximation), we obtain the total work of adsorption under dipolar interaction

$$\tilde{W} = \Delta\tilde{G}_i^0 = \frac{A\mu^2}{d^3}(\tilde{\theta} - \tilde{\theta}) \quad \text{and} \quad \hat{W} = \Delta\hat{G}_i^0 = -\frac{A\mu^2}{d^3}(\hat{\theta} - \hat{\theta}) \tag{16}$$

According to Eq. 15 we can write

$$\tilde{\theta} - \hat{\theta} = \frac{\tilde{n} - \hat{n}}{n^* + \tilde{n} + \hat{n}} \tag{17}$$

Defining

$$X = \frac{\mu\sigma}{kT\varepsilon_{CL}} + \frac{A\mu^2}{kTd^3}(\tilde{\theta} - \hat{\theta}) \quad \text{and} \quad a = 2e^{-A\sigma_0^2/kT} \tag{18}$$

Eq. 7 becomes

$$\hat{n} = n_s\Theta_{H_2O}\frac{a}{2}e^{-X} \quad \text{and} \quad \tilde{n} = n_s\Theta_{H_2O}\frac{a}{2}e^{X} \tag{19}$$

and Eq. 17 becomes

$$\frac{a\sinh[X]}{\frac{n^*}{n_s\Theta_{H_2O}} + a\cosh[X]} = \kappa\sigma - \lambda X$$

$$\text{with } \kappa = \frac{d^3}{\varepsilon_{CL}A\mu} \quad \text{and} \quad \lambda = \frac{kTd^3}{A\mu^2} \tag{20}$$

This transcendental equation in X allows to compute $\tilde{\theta} - \hat{\theta}$ and so $\tilde{n} - \hat{n}$. It has a unique solution for a given value of σ. So, considering Eq. 4 and 5 we obtain

$$\Delta\phi_2 = -\frac{an_s\Theta_{H_2O}\mu\sinh[X]}{\varepsilon_{DL}} \tag{21}$$

Finally, the potential drop $\eta(t)$ can be written as

$$\eta(t) = \Delta\phi_1 + \Delta\phi_2 = -\frac{\sigma d}{\varepsilon_{CL}} - \frac{an_s\Theta_{H_2O}\mu\sinh[X]}{\varepsilon_{DL}} \tag{22}$$

The calculation of the number of free sites per unit of area n_s and its coupling with the electrochemical reactions are presented in the next section. As an example of application of our approach, we show the case of the HOR, describing the oxidation of molecular hydrogen on platinum in a volumetric PEFC electrode. We also introduce the relation between σ and the current demanded to the electrode.

The Inner Layer Model: Electrochemical Reaction Submodel

A Tafel–Heyrovsky–Volmer three-step reaction model for the hydrogen oxidation is considered in order to show how n^* (and so n_s) used in the water adsorption submodel can be calculated. This reaction mechanism is commonly accepted:[10,41,51-53]

$$H_2 + 2s \leftrightarrow 2Hs \text{ (Tafel)} \tag{23}$$

$$s + H_2 \leftrightarrow Hs + H^+ + e^- \text{ (Heyrovsky)} \tag{24}$$

$$Hs \leftrightarrow s + H^+ + e^- \text{ (Volmer)} \tag{25}$$

Assuming noninteraction between adsorbed intermediate species and between intermediates and water, the rates of these elementary steps may be described as:[37,25,24,35-38,41,51-53]

$$v_{TAF} = k_{TAF}\theta_s^2 C_{H_2}(L,t) - k_{-TAF}\theta_{Hs}^2 \tag{26}$$

$$v_{HEY} = k_{HEY}\theta_s C_{H_2}(L,t)e^{(1-\alpha)f\eta(t)} - k_{-HEY}\theta_{Hs}C_{H^+}(L,t)e^{-\alpha f\eta(t)} \tag{27}$$

$$v_{VOL} = k_{VOL}\theta_{Hs}e^{(1-\alpha)f\eta(t)} - k_{-VOL}\theta_s C_{H^+}(L,t)e^{-\alpha f\eta(t)} \tag{28}$$

where $C_{H_2}(L,t)$ is the hydrogen concentration at $x = L$ (see Fig. 1), $C_{H^+}(L,t)$ the proton concentration at the same point, θ_s is the surface coverage by free sites, and θ_{Hs} is the surface coverage by adsorbed monatomic hydrogen. k_i and k_{-i} are the electronic standard rate constants for each step, and $f = F/RT$ and α_i denote the symmetry factors.[42]

Recall that the potential drop $\eta(t)$ appearing in Eq. 27 and 28 is a function of the electronic density σ (Eq. 22). The value of θ_{Hs} is given by the solution of the balance equation

$$\frac{n^{max}}{N_A}\frac{d\theta_{Hs}}{dt} = -v_{VOL} + v_{HEY} + 2v_{TAF} \tag{29}$$

where N_A is the Avogadro number. According to the definition of $n^* = n_s + n_{Hs}$, and using $\theta_i = n_i/n^{max}$, Eq. 20 becomes

$$\frac{a\sinh[X]}{\frac{1}{\Theta_{H_2O}} + \frac{\theta_{Hs}}{\theta_s}\frac{1}{\Theta_{H_2O}} + a\cosh[X]} = \kappa\sigma - \lambda X \tag{30}$$

For the surface coverage by dipoles directed toward the electrode, we have

$$\tilde{\theta} = \frac{\frac{a}{2}e^{-X}}{\frac{1}{\Theta_{H_2O}} + \frac{\theta_{Hs}}{\theta_s}\frac{1}{\Theta_{H_2O}} + a\cosh[X]} \tag{31}$$

and for the opposed ones, we have

$$\hat{\theta} = \frac{\frac{a}{2}e^{X}}{\frac{1}{\Theta_{H_2O}} + \frac{\theta_{Hs}}{\theta_s}\frac{1}{\Theta_{H_2O}} + a\cosh[X]} \tag{32}$$

Then θ_s and n_s can be calculated from

$$\frac{n_s}{n^{max}} = \theta_s = \frac{1 - \theta_{Hs}}{1 + \Theta_{H_2O}a\cosh[X]} \tag{33}$$

σ is calculated from the charge conservation law at the metal/electrolyte interface[43,44] (Fig. 2)

$$J(t) - J_{Fa} = -\frac{\partial\sigma}{\partial t} \tag{34}$$

where J_{Fa} is the faradaic current density given by[54,55]

$$J_{Fa} = F(v_{HEY} + v_{VOL}) \tag{35}$$

In the case of a volumetric electrode with a total electronic current $I(t)$, the current density $J(t)$ in Eq. 34 can be calculated by

$$J(t) = \frac{I(t)}{S_{electrode}\varepsilon_{EA}\gamma} \tag{36}$$

where γ is the specific contact area between metal parts (Pt/C in our PEFC electrode) and electrolyte fractions (Nafion),[56,57] and $S_{electrode}$ and ε_{EA} are, respectively, the geometrical surface and thickness of the volumetric electrode.

To close the system of equations, we have to know $C_{H_2}(L,t)$ and $C_{H^+}(L,t)$ in Eq. 26-28. Their values can be obtained from the diffuse layer model as we show in the following section.

Table I. Parameters used in the model.

Parameters	Units	References
$\gamma = 10^5$	m^2/m^3	40, 41, and 63
$e_{2h} = 50 \times 10^{-9}$	m	40, 41, and 63
$S_{\text{electrode}} = 20 \times 10^{-4}$	m^2	This work
$C_{\text{FIX}} = 2000$	mol/m^3	41 and 57
$\alpha_{\text{HER}} = \alpha_{\text{TAF}} = \alpha_{\text{VOL}} = 0.5$	Dimensionless	This work
$D_{H^+} = 2.97 \times 10^{-14} \times T \times 10^{C(19.551 \times 10^3 - T \times 0.335 + 1.535 \times 10^{-3} \times T^2)/T \times 10^3 \times 1}$	m^2/s	64
$D_{H_2} = 3.02 \times 10^{-10} \times \exp(0.025 \times T)$	m^2/s	39 and 40
$\kappa_{CL} = 7.08 \times \kappa_0$	$C/(V\ m)$	43-47, 55, 65, and 66
$\kappa_{DL} = 80.1 \times \kappa_0$	$C/(V\ m)$	43-47, 55, 65, and 66
$\Delta G_{ad}^0 = 1$	kJ/mol	24
$a_{TAF} = 10^{-7}\ k_{HER} = 10^{-2}\ k_{-HER} = 10^{-6}\ k_{VOL} = 10^{-3}$	m/s	51-53
$K_{-TAF} = 10^{-7}\ k_{VOL} = 10^{-3}$	$mol/(m^2\ s)$	51-53
$\Theta_{H_2O} = 0.95$	Dimensionless	41, 67, and 68

Coupling the Inner Layer Model with a Diffuse Layer Model

In this section we show how the models describing the transport of H_2 and of H^+ in the diffuse layer couple with the inner layer model described previously. This allows calculation of $C_{H_2}(L,t)$, $C_{H^+}(L,t)$, $\phi(L,t)$, and $\psi(t)$.

Description of the diffuse layer model. Balance equations.— The diffuse layer model is based on the diffusion and migration transport of the reaction species coupled with the electric field generated by the resulting charge distribution. All species (H^+, H_2, FIX^-, and water) are considered as punctual, so the interparticle electrical interaction is neglected. The solvatation and convection by water are not considered.

The flux for the electrically neutral species H_2 is assumed to be given by Fick's law of diffusion and the mass balance leads to

$$\frac{\partial C_{H_2}}{\partial t} = -\nabla \cdot \vec{J}_{H_2} = -\nabla \cdot (-D_{H_2} \nabla C_{H_2}) = D_{H_2} \nabla^2 C_{H_2} \quad [37]$$

where we assume that the diffusion coefficient D_{H_2} is constant.

For the case of the electrically charged species H^+, the diffusion coefficient in the medium is also supposed to be independent of the concentration. In a similar way that in the H_2 case, combining the flux related to the Fick's diffusional force to the electrical force, with the mass balance, we obtain the equation representing the H^+ concentration (Nernst–Planck equation)

$$\frac{\partial C_{H^+}}{\partial t} = -\nabla \cdot \vec{J}_{H^+} = -\nabla \cdot (-D_{H^+} \nabla C_{H^+} - fD_{H^+} C_{H^+} \nabla \phi)$$
$$= D_{H^+} \nabla^2 C_{H^+} + fD_{H^+} \nabla C_{H^+} \nabla \phi + fD_{H^+} C_{H^+} \nabla^2 \phi \quad [38]$$

where $\phi(x,t)$ is the electric potential in the electrolyte, which is calculated from the Poisson's equation

$$\frac{F}{\varepsilon_{DL}} (C_{H^+} - C_{FIX}) = -\nabla^2 \phi \quad [39]$$

neglecting magnetic effects (because the frequency range we are interested in is lower than 1 MHz[24,65]). C_{FIX} in Eq. 39 is the Nafion sulfonate concentration,[23,24,30,37,51,54] which we suppose to be constant. These sulfonate sites are supposed to be located outside of the inner layer and to not affect its structure.[23,24,34,36-38,62]

Equations 38 and 39 are introduced because at the nanoscopic scale (near the electrified surface where the electron transfer takes place) electroneutrality cannot be assumed and because there is not any supporting electrolyte (the conductivity of protons in the Nafion is not infinite). Far from the inner layer, the electroneutrality condition is valid because the concentration of protons becomes constant (and equal to the sulfonate concentration which is supposed to be constant) (see the following section).

Boundary conditions and calculation of $\psi(t)$.— The bulk electrolyte is located at $x = 0$, where $C_{H^+}(x = 0,t) = C_{FIX}$ and $C_{H_2}(x = 0,t) = p_{H_2}/[1.09 \times 10^9 \times \exp(77/T)]$ (Henry's law of hydrogen absorption in Nafion behaving as water, where p_{H_2} is the hydrogen–gas pressure in a pore phase,[23]).

The scalar potential $\phi(x = 0,t)$ equals 0. (In our multiscale model[23,24,36-38] it is calculated by the microscopic transport model of protons in the thickness of the volumetric electrode.)

At $x = L$, the boundary conditions for Eq. 37 and 38 are, respectively

$$J_{H_2}(L,t) = -(v_{TAF} + v_{HER}) \quad [40]$$

(negative because H_2 is consumed)

$$J_{H^+}(L,t) = v_{HER} + v_{VOL} = \frac{J_{Pt_H}(t)}{F} \quad [41]$$

(positive because protons are produced), where $J_{Pt_H}(t)$ is given by Eq. 35 (in the case of the HOR).

The boundary condition for Eq. 39 is given by $\partial\phi(L,t)/\partial x$, which is calculated from σ (obtained from Eq. 34), and using Eq. 2. Then, Eq. 39 allows calculation of $\phi(L,t)$, which, using Eq. 1, allows calculation of the electronic potential $\psi(t)$ in the electrode [as $\eta(t)$ is given by Eq. 22].

Numerical Simulations

The model allows analysis of the stationary and dynamic behavior of the different state variables [for example, the proton concentration in the diffuse layer and in the inner layer $C_{H^+}(x,t)$, the ionic potential $\phi(x,t)$ the hydrogen concentration $C_{H_2}(x,t)$, and the electronic potential $\psi(t)$, in response to a current demand $I(t)$. From the decomposition of the model into parts based on first-principle models and their explicit coupling, it becomes easily interpretable and adaptable to different modeling assumptions and working conditions. It may help to analyze the sensitivity of the dynamic response of the electrode to the operating conditions (nominal current, reactant-gas pressure, temperature, platinum loading). In this section we show some simulations of the steady-state and transient (linear EIS) responses of our interface model and analyze the sensitivity to the working conditions. We specifically focus on impedance spectroscopy responses and estimate the contribution of the inner and diffuse layers to the system response, and discuss the sensitivity to some parameters (κ_{CL}, Θ_{H_2O}).

[1]Actually in our complete multiscale electrode model $C_{H_2}(x = 0,t)$ is calculated by a reactant diffusion model through the Nafion layer covering the PAC phase, from the pore.

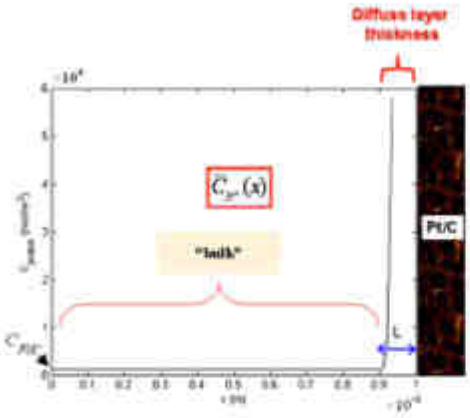

Figure 4. Proton concentration profile in the Nafion phase. The Pt/C phase is located at $x = 10^{-6}$ m.

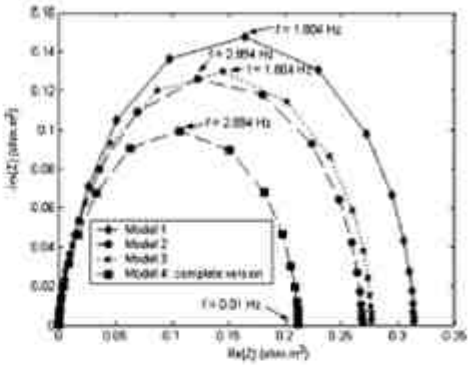

Figure 5. (Model 1) Calculated without concentration changes in the diffuse layer and without the second term in Eq. 22. (Model 2) Performed neglecting transport in the diffuse layer and including the complete Eq. 22. (Model 3) Calculated with transport phenomena in the diffuse layer and without the second term in Eq. 22. (Model 4) Consideration of all coupled phenomena. $\bar{I} = 30$ A, $T = 318$ K, $P_{H_2} = 1.5$ bar.

Computational code and parameters.— To solve our problem numerically, we have developed a code by coupling three softwares: Simulink (describing the boundary conditions in $x = 0$ and in $x = L$ and the interconnection between the different partial differential equations of the model), Femlab (describing the one-dimensional transport phenomena in the electrolyte, using the finite element method), all integrated in Matlab. The computations have been realized on a microcomputer with an Intel Pentium 4 processor 2 GHz, 1 GB of RAM. For the simulations shown here, we have chosen the set of physicochemical parameters given in the Table I.

Different impedance spectra are calculated by simulation in the time domain and subsequent fast Fourier transformation. This approach has been shown previously in the context of solid oxide fuel cells[30,43] and PEFCs.[22,24,30,37] For the determination of the ac impedance shown here, a sufficiently small sinusoidal signal (e.g., 15 mA) has been superimposed on the fixed (dc) current level $\bar{I}$ in order to obtain a linear response of $\psi(t)$. This has been done for frequencies ranging from 0.01 to 10^5 Hz in the anticlockwise direction. Prior to starting the simulation of the periodic signal response, the steady state has been calculated. The time of calculation for an impedance spectrum with 40 frequency points is approximately 50 min.

Simulation results.— In Fig. 4 we show the computed stationary proton concentration profile in the diffuse layer for a given nominal current. We can see that the concentration of protons becomes equal to the sulfonate concentration for $L = 10^{-9}$ m. In other words, the electroneutrality $[C_{H^+}(x,t) - C_{FIX} = 0]$ is reached at 1 nm of the Pt/C phase (we put the origin of the spatial coordinate at $x = 10^{-6}$–10^{-9} m for further simulations). This value is independent of the nominal current but depends on sulfonate concentration and temperature (this is discussed elsewhere[24]).

In Fig. 5, we study, for a given nominal current $\bar{I} = 30$ A, the contributions of the inner and diffuse layer models on the global impedance spectrum. Calculated EIS plots have arc shapes, in accordance with typical experimental results.[9,17,20,21,34] The diameter of the arcs is a function of the coupling between the reaction kinetics and double-layer effect (accumulation and transport of H^+ and H_2 in the diffuse layer, and the behavior of the inner layer). The high-frequency limit for all spectra is very near zero because in this paper we do not take into account transport phenomena in the bulk solution.

The comparison between the EIS curves in Fig. 5 shows that the coupled phenomena taken into account in our model have a significant effect on the computed impedance spectra. The solid-line spectrum is calculated without considering concentration changes in the diffuse layer and without consideration of the second term in Eq. 22 (which introduces the coupling between the potential difference, the dipolar layer structure, and the electrochemical kinetics). The dashed line spectrum is performed by neglecting the transport in the diffuse layer by taking into account the complete Eq. 22. The dotted-line spectrum corresponds to the case where we consider transport phenomena in the diffuse layer without the second term in Eq. 22. Finally the dash-dot-line spectrum corresponds to the consideration of all coupled phenomena: the diameter of the spectrum is reduced significantly. As we show in Fig. 6, our model is able to calculate the influence of the nominal current $\bar{I}$ on the impedance spectra of the

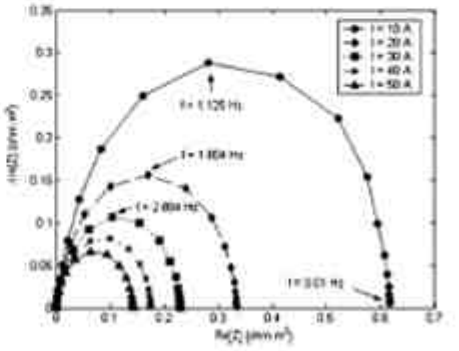

Figure 6. Sensitivity of the EIS spectra to the nominal current $\bar{I}$. $T = 338$ K, $P_{H_2} = 1.5$ bar.

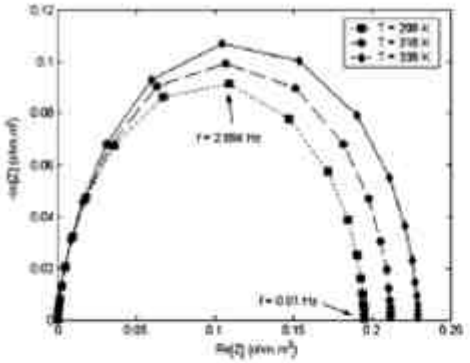

Figure 7. Sensitivity of the EIS spectra to the temperature. $\bar{I} = 30$ A, $P_{H_2} = 1.2$ bar.

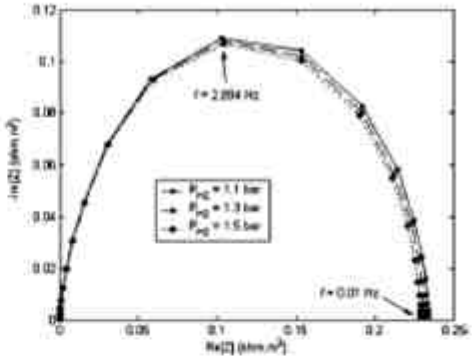

Figure 8. Sensitivity of the EIS spectra to the H_2 pressure. $\bar{I} = 30$ A, $T = 338$ K.

double layer. The increase of the demanded current leads to the diminution of the amplitude of the arcs. In other words, the capacitive effect diminishes. We can also see that the frequency at the maxima of spectra increases with the nominal current value.

In Fig. 7 and 8 we show our model capabilities to simulate the sensitivity of impedance spectra to the temperature and the reactant pressure. In both cases the nominal current is $\bar{I} = 30$ A. The arc diameter increases with temperature and diminishes with pressure, and sensitivity to the temperature is higher than sensitivity to pressure. These simulations are qualitatively in agreement with experimental results.[24]

The effect (less significant) of some parameter values is shown in Fig. 9 and 10. The diminution of the water content in the electrolyte,[5] and so of Θ_{H_2O}, produces the diminution of the impedance plot diameter (Fig. 9). The augmentation of a_{CL} produces a displacement of frequency points (Fig. 10).

Conclusion

Based on a nonequilibrium thermodynamics/electrodynamics description, a mechanistic model of the electrochemical double layer at the interface between a metal, an electrolyte, and in the presence of electrochemical reactions has been proposed. As an example of application, in this paper we have implemented this model to the case of a PEFC anode. The model is based on first-principles modeling and represents explicitly the different physical phenomena as nonlinear submodels in interaction. It is hence nonlinear and can help to analyze the dynamic response sensitivity to the electrode operating conditions (nominal current, reactant-gas pressure, temperature) and composition (platinum loading).

It considers first a 0-D *inner layer* submodel formed by surface-adsorbed water molecules and electrochemical intermediate reaction species which modify the effective water dipolar density. The inner layer model describes the dynamic evolution of the generated electric potential drop between the electronic-conductor and the electrolytic phases. The law of mass action is applied (depending on chemical, electrostatic, and interdipolar interaction energies) to compute the dipolar density as a function of the local electric field. This density allows computation of a first contribution to the generated potential difference. The thickness of the layer allows to computation of a second contribution to the difference using Gauss' theorem.

Second, the model considers a 1-D *diffuse layer* submodel in the electrolyte composed of spatially moving ions (protons) and fixed counterions (Nafion sulfonates). The ionic transport description takes into account diffusion and electric field effects. So, the ionic concentration and the electric potential are computed by coupling a Nernst–Planck equation and a Poisson equation. At the interface, the total current is given by the reaction kinetics, depending on the potential drop between the electronic and electrolytic phases η_s and coupled with the inner layer model.

The numeric model was implemented in a Matlab–Simulink/Femlab environment. Without going up to MC/MD approaches,[33,34,37] but in contrast with analogic circuit models, our model is able to predict the influence of the working conditions of a volumetric electrode, such as nominal current, pressure, temperature, and platinum loading, on impedance spectra characteristics. The model allows also evaluation of the contribution of the different layers (diffuse and inner layers) and physical phenomena (diffusion, electric migration, reaction kinetics). Simulations show that none of these contributions is negligible.

The model has been designed in a modular way, so it is possible to extend it by coupling with other phenomena (Pt aging mechanisms, CO poisoning, etc.).[41,42] Furthermore, this model of the electrochemical interface may be coupled to a microscopic description

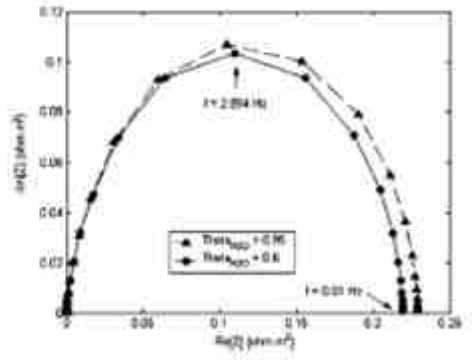

Figure 9. Sensitivity of the EIS spectra to the surface fraction of free water molecules. $\bar{I} = 30$ A, $T = 338$ K, $P_{H_2} = 1.5$ bar.

Note that the augmentation of water content also produces the electrolyte swelling in the Nafion case. This swelling produces a change in the C_{DL} value (supposed constant in this paper).

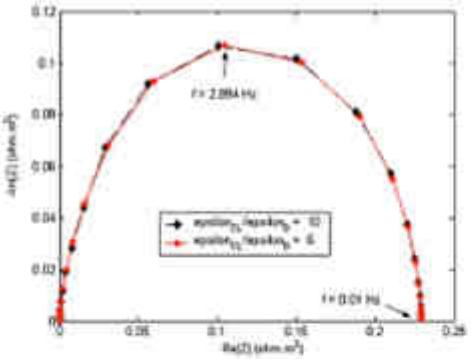

Figure 10. Sensitivity of the EIS spectra to e_{CL}. T = 30 Å, T = 338 K, P_{H_2} = 1.5 bar.

of transport phenomena in a whole membrane/electrode PEFC assembly, as presented elsewhere.[22,24,35-38] EIS on a PEFC has been performed in order to quantitatively validate the simulation results and to analyze their sensitivity to the working conditions.[24,38]

The model of electrochemical interface that we propose has been developed in the context of PEFCs, but it can be extended to other contexts (acid Pb batteries, Li-ion batteries, etc.).

Commissariat à l'energie Atomique assisted in meeting the publication costs of this article.

List of Symbols

- α $2\exp(-\Delta G_{ij}^{\ddagger}/RT)$
- C_{FCX} charged fixed sites concentration, (milliomes of Nafion), mol m^{-3}
- C_{H^+} proton concentration, mol m^{-3}
- C_{H_2} hydrogen or oxygen concentration, mol m^{-3}
- d thickness of a water molecule, 2×10^{-10} m
- D displacement vector, C m^{-2}
- D_{H^+} diffusion coefficient of protons in Nafion, m^2 s^{-1}
- D_{H_2} diffusion coefficient of hydrogen in Nafion, m^2 s^{-1}
- $\vec{E}$ electric field, N C^{-1}
- f F/RT
- F Faraday's constant, 96,485 C mol^{-1}
- $\Delta G_{ij}^{\ddagger}$ Gibbs' free energy for the dipolar adsorption, J mol^{-1}
- $\Delta G_{ij}^{\ddagger}$ dipolar chemical adsorption energy, J mol^{-1}
- $\Delta G_{ij}^{\ddagger}$ dipolar electrostatic adsorption energy, J mol^{-1}
- $\Delta G_{ij}^{\ddagger}$ dipolar interaction adsorption energy, J mol^{-1}
- I total current demanded to the fuel cell, A
- i local electronic current density at the surface of the Pt/C phase (nanoscopic model), A m^{-2}
- j_{Far} faradaic current, A m^{-2}
- j_{H^+} molar flux for the protons in Nafion, mol s^{-1} m^{-2}
- j_{H_2} molar flux of hydrogen in Nafion, mol s^{-1} m^{-2}
- k Boltzmann's constant, 1.38×10^{-23} J K^{-1}
- k_i elementary standard rate constant, m s^{-1}
- n^{ads} sum of free sites and sites covered by intermediate reaction species per unit of area of metallic phase, m^{-2}
- $\vec{n}$ number of dipoles directed toward the metallic phase per unit of area, m^{-2}
- $\overleftarrow{n}$ number of dipoles opposed to the metallic phase per unit of area, m^{-2}
- n_{Hi} number of sites covered by the intermediate reaction species Hi per unit of area of metallic phase, m^{-2}
- n_s number of free sites per unit of area of metallic phase, m^{-2}
- n^{max} maximal quantity of free sites per unit of area of metallic phase, m^{-2}
- N_A 6.02214×10^{23} Avogadro's number, mol^{-1}
- P_{H_2} hydrogen partial pressure in the pore phase, Pa
- R ideal gas constant, 8.3421 K^{-1} mol^{-1}
- $S_{electrode}$ geometric surface of the MEA
- T absolute temperature, K
- v_i electrochemical reaction rate, mol s^{-1} m^{-2}

Greek letters

- α elementary reaction step transfer coefficient
- γ specific active surface area, m^2/m^2
- Γ interfacial dipolar surface density, Debye m^{-2}
- ε_{CL} electric permittivity in the inner layer, C^2 J^{-1} m^{-1}
- ε_{DL} electric permittivity in the diffuse layer (electrolyte phase), C^2 J^{-1} m^{-1}
- ε_0 electric permittivity of vacuum, 8.85×10^{-12} C^2 N^{-1} m^{-2}
- η potential difference at the metal/electrolyte interface (through the inner layer), V
- $\vec{\theta}$ covering fraction of dipoles oriented toward the metallic phase
- $\overleftarrow{\theta}$ covering fraction of dipoles opposed to the metallic phase
- θ_{Hi} covering fraction of the intermediate reaction species Hi
- θ_s covering fraction of free sites
- θ_{H_2O} water surface fraction on the metal surface
- μ dipolar moment of a water molecule, 0.62×10^{-29} C m
- σ electronic surface density, C m^{-2}
- ϕ electric potential in the electrolyte phase, V
- ψ electric potential in the metallic phase (Pt/C), V

References

1. J. P. Dunsl, B. Le Gorrec, C. Montella, C. Poinignon, and G. Vitter, *J. Power Sources*, 74, 244 (1998).
2. E. Antolini, L. Giorgi, A. Pozio, and E. Passalacqua, *J. Power Sources*, 77, 136 (1999).
3. D. D. Macdonald, E. Sikora, and G. Engelhardt, *Electrochim. Acta*, 43, 87 (1998).
4. M. Bautista, Y. Bultel, J.-P. Diard, and S. Wallaszewicz, 144ème Forum sur les Impédances Electrochimiques, Paris, France, Jan 14, 2002, pp. 221-230 (2002).
5. V. A. Paganin, *Electrochim. Acta*, 43, 3761 (1998).
6. Y. Bultel, L. Ceraso, O. Antoine, P. Ozil, and R. Durand, *J. Electroanal. Chem.*, 527, 143 (2002).
7. O. Antoine, Y. Bultel, P. Ozil, and R. Durand, *Electrochim. Acta*, 45, 4493 (2000).
8. O. Antoine, Y. Bultel, and R. Durand, *J. Electroanal. Chem.*, 499, 85 (2001).
9. M. Eikerling and A. A. Kornyshev, *J. Electroanal. Chem.*, 475, 107 (1999).
10. W. Frands, Ph.D. Thesis INPG, no. 03INPL0044N, France (2003).
11. J. Ross Macdonald, in Impedance Spectroscopy, Emphasizing Solid Material and Systems, John Wiley & Sons, New York (1987).
12. J. S. Newman, in *Electrochemical Systems*, 2nd ed., Prentice Hall, Englewood Cliffs, NJ (1991).
13. S. P. Jiang, J. G. Love, and S. P. S. Badwal, *Key Eng. Mater.*, 125, 81 (1997).
14. F. Scholz, in *Electroanalytical Methods*, 1st ed., Springer, New York (2002).
15. S. S. Zhang, K. Xu, and T. R. Jow, *Electrochim. Acta*, 49, 1057 (2004).
16. S. R. Narayan and P. Singh, *J. Power Sources*, 112, 621 (2002).
17. J. P. Diard, B. Le Gorrec, and C. Montella, *J. Power Sources*, 70, 78 (1998).
18. J. P. Diard, N. Glandut, P. Landaud, B. Le Gorrec, and C. Montella, *Electrochim. Acta*, 48, 555 (2003).
19. D. B. Pathapati, X. Xue, and J. Tang, *Renewable Energy*, 30, 1 (2005).
20. H. Eisler, D. Andreaus, A. Wokaun, and G. G. Scherer, *Electrochim. Acta*, 49, 1622 (2004).
21. H. Eisler, B. Andreaus, A. Wokaun, and G. G. Scherer, in *Proceedings of the 1st European PEFC Forum*, Paper no. B078 (in conference CD), Lucern, Switzerland (2003).
22. P. Costamagna and S. Srinivasan, *J. Power Sources*, 102, 242 (2001).
23. A. A. Franco, P. Schott, C. Jallut, and B. Maschke, in *Proceedings of the 1st European PEFC Forum*, Paper no. B063 (in CD Conference, and in press), Lucerne, Switzerland (2003).
24. A. A. Franco, Ph.D. Thesis, UCB Lyon-1, 2005LYO10239, Lyon, France (2005).
25. J. S. Chen, J.-P. Diard, R. Durand, and C. Montella, *J. Electroanal. Chem.*, 486, 1 (2000).
26. Y. Wang and C.-Y. Wang, *Electrochim. Acta*, 50, 1307 (2005).
27. S. Ansukumar, *Electrochim. Acta*, 41, 2057 (1996).
28. R. D. Armstrong and B. R. Horrocks, *Solid State Ionics*, 94, 181 (1997).
29. N. F. Mott and R. J. Watts-Tobin, *Electrochim. Acta*, 4, 79 (1961).
30. R. Guidelli, in *Trends in Interfacial Electrochemistry*, A. F. Silva, Editor, Reidel, Dordrecht (1986).
31. W. Schmickler, *J. Electroanal. Chem. Interfacial Electrochem.*, 157, 1 (1983).
32. R. Guidelli and W. Schmickler, *Electrochim. Acta*, 45, 2317 (2000).
33. X. Cao and R. S. White, *J. Electroanal. Chem.*, 389, 13 (1995).
34. T. Jacob, W. Goddard, and M. Schuffler, *Computational Electrochemistry Workshop*, Santorini, Greece, Sept 26–29, 2004.
35. V. Rai, M. Aryanpour, A. Dhanda, S. Welch, and H. Pitsch, Presented at *The 207th Joint International Meeting of The Electrochemical Society*, Quebec City, Canada, May 15–20, 2005 (http://www.stanford.edu/group/pitschPublications.htm).
36. A. A. Franco, P. Schott, C. Jallut, and B. Maschke, in *Proceedings of the JOMICS Conference*, Lyon, France, Sept 5–9, 2005 (in conference CD).
37. A. A. Franco, P. Schott, C. Jallut, and B. Maschke, e-STA (e-revue, http://www.see.asso.fr/) 2, no. 3 (2003).
38. A. A. Franco, P. Schott, C. Jallut, and B. Maschke, in *Proceedings of the 5th MATHMOD Conference* (ISBN 3-901608-25-7) (in Conference CD), Vienna, Austria, Feb 8–10, 2005.
39. N. P. Siegel, M. W. Ellis, D. J. Nelson, and M. R. von Spakovsky, *J. Power Sources*, 115, 81 (2003).
40. S. Escribano, Ph.D. Thesis INPG, no. 1995INPG0140, Grenoble, France (1995).
41. L. Gerbaux, Ph.D. Thesis INPG, no. 1996INPG0163, Grenoble, France (1996).

42. V. P. Zhdanov and B. Kasemo, *Appl. Surf. Sci.*, 219, 276 (2003).
43. J. O'M. Bockris and K. T. Jeng, *Adv. Colloid Interface Sci.*, 33, 1 (1990).
44. J. O'M. Bockris and M. A. Habib, *Electrochim. Acta*, 22, 41 (1977).
45. S. L. Marshall and B. E. Conway, *J. Electroanal. Chem.*, 337, 1 (1992).
46. S. L. Marshall and B. E. Conway, *J. Electroanal. Chem.*, 337, 19 (1992).
47. S. L. Marshall and B. E. Conway, *J. Electroanal. Chem.*, 337, 45 (1992).
48. J. D. Jackson, in *Classical Electrodynamics*, John Wiley & Sons, Inc., New York (1962).
49. W. Pauli(ky and M. Phillips, in *Classical Electricity and Magnetism*, 2nd ed., Addison-Wesley Publishing Company, Inc., Reading, MA, 1962.
50. J. O'M. Bockris and S. U. M. Khan, in *Surface Electrochemistry: A Molecular Level Approach*, Plenum Press, New York (1993).
51. D. A. Harrington and B. E. Conway, *Electrochim. Acta*, 32, 1703 (1987).
52. L. Bai, D. A. Harrington, and B. E. Conway, *Electrochim. Acta*, 32, 1713 (1987).
53. D. A. Harrington and B. E. Conway, *J. Electroanal. Chem. Interfacial Electrochem.*, 221, 1 (1987).
54. J. P. Diard, B. Le Gorrec, and C. Montella, in *Cinétique Électrochimique*, Hermann, Editeurs Hermann, Courtille, France (1998).
55. H. Gerischer, in *Electrochimie: Physique et Analytique*, Presses Polytechniques et Universitaires Romandes, Lausanne (2001).
56. N. P. Siegel, M. W. Ellis, D. J. Nelson, and M. R. von Spakovsky, *J. Power Sources*, 128, 173 (2004).
57. M. Inaba, M. Uno, J. Maruyama, A. Tasaka, K. Kinukawa, and Z. Ogumi, *J. Electroanal. Chem.*, 417, 105 (1996).
58. T. Bastug, D. M. Le, and N. Djilali, *J. Power Sources*, 106, 264 (2002).
59. W. G. Bessler, *Solid State Ionics*, 176, 997 (2005).
60. D. G. Goodwin, in Solid Oxide Fuel Cells (SOFC-IX), S. C. Singhal and J. Mizusaki, Editors, p. 690–707, The Electrochemical Society Proceedings Series, Pennington, NJ (2005).
61. R. M. Darling and J. P. Meyers, *J. Electrochem. Soc.*, 150, A1523 (2003).
62. S. Jaouen, J. Sidot, R. X. Valenzuela, and L. Dura, *J. Power Sources*, 151, 60 (2005).
63. S. Hamilton, P. Aldebert, and M. Pineri, *Electrochim. Acta*, 43, 2105 (1998).
64. G. Maggio, V. Recupero, and L. Pino, *J. Power Sources*, 101, 275 (2001).
65. V. Climent, R. A. Coles, and R. G. Compton, *J. Phys. Chem. B*, 106, 5258 (2002).
66. S. Levine, G. M. Bell, and A. L. Smith, *J. Phys. Chem.*, 73, 3534 (1969).
67. T. Thampa, S. Malhotra, J. Zhang, and R. Datta, *Catal. Today*, 67, 15 (2001).
68. F. Meier and G. Eigenberger, *Electrochim. Acta*, 49, 1731 (2004).

BIBLIOGRAPHY

([1]) http://www.uns.edu.ar

([2]) http://www.ib.edu.ar

([3]) http://www.cnea.gov.ar

([4]) M. Kolar, G. Gumbs, *Physical Review A*, **45** (2) (1992) 626.

([5]) E. Lorenz. *Journal of the Atmospheric Sciences*, **20** (2) (1963) 130.

([6]) http://www.cea.fr

([7]) http://www.20sim.com/

([8]) A.A. Franco, *A multi-scale mechanistic model for transient analysis of a PEMFC – An infinite dimensional Bond Graph approach*, PhD Thesis Université Claude Bernard Lyon-1 (France) no. 2005LYO10239 (2005) http://tel.archives-ouvertes.fr/tel-00110968/en/ .

([9]) http://www.panstanford.com

([10]) W.R. Grove, *Philosophical Magazine and Journal of Science*, **13** (1838) 430.

([11]) W.R. Grove, *Proceedings of the Royal Society* (1843) (pages 268-278, 346-354, 422-432).

([12]) G.Pancaldi, "Electricity and Life: Volta's Path to the Battery", in: *Historical Studies in the Physical and Biological Sciences*, Vol. 21. Berkeley: University of California Press (1990).

([13]) C. J. Brockman , *J. Chem. Educ.*, **5** (5) (1928) 549.

([14]) published in 1896 Ostwald, Wilhelm, Electrochemistry: History and Theory, trans. N. P. Date, (New Delhi: Amerind for the Smithsonian Institution and the National Science Foundation, 1980), pp. 668-79, 1119

([15]) L. Mond, C. Langer, *Trans. American Electrochem. Soc.* (1889) 1905.

([16]) C. R. Alder Wright, C. Thompson, *Proc. of the Royal Soc. of London* **46** (1889).

([17]) D. Douglas, H. Liebhafsky. *Physics Today* (June 1960) 26.

([18]) E. Baur, H. Preis, *Zeitschrift für Elektrochemie* **43** (1937) 727.

([19]) M. Bischoff, G. Huppmann, *J. Power Sources* **105** (2) (2002) 216.

([20]) J. Weissbart, R. Ruka, *J. Electrochem. Soc.* **109** (8) (1962) 723.

([21]) F.T. Bacon, T. M. Fry. *Proceedings of the Royal Society of London*, Series A, *Mathematical and Physical Sciences*, **334** (1973) 431.

([22]) W.T. Grubb, L.W. Niedrach, *J. Electrochem. Soc.* **107** (1960) 131.

([23]) http://www.nafion.mysite.com/, personal Website of Dr. Walther Grot (last consulted on July 7, 2010).

([24]) Raistrick, L. D. *Electrochem. Soc. Proc. Ser.* **PV 86-13** (1986) 172.

([25]) E. Ticianelli, C. Derouin, A. Redondo, S. Srinivasan, *J. Electrochem. Soc.* **135** (1988) 2209.

([26]) M.S. Wilson, S. Gottesfeld, *J. Electrochem. Soc.* **139** (1992) L28.

([27]) http://www.h2truncado.com.ar/

([28]) Courtesy of Dr. Thierry Priem, CEA-Grenoble (2009).

([29]) D. Jollie, *Fuel Cell Market Survey: Portable Applications*, www.fuelcelltoday.com, 6 September 2005.

([30]) M. Mathias, H.A. Gasteiger, Electrochemical Society Proceedings, vol. PV 2002-31, in: M. Murthy, T.F. Fuller, J.W. Van Zee, S. Gottesfeld (Eds.), Third International Symposium on PEM Fuel Cells, Salt Lake City, UT (2002).

([31]) http://www.hydrogen.energy.gov/., USA DOE Website

([32]) TIAX LLC: D0034, DOE: DE-FC04-01AL67601.

([33]) J. Sinha FY 2009 Annual Progress Report

([34]) M. Eikerling, A. Kornyshev, A. Kulikovsky, *The Fuel Cell Review* (January 2005) 15.

([35]) C.Y. Wang, *Chem. Rev.* **104** (2004) 4727.

([36]) A.Briyikoglu, *Int. J. of Hydrogen Energy* **30** (2005) 1181.

([37]) C.Y. Wang, *Chem. Rev.*, **104** (2004) 4727.

([38]) O. Antoine, Y. Bultel, R. Durand, *J. of Electroanalytical Chemistry* **499** (1) (2001) 85.

([39]) T.E. Springer, T.A. Zawodzinski, S. Gottesfeld, *J. Electrochem. Soc.* **138** (1991) 2334.

([40]) D.M. Bernardi, M.W. Verbrugge, *J. Electrochem. Soc.* **139** (1992) 2477.

([41]) D.M. Bernardi, M.W. Verbrugge, *AIChE J.* **37** (1991) 1151.

([42]) Y.W. Rho, S. Srinivasan, Y.T. Kho, *J. Electrochem. Soc.* **141** (1994) 2089.

([43]) K. Broka, P. Ekdunge, *J. Appl. Electrochem.* **27** (1997) 281.

([44]) F. Jaouen, G. Lindbergh, G. Sundholm, *J. Electrochem. Soc.* **149** (2002) A437.

([45]) N.P. Siegel, M.W. Ellis, D.J. Nelson, M.R. von Spakovsky, *J. Power Sources* **115** (2003) 81.

([46]) N.P. Siegel, M.W. Ellis, D.J. Nelson, M.R. von Spakovsky, *J. Power Sources* **128** (2004) 173.

([47]) W. Sun, B.A. Peppley, K. Karan, *J. Power Sources* **144** (2005) 42.

([48]) W. Sun, B.A. Peppley, K. Karan, *Electrochim. Acta* **50** (2005) 3359.

([49]) K.M. Yin, *J. Electrochem. Soc.* **152** (2005) A583.

([50]) G.Y. Lin, W.S. He, T. Van Nguyen, *J. Electrochem. Soc.* **151** (2004) A1999.

([51]) S.-M. Chang, H.-S. Chu, *J. Power Sources* **161** (2006) 1161.

([52]) G. Lin, T. Van Nguyen, *J. Electrochem. Soc.* **153** (2006) A372.

([53]) T. Navessin, S. Holdcroft, Q.P. Wang, D.T. Song, Z.S. Liu, M. Eikerling, J. Horsfall, K.V. Lovell, *J. Electroanal. Chem.* **567** (2004) 111.

([54]) D.T. Song, Q.P. Wang, Z.S. Liu, M. Eikerling, Z. Xie, T. Navessin, S. Holdcroft, *Electrochim. Acta* **50** (2005) 3347.

([55]) D.T. Song, Q.P. Wang, Z.S. Liu, T. Navessin, M. Eioerling, S. Holdcroft, *J. Power Sources* **126** (2004) 104.

([56]) D.T. Song, Q.P. Wang, Z.S. Liu, T. Navessin, S. Holdcroft, *Electrochim. Acta* **50** (2004) 731.

([57]) Q.P. Wang, M. Eikerling, D.T. Song, Z.S. Liu, *J. Electroanal. Chem.* **573** (2004) 61.

([58]) Q.P. Wang, M. Eikerling, D.T. Song, Z.S. Liu, T. Navessin, Z. Xie, S. Holdcroft, *J. Electrochem. Soc.* **151** (2004) A950.

([59]) Q.P. Wang, D.T. Song, T. Navessin, S. Holdcroft, Z.S. Liu, *Electrochim. Acta* **50** (2004) 725.

([60]) Y. Wang, C.Y. Wang, *Electrochim. Acta* **50** (2005) 1307.

([61]) Y. Wang, C.-Y. Wang, *Electrochim. Acta* **51** (2006) 3924.

([62]) Z.H. Wang, C.Y. Wang, K.S. Chen, *J. Power Sources* **94** (2001) 40.

([63]) U. Pasaogullari, C.Y. Wang, *Electrochim. Acta* **49** (2004) 4359.

([64]) U. Pasaogullari, C.Y.Wang, *J. Electrochem. Soc.* **152** (2005) A380.

([65]) H. Meng, C.-Y. Wang, *J. Electrochem. Soc.* **152** (2005) A1733.

([66]) Y. Wang, C.-Y. Wang, *J. Electrochem. Soc.* **153** (2006) A1193.

([67]) U. Pasaogullari, C.Y. Wang, K.S. Chen, *J. Electrochem. Soc.* **152** (2005) A1574.

([68]) D. Natarajan, T. Van Nguyen, *J. Electrochem. Soc.* **148** (2001) A1324.

([69]) D. Natarajan, T. Van Nguyen, *J. Power Sources* **115** (2003) 66.

([70]) R. A. van Santen, P. Sautet, *Computational Methods in Catalysis and Materials Sciences*, Wiley-VCH (2009).

([71]) K. Kalantar-zadeh, B. Fry, *Nanotechnology-enabled sensors*, Springer (2008).

([72]) B. Fang *et al.*, *Nano-engineered PtVFe catalysts in proton exchange membrane fuel cells: Electrocatalytic performance*, doi:10.1016/j.electacta.2010.02.048

([73]) J.K. Norskov, J. Rossmeisl, A. Logadottir, L. Lindqvist, J.R. Kitchin, T. Bligaard, H.J. Jonsson, *Phys. Chem. B* **108** (2004) 17886.

([74]) J. Greeley, J. Rossmeisl, A. Hellmann, J. K. Norskov, *Zeitschrift für Physikalische Chemie* **221** (9-10) (2007) 1209.

([75]) T. Jacob, W. A. Goddard, *Chem. Phys. Chem.* **7** (2006) 992.

([76]) T. Jacob, *Fuel Cells* **6** (2006) 159.

([77]) T. Jacob, W. A. Goddard III, *J. Am. Chem. Soc.* **126** (2004) 9360.

([78]) A. Eichler, F. Mittendorfer, J. Hafner, *Phys. Rev. B* **62**(7) (2000) 4744.

([79]) A. Eichler, J. Hafner, *Phys. Rev. Lett.* **79** (1997) 4481.

([80]) S. Kandoi, A.A. Gokhale, L.C. Grabow, J.A. Dumesic, M. Mavrikakis, *Catal. Lett.* **93** (2004) 93.

([81]) T. Jacob, W. A. Goddard III, *J. Phys. Chem. B* **108** (2004) 8311.

([82]) Y. Xu, A.V. Ruban, M. Mavrikakis, *J. Am. Chem. Soc.* **126** (2004) 4717.

([83]) R. Carr, M. Parrinello, *Phys. Rev. Lett.*, **55** (1985) 2471.

([84]) A. Grob, *Theoretical Surface Science: A Microscopic Perspective*, Springer, New York, 2003 (Chapter 3).

([85]) W. Goddard III, B. Merinov, A. Van Duin, T. Jacob, M. Blanco, V. Molinero, S.S. Jang, Y.H. Jang, *Molecular Simulation* **32** (3–4) (2006) 251.

([86]) J.S. Filhol, M. Neurock, *Angew. Chem. Int. Ed.*, **45** (2006) 402.

([87]) M. J. Janik, M. Neurock, *Electrochim. Acta* **52** (2007) 5517.

([88]) M.J. Janik, C.D. Taylor, M. Neurock, *J. Electrochem. Soc.* **156** (1) (2009) B126.

([89]) M. Eikerling, K. Malek, Q. Wang, *Catalyst Layer Modeling: Structure, Properties, and Performance*, book chapter in: *PEM Fuel Cells Catalysts and Catalyst Layers - Fundamentals and Applications*, Ed. J.J. Zhang, Springer, London (2008).

([90]) N. Fouquet, C. Doulet, C. Nouillant, G. Dauphin-Tanguy, B. Ould-Bouamama, *J. Power Sources*, **159** (2) (2006) 905.

([91]) Y. Song, H. Xu, Y. Wei, H. R. Kunz, L. J. Bonville, J. A. Fenton, *J. Power Sources*, **154** (1) (2006) 138.

([92]) A. Panchenko, “Polymer Electrolyte Membrane Degradation and Oxygen Reduction in Fuel Cells: an EPR and DFT investigation”, Fakultät Chemie der Universität Stuttgart (2004).

([93]) M. Schulze, N. Wagner, T. Kaz, K.A. Friedrich, *Electrochim. Acta*, **52** (2007) 2328.

([94]) R. Hiesgen, D. Eberhardt, E. Alexandrova, K.A. Friedrich, *Fuel Cells*, **6** (6) (2006) 425.

([95]) E. Aleksandrova, R. Hiesgen, D. Eberhard, K.A. Friedrich, T. Kaz, E. Roduner, *Chem. Phys. Chem.*, **8** (2007) 519.

([96]) M. Loster, D. Balzar, K.A. Friedrich, Jürgen Garche, *J. Phys. Chem. C*, **111** (2007) 9583.

([97]) R. L. Borup, J. R. Davey, F. H. Garzon, D. L. Wood, M. A. Inbody, *J. Power Sources*, **163**, (2006) 76.

([98]) P. J. Ferreira, G.J. la O', Y. Shao-Horn, D. Morgan, R. Makharia, S. Kocha, H. A. Gasteiger, *J. Electrochem. Soc.* **152** (2005) A2256.

([99]) K. L. More, R. Borup, K. S. Reeves, *ECS Transactions* **3** (1) (2006) 717.

([100]) S. Escribano et al, Project "DVD-AME", Program ANR "PAN-H", France (2008).

([101]) A.A. Franco, R. Coulon, R.Ferreira de Morais, S.-K. Cheah, A. Kachmar, M.A. Gabriel, *ECS Trans.* **25** (1) (2009) 65.

([102]) X. Wang, R. Kumar, D. J. Myers, *Electrochemical and Solid-State Letters,* **9** (5) (2006) A225.

([103]) P.J. Ferreira, G.J. la O', Y. Shao-Horn, D. Morgan, R. Makharia, S. Kocha, and H.A. Gasteiger; *J. Electrochem. Soc.* **152** (2005) A2256.

([104]) R. L. Borup, J. R. Davey, F. H. Garzon, D. L Wood, M. A. Inbody; *J. Power Sources* **163** (1) (2006) 76.

([105]) K. Yazuda, A. Taniguchi, T. Akita, T. Ioroi, Z. Siroma; *Phys. Chem. Chem. Phys.*, **8** (6), (2006) 746.

([106]) P. J. Ferreira, Y. Shao-Horn**,** *Electrochemical and Solid-State Letters,* **10** (3) (2007) B60.

([107]) L. Kim, C. G. Chung, Y. W. Sung, J. S. Chung, *J. Power Sources* **183** (2008) 524.

([108]) A. Taniguchi, T. Akita, K. Yasuda, Y. Miyazaki, *Int. J. of Hydrogen Energy*, **33** (2008) 2323.

([109]) S.C. Ball, S. Hudson, B. Theobald, D. Thompsett, 210th ECS Meeting, abstract # 0552.

([110]) S.C. Ball, S. L. Hudson, B. R. Theobald, D. Thompsett, *ECS Trans*. **11**, (1) (2007) 1267.

([111]) S.C. Ball, S. L. Hudson, J. Hei Leung, A. E. Russell, D. Thompsett, B. R. Theobald, *ECS Trans*. **11**, (1) (2007) 1247.

([112]) V. R. Stamenkovic, B. S. Mun, M. Arenz, K. J. J. Mayrhofer, C. A. Lucas, G. Wang, P. N. Ross, N. M. Markovic, *Nat. Mater.* **6** (2007) 241.

(113) M. Watanabe K. Tsurumi, K. Mizukami, T. Nakamura, P. Stoneharf, *J. Electrochem. Soc.* **141** (1994) 2659.

([114]) E. Antolini, J. R.C. Salgado, E.R. Gonzalez, *J. Power Sources* **160** (2006) 957.

([115]) H. R. Colon-Mercado, B. N. Popov, *J. Power Sources* **155** (2) (2006) 253.

([116]) S.C.Ball, S.L.Hudson, D.Thompsett, B. Theobald, *J. Power Sources* **171**, (1) (2007) 18.

([117]) K. Teranishi, K. Kawata, S. Tsushima, S. Hirai; *Electrochemical and Solid-State Letters*, **9** (10) (2006) A475.
([118]) H. Tang, Z. Qi, M. Ramani, J. F. Elter, *J. Power Sources* **158** (2006) 1306.

([119]) M. L. Perry, T. W. Patterson, C. Reiser; *ECS Trans.* **3** (1) (2006) 783.
([120]) J. Li, P. He, K. Wang, M. Davis, S. Ye; *ECS Trans.* **3** (1) (2006) 743.

([121]) Y. Fujii, S. Tsushima, K. Teranishi, K. Kawata, T. Nanjo, S. Hirai, *ECS Trans.* **3** (1) (2006) 735.
([122]) W. R. Baumgartner, E. Wallnöfer, T. Schaffer, J. O. Besenhard, V. Hacker, V. Peinecke, P. Prenninger; *ECS Trans.* **3** (1) (2006) 811.
([123]) C. A. Reiser, L. Bregoli, T. W. Patterson, J. S. Yi, D. Yang, M.L. Perry, T.D. Jarvi, *Electrochemical and Solid-State Letters,* **8** (6) (2005) A273.
([124]) T. F. Fuller, G. Gray; *ECS Trans.* **1** (8) (2006) 345.
([125]) R. M. Darling, D. Jayne; *ECS Trans.* **11** (1) (2007) 975.

([126]) A.A. Franco, M. Gerard, *J. Electrochem. Soc.* **155** (4) (2008) B367.
([127]) Y.Y. Shao, G.P. Yin, Y.Z. Gao, P.F. Shi, *J. Electrochem. Soc.* **153** (2006) A1093.
([128]) F. Coloma, A. Sepulveda Escribano, F. Rodriguez Reinoso, *J. Catal.* **154** (1995) 299.
([129]) L. Merlo, A. Ghielmi, L. Cirillo, M. Gebert, V. Arcella, *J. Power Sources* **171** (2007) 140.
([130]) A. Pozio, R. F. Silva, M. De Francesco, L. Giorgi, *Electrochim. Acta* **48** (2003) 1543.
([131]) M. Inaba *et al.*, *Electrochim. Acta* **51** (2006) 5746.
([132]) M. K. Kadirov, A. Bosnjakovic, S. Schlick, *J. Phys. Chem. B* **109** (16) (2005) 7664.
([133]) A. Bosnjakovic, S. Schlick, *J. Phys. Chem. B* **108** (2004) 4332.
([134]) M. Aoki, H. Uchida, M. Watanabe, *Electrochem. Comm.* **7** (2005) 1434.
([135]) W. Liu and D. Zuckerbrod, *J. Electrochem. Soc.* **152** (2005) A1165.
([136]) V. O. Mittal, H. R. Kunz, and J. M. Fenton, *J. Electrochem. Soc.* **154** (2007) B652.
([137]) V. V. Atrazhev, E. N. Timokhina, S. F. Burlatsky, V. I. Sultanov, T. H. Madden, M. Gummalla, 211th Meeting of the Electrochemical Society – Meeting Abstracts, **701** (2007) 107.
([138]) V. O. Mittal, H. R. Kunz, J. M. Fenton, *Electrochemical and Solid-State Letters,* **9** (6) (2006) A299.

([139]) C. Chen, T.F. Fuller, *ECS Trans.* **11** (1) (2007) 1127.
([140]) J.Y. Shim, S. Tsushima, S. Hirai, *ECS Trans.* **16** (2) (2008) 1705.
([141]) T. Hatanaka, T. Takeshita, H. Murata, N. Hasegawa, T. Asano, M. Kawasumi, Y. Morimoto, *ECS Trans.* **16** (2) (2008) 1961.
([142]) F. Collette, *J. Membr. Sc.*, **330** (2009) 21.

([143]) L. Ghassemzadeh *et al.*, *J. Power Sources* **186** (2009) 334.

([144]) H. Tang *et al.*, *J.Power Sources* **170** (2007) 85.

([145]) I. Tkach, A. Panchenko, T. Kaz, V. Gogel, K.A. Friedrich, E. Roduner, *Chem. Phys. Phys. Chem.*, **6** (23) (2004) 5419.

([146]) G. Gébel, O. Diat, *Fuel Cells* **5** (2) (2005) 261.

([147]) M. Kim *et al.*, *Macromolecules* **39** (2006) 4775.

([148]) G. Lin, W. He, T.V. Nguyen, *J. Electrochem. Soc.* **151** (2004) A1999.

([149]) T.V. Nguyen, *J. Electrochem. Soc.* **143** (1996) L103.

([150]) A.Z. Weber, R. M. Darling, J. Newman, *J. Electrochem. Soc.* **151** (2004) A1715.

([151]) M.V. Williams, H.R. Kunz, J.M. Fenton, *J. Electrochem. Soc.* **151** (2004) A1617.

([152]) U. Pasaogullari, C.-Y. Wang, *J. Electrochem. Soc.* **152** (2005) A380.

([153]) A.Z. Weber, J. Newman, *J. Electrochem. Soc.* **152** (2005) A677.

([154]) Wood, D.; Davey, J.; Garzon, F.; Atanassov, P.; Borup, R. *Proc. Fuel Cell Seminar* (2005).

([155]) W. K. Lee, C. H. Ho, J. W. Van, Zee, M. Murthy, *J. Power Sources* **84** (1999) 45.

([156]) T. Kitahara, T. Konomi, Y. Sasaki, *Jpn. Soc. Mech. Eng.* **72** (2006) 192.

([157]) S. Zhang *et al.*, *Int. J. Hydr. Energy*, **34** (1) (2009) 388.

([158]) Y. Gua, J. St-Pierre, R. Goeke, A. Datye, P. Atanassov, *ECS Trans.*, **16** (2) (2008) 355.

([159]) K.J.J. Mayrhofer *et al.*, *Electrochem. Comm.*, **10** (8) (2008) 1144.

([160]) H-S. Oh, J-G. Oh, B. Roh, I. Hwang, H. Kim, On-Line Mass Spectrometry Study of Carbon Corrosion in Polymer Electrolyte Membrane Fuel Cells, *Electrochemistry Communications* (2008), doi: 10.1016/ j.elecom.2008.05.006

([161]) R. Makharia, S. S. Kocha, P. T. Yu, M. A. Sweikart, W. Gu, F. T. Wagner, H. A. Gasteiger, *ECS Trans.*, **1** (8) (2006) 3.

([162]) F. A. de Bruijn, V. A. T. Dam, G. J. M. Janssen, *Fuel Cells*, **1** (2008) 3.

([163]) F. T. Wagner, H. A. Gasteiger, R. Makharia, K.C. Neyerlin, E. L. Thompson, S. G. Yan, *ECS Trans.* **3** (1) (2006) 19.

([164]) P. T. Yu, W. Gu, R. Makharia, F. T. Wagner, H. A. Gasteiger, *ECS Trans.* **3** (1) (2006) 797.

([165]) M. Schulze, N. Wagner, T. Kaz, K.A. Friedrich, *Electrochim. Acta*, **52** (2007) 2328.

([166]) H. Kuhn, B. Andreaus, A. Wokaun, G. G. Scherer, *Electrochim. Acta*, **51** (2006) 1622.

([167]) N. Yousfi-Steiner, Ph. Mocoteguy, D. Candusso, D.Hissel, A review on PEM Fuel Cell catalyst degradation and starvation issues: causes, consequences and diagnostic for mitigation, *J. Power Sources* (2008), doi:10.1016/j.jpowsour.2009.03.060

([168]) A.A. Franco, M. Guinard, B. Barthe, O. Lemaire, *Electrochim. Acta*, **54** (22) (2009) 5267.

([169]) R. N. Carter, B. K. Brady, K. Subramanian, T. Tighe, H. A. Gasteiger, *ECS Trans.* **11** (1) (2007) 423.

([170]) S. Sugawara, T. Maruyama, Y. Nagahara, S. S. Kocha, K. Shinohra, K. Tsujita, S. Mitsushima, K. Ota, *J.Power Sources* **187** (2009) 324.

([171]) S. Gottesfeld, J. Pafford, *J. Electrochem. Soc.* **135** (10) (1988) 2651.

([172]) W. Wang, W. Lee, J. W. Van Zee, *ECS Trans.* **1** (8) (2006) 131.

([173]) D. Dalle Nogare, P. Baggio, C. Tomasi, L. Mutri, P. Canu ; *Chem. Eng. Sc.* **62** (2007) 5418.

([174]) M. Carré, *International Workshop on the Effects of Fuel & Air Quality to the Performance of Fuel Cells, FCTEDI project*. Available from: http://www.fctedi.eu/symposia/fqaspects/organizercontact/090909_4_4_Carre_H2_quality_from_decarbonized_fuels.pdf, September 9-11, 2009.

([175]) B.M. Besancon, V. Hasanov, R. Imbault-Lastapis, R. Benesch, M. Barrio, M.J. Mølnvik, *Int. J. Hydrogen Energy*, **34** (2009) 2350.

([176]) J.J. Baschuk, X. Li, *Int. J. Energy Res.*, **25** (2001) 695.

([177]) G. A. Camara, E. A. Ticianelli, , S. Mukerjee, S. J. Lee, J. McBreen, *J. Electrochem. Soc.* **149** (6) A748 (2002) A748.

([178]) Z. Ji, J.-Q. Li; *Chemical Physics Letters*, **424** (2006) 111.

([179]) X. Cheng, Z. Shi, N. Glass, L. Zhang, J. Zhang, D. Song, Z. Liu, H. Wang, J. Shen; *J.Power Sources* **165** (2) (2007) 739.

([180]) X. Cheng, Z. Shi, N. Glass, L. Zhang, J. Zhang, D. Song, Z.-S. Liu, H. Wang, J. Shen, *J. Power Sources*, **165** (2007) 739.

([181]) A.A. Franco, M. Gerard, M. Guinard, B. Barthe, O. Lemaire, *ECS Trans.* **13** (15) (2008) 35.

([182]) F. H. Garzon, T. Lopes, T. Rockward, J.-M Sansinena, B. Kienitz, R. Mukundan, T. Springer, *ECS Trans.* **25** (1) (2009) 1575.

([183]) A.A. Franco, M. Gerard, M. Guinard, B. Barthe, O. Lemaire, *ECS Trans.* **13** (15) (2008) 35.

([184]) A.A. Franco, S. Passot, S.-K. Cheah, O. Lemaire, C. Faure, *Chem. Rev.*, submitted (2010).

([185]) Y. Shao, G. Yin, Y. Gao, *J.Power Sources* **171** (2007) 558.

([186]) R. Borup, J. Meyers, B. Pivovar,Y.S. Kim, R. Mukundan, N. Garland, D. Myers, M. Wilson, F. Garzon, D. Wood, P.Zelenay, K. More, K. Stroh, T.Zawodzinski, J.Boncella, J.E. McGrath, M. Inaba, K.Miyatake, M.Hori, K.Ota, Z.Ogumi, S.Miyata, A. Nishikata, Z.Siroma,Y.Uchimoto, K. Yasuda, K.Kimijima, N.Iwashita, *Chem. Rev.* **107** (2007) 3904.

([187]) Y. Morimoto, S. Yamakawa, *Int. Journal of Hydrogen Energy* (2009), doi:10.1016/j.ijhydene.2009.08.059

([188]) A.A. Franco, book chapter: *PEMFC degradation modeling and analysis*, in the book: *Polymer electrolyte membrane and direct methanol fuel cell technology (PEMFCs and DMFCs) - Volume 1: Fundamentals and performance*, edited by C. Hartnig and C. Roth, Woodhead (Cambridge, UK) *in preparation* (2010).

([189]) T.F.Fuller and Gary Gray, *ECS Trans.* **1** (8) (2006) 345.

([190]) R. M. Darling, J. P. Meyers, *J. Electrochem. Soc.* **150** (2003) A1523.

([191]) R. M. Darling and J. P. Meyers, *J. Electrochem. Soc.* **152** (2005) A242.

([192]) W. Bi, T. Fuller, *J. Power Sources* 178 (2008) 188.

([193]) E. Holby, Y. Shao-Horn, D. Morgan, 211th ECS meeting abstract #907. Pennington, NJ: The Electrochemical Society; 2007.

([194]) E. Holby, Y. Shao-Horn, A. Sheng, D. Morgan, 212th ECS meeting abstract #391. Pennington, NJ: The Electrochemical Society; 2007.

([195]) E. Holby, Y. Shao-Horn, A. Sheng, D. Morgan, 214th ECS meeting abstract #798. Pennington, NJ: The Electrochemical Society; 2008.

([196]) T. Takeshita, H. Murata, T. Hatanaka, Y. Morimoto, *ECS Trans.*, **16** (2) (2008) 367.

([197]) S.G. Rinaldo, J. Stumper, M. Eikerling, *J. Phys. Chem. C* **114** (2010) 5773.

([198]) E. F. Holby, W. Sheng, Y. Shao-Horn, D. Morgan, *Energy Environ. Sci.* **2** (2009) 865.

([199]) W. Ostwald, *Z. Phys. Chem*. **37** (1901) 385.

([200]) I.M. Lifshitz, V.V. Slyozov, *J. Phys. Chem. Solids* **19** (1961) 35.

([201]) Wagner, C. *Z. Elektrochem*. **65** (1961) 581.

([202]) W. Bi, G. E. Gray, T. F. Fuller *Electrochemical and Solid-State Letters,* **10** (5) (2007) B101.

([203]) A. Ohma, S. Suga, S. Yamamoto, and K. Shinohara, *ECS Trans.* **3** (1) (2006) 519.

([204]) V.V. Atrazhev, N.S. Erikhman, S.F. Burlatsky, *J. Electroanal. Chem.* **601** (2007) 251.

([205]) W. Liu, D. Zuckerbrod, *J. Electrochem. Soc.* **152** (6) (2005) A1165.

([206]) J. P. Meyers, R. M. Darling, *J. Electrochem. Soc.*, **153** (8) (2006) A1432.

([207]) N. Takeuchi, T. F. Fuller, *ECS Trans.*, **16** (2) (2008) 1563.

([208]) S. Kumar, 210th ECS Meeting, Abstract #**599**, Cancun, October 29 – November 3 (2006).

([209]) J. Hua, P.C. Sui, N. Djilali, S. Kumar, *ECS Trans.*, **16** (2) (2008) 1313.

([210]) A. Gidwania, K. Jainb, S. Kumarc, J. V. Cole, *ECS Trans.*, **16** (2) (2008) 1323.

([211]) N. Takeuchia, T. F. Fuller, *J. Electrochem. Soc.* **157** (1) B135 (2010).

([212]) S. Kundu, M. Fowler, L.C. Simon, R. Abouatallah, N. Beydokhti, *J. Power Sources* **183** (2008) 619.

([213]) A.A. Shah, T.R. Ralph, F.C. Walsh, *J. Electrochem. Soc.*, **156** (2009) B465.

([214]) C. Chen, T. Fuller, *Electrochim. Acta* **54** (16) (2009) 3984.

([215]) S. Kima, M. Khandelwala, C. Chacko, M. M. Mench, *ECS Trans.*, **16** (2) (2008) 1977.

([216]) F. Rong, C. Huang, Z-S. Liu, D. Song, Q. Wang, *J. Power Sources* **175** (2008) 699.

([217]) F. Rong, C. Huang, Z-S. Liu, D. Song, Q. Wang, *J. Power Sources* **175** (2008) 712.

([218]) S. He, M.M. Mench, *J. Electrochem Soc.* **153** (2006) A1724.

([219]) S. He, S.H. Kim, M.M. Mench, *J. Electrochem. Soc.* **154** (2007) B1024.

([220]) S. He, S.H. Kim, M.M. Mench, *J. Electrochem. Soc.* **154** (2007) B1227.

([221]) T. Jacob, *J. Electroanal. Chem.* **607** (2007) 158.

([222]) V. Atrazhev, E. Timokhina, S.F. Burlatsky, V. Sultanov, T. Madden, M. Gummalla, *ECS Trans.* **6**(25) (2008) 69.

([223]) N. Miyake, M. Wakizoe, E. Honda, T. Ohta, *ECS Trans.* **1**(8) (2006) 249.

([224]) N. Hasegawa, T. Asano, T. Hatanaka, M. Kawasumi, Y. Morimoto, *ECS Trans.* **16** (2) (2008) 1713.

([225]) V.O. Mittal, H.R. Kunz, J.M. Fenton. *J. Electrochem. Soc.* **154** (2007) B652.

([226]) A. Panchenko, *J. Membr. Sci.* **278** (2006) 269.

([227]) F.D. Coms, *ECS Trans.* **16**(2) (2008) 235.

([228]) D.E. Curtin, R.D. Losenberg, T.J. Henry, P.C. Tangeman, M.E. Tisack, *J. Power Sources* **131** (2004) 41.

([229]) F. Tian, A. B. Anderson, *J. Phys. Chem. C* **112** (2008) 18566.

([230]) D. V. Talapin, A. L. Rogach, M. Haase, H. Weller. *J. Phys. Chem. B*, **105** (2001) 12278.

([231]) J.Chen, K.-Y. Chan, *Molecular Simulation* **31** (6–7) (2005) 527.

([232]) X.Y. Zhou, *Electrochem. Solid-State Lett.* **11** (2006) B59.

([233]) K. Malek, A.A. Franco, *J. Phys.Chem.C*, *in preparation* (2010).

([234]) Zhu *et al.*, *Journal of Catalysis*, **167** (1997) 408.

([235]) P. Mocoteguy, F. Druart, Y. Bultel, S. Besse, A. Rakotondrainibe, *J. Power Sources* **167** (2007) 349.

([236]) S. S. Jang, B. V. Merinov, T. Jacob, W. A. Goddard III, in *International Conference on Solid State Ionics-15*, Abstract P498, International Solid State Ionics (2005).

([237]) J. X. Wang, T. E. Springer, R. R. Adzic, *J. Electrochem. Soc.* **153** (9) (2006) A1732.

([238]) D. Krapf, B. M. Quinn, M.-Y. Wu, H. W. Zandbergen, C. Dekker, S. G. Lemay, *Nanoletters* **6** (11) (2006) 2531.

([239]) J. Greeley, J. K. Norskov, *Electrochim. Acta* **52** (2007) 5829.

([240]) R. Choukroun, D. de Caro, B. Chaudret, P. Lecante, E. Snoeck, *New J. Chem.,* **25** (2001) 525.

([241]) L. Zhu, R. Wang, T. S. King, A. E. DePristo, *J. Cat?* **167** (1997) 408.

([242]) A. A. Franco, S. Passot, P. Fugier, C. Anglade, E. Billy, L. Guetaz, N. Guillet, S. Mailley, *ECS Trans.*, **13** (17) (2008) 29.

([243]) A. A. Franco, S. Passot, P. Fugier, C. Anglade, E. Billy, L. Guetaz, N. Guillet, E. De Vito, S. Mailley, *J. Electrochem.Soc.*, **156** (3) (2009) B410.

([244]) C.A. Menning, H.H. Hwu, J.G.G. Chen, *J. Phys. Chem. B* **110** (2006) 15471.

([245]) Z.H. Gu, P.B. Balbuena, *J. Phys. Chem. A* **110** (2006) 9783.

([246]) E. Christoffersen, P. Liu, A. Ruban, H. L. Skriver, J. K. Nørskov, *J. Cat.* **199** (2001) 123.

([247]) "The self-operating Napkin", picture from Rube Goldberg, American cartoonist, sculptor and author, 1883-1970 (http://www.rubegoldberg.com/)

([248]) A.A. Franco, P. Schott, C. Jallut, B. Maschke, *Fuel Cells*, **7** (2) (2007) 99.

([249]) A.A. Franco, M. Tembely, *J. Electrochem. Soc.*, **154** (7) B712 (2007).

([250]) A.A. Franco, P. Schott, C. Jallut, B. Maschke, *J. Electrochem. Soc.* **153** (6) A1053 (2006).

([251]) A.A. Franco, P. Schott, C. Jallut, B.M. Maschke, 207th Meeting of the Electrochemical Society (Québec, May 15-20, 2005), abstract #**1296** (2005).

([252]) A.A. Franco, P. Schott, C. Jallut, B. M. Maschke, in *Proceedings of the 3rd European PEMFC Forum*, Luzern, July 4–8, 2005, Paper B063 (in conference CD) (2005).

([253]) A.A. Franco, *ECS Trans.* **6** (10) (2007) 1.

([254]) A.A. Franco, Abstract 954, The Electrochemical Society Meeting Abstracts, Vol. **2007-1**, Chicago, IL, May 6–11, 2007.

([255]) A.A. Franco, M. Gerard, M. Guinard, B. Barthe, O. Lemaire, *ECS Trans.*, **13** (15) (2008) 35.

([256]) S.K. Cheah, O. Lemaire, P. Gelin, A.A. Franco, *ECS Trans.*, **25** (35), (2010) 275.

([257]) H.M. Paynter, *Analysis and design of engineering systems*. Cambridge, Mass.: M.I.T. Press (1961).

([258]) D. Karnopp, D. Margolis, R. Rosenberg, *Systems dynamics: A unified approach*, New York: John Wiley and Sons (2000).

([259]) P. Breedveld, *Physical systems theory in terms of bond graphs*. Ph.D. thesis, Technische Hogeschool Twente: Enschede, The Netherlands. ISBN 90-90005999-4 (1984).

([260]) P. Breedveld, *Journal of the Franklin Institute*, **319** (1985) 136.

([261]) B. Maschke, A.J. van der Schaft, In *Proceedings of the international mechanical engineering congress and exposition*. New-York, USA: ASME (2001).

([262]) F. Couenne, C. Jallut, B. Maschke, P. Breedveld, M. Tayakout, *Mathematical and Computer Modelling of Dynamical Systems* (2006) **12** (2–3) (2006) 159–174.

([263]) A. A. Franco, C. Jallut, B. Maschke, in *Proc. 5th MATHMOD Conference*, (Eds. I. Troch and F. Breitenecker), Vienna, Austria (2006) P103.

([264]) L. Wang, A. Roudgar, M. Eikerling, *J. Phys. Chem. C,* **113** (2009) 17989.

([265]) M. Neurock, *J. Cat.* **216** (1-2) (2003) 73.

([266]) R. Ferreira de Morais, D. Loffreda, P. Sautet, A.A. Franco, *ECS Trans.* **25** (23) (2010) 167.

([267]) R. Ferreira de Morais, D. Loffreda, P. Sautet, A.A. Franco, *in preparation* (2010).

([268]) M. A. Gabriel, T. Deustch, L. Genovese, G. Krosnicki, O. Lemaire, A. A. Franco, *Phys. Chem. Chem. Phys.* (2010), doi: 10.1039/b927111b

([269]) G. Kresse, J. Hafner, *Phys. Rev. B* **47** (1993) RC558.

([270]) G. Kresse, J. Furthmüller, *Phys. Rev. B* **54** (1996) 11169.

([271]) http://www.scm.com/

([272]) http://inac.cea.fr/L_Sim/BigDFT/

([273]) G. Henkelman, B.P. Uberauaga, H. Jonsson, *J. Chem. Phys.*, **113** (2000) 9901.

([274]) Y. Xu, A.V. Ruban, M. Mavrikakis, *J. Am. Chem. Soc.* **126** (2004) 4717.

([275]) T. Jacob, W. A. Goddard, *Chem. Phys. Chem.* **7** (2006) 992.

([276]) A. Kachmar, A.A. Franco, V. Vetere, P. Maldivi, *J. Phys. Chem. C, submitted* (2010).

([277]) Lialikov, Piscounova, Chipilov, Cerdycev, IX Congrès International de Photographie Scientifique et Appliquée, S.277 (Paris, 1935).

([278]) A.A. Franco, J. Letemplier, *paper in preparation* (2010).

([279]) S. Y. Liem, K.-Y. Chan, *Surf. Science* **328** (1-2) (1995) 119.

([280]) Y. Ma, P. B. Balbuena, *Surf. Science*, **602** (2008) 107.

([281]) S. Chen, P. J. Ferreira, W. Sheng, N. Yabuuchi, L. F. Allard, Y. Shao-Horn, *J. Am. Chem. Soc.*, **130** (2008) 13818.

([282]) A.A. Franco, S.-K. Cheah, O. Lemaire, *217th ECS Meeting* (2010) Abstract #257.

([283]) P. Choi, N.H. Jalani, R. Datta, *J. Electrochem. Soc.* **152** (3) (2005) 8.

([284]) R. Coulon, W. Bessler, A.A. Franco, *ECS Trans.* **25** (35) (2010) 259.

([285]) http://www.geodict.com/

([286]) K.Malek, M.Eikerling, Q.Wang, T.Navessin, and Z.Liu, *J. Phys. Chem. C,* **111** (2007) 13627.

([287]) H. Friedrich, P. E. de Jongh, A. J. Verkleij, K. P. de Jong, *Chemical Reviews* **109** (5) (2009) 1613.

([288]) K. Malek, M. Eikerling, Q. Wang, Z. Liu, S. Otsuka, K. Akizuki, M. Abe, *J. Chem. Phys.* **129** (2008) 204702.

([289]) O. Chapuis, M. Prat , M. Quintard, E. Chane-Kane, O. Guillot, N. Mayer, *J. Power Sources* **178** (2008) 258.

([290]) J. T. Gostick, M. A. Ioannidis, M. W. Fowler, M. D. Pritzker, *J. Power Sources* **173** (2007) 277.

([291]) *Courtesy of* M. El-Hannach, PhD student, CEA/LCPEM and *Institut de Mécanique de Fluides de Toulouse* (IMFT) (2009).

([292]) S. Shimpalee, U. Beuscher, J.W. Van Zee, *Electrochim. Acta* **52** (24) (2007) 6748.

([293]) P. K. Sinha, C.-Y. Wang, *J. Power Sources*, **183** (2008) 609.

([294]) K. Tajiri, C.-Y. Wang, Y. Tabushi, *Electrochim. Acta* **53** (2008) 6337.

([295]) S. Litster, N. Djilali, in *Transport Phenomena in Fuel Cells,* Eds. B. Sundén and M. Faghri, WIT Press, Southampton, (2005) 175-213.

([296]) A.C. Fowler, Mathematical Models in the Applied Sciences, Cambridge Texts in Applied Mathematics, Cambridge University Press (1997).

([297]) A. Costa, *Geophysical Research Letters*, **33** (2006) L02318.

([298]) N. Epstein, *Chem. Eng. Sci.*, **44** (3) (1989) 777.

([299]) R.R. Cunningham, R.J.J. Williams, *Diffusion in gases and porous media*, Pleum Press, New York (1980).

([300]) P.K. Das, X. Li, Z.-S. Liu, *Int. J. Hydrogen Energy* **35** (6) (2010) 2403.

([301]) K.S. Udell, *Int. J. Heat Mass Transfer* **28** (2) (1985) 485.

([302]) S. Kamarajugadda, Sandip Muzander, *J. Power Sources*, **183** (2008) 629.

([303]) D. L. Wood III, J. Chlistunoff, J. Majewski, R. L. Borup, *J. Am. Chem. Soc.*, **131** (2009) 18096.

([304]) A.Z. Weber, *J. Electrochem. Soc.*, 151 (2004).

([305]) F. Meier, G. Eigenberger, *Electrochim. Acta*, **49** (2004) 1731.

([306]) V.P. Zhdanov, B. Kasemo, *Surf. Sci.* **554** (2004) 103.

([307]) V.P. Zhdanov, B. Kasemo, *Electroch. Comm.* **8** (2006) 561.

([308]) *Extract from* D. Damasceno Borges, CEA internal report (2010).

([309]) G. Li, P.G. Pickup, *J. Electrochem. Soc.* **150** (11) (2003) C475.

([310]) A. A. Franco, P. Schott, C. Jallut, B. Maschke, in *Proceedings of the 16th World Hydrogen Energy Conference*, Paper 572 (2006) (in conference CD).

([311]) A. A. Franco, M. Tembely, C. Jallut, B. Maschke, in *Proceedings of the II Jornadas Iberoamericanas de Pilas de Combustible e Hidrogeno*, Buenos Aires, July 24–26, 2006, Red Iberoamericana de Pilas de Combustible e Hidrogeno (in conference CD).

([312]) S. Litster, G. McLean, *J. Power Sources* **130** (2004) 61.

([313]) P. Fugier, S. Passot, C. Anglade, L. Guétaz, N. Guillet, E. De Vito, S. Mailley, A. A. Franco, *J. Electrochem. Soc.* **157** (6) (2010) B943.

([314]) A. Le Goff, V. Artero, B. Jousselme, P. Dinh Tran, N. Guillet, R. Métayé, A. Fihri, S. Palacin, M. Fontecave, *Science* **326** (5968) (2009) 1384.

([315]) H. Nagashima, A. Nakoaka, Y. Saito, M. Kato, T. Kawanishi, K. Itoh, *J.Chem.Soc. Chem. Commun.* **4** (1992) 377.

([316]) H. Nagashima, Y. Kato, H. Yamaguchi, E. Kimura, T. Kawanishi, M. Kato, Y. Saito, M. Haga, K. Itoh, *Chem. Lett.* **7** (1994) 1207.

([317]) S. Escribano, R. Vincent, A.A. Franco, CEA report (2009).

(318) L.M. Roen, C.H. Paik, T.D. Jarvi, *Electrochem. Solid-State Lett.* **7** (2004) A19.

([319]) D. A. Stevens, M. T. Hicks, G. M. Haugen, J. R. Dahn, *J. Electrochem. Soc.* **152**, (2005) A2309.

([320]) K. Adjemian, oral comm., Workshop on degradation issues for MEAs, CARISMA Network, Grenoble 3-5 July 2007.

([321]) R. Subbaraman, D. Strmcnik, V. Stamenkovic' N. M. Markovic, *J. Phys. Chem. C* **114** (18) (2010) 8414.

([322]) *Extract from* S. Escribano, L. Guetaz, A.A. Franco, CEA internal report (2010).

([323]) D. Kondepudi, I. Prigogine, *Modern Thermodynamics*, John Wiley & Sons (1998).

([324]) M. Tabor, *Chaos and integrability in nonlinear dynamics*, John Wiley & Sons (1989).

([325]) B. E. Conway, D. M. Novak, *J. Phys. Chem.* **81**, (1977) 1459.

([326]) P. Russell, J. Newman, *J. Electrochem. Soc.* **133** (1986) 59.

([327]) H. Hunger, *J. Electrochem. Soc.* **115** (1968) 492.

([328]) G. Horanyi, C. Visy, *J. Electroanal. Chem.* **103** (1979) 353.

([329]) T. Yamazaki, T. Kodera, R. Ohnishi, M. Masuda, *Electrochim. Acta* **35**, (1990) 431.

([330]) H. Lu, L. Rihko-Struckmann, R. Hanke-Rauschenbach, K. Sundmacher, *Topics in Catalysis* **51** (2008) 89.

([331]) M. Murthy, M. Esayian, A. Hobson, S. MacKenzie, W.K. Lee, J.W. Van Zee, *J.Electrochem. Soc.* **148** (2001) A1141.

([332]) L.P.L. Carrette, K.A. Friedrich, M. Huber, U. Stimming, *Phys. Chem. Chem. Phys.* **3** (2001) 320.

([333]) J.X. Zhang, T. Thampan, R. Datta, *J. Electrochem. Soc.* **149** (2002) A765.

([334]) A.A. Franco, B. Barthe, L. Rouillon, O. Lemaire, *ECS Trans.* **25** (1) (2009) 1595.

([335]) A.A. Franco, O. Lemaire, S. Escribano, FR patent filled (2008).

([336]) V. Parry, J.C. Joud, B. Barthe, L. Guetaz, O. Lemaire, A.A. Franco, *J. Power Sources*, submitted (2010).

([337]) *Courtesy of* S.-K. Cheah, CEA PhD student (2010).

([338]) M. P. Eschenbach, R. Coulon, A. A. Franco, J. Kallo, W. G. Bessler, "Multi-scale simulation of fuel cells: from the cell to the system", *Solid State Ion.* (2010), doi:10.1016/j.ssi.2010.06.041

([339]) A.A. Franco, O. Lemaire, B. Barthe, in preparation (2010).

([340]) L.F. Oliveira Lopes, A.A. Franco and C. Jallut, in preparation (2010).